

Xueming Yang
Kopin Liu
Editors



MODERN TRENDS IN CHEMICAL REACTION DYNAMICS

Experiment and Theory (Part I)

Advanced Series in Physical Chemistry **Vol. 14**

Advanced Series in Physical Chemistry

14

MODERN TRENDS IN CHEMICAL REACTION DYNAMICS

Experiment and Theory (Part I)

Advanced Series in Physical Chemistry

Editor-in-Charge

Cheuk-Yiu Ng, *Department of Chemistry, University of California at Davis, USA*

Associate Editors

Hai-Lung Dai, *Department of Chemistry, University of Pennsylvania, USA*

James M. Farrar, *Department of Chemistry, University of Rochester, USA*

Kopin Liu, *Institute of Atomic and Molecular Sciences, Taiwan*

David R. Yarkony, *Department of Chemistry, Johns Hopkins University, USA*

James J. Valentini, *Department of Chemistry, Columbia University, USA*

Published

Vol. 2: Modern Electronic Structure Theory
ed. D. R. Yarkony

Vol. 3: Progress and Problems in Atmospheric Chemistry
ed. J. R. Barker

Vol. 4: Molecular Dynamics and Spectroscopy by Stimulated Emission Pumping
eds. H.-L. Dai and R. W. Field

Vol. 5: Laser Spectroscopy and Photochemistry on Metal Surfaces
eds. H.-L. Dai and W. Ho

Vol. 6: The Chemical Dynamics and Kinetics of Small Radicals
eds. K. Liu and A. Wagner

Vol. 7: Recent Developments in Theoretical Studies of Proteins
ed. R. Elber

Vol. 8: Charge Sensitivity Approach to Electronic Structure and Chemical Reactivity
R. F. Nolewajski and J. Korchowiec

Vol. 9: Vibration-Rotational Spectroscopy and Molecular Dynamics
ed. D. Papoušek

Vol. 10: Photoionization and Photodetachment
ed. C.-Y. Ng

Vol. 11: Chemical Dynamics in Extreme Environments
ed. R. A. Dressler

Vol. 12: Chemical Applications of Synchrotron Radiation
ed. T.-K. Sham

Vol. 13: Progress in Experimental and Theoretical Studies of Clusters
eds. T. Kondow and F. Mafuné

Advanced Series in Physical Chemistry

14

MODERN TRENDS IN CHEMICAL REACTION DYNAMICS

Experiment and Theory (Part I)

Editors

Xueming Yang

Academia Sinica, Taiwan & Chinese Academy of Sciences, PRC

Kopin Liu

Academia Sinica, Taiwan

 **World Scientific**

NEW JERSEY • LONDON • SINGAPORE • SHANGHAI • HONG KONG • TAIPEI • BANGALORE

Published by

World Scientific Publishing Co. Pte. Ltd.

5 Toh Tuck Link, Singapore 596224

USA office: 27 Warren Street, Suite 401-402, Hackensack, NJ 07601

UK office: 57 Shelton Street, Covent Garden, London WC2H 9HE

British Library Cataloguing-in-Publication Data

A catalogue record for this book is available from the British Library.

**MODERN TRENDS IN CHEMICAL REACTION DYNAMICS: EXPERIMENT
AND THEORY, Part I**

Copyright © 2004 by World Scientific Publishing Co. Pte. Ltd.

All rights reserved. This book, or parts thereof, may not be reproduced in any form or by any means, electronic or mechanical, including photocopying, recording or any information storage and retrieval system now known or to be invented, without written permission from the Publisher.

For photocopying of material in this volume, please pay a copying fee through the Copyright Clearance Center, Inc., 222 Rosewood Drive, Danvers, MA 01923, USA. In this case permission to photocopy is not required from the publisher.

ISBN 981-238-568-1

Typeset by Stallion Press

Email: enquiries@stallionpress.com

Printed in Singapore by World Scientific Printers (S) Pte Ltd

INTRODUCTION

Many of us who are involved in teaching a special-topic graduate course may have the experience that it is difficult to find suitable references, especially reference materials put together in a suitable text format. Presently, several excellent book series exist and they have served the scientific community well in reviewing new developments in physical chemistry and chemical physics. However, these existing series publish mostly monographs consisting of review chapters of unrelated subjects. The modern development of theoretical and experimental research has become highly specialized. Even in a small subfield, experimental or theoretical, few reviewers are capable of giving an in-depth review with good balance in various new developments. A thorough and more useful review should consist of chapters written by specialists covering all aspects of the field. This book series is established with these needs in mind. That is, the goal of this series is to publish selected graduate texts and stand-alone review monographs with specific themes, focusing on modern topics and new developments in experimental and theoretical physical chemistry. In review chapters, the authors are encouraged to provide a section on future developments and needs. We hope that the texts and review monographs of this series will be more useful to new researchers about to enter the field. In order to serve a wider graduate student body, the publisher is committed to making available the monographs of the series in a paperbound version as well as the normal hardcover copy.

Cheuk-Yiu Ng

This page intentionally left blank

PREFACE

Chemical reaction dynamics research has been an important field in physical chemistry and chemical physics research during the last few decades. This field of research has provided crucial support for atmospheric chemistry, interstellar chemistry as well as combustion chemistry. The development in this field has also greatly enhanced our understanding of the nature of bimolecular and unimolecular chemical reactions, and intermolecular and intramolecular energy transfer processes. Even though this field of research reached relative maturity in the 1980s, it has made tremendous progress during the last decade or so. This is largely due to the development of many new and state-of-the-art experimental and theoretical techniques during that period. In view of these significant developments, it is beneficial to all of us that these developments be presented in a review volume to provide both graduate students and experts in the field a detailed picture of the current status of the advanced experimental and theoretical researches in chemical reaction dynamics. This review volume, published in two parts, is dedicated to the recent advances, both theoretical and experimental, in chemical reaction dynamics. All chapters in these books are written by world experts in the chosen special topics.

Experimentally, many new techniques have been developed in the last decade or so to study molecular reaction dynamics. For example, the velocity map imaging method for photochemistry and bimolecular reactions, the high resolution highly sensitive H-atom Rydberg tagging time-of-flight technique, the Doppler selected “core” mapping method, the significantly improved universal crossed molecular beam technique, the coincident imaging method, etc. The application of VUV synchrotron radiation as well as the soft ionization using traditional electron impact ionization in chemical dynamics has somewhat added species selectivity to the study of bimolecular as well as unimolecular reactions. The exciting research field of femtosecond chemistry has also provided us the technique and the drive to look

at chemical reactions in the real time domain. These experimental methodologies are crucial for the advancement of our detailed understanding of the mechanisms of elementary chemical processes, complicated chemical reactions with multiple reaction pathways, photoionization/photodissociation processes, as well as intermolecular and intramolecular energy transfer processes.

On the theoretical front, the fast growing computing power and the development of sophisticated quantum, semiclassical and statistical methods in this research field allows us now to study complicated chemical processes quantitatively. The development of *ab initio* quantum chemistry has provided us with tools for obtaining accurate energetics as well as structural information on both small and large molecular systems. Based on *ab initio* calculations, global potential energy surfaces can now be constructed for elementary chemical reactions for high-level dynamical studies. Dynamical calculations using exact full quantum methods as well as semiclassical methods can be carried out on these global potential surfaces. Combining these calculations with detailed analysis of the calculated results, mechanisms of elementary chemical reactions can now be studied in great detail. Interesting nonadiabatic dynamics involving interesting avoided crossings as well as conical intersections can now be studied using both quantum chemical and dynamical methods. Dynamics of larger systems such as large clusters and biomolecules can also be investigated. Furthermore, the interaction between experiment and theory is becoming stronger than ever. Experiment and theory can now be compared quantitatively in chemical dynamics even for very complicated systems. Such interactions have also enhanced our understanding in almost every front in this research field.

In this second part, we have included a total of ten chapters which describe a variety of new research topics in the chemical dynamics field. Lee and Liu discusses in Chapter 1, a three-dimensional velocity mapping approach to study dynamics in elementary chemical reactions. In Chapter 2, Chao and Skodje provides an overview of the effect of reactive resonance on observables in reactive scattering studies. Chapter 3 by Yang describes the recent advances in the studies of elementary chemical reactions using the Rydberg tagging H-atom transitional spectroscopy technique. Huang *et al.* in Chapter 4 gives a detailed description on the new multimass ion imaging technique for photochemistry studies. Schroden and Davis describes in Chapter 5 the recent dynamics studies of neutral transition metal atom reactions with small molecules using crossed molecular beam method. The elegant study of photodissociation dynamics of ozone using ion imaging

technique in the Hartley band is described in Chapter 6 by Houston. In Chapter 7, Casavecchia *et al.* focuses on the universal crossed molecular beam reactive scattering studies by soft electron-impact ionization. Wodtke describes in Chapter 8 the dynamics of interactions of vibrationally-excited molecules at surfaces. D. Zhang *et al.* provides an overview on the recent advances of the first principles quantum dynamical study of four-atom reactions in Chapter 9. In the last chapter, J. Zhang gives an overview on the recent studies of photodissociation dynamics of free radicals. These chapters represent the most recent advances in the various topics in the chemical dynamics research field.

We want to take this opportunity to thank all the authors who have contributed to these two parts in various research topics. We hope these contributions will provide a general view on the current trends in chemical dynamics research, and will be helpful to both experts and newcomers in the field. We appreciate very much the great efforts made by Ms. Ying Oi Chiew who has done a superb job in editing the books.

Xueming Yang and Kopin Liu
September 2004

This page intentionally left blank

CONTENTS

<i>Introduction</i>	v
<i>Preface</i>	vii
1. Doppler-Selected Time-of-Flight Technique: A Versatile Three-Dimensional Velocity Mapping Approach	1
Shih-Huang Lee and Kopin Liu	
2. The Effect of Reactive Resonance on Collision Observables	43
Sheng Der Chao and Rex T. Skodje	
3. State-to-State Dynamics of Elementary Chemical Reactions Using Rydberg H-Atom Translational Spectroscopy	87
Xueming Yang	
4. Multimass Ion Imaging — A New Experimental Method and Its Application in the Photodissociation of Small Aromatic Molecules	163
Cheng-Liang Huang, Yuan T. Lee and Chi-Kung Ni	
5. Reactions of Neutral Transition Metal Atoms with Small Molecules in the Gas Phase	215
Jonathan J. Schroden and H. Floyd Davis	
6. Photodissociation Dynamics of Ozone in the Hartley Band	281
Paul L. Houston	

7.	Crossed Molecular Beam Reactive Scattering: Towards <i>Universal</i> Product Detection by <i>Soft</i> Electron-Impact Ionization	329
	Piergiorgio Casavecchia, Giovanni Capozza and Enrico Segoloni	
8.	Interactions of Vibrationally-Excited Molecules at Surfaces: A Probe for Electronically Nonadiabatic Effects in Heterogeneous Chemistry	383
	Alec M. Wodtke	
9.	First Principles Quantum Dynamical Study of Four-Atom Reactions	409
	Dong H. Zhang, Minghui Yang, Soo-Y. Lee and Michael A. Collins	
10.	Photodissociation Dynamics of Free Radicals	465
	Jingsong Zhang	
	<i>Index</i>	523

CHAPTER 1

DOPPLER-SELECTED TIME-OF-FLIGHT TECHNIQUE: A VERSATILE THREE-DIMENSIONAL VELOCITY MAPPING APPROACH

Shih-Huang Lee^a and Kopin Liu^b

*Institute of Atomic and Molecular Sciences (IAMS), Academia Sinica,
P. O. Box 23-166, Taipei, Taiwan 10764*

Contents

1. Introduction	2
2. Doppler-Selected Time-of-Flight Technique	4
2.1. Basic Concept	4
2.2. Apparatus	5
2.2.1. Molecular Beam Source	5
2.2.2. Laser Ionization	6
2.2.3. TOF Spectrometer	7
2.3. Data Analysis	9
2.3.1. Crossed Beam Scattering	9
2.3.2. Photodissociation Process	12
2.3.3. Density-to-Flux Transformation	13
3. Applications	14
3.1. Photodissociation Dynamics	14
3.1.1. $\text{C}_2\text{H}_2 + h\nu$ (121.6 nm) \rightarrow $\text{C}_2\text{H} + \text{H}$	15
3.1.2. $\text{H}_2\text{S} + h\nu$ (121.6 nm) \rightarrow $\text{SH} + \text{H}$	19
3.2. Crossed-Beam Reaction Dynamics	25
3.2.1. $\text{S}(^1\text{D}) + \text{H}_2 \rightarrow \text{SH} + \text{H}$	25
3.2.2. $\text{F}(^2\text{P}) + \text{HD} \rightarrow \text{HF} + \text{D}$	30
4. Outlook	37
Acknowledgments	39
References	39

^aPresent address: National Synchrotron Radiation Research Center, Hsinchu, Taiwan 30077.

^bAlso Department of Chemistry, National Taiwan University, Taipei, Taiwan 10764.

1. Introduction

Past decades have witnessed the instrumental role crossed molecular beam technique plays in advancing our understanding of gas phase collision dynamics.¹ The two most important pieces of information derived from a crossed beam experiment are the angular and speed distributions of collision products.² The crossed beam method made these measurements possible by first defining the initial velocities (the vectors) of the two reactants and then allowing one to move the detector (usually the mass spectrometer) around the crossing zone of the two beams so as to detect the angular distribution of the collision products. When combined with a time-of-flight (TOF) method, this detection technique also provides the speed or the translational energy distribution of the products.

With the advent of lasers, there is another way of investigating the angular and speed distribution of the collision products. Instead of using a rotating mass spectrometer, the idea is to first use a laser spectroscopic method to detect the collision products, often in a state-specific manner. Then, advantage is taken of the Doppler effect: the spectroscopic signal originates only from those products that have the right velocity component along the direction of the probe laser to be in resonance with the laser frequency. The Doppler profile, obtained by scanning the frequency of the probe laser, reflects the distribution of this velocity component of collision products. Hence, the Doppler-shift technique is intrinsically a one-dimensional (1D) projection method. Nevertheless, the distribution thus obtained is directly related to the product angular distribution in the center-of-mass (CM) frame when the product speed is well defined. In 1977 Kinsey³ proposed and explored the idea of measuring differential cross-sections by Doppler spectroscopy. Following Kinsey's suggestion, Doppler spectroscopy has found a wide range of applications to problems in gas phase collision dynamics,⁴ including photodissociation processes.⁵

Interestingly, the analogous idea of projecting a three-dimensional (3D) velocity distribution into a 1D distribution has long been recognized by the mass spectroscopy community, particularly in the application of ion TOF mass spectroscopy.⁶ The broadening of an observed mass peak can be ascribed to either the initial spatial distribution or/and the initial kinetic energy spread of the ion packet between the extractor and the repeller. Mons and Dimicoli⁷ were among the first to exploit this feature of ion TOF mass spectroscopy with resonance-enhanced multiphoton ionization (REMPI) detection to determine the angular and speed distributions of photofragments in well-defined internal states.

The Doppler-selected TOF technique grew from the frustration in our initial attempt in the early 1990s to apply the Doppler-shift technique to reactive scatterings.^{8,9} In these experiments, the Doppler-shift technique was applied to the atomic product; thus, the molecular state of the co-product was not selected. As a result, both the product angular and speed distributions are encoded in the Doppler profile. To “decode” the two distributions, Doppler profiles of two experimental configurations (i.e. the laser either propagating along (\parallel) or perpendicular to (\perp) the initial relative velocity vector of the reactants) were typically performed. A trial 3D velocity distribution was then assumed to simultaneously fit the two independent, 1D-projected profiles. Such a forward convoluted approach was time-consuming and not unique; a better experimental approach was needed.

The physical quantity to be determined is the product 3D velocity distribution in the center-of-mass frame. Recognizing that both the Doppler-shift and ion TOF measurement are the 1D projection of a center-of-mass 3D velocity distribution, and that experimentally they can be arranged to be orthogonal to each other, the combination of these two techniques becomes a natural and powerful means to resolve the “dimensionality” problem described above. This is how the idea of a Doppler-selected TOF technique was born and dubbed in 1996.¹⁰ Since then, we have exploited this new approach in a number of photodissociation studies, including H_2S and C_2H_2 (Refs. 10 and 11); CH_4 (Refs. 12 and 13) and CHF_2Cl (Ref. 14); reactive scatterings of $\text{CN} + \text{D}_2$ (Refs. 15 and 16), $\text{O}(^1\text{D}) + \text{H}_2$ (Refs. 17–21), $\text{S}(^1\text{D}) + \text{D}_2$ (Refs. 22–25), $\text{F} + \text{HD}$ (Refs. 26–31) and $\text{Cl} + \text{H}_2$ (Refs. 32–35). To take advantage of the larger Doppler shift of a lighter product, the H- or D-atom was investigated in all these studies. Our initial goal was quite modest, but we were pleasantly surprised when we noticed, shortly after the first trial, that the resolution of this simple approach can be made sufficiently high such that the state-to-state differential cross-section can be realized in favorable cases. This possibility was not in our original agenda when we initially formulated the basic idea and implemented the technique.

For the remaining of this chapter we will first describe the basic concept of this new technique, the details of our experimental setup, and the way to invert the measured data directly to the desired center-of-mass differential cross-section. Two types of applications will then be highlighted to illustrate the power of this exceedingly simple technique. We will conclude the chapter by comparing the technique with other contemporary modern techniques.

2. Doppler-Selected Time-of-Flight Technique

2.1. Basic Concept

The Doppler-selected TOF technique^{11,19} was designed to map out the product 3D, center-of-mass velocity distribution. This new technique can be regarded as a variant of the 3D imaging technique. It exploits high-resolution translational energy spectroscopy by combining three 1D projection techniques in an orthogonal manner. To take advantage of the cylindrical symmetry of the product 3D velocity distribution around the initial relative velocity axis,¹ denoted as the z -axis, in a crossed-beam experiment, the two differentially-pumped source chambers were rotated such that the initial relative velocity axis lies parallel to the probe laser propagation

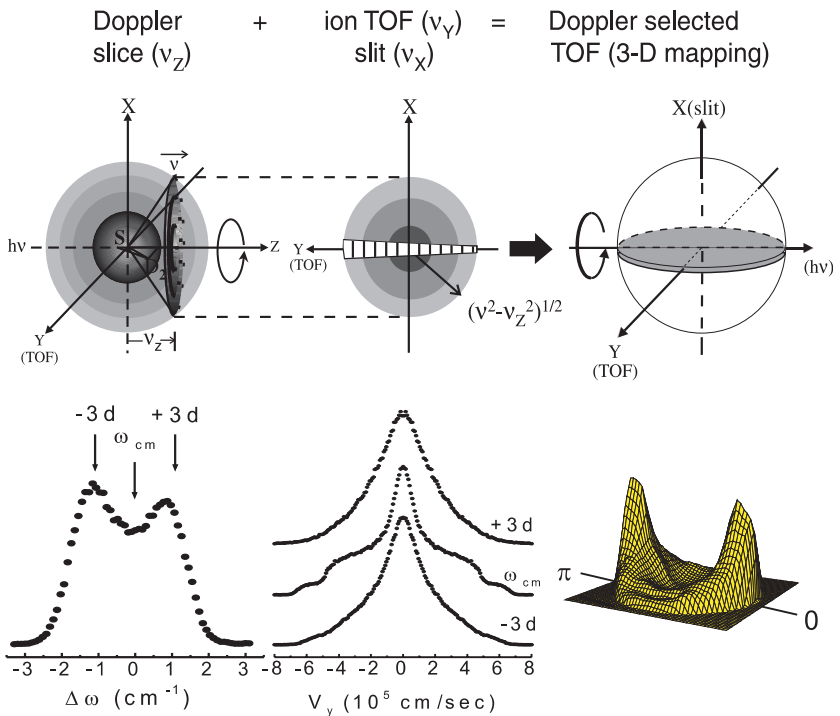


Fig. 1. Schematic illustration of the basic concept of the Doppler-selected TOF technique. The hatched slice on the left represents a Doppler-selection of a given v_z . The strip on the Doppler slice (the middle figure) is the 1D v_y -distribution measured under the v_x -restriction of a slit in front of the TOF spectrometer. The combination of many Doppler-selected TOF measurements yields the result shown on the right. The lower figures are the corresponding actual data at each stage for the reaction of $S(^1D) + H_2$.

axis (which is fixed in the laboratory). As illustrated in Fig. 1, the Doppler-shift technique is first used to selectively (i.e. within the probe laser bandwidth) ionize a subgroup of the H(D)-atom products with $v_z \pm \Delta v_z$ in the center-of-mass frame. Rather than collect all these ions as a single data point in the conventional Doppler-shift technique, the velocity of these Doppler-selected ions in the x - y plane is dispersed both temporally (in y) and spatially (in x) in our approach. By placing a slit (6 mm in height and with its center 1.5 mm offset from the x - z plane to compensate for the center-of-mass speed) at the space-focusing plane just in front of a microchannel plate (MCP) detector to detect only those ions with $v_x \cong 0$, the v_y -distribution is measured through a high-resolution ion TOF velocity spectrometer. Thus, for a given Doppler slice (v_z) the measured TOF profile corresponds to $S(v_y; v_z, v_x \approx 0)$. Due to the symmetry property around the z -axis as mentioned above, the “lost information” (i.e. those with large v_x) can be recovered and the full 3D distribution in the center-of-mass frame can thus be revealed directly from the measurements without simulations.

2.2. Apparatus

The apparatus shown in Fig. 2 consists of three main components: two rotatable molecular beam sources, laser ionization and TOF spectrometer.

2.2.1. Molecular Beam Source

A molecular beam was generated by expanding the reagent into a source chamber through a nozzle using high stagnation pressure. Supersonically-expanded molecules generally have a narrow velocity distribution with a Boltzmann temperature of 1–2 K, but a wide angular divergence which yields a large uncertainty of collision energy in a collision process. Two skimmers in the source chamber were used to collimate the molecular beam and further maintain the vacuum of the main chamber under 10^{-6} Torr, i.e. single collision condition. To generate a radical beam, either the photolysis or dc-discharge method was employed. In the former approach the supersonically-expanded precursor was photolyzed near the throat of the nozzle by a laser. In the latter approach, a discharge device was mounted onto the nozzle to dissociate the appropriate precursor. Both molecular beams then crossed in the center of the main chamber and the probe laser was sent through the scattering center. The advantage of this machine is the ease in changing the interception angle of the two molecular beams, and therefore the collision energy, by rotating each independent molecular beam.

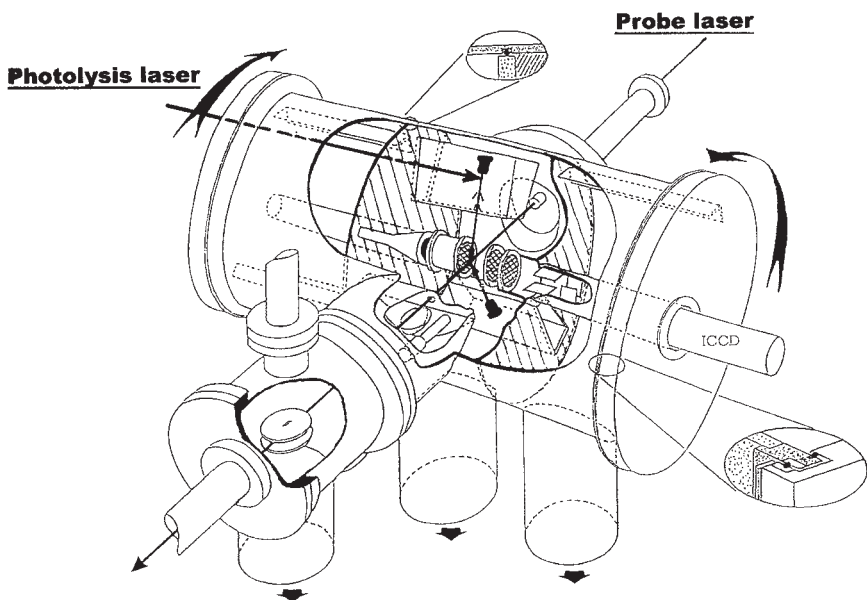


Fig. 2. Schematic of the rotatable sources, crossed-beam machine.

To implement the Doppler-selected TOF measurement, the initial relative velocity is arranged to be parallel to the propagation vector of the probe laser. This critical configuration can readily be achieved in this rotating sources machine.³⁶ Under this configuration, each Doppler-sliced 2D distribution exhibits a cylindrical symmetry. The slit in front of the TOF spectrometer allows only those products with a rather small v_x to be detected. Hence, only the v_y -distribution, obtained by the TOF measurement, is needed to completely characterize the Doppler-sliced 2D ($v_x - v_y$) distribution.

2.2.2. Laser Ionization

For ion TOF measurement a probe laser was used to ionize reaction products in the reaction zone. The $(1+1')$ resonance-enhanced multiphoton ionization (REMPI) method was adapted for H-atom detection. The necessary vacuum ultraviolet (VUV) radiation near 121.6 nm (for Lyman- α transition) can readily be generated by a frequency-tripling technique in a Kr cell.³⁷ The sensitivity of this $(1+1')$ REMPI detection scheme is extremely high owing to the large absorption cross-section of Lyman- α transition,

$\sim 1 \times 10^{-13} \text{ cm}^2/\text{atom}$. More significantly, the lighter mass of the H-atom product has a very large recoil velocity, thus a very large Doppler shift, say 5 cm^{-1} . Even a typical commercial pulsed dye laser, which has $\sim 0.25 \text{ cm}^{-1}$ laser bandwidth near 121.6 nm , is capable of high Doppler selectivity.

2.2.3. TOF Spectrometer

To operate the ion TOF spectrometer in the velocity mode, we adapted a single-stage TOF spectrometer as shown in Fig. 3, which consisted of a repeller, an extractor (and guard rings, not shown) and a free-drift tube. After laser ionization, ions are extracted towards the MCP detector. For an ion with an initial kinetic energy U_0 , the total flight time t can be written as

$$t = 1.0181 \frac{\sqrt{2m}}{qE} \left(\sqrt{U_0 + qS_0E} \pm \sqrt{U_0} \right) + 1.0181 \sqrt{2m} \frac{D}{2\sqrt{U_0 + qS_0E}}, \quad (1)$$

in which S_0 is the distance (cm) from the ionization point to the extractor; D is the length (cm) of the free-drift tube; m is the mass (amu) of the ion; q is the charge number; and E is the extraction field (V/cm). Thus, the initial kinetic energy U_0 can be derived from the measured flight time t according to Eq. 1.

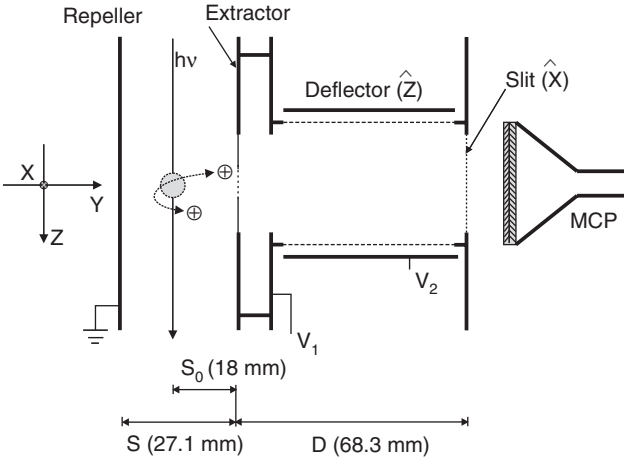


Fig. 3. Schematic of the single-stage TOF device.

The reason for choosing such a simple design is based on the following considerations. If too many ions are created in a small volume, the repulsion force between the ions, i.e. the space charge effect, will perturb the original velocity distribution. To avoid this, an unfocused probe was used, which in general has a size of several mm. Ions generated in this finite and relatively large volume can have different flight times to the detector.⁶ To minimize the flight time difference of ions with the same U_0 but from different space, the dimensions of the TOF spectrometer was kept to fulfill the first-order space-focusing condition, $2U_0 + 2S_0E = ED$. The dimensions shown in Fig. 3 are the optimal values based on the space-focusing condition for $U_0 \approx 0.26$ eV and $E = 3.5$ V/cm. Although in principle the best space-focusing condition appears only for a single value of U_0 as the dimensions and extraction field are fixed, in practice the resolution does not appear to deteriorate for a rather wide range of U_0 .

The TOF spectrum was acquired in the ion-counting mode. The MCP signal was fed through a fast discriminator/amplifier and averaged by a 500 MHz digital oscilloscope as a function of the ion arrival time. The overall temporal resolution of all instruments is approximately 3–4 ns. Further estimation of overall velocity resolution, requires consideration of the individual resolution in v_x , v_y and v_z measurements. The overall velocity resolution can be expressed as $dv/v = (v_x/v^2)dv_x + (v_y/v^2)dv_y + (v_z/v^2)dv_z$. From the Cartesian coordinate defined earlier, dv_z corresponds to the Doppler selection and is determined by the laser bandwidth, dv_y is the speed resolution in the TOF measurement, and dv_x arises from the slit restriction to the spatial spread of the ion packet. Our experimental setup samples those ions with $v_x \cong 0$. Hence, except near the center of the Newton spheres where the center-of-mass recoil velocity is very small, the overall resolution can be approximated as $dv/v \cong (v_y/v^2)dv_y + (v_z/v^2)dv_z$. With our TOF setup and the use of a commercial pulsed dye laser, the resolution is in fact mainly limited by dv_z . Also note that each data point of the Doppler-selected TOF measurement samples the signal within a constant volume element in a center-of-mass velocity frame, $dv_x dv_y dv_z$. When transformed into a center-of-mass polar coordinate, the forward and backward directions (along the z -axis) will have the worst speed resolution, but the best angular distribution. The situation becomes reverse for sideways scattering.

Since the TOF spectrometer is perpendicular to the propagation axis of the probe laser, ions with a large v_z could miss the MCP detector. To overcome this problem, two slots of 6 mm \times 50 mm were cut on the two lateral sides of the free-drift tube and covered with a 90% T-mesh. An

outer tube was arranged to be concentric with the inner free-drift tube and applied with a positive voltage relative to the inner tube. Thus those ions with a large v_z will be reflected back to the inner tube and then reaches the ion detector. Since the electric field of the ion deflector is perpendicular to the TOF axis, it will not distort the original v_y distribution. Though the detection sensitivity is enhanced with the ion deflector, the deflection efficiency is a function of v_z , thus normalization is required for various TOF spectra prior to constructing a 3D velocity contour. A 1D Doppler profile recorded with an extraction field typically $\gtrsim 500$ V/cm was used to normalize all Doppler-selected TOF spectra.

2.3. Data Analysis

2.3.1. Crossed Beam Scattering

In this section, the relationship between the measured quantity and the desired center-of-mass differential cross-section will be established and a brief description of the data analysis procedure will then be given. First, consider a Newton sphere with a single value of the product velocity v (see Fig. 4). From the Doppler-shift formula, at a given laser wavelength, the Doppler effect selectively ionizes those ions with $v_z = v \cos \theta$ in the

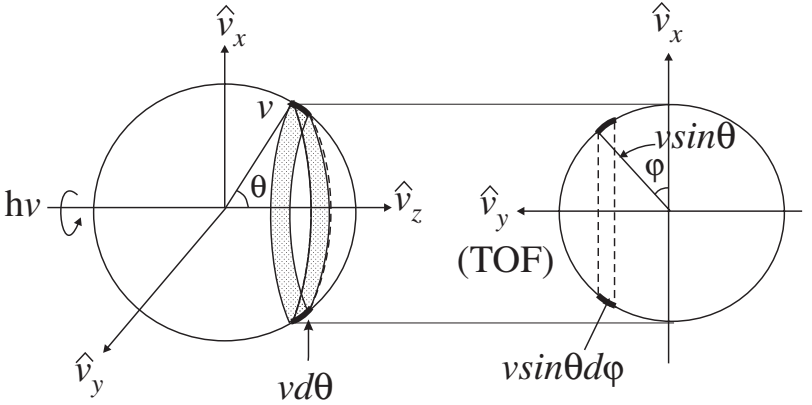


Fig. 4. A quantitative analysis of velocity selectivities in Doppler-selected TOF technique. Shown here is for a single value of the product velocity v . The left panel corresponds to the Doppler selection along the z -axis, and the right panel shows the TOF measurement of the v_y -component for all possible v_x at a selected v_z -slice.

center-of-mass frame with the resolution given by $dv_z = -v \sin \theta d\theta$. For the subsequent ion TOF measurement, one has (from the right panel of Fig. 4)

$$v_y = v \sin \theta \sin \varphi \quad (2)$$

and

$$dv_y = v \sin \theta \cos \varphi d\varphi = v_x d\varphi. \quad (3)$$

Let $D(v_x, v_y, v_z)$ be the product density in the center-of-mass velocity space. The signal under the above condition, i.e. for a given Doppler selection and at a given time bin, is

$$\begin{aligned} S(t; v_z)dt &\propto D(vd\theta)(v \sin \theta d\varphi) \\ &= Dv^2 \sin \theta d\theta d\varphi = D \frac{v}{v_x} dv_y dv_z. \end{aligned} \quad (4)$$

The last equality in Eq. (4) transforms the measured quantity expressed in polar coordinates into the Cartesian one for which the expressions for dv_z given in Eq. (4) and dv_y in Eq. (3) have been used.

Now consider a Newton sphere with a distribution of the center-of-mass velocity v . The corresponding signal can be expressed as

$$S(t; v_z)dt \propto \int_v D \frac{v}{v_x} dv_y dv_z dv. \quad (5)$$

Since v_y and v_z are fixed and $v^2 = v_x^2 + v_y^2 + v_z^2$, one has

$$dv_x = \frac{v dv}{v_x}. \quad (6)$$

It leads to

$$S(t; v_z)dt \propto \left[\int_0^{v_x^{\max}} D dv_x \right] dv_y dv_z \quad (7)$$

where v_x^{\max} is set by the slit restriction or the energetic limit. In other words, except for the extremely small velocity, the measured quantity can be well approximated as

$$S(t; v_z)dt \approx D(v_x, v_y; v_z) dv_z dv_y dv_x. \quad (8)$$

Equation (8) is also what one would anticipate from intuitive arguments.

Experimentally, dv_z is directly proportional to the laser bandwidth and is a constant; dv_x is determined by the slit width and is inversely proportional to the ion arrival time (i.e. a 1D solid angle factor); and dv_y/dt denotes the time-to-speed transformation in the ion TOF measurement, which can readily be derived from the equation of motion. It was found

to be a nearly linear function (i.e. $\Delta v_y \propto \Delta t$) except for extremely low extraction fields, although the exact expression was used in our analysis. Hence, after the v_x -correction and the time-to-speed transformation, the quantity measured in the Doppler-selected TOF method is approximately proportional to the density,

$$S(v_y; v_z, v_x \approx 0) \propto D(v_x, v_y; v_z). \quad (9)$$

Since the density is invariant to the velocity coordinates (Cartesian or polar) used, one has, expressing the density in terms of differential cross-section,

$$D(v_x, v_y, v_z) = \frac{d^3\sigma}{dv^3} = \frac{d^3\sigma}{dv_x dv_y dv_z} = \frac{d^3\sigma}{v^2 dv d\Omega}. \quad (10)$$

The conventional differential cross-section^{1,2} refers to the cross-section per solid angle in the center-of-mass polar coordinate. The desired doubly differential cross-section is then related to the measured quantity by the simple equation

$$\frac{d^2\sigma}{dv d(\cos\theta)} \propto v^2 D(v_x, v_y; v_z) = v^2 S(v_x \approx 0, v_y, v_z). \quad (11)$$

To sum up, the basic idea of the Doppler-selected TOF technique is to cast the differential cross-section $d^3\sigma/dv^3$ in a Cartesian coordinate, and to combine three dispersion techniques with each independently applied along one of the three Cartesian axes. As both the Doppler-shift (v_z) and ion velocity (v_y) measurements are essentially in the center-of-mass frame, and the v_x -component associated with the center-of-mass velocity vector can be made small and be largely compensated for by a slight shift in the location of the slit, the measured quantity in the Doppler-selected TOF approach represents directly the center-of-mass differential cross-section in terms of per velocity volume element in a Cartesian coordinate, $d^3\sigma/dv_x dv_y dv_z$. As such, the transformation of the raw data to the desired doubly differential cross-section becomes exceedingly simple and direct, Eq. (11).

To analyze the data, first perform the v_x - and v_z -corrections and the time-to-speed transformation to make the velocity volume element the same for all data points, and then normalize each Doppler-selected TOF spectrum according to the averaged 1D Doppler profile from several independent scans, $I(v_z) = \sum_{v_y} v_y S(v_y; v_x \approx 0, v_z) dv_y$. Due to the large exothermicity of this reaction, the problematic density-to-flux transformation is not negligible (despite the large probe laser size used to minimize its effects) and needs to be accounted for (the “ v_y -correction”, see Sec. 3.3). By combining all the resulting TOF spectra, the product 3D velocity flux contour

can then be constructed. The major effort in this experimental approach is then to analyze the velocity contour thus obtained (rather than simulating the spectra), and to extract the dynamical information contained in the contour data.

2.3.2. Photodissociation Process

Owing to the symmetry property of an optical dipole transition, the data analysis for a photodissociation study is greatly simplified. The center-of-mass differential cross-section for a single-photon, dissociative process can be expressed as^{38,39}

$$f(\mathbf{v}) = \frac{d^3\sigma}{dv d\Omega} = \frac{1}{4\pi} g(v)[1 + \beta(v) P_2(\cos \theta)] \quad (12)$$

where θ is the polar angle between the fragment recoil velocity and the polarization axis of dissociating light and $P_2(\cos \theta) = (3 \cos^2 \theta - 1)/2$. The goal is then to determine $g(v)$ and $\beta(v)$ experimentally. Three experimental configurations are particularly informative using the Doppler-selected TOF technique. If the probe laser wavelength is chosen such that only those ions with $v_z = 0 \pm \Delta v_z$ (Δv_z determined by the laser bandwidth) will be ionized in the REMPI process and the slit restricts further only those ions with $v_x \approx 0 \pm \Delta v_x$ (Δv_x determined by the slit width and the ion arrival time) to be detected, then one has a nominally 1D “core” speed distribution $f(v_y; v_z \approx 0, v_x \approx 0)$. Recasting Eq. (12) in Cartesian coordinates and omitting the $1/4\pi$ factor, it becomes for $\theta = 0^\circ$, i.e. \parallel -polarization,

$$f^\parallel(v_y; v_x \approx v_z \approx 0) = g(v) [1 + \beta(v)]; \quad (13)$$

for $\theta = 90^\circ$, i.e. \perp -polarization,

$$f^\perp(v_y; v_x \approx v_z \approx 0) = g(v) \left[1 - \frac{1}{2}\beta(v) \right]; \quad (14)$$

and for $\theta = 54.7^\circ$, i.e. magic-angle,

$$f^m(v_y; v_x \approx v_z \approx 0) = g(v). \quad (15)$$

Hence, one has

$$g(v) = f^m = (f^\parallel + 2f^\perp)/3, \quad (16)$$

$$\beta(v) = 2(f^\parallel - f^\perp)/(f^\parallel + 2f^\perp). \quad (17)$$

And the product translational energy distribution becomes

$$P(E_t) = \frac{d\sigma}{dE_t} \propto \frac{g(v)}{v} \quad (18)$$

where E_t is the product translational energy and is related to the translational energy (E) of the fragment being detected by $E_t = E(M/(M - m))$ with m being the detected fragment mass and M the molecular precursor mass. The remaining task is to relate the desired $f^i(v_y)$ to the corresponding TOF profile, just as the above crossed-beam case.

2.3.3. Density-to-Flux Transformation

The density here refers to the spatial coordinate, i.e. the concentration of the reaction product, and is not to be confused with the $D(v_x, v_y, v_z)$ in previous sections which refers to the center-of-mass velocity space. Laser spectroscopic detection methods in general measure the number of product particles within the detection volume rather than a flux, which is proportional to the reaction rate, emerging from it. Thus, products recoiling at low laboratory velocities will be detected more efficiently than those with higher velocities. The correction for this laboratory velocity-dependent detection efficiency is called a density-to-flux transformation.⁴⁰ It is a 3D space- and time-resolved problem and is usually treated by a Monte Carlo simulation.^{41,42}

This problem is greatly simplified here thanks to the nature of the Doppler-selected TOF approach in which three orthogonal dispersion techniques are combined. Products scattered along the laser propagation axis (\hat{z}) with different v_z only manifest themselves as Doppler shifts and will have the same detection efficiency. Thus, only products with different v_x and v_y components need to be considered. In this 3D-mapping approach, however, only those ions with $v_x \approx 0$ are allowed to reach the detector and be detected. Hence, the intrinsic four-dimensional problem, (v_x, v_y, v_z, t) , is reduced to just a (v_y, t) treatment. A Monte Carlo procedure, which takes into account the spatial and temporal profiles of the molecular beams and the laser, was used to model the detection constraints. The resulting correction function is depicted in Fig. 5. As can be seen, the effect is simply to preferentially increase the reactive flux from the experimental measurement for the larger v_y 's. Due to the finite physical length of a typical pulsed molecular beam, for a crossed-beam experiment the density-to-flux problem cannot be completely eliminated if the crossing zone is illuminated. The use of a large probe laser can only reduce the transformation factor. In a typical photodissociation experiment, however, the time delay between the pump and probe lasers can be made sufficiently short so that the detection becomes effectively in the flux mode, i.e. all fragments can be investigated

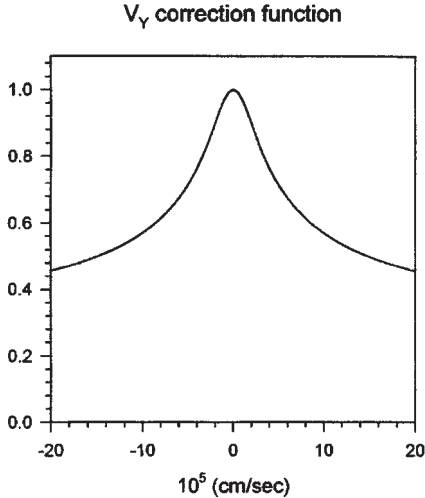


Fig. 5. The v_y -correction (i.e. the density-to-flux transformation) function for the current experimental setup.

in a manner independent of their laboratory recoil speed. In this case, no density-to-flux transformation is needed.

3. Applications

3.1. Photodissociation Dynamics

The studies on photodissociations of C_2H_2 and H_2S are exemplified here to demonstrate the advantages of this experimental technique. For these cases, only a single beam was employed. To minimize the chemical interference from clustering, the leading edge of a mildly expanded pulsed beam was used in all cases. To minimize the difference between the center-of-mass and laboratory velocity frames, the molecular beam was directed nearly collinear (18°) with respect to the laser propagation axis. The detection of H-atom fragments was achieved by using $(1+1')$ REMPI via the Lyman- α transition at 121.6 nm. The 121.6 nm photon, which also served as the photolysis light source, i.e. a one-color experiment, was produced by the third harmonic generation scheme in a Kr gas cell and then recollimated to a parallel light with a few mm in size by a LiF lens. This lens implementation significantly improved the TOF resolution by reducing the higher order effects from the initial spatial-spread of the ion packet. The change of polarization of the 121.6-nm photon was accomplished by inserting a $\lambda/2$ wave plate after a

Glan laser polarizer in the 365-nm beam path. The so-called parallel and perpendicular polarizations are referenced to the ion TOF axis.

3.1.1. $\text{C}_2\text{H}_2 + h\nu$ (121.6 nm) $\rightarrow \text{C}_2\text{H} + \text{H}$

Acetylene (C_2H_2) is one of the simplest hydrocarbons with chemistry highly relevant to a number of natural and human-made phenomena occurring in interstellar processes and combustion. Its spectroscopy and photochemistry in the UV and VUV regions have received considerable attention. The 190–250 nm absorption region is assigned to a weak, linear to trans-bent transition ($\tilde{A}^1A_u \leftarrow \tilde{X}^1\Sigma_g^+$).^{43,44} Fluorescence from the \tilde{A} -state has been observed.^{45,46} A sudden falloff of the fluorescence quantum yield occurs around 214.3–215.8 nm, which was initially attributed to the predissociation of C_2H_2 to $\text{C}_2\text{H} + \text{H}$. A reinvestigation⁴⁷ combining the fluorescence quantum yield and photofragment yield measurement confirms the earlier fluorescence quenching data, which, however, casts some doubts on the original interpretation. Instead, the involvement of the triplet manifold in the \tilde{A} -state predissociation is suggested.

In the VUV region the 165–195 nm spectrum is assigned to the $\tilde{B}^1B_u \leftarrow \tilde{X}^1\Sigma_g^+$ transition,⁴⁸ the spectra become richer at even shorter wavelengths and several (ro)vibrational resolved Rydberg series and valence states have been identified.^{49–51} Near the hydrogen Lyman- α transition at 121.6 nm the vibronic Rydberg state denoted as $3\text{R}''(^1\Pi_u)2_0^1$ is most relevant.⁵⁰ This band is diffused because of predissociation. With 10.2-eV photon energy, three fragmentation channels, the formation of $\text{C}_2 + \text{H}_2$, $\text{CH} + \text{CH}$, and $\text{C}_2\text{H} + \text{H}$ are energetically accessible. Because the excitation of C_2H_2 at 121.6 nm involves a vibronically resolved Rydberg state, the study of its dissociation dynamics offers an opportunity to elucidate the Rydberg-valence interactions^{52–56} and to explore the photochemical consequence of Rydbergization⁵⁶ in a complementary manner to the spectroscopic means which are only sensitive to the Franck–Condon region. The present work focuses only on the characterization of the H-atom elimination process.

The structureless Doppler profile (1D projection) of the H-atom fragment from the photolysis of C_2H_2 is shown in Fig. 6.¹¹ The narrow doublet ($^2P_{3/2,1/2} \leftarrow ^2S_{1/2}$) at the center is the Doppler profile of a supersonically-cooled H-atom beam. The arrows in Fig. 6 indicate the energetic limit associated with the electronic ground state of C_2H co-fragments, which appears to be slightly larger than the maximal Doppler shift of the corresponding

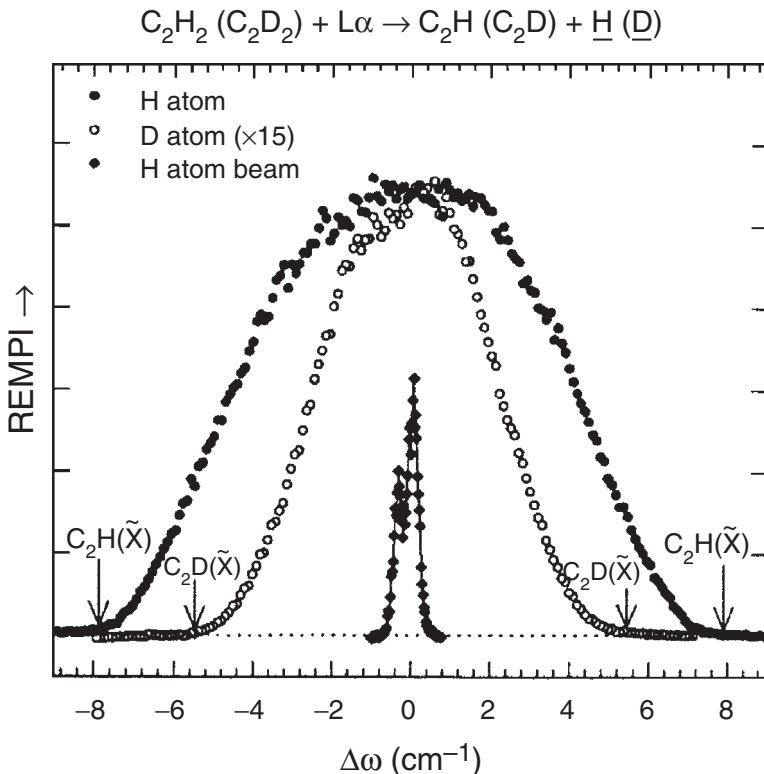


Fig. 6. Doppler profile of H and D fragments from the photolysis of C_2H_2 and C_2D_2 , respectively. The narrow doublet at the center is the Doppler profile of a supersonically-cooled H-atom beam.

profile. Figure 7 displays the raw TOF spectra of H-atom fragments for two different polarization configurations, \parallel and \perp .¹¹ The spectra were obtained with an ion extraction field of 1.85 V/cm at ca. ω_0 , i.e. nominally $v_z \approx 0$. The two spectra were normalized to each other by using high field measurements at 700 V/cm. Clearly, the \perp configuration yields slightly higher intensity than the \parallel , and structures are seen in both configurations for the fast-moving fragments with the \perp configuration far more prominent. The dips in the TOF spectra (at about 4.1 μs ion arrival time, referred to as T_0) correspond to the ions with initial kinetic energy $U_0 = 0$. Ions coming to the detector later than T_0 are those with an initial velocity in the opposite direction to the detector, so-called return ions. The clip-off on return ions at $\sim 4.9 \mu\text{s}$ was due to collision to the repeller plate before turnaround occurred.

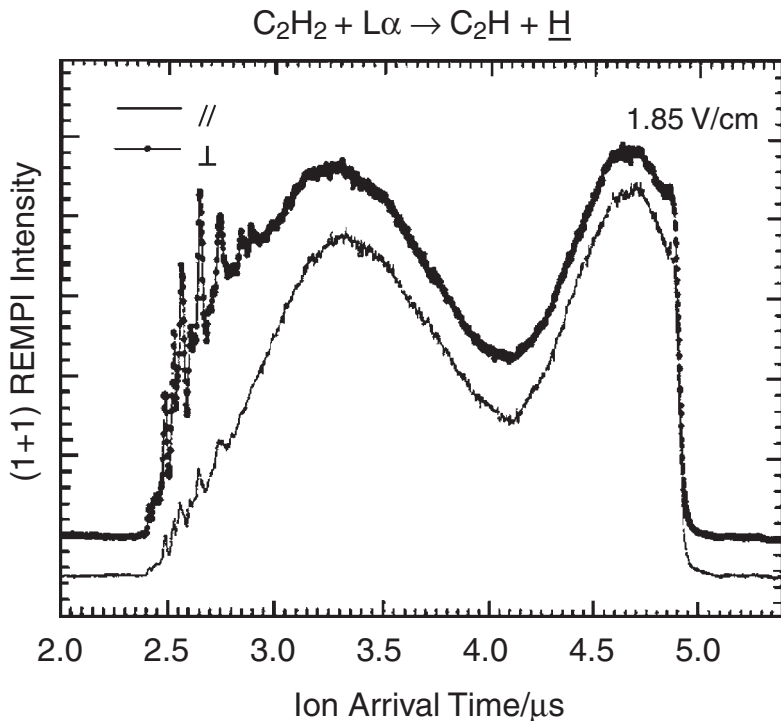


Fig. 7. Raw TOF spectra for the photolysis of C_2H_2 , obtained with two polarization configurations. The laser frequency was set at the center of the Doppler profile, i.e. ω_0 .

The data analysis follows the inversion procedures described in Sec. 2.3. The final results for the product translational energy distribution $P(E_t)$ and recoil anisotropy $\beta(E_t)$ for C_2H_2 are shown in Fig. 8.¹¹ The $P(E_t)$ shows a structural profile at the high kinetic energy part and a propensity against the formation of $\text{C}_2\text{H}(\tilde{X})$ from photodissociation. The $\beta(E_t)$ exhibits a distinct dependence on product translational energy, ranging from zero for slowly moving products to about -0.8 near the observed energetic threshold. The negative β value is consistent with the previous spectroscopic assignment⁴⁹ of a perpendicular transition for the initial excitation of $\text{C}_2\text{H}_2(\tilde{X} \rightarrow 3\text{R}'')$, and its magnitude suggests a rather prompt dissociation process. The out-of-phase correlation between the mild oscillations of β and the peaks in $P(E_t)$ was ascribed to two distinct dissociation pathways with different β parameters and the energy dependence of the observed β values arises from the energy dependence of the branching ratio of these two pathways.

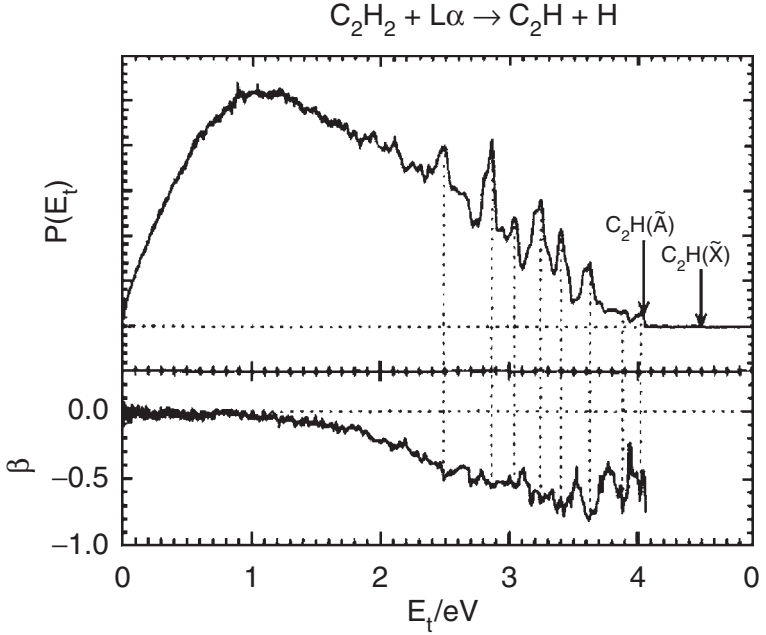


Fig. 8. Photofragment center-of-mass translational energy distribution $P(E_t)$ and anisotropy distribution $\beta(E_t)$ for the photolysis of C_2H_2 . The arrows mark the energetic thresholds for the corresponding electronic states of the fragment C_2H . The out-of-phase correlation between the mild oscillations of β and the structures in $P(E_t)$ is indicated by vertical dashed lines.

Accordingly, Eqs. (16) and (17) can be written as

$$g(v) = g_1(v) + g_2(v) \quad (19)$$

$$\beta(v) = \chi(v)\beta_1 + (1 - \chi(v))\beta_2 \quad (20)$$

respectively, where $\chi(v)$ denotes the branching fraction of two dissociation pathways. With the assumption that $\beta_1 = 0$ and $\beta_2 = -0.8$, the results of two dissociation pathways, i.e. g_1 , g_2 , and χ , are shown in Fig. 9.¹¹ These two pathways are distinguished from each other by the different dissociation timescales with respect to the internal motions of the photoexcited parent molecules. The prompt dissociation yields the fast fragments with a highly structured translational energy distribution and the slow dissociation pathway produces slower fragments with a structureless distribution. Integrating $P_1(E_t)$ and $P_2(E_t)$ yields the branching ratio of these two pathways, i.e. a ratio of 2.8 in favor of the structureless slow component.

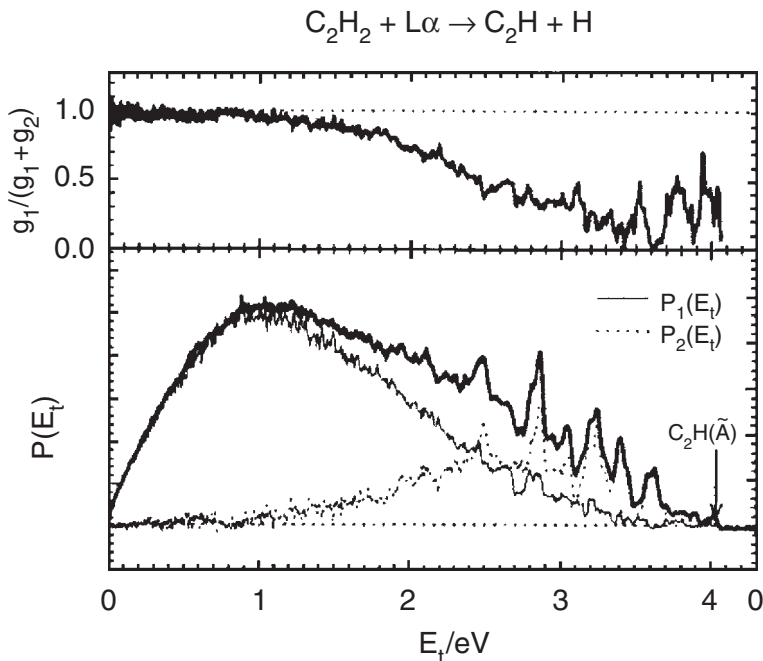


Fig. 9. Partitioned $P(E_t)$ for the photolysis of C_2H_2 under the assumption that $\beta_1 = 0$ and $\beta_2 = -0.8$. The upper panel shows the resulting branching fraction, while the lower panel displays the fragment translational energy distributions of the two corresponding pathways.

There are two remarkable observations for the photodissociation of C_2H_2 at 121.6 nm in this study.¹¹ First, the dissociation of a photoexcited molecule appears to be governed by two distinct pathways characterized by different dissociation lifetimes and product energy distributions. This study shows a strong propensity towards (against) the formation of the $\text{C}_2\text{H}(\tilde{A})(\text{C}_2\text{H}(\tilde{X}))$ fragment, which is in sharp contrast to the photodissociation of C_2H_2 at 193 nm for which both $\text{C}_2\text{H}(\tilde{A})$ and $\text{C}_2\text{H}(\tilde{X})$ are formed.^{57,58} Second, while the slower pathway ($\beta \approx 0$) yields a statistical-like product energy distribution, the faster one ($\beta \approx -0.8$) produces a highly structural and mode-specific distribution.

3.1.2. $\text{H}_2\text{S} + h\nu (121.6 \text{ nm}) \rightarrow \text{SH} + \text{H}$

Hydrogen sulfide (H_2S) is the first heavier analogue of H_2O . As such, it has attracted much experimental and theoretical attention on its

spectroscopy and dissociation dynamics. The first UV absorption band ($\tilde{B}^1A_2/\tilde{A}^1B_1 \leftarrow \tilde{X}^1A_1$), consisting of a progression of diffuse peaks, is located in the region of 240–160 nm and peaks at ~ 195 nm.^{59,60} Towards higher energy, there are several Rydberg transitions extending from 160 to 118 nm.^{59,60} The studies on the photodissociation have been mostly focused in the region between 244 and 193 nm.^{61–63} For wavelengths shorter than 193 nm, the photodissociation dynamics of H₂S for hydrogen elimination has been studied at 157.6 nm and 121.6 nm using the H-atom Rydberg tagging technique.^{64,65} According to the absorption spectrum of H₂S in the VUV region, the excitation at 157.6 nm is assigned to the descending tail of Rydberg transition $\tilde{C}^1A_2 \leftarrow \tilde{X}^1A_1$, and at 121.6 nm to other higher Rydberg states. For hydrogen atom elimination, the hydrogen yield of H₂S photolyzed at 157.6 nm is dominated by the SH($X^2\Pi$)+H channel in accord with the energetics ground. Both spin-orbit and rovibrational state distributions of the SH($X^2\Pi$) co-fragment were obtained from the translational energy distribution of the hydrogen fragment. A prominent bimodal rotational distribution of $v = 0$ and 1 vibrational states was found, indicative of two significantly distinctive dissociation mechanisms being involved in the photodissociation of H₂S at 157.6 nm excitation.⁶⁴ It was argued that the low rotational excitation component is likely due to the dissociation from the first absorption band and the high rotational excitation component is due to the direct dissociation from the \tilde{C}^1A_2 state.

As to the photodissociation of H₂S at 121.6 nm, Schnieder *et al.* have previously recorded the translational spectrum of the hydrogen fragment of H₂S using the H-atom Rydberg tagging technique.⁶⁵ In contrast, it was found that SH($A^2\Sigma^+$) + H and S(1D) + H + H dissociation pathways dominate the hydrogen product yield, and the SH($X^2\Pi$) + H channel is negligibly small. Ignoring the H₂-elimination pathways, a total of four dissociation channels are energetically allowed in the photolysis of H₂S at 121.6 nm: (i) SH($X^2\Pi$) + H, (ii) SH($A^2\Sigma^+$) + H, (iii) S(3P) + H + H, and (iv) S(1D) + H + H with a kinetic energy limit of 6.29, 2.49, 2.65 and 1.50 eV, respectively. The latter two channels (i.e. the three-body dissociation) produce two H-atoms either in a concerted or stepwise process. The $A^2\Sigma^+$ state of SH is of predissociative character which hinders the investigation of $A^2\Sigma^+$ state by fluorescence detection.^{66–70} Hence, each SH($A^2\Sigma^+$) fragment produced via channel (ii) will subsequently decompose into S(3P) + H and/or S(1D) + H, and these “secondary” H-atoms will also contribute to the TOF spectrum together with the “primary” hydrogens.

The title reaction was studied by the Doppler-selected TOF technique to be compared with Schnieder’s results⁶⁵ recorded by the Rydberg tagging

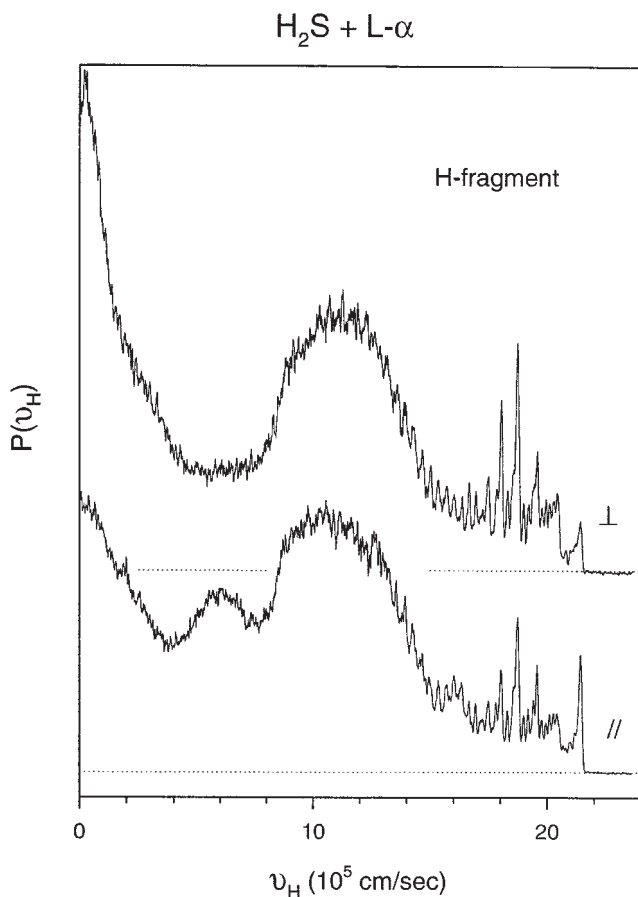


Fig. 10. Velocity distributions of the H-atom fragment recorded at perpendicular (\perp) and parallel (\parallel) configurations in the reaction of H_2S photolysis. For clarity, the perpendicular one is shifted up but not normalized and the base lines for both cases are indicated by dotted lines.

technique. Since our data has never been published anywhere else, more details will be given here. Figure 10 shows the recoil velocity distribution of the H-atom recorded with the laser polarization either parallel or perpendicular to the TOF axis. Both TOF spectra are displayed in the density form, but not yet normalized to each other for a clear representation. Also shown in Fig. 11 are the translational energy distribution and anisotropic parameter distribution derived from Fig. 10 according to Eqs. (16) and (17), respectively. Though the center-of-mass translational energy distribution is quite straightforward for a two-body dissociation

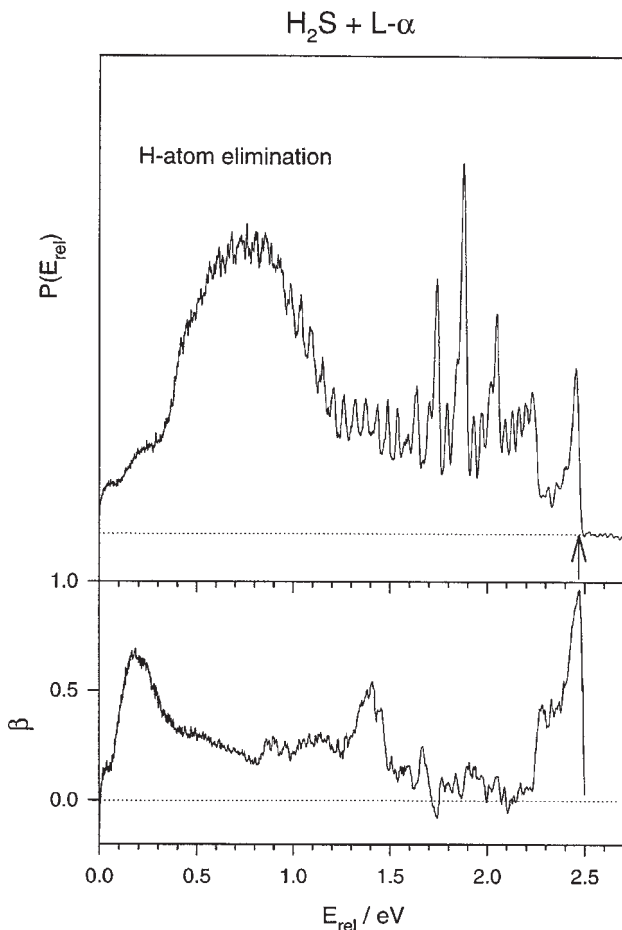


Fig. 11. Photofragment translational energy distribution (upper panel) and anisotropy distribution (lower panel) for the photolysis of H_2S . The arrow in the upper panel marks the energetic onset for the generation of $\text{SH}(A^2\Sigma^+, v') + \text{H}$.

according to the conservation of linear momentum, it becomes troublesome as the fragment undergoes a secondary reaction, i.e. three-body dissociation. As aforementioned, at 121.6 nm excitation, a $\text{SH}(A^2\Sigma^+)$ fragment may decompose into S and H atoms following the primary dissociation of H_2S to $\text{SH}(A^2\Sigma^+) + \text{H}$. Because of the small difference in the energy release ratio $\sim 10^{-3}$ for primary to secondary H-atoms, the total photofragment translational energy distribution shown in Fig. 11 was approximated

by an assumption of two-body dissociation to $\text{SH} + \text{H}$ products. This translational-energy spectrum is in good agreement with Fig. 2 of Ref. 65, though the energy resolution ($\sim 0.5 \text{ kcal/mol}$) in the present work is somewhat less than that ($\sim 0.3 \text{ kcal/mol}$) by the Rydberg-tagging technique. Indicated in Fig. 12 is the assignment of rovibrational states of the SH co-fragment. The sharp peak at 2.46 eV indicates an unambiguous onset of $\text{SH}(A^2\Sigma^+) + \text{H}$ fragmentation process. The undetectably small signal for any faster H -atom implies the dissociation to electronic ground state $\text{SH}(X^2\Pi) + \text{H}$ is negligible. It implies the dissociation undergoes an adiabatic pathway to $\text{SH}(A^2\Sigma^+) + \text{H}$. Five vibrational states $v' = 0-4$ were marked on their onsets and more than forty rotational states of $v' = 0$ can be identified based on Schnieder's assignment.⁶⁵ The rovibrational state distribution of nascent $\text{SH}(A^2\Sigma^+)$ fragment has a maximum near the onset of $v' = 3$ while individual vibrational state exhibits an exponential-like distribution on its rotational states except for $v' = 1$ which seems to have a wider

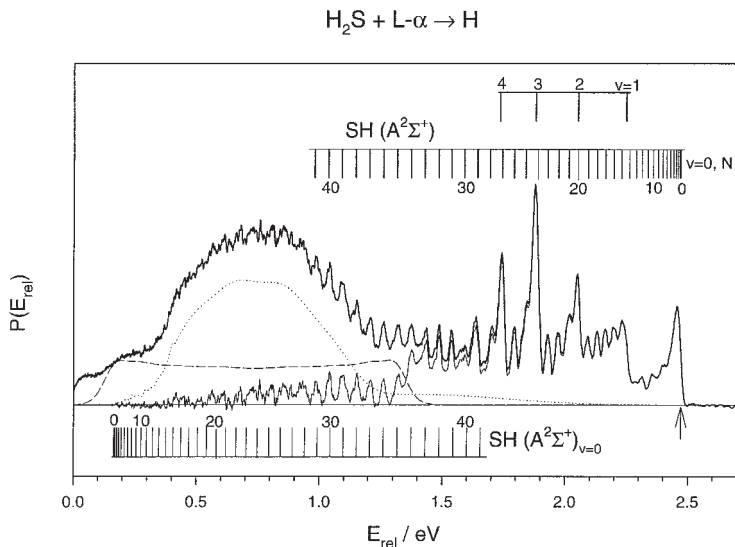


Fig. 12. Partitionings of hydrogen fragment translational energy distribution into three components. The solid line denotes the contribution from $\text{H}_2\text{S} \rightarrow \text{SH}(A^2\Sigma^+) + \text{H}$ which yields a resolved structure with a rovibrational state assignment on the top. The dotted line denotes the contribution of hydrogen from the $\text{SH}(A^2\Sigma^+) \rightarrow \text{S}(^3\text{P}) + \text{H}$ reaction, which is a reflection of the solid curve but the structure is smeared out. The corresponding rotational quantum numbers of the parent molecule $\text{SH}(A^2\Sigma^+)_{v=0}$ is marked on the bottom. The remaining part of the $P(E)$ spectrum is represented by the square-like dashed curve.

rotational distribution. On the other hand, a large broad hump superimposed with a series of small peaks is centered at 0.75 eV of the translational energy spectrum.

Shown in the lower panel of Fig. 11 is the recoil anisotropy of H-fragment which exhibits an intriguing distribution with kinetic energy. The β value near the onset of $v' = 0$ approaches ~ 1 and subsequently decreases with the increase of rotational quantum number of $\text{SH}(A^2\Sigma^+)$. The anisotropy remains oscillatory near zero in the region from 2.2 eV down to 1.5 eV (i.e. $1 \leq v' \leq 6$), whereupon the β value rises suddenly up to ~ 0.5 at 1.4 eV. Thereafter, β varies near a value of 0.25 with kinetic energy and goes up again to ~ 0.7 at kinetic energy 0.2 eV.

As mentioned by Schnieder *et al.*,⁶⁵ the predissociating $\text{SH}(A^2\Sigma^+)$ fragments are originally formed in a specific rovibrational state, i.e. each of which has a well-defined internal energy. Thus, the secondary H-atom resulting from $\text{SH}(A^2\Sigma^+)$ predissociation should in principle yield a spectrum which is essentially a “mirror image” of that structured part of the total kinetic energy spectrum which we have already attributed to $\text{H}_2\text{S} \rightarrow \text{SH}(A^2\Sigma^+) + \text{H}$. On the other hand, rotation of the SH fragment prior to predissociation can blur out this anticipated structure. Inspection of Fig. 12 indicates the total signal of the structureless part is greater than the structured part, thus we partitioned this $P(E)$ spectrum into three components: the contribution from the $\text{H}_2\text{S} \rightarrow \text{SH}(A^2\Sigma^+) + \text{H}$ reaction is denoted by a structured solid line, the kinetic energy distribution of the H-atom resulting from the subsequent predissociation $\text{SH}(A^2\Sigma^+) \rightarrow \text{S}(^3\text{P}) + \text{H}$ is represented by the dotted line which is a rough mirror-image of the solid curve, and the remainder is marked by the dashed line. The third component is also required to account for the angular distribution. In the first component, the decrease in the recoil anisotropy with the increase in fragment vibration can be accounted for by the bending motion of the triatomic molecule.⁷¹ The anisotropic parameter of secondary hydrogen atoms is anticipated to be much less than that of the primary hydrogen atoms owing to the wide range of orientations of predissociating SH fragments. Thus, it is speculated that the third component presumably has a relatively large β value which is averaged with the second component ($\beta \sim 0$) and yields a resultant $\beta \sim 0.2$. This third component is tentatively attributed to a concerted triple fragmentation of H_2S to $\text{S}(^3\text{P}, ^1\text{D}) + \text{H} + \text{H}$, but further investigation is required.

Compared to the analogous photodissociation of H_2O of the \tilde{B}^1A_1 state at 121.6 nm,^{72,73} it was found that $\text{OH}(X)$ product dominates the

dissociation yields though $\text{OH}(A)$ product was also observed. The discrepancy from H_2S dissociation is attributed to the efficient nonadiabatic transition from the \tilde{B} state of H_2O to its lower-lying electronic states. An intriguing finding, an oscillation on the rotational distribution of the $\text{OH}(X, v' = 0)$ product, also supports this suggestion.⁷² A theoretical calculation⁷³ has verified that these oscillations originate from the dynamical interference between HO-H and H-OH nonadiabatic dissociation pathways. The striking difference in the product branching ratio of H_2S from that of H_2O can be rationalized from inspections of their PESs. The electronic ground state of H_2O has a bent geometry with an angle of 105° . After a vertical transition to the Franck-Condon region of the \tilde{B} surface, the H_2O molecule is directed towards the potential well (near linear geometry) where surface hopping occurs through a conical intersection to the electronic ground state and then leads to a dissociation to $\text{OH}(X) + \text{H}$. As to H_2S , its ground state has a smaller equilibrium angle $\sim 92^\circ$. It is proposed that at 121.6 nm excitation H_2S is reflected into a Franck-Condon region of the excited Rydberg state where the potential gradient does not direct H_2S to the conical intersection region. Hence, nonadiabatic transition to the electronic ground state is minor as compared to the dissociation to $\text{SH}(A) + \text{H}$. Alternatively, the underlying continuous absorption of H_2S around 121.6 nm has been suggested to be the Rydberg state transition $\tilde{B}^1A_1 - \tilde{X}^1A_1(4sa_1/6a_1^* - 5a_1)$ based on the *ab initio* calculations.⁷⁴⁻⁷⁶ The PES of the \tilde{B}^1A_1 state calculated by Flouquet⁷⁷ has a conical intersection with the ground state at a linear geometry as H_2O whereas in contrast the potential gradient near the Franck-Condon region ($\sim 92^\circ$) does not favor directing H_2S towards a linear configuration so as to hinder nonadiabatic dissociation to $\text{SH}(X) + \text{H}$.

3.2. Crossed-Beam Reaction Dynamics

3.2.1. $\text{S}(^1\text{D}) + \text{H}_2 \rightarrow \text{SH} + \text{H}$

Analogous to the reaction of $\text{O}(^1\text{D}) + \text{H}_2$, the interaction of the divalent $\text{S}(^1\text{D})$ atom with H_2 molecule leads to the reaction complex of H_2S on the ground PES through the insertion mechanism, in contrast to the 121.6-nm photolysis of H_2S on the excited PES. The reaction products are formed via a subsequent complex decomposition to $\text{SH}(X^2\Pi) + \text{H}$. The well-depth of reaction complex H_2S , 118 kcal/mol is greater than H_2O , 90 kcal/mol as referenced to their product channels. The exoergicity for $\text{S} + \text{H}_2$, however, is 6-7 kcal/mol, substantially smaller than that for $\text{O} + \text{H}_2$, ~ 43 kcal/mol.

Because of the deep potential well and small exoergicity, conventional wisdom will then predict a long-lived complex being involved in the title reaction and the statistical behavior might be borne out.^{1,22,23}

Figure 13(a) shows typical Doppler profiles of the H-atoms from the title reaction at $E_c = 2.24$ and 3.96 kcal/mol.²⁵ The lower energy profile shows a flat top, whereas a prominent double-hump profile is seen at higher energy. The Doppler profiles of the H-atom product span over 6 cm^{-1} in width. Also marked in this figure is the location of the center-of-mass frequency for the $^2\text{P}_{3/2} \leftarrow ^2\text{S}_{1/2}$ transition of the hydrogen atom. In both cases, a slight preference for forward scattered products is discernible. Note that the direction of the hydrogen product being detected is referred to the center-of-mass direction of the reactant H_2 from which the H-atom originates. Figure 13(b) shows a few examples of Doppler-selected TOF spectra for 2.24 kcal/mol (left panel) and for 3.96 kcal/mol (right panel).²⁵ The spectra have been converted into velocity space and for clarity only every other data point is shown. Clear steps and fine-structure features are vividly observed, and their appearance and position are sensitive to the initial v_z selection. The TOF measurements were performed for a total of 33 equally spaced Doppler selections to cover the entire Doppler profiles. After complications arising from the H-atom Lyman- α doublet were removed, the combination of these data yields the direct mapping of the product 3D velocity distribution. The resulting 3D representations of the velocity-flux contour maps for the two collision energies are displayed in Fig. 14. Apparently the contours are quite symmetric, and highly polarized in the forward-backward directions. The degree of polarization becomes more pronounced with the increase in collision energy. Although a nearly symmetric angular distribution for the present reaction cannot be regarded as conclusive evidence for a reaction with long-lived intermediate complex,⁷⁸ it is entirely consistent with the insertion mechanism.

By integrating the doubly differential cross-section over the full speed or angle range for each contour, the product angular distribution $I(\theta)$ or translational energy distribution $P(E_t)$ can be obtained and shown in Fig. 15.²⁵ The product $P(E_t)$ distributions are rather broad at both collision energies, and the vibrational structures of SH are also apparent as can be compared with the stick marks shown on top. The angular distributions are fairly symmetric. Both the slight forward-preference at the two energies and the more polarized distribution at higher collision energy, as noted early, are readily observed. In terms of the fraction of the average translational energy release, $\langle f_t \rangle$, a small variation with the center-of-mass scattering angle can

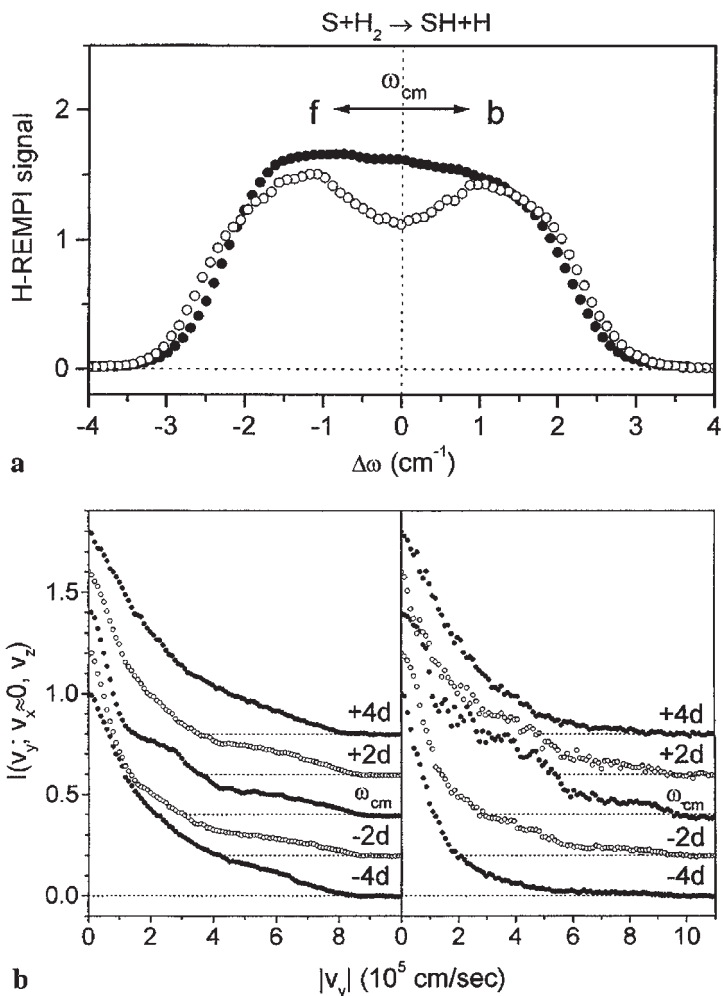


Fig. 13. (a) Doppler profiles for the $S(^1D) + H_2$ reaction at 2.24 kcal/mol (\bullet) and 3.96 kcal/mol (\circ), obtained under the parallel configurations. The vertical dotted line marks the partition between the forward (f) and backward (b) hemispheres for the $^2S_{1/2} \rightarrow ^2P_{3/2}$ transition of the H-atom Lyman- α doublet. (b) A few Doppler-selected TOF spectra of H-atom obtained under the ion extraction field of 1.95 V/cm, the left (right) panel is for 2.24 (3.96) kcal/mol. The label " ω_{CM} " corresponds to the VUV laser frequency that slices through the Newton sphere near the center-of-mass of $^2S_{1/2} \rightarrow ^2P_{3/2}$ transition as marked in panel (a). The label "d" represents the separation of doublet transitions 0.365 cm^{-1} in frequency or $1.335 \times 10^5 \text{ cm/s}$ in speed.

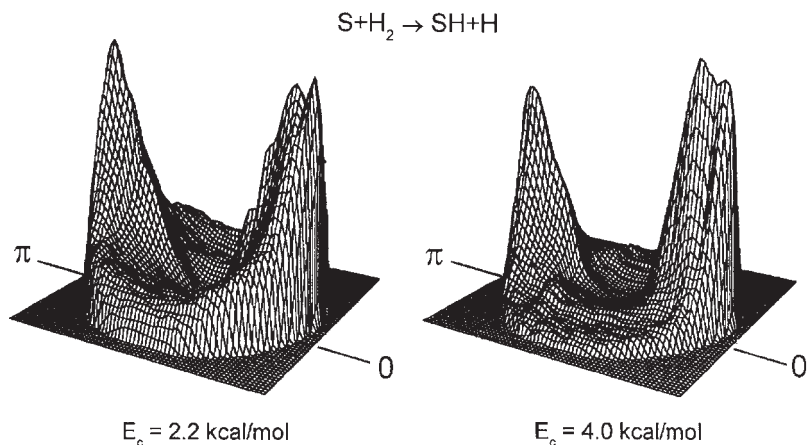


Fig. 14. 3D representation of the H-atom velocity flux contour, $d^2\sigma/dvd(\cos\theta)$. The contours are constructed directly from a total of 33 slices of the Doppler-selected TOF measurements.

be seen. This quantity, $\langle f_t \rangle_\theta$, gives a quantitative measure of the coupling of the product angular and speed distributions. The angle-integrated fractions of kinetic energy release are 0.48 and 0.45 for $E_c = 2.24$ and 3.96 kcal/mol, respectively.

A more informative way to reveal the detailed dynamics afforded by this direct 3D mapping approach is to examine the angle-specific kinetic energy distribution over a limited range of $\Delta\theta$. The results for the two energies are presented in Fig. 16.²⁵ For convenience, they are displayed as a function of $E_{\text{int}} = E_{\text{total}} - E_t$ through energy conservation such that the energetic marks shown in the $0\text{--}15^\circ$ panel apply to all other panels and for both collision energies. Several interesting observations are worth noting. First, the products scattered in different angles clearly display different internal energy distributions. That is a manifestation of the coupling between angle and speed distribution. Second, whereas the global angular distributions are fairly symmetric at both collision energies, the detailed $P(E_{\text{int}}; \Delta\theta)$ distributions behave differently for the two cases. At $E_c = 2.24$ kcal/mol, the f-b symmetry is roughly retained, for example comparing the shape of $P(E_{\text{int}})$ at $0\text{--}15^\circ$ to that at $165\text{--}180^\circ$. At slightly higher energy of 3.96 kcal/mol, such a f-b symmetry apparently breaks down. Third, the vibrational structures in most of the panels can readily be identified by inspections of the $P(E_{\text{int}})$ shape in each panel with respect to the energetic onsets for $\text{SH}(v')$. Since the $P(E_{\text{int}})$ distributions at two energies have been normalized to their integral cross-sections, it becomes apparent that

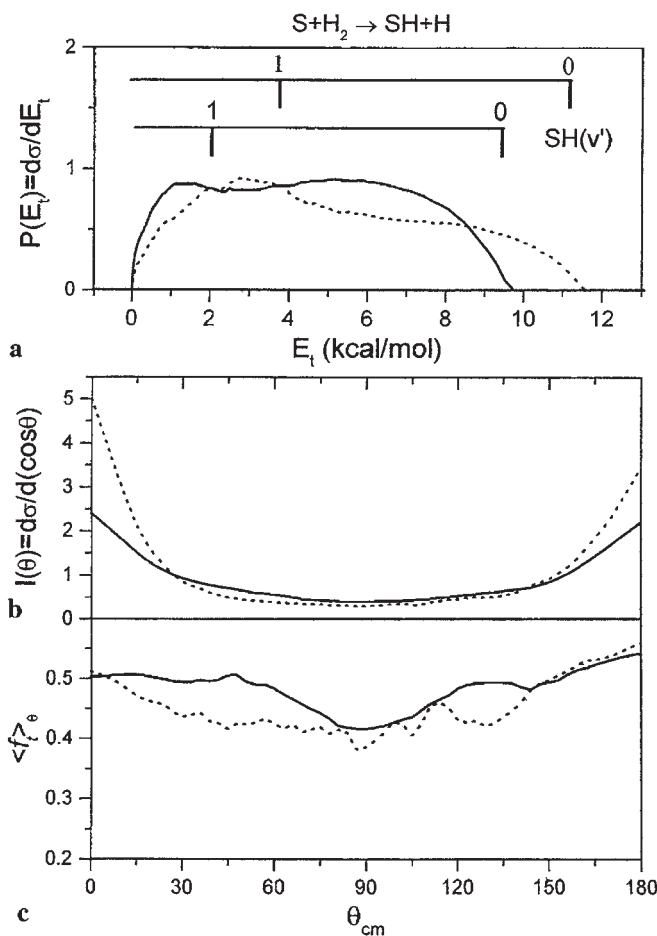


Fig. 15. (a) Product translational energy distributions, (b) product center-of-mass angular distributions, and (c) fractions of the average translational energy release for 2.24 kcal/mol (solid lines) and 3.96 kcal/mol (dashed lines). Also marked in panel (a) is the onset of the vibrational state of the SH product.

with the increase in collision energy, there is a dramatic variation in product state distributions and this variation depends sensitively on scattering angles. Furthermore, some distinct fine structures near sideward direction are seen, which correspond to partially-resolved (high- j') rotational states of the $SH(v' = 0)$ products. Further data analysis and their dynamical implications are beyond the scope of this chapter, the interested reader is referred to the original articles.

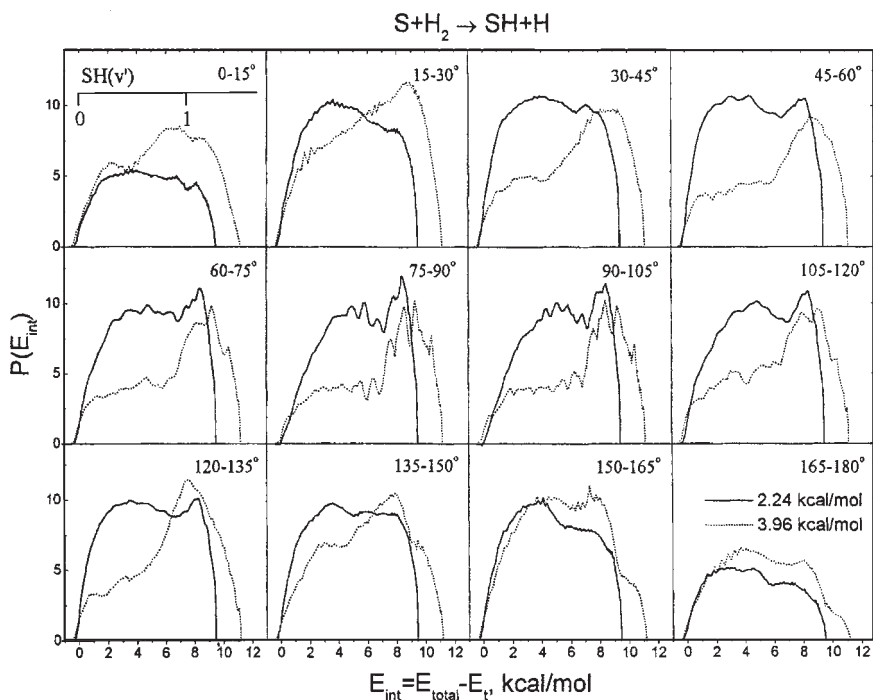


Fig. 16. Angle-specific internal energy distribution of the SH product over every 15° angular segment. The results for the two energies have been normalized to their integral cross-sections (see Fig. 15). The energetic onset of the vibrational state of SH is only shown in the $0\text{--}15^\circ$ panel, though it applies to all other angular segments.

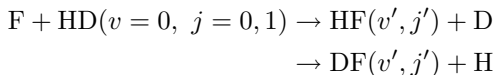
3.2.2. $\text{F}(^2\text{P}) + \text{HD} \rightarrow \text{HF} + \text{D}$

The $\text{F} + \text{H}_2 \rightarrow \text{HF} + \text{H}$ reaction is one of the most studied chemical reactions in science, and interest in this reaction dates back to the discovery of the chemical laser.⁷⁹ In the early 1970s, a collinear quantum scattering treatment of the reaction predicted the existence of isolated resonances.⁸⁰ Subsequent theoretical investigations, using various dynamical approximations on several different potential energy surfaces (PESs), essentially all confirmed this prediction. The term “resonance” in this context refers to a transient metastable species produced as the reaction occurs. Transient intermediates are well known in many kinds of atomic and molecular processes, as well as in nuclear and particle physics.⁸¹ What makes reactive resonances unique is that they are not necessarily associated with trapping

in potential energy wells, but can be localized near the repulsive barrier (or transition state) region of the Born–Oppenheimer PES.

There have been numerous attempts to observe this intriguing phenomenon. In 1985, a molecular beam study by Lee and co-workers^{82,83} revealed an anomalous forward scattering peak in the vibrationally state-resolved angular distribution which was attributed to a resonant mechanism. However, the evidence for reactive resonance in the beam experiments was not conclusive since there are other possible dynamical explanations for the forward scattering peak that could not be ruled out.^{84,85} More recent attempts^{86,87} to locate resonances have employed the techniques of transition-state spectroscopy to probe the dynamics near the transition state via the photodetachment spectrum of FH_2^- . While spectral peaks were observed, the available level of energy resolution was not sufficient to distinguish reactive resonance peaks from other phenomena.

In this study, we focus on the reaction



at collision energies, $E_c = 0.2\text{--}5$ kcal/mol. The choice of the $\text{F} + \text{HD}$ reaction for this study is based on the anticipated resonance hierarchy⁸³: $(\text{F} + \text{HD} \rightarrow \text{HF} + \text{D}) > (\text{F} + \text{H}_2 \rightarrow \text{HF} + \text{H}) > (\text{F} + \text{D}_2 \rightarrow \text{DF} + \text{D}) > (\text{F} + \text{HD} \rightarrow \text{DF} + \text{H})$. In other words, resonance effects are expected to be most (least) pronounced for the $\text{HF} + \text{D}$ ($\text{DF} + \text{H}$) product channel in the very same $\text{F} + \text{HD}$ reaction, because these product channels are kinematically the most (least) constrained. The investigation of both isotopic product channels therefore provides a convenient internal “calibration” in the search for the experimental signatures of a resonance.

Indeed, several identifiable resonance fingerprints in experimental observables were found.^{26–31} Concurrent theoretical simulations and analyses not only confirmed the experimental conjectures, but also provided deeper insights into the nature of this resonance state. For the integral cross-sections, a distinct step for $E_c \leq 1$ kcal/mol was observed in the reactive excitation function (i.e. the translation energy dependence of the reactive cross-section) for the $\text{HF} + \text{D}$ product channel, whereas it is totally absent for the other $\text{DF} + \text{H}$ product channel.²⁶ Anomalous collision energy dependence of the HF vibration branching was also observed.²⁸ For $E_c \leq 1$ kcal/mol more than 90% of the HF products are populated in the $v' = 2$ state. However, as the energetic threshold for the formation of $\text{HF}(v' = 3)$ from

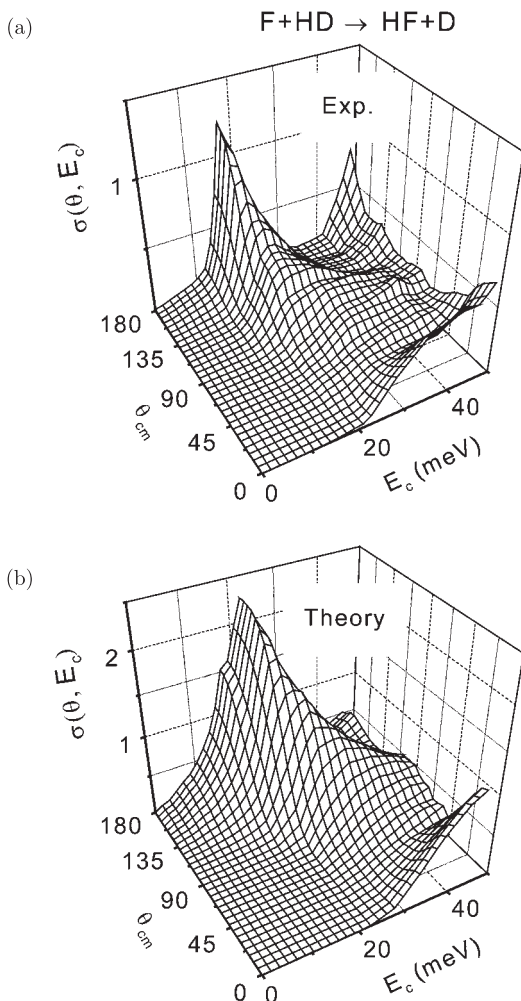


Fig. 17. Total differential cross-section for the $F + HD \rightarrow HF + D$ reaction in the low energy region. (a) shows the experimental results while (b) presents QM. A prominent ridge circumventing the upper corner appears in both experimental and theoretical results.

$F(^2P_{3/2}) + HD$, which occurs at $E_c = 1.16$ kcal/mol, is reached, a sudden drop (growth) of the $v' = 2$ ($v' = 3$) branching was observed. In fact, the vibration state-specific excitation functions displayed two distinctive features: a steplike feature span from 0.2 to 1 kcal/mol was detected for

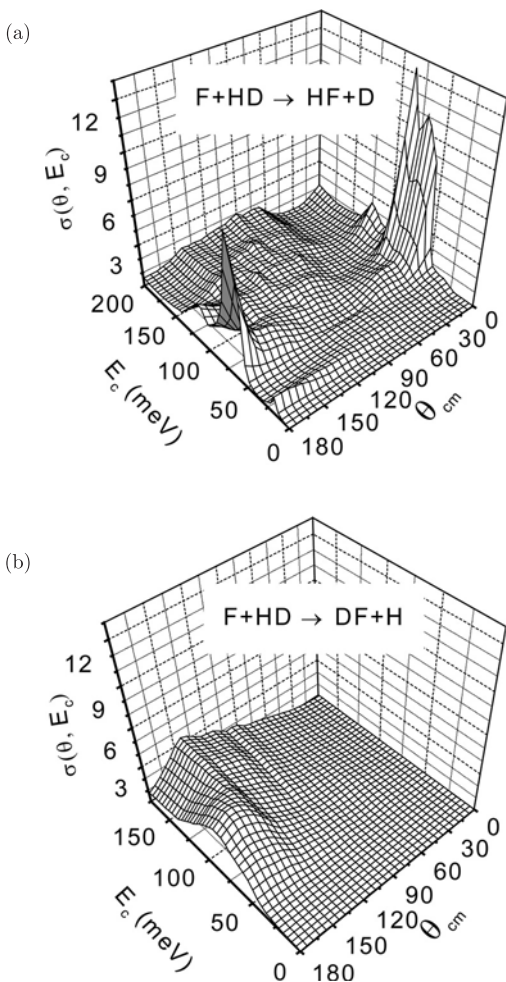


Fig. 18. The experimental total differential cross-section for the $F + HD$ reaction over the full range of collision energies.

$HF(v' = 2)$, and a broad peak feature for $HF(v' = 3)$ starting from its energetic threshold to about 3 kcal/mol.

In the context of the present chapter, only the differential cross-section (DCS) results will be reviewed.^{27,31} The DCS obtained by experiment and theory²⁷ are shown in Figs. 17–19. In Fig. 17 we show the experimental total angular distributions, $d\sigma/d\Omega$, around the 0.5 kcal/mol feature obtained by summing over all (v', j') states of the HF products. (The resolution was sufficiently high to resolve most of the product rovibrational states for $j' \geq 4$

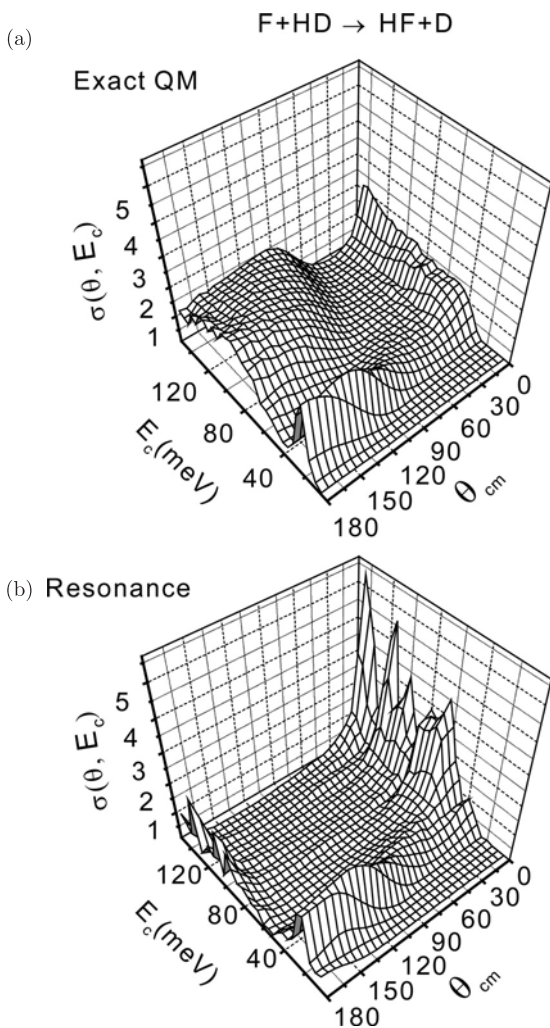


Fig. 19. The computed differential cross-section for $\text{F} + \text{HD} \rightarrow \text{HF} + \text{D}$. (a) is the result of QM while (b) is the pure resonance contribution.

in the DCS.) The product angular distribution starts as backward peaked near the threshold. With increasing collision energy, a dramatic and systematic shift towards the sideways direction is observed. At the same time, a forward peak starts to develop. By 1.18 kcal/mol, it evolves into a predominantly forward-backward peaked distribution. As a result, a ridge which starts at $\theta = 180^\circ$ at 0.4 kcal/mol and moves to about 90° at 1 kcal/mol

was clearly visible in the angle-energy plot. Based on theoretical considerations, Zhang and Miller⁸⁸ have predicted such a ridge to be the signature of a resonance. However, Aoiz *et al.*⁸⁹ subsequently found a similar ridge in a QCT simulation of the $D + H_2$ reaction, and thus it was not conclusive evidence of a resonance. In any event, the striking variation of the angular distributions of reaction products over such a narrow energy range is unprecedented in any previous molecular beam experiment, and is entirely consistent with what we would expect from a resonant mechanism.^{82,83}

In Fig. 18 the experimental differential cross-section $\sigma(\theta, E_c)$ is displayed over an extended energy range for both isotopic product channels. An oscillatory forward-backward peaking in the $HF + D$ distribution is quite apparent. These peaks actually show a rapid exchange of flux as a function of collision energy. In the $DF + H$ channel, the distribution is smoother and localized in a broad swathe in the backward hemisphere. An analogous swathe is also observed in the $HF + D$ channel. From the excitation function results, we know that the $DF + H$ channel is dominated by direct reaction. In terms of the differential cross-section, it is therefore reasonable to conclude that the broad swathe is characteristic of direct reaction. If this conclusion is extended to the $HF + D$ channel, the swathe in this channel is also direct. It is then conjectured that the remaining ridge structure, at low energy, and the highly oscillatory forward-backward peaking, at higher energy, are the fingerprints of the resonant scattering.

Figure 19(a) shows the QM simulation of the differential cross-section (DCS) in the $HF + D$ channel, over the same extended energy range as in Fig. 5. The agreement with experiment is seen to be qualitatively reasonable. The forward-backward peaking and direct reaction swathe observed in the experiment also occur in the QM calculation, although the relative magnitudes are not consistent. Thus fully quantitative agreement between QM calculations and experiment in all of the reaction attributes must await further refinements of the PES, and/or a more rigorous treatment of the open-shell character of the $F(^2P)$ atom.⁹⁰

One property of the $F + HD$ reaction which is particularly unique is the nearly complete absence of direct reaction pathway at energies below about $E_c = 1$ kcal/mol.^{26,27,31} At these low energies the reaction, and all of its observable characteristics, is mediated through a reactive resonance. The total DCS presented so far is a highly averaged quantity, the actual data obtained from the Doppler-selected TOF measurement is however the state-to-state DCS. To illustrate the effect of reactive resonance at the state-to-state level of details, let us focus on the low energy reaction. Figure 20

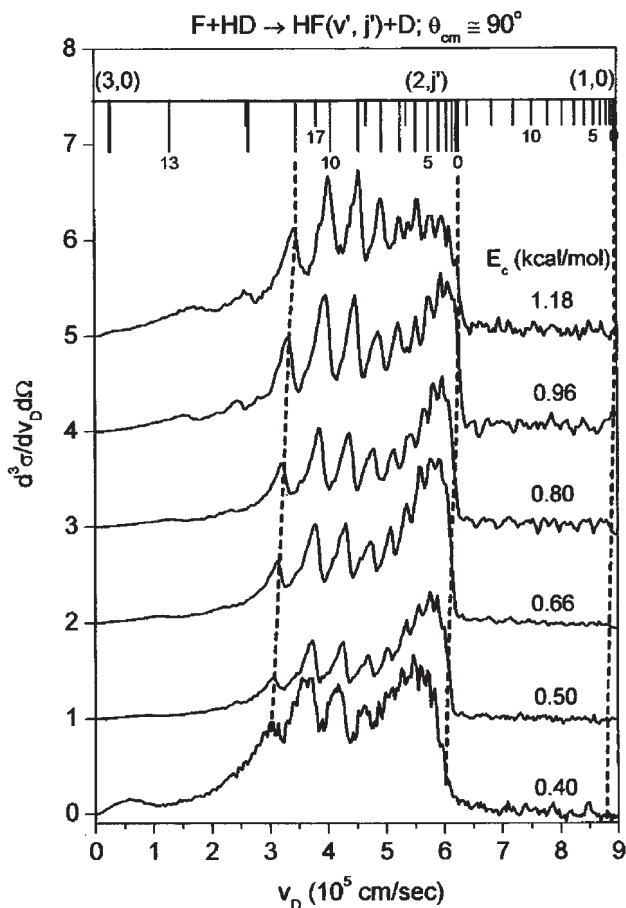


Fig. 20. A few examples of the Doppler-selected TOF data are exemplified. The TOF spectra have been converted into velocity space and weighted by a v_D^2 term. For each spectrum, the VUV laser frequency is selected to slice through the Newton sphere near the center-of-mass, i.e. ω_{CM} . The cap marked on the top corresponds to the (v', j') state of the co-product HF for $E_c = 1.18$ kcal/mol. Note the slight tilt of the dashed lines which act as a visual guide for quantum state assignments.

shows a series of TOF data.³¹ For each spectrum the Doppler slice was selected near ω_{CM} so that it corresponds directly to DCS along $\theta_{CM} \cong 90^\circ$. The raw TOF spectrum has been converted into the speed distribution by a v_D^2 weighting term. Because of that, the small background-subtracted noises are greatly amplified at the larger v_D region. The sticks marked on the top are the calculated HF(v', j') positions for $E_c = 1.18$ kcal/mol,

based on the well-established energetics of this system. The observed peaks can readily be identified as the rotational state distribution of $\text{HF}(v' = 2)$. Similar peaks for the lower E_c 's can also be assigned. The dotted lines act as a visual guide for peak assignment. The lines are slightly slanted (i.e. not exactly vertical) as a result of the small differences in collision energies, i.e. the total available energies.

The relationship between the measured quantity and the desired center-of-mass differential cross-section, and the data analysis procedure have been given above. By combining all ~ 28 TOF spectra over the entire Doppler profile for each E_c , the desired 3D contour map of the product flux-velocity distribution can be constructed. For clarity and to highlight the most prominent feature, the low-resolution (i.e. larger grid-size) contours are presented in Fig. 21. The qualitative variations in angular distributions as inferred from Doppler profiles are now quantitatively and more vividly revealed. Indeed, the change of angular distributions with a small change in E_c is quite dramatic. In addition, there are striking oscillations in angular distributions and these oscillations appear to vary systematically with the increase in E_c 's.

Similar state-to-state DCSs have been obtained for the entire energy range of this reaction. Clearly, the information is overloaded! Studies on such vast amounts of data and their dynamical implication are still in progress.

4. Outlook

The Doppler-selected TOF technique is one of the laser-based techniques for measuring state-specific DCSs.³⁰ It combines two popular methods, the optical Doppler-shift and the ion TOF, in an orthogonal manner such that in conjunction with the slit restriction to the third dimension, the desired center-of-mass three-dimensional velocity distribution of the reaction product is directly mapped out. Using a commercial pulsed dye laser, a resolution of $\sim 1\%$ has been achieved. As demonstrated in this review, such a resolution is often sufficient to reveal state-resolved DCSs.

Compared to the H-atom Rydberg tagging technique,⁶⁵ the resolution of the present method is somewhat worse, by about a factor of two. This loss in resolution, however, is realized in general only for photodissociation studies. In a typical crossed beam experiment, the product translational energy resolution is usually limited by the energy spread of the initial collision energy rather than the detection scheme. On the other hand, the present

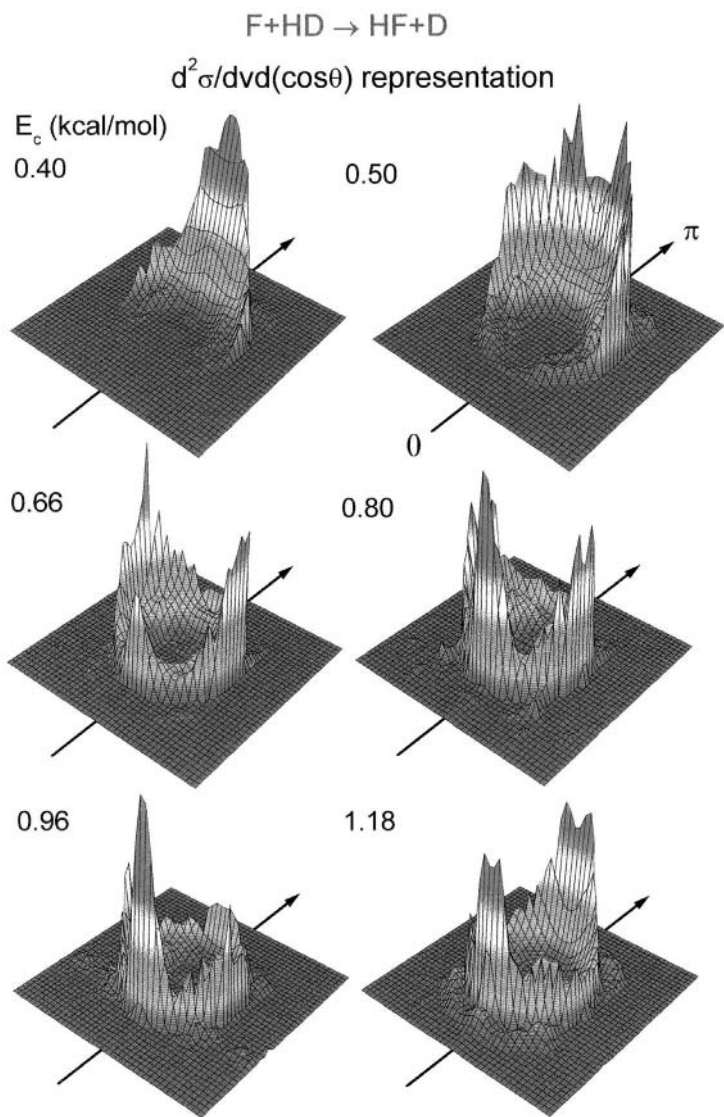


Fig. 21. The product D-atom velocity-flux contour map, $d^2\sigma/dv d(\cos\theta)$, in a 3D isometric representation. Each contour is constructed directly from a total of ~ 28 slices of the Doppler-selected TOF measurements, as exemplified in Fig. 20. For clarity, a coarse grid size is used here. The zero degree is defined as the initial center-of-mass velocity of the HD beam from which the D-atom product is originated. Note the dominance of the $HF(v' = 2)$ co-product for all cases, yet the dramatic variations in angular distributions with a slight change in collision energy (~ 0.1 kcal/mol!).

method has the advantages of generality (applicable to any species which can be detected by REMPI) and simplicity in setup and data analysis. The interested reader is referred to Ref. 30 and other chapters of this book for more detailed comparisons between these two techniques, as well as with the powerful 2D ion imaging technique, for DCS measurements. The concept of a direct center-of-mass 3D mapping, on which the Doppler-selected TOF technique is based, can be put forward further by integrating the time-focusing technique with the velocity mapping of the 2D ion imaging method^{91,92} to form a true 3D imaging technique.⁹³ This new approach will have the multiplexing advantage over the Doppler-selected TOF approach, while retaining the generality and simplicity. More importantly, in principle, it should have sufficient resolution to reveal state-specific DCSs for many polyatomic reactions. Preliminary data have recently been obtained in this laboratory using this new 3D velocity imaging technique, and the results are very promising.^{94–97}

Acknowledgments

The authors thank the past co-workers and colleagues, late Mr. Yen-Tsung Hsu, Mr. Jeng-Han Wang, Dr. Dock-Chil Che, Dr. Lih-Huey Lai, and Dr. Feng Dong for their efforts and contributions to the works described here. The theoretical collaborations with Professors George C. Schatz, David E. Manolopoulos and Rex T. Skodje are also gratefully acknowledged. The financial supports were provided by the National Science Council of Taiwan and the China Petroleum Corporation.

References

1. R. D. Levine and R. B. Bernstein, *Molecular Reaction Dynamics and Chemical Reactivity* (Oxford University Press, New York, 1987).
2. Y. T. Lee, *Science* **236**, 793 (1987).
3. J. L. Kinsey, *J. Chem. Phys.* **66**, 2560 (1977).
4. J. M. Mestdagh, J. P. Visticot and A. G. Suits, in *The Chemical Dynamics and Kinetics of Small Radicals*, ed. K. Liu and A. Wagner (World Scientific, 1995) Part II, Chapter 16.
5. G. E. Hall and P. L. Houston, *Annu. Rev. Phys. Chem.* **40**, 405 (1989).
6. W. C. Wiley and I. H. McLaren, *Rev. Sci. Instrum.* **26**, 1150 (1955).
7. M. Mons and I. Dimicoli, *Chem. Phys. Lett.* **131**, 298 (1986).
8. D.-C. Che and K. Liu, *J. Chem. Phys.* **103**, 5164 (1995).
9. D.-C. Che and K. Liu, *Chem. Phys.* **207**, 367 (1996).
10. L.-H. Lai, D.-C. Che and K. Liu, *J. Phys. Chem.* **100**, 6376 (1996).
11. J.-H. Wang, Y.-T. Hsu and K. Liu, *J. Phys. Chem.* **A101**, 6593 (1997).

12. J.-H. Wang and K. Liu, *J. Chem. Phys.* **109**, 7105 (1998).
13. J.-H. Wang, K. Liu, Z. Min, H. Su, R. Bersohn, J. Preses and J. Z. Larese, *J. Chem. Phys.* **113**, 4146 (2000).
14. L.-H. Lai, Y.-T. Hsu and K. Liu, *Chem. Phys. Lett.* **307**, 385 (1999).
15. L.-H. Lai, J.-H. Wang, D.-C. Che and K. Liu, *J. Chem. Phys.* **105**, 3332 (1996).
16. J.-H. Wang, K. Liu, G. C. Schatz and M. ter Horst, *J. Chem. Phys.* **107**, 7869 (1997).
17. Y.-T. Hsu, J.-H. Wang and K. Liu, *J. Chem. Phys.* **107**, 2351 (1997).
18. Y.-T. Hsu and K. Liu, *J. Chem. Phys.* **107**, 1664 (1997).
19. Y.-T. Hsu, K. Liu, L. A. Pederson and G. C. Schatz, *J. Chem. Phys.* **111**, 7921 (1999); *ibid.* **111**, 7931 (1999).
20. P. Hermine, Y.-T. Hsu and K. Liu, *Phys. Chem. Chem. Phys.* **2**, 581 (2000).
21. S.-H. Lee and K. Liu, *J. Chem. Phys.* **111**, 4351 (1999).
22. S.-H. Lee and K. Liu, *Chem. Phys. Lett.* **190**, 323 (1998); erratum, *ibid.* **317**, 516 (2000).
23. S.-H. Lee and K. Liu, *J. Phys. Chem.* **A102**, 8637 (1998).
24. S.-H. Lee and K. Liu, in *Atomic and Molecular Beam: The State of the Art 2000*, ed. R. Campargue (Springer, 2001), pp. 543–553.
25. S.-H. Lee and K. Liu, *Appl. Phys.* **B71**, 627 (2000).
26. R. T. Skodje, D. Skouteris, D. E. Manolopoulos, S.-H. Lee, F. Dong and K. Liu, *J. Chem. Phys.* **112**, 4536 (2000).
27. R. T. Skodje, D. Skouteris, D. E. Manolopoulos, S.-H. Lee, F. Dong and K. Liu, *Phys. Rev. Lett.* **85**, 1206 (2000).
28. F. Dong, S.-H. Lee and K. Liu, *J. Chem. Phys.* **113**, 3633 (2000).
29. K. Liu, R. T. Skodje and D. E. Manolopoulos, *Phys. Chem. Comm.* **5**, 27 (2002).
30. K. Liu, *Annu. Rev. Phys. Chem.* **52**, 139 (2001).
31. S.-H. Lee, F. Dong and K. Liu, *J. Chem. Phys.* **116**, 7839 (2002).
32. S.-H. Lee, L.-H. Lai, K. Liu and H. Chang, *J. Chem. Phys.* **110**, 8229 (1999).
33. S.-H. Lee and K. Liu, *J. Chem. Phys.* **111**, 6253 (1999).
34. D. Skouteris, D. E. Manolopoulos, W. Bian, H.-J. Werner, L.-H. Lai and K. Liu, *Science* **286**, 1713 (1999).
35. F. Dong, S.-H. Lee and K. Liu, *J. Chem. Phys.* **115**, 1197 (2001).
36. R. G. Macdonald and K. Liu, *J. Chem. Phys.* **82**, 91 (1989).
37. R. Hilbig and R. Wallenstein, *IEEE J. Quantum Electronics*, **QE-17**, 1506 (1981).
38. S. Yang and R. Bersohn, *J. Chem. Phys.* **61**, 4400 (1974).
39. R. Schinke, *Photodissociation Dynamics* (Cambridge University Press, New York, 1993).
40. D. M. Sonnenfroh and K. Liu, *Chem. Phys. Lett.* **176**, 183 (1991).
41. C. Naulin, M. Costes, A. Benseddik and G. Dorthé, *Laser Chem.* **8**, 283 (1988).
42. L. Schnieder, K. Seekamp-Rahn, E. Wrede and K. H. Welge, *J. Chem. Phys.* **107**, 6175 (1997).
43. C. K. Ingold and G. W. King, *J. Chem. Soc. (London)* 2702 (1953).

44. K. K. Innes, *J. Chem. Phys.* **22**, 863 (1954).
45. M. Fujii, A. Haijima and M. Ito, *Chem. Phys. Lett.* **150**, 380 (1988).
46. A. Haijima, M. Fujii and M. Ito, *J. Chem. Phys.* **92**, 959 (1990).
47. N. Hashimoto and T. Suzuki, *J. Chem. Phys.* **104**, 6070 (1996).
48. P. D. Foo and K. K. Innes, *Chem. Phys. Lett.* **22**, 439 (1973).
49. M. Suto and L. C. Lee, *J. Chem. Phys.* **80**, 4824 (1984).
50. M. Herman and R. Colin, *Phys. Scr.* **25**, 275 (1982).
51. M. Herman and R. Colin, *J. Mol. Spectrosc.* **85**, 449 (1981).
52. C. Sandorfy, *Top. Curr. Chem.* **86**, 91 (1979).
53. C. Sandorfy, *J. Mol. Struct.* **19**, 183 (1973).
54. R. J. Buenker and S. D. Peyerimhoff, *Chem. Phys.* **36**, 415 (1975).
55. R. S. Mulliker, *Chem. Phys. Lett.* **46**, 197 (1977).
56. R. S. Mulliker, *Acc. Chem. Res.* **9**, 7 (1976).
57. A. M. Wodtke and Y. T. Lee, *J. Phys. Chem.* **89**, 4744 (1985).
58. B. A. Balko, J. Zhang and Y. T. Lee, *J. Chem. Phys.* **94**, 7958 (1991).
59. H. Masuko, Y. Morioka, M. Nakamura, E. Ishiguro and M. Sasanuma, *Can. J. Phys.* **57**, 745 (1979).
60. L. C. Lee, X. Wang and M. Suto, *J. Chem. Phys.* **86**, 4353 (1987).
61. M. D. Person, K. Q. Lao, B. J. Eckholm and L. J. Butler, *J. Chem. Phys.* **91**, 812 (1989).
62. B. R. Weiner, H. B. Levene, J. J. Valentini and A. P. Baronavski, *J. Chem. Phys.* **90**, 1403 (1989).
63. X. Xie, L. Schnieder, H. Wallmeier, R. Boettner, K. H. Welge and M. N. R. Ashfold, *J. Chem. Phys.* **92**, 1608 (1990).
64. X. Liu, D. W. Hwang, X. F. Yang, S. Harich, J. J. Lin and X. Yang, *J. Chem. Phys.* **111**, 3940 (1999).
65. L. Schnieder, W. Meier, K. H. Welge, M. N. R. Ashfold and C. M. Western, *J. Chem. Phys.* **92**, 7027 (1990).
66. D. A. Ramsay, *J. Chem. Phys.* **20**, 1920 (1952).
67. J. W. C. Johns and D. A. Ramsay, *Can. J. Phys.* **39**, 210 (1961).
68. J. J. Tiee, M. J. Ferris and F. B. Wampler, *J. Chem. Phys.* **79**, 130 (1983).
69. R. R. Friedl, W. H. Brune and J. G. Anderson, *J. Chem. Phys.* **79**, 4227 (1983).
70. G. W. Loge and J. J. Tiee, *J. Chem. Phys.* **89**, 7167 (1988).
71. H.-P. Looock, J. Cao and C. X. W. Qian, *Chem. Phys. Lett.* **206**, 422 (1993).
72. S. A. Harich, D. W. H. Hwang, X. Yang, J. J. Lin, X. Yang and R. N. Dixon, **113**, 10073 (2000).
73. R. N. Dixon, D. W. H. Hwang, X. F. Yang, S. A. Harich, J. J. Lin and X. Yang, *Science* **285**, 1249 (1999).
74. S. Shih, S. D. Peyerimhoff and R. J. Buenker, *Chem. Phys.* **17**, 391 (1976).
75. G. F. Diercksen and S. R. Langhoff, *Chem. Phys.* **112**, 227 (1987).
76. V. Galasso, *J. Phys.* **B22**, 2241 (1989).
77. F. Flouquet, *Chem. Phys.* **13**, 257 (1976).
78. R. J. Buss, P. Casavecchia, T. Hirooka, S. J. Sibener and Y. T. Lee, *J. Chem. Phys.* **82**, 386 (1981).
79. P. H. Corneil and G. C. Pimentel, *J. Chem. Phys.* **49**, 1379 (1968).

80. S.-F. Wu, R. B. Johnson and R. D. Levine, *Mol. Phys.* **25**, 839 (1973).
81. *Resonances in Electron-Molecule Scattering, van der Waals Complexes, and Reactive Chemical Dynamics*, ACS Symposium Series, ed. D. G. Truhlar (American Chemical Society, Washington, DC, 1984) Vol. 263.
82. D. M. Neumark, A. M. Wodtke, G. N. Robinson, C. C. Hayden and Y. T. Lee, *J. Chem. Phys.* **82**, 3045 (1985).
83. D. M. Neumark, A. M. Wodtke, G. N. Robinson, C. C. Hayden, K. Shobatake, R. K. Sparks, T. P. Schafer and Y. T. Lee, *J. Chem. Phys.* **82**, 3067 (1985).
84. F. J. Aoiz, L. Banares, V. J. Herrero, V. Saez Ravanos, K. Stark and H.-J. Werner, *Chem. Phys. Lett.* **104**, 6531 (1996).
85. J. F. Castillo, D. E. Manolopoulos, K. Stark and H.-J. Werner, *J. Chem. Phys.* **104**, 6531 (1996).
86. D. E. Manolopoulos, K. Stark, H.-J. Werner, D. W. Arnold, S. E. Bradforth and D. M. Neumark, *Science* **262**, 1852 (1993).
87. C. L. Russell and D. E. Manolopoulos, *Chem. Phys. Lett.* **256**, 465 (1996).
88. J. Z. H. Zhang and W. H. Miller, *J. Phys. Chem.* **95**, 12 (1991).
89. F. H. Aoiz, V. J. Herrero and V. Saez Rabanos, *J. Chem. Phys.* **97**, 7423 (1992).
90. M. H. Alexander, D. E. Manolopoulos and H.-J. Werner, *J. Chem. Phys.* **113**, 11084 (2000).
91. A. J. R. Heck and D. W. Chandler, *Annu. Rev. Phys. Chem.* **46**, 335 (1995).
92. A. T. J. B. Eppink and D. H. Parker, *Rev. Sci. Instrum.* **68**, 3477 (1997).
93. C. R. Gebhart, T. P. Rakitzis, P. C. Samartzis, V. Ladopoulos and T. N. Kitsopoulos, *Rev. Sci. Instrum.* **72**, 3848 (2001).
94. J. J. Lin, J. Zhou, W. Shiu and K. Liu, *Rev. Sci. Instrum.* **74**, 2495 (2003).
95. J. J. Lin, J. Zhou, W. Shiu and K. Liu, *Science* **300**, 966 (2003).
96. W. Shiu, J. J. Lin and K. Liu, *Phys. Rev. Lett.* **92**, 103201 (2004).
97. J. Zhou, W. Shiu, J. J. Lin and K. Liu, *J. Chem. Phys.* **120**, 5863 (2004).

CHAPTER 2

THE EFFECT OF REACTIVE RESONANCE ON COLLISION OBSERVABLES

Sheng Der Chao and Rex T. Skodje
Department of Chemistry and Biochemistry
University of Colorado, Boulder, CO 80309, USA

While the existence of reactive resonances has long been predicted based on theoretical quantum reaction dynamics, it has remained an open question as to how resonance phenomenon may be observed in a molecular beam experiment. Many of the simple ideas for resonance signature are based on the idealization of the isolated narrow resonance, which generally does not apply to reactive resonances. Due to the occurrence of impact parameter averaging, the resonant scattering becomes smeared over broad ranges of collision energy making it difficult to distinguish between direct and complex scattering mechanisms. In this chapter, recent advances in the study of short-lived reactive resonances are reviewed. The imprint of resonances upon dynamical observables is discussed. Three case studies are presented for simple triatomic systems that are believed to exhibit resonance phenomena: $F + HD \rightarrow D + HF$, $F + H_2 \rightarrow H + HF$, and $H + HD \rightarrow D + H_2$. It is seen that reactive resonances do strongly influence collision observables, but in a different way for each case. At this stage, there does not appear to be a unique resonance signature that can be applied to all reactions.

Contents

1. Introduction	44
2. Theoretical Methods for Resonance Phenomena	46
2.1. Integral Cross-Sections	52
2.2. Time Delay	53
2.3. Exponential Decay	56
2.4. Angular Product Distributions	57
2.5. Product Rovibrational Branching Ratios	59
3. Three Examples of Reactive Resonance	60
3.1. $F + HD \rightarrow HF + D$	60

3.2. $F + H_2$	67
3.3. $H + HD$	72
4. Conclusions	81
Acknowledgments	82
Note Added in Proof	82
References	82

1. Introduction

Simple chemical reactions are often divided into those that proceed directly over a transition state and those, which pass through an intermediate complex. Complex-forming reactions can thus be viewed as a two-step process involving formation and decay of the complex intermediate. Often times the occurrence of reactive complexes is completely predictable based on the existence of deep potential energy wells along the reaction coordinate. Ion-molecule reactions and insertion-type reactions are well known examples. When deep-well trapping occurs, the complex lifetimes are typically quite long, often hundreds of internal vibrational periods. This permits the “complex molecules” to be studied, at least in principle, as distinct chemical species from either the reactants or products. On the other hand, complexes are also believed to occur for systems where the potential energy surface (PES) is purely (or dominantly) repulsive. These intermediates tend to be extremely short-lived and are often viewed inseparably from the collision process itself.^{1–4} In such systems, which include a number of hydrogen abstraction reactions like $F + H_2 \rightarrow HF + H$, the trapping occurs due to dynamical effects near the transition state and is not obvious from the landscape of the PES. The predicted lifetimes of these intermediates are often just a few, or merely one, internal vibrational period. In spite of their transitory existence, these “reactive resonances” can strongly influence both the rate of reaction and the resulting product distribution. However, it is on more fundamental grounds that reactive resonances have proven to be of most interest. Since resonance energies and lifetimes are extremely sensitive functions of the PES and dynamics near the transition state, these elusive states can be viewed as probes of the transition states region. The spectroscopy of resonance states can provide critical information about bond forming and bond breaking at the most basic level.

The possibility of the existence of short-lived reactive resonances has been discussed often over the years. The early advances in this field were largely theoretical and based on the analysis of quantum reaction dynamics using approximate PESs.^{5–10} These studies provided much insight into the dynamical origin of complex formation. However, they were speculative

in that the PES and dynamics calculations were too approximate to permit quantitative comparisons with experiment. The extreme sensitivity of resonance properties to the PES and dynamical approximations greatly reduced the usefulness of these calculations in studying real systems. With the dramatically increased computational power now available, theory has evolved to the point where very accurate potential surfaces and essentially converged quantum scattering calculations can be used to predict the existence of reactive resonances *a priori* for sufficiently simple systems.^{11–14} Furthermore, techniques of analysis have been developed that allow the resonance wavefunction to be extracted, and hence, the full assignment of quantum numbers and other physical characteristics.^{15–18}

While theoretical techniques for the characterization of resonance states advanced, the experimental search for reactive resonances has proven to be a much more difficult task. The extremely short lifetime of reactive resonances makes the direct observation of these species very challenging. In some reactions, transition state spectroscopy can be employed to study resonances through “half-collision experiments” where even very short-lived resonances may be detected at peaks in a Franck–Condon spectrum.¹⁹ Neumark and co-workers²⁰ were able to assign peaks in the $[\text{IHI}]^-$ photo-detachment spectrum to resonance states for the neutral $\text{I} + \text{HI}$ reaction. Unfortunately, transition state spectroscopy is not always feasible, due to the absence of an appropriate Franck–Condon transition or to practical limitations in the required level of energetic resolution. The direct study of reactive resonances in a full collision experiment, such as with a molecular beam apparatus, is the traditional and more universal environment in which to work. Unfortunately, observing resonance behavior in such experiments has proven to be exceedingly difficult. The heart of the problem is not a technical issue in experiment, but rather it is a lack of knowledge about how the existence of a resonance will affect the collision observables in a uniquely identifiable way. As of this point, there is no known general and unique resonance signature that can be sought, even given perfectly resolved scattering cross-section data.

In this article, we shall review recent advances that have been made in detecting and understanding short-lived reactive resonances. Theory and experiment have matured to the point where state- and angle-resolved reactive cross-sections can be measured accurately in the laboratory and brought into quantitative agreement with the results of converged scattering calculations on an accurate PES. We shall attempt to illustrate how theory and experiment can work in tandem to identify resonance signatures in reactive collisions. In Sec. 2, a brief discussion of the theory of reactive

resonances is presented, with special emphasis given to how collision observables are affected by the existence of a resonance. In Sec. 3, we shall present three case studies of systems where reactive resonances are believed to exist: $F + HD$, $F + H_2$, and $H + HD$. Although these three hydrogen abstraction reactions are seemingly quite similar, we shall see that, in fact, the resonance signatures are very different in each case. We are thus led to the conclusion that the search for resonance signatures in collision experiments must still be pursued on a case-by-case basis with close interplay between theory and experiment. Finally, in Sec. 4 we present a brief conclusion.

2. Theoretical Methods for Resonance Phenomena

As noted above, the theory of chemical resonances has been the object of considerable effort for many years. Thus, it is not possible here to concisely review all the important developments. Thus, we shall be content to note a few of the main themes for studying resonances using quantum methods. Furthermore, we shall specialize to reactive resonances for systems described by a single Born–Oppenheimer PES that exhibits no deep trapping wells. Of course, this excludes interesting behavior associated with nonadiabatic coupling, as well as issues arising from dense manifolds of overlapping resonances. This is consistent with our goal to investigate how resonances affect scattering observables for simple barrier-type reactions, rather than providing an exhaustive review.

All resonance behavior in collision problems can be associated with some form of dynamical trapping in the interaction region. The trapping involved in the formation of reactive resonances occurs near the transition state barrier, and we will distinguish “reactive resonances” from van der Waals type states located in shallow wells that may exist in entrance or exit channels. As noted above, the nature of the trapping is dynamical in origin, and cannot be easily inferred from the PES directly. The conventional interpretation of reactive resonances makes use of one-dimensional dynamical potentials, constructed, e.g., using decoupling approximations such as the vibrationally adiabatic theory of reaction. In this way, the multidimensional reaction dynamics is modelled using a set of potential barriers constructed along a reaction coordinate; each of these curves represents different internal excitations of the collision complex. In natural collision coordinates, the coordinate “ s ” then represents distance along the minimum energy path, while the orthogonal vibrational modes are described by the normal mode coordinates “ u ”. In the simplest form, the vibrationally adiabatic theory is constructed assuming that the quantum numbers n , corresponding to

coordinates u , are conserved during the collision.^{21,22} Thus, one obtains vibrationally adiabatic potential curves of the form

$$V_{\text{ad}}(s; n) = V_0(s) + \varepsilon_n(s) \quad (1)$$

where $V_0(s)$ is the potential along the reaction path and $\varepsilon_n(s)$ are the quantized state energies of the orthogonal motion. Since the vibrational frequencies change dramatically near the transition state, $V_{\text{ad}}(s; n)$ can be quite different from the Born–Oppenheimer surface, and can even exhibit wells although the PES is purely repulsive. Although the dynamical conditions for the technical validity of the vibrationally adiabatic model are virtually never satisfied, this simple model often captures the essence of reaction dynamics near the transition state.

When expressed in terms of vibrationally adiabatic curves, the resonance trapping can be viewed in a simple one-dimensional way. There are two common scenarios for resonance formation. First, resonance states can exist as intermediates trapped in wells on the adiabatic potential curves, as shown in Fig. 1(a). This requires the adiabatic wells to be deep enough to support a quantum state, which generally occurs only for internally-excited complexes. The resonance decay can take place either by tunnelling through the barrier, or by energy transfer resulting in a transition to a lower adiabatic curve. The lifetime of the resonance depends strongly on the vibrationally nonadiabatic coupling and tends to be longest for heavy–light–heavy mass combinations. States trapped in adiabatic wells (often referred to as Feshbach-type resonances) are quite familiar and do not

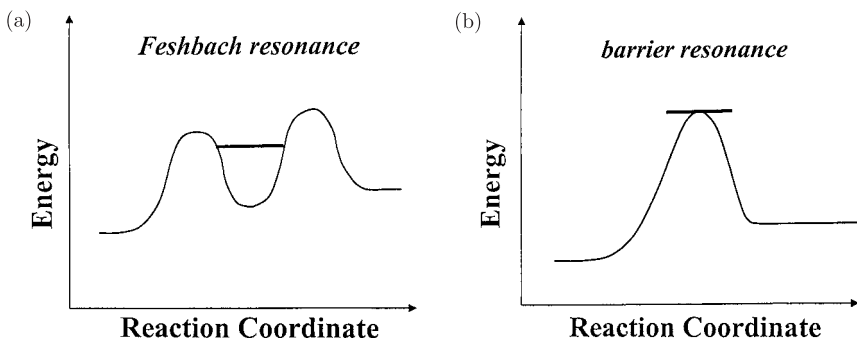


Fig. 1. A schematic diagram of the relationship between adiabatic potential curves and reactive resonances. (a) shows the conventional Feshbach resonance trapped in a well of an adiabatic curve. (b) illustrates barrier trapping, which occurs near the energy of the barrier maximum of an adiabatic curve.

require extensive review. We note only that in a semiclassical picture, Feshbach resonances correspond to trapped volumes of phase space larger than the quantizing volume h^D , where D is the appropriate dimension.

A more novel scenario occurs for the second case, barrier type resonances. Even when there is no well in $V_{\text{ad}}(s; n)$, it is possible to show that trapping occurs near the barrier maximum simply because the motion slows down passing over the barrier, as in Fig. 1(b).^{16,23,24} This sort of kinematic trapping occurs even in classical mechanics and is related to the existence of a periodic orbit perched on top of the dynamical barrier.^{16,25–27} Although there are some important differences between “barrier states” and more conventional Feshbach resonances, it can be shown^{16,23,24,28–32} that barrier states behave much like resonances with energy $E_R = V_{\text{ad}}(s = \text{barrier}; n)$ and width $\Gamma = \hbar\omega$, ω being the barrier frequency of $V_{\text{ad}}(s; n)$. In the most technically correct sense, barrier states are not true resonances since they do not correspond to single poles, but for the purposes of this review we shall consider them together with Feshbach resonances as sources of transition state trapping. The lifetimes of barrier states are typically about one period of vibration for the u -coordinates even if ω should happen to be (accidentally) small.

Since chemical reactions generically exhibit energetic barriers, they will generically possess barrier-type resonances. Barrier resonances are distinguished from the more conventional Feshbach resonances by the nature of the trapping mechanism. As noted, barrier states correspond to trapping at a turning point located at the top of an effective potential barrier. One is tempted to conclude that the distinction between barrier and Feshbach resonances is purely model-dependent, since a trapping well may exist on one type of adiabatic potential, say in hyperspherical coordinates, while only a barrier may exist on another type, say in natural collision coordinates. However, this is not correct since there are in principle fundamental differences between barrier and Feshbach states. First, the pole structure of the \mathbf{S} -matrix is intrinsically different in the two cases. A Feshbach resonance corresponds to a single isolated pole of the scattering matrix below the real axis of the complex energy plane (see the discussion below). On the other hand, the barrier resonance corresponds to an infinite sequence of poles extending into the lower half plane. For a parabolic barrier it is easy to show that the pole positions are given by

$$E_n = V_0 - i\hbar\omega \left(n + \frac{1}{2} \right) \quad (2)$$

where V_0 is the (real) barrier height and ω is the barrier frequency. In a previous work on transition state spectroscopy of barrier resonance, we have demonstrated that this pole structure gives rise to a line-shape formula completely different from the usual Lorentzian form corresponding to conventional Breit–Wigner resonances.³⁰ Another distinction between Feshbach and barrier-type resonances concerns their behavior in the semi-classical limit. While Feshbach states correspond to trapped volumes of phase space, which is a coordinate-independent quantity, barrier states arise from single trapped orbits that obviously have zero volume in phase space. Indeed, Sadeghi and Skodje³⁰ have shown that the lowest-order term in a \hbar -expansion of the Wigner phase space distribution for a decaying barrier state is localized on the unstable manifolds of the periodic orbit, i.e.

$$W(p, q, t) \xrightarrow[t \rightarrow \infty]{} e^{-t/\tau} \sum \delta(p - p_i(q)) \quad (3)$$

where τ is the classical lifetime (the inverse barrier frequency) and $p_i(q)$ are the unstable branches of the reactive separatrix. Finally, we note that the shape of the reaction probability for a barrier shows a threshold structure while a Feshbach state is expected to lead to a generalized Lorentzian peak. From model problems, we can conclude that the steplike threshold behavior of the reaction probability is due to the collective influence of the infinite sequence of poles. For example, an Eckart barrier, $V = V_0/\cosh^2(\alpha x)$, is shown to have a reaction probability, $P_R(E)$, that can be written as³³

$$P_R(E) = 1 - \left| \prod_{n=0}^{\infty} \frac{k_n}{k - k_n} \right|^2 \quad (4)$$

where $k = \sqrt{2\mu E/\hbar^2}$, k_n are the pole positions,

$$k_n = \frac{\hbar\alpha}{2} \left[\sqrt{\frac{8\mu V_0}{\hbar^2 \alpha^2} - 1} - i(1 + 2n) \right] \quad (5)$$

and μ is the mass.

Since chemical reactions usually show significant nonadiabaticity, there are naturally quantitative errors in the predictions of the vibrationally adiabatic model. Furthermore, there are ambiguities about how to apply the theory, such as the optimal choice of coordinate system. Nevertheless, this simple picture seems to capture the essence of the resonance trapping mechanism for many systems. We also point out that the recent work of Truhlar and co-workers^{24,34} has demonstrated that the reaction dynamics is largely controlled by the quantized bottleneck states at the barrier maxima in a much more quantitative manner than expected.

In the framework of quantum scattering theory, the properties of trapped intermediate states have been studied extensively as the formal theory of scattering resonances.³⁵ While every resonance has its own distinct physical character, it has been found that essentially all resonant problems share certain generic characteristics that derive from their mathematical nature. This viewpoint is quite useful since it provides a collection of expected behavior that guide both experimental and theoretical studies in searching for resonance signatures. The standard picture of resonance phenomena is based on the concept of the isolated narrow resonance (INR) proposed by Breit and Wigner.³⁶ The INR is pictured as a “nearly bound” state of the system lying at energies above the threshold for complex breakup, i.e. in the continuum region of the energy spectrum. In the Breit–Wigner treatment, the fundamental characteristic of the INR is the existence of complex energy pole in the scattering-matrix (**S**-matrix), i.e.

$$\mathbf{S}(E) = \mathbf{S}_d(E) \left[1 - \frac{i\mathbf{A}}{E - E_R + i\Gamma/2} \right] \quad (6)$$

where E_R is the (real) resonance energy and Γ is the total width.³⁷ In Eq. (6), $\mathbf{S}_d(E)$ is the direct, or background, contribution which is assumed to be a slowly varying function of the total system energy E . In this form, both $\mathbf{S}(E)$ and $\mathbf{S}_d(E)$ are assumed to be unitary. This requires the matrix \mathbf{A} to be Hermitian and of the form

$$\mathbf{A}_{i,j} = \gamma_i^* \gamma_j. \quad (7)$$

The quantities γ_i are related to the partial widths of the resonance according to

$$\Gamma_i = |\gamma_i|^2 \quad (8)$$

which, in turn, satisfy

$$\Gamma = \sum_i \Gamma_i. \quad (9)$$

The amplitudes γ_i are generally complex and the relative phase between the resonant term and the background term determines the precise line-shape that will be observed. An alternative to Eq. (6) makes use of the sum form:

$$\mathbf{S}(E) = \mathbf{S}'_d(E) - \frac{i\mathbf{A}'}{E - E_R + i\Gamma/2}. \quad (10)$$

In this form, which is the more common expression used in numerical fitting, the matrix \mathbf{A}' is not as simply related to the partial widths. For an INR,

we assume that the complex energy

$$z = E_R - i\Gamma/2 \quad (11)$$

lies very close to the real axis, i.e. Γ is small, so that the background contribution to $\mathbf{S}(E)$ may be readily separated from the resonance pole. Furthermore, it is assumed that no other poles of the \mathbf{S} -matrix lies nearby in energy as defined on the scale set by Γ . When these conditions are met, the existence of a resonance is heralded by the occurrence of a set of well-defined effects that are amenable to observation or computation.

The simple INR concept has succeeded beautifully for many problems in atomic and nuclear physics. Unfortunately, the INR picture is seldom valid for reactive resonances, which, on the contrary, tend to be broad and overlapping. The breakdown of the INR idealization for reactive resonances was appreciated long ago in terms of the impact parameter averaging implicit in reactive collisions.³⁸ If we imagine that an “isolated” reactive resonance corresponds to a vibrational state of an intermediate molecule, then the rotational energy levels built on that state have energies given by

$$E_R(J) = E_0 + B_0 \cdot J(J+1) \quad (12)$$

where E_0 is the ground rotational energy and B_0 is the rotation constant of the complex. (For simplicity we have specialized to the case of a collinear collision complex.) Hence, each resonance state is part of rotational progression with spacing $2JB_0$. The typical B -constant for a reactive resonance can be inferred from the geometry of the saddlepoint on the PES and is usually in the order of several wavenumbers. On the other hand, the resonance lifetimes tend to be <100 fs, corresponding to widths >50 cm^{-1} thus implying that the rotational states are overlapping, i.e. their spacings are smaller than their widths. Stated in dynamical terms, the rotation period of the complex is significantly greater than the lifetime of the resonance. The rotational quantum number of the resonance is expected to correlate to the total angular momentum, J , which labels the partial waves in an expansion of the cross-sections. Since dozens of partial wave generally contribute to the cross-section at typical collision energies, this congestion of resonance states is expected to occur generically in a collision experiment. Thus, the sharp structure (on the scale set by Γ) in the cross-sections versus energy that one might expect to observe for an INR will generally be smeared out over a much larger energy range. Since the background scattering has some energy dependence as well, it becomes very difficult to identify resonance signatures for reactive resonances.

In light of the preceding discussion, it is clear that the unmistakable resonance fingerprint provided by a narrow Lorentzian peak in the integral cross-section will likely never be observed for reactive resonance in a collision experiment. However, a fully resolved scattering experiment provides a wealth of data concerning the reaction dynamics. One hopes that the state-to-state differential cross-sections as functions of collision energy can, in some way, be analyzed for the presence of reactive resonance. In the following subsections, we discuss how various collision observables are influenced by existence of a complex intermediate. Many of the resonance detection schemes that have been proposed, such as the use of collision time delay, are purely theoretical in that the observations required are not currently feasible in the laboratory. Nevertheless, these ideas are also discussed since it is useful to have a method available to determine whether a given PES supports resonances for comparison and interpretation of experiment.

2.1. Integral Cross-Sections

The most well-known and dramatic manifestation of an INR is the appearance of a narrow feature in the integral cross-section (ICS), $\sigma(E)$ at total energy $E = E_R$ of width Γ . Obviously the resonance peak is closely related to the existence of the resonance pole in the **S**-matrix. Using the normal body-fixed representation for an $A + BC(v, j) \rightarrow AB(v', j') + C$ reaction, the ICS is related to the **S**-matrix by

$$\sigma_R(v, j \rightarrow v', j'; E_C) = \frac{\pi}{k^2} \sum_J (2J+1) \cdot P_R(v, j \rightarrow v', j'; E_C, J) \quad (13)$$

with

$$P_R(v, j \rightarrow v', j'; E_C, J) = \frac{1}{2k+1} \sum_{k, k'} |\mathbf{S}_J(v, j, k \rightarrow v', j', k'; E_C)|^2 \quad (14)$$

where the (presumably) unobserved helicity quantum numbers k and k' are averaged over. It is clear from Eq. (6) that, for a given partial wave, the resonance peak should occur at the same total energy for all state-to-state ICSs with the relative heights set by the partial widths. When the resonance exists for only a single partial wave, such as in many nuclear physics problems, a resonance feature of width Γ should survive in the ICS even if other partial waves contribute to a smooth background. When many partial waves support resonance states, as with reactive resonances, the individual peaks that may be quite apparent in $P_R(v, j \rightarrow v', j'; E_C, J)$ merge together in the ICS over a broad energy range and is difficult to distinguish from

background scattering. A special case, of relevance to the $F + HD$ reaction considered below, is when the background scattering happens to be nearly zero around the resonance energy. In this case, the reaction is purely resonance mediated and we can approximately construct the behavior of the ICS from a combination of Lorentzian profiles. Using J -shifting approximation, the reaction probability for the J th-partial wave is given by

$$P_R(v, j \rightarrow v', j'; E_C, J) \approx \frac{C\sqrt{E_C}\sqrt{E'_C}}{(E - E_R(J))^2 + \Gamma^2/4} \quad (15)$$

where E_C and E'_C are the initial and final translational energies, E is the total energy, C is a constant and

$$E_R(J) = E_0 + B_0J(J+1) \quad (16)$$

is the J -shifted resonance energy with B -constant B_0 . When the partial cross-sections are combined according to Eq. (13), a steplike feature occurs in the ICS that can be analytically modelled using the formula⁶⁵

$$\sigma_R \approx \frac{C}{\sqrt{E_C}} \text{Im} \left[\theta(E_C) \ln \left(\frac{\theta(E_C) + 1}{\theta(E_C) - 1} \right) \right] \quad (17)$$

where

$$\theta(E_C) = \sqrt{\frac{E_0 - i\Gamma/2}{E_C}}. \quad (18)$$

The inclusion of J -dependence into the resonance width generally produces only a small change in the shape of the resonance step. Schatz *et al.* have noted that such a step feature may occur for the $Cl + HCl$ reaction.³⁹

2.2. Time Delay

Cross-sections for reactive scattering may exhibit a structure due to resonance or to other dynamical effects such as interference or threshold phenomenon. It is useful to have techniques that can identify resonance behavior in a system and distinguish it from other sorts of dynamics. Since resonance is associated with dynamical trapping, the concept of the collision time delay proves quite useful in this regard. Of course since collision time delay for chemical reactions is typically in the sub-picosecond domain, this approach is, at present, only useful in analyzing theoretical scattering results. Nevertheless, time delay is a valuable tool for the theoretical identification of reactive resonances.

There are two common definitions of collision time delay: one proposed by Wigner and Eisenbud,⁴⁰ and another suggested by Smith.⁴¹ While identical for single channel scattering, these two definitions can yield very different results in multichannel scattering, such as chemically reactive collisions. Both definitions were formulated for the scattering of a single partial wave (single J -values), but an extension of the Wigner–Eisenbud model to full scattering is possible (see below). The Wigner–Eisenbud approach is based on the shift in the center of a spatially-localized wavepacket relative to dynamics in the absence of an interaction potential. At early times, long before the collision, a wavepacket started in the n th internal channel of the J th partial wave is represented as

$$\Psi = \phi(R - v_n t) \chi_n \quad (19)$$

where ϕ is broadly peaked at $R - v_n t = 0$ in position space but is narrowly peaked in translational momentum space at μv_n , R is the collision coordinate, v_n is the channel velocity, and χ_n is the initial internal state wavefunction. Then, long after the collision, the n' th component of the wavepacket takes the form

$$\Psi = C \phi(R - v_{n'} t + v_{n'} \tau_{n,n'}) \chi_{n'} \quad (20)$$

where the quantity $\tau_{n,n'}$ is the state-to-state collision time delay defined by

$$\tau_{n,n'} = \text{Re} \left[\frac{-i\hbar}{\mathbf{S}_{n,n'}(E)} \frac{d\mathbf{S}_{n,n'}(E)}{dE} \right]. \quad (21)$$

The Wigner–Eisenbud definition is physically equivalent to the idea of a signal time delay. Clearly, each channel will display a different value for this quantity, although for an INR each approaches $2\hbar/\Gamma$ at $E = E_R$. Smith's definition of the time delay is based on a different concept, namely the residence time within the interaction region of the collision, referred to as the collision lifetime. It can be shown that for a multidimensional scattering problem, the residence time (relative to free particle motion) within a large sphere enclosing the interaction is given in terms of a Hermitian lifetime matrix,

$$Q_{n,n'} = -i\hbar \sum_j \frac{d\mathbf{S}_{n,j}(E)}{dE} \mathbf{S}_{n',j}^*(E). \quad (22)$$

The average time delay for a particle injected into the n th channel but emerging in any final channel is given by the diagonal element $Q_{n,n}$. The

resonance contribution to the time delay is expected to emerge more distinctly from the background when Q is diagonalized. In this case, the largest eigenvalue should show a peak versus energy near a resonance energy.

Both the Wigner–Eisenbud and Smith definitions of time delay require as the basic input the calculation of \mathbf{S} on a sufficiently fine grid of energies to compute $d\mathbf{S}/dE$. However, the Smith version generally requires a much larger calculation since the determination of the eigenvalues of Q requires the full \mathbf{S} -matrix between all open channels at energy E while the Wigner–Eisenbud theory requires only a single element.

While every resonance is expected to yield extra time delay at energies near E_R , it is extremely dangerous to interpret all sharp structures in the function $\tau_{n,n'}(E)$ as due to resonance. For example, it is easy to see that if $\mathbf{S}_{n,n'}(E)$ should accidentally pass near zero at an energy E_0 , then the τ will show a positive or negative spike at $E = E_0$ that is not necessarily related to any resonance state. If a peak of the time delay occurs near the minimum of the reaction probability, great caution should be exercised before concluding that the peak is due to resonance. Furthermore, near energetic thresholds it is known that the elastic phase shift for $J = 0$ has a singularity of the form $\delta \sim \sqrt{E_C}$. This leads to (elastic) time delays that diverge at threshold. Since thresholds are quite dense in energy for a typical chemical reaction, this can yield very erratic behavior of the Smith lifetime matrix, and hence the eigenvalues.

Since the time delay as defined above applies directly only to scattering of a single partial wave, it cannot be used to compute the scattering angle-resolved time delay, $\tau_{n,n'}(E, \theta)$. This quantity, which is theoretically observable, measures the delay of a plane wave signal as a function of the final center-of-mass scattering angle. To this end, Goldberger and Watson⁴² have generalized the Wigner–Eisenbud time delay using the scattering amplitude, $F_{n,n'}(E, \theta)$ in place of the \mathbf{S} -matrix. It was found that the quantity

$$\tau_{n,n'}(E, \theta) = \hbar \frac{d}{dE} \text{Arg}(F_{n,n'}(E, \theta)) \quad (23)$$

provided a sensible extension of the signal time delay concept to angle-resolved scattering. Kuppermann and co-workers⁴³ have used a somewhat different definition based on the same approach for the $\text{H} + \text{D}_2$ reaction. We note that the angle-resolved time delay may prove quite useful for reactive resonances since resonant scattering may occur much more strongly into certain scattering angles, such as the forward direction.

2.3. Exponential Decay

Associated with the pole of the \mathbf{S} -matrix is a Seigert state, Ψ_{res} , which has purely outgoing boundary conditions and satisfies (with some caveats) the equation, $H\Psi_{\text{res}} = z\Psi_{\text{res}}$, H being the system Hamiltonian.⁴⁴ If a square integrable approximation to Ψ_{res} is constructed, then its time evolution, $\Psi_{\text{res}}(t)$, will exhibit pure exponential decay after a transient induction period. Of course any L^2 state will show quadratic, and hence non-exponential, decay at short times since

$$|\langle\Psi(0)|\Psi(\Delta t)\rangle|^2 \approx 1 - \Delta t^2 \langle\Psi(0)|\hat{H}^2|\Psi(0)\rangle/\hbar^2. \quad (24)$$

However at long times a sample of prepared “complex” molecules will deplete according to the law, $N(t) = N(0)e^{-t/\tau}$, where the lifetime τ is related to the resonance width according to $\tau = \hbar/\Gamma$. Furthermore, the decay flux into each outgoing channel is locked in fixed proportion at all times.

While it is not feasible to measure exponential decay of resonance states in the environment of a molecular beam experiment, in theoretical work the exponential decay law provides a necessary condition that a proposed state, generated by some method, is in fact a resonance state. Furthermore, the rate of exponential decay provides probably the most accurate method for the numerical determination of the lifetime.

Seigert states can be generated from quantum dynamics using several available techniques. The most straightforward approach involves the use of a real stabilization calculation.^{45,46} Unfortunately, real stabilization tends to become rather inconclusive for broad resonances especially at high state densities required to treat 3D reaction dynamics. The performance of stabilization calculations can be greatly improved by including an absorbing optical potential outside the interaction region to enforce outgoing boundary conditions.^{17,47} Direct calculation of a state corresponding to complex energy eigenvalue is possible within the framework of the complex coordinate rotation method.⁴⁸ In our work, we have generally preferred the use of the spectral quantization (SQ) method since it is ideally suited for the study of broad transition state resonances.^{13,15,16,30,49–51} The SQ method is a straightforward application of conventional techniques available for the study of time-dependent quantum wavepacket dynamics. In the first stage of the method, energy spectra are obtained for various initial wavepackets launched in the transition state region, i.e.

$$I(E) \sim \int_{-\infty}^{\infty} \langle\phi(0)|\phi(t)\rangle e^{iEt/\hbar} dt. \quad (25)$$

Peaks in the spectrum, $I(E)$, identify the location of possible resonance states. Then, the initial state $\phi(0)$ is optimized to reduce direct background scattering and the resonance state is extracted using the standard relation

$$\Psi_{\text{res}}(x) \sim \int_{-\infty}^{\infty} \phi(t) e^{iE_p t/\hbar} dt \quad (26)$$

where E_p is a peak energy.

2.4. Angular Product Distributions

For an INR, a pole of the \mathbf{S} -matrix can lead to a peak in the ICS if the resonance exists for just one partial wave, or if the resonances for each J are well-separated in energy. It is not surprising that similar conclusions can be drawn for the differential cross-sections (DCS). The DCS is defined from the usual body fixed \mathbf{S} -matrix for $A + BC \rightarrow AB + C$

$$\begin{aligned} & \frac{d\sigma_R(v, j, k \rightarrow v', j', k')}{d\Omega} \\ &= \frac{1}{4k_{vj}^2} \left| \sum_J (2J+1) \cdot d_{k,k'}^J(\pi - \theta) \cdot \mathbf{S}_R(v, j, k \rightarrow v', j', k') \right|^2 \end{aligned} \quad (27)$$

where $d_{k,k'}^J$ are the Wigner functions. If the \mathbf{S} -matrix is slowly varying versus E except near a pole for some value of J , then it is obvious that the DCS will show rapid variation around $E = E_R$ at all scattering angles where $d_{k,k'}^J$ is significant. As we have noted already, however, this behavior is not to be expected for reactive resonances because of impact parameter averaging. A progression of poles of the form (6) must be combined coherently (with phases) to obtain the resonance signature in the DCS. Making this undertaking complicated is the variation of the background phase as a function of J . Unlike the ICS, which depends only on $|\mathbf{S}|^2$, the relative phase of the partial wave contributions is crucial in determining the angular product distributions. This issue has been understood for quite a long time, and the question of how the existence of an intermediate complex might affect the DCS has received considerable discussion. For an intermediate with a lifetime long period compared to the rotation period, Herschbach⁵² has noted that the DCS should become forward-backward symmetric in the center-of-mass frame. Unfortunately, reactive resonances are often short-lived compared to the rotation period, making subtler the angular signature of resonance.

Miller and Zhang suggested searching for a ridge structure in the DCS as a function of E_C and θ . The ridge is an $E_C - \theta$ correlation resulting from

the J -shifting of the dominant resonance decay angle, which appears, in the DCS. Miller and Zhang⁵³ observed clear ridge features in the $\text{H} + \text{H}_2$ and $\text{D} + \text{H}_2$ systems. However, it is unclear whether ridge structures uniquely correlate to quantum resonances since Aoiz and co-workers⁵⁴ have noted similar ridges occur in QCT simulations. In another discussion of angular correlation, Connor and Sokolovski have recently proposed decomposing the scattering amplitude into nearside/farside contributions that may elucidate resonance behavior.^{55,56}

In a very important work, Lee and co-workers^{57,58} surmised that forward peaks in the state resolved DCS might indicate the existence of resonances. The physical picture behind this idea is somewhat subtle and involves resonant time delay. As the impact parameter (or J) of the collision increases, the total reactive product distribution generally shifts from backward to more sideways scattering reflecting the orientation of the complex. One expects that the resonant contribution to the product distribution will show greater angular deflection (towards forward) since the complex will rotate further due to the time delay. Thus, in the most forward direction the dynamics will be filtered to enhance the resonant contribution to the reaction. A schematic diagram illustrating the forward peaking is given in Fig. 2. Forward peaks have in fact been observed experimentally in the $\text{F} + \text{H}_2$ (Ref. 57), $\text{H} + \text{D}_2$ (Refs. 59–61) and $\text{H} + \text{HD}$ (Ref. 62) reactions. To determine the range of J (and hence the impact parameter) that gives rise to a feature in the DCS, it is useful to compute the angle-resolved

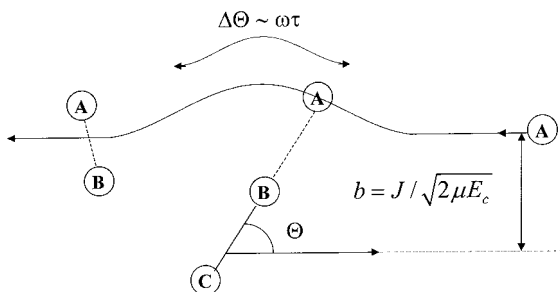


Fig. 2. A schematic diagram illustrating how a time delay, τ , permits the product molecule of an $A + BC$ reaction to rotate into the forward scattering direction. The frequency ω of the rotating complex is set by the angular momentum of the collision, J , and hence by the impact parameter, b .

integrated opacity function,

$$\begin{aligned} & \frac{d\sigma_R^{J_{\max}}(\theta)}{d\Omega} \\ &= \frac{1}{4k_{vj}^2} \left| \sum_{J=0}^{J_{\max}} (2J+1) \cdot d_{k,k'}^J(\pi-\theta) \cdot \mathbf{S}_R(v, j, k \rightarrow v', j', k') \right|^2. \end{aligned} \quad (28)$$

This quantity gives the truncated contribution to the DCS of partial wave up to J_{\max} . Thus, holding E and θ fixed, the most important J values for a process can be determined by plotting Eq. (28) versus J_{\max} .

2.5. Product Rovibrational Branching Ratios

The dynamics of a reaction that proceeds directly over the transition state is expected to be qualitatively different from that of a resonance-mediated reaction. In particular, one expects that the branching ratios into the product rovibrational states will be very different between the direct and the resonant mechanisms. For example, if a given Feshbach resonance corresponds to trapping on the $v = 1$ vibrationally adiabatic curve, then one might expect that the population of the $v' = 1$ vibrational state of the product molecule may be greatly enhanced by the resonant mechanism. Similarly, the rotational product distribution resulting from the fragmentation of a resonance molecule may show a quite distinct pattern from that of a direct reaction. Indeed, Liu and co-workers,⁶³ and Nesbitt and co-workers⁶⁴ have noted distinct rotational patterns in the $F + HD$ resonant reaction.

As always, the phenomenon of impact parameter averaging will lead to a smearing of the resonance decay products over large energy range. Nevertheless, under certain circumstances the influence of resonance may still be discerned. For example, if the resonance energy for the $J = 0$ state occurs at $E_R(0)$, then any reaction occurring at $E < E_R(0)$ must necessarily take place through the direct mechanism. If the product branching ratios are monitored versus E , one might expect to see a sudden change in the branching ratios which begins at $E = E_R(0)$ and persists continuously to higher energy. Conversely, if $E_R(0)$ is below the threshold for direct reaction, as in a resonance tunneling mediated reaction, then there will be a range of energies $E_R(0) < E < E_{\text{thr}}$ in which the reaction proceeds solely through the resonance mechanism. In this case, product branching ratios for $E < E_{\text{thr}}$ are then completely determined by the partial widths of the resonance. Since the partial widths are generally rather weak functions of J , the branching ratios should be relatively constant up to $E = E_{\text{thr}}$. At higher

energies, the direct mechanism begins to contribute and one expects the branching ratios will begin to show much more rapid variation versus E .

3. Three Examples of Reactive Resonance

From the preceding discussion, it is clear that reactive resonance can potentially affect many scattering observables. It is not obvious *a priori*, however, which particular quantities may prove the most effective in identifying the existence of a resonance state. In order to assess the utility of various ideas for resonance signatures, in this section we shall consider three case studies of benchmark chemical reaction believed to support reactive resonances. These are the hydrogen exchange reactions: $\text{F} + \text{HD} \rightarrow \text{HF} + \text{D}$, $\text{F} + \text{H}_2 \rightarrow \text{HF} + \text{H}$, and $\text{H} + \text{HD} \rightarrow \text{D} + \text{H}_2$. For each case, state-of-the art molecular beam experiments have recently been performed. Furthermore, very accurate PESs have also been computed for these reactions, which have been used to carry out converged quantum scattering calculations. Given the general similarity of these reactions, one might expect that their resonance fingerprints would be closely related. Indeed, each of these systems is a triatomic hydrogen abstraction reaction dominated by the lowest PES that exhibits no potential well near the transition state. However, on the contrary, we shall see that the presence of resonances is manifested in different observables for each case. The chameleon-like nature of the resonance emphasizes the need for combined theoretical and experimental work to firmly establish the resonance on a case-by-case basis.

3.1. $\text{F} + \text{HD} \rightarrow \text{HF} + \text{D}$

Perhaps the first clear observation of a reactive resonance in a collision experiment was recently made for the $\text{F} + \text{HD} \rightarrow \text{HF} + \text{D}$ reaction.^{65–67} This reaction was one isotopomer of the $\text{F} + \text{H}_2$ system studied in the landmark molecular beam experiments of Lee and co-workers in 1985.⁵⁸ Unlike the $\text{F} + \text{H}_2$ case, no anomalous forward peaking of the product states was reported, and results for $\text{F} + \text{HD}$ were described as the most classical-like of the isotopes considered. Furthermore, a detailed quantum mechanical study⁶⁸ of $\text{F} + \text{HD} \rightarrow \text{HF} + \text{D}$ reaction on the accurate Stark–Werner (SW)-PES⁶⁹ failed to locate resonance states. Therefore, it was surprising that the unmistakable resonance fingerprints emerged so clearly upon re-examination of this reaction.

The molecular beam experiments of Liu and co-workers^{65,66} employed the Doppler profile time-of-flight technique that allowed the ready observation of the excitation function (i.e. the total reactive ICS summed over

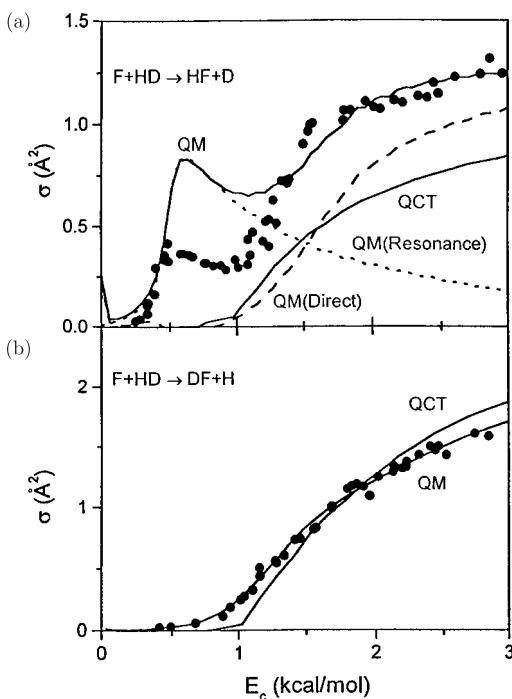


Fig. 3. The normalized excitation functions in \AA^2 versus collision energy for the two isotopic channels for the F+HD reaction. The solid line is the result of quantum scattering theory using the SW-PES. The QCT simulations from Ref. 71 are plotted for comparison. The experiment, shown with points, is normalized to theory by a single scaling factor for both channels. Also shown in (a) is the theoretical decomposition of the excitation function into direct and resonant contributions using the J -shifting procedure.

final product state) at many collision energies for a HD reagent molecule 90% populated in its ground rovibrational state. The excitation function for both possible product channels, HF + D and DF + H, over the range of collision energies 0.2–3 kcal/mol is shown in Fig. 3. A pronounced steplike feature occurs in $\sigma_R(E)$ for the HF + D channel near $E_C = 0.5$ kcal/mol that is clearly absent for the DF + H channel. A converged quantum scattering calculation^{65,66,70} on the SW-PES is found to yield similar results, as seen in the figure. The QCT results of Aoiz and co-workers⁷¹ showed reasonable agreement with the experiment for the H + FD channel, but completely failed to predict the step-feature for the D + HF product. Since the step occurs below the adiabatic barrier, one is led to the conclusion that the reaction step is due to quantum effects. With close interaction between

theory and experiment, the interpretation that emerged^{65,66} for this result was that the reactive step was due to the existence of a reactive resonance with an F–H–D collinear geometry. The step was not seen in the DF + H channel since the decay probability of an F–H–D configured resonance into that unfavorable product channel was very small. The difference in the step height predicted by quantum scattering and that observed in the experiment, is likely due to small errors in SW-PES affecting the rate of resonant tunnelling.

In light of the discussion above, it is very surprising that a clear resonant feature should survive in $\sigma_R(E)$, which, after all, involves averaging over impact parameter, scattering angle, and final states. Some insight into this result is obtained by considering the partial cross-sections computed for the individual partial waves that are shown in Fig. 4. As a function of E_C , each of the partial cross-sections shows a clear Lorentzian-like peak at low E_C followed by the normal threshold-type behavior at higher E_C . The individual

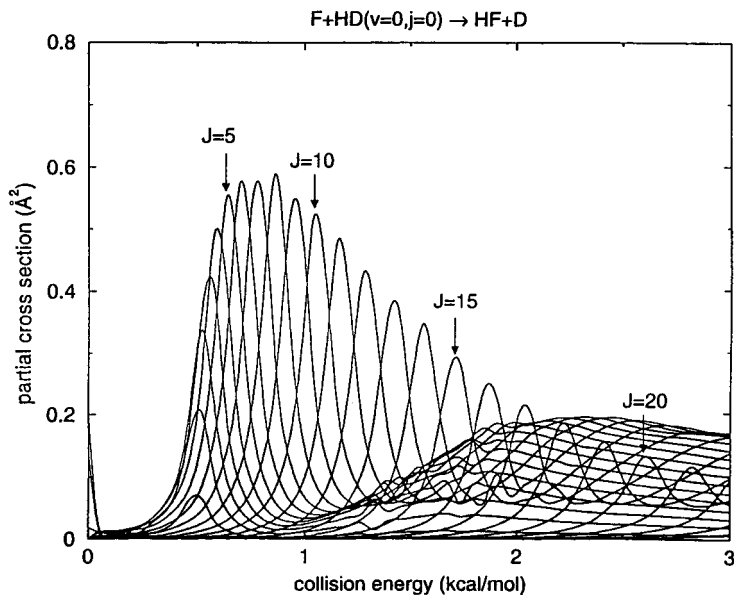


Fig. 4. Computed partial cross-sections in \AA^2 for the $\text{F} + \text{HD} (v = 0, j = 0) \rightarrow \text{HF} + \text{D}$ reaction as a function of the total angular momentum quantum number, J , up to collision energies of 3 kcal/mol.

peaks fit well to a Lorentzian shape function with peak positions at

$$E_{\text{res}}(J) = E_0 + B_0 \cdot J(J+1) \quad (29)$$

with $E_0 = 0.52$ kcal/mol and $B_0 = 0.0051$ kcal/mol, and widths given by the fitted form

$$\Gamma(J) = \Gamma_0 + a(\exp(bJ) - 1) \quad (30)$$

with $\Gamma_0 = 0.15$ kcal/mol, $a = 0.00127$ kcal/mol, and $b = 0.2635$. Since the threshold energy for the “direct” $\text{F} + \text{HD} \rightarrow \text{HF} + \text{D}$ reaction obtained from the lowest vibrationally adiabatic barrier is at about 1.1 kcal/mol, the reactive step in $\sigma_R(E)$ is due almost entirely to the superposition of the Lorentzian peaks. Indeed, by numerically decomposing the partial cross-sections into separate peak and direct contributions, and then summing over J to obtain $\sigma_R(E)$, we see in Fig. 3 that the step is essentially the J -shifted analog of a pure Lorentzian peak. If the Lorentzian feature is indeed taken as a resonance peak, this implies that the reaction occurs almost exclusively as resonance mediated tunnelling at energies below about 1 kcal/mol.

The quantum product state distributions from the reaction show a similar dichotomy for $E_C < 1$ kcal/mol and $E_C > 1$ kcal/mol. Focusing on the rotational state distribution for the dominant $\text{HF}(v' = 2)$ product, in Fig. 5 we show the ICS for $\text{F} + \text{HD} \rightarrow \text{HF}(v' = 2, j')$ as a function of j' and E_C . The scattering calculations show a clear change in the rotational product distribution between low- and high-energy scattering. The rotational distribution at low E_C is rather flat, yet hot extending up to about $j' = 10$. By contrast, the higher E_C results show the more usual envelop peaking at much lower values of j' . Recently, Nesbitt and co-workers⁷² measured the product distribution in a “crossed jet” experiment and obtained results consistent with Fig. 5. Again, the result is consistent with a resonance state picture in that the low E_C distribution is due entirely to a resonance decay mechanism that is expected to be quite different from the direct reaction mechanism that dominates at higher E_C .

The DCS for the $\text{F} + \text{HD} \rightarrow \text{HF} + \text{D}$ reaction is also imprinted with resonance signatures. In Fig. 6, we show the DCS versus E_C and θ , for the $\text{HF}(v' = 2) + \text{D}$ product, summed over j' -states, obtained experimentally and theoretically. At low collision energies, a resonance ridge of the sort proposed by Miller and Zhang⁵³ is clearly apparent. The product distribution is backward peaked at the lowest energy, and then shifts progressively towards the sideways direction. At high E_C , the DCS develops strong

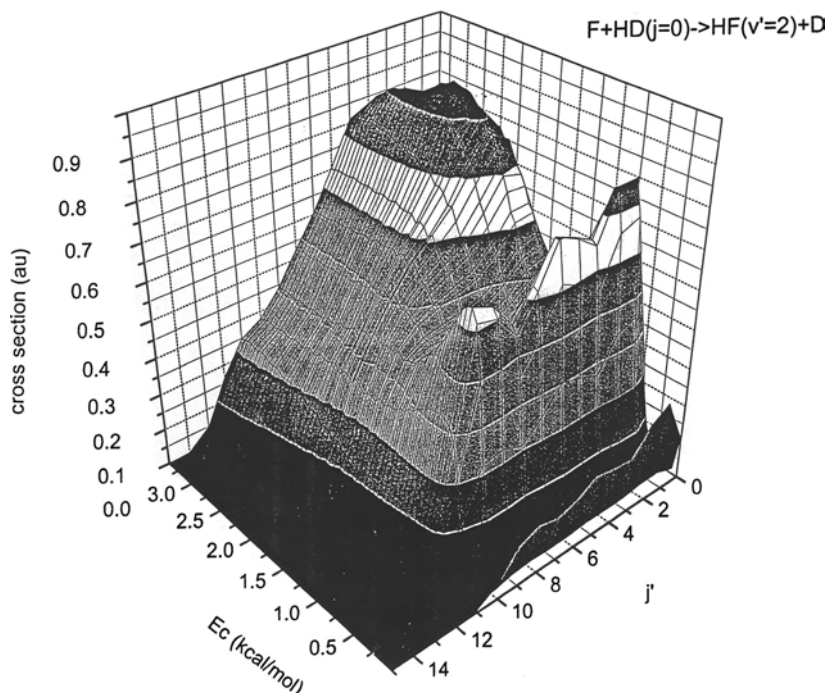


Fig. 5. The ICS for $F + HD (v = 0, j = 0) \rightarrow HF (v' = 2, j') + D$ versus E_C and j' computed from quantum scattering theory using the SW-PES.

forward-backward peaking. A decomposition of the DCS into resonant and direct components, by fitting each **S**-matrix element to a Breit–Wigner pole plus a background, verifies that this peaking is in fact due primarily to the resonant contribution.

To uniquely associate the unusual behavior of the collision observables with the existence of a reactive resonance, it is necessary to theoretically characterize the quantum state that gives rise to the Lorentzian profile in the partial cross-sections. Using the method of spectral quantization (SQ), it is possible to extract a Seigert state wavefunction from time-dependent quantum wavepackets using the Fourier relation Eq. (21). The state obtained in this way for $J = 0$ is shown in Fig. 7; this state is localized in the collinear $F - H - D$ arrangement with 3-quanta of excitation in the asymmetric stretch mode, and 0-quanta of excitation in the bend and symmetric stretch modes. If the state pictured in Fig. 7 is used as an initial (prepared) state in a wavepacket calculation, one observes pure

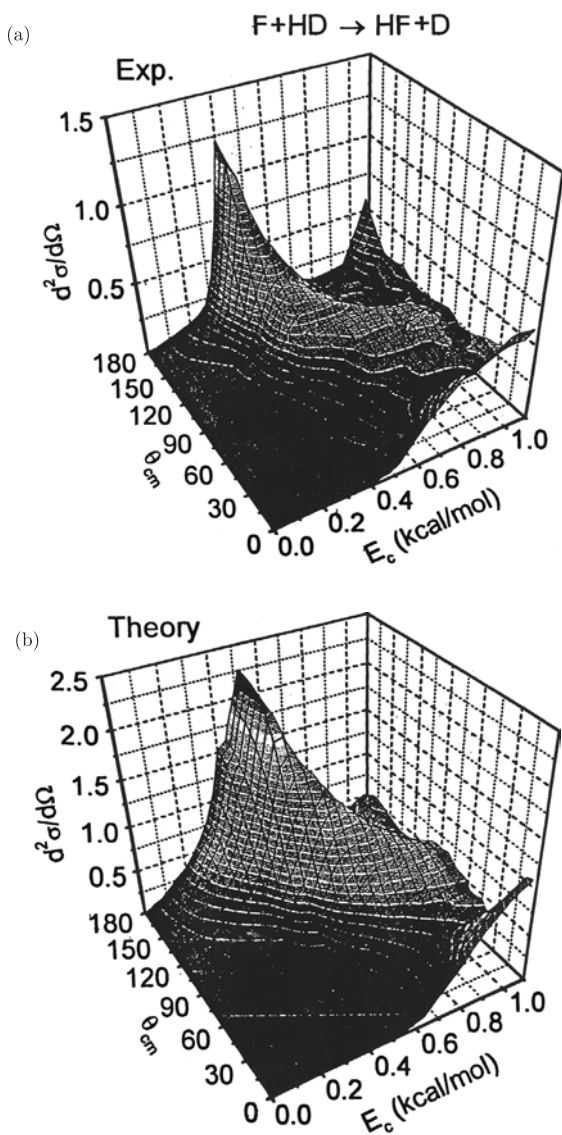


Fig. 6. The total differential cross-section in $\text{\AA}^2/\text{sr}$ for the $\text{HF} + \text{D}$ reactive channel. (a) Shows the experimental results while (b) presents the result of the scattering calculation. Note the ridge running from large θ (backward) at low energies to small θ (sideways) at higher E_C 's.

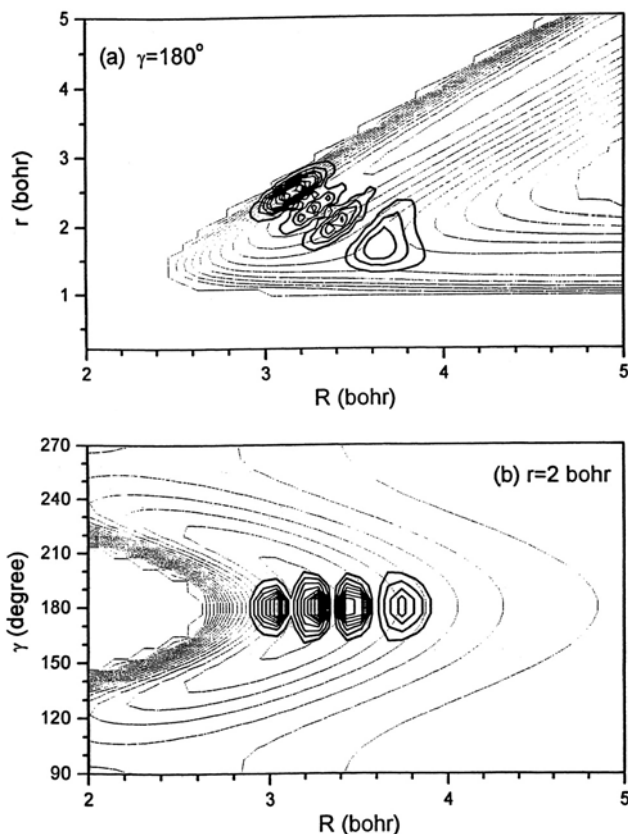


Fig. 7. The probability density of the reactive resonance at $E_C = 0.52$ kcal/mol. In (a) the F-H-D collinear subspace is shown using the Jacobi coordinates (R, r) . In (b), the probability density is sliced $r = 2$ Bohr and is shown in the (R, γ) coordinates. The plot clearly shows a state with 3 nodes along the asymmetric stretch and 0 nodes in the symmetric stretch and bend.

exponential decay with a lifetime of 109 fs, consistent with the width of the Lorentzian peak in the partial cross-section. Furthermore, the product state distribution of the decaying resonance is consistent with the results of the scattering calculations for $E_C < 1$ kcal/mol. Takayanagi and Wada⁷³ have performed a stabilization calculation that confirmed the existence of the resonance state on the SW-PES.

Finally, quantum mechanical trapping at the resonance energy can be verified using a time-delay analysis on the quantum **S**-matrix. In Fig. 8, the average time delay for the $J = 0$ partial wave of the $F + HD \rightarrow HF + D$ reaction, defined using Eq. (22), is plotted versus collision energy. A clear

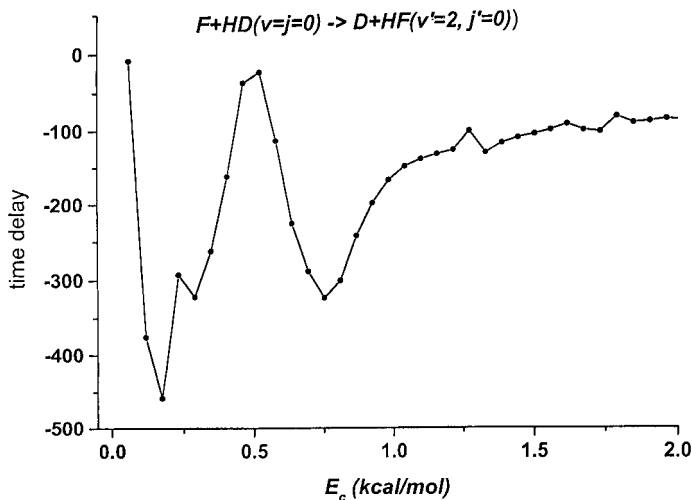


Fig. 8. The time delay versus E_C for the reaction $F + HD(0, 0) \rightarrow D + HF(v' = 2, j' = 0)$ with $J = 0$. The time delay was computed using Wigner's definition.

peak in the time-delay is observed near the resonance energy. Higher partial waves exhibit similar behavior with the peak of the time-delay J -shifting according to Eq. (29).

In summary, the reactive resonance for the $F + HD \rightarrow HF + D$ reaction is found to leave clear signatures on a variety of collision observables. The resonance state itself is readily extracted from the quantum dynamics on the SW-PES, and the scattering observables are found to correlate well with the predictions of theory.

3.2. $F + H_2$

Resonance phenomenon in the $F + H_2$ system was predicted^{74,75} in the early 1970s based on theoretical modelling of the collinear reaction dynamics employing the Muckerman-5 empirical PES.⁷⁶ The case for a reactive resonance was strongly bolstered by the molecular beam experiments of Lee and co-workers,⁵⁷ who observed an anomalous forward peak in the product distribution of the $HF(v' = 3)$ product state. However, the issue was thrown into some doubt when the quantum scattering calculations on the accurate SW-PES failed to yield a clear resonance signature in the quantum time delay.⁷⁷ Furthermore, QCT calculations⁷¹ also revealed a forward peak in

the $\text{HF}(v' = 3)$ product, which seemed to suggest that the hypothesis of a quantum scattering resonance was not necessary to explain the experiment. A direct measurement of the transition state spectrum using anion photodetachment by Neumark and co-workers⁷⁸ was finally assigned to van der Waals states without need for transition state resonances.

The excitation function for the $\text{F} + \text{H}_2 \rightarrow \text{HF} + \text{H}$ reaction was recently measured by Liu and co-workers⁷⁹ in a molecular beam apparatus over the range of collision energies 0.1–3.0 kcal/mol for both *normal*- and *para*- H_2 reagent. Unlike the $\text{F} + \text{HD}$ reaction, no clear resonance step was apparent in $\sigma_R(E)$. However, there was a significant difference between the $\text{H}_2(n)$ and $\text{H}_2(p)$ reactivity implying a fairly strong dependence on the reagent rotational state. As seen in Fig. 9, the quantum scattering calculations of Chao and Skodje⁸⁰ are in reasonable agreement with experiment, although some inaccuracies in the SW-PES are apparent. However, the theory does yield a small double step feature in $\sigma_R(E)$ for $\text{H}_2(p)$ at $E_C = 0.34$ kcal/mol that was too faint to resolve in the beam experiment. The partial cross-sections for the individual partial waves, shown in Fig. 10, reveal that the double step in $\sigma_R(E)$ is the by-product of two Lorentzian peaks spaced by

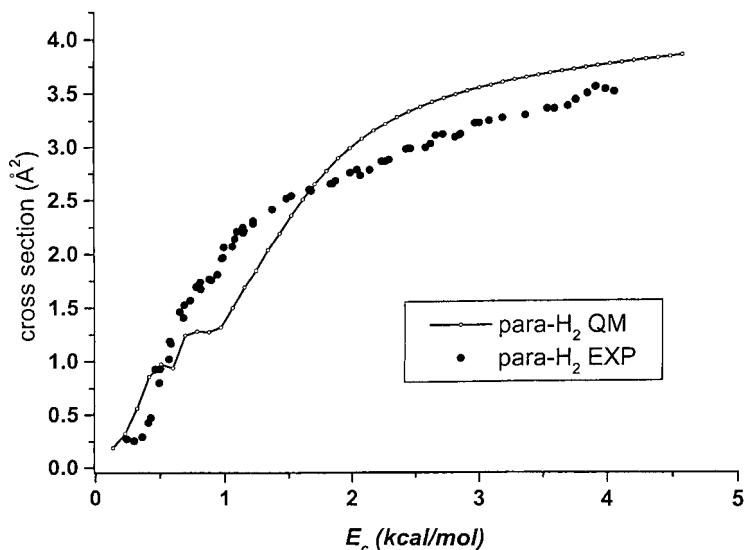


Fig. 9. The excitation function in \AA^2 for the reaction $\text{F} + p\text{-H}_2 \rightarrow \text{H} + \text{HF}$ versus collision energy. The solid line is the result of quantum scattering calculations done with the SW-PES and the points are the molecular beam experiments.

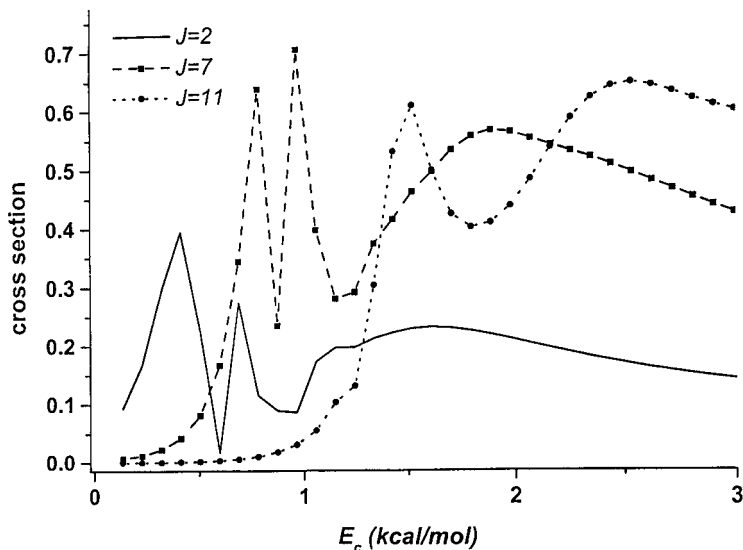


Fig. 10. The partial cross-section summed over all final states in A^2 for $F + H_2(0, 0) \rightarrow H + HF$ for several values of the total angular momentum J . The partial cross-section shows a double peak structure which J -shift to higher energy with J , and eventually merge at about $J = 10$.

about 0.3 kcal/mol. These peaks move closer together as J is increased, until they merge into a single peak for $J > 10$. The effective B -constants obtained by fitting the two peak energies to Eq. (29) imply that the geometry of the lower energy peak is consistent with the transition state, while the higher energy peak gives a smaller B -constant more in keeping with the geometry of the minimum of the van der Waals well in the $H-HF$ channel. Thus, while some hint of resonant behavior in $\sigma_R(E)$ may exist, the effect is too small to be clearly seen in the experiment.

The origin of the double peak structure in the partial cross-sections was clearly established by use of the SQ procedure.⁸⁰ It was found that the lower energy peak was due to a reactive resonance with an identical mode assignment as for $F + HD$ with $E_R(J = 0) = 0.34$ kcal/mol and $\Gamma = 0.26$ kcal/mol, while the higher peak was assigned to the $H - HF(v' = 3, j' = 0)$ van der Waals state at 0.62 kcal/mol.⁸¹ The complexity of the $F + H_2$ reaction, compared to $F + HD$, is largely the result of the overlapping (and interfering) contributions of these two states to the collision observables. In contrast, for the $F + HD$ reaction, the corresponding $D - HF(v' = 3, j' = 0)$ state

lies at 1.31 kcal/mol that is high enough not interfere with the resonance contribution.

While it is clear that a resonance does exist for $F + H_2$ on the SW-PES, many of the INR probes for resonant behavior fail. As noted above, Manolopoulos and co-workers⁷⁷ did not detect a peak in the time delay function at the resonance energy. In Fig. 11, we have reproduced that calculation (using a finer energy grid). At the purported resonance energy, $E_C = 0.34$ kcal/mol, a vague shoulder is seen in the time delay rather than a peak. Obviously complicating the analysis, however, is the rapidly varying “background” time delay, which is reflecting the nearby energetic threshold to reaction. Similarly, the calculated rotational product state distributions, shown in Fig. 12, show no clear imprints of the resonance behavior. Any unusual rotational signatures from the nascent resonance decay are apparently damped by passage through the van der Waals region.

As presaged by Lee and co-workers,⁵⁷ it is in the angular distributions that the clearest sign of resonance behavior is observed. In Fig. 13, we plot the calculated DCS versus E_C and θ for $F + H_2 (p) \rightarrow HF (v' = 2) + H$ summed over j' -states. Near the resonance energy, we observe a very dramatic change in the angular product distribution. At $E_C = 0.34$ kcal/mol

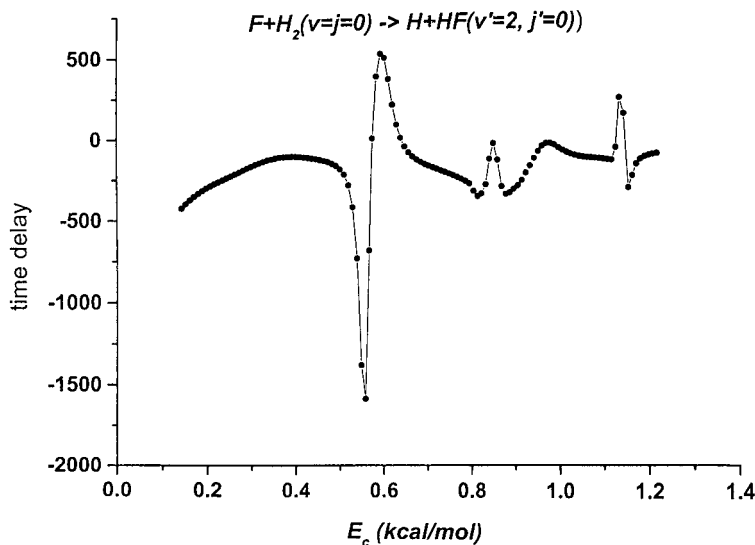


Fig. 11. The (Wigner) time delay versus E_C for the reaction $F + H_2(0, 0) \rightarrow H + HF(v' = 2, j' = 0)$ with $J = 0$, where the same expression used for $F + HD$ was employed.

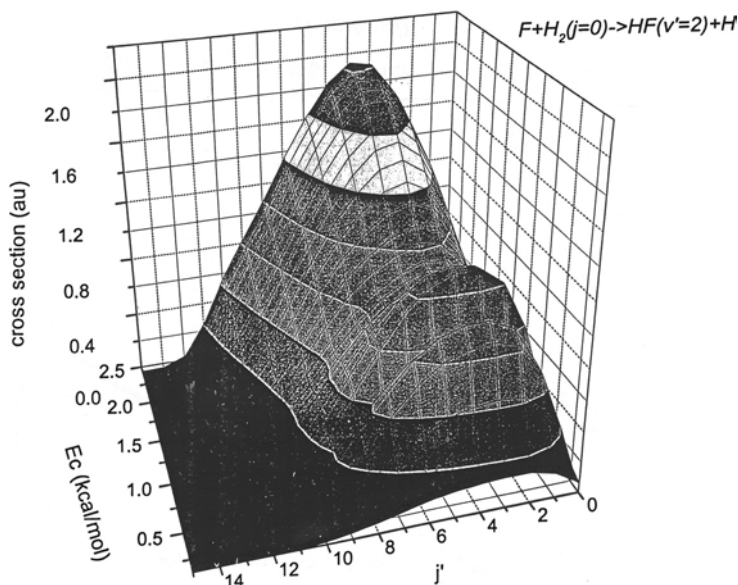


Fig. 12. The ICS for $F + H_2(v = 0, j = 0) \rightarrow H + HF(v' = 2, j')$ versus E_C and j' computed from quantum scattering theory using the SW-PES.

the DCS is backward peaked, at $E_C = 0.55$ kcal/mol it swings to the forward direction, then again by $E_C = 0.8$ kcal/mol it shifts again into the backward direction. This very pronounced oscillation in the DCS is the result of interference between contributions from the reactive resonance and the van der Waals state. At higher energies, such as those considered by Lee and co-workers, the resonance contributions to the DCS are most apparent in the forward scattering direction.

Unfortunately, the experimental confirmation of the dramatic energy/angle correlations predicted by theory has not yet been obtained in the laboratory. Lee and Liu did not obtain the DCS in the critical 0.2–1.0 kcal/mol range of collision energies. An experimental determination of the DCS on a fine grid of energies would be quite useful, both as a confirmation of the theory and for new information about the potential energy surface. It is our experience that the details of the DCS are extremely sensitive to the PES. Indeed, we expect that errors as small as 0.1 kcal/mol in the PES would be apparent from disagreements between theory and experiment. The SW-PES is certainly in error in the exit channel, both in the predicted exothermicity and in the details of the vdW-well which will likely greatly modify DCS for $F + H_2$ at low collision energies.

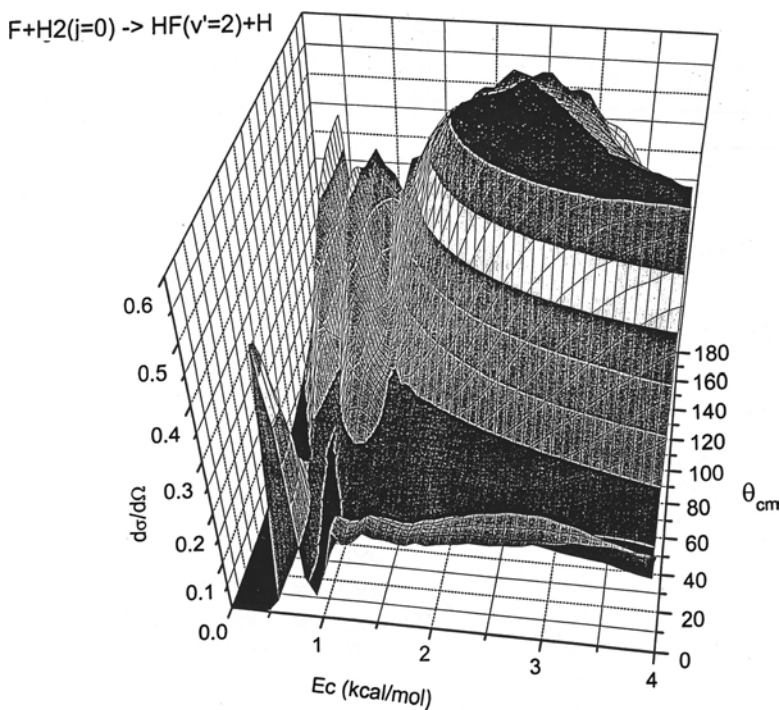


Fig. 13. The differential cross-section in $\text{\AA}^2/\text{sr}$ for $F + H_2$ ($v = 0, j = 0$) \rightarrow $H + HF$ ($v' = 2, j' = \text{all}$). Notice the strong energy-angle correlation at low collision energy.

3.3. H + HD

The search for reactive resonances in the $H + H_2$ reaction (and its isotopomers) has a long history.^{1-4,82} The existence of resonances was first conjectured based on theoretical collinear quantum dynamics simulations using approximate PES.⁵⁻⁸ Subsequent improvements in theory, such as the use of a very accurate PES and the implementation of full 3D-dynamics, strongly implied that the resonances should actually exist in the “real” system.¹¹⁻¹³ Despite the simplicity of this reaction, it has only been rather recently that *ab initio* theoretical reaction dynamics have been brought into agreement with state-resolved experimental results.^{62,83,84} Nevertheless, clear signatures of resonant behavior have proven to be very difficult to identify in experiment, and there have been several false sightings reported. By any measure, experimental conditions required for the measurements are

quite rigorous. The resonances are predicted to exist at high E_C , requiring hot-atom beam sources such as HI-photolysis products for which it is difficult to obtain a well-calibrated energy tunable beam. Furthermore, the resonances will likely have very short lifetimes (~ 20 fs) and thus will display very large widths as a function of collision energy, ~ 0.5 kcal/mol. Therefore, it becomes a subtle matter to distinguish between the direct and resonance contributions to the scattering cross-sections. Further complicating the analysis is the possible influence of the geometrical phase⁸⁵ that might have significant effects on the resonance properties, as stressed by Kuppermann and co-workers.⁸⁶ Weak undulations in certain state-resolved ICSs versus E_C for $\text{H} + \text{D}_2$ have been predicted by Chao and Skodje⁸⁷ but are likely to be at or below the detection threshold. These undulations, seen most strongly for the ICSs $\sigma_R(00 \rightarrow 00)$ and $\sigma_R(00 \rightarrow 02)$, are problematic as resonance fingerprints since they are not uniquely correlated to the barrier states of the reaction. Zare and co-workers⁵⁹ have observed a forward peak in the $\text{H} + \text{D}_2$ DCS, which is consistent with a resonance picture. Theoretical simulations have in fact demonstrated that the forward peak does exhibit extra time delay in line with the physical picture outlined above.^{61,88}

Here we consider the $\text{H} + \text{HD} \rightarrow \text{D} + \text{H}_2$ reaction, which has recently been studied experimentally and theoretically by Harich *et al.*⁶² The reaction was investigated experimentally in a cross-molecular beam apparatus employing the D-atom Rydberg tagging detection scheme originally proposed by Welge and co-workers.⁸³ The hot H-atom beam source was provided by HI-photolysis that produced two well-separated collision energies, $E_C = 0.499$ eV and 1.200 eV. The initial HD beam was cooled to the point where only the ground state, HD (0,0), was represented in the beam. The state-resolved DCSs were obtained for all the important rovibrational product channels. The theoretical analysis involved QCT, quantum scattering, and wavepacket calculation on the accurate BKMP2-PES,⁸⁹ but without the geometrical phase.

In Fig. 14, the ICSs for several channels are plotted versus total energy, $E = E_C + 0.235$ eV. The experiment (plotted with symbols) and theory are in good agreement, but show no clear sign of resonance behavior over the energy range considered. Although the underlying reaction probabilities $P_R(v, j \rightarrow v', j'; E_C, J)$ do exhibit modest oscillation versus E_C , the impact parameter averaging effectively washes out this structure in the cross-sections. Similarly, the j' -dependence of the $\text{D} + \text{H}_2(v' = 0, j')$ products (Fig. 15) show no unusual energy dependence of the sort seen previously for $\text{F} + \text{HD}$. We note parenthetically, however, there is a dramatic

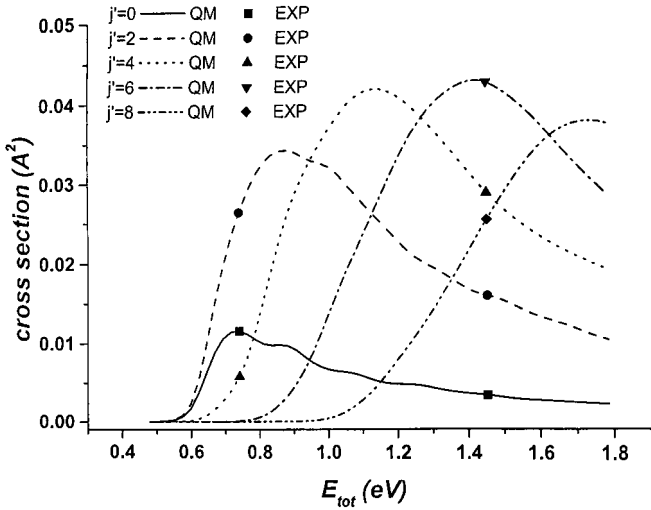


Fig. 14. The ICS for $\text{H} + \text{HD}(v = 0, j = 0) \rightarrow \text{D} + \text{H}_2(v' = 0, j')$ versus total energy for several final rotational channels. The curves are obtained from quantum scattering theory while the symbols are experimental results.

effect of spin-statistics that causes the distributions to exhibit a saw-toothed dependence on j' . The state resolved DCSs for several states is shown in Fig. 16. Several of the DCSs do show weak vestiges of the resonance ridge, such as the $d\sigma_R(0, 0 \rightarrow 0, 0)/d\Omega$. The ridge in these cases is clearly associated with the maximum of the ground adiabatic potential (i.e. the lowest barrier state) and not with any higher-lying Feshbach-type resonances. The most dramatic effect in the angular distributions is the presence of a strong and very narrow forward scattering peak in the DCS for low rotational product states. This forward peak was observed in both the theoretical and experimental results. As seen in Fig. 16, the forward peak for the $(0, 0 \rightarrow 0, 0)$ case begins at about $E_C = 1$ eV and persists to the highest energies considered. Other final rotational states likewise show a forward peak, but at progressively higher energies.

The results indicate that the strongest case for reactive resonances in the $\text{H} + \text{HD}$ reaction is to be found in the forward peaking of the DCS. To establish the link between the forward peak and resonance behavior, it is necessary to analyze the underlying reaction dynamics that give rise to the forward peaking. First, as noted in other reactions, the forward peak is the by-product of high impact parameter (i.e. high J) reactive scattering. As an illustration, in Fig. 17 we plot forward scattering integrated opacity

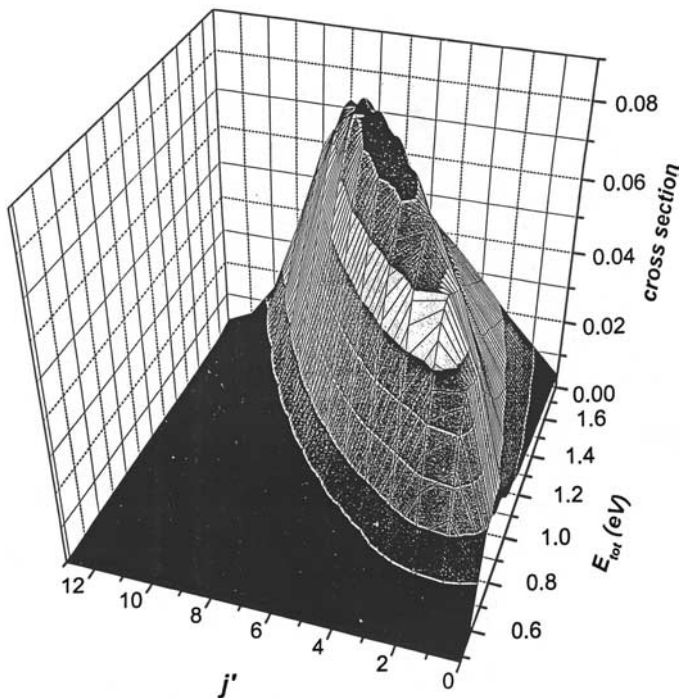
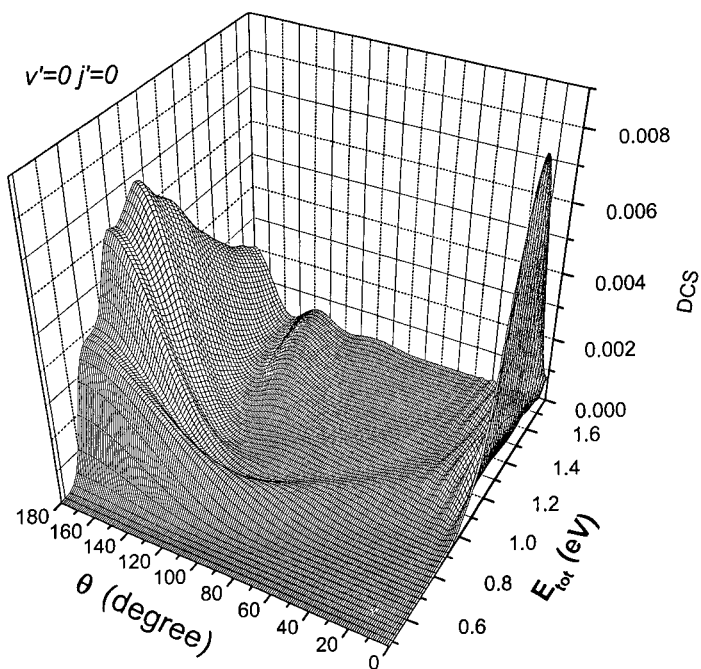


Fig. 15. The ICS for $\text{H} + \text{HD}(v = 0, j = 0) \rightarrow \text{D} + \text{H}_2(v' = 0, j')$ versus E_C and j' computed from quantum scattering theory using the BKMP2-PES.

function, Eq. (28), $d\sigma_R(00 \rightarrow 00; \theta = 0, E_C, J_{\max})/d\Omega$ versus J_{\max} at the experimental collision energy of $E_C = 1.200$ eV. As seen in the figure, the forward peak comes from just a small number of partial waves near the value $J_{\max} = 25$; at this value of J , the vibrationally adiabatic barriers are centrifugally-shifted upward by about 0.5 eV relative to the non-rotating barriers. Next, we note that the forward scattering peak is rotationally cold and vibrationally hot compared to scattering in other directions. By averaging the DCS over the narrow interval $\theta = [0-5^\circ]$, it is found that $\langle j' \rangle_{\theta=0} = 1.3$ and $\langle E'_{\text{vib}} - E_{\text{H}_2}(v' = 0, j' = 0) \rangle_{\theta=0} = 1155 \text{ cm}^{-1}$. These numbers can be contrasted with the ICSs results that are averaged over all scattering angles: $\langle j' \rangle_{\text{all}} = 5.3$ and $\langle E'_{\text{vib}} - E_{\text{H}_2}(v' = 0, j' = 0) \rangle_{\text{all}} = 574 \text{ cm}^{-1}$. In Fig. 18, we plot the mean product vibrational energy versus scattering angle for $\text{H} + \text{HD}(0,0) \rightarrow \text{D} + \text{H}_2(v', j')$ at $E_C = 1.200$ eV, which clearly reveals the special product distribution in the forward direction. Finally, to connect the forward scattering to dynamical trapping phenomena, we

(a)



(b)

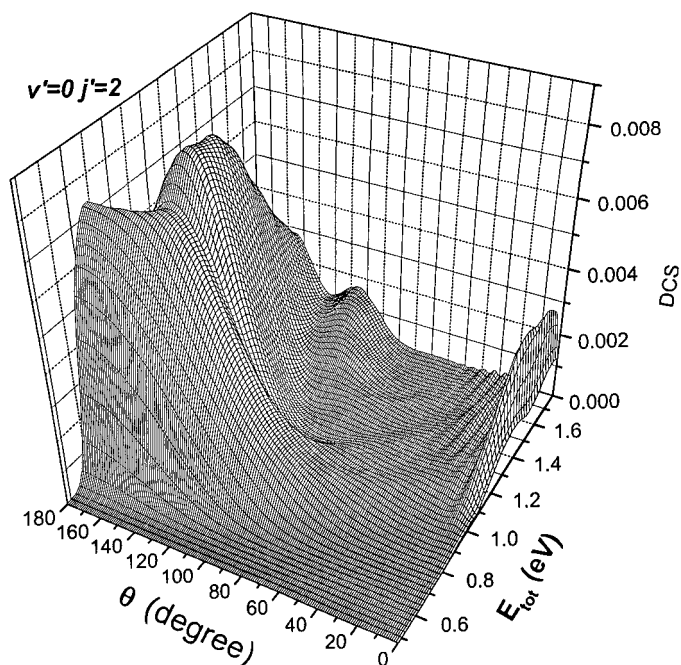


Fig. 16. The DCS in $\text{\AA}^2/\text{sr}$ for the several final states of the $\text{H} + \text{HD}(v=0, j=0) \rightarrow \text{D} + \text{H}_2(v', j')$ reaction. The results were computed from quantum scattering theory using

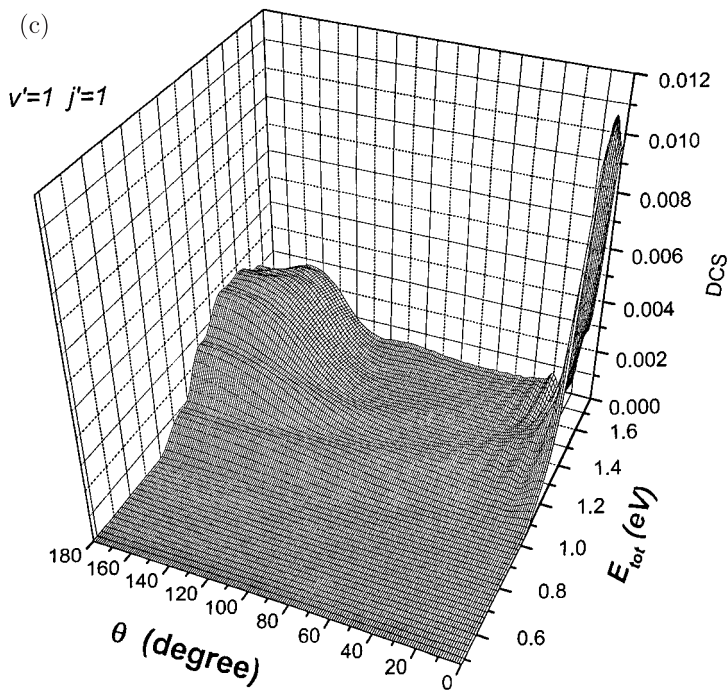


Fig. 16. (Continued)

consider the behavior of the angle-dependent time delay. In Fig. 19, we plot the j' -averaged time-delay for $\text{H} + \text{HD}(0,0) \rightarrow \text{D} + \text{H}_2(v' = 0)$ versus scattering angle at $E_C = 1.200 \text{ eV}$. The forward direction is seen to exhibit a time delay about 20 fs longer than the other scattering directions.

The state assignment of resonance which gives rise to the forward peaking is a delicate issue. It is clear from Fig. 17 that the state involved is highly rotationally excited thus the resonance states are distorted from their $J = 0$ counterparts. However, it is possible to demonstrate on energetic grounds that the $J = 25$ resonance corresponds to the adiabatic barrier maximum of two internal states of the H-H-D complex, viz. the $(v_{ss}, v_{\text{bend}}) = (1, 0)$ and $(0, 2)$. Since neither adiabatic potential curve, $V_{\text{ad}}(s; 1, 0)$ nor $V_{\text{ad}}(s; 0, 2)$, exhibit sufficiently deep wells to trap a Feshbach resonance at $J = 25$, the resonance state is a barrier state. Because of the near degeneracy of the two barrier heights, the trapping will involve a combination of symmetric stretch and bend excitations at the transition state.

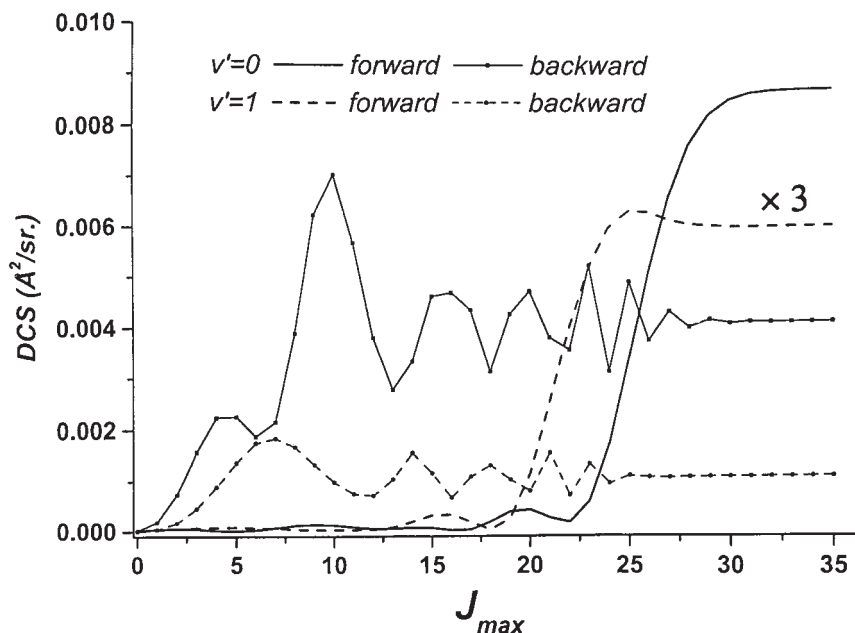


Fig. 17. The angle-dependent integrated opacity function $d\sigma_R(00 \rightarrow v' = 0, 1, j' = 0; \theta, E_C, J_{\max})$ versus J_{\max} computed for the experimental energy $E_C = 1.200$ eV. This quantity is computed by restricting the partial wave sum in the DCS to the terms $J \leq J_{\max}$. The result is shown for forward and backward scattering to illustrate the J -contributions to scattering at different θ .

The SQ method extracts resonance states for the $J = 25$ dynamics by using the centrifugally-shifted Hamiltonian. In Fig. 20, the SQ wavefunction for a trapped state at $E_C = 1.2$ eV is shown. The wavefunction has been sliced perpendicular to the minimum energy path and is plotted in the symmetric stretch and bend normal mode coordinates. As anticipated, the wavefunction shows a combination of one quanta of symmetric stretch excitation and two quanta of bend excitation. The extracted state is barrier state (or quantum bottleneck state) and not a Feshbach resonance.

In summary, the $\text{H} + \text{HD}$ reaction shows little sign of resonance scattering in the ICS. Furthermore, the product distributions without angle resolution show no unusual behavior as functions of energy that might indicate resonance behavior. On the other hand, the forward peaking in the angular product distribution does appear to reveal resonance structure. Since time-delay analysis is at present not possible in a molecular beam experiment, it is the combination of a sharp forward peak with the unusual

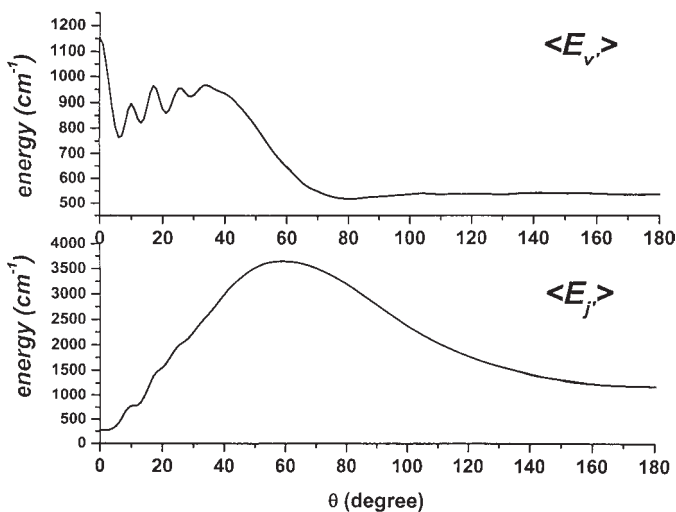


Fig. 18. The average product rotational and vibrational excitation versus scattering angle for $\text{H} + \text{HD}(v = 0, j = 0) \rightarrow \text{D} + \text{H}_2$ at $E_C = 1.200 \text{ eV}$ computed by quantum scattering theory.

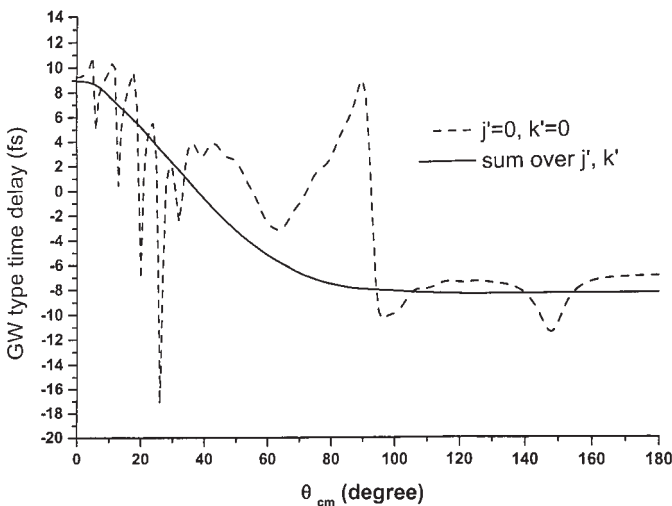


Fig. 19. The scattering time delay versus θ for $\text{H} + \text{HD}(v = 0, j = 0) \rightarrow \text{D} + \text{H}_2$ at $E_C = 1.200 \text{ eV}$. The dashed curve is the result obtained using the formula of Goldberger for the final state $\text{H}_2(v' = 0, j' = 0)$, while the solid line is the result of averaging over the final rotational states, j' for the dominant $v' = 0$ product. Both curves show roughly an extra 20 fs of time delay in the forward direction, but the averaging eliminates the spurious structures that are related to minima in the DCS versus θ .

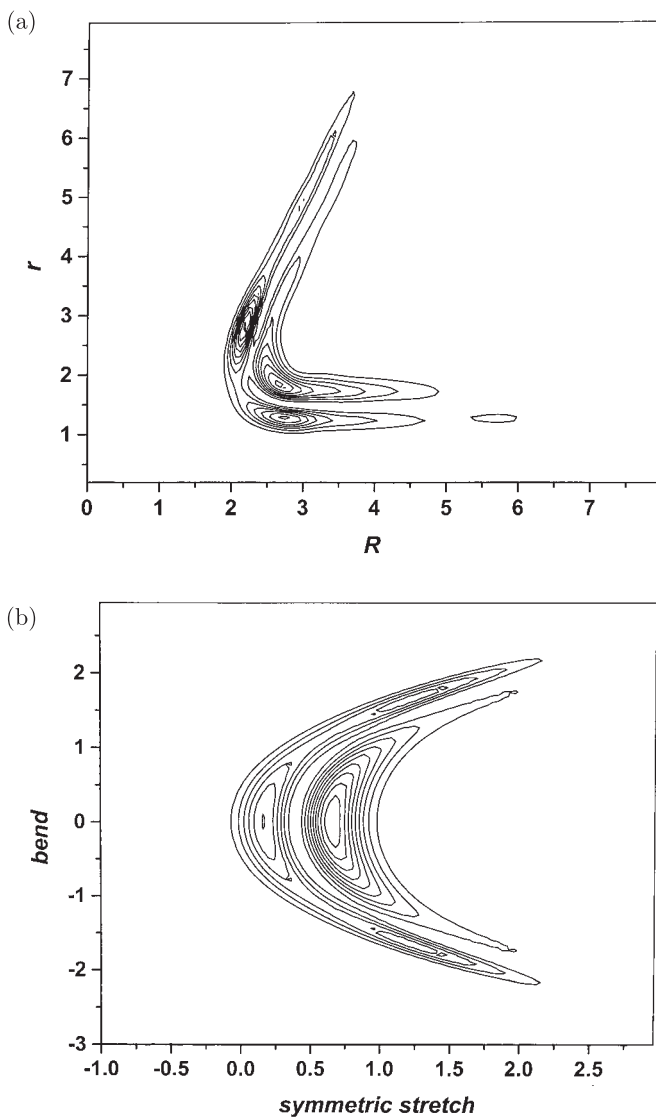


Fig. 20. A resonance state for the H + HD system at $E_C = 1.2$ eV at a total angular momentum of $J = 25$. In (a) the wavefunction is shown in the H+HD Jacobi coordinates for the collinear subspace. In (b) the wavefunction has been sliced perpendicular to the minimum energy path and is plotted in symmetric stretch and bend normal mode coordinates.

angular product distribution that most clearly indicates the presence of a resonance.

4. Conclusions

As we have discussed, the influence of reactive resonance on the outcome of a collision experiment is a subtle one. Unlike the dramatic resonance phenomena observed in nuclear and atomic collision processes, reactive resonances are often only revealed after very careful analysis. The important point to make is that the required analysis can now be accomplished for many reactions. The field of gas phase reaction dynamics has reached a level of maturity where accurate theory and experiment can be combined to reveal the fundamental characteristics of the reaction process. Short-lived resonance states play an essential role in the detailed dynamical analysis of many systems. As we have seen, resonances can have a large influence on physical observables such as excitation functions, state-to-state branching ratios, and angular product distributions. Even highly averaged quantities, like the low temperature reaction rate constant for $F + HD \rightarrow D + HF$, can be strongly affected by processes like resonance tunnelling. In addition to large quantitative effects on the reaction attributes, we should also emphasize that these effects are also very sensitive to details of the PES and to dynamical approximation. Agreement between theory and experiment for resonant observables provides, for both, a very stringent test of accuracy.

Undoubtedly, many reactions investigated in the future will possess reactive resonances. It would be desirable to have in place unambiguous diagnostic tests that would reveal whether or not a new system supported resonance states. The case studies considered above should make it clear, however, that such diagnostics are not easily identified. Perhaps as more systems are investigated, a more or less complete set of possible resonance signatures may be determined. At this point, however, each new system shows some novel resonance features. Given an accurate PES, theoretical analysis can, in principle, provide a more definitive determination of whether or not a reactive resonance exists for a system. Since scattering can be investigated for single partial waves, resonance signatures are identified using techniques such as time-delay analysis or spectral quantization without the complication of impact parameter averaging. Given that theory shows the existence of a reactive resonance on a reliable PES, it then becomes a somewhat empirical undertaking to determine which dynamical observables are the most strongly affected.

Acknowledgments

We are grateful to our collaborators, K. Liu, S. H. Lee, F. Dong, D. E. Manolopoulos, D. Skouteris, X. Yang, S. Harich, D. Dai and C. C. Wang. This work was supported by the National Science Foundation.

Note Added in Proof

Since the submission of this article in 2002, there has been a great deal of new work published on the subject of resonances and quantum bottleneck states in chemical reactions. Unfortunately, a discussion of these exciting new results was not possible here.

References

1. A. Kuppermann, in *Potential Energy Surfaces and Dynamics Calculations*, ed. D. G. Truhlar (Plenum Press, New York, 1981), p. 375.
2. B. C. Garrett, D. W. Schwenke, R. T. Skodje, D. Thirumalai, T. C. Thompson and D. G. Truhlar, ACS Symposium Series 263 (American Chemical Society, Washington D.C., 1984), pp. 375–400.
3. K. Liu, *Annu. Rev. Phys. Chem.* **52**, 139 (2001).
4. F. Fernandez-Alonso and R. N. Zare, *Annu. Rev. Phys. Chem.* **53**, 67 (2002).
5. D. G. Truhlar and A. Kuppermann, *J. Chem. Phys.* **52**, 3841 (1970).
6. D. G. Truhlar and A. Kuppermann, *J. Chem. Phys.* **56**, 2232 (1972).
7. R. D. Levine and S.-F. Wu, *Chem. Phys. Lett.* **11**, 557 (1971).
8. S.-F. Wu and R. D. Levine, *Mol. Phys.* **22**, 881 (1971).
9. G. C. Schatz and A. Kuppermann, *J. Chem. Phys.* **59**, 964 (1973).
10. G. C. Schatz and A. Kuppermann, *Phys. Rev. Lett.* **35**, 1266 (1975).
11. M. S. Zhao, M. Mladenovic, D. G. Truhlar, D. W. Schwenke, O. Sharafeddin, Y. Yan and D. J. Kouri, *J. Chem. Phys.* **91**, 5302 (1989).
12. S. A. Cuccaro, P. G. Hipes and A. Kuppermann, *Chem. Phys. Lett.* **157**, 440 (1989).
13. R. T. Skodje, R. Sadeghi, H. Koppel and J. L. Krause, *J. Chem. Phys.* **101**, 1725 (1994).
14. S. K. Gray, *J. Chem. Phys.* **96**, 6543 (1992).
15. R. Sadeghi and R. T. Skodje, *J. Chem. Phys.* **98**, 9208 (1993); *ibid.* **99**, 5126 (1993).
16. R. Sadeghi and R. T. Skodje, *J. Chem. Phys.* **102**, 193 (1995).
17. G. Jolicard, C. Leforestier and E. J. Austin, *J. Chem. Phys.* **88**, 1026 (1988).
18. V. Mandelstam and H. S. Taylor, *J. Chem. Phys.* **107**, 5756 (1997).
19. D. M. Neumark, *Annu. Rev. Phys. Chem.* **43**, 153 (1992).
20. A. Weaver, R. B. Metz, S. E. Bradforth and D. M. Neumark, *J. Phys. Chem.* **92**, 5558 (1988).
21. W. H. Miller, N. C. Handy and J. E. Adams, *J. Chem. Phys.* **72**, 99 (1980).
22. A. D. Isaacson and D. G. Truhlar, *J. Chem. Phys.* **76**, 1380 (1982).

23. R. S. Friedman and D. G. Truhlar, *Chem. Phys. Lett.* **183**, 539 (1991).
24. D. C. Chatfield, R. S. Friedmann, D. W. Schwenke and D. G. Truhlar, in *Dynamics of Molecules and Chemical Reactions*, eds. R. E. Wyatt and J. Z. H. Zhang (Marcel Dekker, New York, 1996), p. 323.
25. E. Pollak and P. Pechukas, *J. Chem. Phys.* **69**, 1218 (1978).
26. O. Zobay and G. Alber, *J. Phys.* **B26**, L539 (1993).
27. I. Burhardt and P. Gaspard, *J. Chem. Phys.* **100**, 6395 (1994).
28. T. Seideman and W. H. Miller, *J. Chem. Phys.* **95**, 1768 (1991).
29. V. Ryaboy and N. Moiseyev, *J. Chem. Phys.* **98**, 9618 (1993).
30. R. Sadeghi and R. T. Skodje, *Phys. Rev.* **A52**, 1996 (1995).
31. R. S. Friedman and D. G. Truhlar, in *Multiparticle Quantum Scattering with Applications to Nuclear, Atomic, and Molecular Physics*, eds. D. G. Truhlar and B. Simon (Springer-Verlag, New York, 1997), p. 243.
32. H.-D. Meyer, *J. Phys.* **B16**, 2265 (1983).
33. S. D. Chao and R. T. Skodje, *Theoretical Chem. Acc.* **108**, 273 (2002).
34. D. C. Chatfield, S. L. Mielke, T. C. Allison and D. G. Truhlar, *J. Chem. Phys.* **112**, 8387 (2000).
35. M. L. Goldberger and K. M. Watson, *Collision Theory* (Wiley, New York, 1964).
36. G. Breit and E. P. Wigner, *Phys. Rev.* **49**, 519 (1936).
37. J. R. Taylor, *Scattering Theory* (Wiley, New York, 1972).
38. M. J. Redmon and R. E. Wyatt, *Chem. Phys. Lett.* **63**, 209 (1979).
39. G. C. Schatz, D. Sokolovski and J. N. L. Connor, *J. Chem. Phys.* **94**, 4311 (1991).
40. E. P. Wigner, *Phys. Rev.* **98**, 145 (1955); L. Eisenbud, PhD thesis, Princeton University.
41. F. T. Smith, *Phys. Rev.* **118**, 349 (1960).
42. Ref. 35, p. 494; also see, M. L. Goldberger, K. M. Watson, *Phys. Rev.* **127**, 2284 (1962); M. Froissart, M. L. Goldberger and K. M. Watson, *Phys. Rev.* **131**, 2820 (1963).
43. A. Kuppermann and Y.-S. M. Wu, *Chem. Phys. Lett.* **241**, 229 (1995); **243**, 586 (1995) (E).
44. A. J. Seigert, *Phys. Rev.* **56**, 750 (1939).
45. A. U. Hazi and H. S. Taylor, *Phys. Rev.* **A1**, 1109 (1970).
46. T. C. Thompson and D. G. Truhlar, *J. Phys. Chem.* **88**, 210 (1984).
47. S. Skokov and J. M. Bowman, *J. Chem. Phys.* **111**, 4933 (1999).
48. W. P. Reinhardt, *Annu. Rev. Phys. Chem.* **33**, 223 (1982).
49. R. T. Skodje, R. Sadeghi and J. L. Krause, *Chem. Phys.* **240**, 129 (1999).
50. B. Maiti, S. Mahapatra and N. Sathyamurthy, *J. Chem. Phys.* **113**, 59 (2000).
51. A. J. C. Varandas and H. G. Yu, *Chem. Phys.* **209**, 31 (1996).
52. W. B. Miller, S. A. Safron and D. R. Herschbach, *Discuss. Faraday Soc.* **44**, 108 (1967).
53. W. H. Miller and J. Z. H. Zhang, *J. Phys. Chem.* **95**, 12 (1991).
54. F. J. Aoiz, V. J. Herrero and V. S. Rabanos, *J. Chem. Phys.* **95**, 7767 (1991); *ibid.* **97**, 7423 (1994).
55. D. Sokolovski and J. N. L. Connor, *Chem. Phys. Lett.* **305**, 238 (1999).

56. D. Sokolovski, J. F. Castillo and C. Tully, *Chem. Phys. Lett.* **313**, 225 (1999).
57. D. M. Neumark, A. M. Wodke, G. N. Robinson, C. C. Hayden, R. Shobatake and Y. T. Lee, *J. Chem. Phys.* **82**, 3045 (1985).
58. D. M. Neumark, A. M. Wodke, G. N. Robinson, C. C. Hayden, R. Shobatake, R. K. Sparks, T. P. Schafer and Y. T. Lee, *J. Chem. Phys.* **82**, 3067 (1985).
59. F. Fernandez-Alonso, B. D. Bean, J. D. Ayers, A. E. Pomerantz, R. N. Zare, L. Banares and F. J. Aoiz, *Angew. Chem. Int. Ed.* **39**, 2748 (2000).
60. F. Fernandez-Alonso, B. D. Bean and R. N. Zare, *J. Chem. Phys.* **111**, 1022 (1999); *ibid.*, **111**, 2490 (1999); F. Fernandez-Alonso, B. D. Bean, R. N. Zare, F. J. Aoiz, L. Banares and J. F. Castillo, *J. Chem. Phys.* **114**, 4534 (2001).
61. S. C. Althorpe, F. Fernandez-Alonso, B. D. Bean, J. D. Ayers, A. E. Pomerantz, R. N. Zare and E. Wrede, *Nature* **416**, 67 (2002).
62. S. A. Harich, D. X. Dai, C. C. Wang, X. Yang, S. D. Chao and R. T. Skodje, *J. Chem. Phys.* **116**, 4769 (2002); S. D. Chao, S. A. Harich, D. X. Dai, C. C. Wang, X. Yang and R. T. Skodje, *J. Chem. Phys.* **117**, 8341 (2002).
63. S.-H. Lee, F. Dong and K. P. Liu, *J. Chem. Phys.* **116**, 7839 (2002).
64. W. W. Harper, S. A. Nizkorodov and D. J. Nesbitt, *J. Chem. Phys.* **116**, 5622 (2002).
65. R. T. Skodje, D. Skouteris, D. E. Manolopoulos, S.-H. Lee, F. Dong and K. Liu, *J. Chem. Phys.* **112**, 4536 (2000).
66. R. T. Skodje, D. Skouteris, D. E. Manolopoulos, S.-H. Lee, F. Dong and K. Liu, *Phys. Rev. Lett.* **85**, 1206 (2000).
67. K. Liu, R. T. Skodje and D. E. Manolopoulos, *Phys. Chem. Comm.* **4** (2002).
68. J. F. Castillo and D. E. Manolopoulos, *Faraday Discuss.* **110**, 119 (1998); *ibid.* p. 213.
69. K. Stark and H.-J. Werner, *J. Chem. Phys.* **104**, 6515 (1996).
70. D. Skouteris, J. F. Castillo and D. E. Manolopoulos, *Comput. Phys. Commun.* **133**, 128 (2000).
71. F. J. Aoiz, L. Banares, V. J. Herrero, V. S. Rabanos, K. Stark and H.-J. Werner, *Chem. Phys. Lett.* **223**, 215 (1994); *J. Chem. Phys.* **102** (1995).
72. W. W. Harper, S. A. Nizkorodov and D. J. Nesbitt, *J. Chem. Phys.* **116**, 5622 (2002).
73. T. Takayanagi and A. Wada, *Chem. Phys. Lett.* **348**, 524 (2001).
74. S. F. Wu, B. R. Johnson and R. D. Levine, *Mol. Phys.* **25**, 839 (1973).
75. G. C. Schatz, J. M. Bowman and A. Kuppermann, *J. Chem. Phys.* **63**, 674 (1975).
76. J. T. Muckerman, in *Theoretical Chemistry — Advances and Perspectives*, eds. H. Eyring and D. Henderson (Academic Press, New York, 1981), Vol. 6A, p. 1.
77. J. F. Castillo, D. E. Manolopoulos, K. Stark and H.-J. Werner, *J. Chem. Phys.* **104**, 6531 (1996).
78. D. E. Manolopoulos, K. Stark, H.-J. Werner, D. A. Arnold, S. E. Bradforth and D. M. Neumark, *Science* **262**, 1852 (1993).
79. F. Dong, S. H. Lee and K. Liu, *J. Chem. Phys.* **113**, 3633 (2000).
80. S. D. Chao and R. T. Skodje, *J. Chem. Phys.* **113**, 3487 (2000).
81. T. Takayanagi and Y. Kurosaki, *J. Chem. Phys.* **109**, 8929 (1998).

- 82. W. H. Miller, *Annu. Rev. Phys. Chem.* **41**, 245 (1990).
- 83. L. Schnieder, K. Seekamp-Rahn, J. Borkowski, E. Wrede, K. H. Welge, F. J. Aoiz, L. Banares, M. J. D'Mello, V. J. Herrero, V. Saez Rabanos and R. E. Wyatt, *Science* **269**, 207 (1995); L. Schnieder, K. Seekamp-Rahn, E. Wrede and K. H. Welge, *J. Chem. Phys.* **107**, 6175 (1997); E. Wrede, L. Schnieder, K. H. Welge, F. J. Aoiz and L. Banares, *J. Chem. Phys.* **106**, 7862 (1996).
- 84. T. N. Kitsopoulos, M. A. Buntine, D. P. Baldwin, R. N. Zare and D. W. Chandler, *Science* **260**, 1605 (1993).
- 85. C. A. Mead and D. G. Truhlar, *J. Chem. Phys.* **70**, 2284 (1979).
- 86. A. Kuppermann and Y.-S. M. Wu, *Chem. Phys. Lett.* **205**, 577 (1993); *ibid.* **349**, 537 (2001).
- 87. S. D. Chao and R. T. Skodje, *Chem. Phys. Lett.* **336**, 364 (2001).
- 88. S. D. Chao and R. T. Skodje, *J. Chem. Phys.* **119**, 1462 (2003).
- 89. A. I. Boothroyd, W. J. Keogh, P. G. Martin, M. R. Peterson, *J. Chem. Phys.* **104**, 7139 (1996).

This page intentionally left blank

CHAPTER 3

STATE-TO-STATE DYNAMICS OF ELEMENTARY CHEMICAL REACTIONS USING RYDBERG H-ATOM TRANSLATIONAL SPECTROSCOPY

Xueming Yang

*State Key Laboratory of Molecular Reaction Dynamics,
Dalian Institute of Chemical Physics,
Chinese Academy of Sciences, Dalian, China
E-mail: xmyang@dicp.ac.cn*

Contents

1. Introduction	88
2. The H-atom Rydberg “Tagging” TOF Method	90
3. Unimolecular Dissociation of H ₂ O	95
3.1. H ₂ O on the \tilde{A}^1B_1 Surface: A Direct Dissociation	96
3.2. H ₂ O on the \tilde{B}^1A_1 Surface: Dissociation through Conical Intersections	104
3.2.1. OH Product Quantum State Distributions	107
3.2.2. Rovibrational Dependent Anisotropy Parameters	110
3.2.3. Effect of Parent Rotational Excitation on the OH(A) Product	111
3.2.4. Accurate Dissociation Energy of H ₂ O:D ₀ ⁰	113
3.2.5. Population Alternations and Quantum Interference	113
3.2.6. Extremely Rotationally Excited OH from HOD Dissociation through Conical Intersection	114
3.2.7. The Single N Propensity in the HOD + $h\nu \rightarrow$ OD + H Dissociation Process	117
4. The O(¹ D) + H ₂ Reaction: From Insertion to Abstraction	119
4.1. Reaction at 1.3 kcal/mol: Barrierless Insertion Reaction	120
4.2. Effect of a Single Quantum Rotational Excitation	128
4.3. Experimental Evidence for a Collinear Abstraction Mechanism in O(¹ D) + D ₂ \rightarrow OD + D	132
4.4. Quantum State Specific Dynamics for the O(¹ D) + HD \rightarrow OD + H Reaction: Isotope Effect	136

5. Quantum-State Resolved Dynamics in the H_3 System: Probing Structures and Dynamics of the Quantized Transition States	140
5.1. The $H + HD$ Reaction at $E_c = 0.498$ eV and 1.200 eV	141
5.2. Probing the Structures of Quantized Transition States in the $H +$ D_2 Reaction	149
6. Concluding Remarks	155
Acknowledgments	156
References	157

1. Introduction

Significant advances have been made on the experimental and theoretical studies of the dynamics of elementary chemical reactions during the last few decades. On the theoretical front, exact quantum scattering calculations as well as semiclassical trajectory calculations based on accurate potential energy surfaces could now provide the most detailed dynamical pictures for elementary chemical reactions. On the experimental front, on the other hand, the accurate measurements of the state-resolved scattering quantities for elementary chemical reactions are also becoming feasible. Nascent product quantum state distribution in chemical reactions can be routinely measured using many advanced laser techniques, such as laser-induced fluorescence (LIF), resonance-enhanced multiphoton ionization (REMPI), etc. In an elementary chemical reaction, quantum state distribution of nascent chemical products, however, only carries part of the product information in a molecular beam scattering experiment. Likewise, information on the angular distributions of reactive scattering products is at least as important as the product quantum state distribution to the understanding of the whole picture of chemical reactions. The development of various translational spectroscopy techniques for reactive scattering measurement has been instrumental to the understanding of bimolecular and unimolecular chemical reactions over the last few decades. Important information has been derived on primary reaction mechanisms of elementary chemical processes.¹⁻⁵ However, the lack of high resolution translational spectroscopic methods has prevented us from probing the most detailed state-to-state dynamics of many elementary bimolecular and unimolecular dissociation processes. Ideally, quantum state resolved differential cross-section measurements would provide the most detailed mechanistic information on an elementary chemical reaction, and also the most stringent test for a quantitatively accurate theoretical picture for the reaction. However, measuring the quantum state resolved differential cross-sections

are difficult, to say the least. This is largely due to the limited translational energy resolution of various translational spectroscopic techniques and poor molecular beam conditions under which molecular beam experiments are routinely carried out. Recent development of the H-atom Rydberg “tagging” time-of-flight (HRTOF)⁶ technique has provided us an extremely powerful tool for measuring state-resolved differential cross-sections for both unimolecular and bimolecular reactions with unprecedented translational energy resolution and extremely high sensitivity. This technique has been applied successfully to recent⁷ studies of the important benchmark reaction $\text{H} + \text{D}_2 \rightarrow \text{HD} + \text{H}$ and many important unimolecular dissociation processes.⁸ Recent studies on H_2O photochemistry,⁹ the $\text{O}(^1\text{D}) + \text{H}_2$ reaction¹⁰ and the $\text{OH} + \text{D}_2$ reaction¹¹ using this technique have further demonstrated the powerfulness of this method in obtaining experimentally the most detailed dynamics of these benchmark systems.

Since H-atom products from chemical reactions normally do not carry any internal energy excitation with its first excited state at 10.2 eV, which is out of reach for most chemical activations, the high-resolution translational energy distribution of the H-atom products directly reflects the quantum state distribution of its partner product. For example, in the photodissociation of H_2O in a molecular beam condition,



where α, v, N represent the electronic, vibrational and rotational states of the OH product. Total energy and linear momentum in the photodissociation process should be conserved:

$$E_i(\text{H}_2\text{O}) + E_{h\nu} - D_0(\text{H-OH}) = E_i(\text{OH}) + E_t(\text{OH}) + E_t(\text{H}) \quad (1)$$

$$m_{\text{OH}}E_t(\text{OH}) = m_{\text{H}}E_t(\text{H}). \quad (2)$$

Normally, in a molecular beam condition, $E_{\text{int}}(\text{H}_2\text{O}) \approx 0$ is not difficult to achieve. Therefore,

$$E_{\text{int}}(\text{OH}) = E_{h\nu} - D_0(\text{H-OH}) - (1 + m_{\text{H}}/m_{\text{OH}})E_{\text{trans}}(\text{H}) \quad (3)$$

Since the photon energy, $E_{h\nu}$, and the dissociation energy, $D_0(\text{H-OH})$, are constants and already known, the measured laboratory (LAB) H-atom product translational energy ($E_{\text{trans}}(\text{H})$) distribution could easily be converted into the center-of-mass (CM) OH product internal energy ($E_{\text{int}}(\text{OH})$) distribution. With sufficiently high translational energy resolution for the H-atom product, the OH quantum state distribution can be determined for this photodissociation process by simply measuring the H-atom product TOF spectra. The OH product angular distribution can also be determined

from the H-atom product angular distribution since H and OH always run in opposite directions in the CM frame. Similarly, these considerations also apply to the case of bimolecular reactions such as the $\text{O}(^1\text{D}) + \text{H}_2 \rightarrow \text{OH}(^2\Pi) + \text{H}$ reaction. In a crossed molecular beam study of a bimolecular reaction, translational energy resolution is normally limited by the spread in the collision energy rather than the intrinsic resolution of the Rydberg tagging method. In the photodissociation, higher translational energy resolution can be achieved by detecting H-atom products at the perpendicular direction of the molecular beam.

In this chapter, we will describe the most recent advances made in our laboratory on the unimolecular dissociation of the important H_2O molecule as well as the bimolecular reactions, $\text{O}(^1\text{D}) + \text{H}_2 \rightarrow \text{OH} + \text{H}$ and $\text{H} + \text{HD} \rightarrow \text{H}_2 + \text{D}$, using the H-atom Rydberg “tagging” TOF technique. Through these studies, detailed dynamical information can be extracted experimentally for these important systems.

2. The H-atom Rydberg “Tagging” TOF Method

The H-atom Rydberg “tagging” time-of-flight (HRTOF) technique was developed in the early 1990s by Welge and co-workers.⁶ The detailed experimental methods used to study the crossed beam $\text{H} + \text{D}_2 \rightarrow \text{HD} + \text{H}$ reaction have been described in great detail before.⁷ Detailed descriptions of this technique used for studying molecular photodissociation can also be found in Ref. 8. The central scheme of this technique is the two-step efficient excitation (see Fig. 1) of the H atom from its ground state to its high Rydberg levels ($n = 35 \sim 90$) without ionizing the H-atom product directly as in the $(1+1')$ -multiphoton ionization scheme used earlier. Figure 2 shows the spectrum of Rydberg transitions of the H atom from the $n = 2$ level. These high Rydberg H atoms are known to be long-lived to the millisecond timescale in a small electric field ($\sim 20 \text{ V/cm}$). The enhancement of the Rydberg H atom lifetime in a small electric field is likely to be caused by the mixing of the l quantum number in the Rydberg H atom.^{12,13} These long-lived neutral H atoms allow us to measure the time-of-flight spectrum of the neutral H-atom chemical product with extremely high translational energy resolution (as high as 0.1% in translational energy has been achieved in our laboratory). The neutral Rydberg H atoms are easy to detect using field ionization. The extremely high translational energy resolution can be achieved by minimizing the physical sizes of the “tagging” region and the field ionization region.

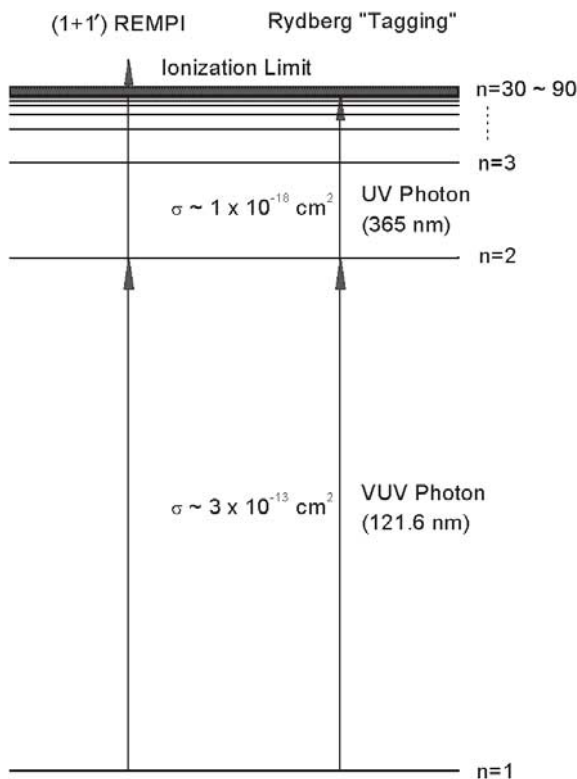
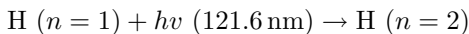
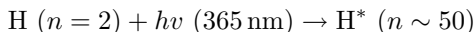


Fig. 1. Detection schemes for H-atoms. Rydberg "tagging" technique is slightly different from the $(1 + 1')$ -REMPI detection scheme in which the H atom is directly ionized; Rydberg "tagging" only pumps the H atom to a high Rydberg state.

The excitation of the ground state H-atom product ($n = 1$) is made by the following two-step excitation scheme:



and



The 121.6 nm VUV light used in the first step excitation is generated using a two-photon resonant ($2\omega_1 - \omega_2$) four-wave mixing scheme in the Kr gas cell. $2\omega_1$ (212.5 nm) is resonant with the Kr ($4p-5p$) transition.¹⁴ ω_1 is generated by doubling a dye laser pumped by a Nd:YAG (355 nm) laser, while ω_2 (845 nm) is the direct output of a dye laser pumped by the second harmonic of the same YAG laser. During the experiment, a few mJ of 212.5 nm

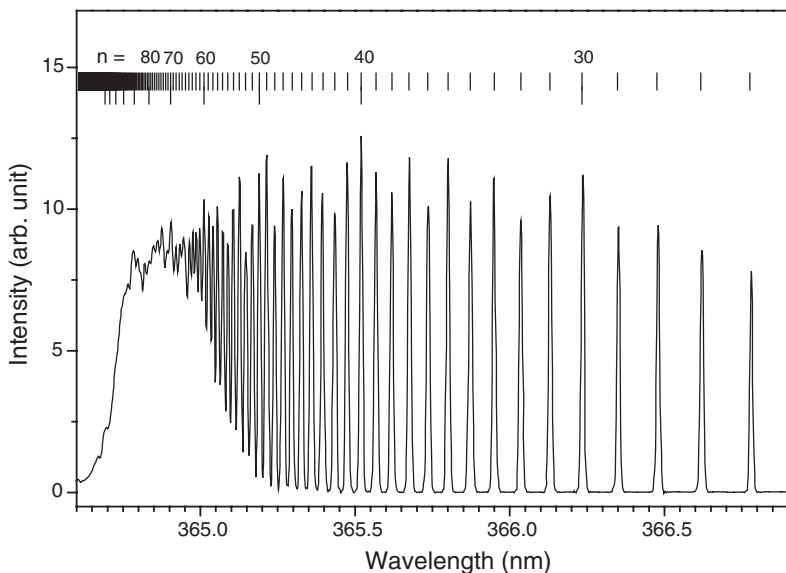


Fig. 2. The H-atom Rydberg transition spectrum from the $n = 2$ level to the higher n states.

and 845 nm laser light are generally used. By generating about $50 \mu\text{J}$ of the 121.6 nm laser light, the first step can be easily saturated since this transition has a huge excitation cross-section ($3.0 \times 10^{-13} \text{ cm}^2$). Following the first step VUV excitation, the H-atom product is then sequentially excited to a high Rydberg state with $n \approx 50$ using a 365 nm light in near saturation, which is generated by doubling a dye laser pumped by the same YAG laser. This excitation scheme allows us to pump the H-atom to a high Rydberg state in nearly unity efficiency. These two excitation laser pulses have to be overlapped exactly both in space and time. The neutral Rydberg H-atom then flies a certain TOF distance to reach a multi-channel plate (MCP) detector with a fine metal grid (grounded) in the front. After passing through the grid, the Rydberg tagged H-atom products are then immediately field-ionized by the electric field applied between the front plate of the Z-stack MCP detector and the fine metal grid. The signal detected by the MCP is then amplified by a fast pre-amplifier, and counted by a multichannel scaler.

Two types of experiments, photodissociation (H_2O) as well as crossed beam bimolecular reactions $[\text{O}(^1\text{D}) + \text{H}_2(\text{HD}, \text{D}_2) \rightarrow \text{OH}(\text{OD}) + \text{H}(\text{D})]$ and $\text{H} + \text{HD}(\text{D}_2) \rightarrow \text{H}_2(\text{HD}) + \text{D}]$, have been carried out using the

experimental technique described above. In the photodissociation experiments, dissociation dynamics at two photolysis wavelengths (157 nm and 121.6 nm) were studied. At 157 nm excitation, H_2O is excited to the \tilde{A}^1B_1 surface; while at 121.6 nm, H_2O is excited to the \tilde{B}^1A_1 surface. The experimental setup used to study the H_2O photodissociation is described by a simple schematic shown in Fig. 3. A fluorine laser (Lambda Physik) is used as the photolysis laser source for the photodissociation of H_2O at 157 nm; while the same laser to pump the H-atom Lyman- α transition is also used as the photolysis laser for the 121.6 nm photodissociation. The 157 nm laser light is unpolarized, while the 121.6 nm laser light is polarized. The polarization direction of the 121.6 nm photolysis light can be changed by rotating the polarization of the 845 nm laser using a rotatable half-waveplate for

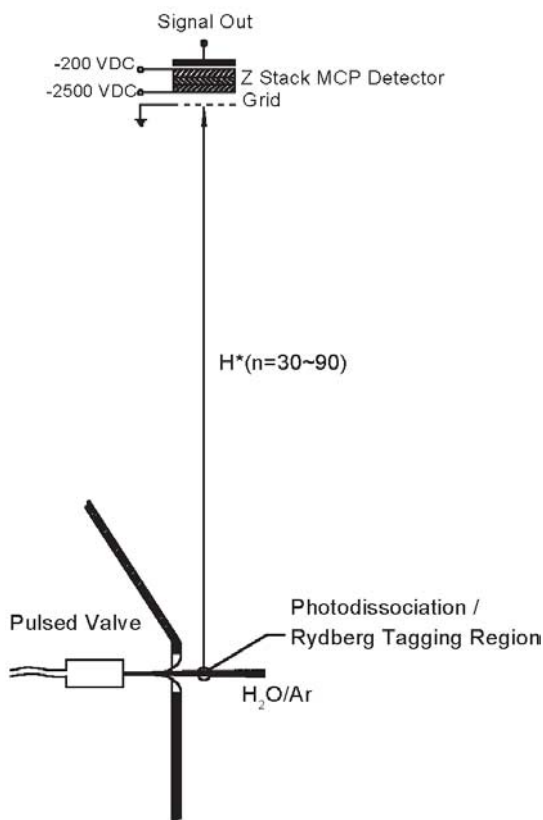


Fig. 3. Experimental setup for the H_2O photodissociation studies.

product angular anisotropy measurement. In the H_2O photodissociation, a molecular beam of H_2O was generated by expanding a mixture of H_2O and Ar ($\sim 3\%$) at a stagnation pressure of 600 torr through a 0.5 mm diameter pulsed nozzle. The mixture of H_2O and Ar was made by bubbling Ar through the water sample at room temperature. The rotational temperature of the H_2O molecules in the molecular beam is about ~ 10 K. The detector in the photodissociation experiment is fixed at the perpendicular direction of the molecular beam. The molecular beam and the photolysis laser beam are all perpendicular to each other.

The setup used for crossed beam experiments is basically the same apparatus used in the H_2O photodissociation studies but slightly modified. In the crossed beam study of the $\text{O}(^1\text{D}) + \text{H}_2 \rightarrow \text{OH} + \text{H}$ reaction and the $\text{H} + \text{HD}(\text{D}_2) \rightarrow \text{H}_2(\text{HD}) + \text{D}$ reaction, two parallel molecular beams (H_2 and O_2) were generated with similar pulsed valves. The $\text{O}(^1\text{D})$ atom beam was produced by the 157 photodissociation of the O_2 molecule through the Schumann–Runge band. The $\text{O}(^1\text{D})$ beam was then crossed at 90° with the

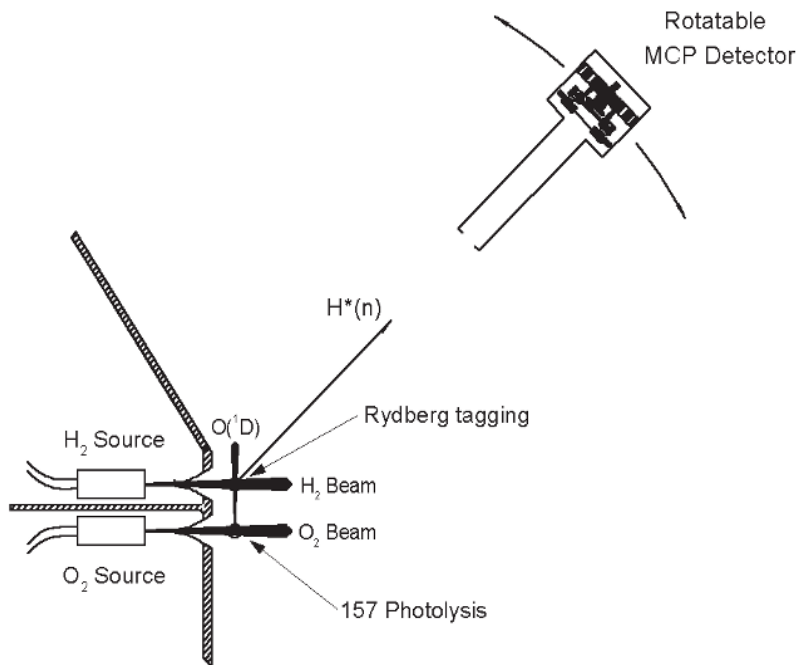


Fig. 4. The schematic of the experimental setup for studying the crossed beam $\text{O}(^1\text{D}) + \text{H}_2 \rightarrow \text{OH} + \text{H}$ reaction.

H₂ molecular beam. The H-atom products were detected by the Rydberg “tagging” TOF technique using the same scheme described in the last paragraph with a rotatable MCP detector. Figure 4 shows the experimental scheme of the crossed beam setup for the O(¹D) + H₂ reactive scattering studies. The scheme used for the H + D₂(HD) studies is very similar to that used in the O(¹D) + H₂ except that the H-atom beam source is generated from HI photodissociation rather than the O(¹D)-atom beam source from O₂ photodissociation.

3. Unimolecular Dissociation of H₂O

Photodissociation of the water molecule is a model system for both experimental and theoretical studies. Extensive experimental and theoretical studies have been performed on this system during the last few decades. Excitation in its longest wavelength ultraviolet absorption band around 150–200 nm leads to the lowest excited singlet state (\tilde{A}^1B_1). Dissociation from this state proceeds on a single potential energy surface leading to a H atom and a ground state OH(*X*²Π) molecular product with little internal excitation.¹⁵ This is a prototype example of direct dissociation. In contrast, three electronic states of the water molecule are implicated in its photochemistry at the Lyman-α wavelength (121.6 nm).^{16–18} The initial excitation of H₂O at the Lyman-α wavelength is to the third singlet electronic state (\tilde{B}^1A_1), which correlates adiabatically with a H atom and an excited electronic state of the OH partner (*A*²Σ⁺). However, although OH radicals in the *A* state are produced,¹⁹ the dominant dissociation leads to a H atom plus a rovibrationally excited ground state OH molecule via non-adiabatic crossing from the \tilde{B}^1A_1 state to the potential energy surfaces of either the \tilde{A} state or the ground state of water (\tilde{X}^1A_1). Even though extensive information on the photodissociation through the \tilde{B}^1A_1 state has been obtained through these studies,^{20,21} a quantitative picture of H₂O dissociation from this surface is still lacking.

Conical intersections of potential energy surfaces have been recognized as playing an important role in the dynamics of excited electronic state photochemistry and chemical reactions; the H₂O \tilde{B}^1A_1 state is a well-known example. One of the notable observations from previous experimental studies is the extremely high rotational excitation of the OH product. This is attributed to a conical intersection at a collinear (H–O–H) geometry. Dynamical calculations have shown that the high average rotational angular momentum of the OH product is the consequence of the high torque acting

in the vicinity of this conical intersection of the excited and ground state potential energy surfaces. This conical intersection arises because a linear approach of H to OH on the repulsive potential curve from $\text{H} + \text{OH}(X^2\Pi)$ can cross an attractive potential curve from $\text{H} + \text{OH}(A^2\Sigma^+)$, whereas there is an avoided crossing of these curves in the lower symmetry of a bent geometry.

In addition to this well-known conical intersection for the H–O–H geometry, there is a second symmetry-determined conical intersection on the \tilde{B}^1A_1 state for the collinear O–H–H geometry. The importance of this second conical intersection in the $\text{O}(^1\text{D}, ^3\text{P}) + \text{H}_2$ reaction system has been noted before.²² However, only very recently has its possible influence on the photodissociation of H_2O been seriously addressed. Mordaunt *et al.* pointed out,²³ in a recent wavepacket calculation, that a small part of the dissociative flux on the \tilde{B}^1A_1 surface goes towards the second conical intersection (O–H–H), thus indicating that this second intersection might also play a role in the \tilde{B} -state photodissociation. Following various improvements in the experiments, many features of the photofragment translational spectra have been more clearly revealed in an even more fine-tuned experimental investigation of the H_2O photodissociation at 121.6 nm in our laboratory.

Here, we will describe the recent experimental study of water photodissociation at both 157 and 121.6 nm in our laboratory, providing further insights into the detailed dynamics of this interesting and also fundamentally important system.

3.1. H_2O on the \tilde{A}^1B_1 Surface: A Direct Dissociation

The time-of-flight spectrum of the H-atom product from the H_2O photodissociation at 157 nm was measured using the HRTOF technique described above. The experimental TOF spectrum is then converted into the total product translational distribution of the photodissociation products. Figure 5 shows the total product translational energy spectrum of H_2O photodissociation at 157.6 nm in the molecular beam condition (with rotational temperature 10 K or less). Five vibrational features have been observed in each of this spectrum, which can be easily assigned to the vibrationally excited OH ($v = 0$ to 4) products from the photodissociation of H_2O at 157.6 nm. In the experiment under the molecular beam condition, rotational structures with larger N quantum numbers are partially resolved. By integrating the whole area of each vibrational manifold, the OH vibrational state distribution from the H_2O sample at 10 K can be obtained. In

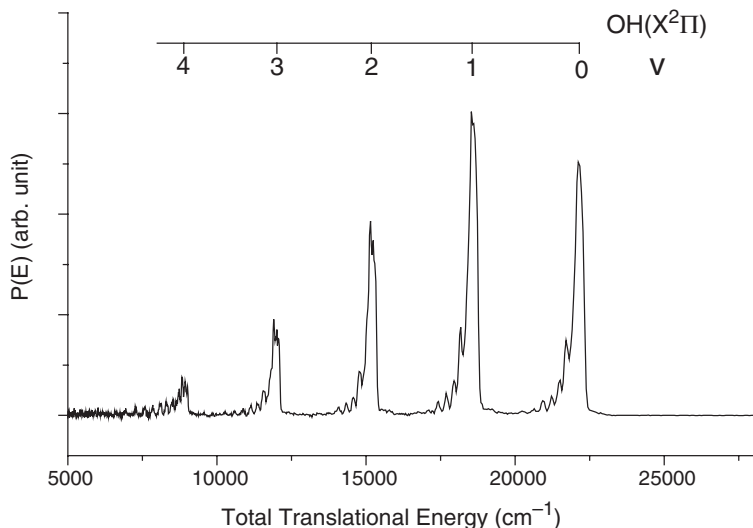


Fig. 5. The total translational energy distribution of H_2O photodissociation at 157 nm. The peaks correspond to the different rovibrationally excited OH products.

order to get an estimate of the rotational excitation of the OH product, the product translational energy distribution is simulated using fixed parameters. Translational energy distribution for H_2O photodissociation in Fig. 5 has been simulated. From the simulation, it is clear that the rotational excitation of the OH products at the $v = 0, 1, 2, 3$ states is quite cold, with an estimated rotational temperature of about 340 K. Interestingly, the rotational temperature of the OH products at the $v = 4$ state is notably higher than that at the lower vibrational states. The estimated rotational temperature for OH ($v = 4$) is about 650 K. These results are similar to that obtained by Andresen *et al.*²⁴ using the LIF technique.

In order to see the effect of the rotational excitation of the parent H_2O molecules on the OH vibrational state distribution, the experimental TOF spectrum of the H atom from photodissociation of a room temperature vapor H_2O sample has also been measured with longer flight distance (~ 78 cm). By integrating each individual peak in the translational energy spectrum, the OH product vibrational distribution from H_2O photodissociation at room temperature can be obtained.

The OH product vibrational state distributions obtained from the above experimental studies are listed in Table 1. From the results obtained under the two extreme conditions (molecular beam and room temperature vapor)

Table 1. Vibrational state distribution of OH/OD from H₂O/D₂O/DOH photodissociation at 157.6 nm.

Species	V							Remark
	0	1	2	3	4	5	6	
H ₂ O	1.0	1.11	0.61	0.30	0.15	0	0	Beam ^a
H ₂ O	1.0	1.06	0.56	0.24	0.11	0	0	Vapor ^a
H ₂ O	1.0	1.03	0.57	0.27	0.11	0	0	EI ^b
H ₂ O	1.0	0.96	0.15	—	—	—	—	Exp. ²⁴
H ₂ O	1.0	0.56	0.10	0.02	0.003	$<3 \times 10^{-4}$	—	Exp. ²⁵
H ₂ O	1.0	0.89	0.63	0.41	0.28	0.24	—	Theory ²⁶
H ₂ O	1.0	0.81	0.53	0.34	0.18	0.10	—	Theory ²⁷
H ₂ O	1.0	1.06	0.59	0.27	0.13	0.01	0.00	Theory ²⁸
D ₂ O	1.0	1.49	1.09	0.67	0.39	0.16	0.03	Beam ^a
D ₂ O	1.0	1.39	1.00	0.49	0.29	0.14	0.01	Theory ²⁸
DOH/OH	1.0	1.56	1.02	0.60	0.13	0	0	Beam ^a
DOH/OH	1.0	1.18	0.73	0.46	0.09	0	0	Theory ²⁸
DOH/OD	1.0	1.19	0.76	0.45	0.29	0.16	0.09	Beam ^a
DOH/OD	1.0	1.08	0.56	0.29	0.15	0.09	0.03	Theory ²⁸

^aResults obtained using the H-atom Rydberg tagging TOF technique.^bResults obtained using a universal electron impact ionization detector.

in this work, it is clear that the rotational excitation of the parent molecule has a negligible effect on the product vibrational state distribution of the OH product from H₂O photodissociation at 157.6 nm excitation. Previous experimental and theoretical results are also shown in Table 1.

From Table 1, it is quite obvious that the OH product vibrational state distribution obtained in our laboratory is significantly different from the one measured using the LIF method, especially at the higher vibrational states. This implies that the vibrational distribution of OH obtained by previous LIF measurements may have serious errors. This conclusion may have a significant impact since LIF has been widely used in measuring the product OH vibrational state distribution in the studies of many important chemical reactions. The vibrational distributions obtained here for high vibrational states are as much as 50 times larger than that obtained by the LIF technique. These results indicate that one must be very careful when using LIF to measure vibrational distributions of the OH product. Generally speaking, LIF is a sensitive detection technique for molecular species. However, there are a few problems when one uses this technique to measure relative product vibrational populations. Firstly, in order to determine the relative population distributions in many vibrational states, one normally could not cover all vibrational states within the tuning range of one laser dye. This would

likely cause propagation errors in measuring the relative LIF signals from different OH vibrational states. Secondly, saturation effects may also cause significant errors when one calculates relative populations using relative LIF intensities. When converting relative LIF intensities to relative populations, one usually needs information that is usually not available, such as transition dipole moments, etc. If one uses transitions with small off-diagonal Franck-Condon (FC) factors, by which many previous LIF measurements of OH were carried out, errors in the calibration might originate from the inaccuracy of the small off-diagonal FC factors which are harder to calculate accurately. Furthermore the inaccuracy of the vibrational overlap integrals will also make the estimation of the transition dipole much more difficult since accurate r -centeroid is even harder to obtain for each transition. Predissociation of OH in the excited electronic state in the LIF scheme can also cause serious problems. And it is well known that OH predissociates in the $A^2\Sigma$ state. This could also be a major source of error in measuring the vibrational distribution of OH because the effect of predissociation is hard to account for quantitatively in many cases.

From Table 1, it is clear that vibrational state distributions of the OH product obtained here under the two experimental conditions in our work are in rather good agreement with the theoretical results, indicating that the overall accuracy of the theoretical calculations are fairly good for the $v \leq 4$ levels. There is, however, a large discrepancy between the previous theoretical results^{3,9} and our experimental measurement at $v = 5$. In fact, no signal has been observed for the OH products at $v = 5$ in our experiment. Since detection efficiencies for H atoms with different velocities are quite uniform using the Rydberg tagging technique, as we have demonstrated in the photodissociation of H_2O at 121.6 nm²⁹ and also in this experiment, the discrepancies between theory and experiment therefore likely come from the inaccuracies of the H_2O \tilde{A} state potential energy surface on which all previous theoretical calculations are based. Improvement on the theoretical calculations should also be possible using a more accurate \tilde{A} state potential energy surface. Recent theoretical studies based on an improved potential energy surface²⁸ have shown that this is truly the case. The agreement between the product state distributions from theory and experiment is much improved for H_2O . This improved \tilde{A} state potential energy surface is now believed to be one of the most accurate model potentials for direct dissociation processes in triatomic molecules.

Photodissociation of D_2O on the \tilde{A} surface at 157 nm has also been investigated. The time-of-flight spectrum of the D-atom product from the D_2O

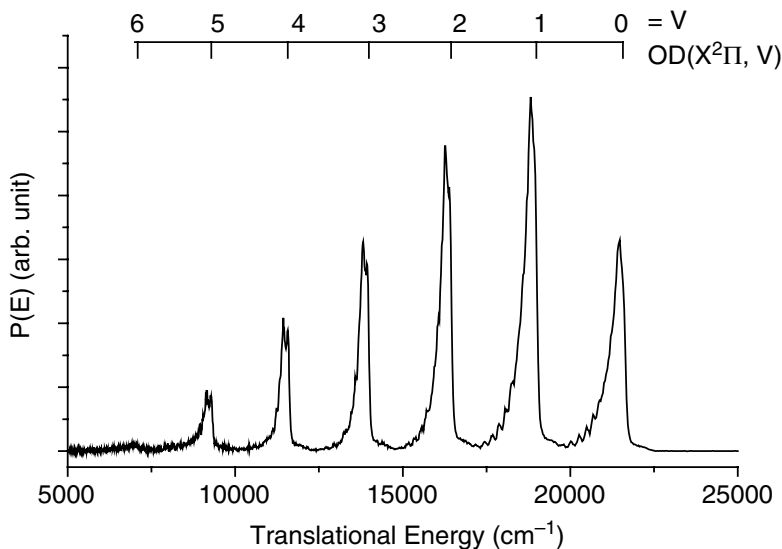


Fig. 6. The total translational energy distribution of D_2O photodissociation at 157 nm. The peaks correspond to the different rovibrationally excited OD products.

photodissociation was measured using the Rydberg tagging TOF technique. The experimental TOF spectrum is then converted into the total translational distribution of the photodissociation products. Figure 6 shows the total product translational energy spectrum of D_2O photodissociation at 157.6 nm in the molecular beam condition. Seven vibrational features have been observed in the spectrum. These features can be easily assigned to the vibrationally excited OD products at $v = 0$ to 6 from the photodissociation of D_2O at 157.6 nm. Because of the smaller OD rotational constant, the rotational structures are not as well resolved as in the H_2O case. By integrating the whole area of each vibrational manifold, the OD vibrational state distribution from a D_2O beam sample at 10 K can be obtained. The relative distribution obtained is also listed in Table 1 with the HOD photodissociation results. It is quite clear that the rotational excitation of the OD products is also quite cold for different OD vibrationally-excited products. It is interesting to point out that even though more vibrational states of the OD product in the D_2O photodissociation are populated in comparison with the OH product from H_2O photodissociation, the vibrational energy deposited into the OD product is quite similar to the OH product. The averaged vibrational energy deposited in the OH product from H_2O

is about 4170 cm^{-1} , while that deposited in the OD product from D_2O is about 4310 cm^{-1} .

Photodissociation of HOD on the $\tilde{\text{A}}^1\text{B}_1$ surface at 157 nm in the molecular beam condition has also been studied using the Rydberg tagging technique. Since a pure sample of HOD could not be obtained practically because of the fast H/D exchange rate, a sample of 1:1 mixture of H_2O and D_2O is prepared in order to obtain the HOD sample. Due to the fast exchange of the H and D atoms in this water sample, the final mixed ratio of the three isotopomers, H_2O , HOD and D_2O , should be 1:2:1, respectively, after reaching equilibrium. Therefore, in the photodissociation of this mixed sample, there will be two different sources for the H atom: one from the H_2O molecule, and the other from the HOD molecule. Similarly, there will also be two different sources for the D atom: one from the D_2O molecule, and the other from the HOD molecule. The time-of-flight spectrum of both the H-atom product (with OD partner product) and the D-atom product (with OH partner product) from the mixed water sample has to be measured in order to acquire the whole picture of the HOD photodissociation. Figure 7(a) shows this translational energy distribution for the H detection

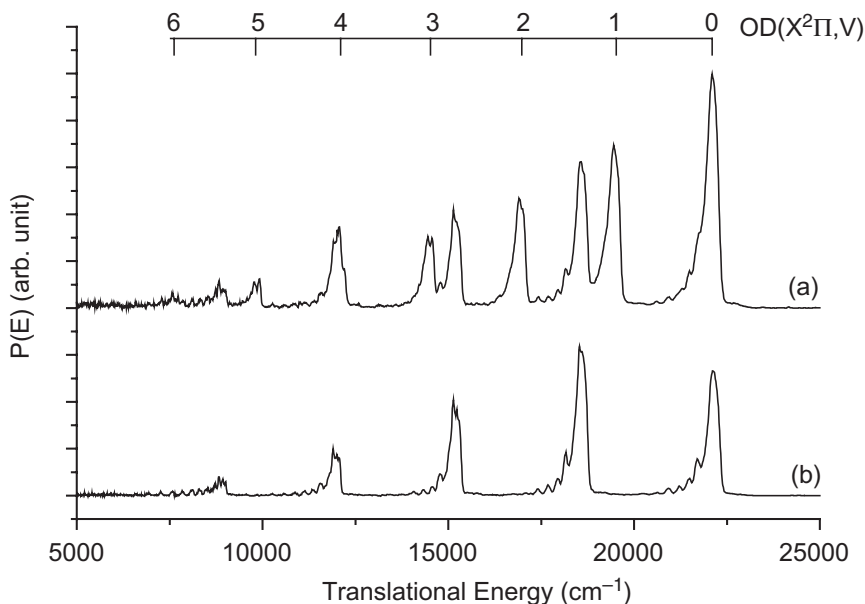


Fig. 7. The total translational energy distribution of the H-atom product from (a) the mixed sample using 1:18 mass ratio, (b) pure H_2O sample using 1:18 mass ratio.

from the mixed sample. In order to show the contribution from the H_2O photodissociation, Fig. 7(b) presents the translational energy distribution for pure H_2O photodissociation converted from the H-atom TOF spectrum using a mass ratio of 1:18. From this figure, one can see immediately the contribution from HOD photodissociation (H-atom product). It is quite obvious that a total of seven vibrational states ($v = 0$ to 6) in the OD product from the HOD photodissociation have been observed. By integrating each individual peak and subtracting the contribution from H_2O , the OD product vibrational state distribution from HOD photodissociation can be determined. The results obtained are listed in Table 1.

Similarly, the TOF spectrum of the D-atom product from the mixed sample has also been measured. Figure 8(a) shows the translational energy distribution for the D-atom product from the mixed sample. In order to show the contribution from the D_2O photodissociation, Fig. 8(b) also shows the translational energy distribution for the photodissociation of the pure D_2O sample converted from the D-atom TOF spectrum using a mass ratio

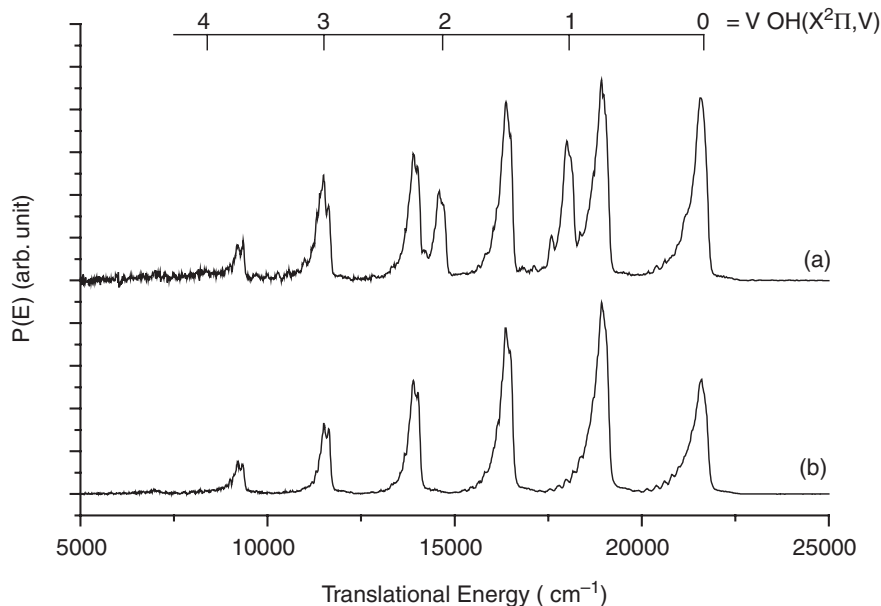


Fig. 8. The total translational energy distribution of (a) the D-atom product channel from the mixed sample using 2:17 mass ratio, (b) the H-atom product from the pure D_2O sample using 2:17 mass ratio.

of 2:17. A total of five vibrational states ($v = 0$ to 4) in the OH product from the HOD photodissociation have been observed. By integrating each individual peak and subtracting the contribution from D₂O, the OH product vibrational state distribution for the HOD photodissociation can be experimentally determined. The results obtained are listed in Table 1.

The overall OD vibrational distribution from the HOD photodissociation resembles that from the D₂O photodissociation. Similarly, the OH vibrational distribution from the HOD photodissociation is similar to that from the H₂O photodissociation. There are, however, notable differences for the OD products from HOD and D₂O, similarly for the OH products from HOD and H₂O. It is also clear that rotational temperatures are all quite cold for all OH (OD) products. From the above experimental results, the branching ratio of the H and D product channels from the HOD photodissociation can be estimated, since the mixed sample of H₂O and D₂O with 1 : 1 ratio can quickly reach equilibrium with the exact ratios of H₂O, HOD and D₂O known to be 1 : 2 : 1. Because the absorption spectrum of H₂O at 157 nm is a broadband transition, we can reasonably assume that the absorption cross-sections are the same for the three water isotopomer molecules. It is also quite obvious that the quantum yield of these molecules at 157 nm excitation should be unity since the \hat{A}^1B_1 surface is purely repulsive and is not coupled to any other electronic surfaces. From the above measurement of the H-atom products from the mixed sample, the ratio of the H-atom products from HOD and H₂O is determined to be 1.27. If we assume the quantum yield for H₂O at 157 is unity, the quantum yield for the H production should be 0.64 (i.e. 1.27 divided by 2) since the HOD concentration is twice that of H₂O in the mixed sample. Similarly, from the above measurement of the D-atom product from the mixed sample, we can actually determine the ratio of the D-atom products from HOD and D₂O to be 0.52. Using the same assumption that the quantum yield of the D₂O photodissociation at 157 nm is unity, the quantum yield of the D-atom production from the HOD photodissociation at 157 nm is determined to be 0.26. Therefore the total quantum yield for the H and D products from HOD is $0.64 + 0.26 = 0.90$. This is a little bit smaller ($\sim 10\%$) than 1 since the total quantum yield of the H and D productions from the HOD photodissociation should be unity because no other dissociation channel is present for the HOD photodissociation other than the H and D atom elimination processes. There are a couple of sources of error, however, in this estimation: (a) the assumption that the absorption cross-sections of all three water isotopomers at 157 nm are exactly the same, and (b) the accuracy of the volume mixture in the

H₂O and D₂O mixed sample used in the experiment. For the absorption cross-sections, there are probably some small differences among the three isotopomers in reality. Nevertheless, this estimation should be quite realistic. The estimated branching ratios of the H and D productions from HOD at 157 nm excitation should be 2.46 with about $\pm 15\%$ estimated error bar. More accurate measurement on the branching ratio should be possible with the experimentally measured cross-section values for H₂O and D₂O.

3.2. H₂O on the \tilde{B}^1A_1 Surface: Dissociation through Conical Intersections

Dissociation of H₂O on the \tilde{A} surface is clearly a prototype direct dissociation process. Dissociation of H₂O on the \tilde{B}^1A_1 surface, however, is much more complicated. Three electronic states have been implicated in the photochemistry of H₂O at 121.6 nm. The initial excitation is to the third singlet state, \tilde{B}^1A_1 , which correlates adiabatically with a H atom and an excited electronic state of the OH partner (OH, $A^2\Sigma^+$). However, the dominant dissociation, to a H atom plus a ground state OH molecule (OH, $X^2\Pi$), is brought about by nonadiabatic crossings from the \tilde{B}^1A_1 state to the potential energy surfaces of either the \tilde{A}^1B_1 state or the \tilde{X}^1A_1 ground state of water. These are mediated respectively by electronic Coriolis interactions, and through conical intersections of the \tilde{B}^1A_1 and \tilde{X}^1A_1 surfaces.

Experimentally, the TOF spectra of the H-atom product from the photodissociation of H₂O at 121.6 nm have been measured using the same experimental method used at 157 nm above except that the 157 nm laser is absent. Two TOF spectra were obtained with the photolysis laser polarization parallel and perpendicular to the detection axis. The two TOF spectra have been converted to the total translational energy distribution of the photodissociation process using a computer program that includes allowance for the velocity of the molecular beam. Figure 9(a) shows the experimental product translational energy distribution in the parallel direction, while Fig. 10(a) shows the experimental product translational energy distribution in the perpendicular direction.

From the translational energy distributions obtained above, the quantum state distributions and the quantum state-specific anisotropy parameters can be determined. In a molecular photodissociation process, the photodissociation product detected at an angle in the center-of-mass

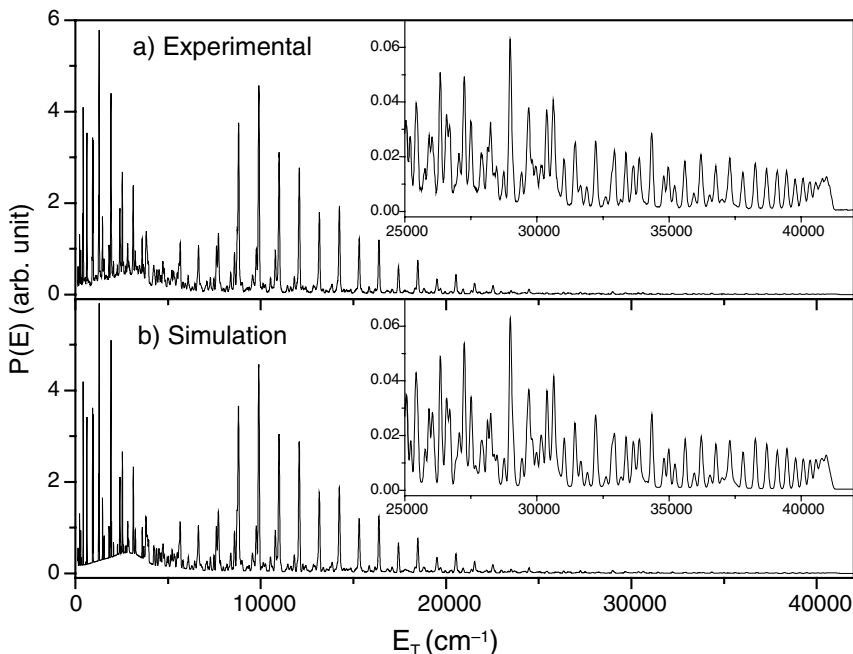


Fig. 9. The translational energy distributions of H_2O photodissociation at 121 nm obtained with photolysis laser polarization parallel to the detection direction. (a) The upper trace was acquired experimentally. (b) The lower trace is the simulated distribution.

(CM) frame of θ_{CM} relative to the photolysis laser polarization can be represented by the following formula:

$$\psi(E_{\text{T}}, \theta_{\text{CM}}) = \varphi(E_{\text{T}}) \{1 + \beta(E_{\text{T}}) P_2(\cos \theta_{\text{CM}})\} \quad (4)$$

where $\varphi(E_{\text{T}})$ is the product translational energy distribution and $\beta(E_{\text{T}})$ is the energy-dependent anisotropy parameter. In order to determine both $\varphi(E_{\text{T}})$ and $\beta(E_{\text{T}})$ in the experiment, translational energy distributions at two polarizations (parallel and perpendicular to the detection axis) in the laboratory frame have to be measured. θ_{CM} is dependent on E_{T} , but can be calculated from θ_{LAB} provided the beam velocity is known. $\sigma(E_{\text{T}})$ and $\beta(E_{\text{T}})$ can therefore be calculated by solving the following two equations, in which the angles for $\psi^{\perp}(E_{\text{T}}, \theta_{\text{CM}}^{\perp})$ and $\psi^{\parallel}(E_{\text{T}}, \theta_{\text{CM}}^{\parallel})$ have first been derived using a laboratory to center-of-mass transformation,

$$\psi^{\perp}(E_{\text{T}}, \theta_{\text{CM}}^{\perp}) = \sigma(E_{\text{T}}) \{1 + \beta(E_{\text{T}}) P_2(\cos \theta_{\text{CM}}^{\perp})\} \quad (5)$$

$$\psi^{\parallel}(E_{\text{T}}, \theta_{\text{CM}}^{\parallel}) = \sigma(E_{\text{T}}) \{1 + \beta(E_{\text{T}}) P_2(\cos \theta_{\text{CM}}^{\parallel})\} \quad (6)$$

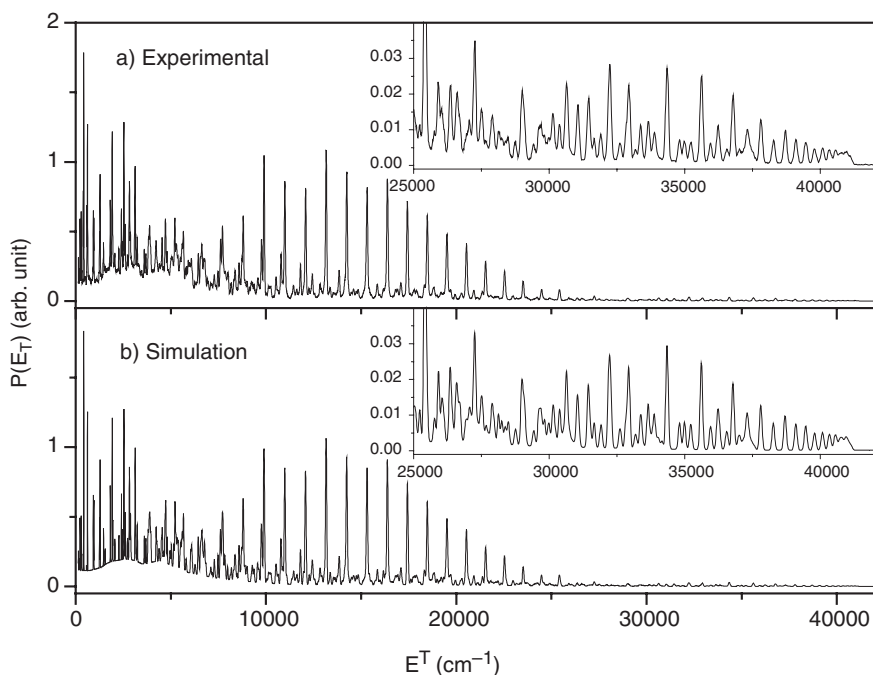


Fig. 10. The translational energy distributions of H_2O photodissociation at 121 nm obtained with photolysis laser polarization perpendicular to the detection direction. (a) The upper trace was acquired experimentally. (b) The lower trace is the simulated distribution.

Extensive sharp structures in the product translational energy distributions (Figs. 9(a) and 10(a)) have been observed. Since the H-atom product has no internal excitation, these sharp features all correspond to the electronically and rovibrationally excited OH products. OH quantum state distributions have been determined from the simulations of the product translational energy distributions obtained above for the two polarizations. Figures 9(b) and 10(b) show the simulated product translational energy distributions for the two corresponding polarizations (parallel and perpendicular). The energy resolution in the experiment varies with the translational energy of the H-atom product, so that the line-width of each peak in the simulation is a function of the translational energy. In addition to the OH(*X*) and OH(*A*) products, a broad underlying peak has also been observed at low translational energy. This underlying peak is also simulated using a broad energy distribution. From the above simulations, rovibrational state distributions have been determined for both the OH(*X*) and OH(*A*) products.

3.2.1. OH Product Quantum State Distributions

Assignments have been made for almost all the peaks in the translational energy spectra using the complete set of bound states of OH in its X and A states. In total, 10 vibrational states ($v = 0$ to 9) of OH(X) have been included in the fitting of the translational distributions. From the simulations, it is clear that the most important pathway leads to the OH ground electronic state products in the $v = 0$ state. Figure 11 shows the rotational distributions of the OH($X, v = 0$) product obtained from the simulations. It is apparent that most of the OH($X, v = 0$) products are extremely rotationally excited with a peak at $N = 45$, corresponding to about $32,000\text{ cm}^{-1}$ rotational excitation. This is truly a phenomenal case in that almost 75% of the available energy is deposited into purely rotational excitation. It is also interesting to point out that the rotational distribution shows a clear oscillation around $N = 40$, with the odd N levels having enhanced population with respect to the neighboring even N levels. There is also another oscillation in the weaker peaks of the rotational distribution near $N = 18$. Such oscillations have been attributed to the dynamical interference arising through the existence of two conical intersections on the excited surface.³⁰

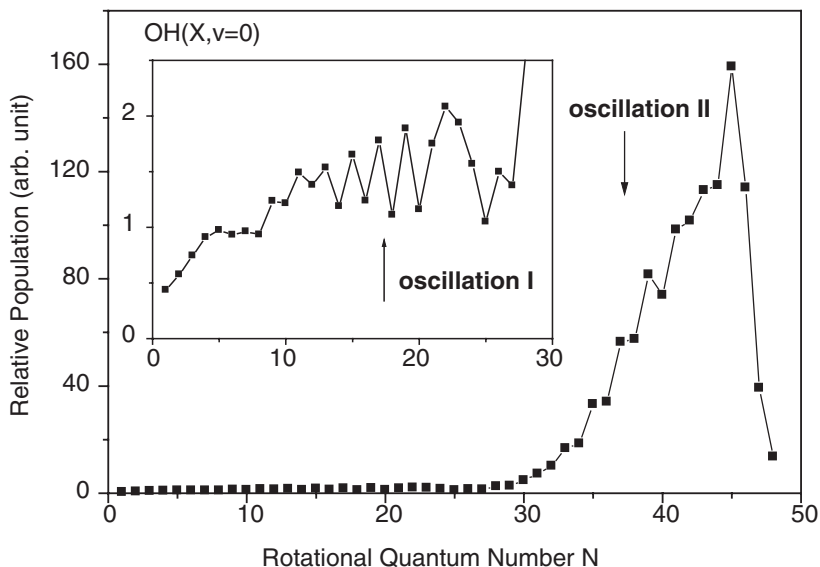


Fig. 11. The rotational distribution of the OH($X, v = 0$) products from H_2O photodissociation at 121.6 nm.

Rotational state distributions for the $\text{OH}(X)$ products at $v = 1$ to 4 have also been determined. These products are also highly rotationally excited, indicating that they are probably produced through the same dynamical pathway as the $\text{OH}(X, v = 0)$ product. $\text{OH}(X)$ products for $v = 5$ to 9 have also been observed. However, the increasing density of rovibronic states leads to severe overlapping of the rotational manifolds for these higher vibrational levels. Figure 12(a) shows the vibrational state distribution of the $\text{OH}(X)$ product. While the $\text{OH}(X, v = 0)$ product is by far the most important single channel, vibrationally excited OH products comprise approximately half the total $\text{OH}(X)$ population for vibrational states up to $v = 11$. A significant population of the vibrationally excited $\text{OH}(X)$ products is required in order to account for the complicated structures in the translational energy spectrum between 4000 and 10,000 cm^{-1} .

Rotational state distributions of the $\text{OH}(A)$ product for $v = 0$ to 3 have also been determined. Highly rotationally excited $\text{OH}(A, v = 0, 1)$ products are dominant as in the ground state, indicating that the angular anisotropy of the potential is also very important to the production of these product states on the $\text{H}_2\text{O } \tilde{B}^1A_1$ state surface. The vibrational distribution

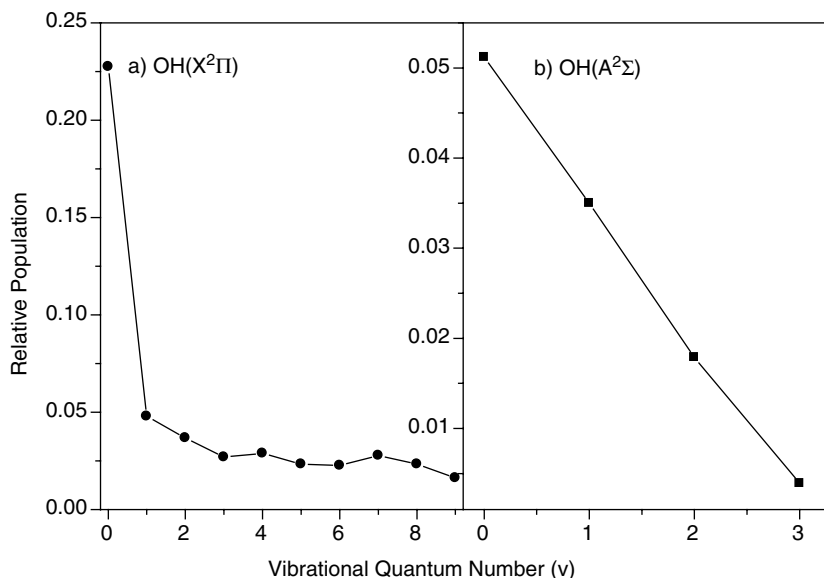


Fig. 12. Vibrational state distribution of (a) the $\text{OH}(X^2\Pi)$ product, (b) the $\text{OH}(A^2\Sigma)$ product.

for the OH(A) product has been obtained by integrating the rotational distributions for each vibrational level. Figure 12(b) shows this vibrational state distribution. The population for the OH(A) product decreases almost linearly as the vibrational energy increases. The relative branching ratio of the OH(X) product versus the OH(A) product is well determined to be about 5 : 1.

Early dynamical calculation using time-dependent wavepackets was able to reproduce the general form of the OH rotational population distribution for the OH($X^2\Pi$, $v = 0$) level.²³ This was based on the rather limited *ab initio* surfaces of Theodorakopoulos *et al.*³¹ The branching fraction for the $\tilde{B}^1A_1 \rightarrow \tilde{A}^1B_1$ route to the ground state OH radical relative to the $\tilde{B}^1A_1 \rightarrow \tilde{X}^1A_1$ route was shown to increase with a -axis rotational excitation of the parent molecule, whilst the second of these routes is associated with higher angular acceleration of the OH on the final surface than for the first route. Recently, van Harreveld and van Hemert used their new potential energy surfaces for water to carry out a complete three-dimensional quantum mechanical description of its photodissociation at a number of energies following $\tilde{B} \leftarrow \tilde{X}$ excitation from the rotational ground state.³² Diabatic electronic surfaces were constructed from the adiabatic electronic states and matrix elements of the electronic angular momentum operators, following a well-defined procedure.³³ The dynamics were studied using wavepacket methods, and the evolution of the time-dependent wavefunction discussed in detail. These calculations show that both the absorption spectrum and the product state distributions are strongly influenced by transient resonances on the adiabatic \tilde{B}^1A_1 state surface, which probably involve both stretching and bending motions.³⁴ As a consequence the branching ratios between the dissociation channels and the vibrational and rotational distributions are strongly energy dependent. These theoretical results agree at least qualitatively with the available experimental data. It is also shown that molecular rotation plays an important role in the photofragmentation process. Three-dimensional trajectory calculations have also been performed on this system recently. Further insights on the dynamics of dissociation processes were provided in these investigations. The essential dynamical features in the trajectory studies also agree well with the quantum calculations by van Harreveld and van Hemert.³² Of particular note, it was concluded that the highly vibrationally excited OH products are produced by indirect trajectories, whereas the $v = 0$ OH products are mainly due to direct dissociation.

3.2.2. Rovibrational Dependent Anisotropy Parameters

The distributions of the angular anisotropy parameter have also been determined for the different rovibrational levels of the OH product. Figure 13 shows the $\beta(N)$ distribution for the OH(X) product in the $v = 0$ state. This distribution shows a marked variation in the β parameter over the observed range of N values. For N less than 10, N between 23 and 28, and N greater than 42, the β parameter is of the order $+1$. In between these ranges there are two regions of local oscillation in β . Starting from $N = 10$ to $N = 22$, the β parameter alternates with higher β at even N and lower β at odd N . However, for the second local oscillation (from $N = 29$ to 40), the β parameter alternates in an opposite way with higher β at odd N and lower β at even N . Note that these two regions of oscillation in β are the same as the two regions of oscillation in the rotational population (Fig. 11). These observed oscillations are very intriguing and indicate that there could be more than one dissociation mechanism leading to the ground state OH. Closer inspection reveals that in the lower N range the population

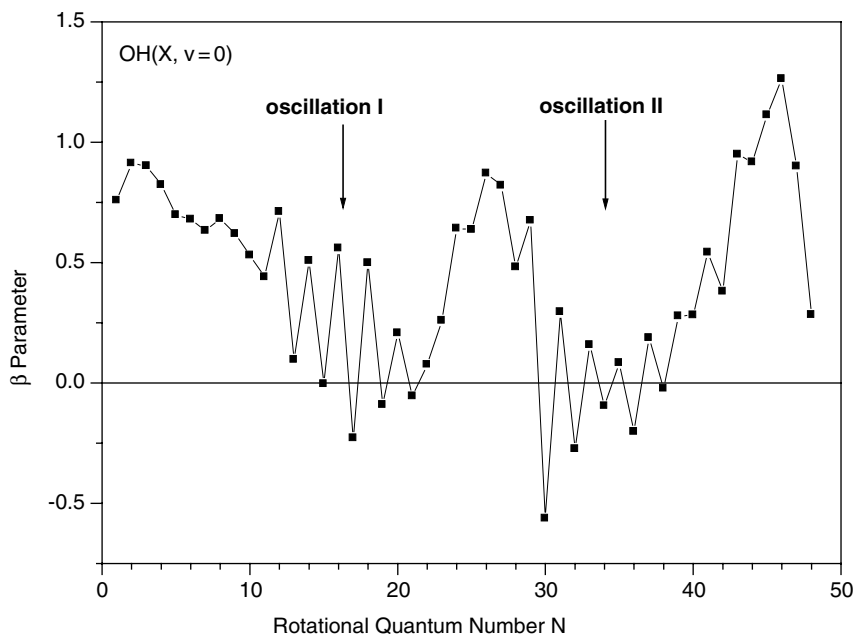


Fig. 13. The anisotropy parameters for the OH($X, v = 0, N$) products. The two oscillation sites correspond exactly to the population oscillations exhibited in Fig. 11.

alternation is much more prominent in perpendicular polarization than in parallel polarization, whereas the reverse is true in the higher N range. The source of these oscillations for the most important $\text{OH}(X, v = 0)$ channel is discussed below.

Anisotropy parameters have also been determined for the $\text{OH}(X)$ product from $v = 1$ to 4 in the same way. These distributions are significantly different from each other. β again varies widely with N , but the distributions are very different from that for the $\text{OH}(X, v = 0)$ product, indicating the complex nature of H_2O photodissociation at 121.6 nm. For higher vibrational levels the β parameters cannot be determined accurately because of significant correlations through overlapping lines. The anisotropy parameters have also been determined for the $\text{OH}(A)$ product for $v = 0$ to 3. The variations in β are again quite different from each other. Except for $v = 3$, the anisotropy parameter oscillates as the N quantum number increases. There are also some general features for these distributions. Near the energetic limit, the anisotropy parameter is normally higher than for the lower N states. This probably arises because the generation of high N products requires the experience of large angular forces during the dissociation.

3.2.3. Effect of Parent Rotational Excitation on the $\text{OH}(A)$ Product

The rotational temperature of H_2O in the molecular beam is quite low, about 10 K. As in the hydrogen molecule, the water molecule has *para* and *ortho* rotational levels with nuclear spin-statistics of 1:3 respectively. Since the *para* and *ortho* rotational levels have different nuclear wavefunctions, the conversion between the *para* and *ortho* levels is extremely slow, as in the hydrogen molecule. In H_2O , the nuclear spin-statistics for the lowest rotational levels are as follows:

Level	Energy (cm^{-1})	Nuclear Spin Statistics
0 ₀₀	0.00	1
1 ₀₁	23.80	3
1 ₁₁	37.16	1
1 ₁₀	42.39	3

Consequently, even at the lowest rotational temperature both the 0₀₀ and 1₀₁ levels will be populated, with a ratio of 1:3 respectively. The

spacing between these different rotational levels of H_2O is such that the parent rotational levels are not well resolved in the product translational energy distribution for the high translational energy region because of the limited translational energy resolution. In the very low translational energy region associated with the $\text{OH}(A)$ product, however, peaks from the same $\text{OH}(A)$ product from different parent rotational states can be resolved because of their different available energies and the higher translational energy resolution. Figure 14 shows an expanded plot of the product translational energy distributions (Figs. 9(a) and 10(a)) in the very low translational energy region (from 100 to 1500 cm^{-1}). Each product rotational level is associated with multiple peaks (see the peak labelled $v = 1$, $N = 18$). These multiplets arise from the different parent rotational levels of H_2O : 0_{00} , 1_{01} and 1_{11} from low to high energy. From this figure we can investigate the effect of the parent rotational excitation. By simulating the translational energy distributions, relative dissociation cross-sections can be derived for different parent rotational levels. The dashed curves in

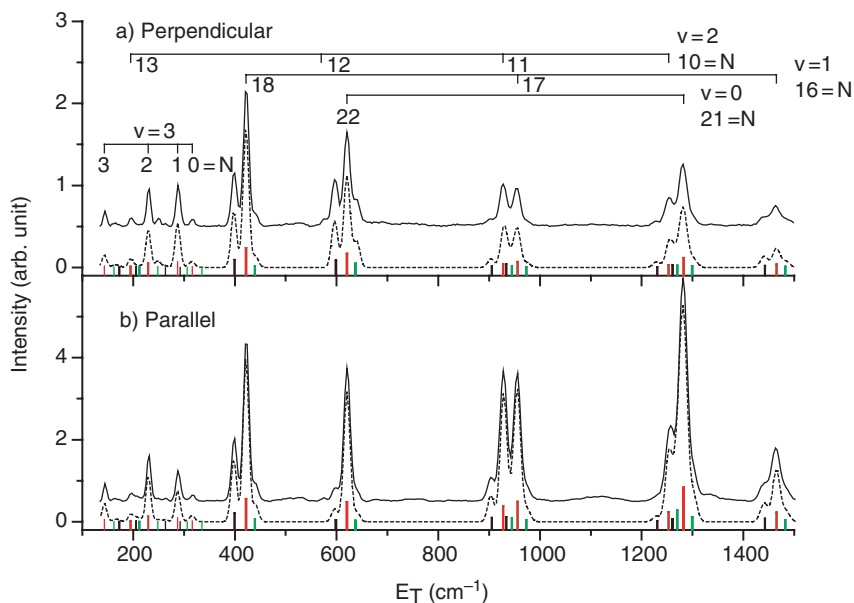


Fig. 14. The product translational energy distributions at very low translational energy region. The solid lines are the experimental results while the dotted lines are the simulated distributions. (a) The photolysis laser polarization is perpendicular to the detection axis, (b) the photolysis laser polarization is parallel to the detection axis.

Fig. 14 are the simulated distributions including the different parent rotational levels. An interesting observation from these distributions is that the shape of the multiplet peak corresponding to each OH(*A*) rotational level for the perpendicular polarization is not necessarily the same as that for the parallel polarization: see for example the peak labelled $v = 0$, $N = 22$. From the simulations, relative populations are determined for the OH(*A*) product in the low translational energy region from H₂O in different rotational levels for both polarizations. The anisotropy parameters for the OH product from different parent rotational levels are determined. Experimental results indicate that the β parameters for the OH(*A*) product from the three parent H₂O levels: 0_{00} , 1_{01} , 1_{11} , are quite different from each other. Most notably, for the OH(*A*, $v = 0$, $N = 22$) product the β parameter from the 1_{01} H₂O level is positive while the β parameters from the 0_{00} and 1_{11} levels are negative, indicating that the parent molecule rotation has a remarkable effect on the product anisotropy distributions of the OH(*A*) product. The state-to-state cross-sections have also been determined, which also are different for dissociation from different rotational levels of H₂O.

3.2.4. Accurate Dissociation Energy of H₂O:D₀⁰

The term values for all the available OH(*A*) rovibrational levels have been determined accurately from spectroscopic data. From the simulation of the translational energy distributions shown in Fig. 14, including the parent rotational levels, the translational energy release for each OH(*A*) level can be calculated with high precision. The Lyman- α transition energy is known accurately to be 82259.1 cm^{-1} , while the total available energy of dissociation from the 0_{00} level of H₂O to produce the lowest quantum level of OH($X^2\Pi_{3/2}$, $v = 0$, $N = 1$) derived from the simulation is 41108.0 cm^{-1} . The dissociation energy D_0^0 , defined as from the lowest H₂O state to the lowest OH level, is therefore determined to be 41151.1 cm^{-1} . The error bar on D_0^0 is estimated to be 5 cm^{-1} and should have a confidence of at least 95%. The new value provides the most accurate bond dissociation energy for the water molecule thus far.

3.2.5. Population Alternations and Quantum Interference

Recently, two-dimensional quantum dynamical calculations using *ab initio* surfaces from Murrell and co-workers^{35,36} which span the regions that include the O–H–H conical intersections of the \tilde{B}^1A_1 and \tilde{X}^1A_1 surfaces

as well as those with H–O–H geometry, shows that the even/odd intensity alternation in the OH($v = 0$) rotational distribution could arise through a quantum interference between components of the wavefunction emanating on the \tilde{X}^1A_1 surface from these two types of conical intersections.³⁰ However, for both these sets of calculations one OH bond-length was fixed, so that vibrational excitation of an OH fragment, or three-body dissociation, could not occur. This explanation was questioned by van Harreveld and van Hemert on the grounds that their calculations yielded even/odd oscillations, not only for OH(X) but also for OH(A).³² Although there are rapid fluctuations with N in the rotational populations and anisotropy parameters of most vibrational states of both OH(X), and OH(A), a clear even/odd alternation sustained over more than ten consecutive N values is observed only for OH(X, $v = 0$). Furthermore, the two spectra recorded in limiting polarizations differ in that the high N alternation ($N \sim 40$) is most prominent in parallel polarization, whereas the lower N alternation ($N \sim 15$) is most prominent in perpendicular polarization. This contrasting behavior is not apparent from the summed populations in Fig. 11. Further detailed three-dimensional wavepacket analysis, which uses attenuated waves near the second conical intersection (O–HH), shows that the population alternations are strongly related to that conical intersection pathway, indicating strongly that the population alternations in the OH(X, $v = 0$) rotational distribution are caused by the dynamical interference between the two unlike conical intersections between the \tilde{B} and \tilde{X} surfaces.

3.2.6. *Extremely Rotationally Excited OH from HOD Dissociation through Conical Intersection*

The substitution of hydrogen by deuterium often leads to significant changes in processes under dynamical control, particularly where non-adiabatic forces such as conical intersections are involved. Photodissociation of HOD has been recently studied in order to study such dynamical effect in our laboratory using the same method described above.³⁷ The experiment was carried out using a mixed sample of H₂O/HOD/D₂O. The contributions from D₂O were then subtracted from the results using the mixed sample. Figure 15 shows the resulting translational energy spectra for the D + OH products at 121.6 nm excitation at two polarizations (parallel and perpendicular to the detection axis). Since translational energy distributions were measured for both parallel and perpendicular polarizations, the

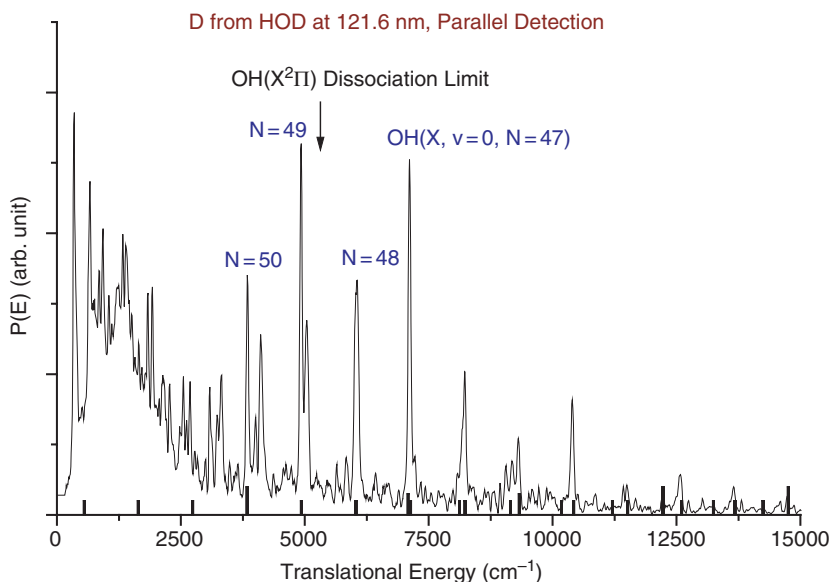


Fig. 15. The product translational energy distributions for the OH + D channel from the HOD photodissociation at 121.6 nm with the photolysis laser polarization parallel as well as perpendicular to the detection direction.

angular dependent translational energy distribution $f(E, \theta)$ can be determined for any angle θ . The peaks of the distribution clearly shows that the main products recoil along the direction of the photolysis laser polarization, indicating that these ground state products are mainly produced by passage through the conical intersection between the \tilde{B} and \tilde{X} surfaces in a collinear geometry.

The sharp peaks in Fig. 15 arise from the rovibronic states of the OH product from the HOD photodissociation at the D-Lyman α wavelength. Most of these peaks can be assigned to the highly rotationally excited levels of $v = 0$ to 5 of OH($X^2\Pi$) and those of $v = 0$ of OH($A^2\Sigma$). The strongest peaks are due to the ground OH products with $v = 0$ and 1. The highest peak in the product translational energy spectrum of Fig. 15 below the dissociation limit is due mainly to the $N = 47$ level of OH($X^2\Pi, v = 0$), which has a rotational energy of $33,400\text{ cm}^{-1}$, already 94% of the bond dissociation energy of the OH molecule (35426 cm^{-1}). Through careful assignments based on calculated energy levels, higher levels still ($N = 48$ to 50) have been clearly observed. The strongest peak above the dissociation limit is

due to $N = 49$. Rotational levels of vibrationally excited OH states that lie above the OH dissociation limit have also been observed.

In comparison with H_2O , the rotational excitation of the $\text{OH}(X)$ product from HOD photodissociation is noticeably higher than that from H_2O , in which the highest observed rotational level of $\text{OH}(X, v = 0)$ is $N = 46$. This can be directly attributed to the kinetic consequences of the difference in product masses. In H_2O , or in D_2O , as the two H (or D) atoms start to accelerate away from the symmetrical Franck–Condon configuration, the developing kinetic energy will tend initially to be equally shared between them. One of these atoms will dissociate, while the motion of the other will become the internal energy of the OH (or OD) product. Thus the internal energy distribution of OH from H_2O is very similar to that of OD from D_2O , given the almost identical available energies at 121.6 nm.³⁸ In contrast, this sharing will tend to be 2/3 to the H atom and 1/3 to the D atom for HOD. Thus if the H atom dissociates, its partner OD will tend to have a lower internal energy distribution than OD from D_2O . Conversely, if the D atom dissociates, its partner OH will tend to have a higher internal energy distribution than OH from H_2O , as observed. It is unusual to generate such an extreme rotational excitation.

These extremely rotationally excited levels, lying above the dissociation limit, are only quasibound through the support of centrifugal barriers. Rotational levels that are only slightly above the dissociation limit have substantial centrifugal barriers to dissociation, therefore the tunnelling probability is expected to be extremely small. However, as rotational excitation further increases, the centrifugal barrier is significantly reduced and thus the tunnelling probability through the centrifugal barrier is dramatically increased. Figure 16 shows the tunnelling lifetimes of these extremely OH rotationally excited levels that are above its dissociation limit, calculated using the semiclassical phase integral method.³⁹ It is interesting to point out that even though the $N = 50$ pure rotational level of $\text{OH}(X^2\Pi, v = 0)$ is already more than 1000 cm^{-1} above its dissociation limit, the tunnelling lifetime of this state through the centrifugal barrier is much longer than the age of the universe, about 13.4 billion years.⁴⁰ This indicates that the first few super-rotationally excited levels above the dissociation limit are essentially stable quantum states. However, as the rotational energy increases, the tunnelling lifetime drops very rapidly. For the $N = 53$ rotational level of $\text{OH}(X^2\Pi, v = 0)$, which is $\sim 0.5\text{ eV}$ above the dissociation limit, the tunnelling lifetime is about 1 day, and at $N = 60$ it is already in the femto-second timescale, indicating that this rotational level is only stable for a few

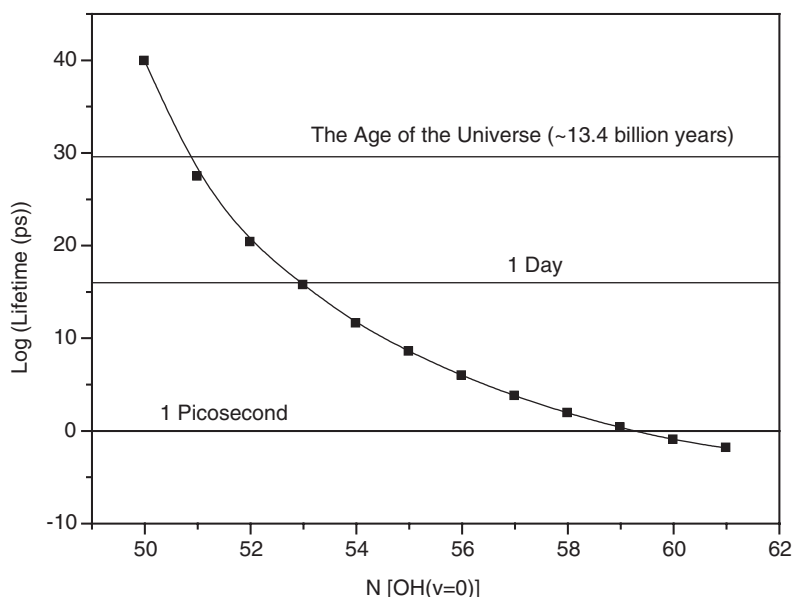


Fig. 16. Tunnelling lifetimes of the super-rotationally excited OH molecules.

vibrational periods. From these theoretical predictions, no quasibound levels of $\text{OH}(X^2\Pi, v=0)$ should exist above $N = 62$. These highly excited OH molecules are substantially stretched by the centrifugal force. For example, the mean bond length for $N = 47$ is about 34% longer than for the rotationless OH molecule, while that for $N = 50$ is about 43% longer. Since these rotationally excited molecules are significantly stretched like highly vibrationally excited molecules, it would be interesting to compare the physical and chemical properties of these two extremely different excited species.

3.2.7. The Single N Propensity in the $\text{HOD} + h\nu \rightarrow \text{OD} + \text{H}$ Dissociation Process

Recently, the photodissociation process, $\text{HOD} + h\nu \rightarrow \text{OD} + \text{H}$, has also been studied at the 121.6 nm using the experimental technique described above. Contributions from H_2O were then subtracted from the results of the mixed sample. The experimental TOF spectra of the H atom from HOD were then converted into translational energy spectra in the center-of-mass frame. Figure 17 shows the translational energy spectra of the H-atom products at 121.6 nm excitation using two different polarization schemes

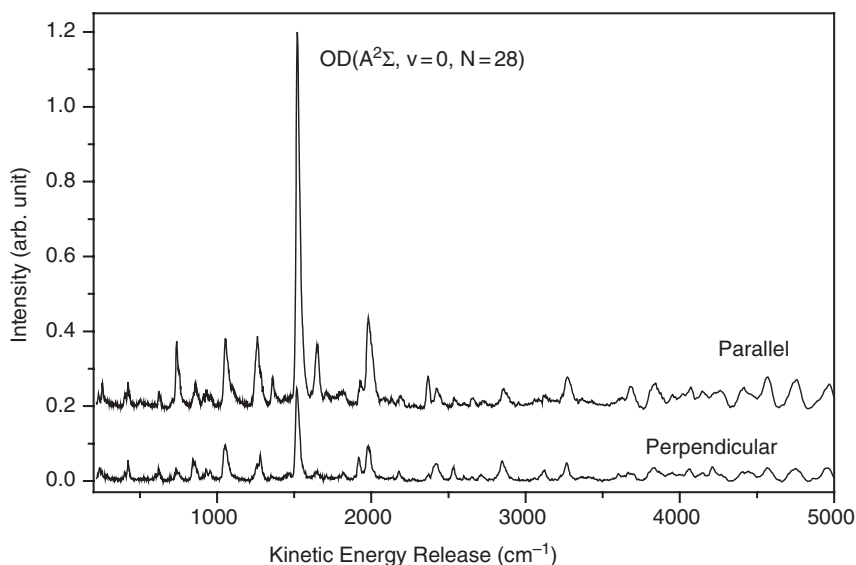


Fig. 17. The product translational energy distributions for the OD + H channel from the HOD photodissociation at 121.6 nm with the photolysis laser polarization parallel as well as perpendicular to the detection direction.

(parallel and perpendicular to the detection axis). The spectra were taken at a total stagnation pressure of 600 torr of a sample of 3% H₂O/HOD/D₂O in Ar. Based on previous spectroscopic data on the OD molecule, all sharp features in the translational energy spectra shown in Fig. 17 can be clearly assigned. The OD products with translational energy above 8000 cm⁻¹ are all in the ground electronic state ($X^2\Pi$), while the sharp structures below 5000 cm⁻¹ are mostly attributed to the OD products in the electronic excited $A^2\Sigma$ state. From the translational energy distribution, it is obvious that most of the OD($A^2\Sigma$) products are in the $v = 0$ state. The rotational state distribution shows that the population of the OD($A^2\Sigma$) product at $v = 0$ and $N = 28$ is much larger than that of OD at other rotational states. This is a very interesting phenomenon since only the population of a single rotational state OD product ($v = 0$, $N = 28$) is significantly enhanced. It is also interesting to notice that the anisotropy parameter for the $N = 28$ OD($A^2\Sigma$) is also significantly larger than the rest of the OD products at other rotational levels, indicating that some interesting mechanism behind this single J enhancement. This type of phenomenon was not observed in the photodissociation of other similar systems such as

H₂O, D₂O and HOD with D detection at the Lyman- α wavelength excitation. Based on theoretical analysis, this single rotational state product propensity is attributed to a dynamically constrained threshold effect in the HOD photodissociation process.⁴¹

4. The O(¹D) + H₂ Reaction: From Insertion to Abstraction

The reaction of O(¹D) + H₂ plays a significant role in atmospheric⁴² and combustion chemistry.⁴³ This reaction is also a well-known benchmark system for an insertion type chemical reaction at low collision energies. Extensive experimental and theoretical studies have been carried out in order to elucidate the dynamics of this reaction (and isotope variants).^{44–65} A more complete review of the studies on the O(¹D) + H₂ reaction during the last decade or so can be found in a very recent review article by Casavecchia.² Previous experimental studies found that this reaction is dominated by the insertion reaction mechanism. Very recently, Liu and co-workers^{61–65} have measured the excitation function and the differential cross-sections at different energies for the O(¹D) + HD reaction using the Doppler-selected time-of-flight methods. Their experimental results show that at low collision energies (<1.8 kcal/mol), the reaction is mainly through the insertion pathway that shows roughly a forward-backward symmetric product angular distribution. At higher collision energies (>1.8 kcal/mol), however, an additional abstraction channel becomes important. This abstraction reaction mechanism is likely caused by the excited state reactive surfaces,^{64,65} even though not all experimental results point to this direction.^{64,65} Due to the limited resolution of the above experiments, quantum state-specific information on the radical products (OH) has not been derived for this reaction in their experimental studies.

In this section, we will describe detailed experimental results on the O(¹D) + H₂(HD, D₂) reactions at different collision energies to probe the fine dynamics in this interesting system. In the first two parts, we will first describe the study of the O(¹D) + *p*-H₂ reaction at 1.3 kcal, to show an example of the state-to-state dynamics of a barrierless insertion reaction, and then the single rotational excitation effect on the dynamics of this reaction. In the third part of this section, we will describe the experimental results of the O(¹D) + D₂ reaction at two different collision energies to provide clear experimental evidence of the appearance of the collinear abstraction mechanism at higher collision energies in this reaction. In the last part of this section, an interesting isotope effect will also be discussed in the O(¹D) + HD reaction.

4.1. Reaction at 1.3 kcal/mol: Barrierless Insertion Reaction

The $\text{O}(^1\text{D}) + \text{H}_2 \rightarrow \text{OH} + \text{H}$ reaction was studied at the collision energy of 1.3 kcal/mol, which is significantly below the 1.8 kcal/mol barrier for the abstraction channel inferred from previous experimental studies.⁶³ This allows us to look at the reaction dynamics of a pure insertion chemical reaction at the state-to-state level. The experimental scheme for this reaction is shown in Fig. 4. The detection scheme used in the crossed beam experiment is almost exactly the same as the photodissociation experiment described above, except that a rotating MCP detector is used here instead of a fixed angle detector. Two parallel molecular beams (*para*- H_2 and O_2) were generated with similar pulsed valves in this experiment. The $\text{O}(^1\text{D})$ atom beam was produced by the 157 nm photolysis of the O_2 molecule. The 157 nm laser light is produced by a F_2 laser (Lambda Physik LPX 210I). The $\text{O}(^1\text{D})$ beam was then crossed at 90° with the H_2 molecular beam. The *para*- H_2 molecular beam is generated by expanding the H_2 sample through a pulsed nozzle, which is cooled to liquid nitrogen temperature. This is to reduce the uncertainties of the collision energy by minimizing the beam velocity spread. A small aperture is used to define the $\text{O}(^1\text{D})$ beam between the O_2 and H_2 beams. The H atom products were detected using the technique described above with a rotatable MCP detector. The velocity of the $\text{O}(^1\text{D})$ beam has been measured to be 2050 m/s with very narrow velocity distribution ($v/\delta v > 50$), while the velocity of the liquid nitrogen cooled *para*- H_2 beam is 1384 m/s with a speed ratio ($v/\delta v$) of about 15. Since *para*- H_2 is expanded under the liquid nitrogen temperature, H_2 molecules in the beam should all be in the $j = 0$ state.⁷ In order to understand the kinematics of reactive scattering, Fig. 18 shows the Newton diagram for this reaction investigated using the above experimental conditions.

TOF spectra of the H atom products have been measured at 18 laboratory angles (from 117.5° to -50° at about 10° intervals). Figure 19 shows a typical TOF spectrum at the laboratory (LAB) angle of -50° (forward direction). By definition, the forwardness and backwardness of the OH product is defined here relative to the $\text{O}(^1\text{D})$ beam direction. The TOF spectrum in Fig. 19 consists of a lot of sharp structures. All these sharp structures clearly correspond to individual rotational states of the OH product, indicating that these TOF spectra have indeed achieved rotational state resolution for the $\text{O}(^1\text{D}) + \text{H}_2 \rightarrow \text{OH} + \text{H}$ reaction. By converting these TOF spectra from the laboratory (LAB) frame to the center-of-mass (CM) frame

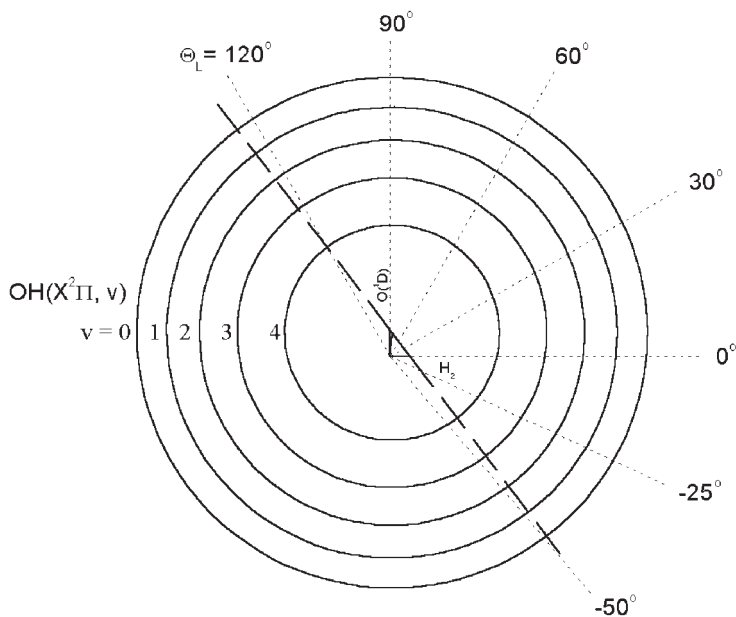


Fig. 18. The Newton diagram for the $\text{O}(^1\text{D}) + \text{H}_2 \rightarrow \text{OH} + \text{H}$ reaction.

using a standard Jacobian transformation, the product translational energy distributions obtained at different LAB angles for the title reaction can be obtained. Figure 20 shows the total product translational energy distribution at the LAB angle of -50° . All the peaks in the distribution can be assigned to the OH products at different spin-orbit rovibrational levels. In this reaction, the total available energy is about 45 kcal/mol, which can produce OH products up to $v = 4$ in the ground electronic state.

By integrating the total intensity of the translational energy distribution at each LAB angle, total product angular distribution can be determined, which is shown in Fig. 21. From this distribution, it is apparent that the total H product is essentially forward and backward symmetrically scattered with regard to the H_2 beam direction. This result is quite consistent with previous experimental studies.^{59,62,63} The forward and backward symmetry of the total H product is a clear signature of the dominant role of the insertion mechanism in this reaction. Since the CM angles are not constant for a certain laboratory angle at different product (H) velocities, a translational energy distribution obtained from the direct conversion of the TOF spectra contains scattering information in a range of CM angles. In analyzing these

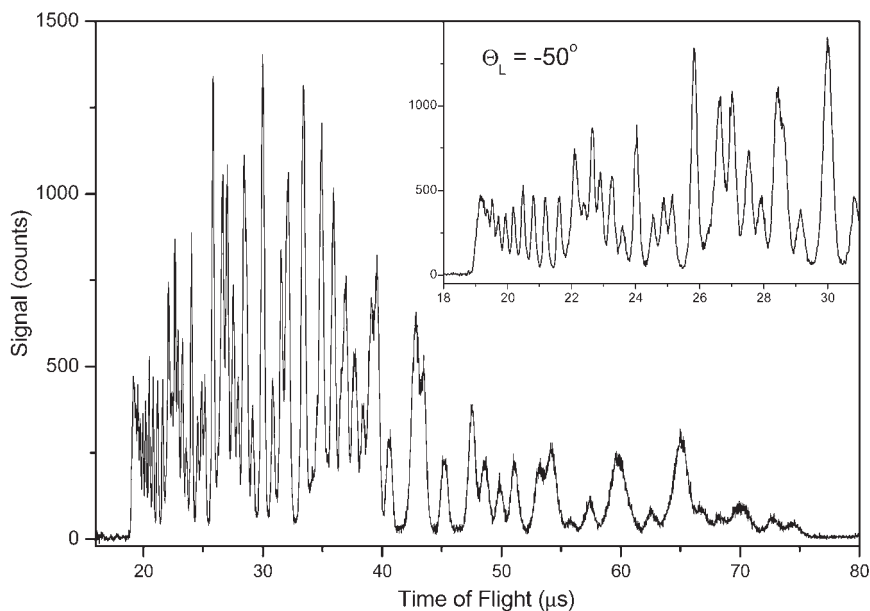


Fig. 19. Time of flight spectra of the H atom product from the $\text{O}(^1\text{D}) + \text{H}_2 \rightarrow \text{OH} + \text{H}$ reaction at -50° laboratory scattering angle at the collision energy of 1.3 kcal/mol.

experimental data, all rovibrational states ($v \leq 4$) of the OH product are included in fitting each translational energy distribution obtained. From the simulations, relative population distributions of each rovibrational state of the OH product were determined at 18 different LAB angles. From these results, quantum state distributions of the OH product in the CM frame ($\Theta_{\text{CM}} = 0^\circ$ to 180° at 10° steps) can then be determined using polynomial interpolations of the above results. Thus, rotational state resolved differential cross-sections are determined. From these typical distributions, detailed dynamical features have been revealed. As we have pointed out above, the total product angular distribution is roughly forward and backward symmetric. For individual quantum state OH product, however, the angular distribution is not necessarily symmetric as shown in Fig. 22. From Fig. 22, the difference between the translational energy distribution at $\Theta_{\text{CM}} = 0^\circ$ or 180° and that at 90° is even more remarkable. From the quantum state distributions, it is clear that the main difference between the side scattering and the forward or backward scattering is the low rotationally excited OH product relative to the $\text{O}(^1\text{D})$ beam direction. At forward and backward scatterings, significant amounts of the OH products are found in the lower

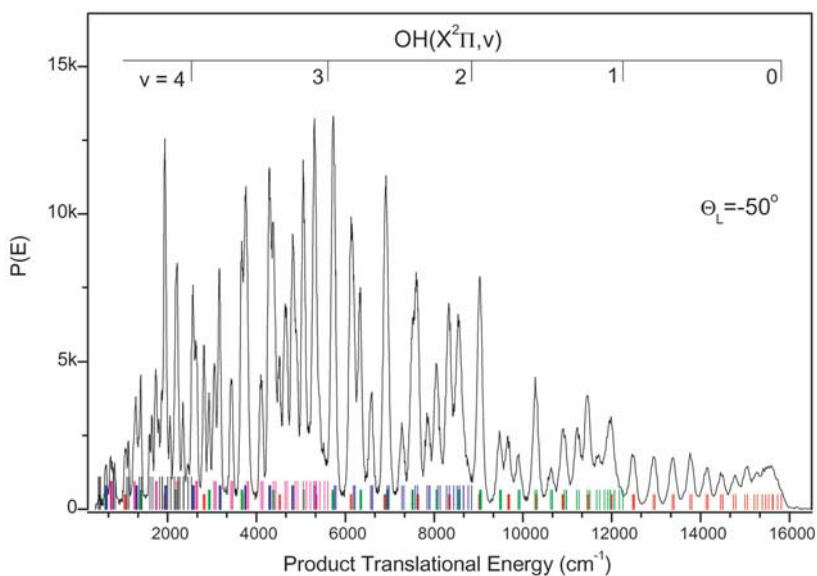


Fig. 20. The directly converted CM translational energy distributions at the lab angle of -50° .

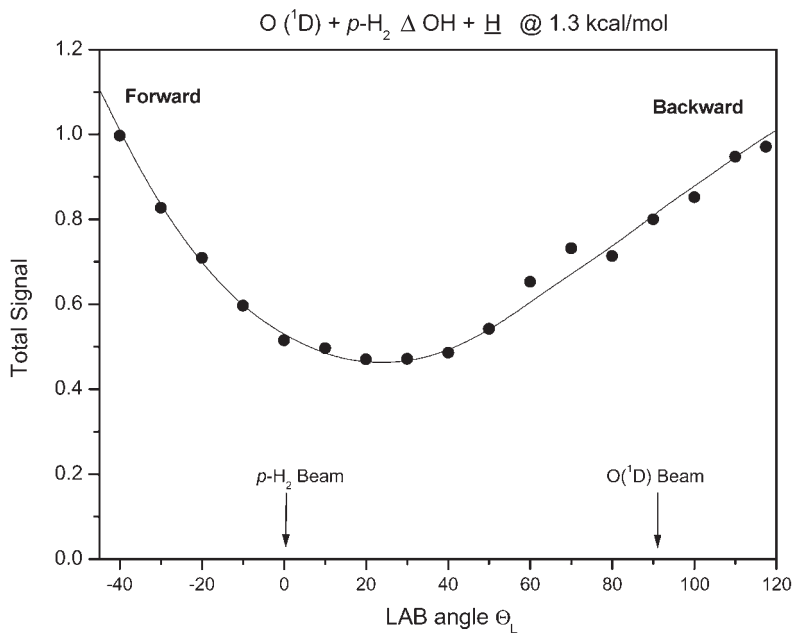


Fig. 21. The H atom product angular distribution in the laboratory frame for the $\text{O}(^1\text{D}) + \text{H}_2 \rightarrow \text{OH} + \text{H}$ reaction.

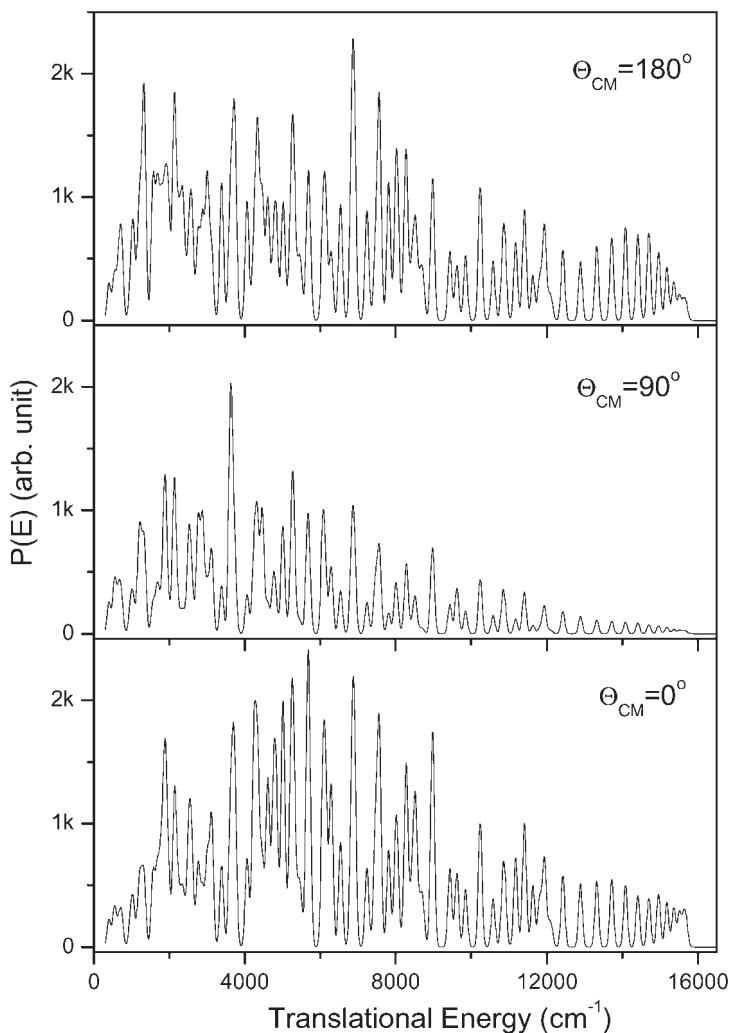


Fig. 22. The CM translational energy distributions at three different lab angles corresponding to the forward (0°), sideways (90°) and backward (180°) scattering.

rotationally excited states of different vibrational states. This is quite obvious from the translational energy distributions shown in Fig. 22 in which lower rotationally excited OH products (near each vibrational state energy limit) are much more pronounced at the forward-backward directions than at the sideways scattering. The highly rotationally excited OH products,

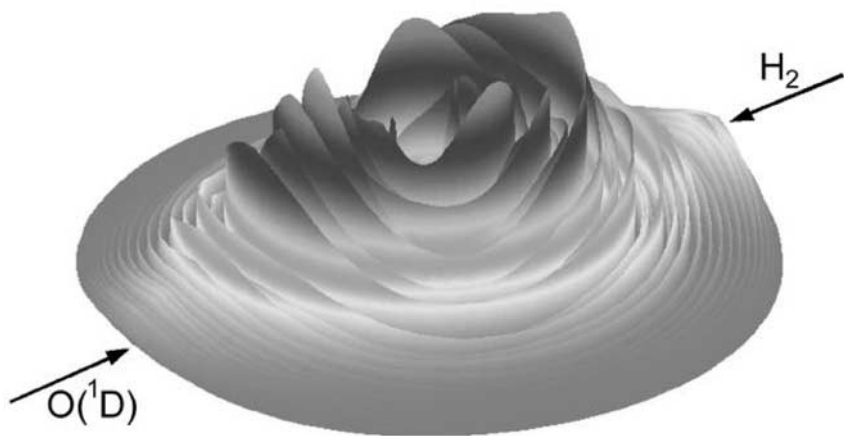


Fig. 23. The three-dimensional plot of the product flux contour diagram for the $\text{O}(^1\text{D}) + \text{H}_2 \rightarrow \text{OH} + \text{H}$ reaction at the collision energy of 1.3 kcal/mol.

however, are more isotropic in their angular distributions, and sometimes even strongly sideways scattered. These results are easily understandable. In the $\text{O}(^1\text{D})$ insertion reaction with the H_2 molecule, significant numbers of trajectories should have low impact parameters. The OH product at the forward-backward directions should carry small angular momentum because of angular momentum conservation in these low impact collisions. For higher rotationally excited OH products, however, angular distributions should not be as simple.

By incorporating all translational energy distributions in the CM frame, a three-dimensional contour plot of the differential cross-sections in terms of angle and translational energy can be constructed, as shown in Fig. 23. As a whole distribution, it is clear that at higher translational energies (or lower internal excitation for OH), the products are more forward-backward scattering than sideways scattering relative to the $\text{O}(^1\text{D})$ beam direction. At lower translational energies (or higher OH internal excitation), however, the OH product scattering is more complicated with strong side scattering in certain regions. Figure 24 shows the angular distribution of different vibrational excited OH products, in which the angular distribution for each vibrational state OH product are mostly forward-backward symmetric, except for the $v = 4$ OH product. This indicates that rotational product asymmetry in the angular distribution does not sustain in the rotationally summed $\text{OH}(v)$ product. Since OH quantum state distributions have been determined at

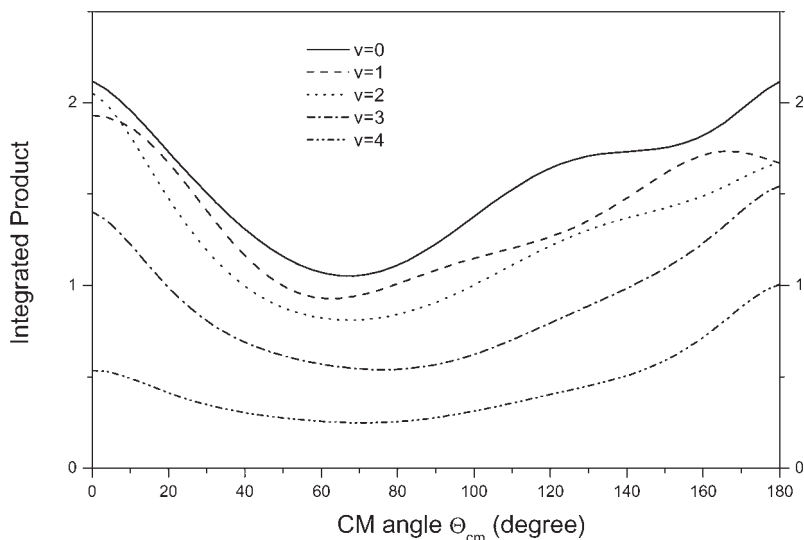


Fig. 24. The angular distribution of different vibrational excited OH products for the $O(^1D) + H_2 \rightarrow OH + H$ reaction at the collision energy of 1.3 kcal/mol.

different CM scattering angles, total quantum state distributions for this reaction can easily be determined by simply integrating these distributions over different CM angles. Figure 25 shows the full quantum state distributions obtained for the title reaction. Such measurements are not possible previously because of problems associated with the OH laser induced fluorescence (LIF) detection.⁶⁶ In Fig. 25(b), OH rotational distributions for each vibrational state are presented. The distributions at different vibrational states are actually quite similar in that all distributions peak near their energetic limit, indicating that the majority of the OH products from this reaction are rotationally excited. In Fig. 25(a), the total OH product vibrational state distribution is shown. The population in different vibrational states monotonically decreases as the vibrational energy increases. In this experiment, even though extremely high translational energy resolution has been achieved, it is still not sufficient to resolve the spin-orbit states of the OH product at $v = 0$ to 3 and the Lambda doublet states for all the vibrational states. For OH($v = 4$) products, however, the spin-orbit components (F_1 and F_2) have been resolved. A clear propensity for the F_1 component OH($v = 4$) product has been observed for this reaction.

In this part, we have shown an excellent example of quantum state resolved reactive scattering studies on the important $O(^1D) + H_2 \rightarrow OH + H$

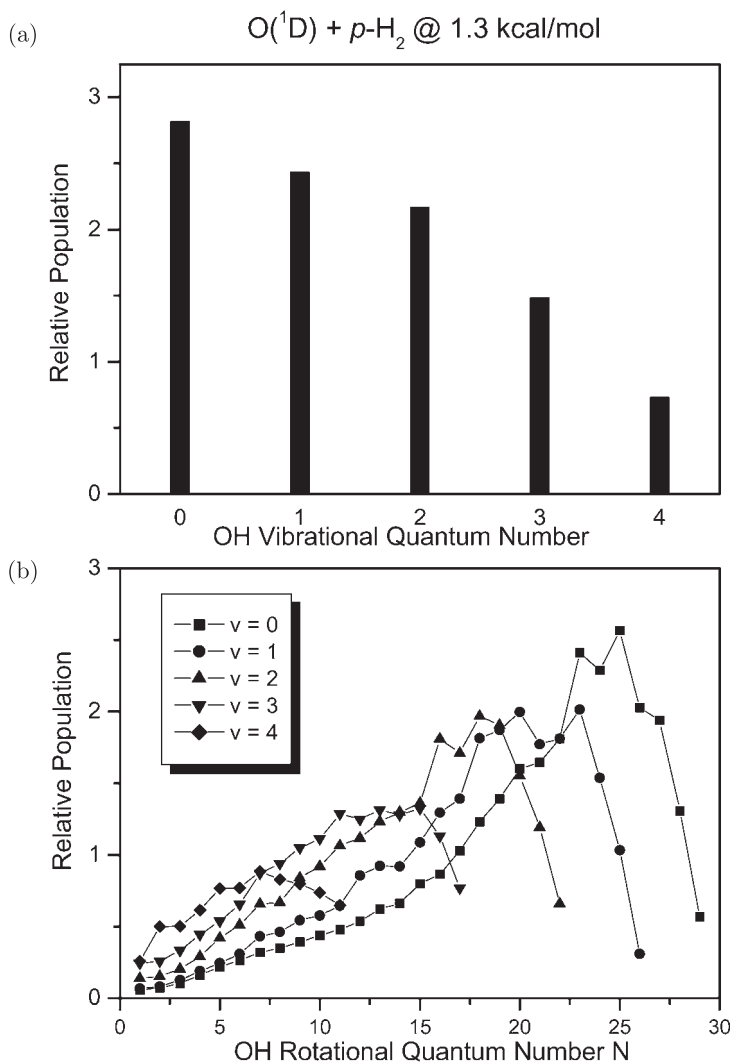


Fig. 25. The total OH product vibrational and rovibrational state distributions for the $O(^1D) + H_2 \rightarrow OH + H$ reaction.

reaction using the high resolution H-atom Rydberg “tagging” TOF technique. Rotational state resolved differential cross-sections have been measured for this reaction for the first time. A full analysis of the experimental results has revealed many interesting dynamics for this prototype system.

The experimental results obtained in this work should be able to provide an excellent test ground for theoretical studies of this benchmark insertion reaction.

4.2. Effect of a Single Quantum Rotational Excitation

The effect of the reagent rotational and vibrational excitation on the reactivity is an interesting issue. In the above experiment, the study was performed for the $O(^1D)$ reaction with the H_2 molecule purely in the $v = 0$, $j = 0$ level using cooled *para*- H_2 beam. Clearly the H_2 reagent in this experiment is without any rotation. In this part, we would like to describe the results of a sophisticated experimental study of the $O(^1D)$ reaction H_2 with the H_2 reagent in the $j = 0$ and $j = 1$ level to look at the effect of a single rotational quantum reagent excitation on the dynamics of this reaction. The experiment was carried in exactly the same way as described in the last part, except that two H_2 samples, *para* and *normal*, were used for exact comparisons. In this experiment, *para*- H_2 is purely in the $j = 0$ level in the cooled beam, while *normal*- H_2 has one part in $j = 0$ and three parts in $j = 1$. In this experiment, TOF spectra at eight LAB scattering angles were measured for both H_2 samples with exactly the same experimental conditions. These spectra were measured by switching the two H_2 samples back and forth many times to reduce the systematic errors in the measurements. Since the numbers of density for the two H_2 samples in the beam are controlled to be exactly the same, the TOF spectra (TOFS) of the H-atom products from the $O(^1D)$ reactions with H_2 at both $j = 0$ and 1 can be obtained from these two samples using simple arithmetic. Since normal H_2 has two components: $j = 0$ (1) and $j = 1$ (3), the TOFS observed for the *p*- H_2 and *n*- H_2 reactions can be described in terms of that from H_2 at $j = 0$ and $j = 1$,

$$\text{TOFS } (p\text{-}H_2) = \text{TOFS } (j = 0) \quad (7)$$

$$\text{TOFS } (n\text{-}H_2) = 0.75 \times \text{TOFS } (j = 1) + 0.25 \times \text{TOFS } (j = 0). \quad (8)$$

Therefore, the TOF spectra (TOFS) for the H_2 reactions for the pure $j = 0$ and 1 levels can be determined from the experimentally-measured TOFS for the *p*- H_2 and *n*- H_2 reactions,

$$\text{TOFS } (j = 0) = \text{TOFS } (p\text{-}H_2) \quad (9)$$

$$\text{TOFS } (j = 1) = (\text{TOFS } (n\text{-}H_2) - 0.25 \times \text{TOFS } (p\text{-}H_2)) \times 4/3 \quad (10)$$

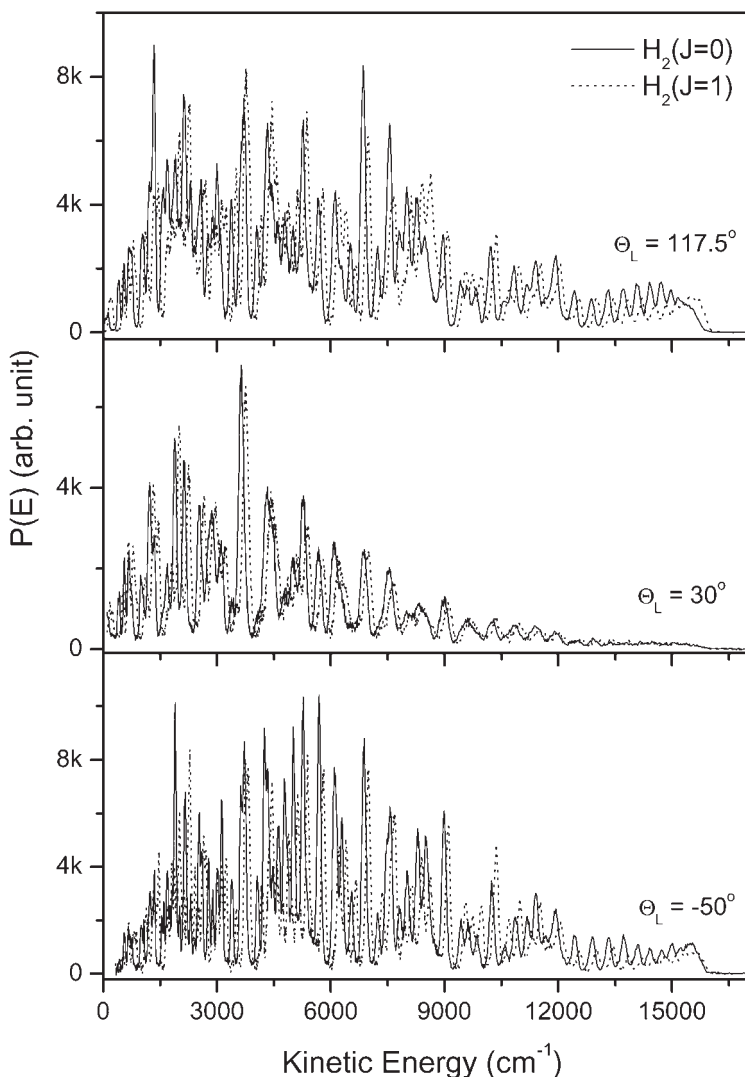


Fig. 26. The translational energy distributions obtained for the $\text{O}(^1\text{D}) + \text{H}_2(j=0) \rightarrow \text{OH} + \text{H}$ and the $\text{O}(^1\text{D}) + \text{H}_2(j=1) \rightarrow \text{OH} + \text{H}$ reaction at the collision energy of 1.3 kcal/mol.

The TOF spectra were then converted into the product translational energy distributions. Figure 26 shows the product translational energy distributions at the LAB angles of 117° , 30° and -50° for the $\text{O}(^1\text{D})$ reaction with H_2 at both $j=0$ and 1 rotational levels. These angles correspond

dynamically to the backward, sideway and forward scattering directions for the OH product relative to the $\text{O}(^1\text{D})$ atom beam direction or H-atom products relative to the H_2 beam direction. The relative distributions for the $\text{O}(^1\text{D})$ reaction with H_2 at $j = 0$ and $j = 1$ were therefore determined at the eight scattering angles. The ratios of the total products from $\text{H}_2(j = 0)$ and $\text{H}_2(j = 1)$ at eight different LAB angles were also determined. By integrating the differences in all eight LAB angles including the $\sin \theta$ weighting factor for the spherical integration, the ratio between the total cross sections of $\text{O}(^1\text{D})$ reaction with H_2 at $j = 0$ and $j = 1$ are determined to be $\sigma(j = 1)/\sigma(j = 0) = 0.95 \pm 0.02$. This shows that the H_2 molecule at $j = 0$ is slight more reactive than that at $j = 1$, which agrees quite well with quantum theoretical calculations.⁶⁷

Clearly, the single quantum H_2 rotational excitation effect on the integral cross section of the $\text{O}(^1\text{D}) + \text{H}_2$ reaction seems quite small though detectable. The more interesting question is how the single quantum rotational excitation of the H_2 reagent affects the OH product state resolved differential cross sections. From Fig. 26, the product translational energy distributions of the $\text{O}(^1\text{D}) + \text{H}_2(j = 1)$ reaction are shifted slightly to higher energy with respect to that of the $\text{O}(^1\text{D}) + \text{H}_2(j = 0)$ reaction. This is because the total energy of the $\text{O}(^1\text{D}) + \text{H}_2(j = 1)$ reaction is slightly more than that of the $\text{O}(^1\text{D}) + \text{H}_2(j = 0)$ reaction by $2B_{\text{rot}}(\text{H}_2)$, i.e. 120 cm^{-1} . If we shift the product translational energy distributions of the $\text{O}(^1\text{D}) + \text{H}_2(j = 1)$ reaction by 120 cm^{-1} , all the peak positions in the distributions will be aligned exactly to those of the $\text{O}(^1\text{D}) + \text{H}_2(j = 0)$ reaction.

From the translational energy distributions shown in Fig. 26, the distributions at the backward (117°) and forward (-50°) directions show some significant differences for the $\text{H}_2(j = 0)$ and $\text{H}_2(j = 1)$ reactions even though the distributions at the sideway scattering direction (30°) are very similar to each other for the two reactions. Since the rovibrational states of the OH radical are well known through previous spectroscopic studies, the translational energy distributions observed can be simulated quite conveniently. From the simulations, state-specific differential cross-sections can be determined for the eight LAB angles measured. From the product state distributions at the backward scattering distribution shown in Fig. 27, it is clear that a single quantum rotational excitation in the H_2 reagent has a rather significant effect on the OH. The rotational excitation seems to have a rather irregular effect on a specific OH state product, indicating that whether a single rotational excitation would enhance or reduce the

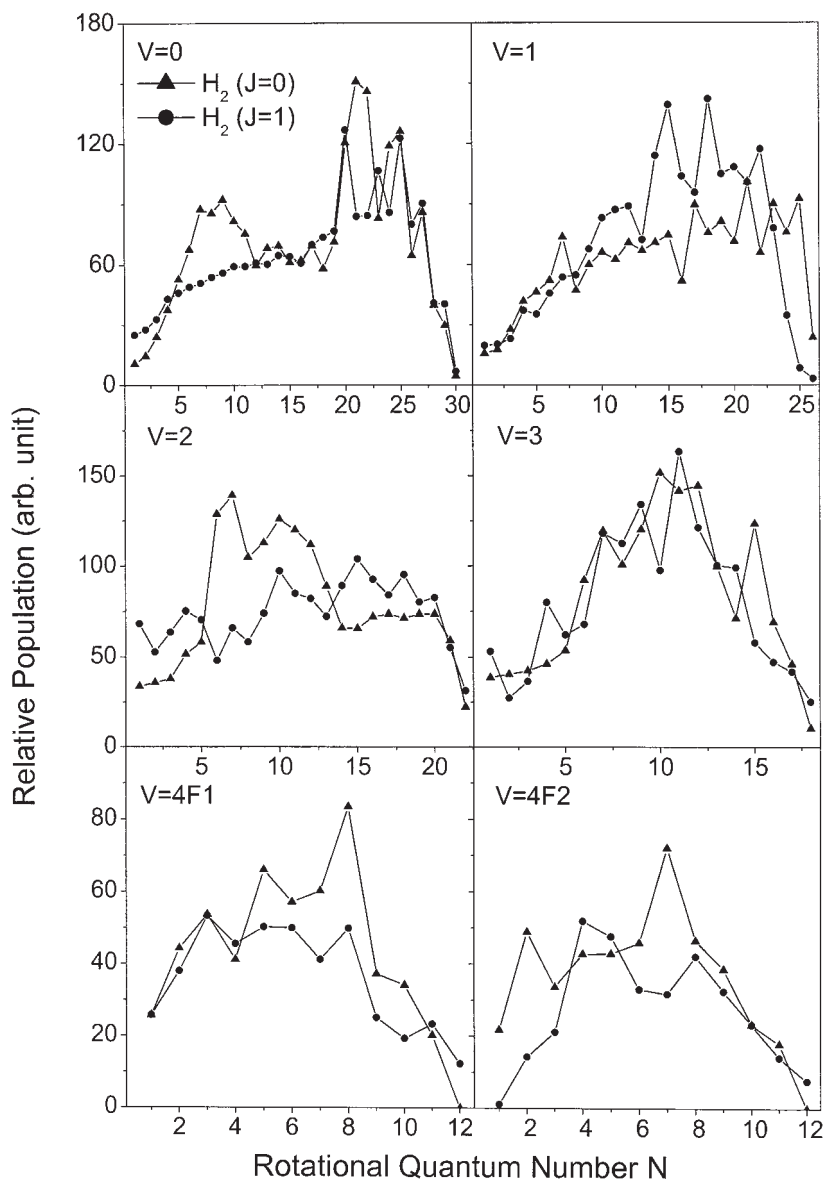


Fig. 27. Comparisons of the rovibrational state distributions obtained from the $O(^1D)$ reaction with H_2 at the $j = 0$ and $j = 1$ levels at the backward scattering 117° LAB angle.

state-specific differential cross-sections for a specific state seems to be very unpredictable. These observations are also true for the forward scattering direction even though the effects are quite different from that of the backward scattering direction. For the sideways scattering, however, the single quantum rotational excitation in H_2 seems to have a very limited effect on the OH-product state distributions, though slightly noticeable. This is very different from that of the forward and backward scattering products.

Qualitatively, this phenomenon can be understood in that the sideways scattering products are normally produced through larger impact parameter (b) collisions, i.e. larger orbital angular momentum, $L = \mu vb$, while forward-backward scattering products are produced via relatively smaller impact parameter (b) collisions, i.e. smaller orbital angular momentum. Therefore, a single quantum rotational excitation (j) in H_2 should have a larger effect at the forward and backward directions because the total angular momentum $J = L + j$ for the small L collisions is significantly changed relative to a single rotational quantum excitation in H_2 . However, relatively speaking, the total angular momentum $J = L + j$ is altered only slightly by a single rotational quantum excitation in H_2 for larger impact parameter (larger L) collisions which is mostly responsible for the sideways scattering products. The specific effect of the single quantum rotational excitation on the differential cross-sections is also very interesting. The lack of the specific patterns for the forward and backward directions in this effect is probably due to the nature of this insertion reaction, which has a large number of reaction resonance states. Interestingly, in a similar experiment in our laboratory, it was found that a rotational quantum excitation in D_2 does not have any noticeable effect in the $\text{O}(^1\text{D}) + \text{D}_2$ reaction.

4.3. *Experimental Evidence for a Collinear Abstraction Mechanism in $\text{O}(^1\text{D}) + \text{D}_2 \rightarrow \text{OD} + \text{D}$*

The $\text{O}(^1\text{D}) + \text{D}_2$ reaction was also investigated using the Rydberg “tagging” technique described above. As we have pointed out, there is an abstraction mechanism present at higher collision energies, in addition to the insertion mechanism which is dominant for this reaction at the low collision energies.^{61–65} The nature of this abstraction reaction was, however, not very clear from previous experimental studies. The experiment designed here was intended to clarify the source of this abstraction mechanism. The experiment described here was carried out at the collision energies of 2.0 kcal/mol and 3.2 kcal/mol, respectively. The 2.0 kcal/mol collision

energy is only slightly above the inferred 1.8 kcal/mol abstraction barrier for the abstraction, which implies that the reaction at this collision energy is mainly due to the insertion mechanism. While the collision energy of 3.2 kcal/mol is significantly above the inferred 1.8 kcal/mol barrier for the possible abstraction channel, providing us a good opportunity to probe the dynamics of this elusive abstraction channel.

Time-of-flight spectra of the D atom products have been measured at many laboratory angles at both collision energies. Translational energy distributions can be derived by direct conversion of these TOF spectra. For the experiment carried out at 2.0 kcal/mol, Fig. 28(a) shows the total product angular distribution from $\Theta_L = -60^\circ$ to 117.5° , which correspond to the forward (-60°), the sideward (30°) and the backward (117.5°) scattering directions. The direction of the D_2 beam is at $\Theta_L = 0^\circ$, while the direction of the $O(^1D)$ beam is at $\Theta_L = 90^\circ$. By definition, the forwardness and backwardness of the D-atom products are with respect to the D_2 beam direction, while those of the OD products are with respect to the $O(^1D)$ beam direction. From the angular distribution shown in Fig. 28(a), it is quite obvious that the angular distribution of the reaction product (D) is essentially forward and symmetric. That is not too surprising since 2.0 kcal/mol is only slightly above the barrier (1.8 kcal/mol) for the abstraction mechanism inferred from previous experimental studies. It is interesting that even though the total product distribution is forward and backward symmetric, the product translational energy distributions at the forward and backward directions in the CM frame are noticeably different. Figure 29(a) shows the product translational distributions at $\Theta_L = -60^\circ$ and 117.5° for the $O(^1D) + D_2$ reaction at 2.0 kcal/mol collision energy. Extensive sharp features are present in these translational energy distributions. These sharp structures correspond to the rovibrational structures of the OD products since the D atom has no internal energy distribution. Most of these structures are overlapped structures of different OD rovibrational states from $v = 0$ to 6. Spin-orbit states of the OD product are not resolved in these TOF spectra. Upon examining the translational energy distributions, it is clear that most of the OD products are highly rotationally excited since the low rotational OD product at the onset of each vibrational state of OD is not significant in comparison with other regions. The two translational energy distributions possess similar shapes overall. However, the detailed structures of these two distributions are noticeably different, indicating that state-specific OD product is clearly not exactly forward and backward symmetric. This result is quite similar to that of the $O(^1D) + H_2$ reaction. The

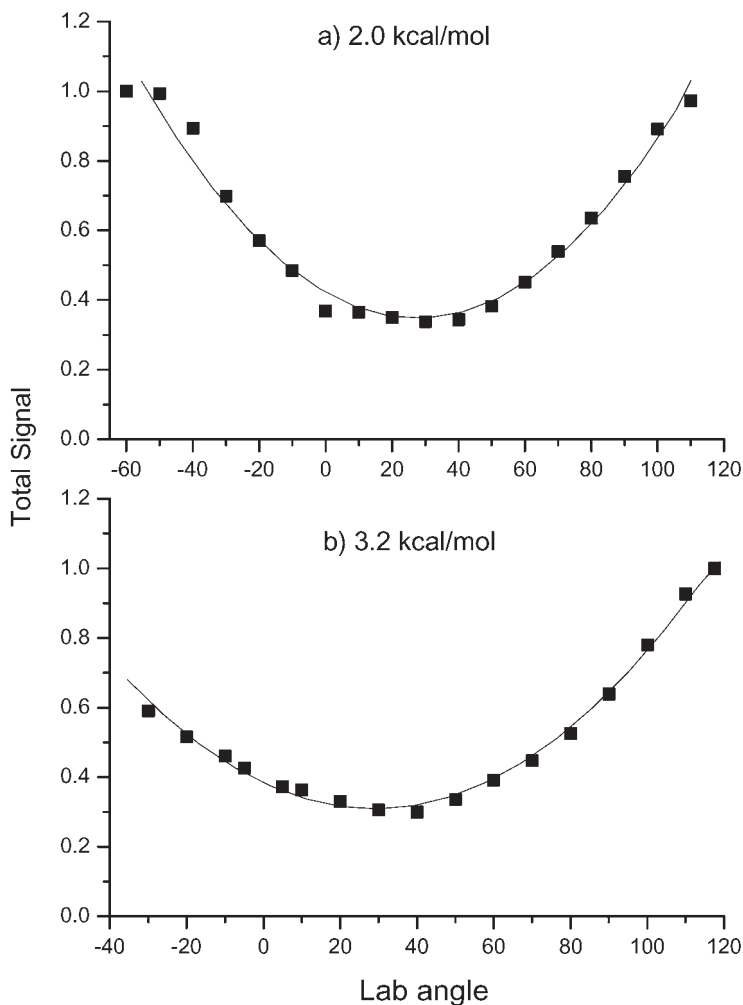


Fig. 28. The D atom product angular distribution in the laboratory frame for the $\text{O}(^1\text{D}) + \text{D}_2 \rightarrow \text{OD} + \text{D}$ reaction at two collision energies: (a) 2.0 kcal/mol, and (b) 3.2 kcal/mol.

overall symmetric OD product distribution at 2.0 kcal/mol is indicative of an insertion type mechanism.

The $\text{O}(^1\text{D}) + \text{D}_2$ reaction is also studied at a higher collision energy, 3.2 kcal/mol, with a room temperature D_2 beam, in order to better understand the reaction mechanisms involved at higher collision energies. When

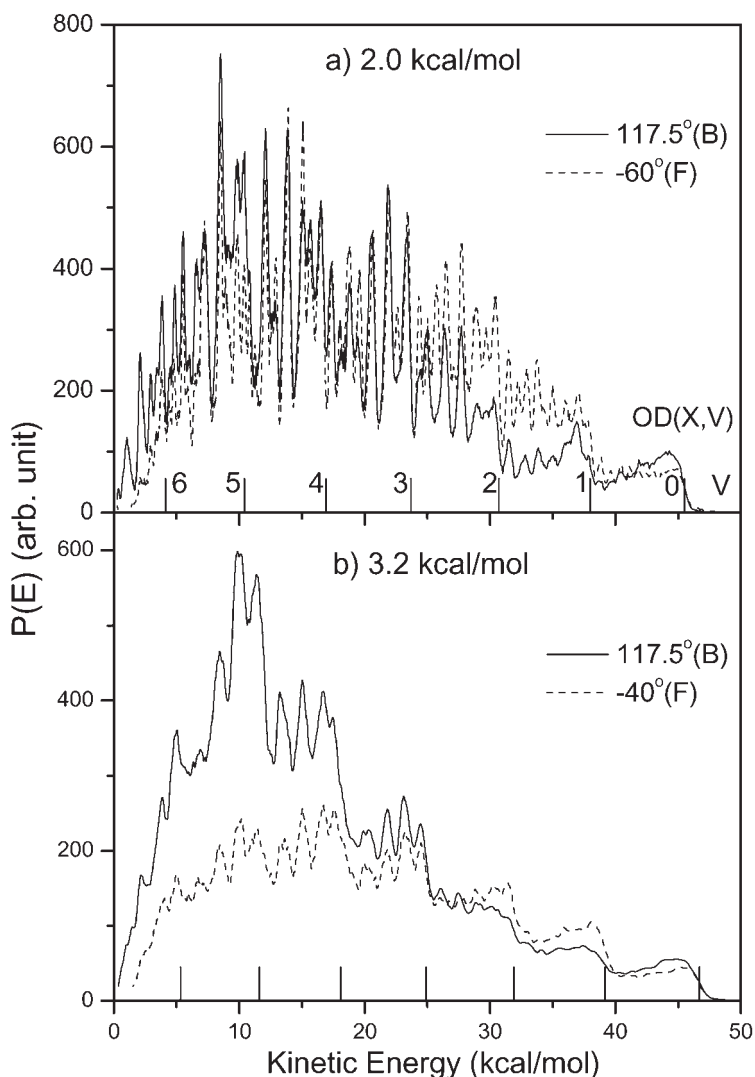


Fig. 29. The CM product translational energy distributions at the forward and backward scattering direction for the $O(^1D) + D_2 \rightarrow OD + D$ reaction at two collision energies: (a) 2.0 kcal/mol, and (b) 3.2 kcal/mol.

the collision energy of the reaction is increased from 2.0 to 3.2 kcal/mol, the total product angular distribution changes from a roughly forward-and-backward symmetric distribution to a clearly more backward distribution. Figure 28(b) shows the total product angular distribution at 3.2 kcal/mol

collision energy. The increase in the backward scattering signal is quite obvious in comparison with that at 2.0 kcal/mol. The nature of these backward scattered products is a very important issue, since that can provide important insight into the reaction mechanism responsible for these backward products. Figure 29(b) shows the two product translational energy distributions at the forward ($\Theta_L = -40^\circ$) and backward ($\Theta_L = 117.5^\circ$) directions in the CM frame at 3.2 kcal/mol collision energy. Apparently, the resolution of these translational energy distributions is worse than those at 2.0 kcal/mol, because the room temperature beam has a much larger beam velocity spread. Although the resolution is much lower at this collision energy, the basic information is not all lost in these translational energy distributions. By comparing the two distributions, it is quite obvious that the translational energy distribution at the backward direction is significantly different from that of the forward direction. At higher translational energy or lower OD internal energy, the distributions at the forward and backward directions are similar, which resembles the results at 2.0 kcal/mol. At lower translational energy or higher internal energy, the backward product is much more pronounced than that of the forward direction. These more backward products are likely the OD($v = 4, 5, 6$) products. Clearly, these backward products are not rotationally hot. These results are quite different from that at the collision energy of 2.0 kcal/mol, in which the forward and backward translational energy distributions are generally similar. From the above analysis, it is not difficult to draw the conclusion that the extra backward OD products appearing at higher collision energy are likely vibrationally hot ($v = 4, 5, 6$) and rotationally cold, which is typical of a collinear abstraction mechanism. This result indicates that the abstraction pathway for the O(^1D) + H₂ reaction at higher collision energies is clearly due to a collinear abstraction mechanism through the excited state surface.

4.4. *Quantum State Specific Dynamics for the O(^1D) + HD \rightarrow OD + H Reaction: Isotope Effect*

The O(^1D) + HD reaction was also studied using the same Rydberg tagging TOF technique described above. The experiment was carried out at a collision energy of ~ 1.7 kcal/mol, which is below the 1.8 kcal/mol barrier for the abstraction mechanism inferred from previous experimental studies.⁶³ The purpose of this experimental study is to investigate the isotope effect on this reaction.

Time-of-flight spectra of the H atom products have been measured at many laboratory angles (from 117.5° to -60° degree at 10° intervals). The laboratory angles at which the TOF spectra are shown are indicative of forward (-60°), backward (117.5°) and sideward scattering (30°). The direction of the HD beam is $\Theta_L = 0^\circ$, while the direction of the $O(^1D)$ beam is $\Theta_L = 90^\circ$. By definition in this work, the forwardness and backwardness for the H atom products are with respect to the HD beam direction, while those for the OD products are with respect to the $O(^1D)$ beam direction. From these TOF spectra, it is quite clear that these spectra consist of a lot of sharp structures. These sharp structures correspond to the rovibrational structures of the OD products. Most of these structures are overlapped structures by different OD rovibrational states. Spin-orbit states were not resolved in these TOF spectra. By directly converting these TOF spectra from the laboratory frame to the center-of-mass (CM) frame including the standard Jacobian transformation, the product translational energy distributions at different CM scattering angles of the title reaction can be obtained. Figure 30 shows the translational energy distributions obtained from the experimental measured TOF spectra. Since the center-of-mass angles are not constant for a certain laboratory angle at different product (H) velocities, each of the translational energy distributions obtained from the three different laboratory angles contains information in a range of CM angles. However, the three translational energy distributions still carry the basic information on forward, backward and sideward scatterings.

The available energy of the title reaction is about 45 kcal/mol, which can produce OD radical product up to $v = 6$. From Fig. 30(a), the energetic limit of different vibrationally excited OD products are indicated. The peaks shown in the translational energy distribution in Fig. 30(a) at these energetic limits are rotationally cold OD products at different vibrationally excited states. In principle, angular distributions can be obtained for the OD product at different rovibrational states by careful simulations of the translational energy distributions at different laboratory angles. This type of analysis takes enormous amount of time, and work in this direction is under way. Even though angular distributions for each rovibrational state are not available yet, important dynamical information on this reaction can still be derived from the translational energy distributions at typical scattering angles. From Fig. 30, it is quite obvious that the rotationally cold OD products are more pronounced at the forward and backward scattering directions than that at the sideward scattering direction with respect to the $O(^1D)$ beam direction. While almost all OD products at the sideward

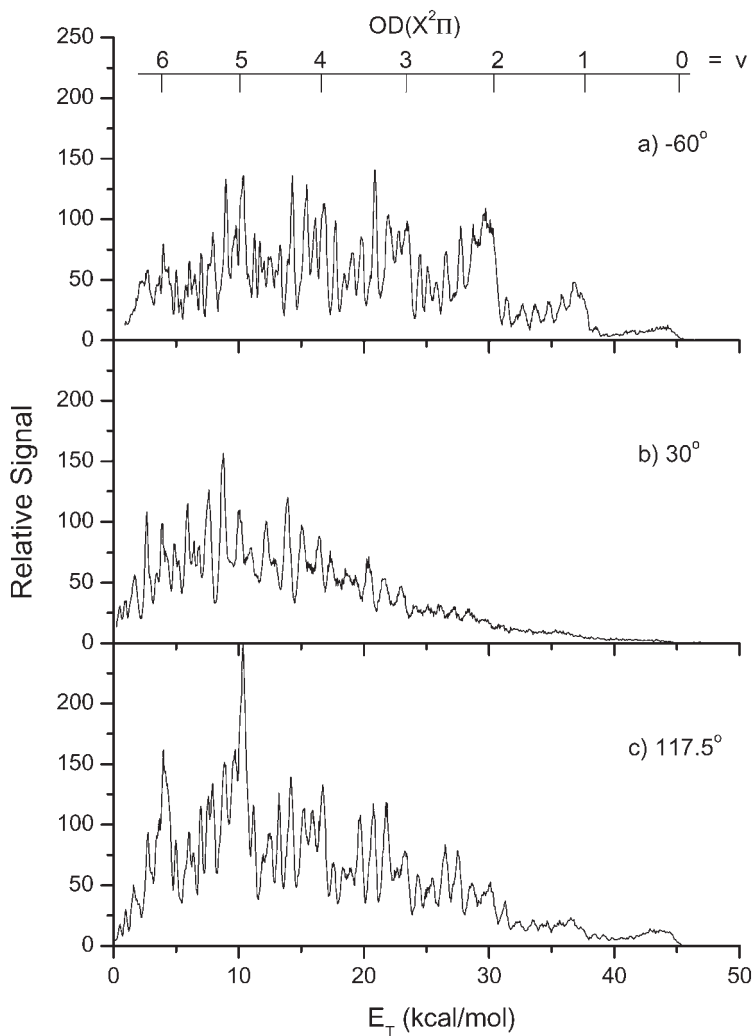


Fig. 30. The CM product translational energy distributions at the forward (-60°), sideways (30°) and backward (117.5°) scattering direction for the $O(^1D) + HD \rightarrow OD + H$ reaction at the collision energy of 1.7 kcal/mol.

scattering direction are rotationally hot, both cold and hot OD products are present at both forward and backward directions even though hot OD products are still more important. Over all, it is not difficult to notice that most of the OD products for the title reaction are rotationally hot, while

small amounts of OD products are rotationally cold and are mainly scattered in the forward and backward directions with respect to the $O(^1D)$ beam direction.

The total product angular distribution of the H-atom product in this reaction is roughly forward-backward symmetric. The total products at the backward direction are slightly more pronounced than that at the forward direction, indicating that the forward-backward scattering for the $O(^1D) + HD \rightarrow OD + H$ might not be exactly symmetric even though the collision energy of this reaction is below the reaction barrier for the abstraction channel. This means that insertion reaction does not necessarily produce forward-backward symmetric product angular distribution. In this reaction, since HD is not exactly symmetric, therefore the interaction with H and D might not be exactly the same. From the angular resolved translational energy distributions, it is clear that the total translational energy distribution or the OD product state distribution is also not forward and backward symmetric. In reality, there are actually significant differences between the forward and backward translational energy distributions. Since exact simulation is not available yet, a full-fledged comparison between theory and experiment is not realistic at this time. From Fig. 30, it is obvious that the product state distribution for the rotationally cold OD products are quite asymmetric. For $v = 0$ of OD, the rotationally cold peak at forward direction (-60°) is roughly the same as that at the backward direction, indicating that the rotationally cold OD products at $v = 0$ are roughly forward and backward symmetric. For rotationally cold $OD(v = 1)$ products, the forward and backward scatterings are clearly not symmetric. With respect to the $O(^1D)$ beam direction, the $OD(v = 1)$ products at low rotational levels are clearly forward scattered. And the $OD(v = 2)$ products at low rotational levels are even more forward scattered. For $v = 3$, the OD products at low rotational levels are still forward scattered, however, less so than the $OD(v = 2)$ products. For $v = 4$, the OD product peak height at low rotational levels is similar for forward and backward scattering directions, indicating the $OD(v = 4)$ products at low rotational levels are roughly forward-backward symmetric. At $v = 5$, however, the OD products at low rotational levels are clearly backward scattered with respect to the $O(^1D)$ beam, in which the corresponding peak at the backward direction is significantly more than that at the forward scattering direction. Similarly, the $v = 6$ OD products at low rotational excitation is also backward scattered. The above experimental observations are quite striking in that the OD

rotationally cold products undergo forward to backward scattered angular distributions. The underlying dynamics responsible for these interesting experimental observations are not immediately clear for the $\text{O}(^1\text{D}) + \text{HD}$ reaction since such phenomenon has not been observed for the $\text{O}(^1\text{D}) + \text{H}_2$ reaction. Much theoretical work is needed to understand the nature of this interesting phenomenon.

5. Quantum-State Resolved Dynamics in the H_3 System: Probing Structures and Dynamics of the Quantized Transition States

Extensive studies on the H_3 system have been performed both experimentally^{67–70} and theoretically.^{71–77} Even though this is simplest chemical reaction in nature, many of the interesting and also important questions involved this system have never been clearly answered. One of the most outstanding questions is the existence of the dynamical resonances in this reaction. Experimentally, a few attempts to observe the dynamical resonance effect in this reaction have largely failed. Theoretically, the existence and the nature of such resonances have never been clarified. In this work, the $\text{H} + \text{HD}(\text{D}_2) \rightarrow \text{H}_2(\text{HD}) + \text{D}$ reaction was studied experimentally in our laboratory using the Rydberg time-of-flight technique, in close collaboration with the theoretical calculations by Skodje, in the hope of trying to answer some of these intriguing questions in this system.

The experimental apparatus employed in this study is the same one used in the study of the $\text{O}(^1\text{D}) + \text{H}_2$ reaction in the last section.^{78,79} The only significant difference is the H beam source which is generated from HI photodissociation while the $\text{O}(^1\text{D})$ atom beam described in the previous section is generated from O_2 photodissociation. Briefly, two parallel molecular beams (HI and HD or D_2) are generated with similar pulsed valves in this experiment. In the reaction of $\text{H} + \text{HD}$, the H-atom beam is produced by the photolysis of the HI molecule at 266 nm using a Nd:YAG 4th harmonic laser output. There are two different photolysis channels, corresponding to the two spin-orbit states of the iodine atom, which gives rise to two sharp peaks of H-atom velocity distribution: a fast component at 17,470 m/s and a slow component at 11,230 m/s. The H beam is then crossed at 90° with the HD molecular beam. The HD beam was produced by an adiabatic expansion through a nozzle cooled to liquid nitrogen temperatures with almost all of the HD molecules in the $j = 0$ level. Using the slow and fast H atoms separately in the reactive scattering experiment

with HD, two collision energies are obtained, $E_c = 0.498$ eV and 1.200 eV, correspondingly. The experimental results obtained at these two collision energies are described in the following paragraphs. In the reaction of $\text{H} + \text{D}_2$ described below, a tunable wavelength photolysis laser is used to generate the H-atom beam with variable speed. This allows us to study the dynamics of this reaction at different collision energies.

5.1. The $\text{H} + \text{HD}$ Reaction at $E_c = 0.498$ eV and 1.200 eV

TOF spectra of D atom at different laboratory scattering angles were measured using the technique described above at the collision energy of 0.498 eV for the title reaction.⁸⁰ These TOF spectra were then converted to the product translational energy distributions using a home-written LAB-CM conversion program. Figure 31 shows four typical such distributions. These are many sharp structures in these distributions which can be assigned to different H_2 -product rotational states from the $\text{H} + \text{HD}$

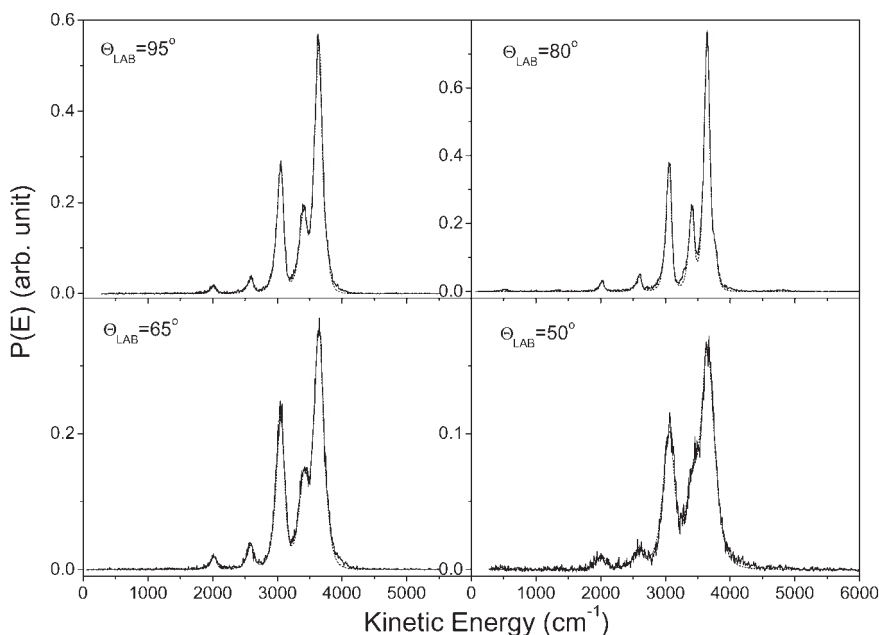


Fig. 31. The product translational energy distributions measured at different laboratory angles for the $\text{H} + \text{HD} \rightarrow \text{H}_2 + \text{D}$ reaction at the collision energy of 0.5 eV.

reaction. From these distributions, relative rotational-state-resolved differential cross-sections can be determined. Experimental apparatus functions on a realistic experimental model are used to correct the detections at different detection time delays and laboratory angles. These corrections are essentially the same as the method used by Schnieder *et al.*⁷ The experimental differential cross-sections for the $\text{H}_2(v=0, j')$ product obtained are presented in Fig. 32(a) along with the theoretical values. All experimental

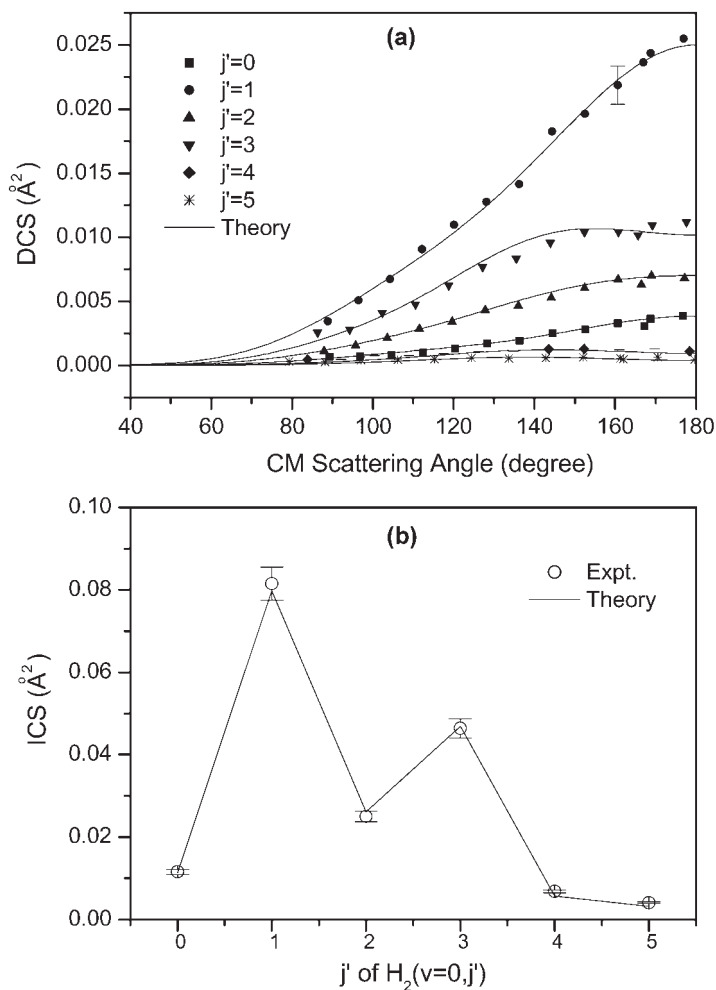


Fig. 32. The differential cross-sections and the state-specific integral cross-sections for the $\text{H} + \text{HD} \rightarrow \text{H}_2 + \text{D}$ reaction at the collision energy of 0.5 eV.

results in Fig. 32(a) are scaled to the theoretical value using one scaling factor for all different product states. State-specific integral cross-sections (ICS) have also been determined by integrating the DCS data in Fig. 32(a), and are shown in Fig. 32(b). Clearly the experimental results show that all H_2 products are backward scattered relative to the H-atom beam direction. Another interesting observation is that the state-specific integral cross-sections of the $\text{H}_2(v=0, j')$ oscillate quite significantly. Clearly, this oscillation follows the $\text{H}_2(j')$ -product nuclear spin statistics. Therefore, the H_2 -product rotational-state distribution seems to be dramatically affected by the H-atom nuclear spin statistics. This result is similar to that of the $\text{H} + \text{HI}$ reaction by Zare *et al.*⁸¹

The title reaction has also been investigated at the collision energy of 1.200 eV using the faster H-atom component generated by the HI photolysis at 266 nm. TOF spectra of the D-atom at many different laboratory scattering angles were measured using the technique described above at the collision energy of 1.200 eV. These TOF spectra can be converted to the product translational energy distributions using the same LAB-CM conversion program. Figure 33 shows six typical product translational energy distributions converted at the backward and sideways scattering directions. These are

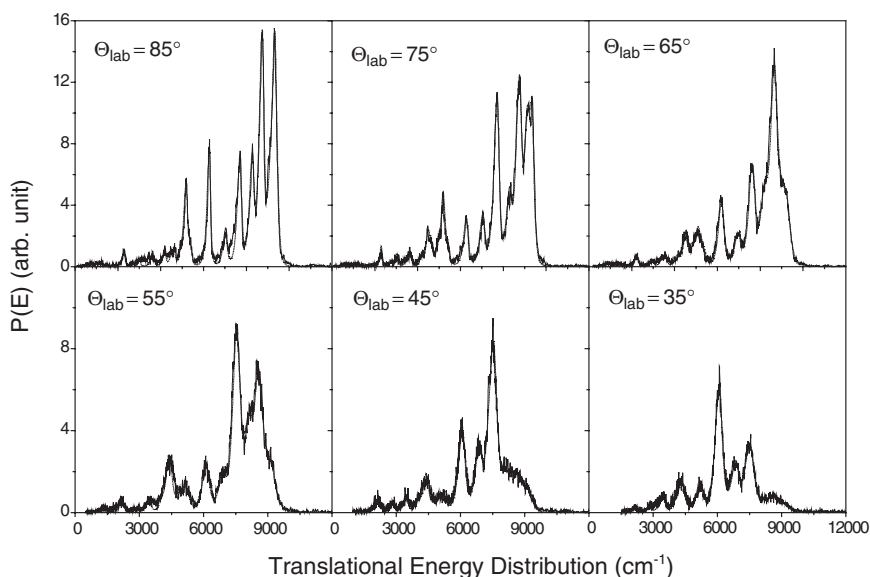


Fig. 33. The product translational energy distributions measured at different laboratory angles for the $\text{H} + \text{HD} \rightarrow \text{H}_2 + \text{D}$ reaction at the collision energy of 0.5 eV.

many sharp structures in these distributions which can be assigned to different H_2 -product rovibrational states from the $\text{H}+\text{HD}$ reaction. In addition to the backward and sideways scattering, we have also measured scattering products at the forward scattering direction, which is very hard to measure because of the unfavorable kinematics and also signal attenuation due to the HI beam. Nevertheless, great efforts have been devoted to the forward scattering product detection. TOF spectra at several laboratory angles at the forward scattering direction have been measured. Figure 34 shows the D-atom TOF signal at -58° for the $v = 0$ H_2 -product in the forward direction. From experimental results, relative quantum state-resolved differential cross-sections can be determined. Experimental apparatus functions on a realistic experimental model are used, as discussed above, to correct the detections at different detection time delays and laboratory angles. The three-dimensional experimental differential cross-sections obtained for the $\text{H}_2(v = 0, j')$ products are presented in Fig. 35.^{82,83} All experimental results are scaled to the theoretical value using one scaling factor for all different product states. Rovibrational state specific integral cross-sections (ICS) for

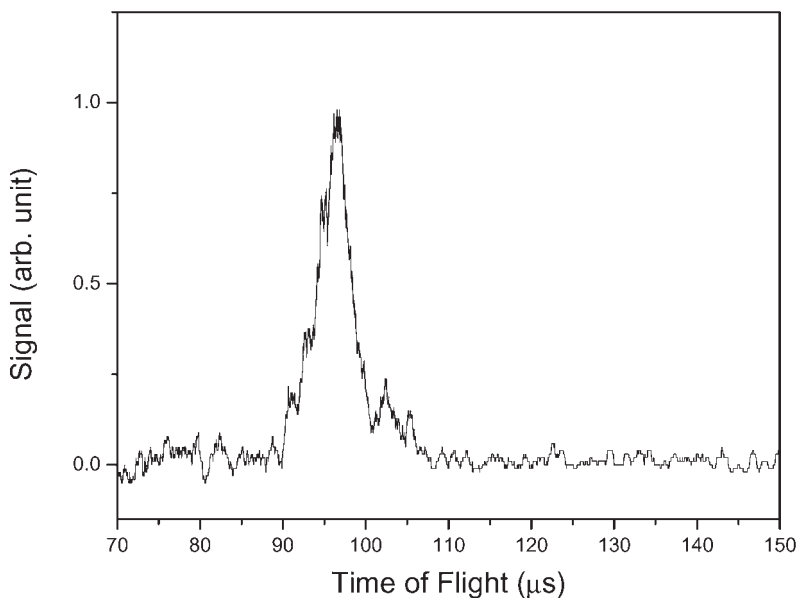


Fig. 34. The D-atom TOF spectrum at the forward scattering direction ($\Theta_L = -58^\circ$) for the $\text{H} + \text{HD} \rightarrow \text{H}_2 + \text{D}$ reaction at the collision energy of 1.200 eV.

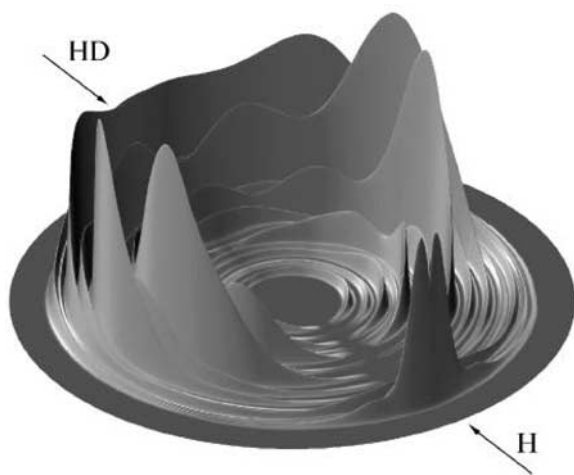


Fig. 35. The three-dimensional plot of the differential cross-sections for the $\text{H} + \text{HD} \rightarrow \text{H}_2 + \text{D}$ reaction at the collision energy of 1.200 eV (detecting the D-atom product).

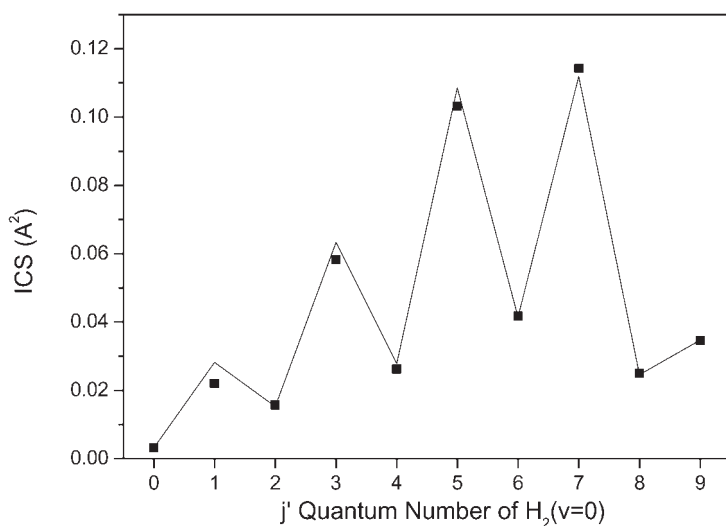


Fig. 36. The state-specific integral cross-sections for the $\text{H}_2(v=0)$ product from the $\text{H} + \text{HD} \rightarrow \text{H}_2 + \text{D}$ reaction at the collision energy of 1.200 eV.

the $\text{H}_2(v=0)$ products have also been determined by integrating the DCS data in Fig. 33 and are shown in Fig. 36.

The experimental results show that all H_2 -products are more backward and sideways scattered relative to the H-atom beam direction. In addition

to the backward and sideway scattering, there is a narrow forward scattering peak for the $v = 0$ H_2 -product. The simulations show that the $v = 0$ H_2 forward peak is attributed to predominantly low rotationally excited H_2 -products ($j' = 0, 1$ and 2). This is in contrast to the backward and sideway scattering products which are significantly more rotationally excited with averaged rotational quantum number $j' \sim 5$. This observation is rather peculiar because the product state distributions at the forward and backward scattering directions are significantly different from each other, indicating that the reaction dynamics responsible for the forward scattering products are very unique. In Fig. 35, state-specific DCSs for high j' H_2 products shows some significant angular oscillations. As j' increases, there are actually multiple oscillations. This phenomenon has also been observed in the $\text{H} + \text{D}_2$ reaction by Schnieder *et al.*⁷ However, the nature of these angular oscillations has not been clearly addressed in previous theoretical investigations. Furthermore, state-specific integral cross-sections (Fig. 36) of $\text{H}_2(v = 0, 1, j')$ at this collision energy oscillate more dramatically than that at the lower collision energy, which is attributed to the nuclear spin statistics.

One of the most interesting observations in this experiment is the forward scattering, similar to the forward scattering observed in the $\text{H} + \text{D}_2$ reaction at higher collision energies.⁸⁶ The characteristics of the forward scattering H_2 products are quite unique. Firstly, it is clear that the forward scattering H_2 -products are significantly colder rotationally, with mainly $\text{H}_2(j = 1)$ populated, than the backward and sideway scattering products. Secondly, the angle range of the observed forward scattering peak is extremely narrow. Experimental characteristics of the forward scattering peak including the rotational distribution and angular width can be readily reproduced by the quantum calculations. However, to assign the forward peak to specific dynamical behavior requires further theoretical analysis.

In order to understand the detailed dynamics observed for this reaction, especially the forward scattering, quantum reactive scattering calculations (QM) were carried out based on the BKMP2 PES⁸⁴ by Skodje. State-specific integral cross-section (ICS) and differential cross-section (DCS) were obtained from these calculations. From the scattering calculation, the state- and angle-resolved integrated opacity function is computed, i.e., $d\sigma_{J_{\max}}(0, 0 \rightarrow 0, 0; \theta = 0)/d\Omega$ versus J_{\max} , where the DCS is the partial sum of waves with $J \leq J_{\max}$, J being the total angular momentum. This analysis shows that the forward peak in the $\text{H}_2(v' = 0)$ product for $E_c = 1.200$ eV is dominated by the contribution from just several partial

waves near $J = 25$, while for the $\text{H}_2(v' = 1)$ product the dominant contribution occurs near $J = 21$. The narrow range, high J collisions responsible for the forward scattering implies that the reaction intermediate is formed at a very high impact parameter and should rotate quite rapidly. To further probe the dynamics associated with the forward peak, a time-delay analysis was carried out using the concept of the angle-resolved scattering time-delay proposed by Goldberger and Watson.⁸⁵ An extra ~ 20 fs of time delay in the forward direction, similar to the result obtained by Althorpe *et al.*,⁸⁶ is clearly seen compared to other scattering angles. This clearly shows that the forward scattering product results from a time-delayed mechanism.

Since the forward peak is clearly from high J collisions, it is clearly produced via a rapidly rotating intermediate exhibiting an enhanced time delay. Further insight into the associated dynamics is provided by a classical trajectory simulation by Skodje. The forward peak results from the sideways collisions of the H atom on the HD-diatom (see Fig. 37). At the point where the transition state region is first reached, the collision complex is already oriented about 70° relative to the center-of-mass collision axis. The intermediate then rotates rapidly with an angular frequency of $\omega \sim J/I$, where I is the moment of inertia of the intermediate. If the intermediate with a time delay of the order of the lifetime τ , the intermediate can rotate

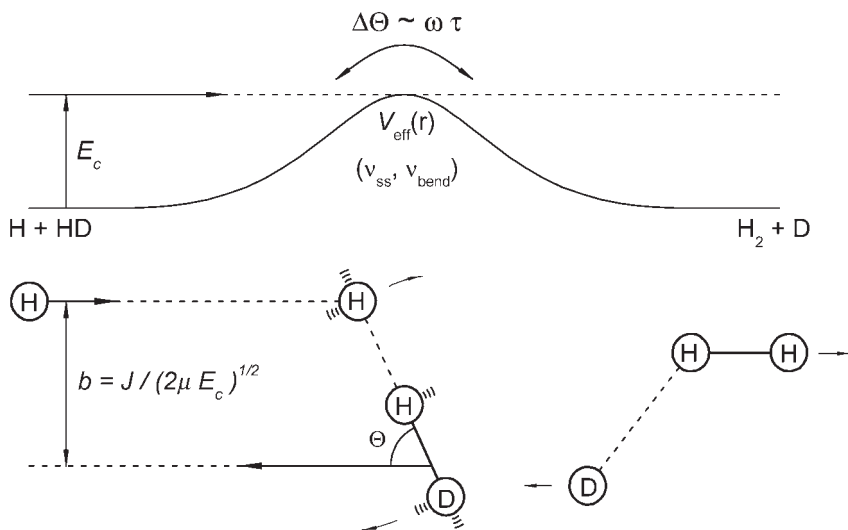


Fig. 37. Reaction mechanism for the forward scattering product from the $\text{H} + \text{HD} \rightarrow \text{H}_2 + \text{D}$ reaction at the collision energy of 1.200 eV.

an additional amount $\Delta\theta = \omega\tau$, or about 50° for a 20 fs time delay. Since the intermediate is expected to decay exponentially $e^{-t/\tau}$, there will still be significant probability density at $t = 2.2\tau$ which can take the product into the forward direction. Consistent with this simple picture, we have found that the smallest scattering angles consistently show the longest time delays, both classically and quantum mechanically.

The next interesting question, of course, is the physical origin of the time-delay in the transition state region for the forward scattering products. Using the centrifugally-shifted Hamiltonian, $H(J) = H(0) + \hbar^2 \hat{J}^2 / 2\mu R^2$, with R being the H–HD distance, the theoretical spectra of quantized bottleneck states and the wavefunctions of the bottleneck states^{87–90} have been obtained using the spectral quantization technique. A quantized bottleneck state is clearly identified at exactly the collision energy ($E_c = 1.200$ eV) of this experiment.

In the above analysis, we have shown that the forward scattering in the $\text{H} + \text{HD} \rightarrow \text{H}_2 + \text{D}$ reaction is clearly produced via a time-delayed mechanism, similar to that for the $\text{H} + \text{D}_2$ reaction, that is somehow related to a quantized bottleneck state. Generally, time-delay in the transition state region could be caused by different mechanisms, i.e., (a) via a Feshbach resonance state trapped in an adiabatic potential well as in the $\text{F} + \text{HD} \rightarrow \text{HF} + \text{D}$ reaction, and (b) via a quantized bottleneck state in which time delay results from the slow-down of the motion of the intermediate near the top of the adiabatic reaction barrier rather than trapping, during which a few vibrations take place in the coordinates perpendicular to the reaction coordinate. The distinction between these two types of mechanisms and, in fact, the existence of quantized bottleneck states as a distinct category of quasi-bound state has only become clear in recent years.^{90,91} The spectral quantization method shows that no clear Feshbach resonance state is present in the centrifugally-shifted vibrationally adiabatic potentials in the $\text{H} + \text{HD} \rightarrow \text{H}_2 + \text{D}$ system near the energy of the experiment; on the other hand our results show clearly that the collision energy ($E_c = 1.200$ eV) in this experiment is nearly resonant with the energy of a quantized bottleneck state for the $J = 25$ collisions predominantly responsible for the forward scattering. Therefore all analyses indicate that the time-delay mechanism observed in the forward scattering is produced via the slow-down of the intermediate's motion near the top of the barrier of the specific quantized bottleneck state at about $E_c = 1.2$ eV. It is obvious that this mechanism is significantly different from the Feshbach resonance mechanism in which trapping occurs in an

effective potential well. However, there are also similarities between the two mechanisms. In the Feshbach resonance mechanism, the collision energy (E_c) has to be resonant with the trapped resonance state. Similarly, in the time-delayed mechanism via a quantized bottleneck state, the collision energy (E_c) has also to be resonant with the quantized bottleneck state, i.e. the barrier height. The quantized bottleneck state responsible for the time delay is also an interesting issue. Theoretical analysis shows that the wavefunction of the quantized bottleneck state has one node in the symmetric stretch and two nodes along the bending coordinate, corresponding clearly to a quantized bottleneck state with one quantum of symmetric stretch excitation and two quanta of bend. This barrier state is a mixed state of two adiabatic barrier states with $(v_{ss}, v_{bend}) = (1, 0)$ and $(0, 2)$. It is also interesting to point out here that a quantized bottleneck state could essentially affect the reaction dynamics in a similar way (producing forward scattering) to a trapped Feshbach resonance state as in the $F + HD \rightarrow HF + D$ reaction.⁹⁵ Such a mechanism should also play an important role in many chemical reactions with barriers at high collision energies.

5.2. *Probing the Structures of Quantized Transition States in the $H + D_2$ Reaction*

The concept of the transition state is essential to our view of the dynamics of chemical reactions as well as to the chemical reaction rate theory. In a chemical reaction, the transition state acts as a bottleneck to reaction so that incident reagent flux below the transition state energy is reflected while above the transition state energy it is transmitted to products. In practice, transition state theory is based on the existence of rovibrational quantum states of the collision complex lying near the maxima of effective potential barriers.⁸⁹ Despite the crucial importance of the QBS to the framework of chemical reaction dynamics, they have proven quite elusive to direct experimental observation. Recently, the quantum dynamics near the transition state has been investigated in “half-collision” experiments using the methods of transition state spectroscopy⁹² and photodissociation spectroscopy.⁹³ In particular, the recent work of Moore and co-workers⁹³ on the laser photolysis of the ketene molecule in a cold jet environment revealed step-like structures in the rate for $C_2H_2O + h\nu \rightarrow CO + CH_2$ as the deposited energy passed through threshold values. However, the suggestion in that work that the steps were associated with the energies of the

QBS was cast into doubt by strong disagreement with theoretical results.⁹⁴ In a full collision experiment, appropriate to bimolecular reactions, direct observation of quantized states in the transition state region is even more difficult. The core problem is that the impact parameter averaging in a crossed beam scattering experiment smears the bottleneck energies over a large range, making them very difficult to identify in observables. In order to partly undo the effects of impact parameter averaging, it would be very helpful to carry out angle- and state-resolved measurements^{86,95,96} at different collision energies. In this section, the recent results of a new experiment on the $\text{H} + \text{D}_2 \rightarrow \text{D} + \text{HD}$ reaction^{97–100} and the results of theoretical simulations are described here to demonstrate the influence of QBSs in a full collision environment.

In order to observe the effects of quantized transition states in a reactive collision on the reaction dynamics, it is essential to accurately measure the reactive cross-sections as a function of variable collision energy, E_c . In the previous part on the $\text{H} + \text{HD} \rightarrow \text{H}_2 + \text{D}$ reaction, we have measured the state-to-state differential cross-section (DCS) at two isolated collision energies with a crossed molecular beam apparatus using a HI-photolysis source for the H-atom beam using fixed laser frequencies. In the present work on the related $\text{H} + \text{D}_2 \rightarrow \text{D} + \text{HD}$ reaction, we have modified our previous experimental design to permit the use of a tunable photolysis laser to generate the H-atom beam with variable speed, which thus allows the continuous variation of E_c . Except for the photolysis source, the present experiment is similar to the experiment described in the last sections. Two parallel molecular beams (HI and *ortho*-D₂) are generated with pulsed valves. The *ortho*-D₂ beam was produced by an adiabatic expansion through a nozzle cooled to the liquid nitrogen temperature, which ensures that almost all molecules in the beam are in the $\text{D}_2(v=0, j=0)$ state.¹⁰¹ The H-atom beam is produced by HI-photolysis using a tunable, narrow band doubled dye laser output. By varying the laser frequency, center-of-mass (CM) collision energies in the range $E_c = [0.4\text{--}1.0\text{ eV}]$ were obtained with a spread estimated to be about $\Delta E_c = 10\text{ meV}$. The reaction products were monitored using the same hydrogen Rydberg atom time-of-flight technique described above. The TOF-spectra of D-atoms at different E_c was measured using this method and then converted to the CM translational energy distribution. Sharp structures are observed in the TOF-spectra at different E_c , which can be assigned to HD-product rovibrational states, which then yield relative quantum state-specific DCSs. Experimental error bars on the DCSs are about $\pm 10\%$ or less. The experimental design, which

could monitor conveniently the H-atom beam intensity *in situ*, allows the measurement of absolute DCS up to a single overall scaling factor for all energies and, thus, all product states. The D-atom TOF spectrum was measured at 19 energies at the same (nearly) backward scattering direction at the laboratory angle of 70° , corresponding to CM angles around 160° for $\text{H} + \text{D}_2(v = 0, j = 0) \rightarrow \text{HD}(v = 0, j' = 2) + \text{D}$. Eight typical translational energy distributions at different collision energies, obtained from the measured D-atom TOF spectra, are shown in Fig. 38. The measured DCS at $\Theta_L = 70^\circ$ for the $\text{HD}(v = 0, j' = 2)$ products at different collision energies, which were clearly resolved in the TOF spectra, are shown in Fig. 39. Three oscillations in the measured DCS are clearly apparent over the energy range considered. Similar oscillations are also observed for other final states. The observation of this oscillation is very intriguing since the nature of such structures has not been clearly characterized theoretically despite their obvious importance in the understanding of fundamental reaction dynamics in this benchmark system.

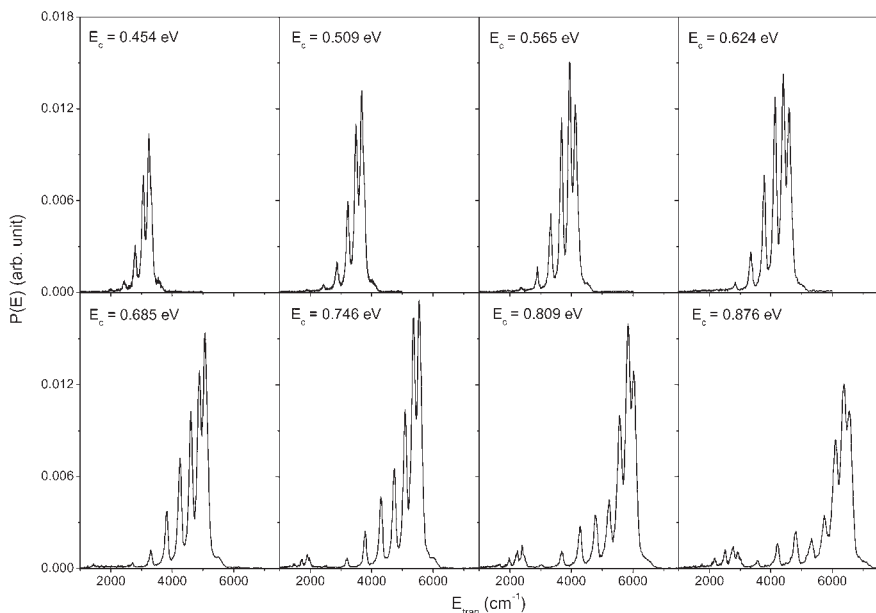


Fig. 38. Typical translational energy distributions for $\text{H} + \text{D}_2(v = 0, j = 0) \rightarrow \text{D} + \text{HD}(v', j' = 2)$, which were obtained from the measured D-atom TOF spectra, at nine different collision energies.

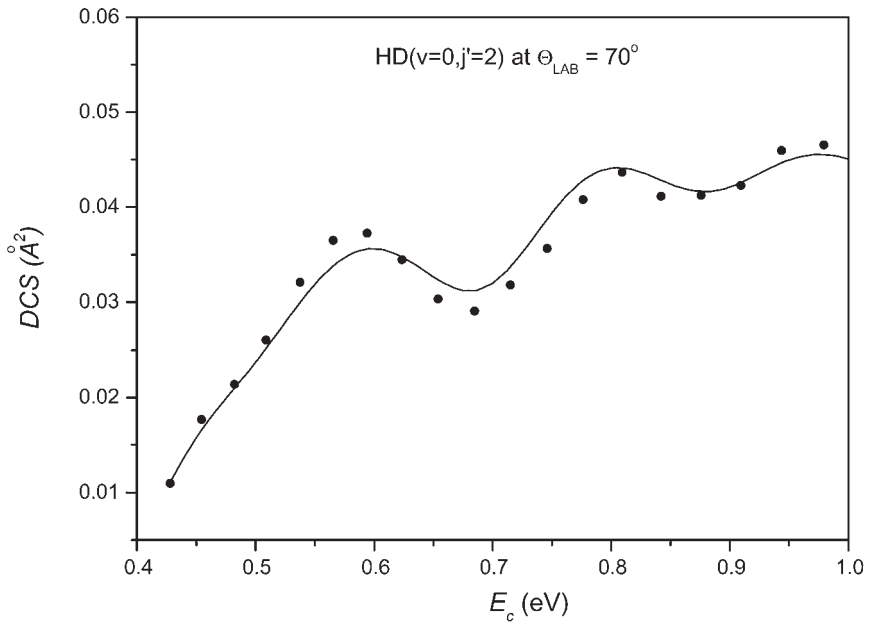


Fig. 39. The experimental differential cross-section (dots) for $\text{H} + \text{D}_2(v = 0, j = 0) \rightarrow \text{D} + \text{HD}(v' = 0, j' = 2)$, measured at the laboratory angle of 70° , versus CM collision energy, E_c . The curve is the result of the quantum scattering calculation.

In order to clarify the nature of these oscillations, the dynamics for $\text{H} + \text{D}_2 \rightarrow \text{D} + \text{HD}$ has been theoretically modelled using a fully converged coupled channel scattering calculation that employed the highly accurate BKMP2-PES.¹⁰² These computations produce the \mathbf{S} -matrix from a coupled-channel calculation in a hyperspherical coordinate system^{103–107} using a partial wave expansion up to total angular momentum $J = 32$ on a grid of 90 total energies (including zero-point) from $E = 0.5$ – 1.6 eV. The details of the calculations have been presented elsewhere, and it is sufficient to note that the state-to-state DCS and ICS are converged with respect to basis set size and propagation steps. As seen in Fig. 39, the experimental DCS at $\Theta_{\text{LAB}} = 70^\circ$ ($\Theta_{\text{CM}} \approx 160^\circ$) for $\text{H} + \text{D}_2(0, 0) \rightarrow \text{HD}(0, 2) + \text{D}$ is well reproduced by theory. The agreement between theory and experiment provides an excellent check that the theoretical model used is accurate and reliable as the basis for further analysis.

Using the accurate theoretical model, the physical origin of the intriguing oscillatory structure of the DCS can be traced. One striking feature that emerges from the scattering calculations is the occurrence of very

strong oscillations in the **S**-matrix elements vs. E . Similar oscillation in $P_R(v, j \rightarrow v', j'; E)$ has been computed for other isotopic combination of this reaction,¹⁰⁸ but is most pronounced in the present case. The oscillatory structure taken as a function of J reveals that the “peak” positions progressively shift to higher energy with increasing J . This “ J -shifting” of features in P_R vs. J is a well-known manifestation of impact parameter averaging and leads to the energy smearing of features, such as resonance energies, in collision experiments. Indeed, when the partial wave are combined to form the cross sections, $\sigma_R(v, j \rightarrow v', j'; E)$, the oscillations are generally averaged out. The situation is clearly different for the DCS. As shown in Fig. 39, the oscillatory structures in the backward (i.e. rebound) direction appear much more strongly than the corresponding structures in the ICS. The reason is that the angle selection suppresses the impact parameter averaging allowing the strong oscillation of the individual **S**-matrix elements persist in the final observable. Therefore, detecting backward scattering products at low rotational excitation is “selectively” probing reactive products from collisions with a reduced range of small impact parameters.

While it is now clear that the oscillation in the DCS is the result of an underlying oscillation in P_R , it still remains to explain why P_R oscillates in the first place. In previous discussions of the $\text{H} + \text{H}_2$ reaction family, there is occasional reference to such structures as resonance peaks, although a systematic assignment has not appeared. However it does not appear that this simple identification is tenable. Using the spectral quantization method¹⁰⁹ we computed all the localized quantum states for $E_c < 1.2$ eV, and we have found that all the relevant lowest energy states can be assigned to the QBSs: $E_c(0, 0^0) = 0.41$ eV, $E_c(0, 2^0) = 0.59$ eV, and $E_c(1, 0^0) = 0.71$ eV, all for $J = 0$. While the QBSs are sometimes referred to as “barrier resonances”, this nomenclature is controversial precisely because P_R does not show resonant peaks. Moreover, the peak positions¹⁰⁷ are out-of-phase for the various transitions $(v, j \rightarrow v', j')$, whereas resonance peaks should appear at nearly the resonance energy. Finally, the amount of J -shifting of the peaks is inconsistent¹⁰⁷ with a progression of rotationally excited resonance states. Even though the oscillations are not resonance peaks *per se*, they are intimately connected to the QBSs. It appears that the energy-dependent oscillation observed in the experiment is an interference effect somewhat similar to Stuckelberg oscillations¹¹⁰ familiar from atomic physics. The correlation diagram shown in Fig. 40(a) provides a simple view of the reaction dynamics. The QBSs near the saddle point are correlated along the reaction coordinate to the asymptotic rovibrational states through vibrationally

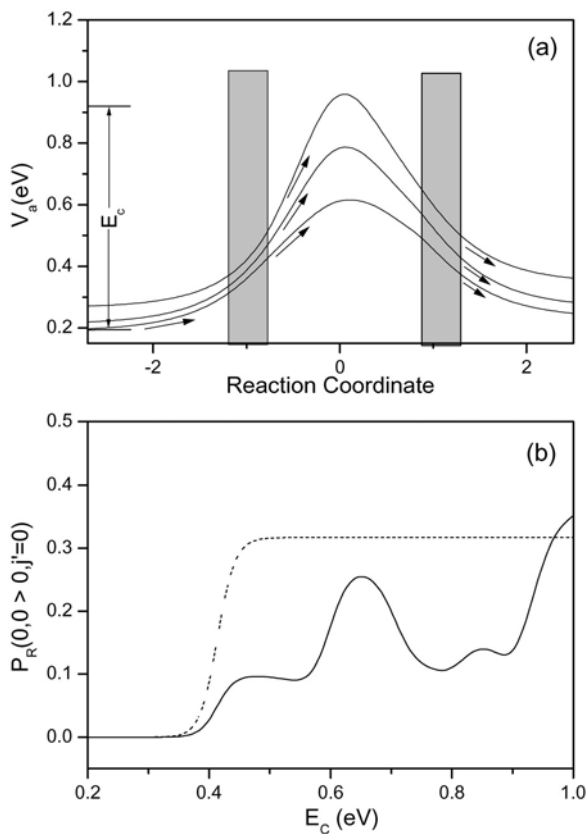


Fig. 40. (a) A schematic correlation diagram illustrating the role of quantized bottlenecks on the reaction dynamics. Because of nonadiabatic coupling in the entrance channel (shaded area), flux in a given initial state will pass the transition state through several bottleneck states. Nonadiabatic coupling in the exit channel (shaded area) will further mix the reactive flux into the final product states. (b) The state-to-state reaction probabilities, $P_R(0,0 \rightarrow 0,j'; E)$ versus E_c for $j' = 0$. The solid lines show that the full model, with coupling in both the entrance and exit channel, exhibits the out-of-phase oscillations observed in the exact dynamics. The dashed lines show the results when the coupling in the exit channel is switched off, which then show only simple threshold behavior. The essential point is that all physically reasonable models of this form show oscillations qualitatively similar to those observed in the exact calculation.

adiabatic potential curves.⁹⁴ Significant coupling between the curves occurs in the entrance and exit channels due to, e.g., avoided crossings. Near the saddle point, where the levels are further apart, the dynamics is more uncoupled. As illustrated in the figure, the incident flux in a particular reagent

channel, $\text{H} + \text{D}_2(v, j)$ is redistributed among several neighboring states due to vibrationally nonadiabatic coupling in the entrance channel. Thus, several QBS thresholds control the reactive flux as it passes the transition state. Similar coupling again scrambles the flux in the exit channel of the reaction. Hence, one expects that each state-to-state reaction probability is affected by a number of QBS pathways, and is formed from the coherent sum of amplitudes corresponding to a variety of pathways as depicted schematically in Fig. 40(a).

Based on this physical view of the reaction dynamics, a very broad class of models can be constructed that yield qualitatively similar oscillations of the reaction probabilities. As shown in Fig. 40(b), a model based on Eckart barriers and constant non-adiabatic coupling to mimic $\text{H} + \text{D}_2$, yields out-of-phase oscillations in $P_R(0, 0 \rightarrow 0, j'; E)$ analogous to those observed in the full quantum scattering calculation. Note, however, that if the re-coupling in the exit-channel is omitted (as shown in Fig. 40(b) with dashed lines) then oscillations disappear and P_R exhibits simple steps at the QBS energies. As the occurrence of the oscillation is quite insensitive to the details of the model, the interference of pathways through the network of QBS seems to provide a robust mechanism for the oscillating reaction probabilities.

In conclusion, we have demonstrated that the DCS for the $\text{H} + \text{D}_2 \rightarrow \text{HD} + \text{H}$ reaction exhibits pronounced oscillatory structures in the backward scattering direction both in experimental and in theory. The physical origin of this structure has been traced to the opening of a sequence of quantized transition state thresholds.

6. Concluding Remarks

In this chapter, we have demonstrated a few examples of quantum state resolved reactive scattering studies of both unimolecular and bimolecular reactions using the elegant H atom Rydberg “tagging” TOF technique. Detailed dynamical information can be learned from these well-controlled experimental investigations. Photodissociation of H_2O at both 157 nm and 121.6 nm have been studied in great details. From the studies of H_2O at 157 nm, the OH vibrational state distribution was measured. Experimental results here also pointed out the inaccuracies in using the LIF technique to measure the OH vibrational state distributions. Photodissociation of H_2O at 121.6 has provided an excellent dynamical case of complicated, yet

direct dissociation process through conical intersections. These experimental investigations have provided a solid ground to test the accuracy of the currently available H_2O potential energy surfaces and to improve these surfaces. The $\text{O}(^1\text{D}) + \text{H}_2 \rightarrow \text{OH} + \text{H}$ reaction has also been investigated using the Rydberg tagging TOF method. Rotational state-resolved differential cross-sections have been measured for this reaction for the first time. The effect of the reagent rotational excitation on the dynamics of this reaction has also been investigated. The $\text{O}(^1\text{D}) + \text{D}_2 \rightarrow \text{OD} + \text{D}$ reaction at two collision energies has been studied in order to clarify the nature of the abstraction mechanism. The $\text{O}(^1\text{D}) + \text{HD} \rightarrow \text{OH}(\text{OD}) + \text{D}(\text{H})$ reaction has also been investigated to demonstrate the interesting isotope effect in the insertion reaction. These measurements provided the most detailed experimental results for this prototype insertion reaction. The simplest neutral chemical reaction in nature, the H_3 system, has also been studied using the H atom Rydberg “tagging” method in an effort to clarify some of the important basic concepts involved in this reaction. Through extensive collaborations between theory and experiments, the mechanism for forward scattering product at high collision energies for the $\text{H} + \text{HD}$ reaction was clarified, which is attributed to a slow-down mechanism on the top of a quantized barrier transition state. Oscillations in the product quantum state resolved different cross-sections have also been observed in the $\text{H} + \text{D}_2$ reaction, which is due to the interference of vibrationally adiabatic transition state pathways. The studies on this simple yet important system have provided clarifications on many important concepts on the structures and dynamics of the quantized state states in chemical reactions. It is important to note that all experimental investigations on these different systems described here are in extensive collaborations with the theoretical studies in different research groups in the world. Only through these close collaborations, clear physical pictures on these benchmark systems could emerge. The works described here clearly demonstrate the importance of close collaborations between experiment and theory in this field.

Acknowledgments

I am deeply indebted to Prof. Yuan T. Lee and Prof. Kopin Liu, who have supported and inspired me throughout these research works. Most of the research works described here are in extensive collaboration with many outstanding theoreticians, amongst them, Prof. Richard N. Dixon, Prof. Xuefeng Yang, and Prof. Marc van Hemert on the H_2O photodissociation.

Professors George C. Schatz, F. Javier Aoiz and Jean-Michel Launay have provided important insight into the research work on the $\text{O}(^1\text{D}) + \text{H}_2$ reaction. I am especially grateful to Prof. Rex T. Skodje for the inspiring collaborations on the $\text{H} + \text{HD}(\text{D}_2)$ work. The experimental works described here were carried out by many students and postdocs in my research group over the last six years. Here, I want to especially thank Drs. Xianghong Liu, Steve A. Harich, Dennis W. Huang, Jim J. Lin, Dongxu Dai, Mrs. Chia C. Wang and many others who have contributed to the research works described here. Without their efforts, these research projects would not be finished. The experimental works reviewed here are supported by the Academia Sinica and the National Science Council of Taiwan, and in part by the Chinese Academy of Sciences and the Ministry of Science of China.

References

1. Y. T. Lee, *Science* **236**, 793 (1987).
2. P. Casavecchia, *Rep. Prog. Phys.* **63**, 355 (2000).
3. P. Casavecchia, N. Balucani, M. Alagia, L. Cartechini and G. G. Volpi, *Acc. Chem. Res.* **32**, 503 (1999).
4. K. Liu, *Annu. Rev. Phys. Chem.* **52**, 139 (2001).
5. J. Helpburn, *Photofragment translational spectroscopy, Atomic and Molecular Beam Methods*, ed. G. Scoles (Cambridge Press).
6. L. Schnieder, W. Meier, K. H. Welge, M. N. R. Ashfold and C. M. Western, *J. Chem. Phys.* **92**, 7027 (1990).
7. L. Schnieder, K. Seekamp-Rahn, J. Borkowski, E. Wrede, K. H. Welge, F. J. Aoiz, L. Bañares, M. J. D'Mello, V. J. Herrero, V. Saez Rabanos and R. E. Wyatt, *Science* **269**, 207 (1995); L. Schnieder, K. Seekamp-Rahn, E. Wrede and K. H. Welge, *J. Chem. Phys.* **107**, 6175 (1997).
8. M. N. R. Ashfold, D. H. Mordaunt and S. H. S. Wilson, *Advances in Photochemistry*, eds. D. C. Neckers, D. H. Volman and G. v. Bunau (John Wiley & Sons, Inc., 1996), Vol. 21, p. 217.
9. R. N. Dixon, D. W. Huang, X. F. Yang, S. Harich, J. J. Lin and X. Yang, *Science* **285**, 1249 (1999).
10. X. Liu, J. J. Lin, S. A. Harich, G. C. Schatz and X. Yang, *Science* **289**, 1536 (2000).
11. B. R. Strazisar, C. Lin and H. F. Davis, *Science* **290**, 958 (2000).
12. W. A. Chupka, *J. Chem. Phys.* **98**, 4520 (1993).
13. A. ten Wolde, L. D. Noordam, A. Lagendij and H. B. van Linden van den Heuvell, *Phys. Rev.* **A40**, 485 (1989).
14. J. P. Marangos, N. Shen, H. Ma, M. H. R. Hutchinson and J. P. Connerade, *J. Opt. Soc. Am.* **B7**, 1254 (1990).
15. P. Andresen and R. Schinke, in *Molecular Photodissociation Dynamics*, eds. M. N. R. Ashfold and J. E. Baggott (Royal Society of Chemistry, London, 1987), Chap. 3.

16. E. Segev and M. Shapiro, *J. Chem. Phys.* **77**, 5604 (1982).
17. R. N. Dixon, *Mol. Phys.* **85**, 333 (1985).
18. K. Weide and R. Schinke, *J. Chem. Phys.* **87**, 4627 (1987).
19. M. P. Docker, A. Hodgson and J. P. Simons, in *Molecular Photodissociation Dynamics*, eds. M. N. R. Ashfold and J. E. Baggott (Royal Society of Chemistry, London, 1987), Chap. 4.
20. H. J. Krautwald, L. Schnieder, K. H. Welge and M. N. R. Ashfold, *Faraday Discuss. Chem. Soc.* **82**, 99 (1986).
21. A. Hodgson, *Faraday Discuss. Chem. Soc.* **82**, 190 (1986); L. J. Dunne, *ibid.*, **82**, 190 (1986); J. N. Murrell, *ibid.*, **82**, 191 (1986); M. N. R. Ashfold and R. N. Dixon, *ibid.*, **82**, 193 (1986).
22. G. C. Schatz, *J. Chem. Phys.* **83**, 5677 (1985).
23. D. H. Mordaunt, M. N. R. Ashfold and R. N. Dixon, *J. Chem. Phys.* **100**, 7360–7375 (1994).
24. P. Andresen, G. S. Ondrey, B. Titze and E. W. Rothe, *J. Chem. Phys.* **80**, 2548 (1984).
25. K. Mikulecky, K.-H. Gericke and F. J. Comes, *Chem. Phys. Lett.* **182**, 290 (1991).
26. H. Guo and J. N. Murrell, *Mol. Phys.* **65**, 821 (1988).
27. V. Engel, R. Schinke and V. Staemmler, *Chem. Phys. Lett.* **130**, 413 (1986); *J. Chem. Phys.* **88**, 129 (1988).
28. R. van Harrevelt and M. C. van Hemert, *J. Chem. Phys.* **114**, 9453 (2001).
29. D. W. Hwang, X. F. Yang, S. Harich, J. J. Lin and X. Yang, *J. Chem. Phys.* **110**, 4123 (1999).
30. R. N. Dixon, D. W. Huang, X. F. Yang, S. Harich, J. J. Lin and X. Yang, *Science* **285**, 1249 (1999).
31. G. Theodorakopoulos, I. D. Petsalakis and R. J. Buenker, *Chem. Phys.* **96**, 217 (1985).
32. R. van Harrevelt and M. C. van Hemert, *J. Chem. Phys.* **112**, 5787 (2000).
33. A. J. Dobbyn and P. J. Knowles, *Mol. Phys.* **91**, 1107 (1997).
34. K. Weide and R. Schinke, *J. Chem. Phys.* **90**, 7150 (1989).
35. H. Guo and J. N. Murrell, *J. Chem. Soc. Farad. Trans. 2*, **84**, 949 (1988).
36. J. N. Murrell, S. Carter, S. C. Farantos, P. Huxley and A. J. C. Varandas, *Molecular Potential Energy Functions* (Wiley-Interscience, New York, 1984).
37. S. A. Harich, X. F. Yang, R. N. Dixon and X. Yang, *Phys. Rev. Lett.* **87**, 253201 (2001).
38. S. A. Harich, X. F. Yang, X. Yang and R. N. Dixon, *J. Chem. Phys.* **114**, 7830 (2001).
39. R. J. Le Roy and W. K. Lui, *J. Chem. Phys.* **69**, 3622 (1978).
40. C. H. Lineweaver, *Science* **284**, 1503 (1999).
41. R. van Harrevelt, M. van Hemert, S. A. Harich, X. F. Yang and X. Yang, *Phys. Rev. Lett.* **87**, 263001 (2001).
42. G. Anderson, *Annu. Rev. Phys. Chem.* **38**, 489 (1987), and references therein.

43. G. Dixon-Lewis and D. J. Williams, *Comprehensive Chem. Kinet.* **17**, 1 (1977).
44. P. A. Whitlock, J. T. Muckerman and E. R. Fisher, *J. Chem. Phys.* **76**, 4468 (1982).
45. R. Schinke and W. A. Lester Jr., *ibid.* **72**, 3754 (1980).
46. S. W. Ransome and J. S. Wright, *ibid.* **77**, 6346 (1982).
47. P. J. Kuntz, B. I. Niefer and J. J. Sloan, *ibid.* **88**, 3629 (1988).
48. G. C. Schatz *et al.*, *ibid.* **107**, 2340 (1997).
49. J. E. Butler, R. G. Macdonald, D. J. Donalson and J. J. Sloan, *Chem. Phys. Lett.* **95**, 183 (1983).
50. J. E. Butler, G. M. Jursich, I. A. Watson and J. R. Wiesenfeld, *J. Chem. Phys.* **84**, 5365 (1986).
51. R. J. Buss, P. Casavecchia, T. Hirooka, S. J. Sibener and Y. T. Lee, *Chem. Phys. Lett.* **82**, 386 (1981).
52. K. Tsukiyama, B. Katz and R. Bersohn, *J. Chem. Phys.* **83**, 2889 (1985).
53. Y. Matsumi, K. Tonokura, M. Kawasaki and H. L. Kim, *J. Phys. Chem.* **96**, 10622 (1992).
54. M. S. Fritzcharles and G. C. Schatz, *ibid.* **90**, 3634 (1986).
55. L. J. Dunne, *Chem. Phys. Lett.* **158**, 535 (1989).
56. A. J. Alexander, F. J. Aoiz, M. Brouard and J. P. Simons, *ibid.* **256**, 561 (1996).
57. K. Badenhop, K. Koizumi and G. C. Schatz, *J. Chem. Phys.* **91**, 142 (1989).
58. T. Peng, D. M. Zhang, J. Z. H. Zhang and R. Schinke, *Chem. Phys. Lett.* **248**, 37 (1996).
59. M. Alagia, N. Balucani, L. Cartechini, P. Casavecchia, E. H. van Kleef, G. G. Volpi, P. J. Kuntz and J. J. Sloan, *J. Chem. Phys.* **108**, 6698 (1998).
60. M. Ahmed, D. S. Peterka and A. G. Suits, *Chem. Phys. Lett.* **310**, 372 (1999).
61. D.-C. Che and K. Liu, *J. Chem. Phys.* **103**, 5164 (1995).
62. Y.-T. Hsu and K. Liu, *ibid.* **107**, 1664 (1997).
63. Y.-T. Hsu, J. H. Wang and K. Liu, *ibid.* **107**, 2351 (1997).
64. Y.-T. Hsu, K. Liu, L. A. Pederson and G. C. Schatz, *ibid.* **111**, 7921 (1999).
65. Y.-T. Hsu, K. Liu, L. A. Pederson and G. C. Schatz, *ibid.* **111**, 7931 (1999).
66. D. W. Hwang, X. F. Yang and X. Yang, *J. Chem. Phys.* **110**, 4119 (1999).
67. S. K. Gray, G. G. Balint-Kurti, G. C. Schatz, J. J. Lin, X. Liu, S. Harich and X. Yang, *J. Chem. Phys.* **113**, 7330 (2000).
68. S. A. Buntin, C. F. Giese and W. R. Gentry, *J. Chem. Phys.* **87**, 1443–1145 (1987).
69. D. A. Kliner, D. E. Adelman and R. N. Zare, *J. Chem. Phys.* **95**, 1648 (1991).
70. T. N. Kitsopoulos, M. A. Buntine, D. P. Balwin, R. N. Zare and D. W. Chandler, *Science* **260**, 1605 (1993).
71. J. Z. H. Zhang and W. H. Miller, *J. Chem. Phys.* **91**, 1528–1547 (1991).
72. M. Zhao, D. G. Truhlar, D.W. Schwenke and D. J. Kouri, *J. Phys. Chem.* **94**, 7074 (1990).

73. M. Zhao, M. Mladenovic, D. G. Truhlar, D. W. Schwenke, O. Sharafeddin, Y. Sun and D. J. Kouri, *J. Chem. Phys.* **91**, 5302 (1989).
74. M. J. D'Mello, D. E. Manolopoulos and R. E. Wyatt, *J. Chem. Phys.* **94**, 5985 (1991).
75. R. T. Pack and G. A. Parker, *J. Chem. Phys.* **87**, 3888–3921 (1987).
76. D. M. Skouteris, J. F. Castillo and D. E. Manolopoulos, *Comput. Phys. Commun.* **133**, 128 (2000).
77. S. D. Chao and R. T. Skodje, *Chem. Phys. Lett.* **336**, 364 (2001).
78. X. Liu, J. J. Lin, S. A. Harich, G. C. Schatz and X. Yang, *Science* **289**, 1536 (2000).
79. X. Liu, J. J. Lin, S. A. Harich and X. Yang, *Phys. Rev. Lett.* **86**, 408 (2001).
80. S. A. Harich, D. Dai, X. Yang, S. D. Chao and R. T. Skodje, *J. Chem. Phys.* **116**, 4769 (2002).
81. K. D. Rinnen, D. A. V. Kliner, M. A. Buntine and R. N. Zare, *Chem. Phys. Lett.* **169**, 365 (1990).
82. S. A. Harich, D. Dai, C. C. Wang, X. Yang, S. D. Chao and R. T. Skodje, *Nature* **419**, 281 (2002).
83. S. A. Harich, D. Dai, C. C. Wang, X. Yang, S. D. Chao and R. T. Skodje, *J. Chem. Phys.* **117**, 8341 (2002).
84. A. I. Boothroyd, W. J. Keogh, P. G. Martin and M. R. Peterson, *J. Chem. Phys.* **104**, 7139 (1996).
85. M. L. Goldberger and K. M. Watson, *Collision Theory* (Wiley, New York, 1964).
86. S. C. Althorpe, F. Fernández-Alonso, B. D. Bean, J. D. Ayers, A. E. Pomerantz, R. N. Zare and E. Wrede, *Nature* **416**, 67–70 (2002); F. Fernández-Alonso, B. D. Bean, J. D. Ayers, A. E. Pomerantz, R. N. Zare, L. Bañares and F. J. Aoiz, *Ang. Chemie.* **39**, 2748–2752 (2001).
87. S. A. Cucaro, P. G. Hipes and A. Kuppermann, *Chem. Phys. Lett.* **157**, 440 (1989).
88. R. T. Skodje, R. Sadeghi, H. Koppel and J. L. Krause, *J. Chem. Phys.* **101**, 1725 (1994).
89. D. C. Chatfield, S. L. Mielke, T. C. Allison and D. G. Truhlar, *J. Chem. Phys.* **112**, 8387 (2000).
90. R. Sadeghi and R. T. Skodje, *J. Chem. Phys.* **102**, 193 (1995).
91. D. C. Chatfield, R. S. Friedman, D. W. Schwenke and D. G. Truhlar, *J. Phys. Chem.* **96**, 2414 (1992).
92. D. E. Manolopoulos, K. Stark, H.-J. Werner, D. W. Arnold, S. E. Bradforth and D. M. Neumark, *Science* **262**, 1852 (1993).
93. E. R. Lovejoy, S. K. Kim and C. B. Moore, *Science* **256**, 1541 (1992); S. K. Kim, E. R. Lovejoy and C. B. Moore, *J. Chem. Phys.* **102**, 3202 (1995).
94. W. H. Miller, N. C. Handy and J. E. Adams, *J. Chem. Phys.* **72**, 99 (1980).
95. R. T. Skodje, D. Skouteris, D. E. Manolopoulos, S.-H. Lee, F. Dong and K. Liu, *Phys. Rev. Lett.* **85**, 1206 (2000).
96. D. M. Neumark, A. M. Wodtke, G. N. Robinson, C. C. Hayden and Y. T. Lee, *Phys. Rev. Lett.* **53**, 226 (1984).

97. T. N. Kitsopoulos, M. A. Buntine, D. P. Baldwin, R. N. Zare and D. W. Chandler, *Science* **260**, 1605 (1993).
98. M. J. D'Mello, D. E. Manolopoulos and R. E. Wyatt, *J. Chem. Phys.* **94**, 5985 (1991).
99. Y. S. M. Wu and A. Kuppermann, *Chem. Phys. Lett.* **235**, 105 (1995).
100. B. K. Kendrick, *J. Chem. Phys.* **114**, 8796 (2001).
101. L. Schnieder, K. Seekamp-Rahn, F. Liedeker, H. Steuwe and K. H. Welge, *Faraday Discuss.* **91**, 259 (1991).
102. A. I. Boothroyd, W. J. Keogh, P. G. Martin and M. R. Peterson, *J. Chem. Phys.* **104**, 7139 (1996).
103. R. T. Pack and G. A. Parker, *J. Chem. Phys.* **87**, 3888 (1987).
104. G. C. Schatz, *Chem. Phys. Lett.* **150**, 92 (1988).
105. J. M. Launay and M. Le Dourneuf, *Chem. Phys. Lett.* **163**, 178 (1989).
106. D. M. Skouteris, J. F. Castillo and D. E. Manolopolous, *Comput. Phys. Commun.* **113**, 128 (2000).
107. S. D. Chao and R. T. Skodje, *Chem. Phys. Lett.* **336**, 364 (2001).
108. W. H. Miller, *Annu. Rev. Phys. Chem.* **41**, 245 (1990).
109. R. Sadeghi and R. T. Skodje, *J. Chem. Phys.* **102**, 193 (1995); R. T. Skodje, R. Sadeghi, H. Koppel and J. L. Krause, *J. Chem. Phys.* **101**, 1725 (1994).
110. M. S. Child, *Molecular Collision Theory* (Dover, New York, 1996) p. 167.

This page intentionally left blank

CHAPTER 4

MULTIMASS ION IMAGING — A NEW EXPERIMENTAL METHOD AND ITS APPLICATION IN THE PHOTODISSOCIATION OF SMALL AROMATIC MOLECULES

Cheng-Liang Huang, Yuan T. Lee and Chi-Kung Ni*

*Institute of Atomic and Molecular Sciences, Academia Sinica,
P. O. Box 23-166, Taipei, 106 Taiwan R.O.C.*

Contents

1. Introduction	163
2. New Experimental Method: Multimass Ion Imaging	167
2.1. Overview	167
2.2. Mass Spectrometer	171
2.3. Mass Resolution and Mass Range	174
2.4. Fragment Recoil Velocity Resolution	174
2.5. Dissociation Rate	176
3. Application in the Photodissociation of Small Aromatic Molecules	179
3.1. Benzene	179
3.2. Toluene	192
3.3. Ethylbenzene and Propylbenzene	201
4. Conclusions	210
Acknowledgments	211
References	211

1. Introduction

The advancement of the application of lasers in combination with the molecular beam technique has made a great impact in the understanding of primary photodissociation processes. For state-specific detection of small fragments, laser-induced fluorescence, multiphoton ionization, and coherent laser scattering have provided extremely detailed information on the dynamics of photodissociation. Unfortunately, a large number of interesting

* Author to whom correspondence should be addressed:
e-mail: ckni@po.iam.s.sinica.edu.tw.

polyatomic photofragments cannot be detected by these techniques, due to the complexities of the spectra. The main virtue of photofragment translational spectroscopy using the ionization detection method is that it is universally applicable to all products, although the information obtained from the product translational energy distributions is not as detailed as that from the spectra.

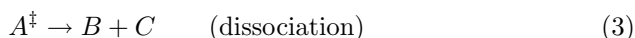
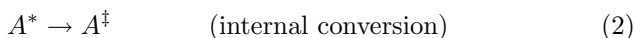
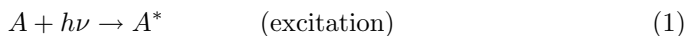
Photofragment translational spectroscopy traditionally uses a mass spectrometer to detect and to measure the velocity distributions of photodissociation products.¹ Photofragmentation occurs in the crossing volume between a collimated molecular beam and a pulsed photolysis laser beam. The detector is located at an angle from the molecular beam axis and is displaced some distance from the photolysis volume. Angle-resolved time-of-flight, or velocity of the products, is obtained by measuring the arrival time of various mass selected products after the laser pulse. Photodissociation mechanisms and the primary dissociation products of many molecules have been studied by this method. However, there are some disadvantages. First, the velocities of the photofragments are measured in the laboratory frame; they have to be converted to the center-of-mass frame for data analysis. Second, photofragments are usually ionized by electron impact and detected by the quadrupole mass spectrometer. Fragments ionized by electron impact easily produce daughter fragment ions through the fragment cracking due to the large energy of electrons. If the mass of the daughter ions is the same as one of the primary fragment masses from other dissociation channels, the data analysis becomes complicated due to the interference from each other. Finally, only a single mass at a given angle can be detected each time. It makes the measurement time consuming for large molecules having many channels in the photodissociation process.

Conventional ion-imaging techniques can also be used to measure photofragment translational spectroscopy.^{2,3} In these experiments, the photolysis laser beam crosses the molecular beam and causes photodissociation. The same laser pulse or the second laser pulse which arrives within a very short delay time ionizes the fragments, creating a group of ions which radiate from their origins due to the recoil velocity and are distributed in an expanding sphere. The fragment ions are accelerated towards the two-dimensional detector by an electric field, and the product image is a 2D projection of the photofragment's 3D-recoil velocity distribution. The 3D distribution can be reconstructed from the 2D image by applying the inverse Abel transformation. Mass selectivity of the conventional ion-imaging techniques is achieved using the resonance enhanced multiphoton ionization (REMPI). Therefore, only the fragments produced by REMPI

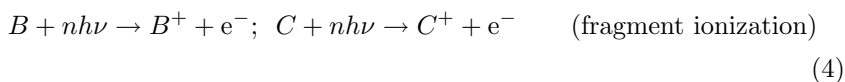
can be detected. Recently, vacuum ultraviolet (VUV) photoionization has been applied in the conventional ion-imaging experiments.⁴ The detector has to be properly gated to the arrival time of the mass of interest in order to have mass selectivity. Replacement of REMPI by VUV photoionization achieves the universal detection capability, however, quantum state information is lost. Both the REMPI and the VUV ionization in the conventional ion-imaging techniques can only detect one mass at a time.

Time-of-flight mass spectrometry has also been used to measure the photofragment kinetic energy.^{5,6} The fragment velocity distributions are obtained from the broadening of the features in the time-of-flight mass spectrum. In principle, the velocity distributions of all the different fragments can be obtained simultaneously if VUV photons or electron impact are used in the fragment ionization. However, the obtained velocity distribution is a 1D projection of the photofragment's 3D-recoil velocity distribution, and the velocity distribution obtained by this method is crude.

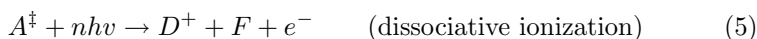
In addition to the previously mentioned disadvantages, all of these methods have another drawback in the large molecule photofragment velocity measurements. For example, in the studies of UV photon photodissociation of polyatomic molecules, like alkene and aromatic molecules, molecules excited by the UV photons quickly become highly vibrationally excited in the ground electronic state through fast internal conversion, and dissociation occurs in the ground electronic state.



Here, A^* represents molecules in the excited state, and A^\ddagger represents highly vibrationally excited molecules in the ground electronic state. The dissociation rates of these molecules have been shown to be very slow and the lifetimes of A^\ddagger are in the microsecond region.⁷ In the traditional translational spectroscopy measurement, most of the highly vibrationally excited molecules fly out of the reaction region before dissociation. As a result, signals are very small. On the other hand, in the conventional ion-imaging techniques and time-of flight mass spectrometry, the fragment detection is through the multiphoton ionization or VUV photoionization by the same laser pulse or using a second laser pulse.



The delay time between the pump and the probe laser pulses is usually very short in these experiments. The delay time is less than 5 ns when the pump and the probe laser pulses are the same, and the delay time is as long as several hundred nanoseconds when the pump and the probe laser pulses are from two different sources. The short delay time ensures that the fragments flying with different velocities are equally sampled before they leave the detection region. Since the delay time is much shorter than the lifetime of the excited molecules (A^\dagger), most of these molecules do not dissociate into fragments when the probe laser pulse arrives. As a result, the probe laser can easily cause dissociative ionization of the vibrationally excited molecules due to their large internal energy.



The photofragment translational energy distributions of the dissociative ionization (reaction 5) are different from those of the products obtained from the dissociation processes (reaction 3). However, if the masses of fragments B and D happen to be the same, the images or the broadening of the arrival time of fragments B^+ and D^+ will be overlapped. These two reactions cannot be distinguished from the images obtained by the conventional ion-imaging techniques, or from the broadening of the features in the time-of-flight mass spectrum. The probability that B and D have the same value of mass is high for large molecules having many dissociation channels.

A completely new design to measure the product translational spectra was proposed by one of us.⁸ The goal was to overcome the difficulties of the other available techniques mentioned previously. Basically, a mass spectrometer with a long entrance slit and a position-sensitive detector are combined with a pulsed VUV laser to detect the translational spectroscopy of many different photofragments simultaneously. The translational spectroscopy is measured in the center-of-mass frame, based on the displacement from the origin of the center-of-mass frame, thus eliminating the effort of conversion between the laboratory frame and the center-of-mass frame. Fragments are ionized by a VUV laser pulse with the photon energy above the ionization threshold. The VUV photon energy is chosen such that the fragment's dissociation after ionization is minimized. This avoids the fragment cracking due to the large energy in electron impact ionization, but it maintains the universal detection capability. Delay time between pump and probe laser pulses can be as short as a few nanoseconds in order to measure the fast dissociation rate. On the other hand, a long delay time between the pump and the probe laser pulses ($>10\text{--}100\ \mu\text{s}$) is used in order

to distinguish the reactions between dissociative ionization (reaction 5) and neutral molecule dissociation (reaction 3).

In the following sections, we describe the principles of this new experimental technique,⁹ and show the application of this technique in the photodissociation of small aromatic molecules.

2. New Experimental Method: Multimass Ion Imaging

2.1. Overview

The apparatus consists of a pulsed molecular beam, a pulsed ultraviolet (UV) photolysis laser beam, a pulsed vacuum ultraviolet (VUV) probe laser beam, a mass spectrometer, and a two-dimensional ion detector. The schematic diagram is shown in Fig. 1.

The molecular beam is formed by the supersonic expansion of gas through a pulsed nozzle. It is then collimated by two skimmers, and enters

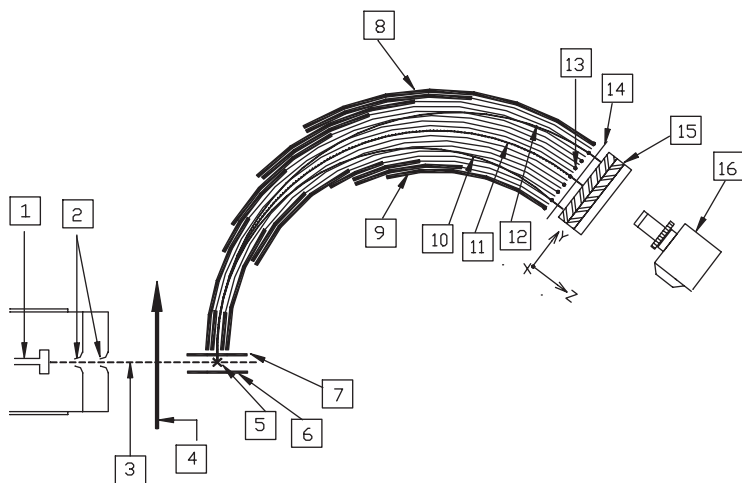


Fig. 1. Schematic diagram of the multimass ion imaging detection system. (1) Pulsed nozzle; (2) skimmers; (3) molecular beam; (4) photolysis laser beam; (5) VUV laser beam, which is perpendicular to the plane of this figure; (6) ion extraction plate floated on V_0 with pulsed voltage variable from 3000 to 4600 V; (7) ion extraction plate with voltage V_0 ; (8) outer concentric cylindrical electrode; (9) inner concentric cylindrical electrode; (10) simulation ion trajectory of $m/e = 16$; (11) simulation ion trajectory of $m/e = 14$; (12) simulation ion trajectory of $m/e = 12$; (13) 30 μm diameter tungsten wire; (14) 8 \times 10 cm metal mesh with voltage V_0 ; (15) z-stack multichannel plates and phosphor screen. In the two-dimensional detector, the Y-axis is the mass axis, and X-axis (perpendicular to the plane of this figure) is the velocity axis; (16) CCD camera.

the main chamber. The VUV laser beam is generated by frequency tripling or four-wave mixing of UV/VIS laser beams in rare gas. After the generation of VUV radiation, the coaxial UV/VIS and VUV laser beams are sent to a homemade vacuum monochromator to separate the UV/VIS laser beam from the VUV laser beam. The VUV laser beam alone is sent to the ionization region. A concave grating with 1200 l/mm and radius of 98.5 cm is used in the vacuum monochromator. The distances are set such that the focal point of UV/VIS laser beams in rare gas is 120 cm away from the grating. The concave grating refocuses the expanding VUV radiation onto the molecular beam, which is 88 cm away from the grating. The grating is set near the normal incidence (15°), therefore, the focal point of the VUV laser beam does not move away from the molecular beam as the VUV wavelength changes. The first order of the VUV radiation from the grating is used.

The molecular beam, photolysis laser beam, and VUV laser beam are perpendicular to each other. However, the crossing points of the photolysis laser beam and the VUV laser beam with the molecular beam are not the same. The crossing point of the photolysis laser beam with the molecular beam is adjustable. It is 3–10 cm upstream with respect to the crossing point of the VUV laser with the molecular beam. For short distances (<3 cm) between these two crossing points, the direction of the UV laser beam is changed. It is in the plane formed by molecular beam and VUV laser beam, but the angle between the photolysis laser beam and the VUV laser beam is 15 degrees.

Molecules in the molecular beam are photodissociated by a UV photolysis laser pulse. Due to the recoil velocity of dissociation products and the center-of-mass velocity (molecular beam velocity), the fragments radiate from their origins and are distributed in an expanding sphere on their flight to the ionization region, and are then ionized by a VUV laser pulse. Fragment ions are generated by VUV photoionization and are distributed in a segment of line along the VUV laser beam path. The distance between the crossing points of UV and VUV laser beams with the molecular beam is set such that it is equal to the delay time between UV and VUV laser pulses multiplied by the molecular beam velocity. This distance ensures that the VUV laser beam passes through the center of the fragment sphere and, therefore, the fragment's velocity distribution is measured in the center-of-mass frame. There could be many fragment ions of different masses within this segment according to the photodissociation mechanisms of parent molecules. Each fragment has its own intensity distribution along the segment. The length of the segment is proportional to

the fragment recoil velocity in the center-of-mass frame multiplied by the delay time.

After the ions have been generated by the VUV laser pulse, a pulsed electric field is used to extract the ions into a mass spectrometer in order to separate different masses within the ion segment. The entrance of the mass spectrometer has a long slit parallel to the VUV laser beam to accept the ions produced at various positions along the line of VUV laser irradiation. The mass spectrometer basically is a radial cylindrical energy analyzer.¹⁰ In this instrument, the pulsed electric field used to extract ions is very short so that the electric field is turned off before any ions leave the extraction region and enter the energy analyzer. The momentum, P , of the ions obtained from the pulsed field can be expressed by the following equations:

$$P = \int F dt = \int m \times a dt = \int m \times (qE/m) dt = \int q \times E dt. \quad (6)$$

Here, m is the mass of the ion, a is the acceleration of the ion by the electric field E in the extraction region, q is the charge of the ion, and F is the force. The range of time t in the integral is equal to the duration which the ion is accelerated by the electric field. In a conventional time-of-flight mass spectrometer, the electric field is turned on all the time when ions travel through the extraction region. Because different masses require different times to travel through the extraction region, the range of time t in the integral of Eq. (6) is different for different masses. Thus, the momentum obtained from the electric field is different for different masses, though the energy obtained from the electric field is the same. However, in our instrument, the pulsed electric field is turned off before any ions leave the extraction region, thus the range of time in the integral of Eq. (6) is the same for all masses. Therefore, all the ions will be accelerated to the same linear momentum along the direction of the field. Since the momentums are the same, the ion's translational energy that is obtained from the pulsed electric field is proportional to the reciprocal of the fragment's mass. Different fragment ions entering the radial cylindrical energy analyzer, therefore, can be separated according to the difference of energies obtained from the pulsed electric field.

Since the VUV laser beam passes through the center of the fragment sphere, fragments ionized by the VUV laser have the recoil velocity only in the direction of the VUV laser beam axis. These recoil velocities are perpendicular to both the electric field in the extraction region and the field inside the energy analyzer. They would not be affected by these electric fields. During the flight through the energy analyzer, the length of the

fragment ion segment keeps expanding according to the fragment recoil velocity. Meanwhile, ions of different masses start separating from each other in the energy analyzer. The trajectories of different masses are illustrated in Fig. 1. Charge particles of smaller m/e values have larger radii and reach the upper part of the exit port. At the exit port of the energy analyzer, a 7×8 cm two-dimensional ion detector is used to detect the ion position and intensity distributions. In this two-dimensional detector, one direction is the recoil velocity axis (X -axis, as shown in Fig. 1) and the other is the mass axis (Y -axis, as shown in Fig. 1). The ion image obtained from this two-dimensional detector contains many segments of line parallel to the X -axis. The intensity distribution and the length of each segment in the image represent translational energy distribution of a given fragment. The recoil velocity distributions in the center-of-mass frame of many different fragments are obtained simultaneously from the position and intensity distributions of the image.

The change in the delay time between these two laser pulses has to match with the distance between the crossing points of the photolysis laser and VUV laser with the molecular beam, according to the velocity of the molecular beam to ensure the ionization laser passes through the center-of-mass of the products. This adjustment also changes the length of the fragment ion segment in the image. The relation between the length of the ion image and the change of photolysis laser position (or delay time) is shown in Fig. 2. In general, the distance between these two crossing points is set to be long for the detection of fragments with small recoil velocity, whereas it is set to be short for the detection of fragments with large recoil velocity.

If molecules do not dissociate after the absorption of photolysis photons, those molecules with large internal energy will stay within the molecular beam. They fly with almost the same velocity to the ionization region and are ionized by the VUV laser, resulting in the dissociative ionization (reaction 5). The ion image from the dissociative ionization is very different from the image due to the dissociation products of neutral molecules (reactions 3 and 4). Since the dissociation and ionization occur at the same position, the image from dissociative ionization is a 2D projection of the photofragment ion's 3D-recoil velocity distribution. It is a disk-like image and is different from the line-shape image resulted from dissociation products of neutral molecules. With the VUV laser fixed in position, only the intensity of the disk-like image changes with the delay time between two laser pulses, but the size of the disk-like image would not change with the

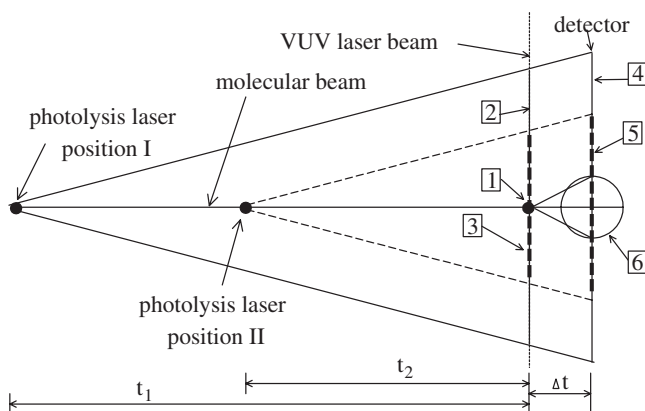


Fig. 2. Relation between the lengths of the image resulting from different photolysis laser positions and the disk-like image from the dissociation after ionization. (1) represents the crossing point of the molecular beam and the VUV laser beam, where the dissociative ionization occurs. (2) and (3) represent the lengths of the fragment ion segments created by the VUV laser photoionization from two different photolysis laser positions. (4) and (5) represent the lengths of the line-shape fragment ion image on the detector from two different photolysis laser positions. (6) represents the disk-like image. t_1 and t_2 represent the two different delay times between the photolysis laser pulse and the VUV laser pulse. Δt is the flight time in the mass spectrometer.

delay time. Therefore, the ion image resulted from the dissociative ionization can be distinguished easily from the image resulted from dissociation products of neutral molecules by the shape of the image as well as the change with the delay time.

2.2. Mass Spectrometer

One of the key components in the system is the mass spectrometer. Fragments are ionized by a VUV laser pulse between a pair of plane parallel-plate electrodes (6×14 cm). One of the plane electrodes has a slit of 1×10 cm, which is covered by a metal mesh. The slit is parallel to the VUV laser beam and is the entrance of the mass spectrometer. Ions are accelerated by a pulsed electric field present between the plane parallel-plate electrodes, and then pass through the slit before they enter the mass spectrometer.

The mass spectrometer is a homemade radial cylindrical energy analyzer. A radial electric field is produced by an electrical potential applied to the inner and outer concentric cylindrical electrodes. The radii of the inner and outer electrodes are 18 cm and 26 cm, respectively. In order to reduce

the fringing field effect, fifteen U-shaped concentric cylindrical electrodes, which are mounted on two grooved parallel ceramic plates, are placed in equal distance between the inner and outer cylindrical electrodes, as shown in Fig. 3. The distance between these two parallel ceramic plates is 12 cm. The voltages of these concentric cylindrical electrodes V_i with a radius R_i are related to the central concentric cylindrical electrode voltage V_o with a radius R_o by the following equation:

$$V_i = V_o + 2V_o \times \ln(R_i/R_o). \quad (7)$$

At the exit port of the energy analyzer, nine tungsten wires of $30\text{ }\mu\text{m}$ diameter are spot-welded on every other concentric cylindrical electrode, as shown in Fig. 3. These wires effectively reduce the fringing field and also provide high ion transmission efficiency. An $8 \times 10\text{ cm}$ metal mesh, having a voltage equal to the central cylindrical electrode voltage, is placed between the analyzer exit port and the two-dimensional detector to reduce further the fringing field effect. Ions from the exit port of the energy analyzer pass through this mesh and fly to the detector. The detector is an assembly of z -stack microchannel plates (MCP) and a phosphor screen. Signals are recorded by a CCD video camera, and are accumulated in the computer.

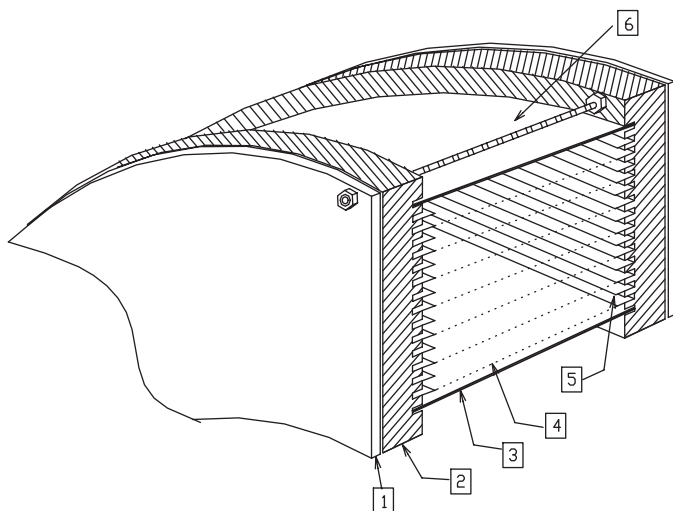


Fig. 3. Exit port of the energy analyzer. (1) Stainless steel plates to support the ceramic plates; (2) grooved ceramic plates to support the concentric cylindrical electrodes; (3) inner cylindrical electrode; (4) $30\text{ }\mu\text{m}$ diameter tungsten wire; (5) 15 concentric cylindrical electrodes separated equally between the inner and outer cylindrical electrodes; (6) outer cylindrical electrode.

We use a thresholding algorithm to discriminate the low level noise from the video CCD.

One of the major advantages of this design is the multimass ion detection capability, i.e., the translational energy distributions of many different masses can be detected simultaneously. In order to detect different masses simultaneously, good mass resolution is necessary. It depends on the distance between the images of adjacent masses and the image width of each mass in the mass axis.

The distance between the images of adjacent masses depends on the radius of the central electrode and the mass values. The first factor sets the separation distance of different energies at the exit port of the analyzer. The second factor is due to the energy difference between different masses. Since the energy of the ions obtained from the pulsed electric field is proportional to the reciprocal of the fragment's mass, the energy difference between adjacent masses m and $m + 1$ is equal to $\Delta E = 1/[m(m + 1)]$. The energy difference between adjacent masses is small for higher values of masses, but it is large for lower values of masses. Therefore, a large range of masses can be detected simultaneously for high values of masses, and the separated distance between the images of adjacent masses is small. On the other hand, a small range of masses can be detected simultaneously for low values of masses, and the separated distance between the images of adjacent masses is large. Detection of different mass ranges simply requires a matching of the ion's kinetic energy obtained from the pulsed field with the energy setting of the energy analyzer. It can be achieved by (1) changing the strength or the duration of the pulsed electric field, or (2) changing the voltage of the energy analyzer.

The cylindrical electrodes subtend an angle of 127.3° to obtain first-order focusing. However, this focusing condition is valid only for the incident ion kinetic energy related to the central cylindrical electrode voltage V_o by $E = qV_o$, where E is the ion kinetic energy with the velocity in the plane perpendicular to VUV laser beam. For ions with kinetic energy other than $E = qV_o$, the focusing condition is not valid. In order to have good mass resolution, ions of a given mass with a kinetic energy other than $E = qV_o$ have to remain within a small width in the mass axis of the detector. This can be accomplished only if both the ions spatial distribution and velocity distribution in the plane perpendicular to the VUV direction are small. This requires a small VUV laser beam diameter and a small molecular beam velocity distribution. In our apparatus, the molecular beam is collimated by two skimmers which are separated by one inch in order to obtain a

small velocity distribution in the direction perpendicular to the molecular beam axis. Molecules mixed with He or Ar are expanded through a pulsed nozzle, and the small velocity distribution in the direction of the molecular beam is achieved through adiabatic expansion. The diameter of the VUV laser beam is about $100\text{ }\mu\text{m}$ at the ionization region after focusing by the concave grating. These experimental conditions allow us to have a good mass resolution of ions with kinetic energy other than $E = qV_0$.

2.3. Mass Resolution and Mass Range

Figure 4(a) shows the ion image of the mixture of chlorobenzene, chlorotoluene, and trifluorotoluene ionized by 118.2 nm VUV photons with the dissociation laser turned off. The mass difference due to the isotopes ^{12}C , ^{13}C , ^{35}Cl , and ^{37}Cl in these species can be seen clearly. At the center of the mass axis on the image, the ion energy E obtained from the pulsed field is equal to the central electrode voltage V_0 by $E = qV_0$. Above the center, the ion energy is larger than the central electrode voltage by $E > qV_0$, and below the center, the ion energy is smaller than the central electrode voltage by $E < qV_0$. Though the focusing condition is not valid for the area away from the central horizontal line, the mass resolution is still as good as the mass resolution around the center. We estimate the mass resolution to be better than $\Delta m/m = 1/200$ for the entire detector. Although this is not a very high mass resolution, it is certainly high enough for most of the photodissociation studies. Figure 4(a) further demonstrates that the molecular masses ranging from $m/e = 112$ to 146 can also be detected simultaneously. At low values of masses the separated distance between the images of adjacent masses is large, therefore the range of masses that can be detected is small. For instance, if the mass is as low as $m/e = 16$, only those masses from 15 to 18 can be detected simultaneously.

2.4. Fragment Recoil Velocity Resolution

The fragment recoil velocity resolution depends on the divergence of the molecular beam, molecular beam velocity distribution in the direction of the molecular beam axis, and the distance of fragments expanded in the velocity axis of the two-dimensional detector. If the divergence of the molecular beam is small and the fragment recoil velocity is much larger than the velocity difference of parent molecules, the recoil velocity resolution can be simply expressed as $\Delta V/V = s/L$, where L is the length of expansion of

fragments in the velocity axis on the image and s is the width of the molecular beam. In our apparatus, the largest distance L is limited by the size of the detector, which is equal to half of that of the detector in the velocity axis (40 mm). The width of the molecular beam of parent molecules can be measured directly from the image. Figure 4(b) shows that the FWHM of the molecular beam profile in the velocity axis is 2.4 mm. Therefore, the best apparent velocity resolution is $\Delta V/V = 2.4 \text{ mm}/40 \text{ mm} = 6\%$.

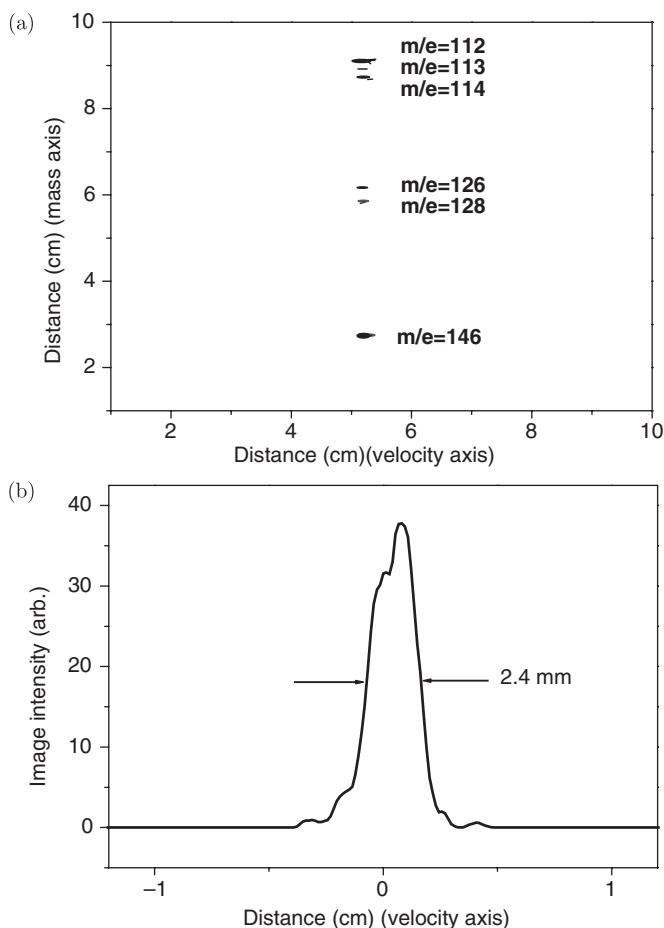


Fig. 4. (a) Image of the mixture of chlorobenzene, chlorotoluene, and trifluorotoluene ionized by 118.2 nm VUV laser pulses. The vertical axis is the mass axis and the horizontal axis is the velocity axis. (b) Molecular beam profile of the image in the velocity axis at mass = 114.

The formula, $\Delta V/V = s/L$, also indicates that the resolution changes with the recoil velocity. For a given image, the velocity resolution on both wings is better than that at the center due to the different lengths of expansion. However, if the fragment recoil velocity is small and is close to the velocity difference of parent molecules, or the distance of the fragment expanded is not very large compared to the width of the molecular beam, the velocity resolution $\Delta V/V = s/L$ will not be valid. Deconvolution of the final measurement by the width of the molecular beam and the velocity distributions of parent molecules is necessary in these cases to obtain the recoil velocity distribution.

One of the advantages of this apparatus is that the distance between the photolysis laser beam and the VUV laser beam is changeable. A large distance between the photolysis laser beam and the VUV laser beam can be set for the detection of fragments with small recoil velocity in order to achieve the maximum velocity resolution. A small distance is set for the detection of fragments with large recoil velocity in order to collect all of the fragments within the detector. In addition, if the signal is small, one can move the photolysis beam closer to the VUV beam to maintain a reasonable signal-to-noise ratio.

2.5. Dissociation Rate

The dissociation rate can be measured using the multimass ion imaging techniques. There are several methods to determine the dissociation rate, depending on the values of the rate. The dissociation rate can be obtained from the product growth with respect to the delay time between the pump and probe lasers. An accurate measurement can be obtained only if two conditions are satisfied. First, the dissociation rate must be fast enough before the parent molecules and fragments fly out of the detection region due to the large molecular beam velocity and fragment recoil velocity. Second, the contribution from dissociative ionization (reaction 5) for a given mass of fragment ion must be small compared to that from dissociation products (reactions 3 and 4). This ensures the low background in the measurement. In this method, both the photolysis and probe laser pulse durations set the upper limit in the dissociation rate measurement, and the values of the lower limit is determined by the molecular beam velocity and fragment recoil velocity. The values between 10^8 s^{-1} and 10^6 s^{-1} can be accurately measured using nanosecond laser pulse and $\sim 10^5 \text{ cm/s}$ molecular beam velocity if fragment recoil velocity is small. This method has

been applied in many photodissociation studies. However, some aromatic molecules have dissociation rates much slower than these values, and a different approach is necessary for the rate measurement.

Another method is to measure the disappearance rate of the excited parent molecules, that is, the intensity changes of the disk-like images at various delay times (therefore, at various photolysis laser positions) along the molecular beam. This is very useful when the dissociation rate is slow and the method described above cannot be applied. This measurement requires a small molecular beam velocity distribution and a large variable distance between the crossing points of the pump and probe laser beams with the molecular beam. The small velocity distribution can be obtained through adiabatic expansion, and the available distances between the pump and probe laser beams depend on the design of the chamber. For variable distances from 0 to 10 cm in our system and $\Delta V/V = 10\%$ molecular beam velocity distribution, dissociation rates as slow as $3 \times 10^3 \text{ s}^{-1}$ under collisionless condition can be measured.

In addition to these methods, the dissociation rate can be obtained from the line-shape image intensity distribution. Since the intensity of the line-shape image results from the accumulation of the products produced during the time period from the pump pulse to the probe pulse, the ion image intensity distribution is a function of both the fragment recoil velocity distribution and the dissociation rate. Therefore, both the velocity distribution and the dissociation rate can be obtained from the image. The simulation in Fig. 5 shows the effect of the dissociation rate on the ion image intensity distribution. For a given fragment recoil velocity distribution, as shown in Fig. 5(a) for a large recoil velocity distribution and Fig. 5(d) for a small velocity distribution, the image intensity distributions from a fast dissociation rate, as illustrated in Figs. 5(b) and 5(e), are different from that of a slow dissociation rate, as presented in Figs. 5(c) and 5(f). The image intensity profiles are not sensitive to the change of the dissociation rate when they are larger than 10^6 s^{-1} or smaller than 10^4 s^{-1} . These set the limits of this method. However, the advantage of the measurement from the images is the following. If the fragment image contains more than one component (either the disk-like images or multi-components in the line-shape image), the dissociation rates and velocity distributions of each component can be determined separately. This avoids the fit of the experimental data obtained from the product growth or the parent decay to the multi-exponential functions in a low signal to noise ratio situation.

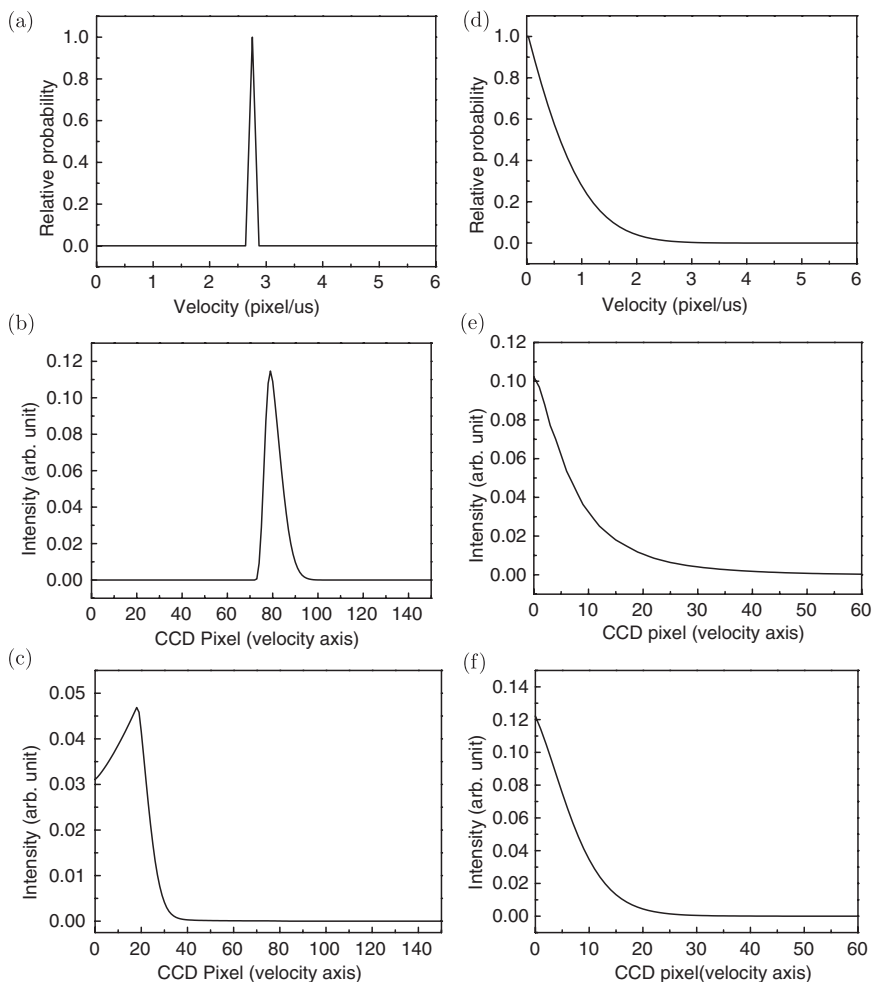


Fig. 5. Effect of the dissociation rate on the ion image intensity distribution. (a) Simulated translational energy distribution. (b), (c) Image intensity distributions that would result from (a) if the dissociation lifetime was $0.1\ \mu\text{s}$ and $15\ \mu\text{s}$, respectively. (d) Simulated translational energy distribution. (e), (f) Image intensity distributions that would result from (d) if the dissociation lifetime was $0.1\ \mu\text{s}$ and $15\ \mu\text{s}$, respectively. The total delay time between pump laser pulse and detection is $30.5\ \mu\text{s}$.

In the work described below, the dissociation rates were obtained from the product growth with respect to the delay time if the dissociation rate is fast enough before the parent molecules and fragments fly out of the probe region. This is demonstrated in the photodissociation study of toluene. Alternately, dissociation rates were obtained from the disk-like image intensity decay for slow dissociation rate, as illustrated in the rate

measurement of benzene. For multi-component dissociation channels, like the dissociation of ethylbenzene at 248 nm, the dissociation rate of each component was determined separately by forward convolution simulation of the images.

3. Application in the Photodissociation of Small Aromatic Molecules

3.1. Benzene

The photophysics and photochemistry processes of benzene have been extensively studied in the past few decades. It is frequently used as an example for both the theoretical and experimental investigation. It has been found that the fluorescence quantum yield of benzene decreases rapidly when the excitation wavelength is shorter than 244.5 nm.^{11–13} This is interpreted as the result from a non-radiative pathway, called channel three, by which vibrational energy in excess of $\sim 3000\text{ cm}^{-1}$ is lost at an anomalously rapid rate. The decay rate of benzene after excitation to the S_1 state has been measured below and above the channel-three threshold of 244.5 nm under collision-free condition. As a result of these experiments, it can be concluded that the lifetimes are in the nanosecond and picosecond regions, corresponding to the decay of the singlet S_1 below and above the channel-three threshold, respectively. The triplet state produced by inter-system crossing from the S_1 state has longer lifetime, in the region of several hundred nanoseconds.¹⁴

There have also been many works on the study of benzene after the excitation to the S_2 state. In the photolysis of benzene at 184.9 nm,^{15,16} the quantum yield for the disappearance of benzene was found to decrease from unity at the low pressure limit with increasing benzene or N_2 buffer gas pressure. From the pressure dependence of the quantum yields for the disappearance of the benzene and the production of benzene isomers, a reaction mechanism proceeding through the vibrationally excited ground electronic state of benzene, “hot benzene”, was proposed.^{16,17} Hot benzene was produced through internal conversion from the electronically excited singlet state ($^1E_{1u}$ or $^1B_{1u}$) populated by 184.9 nm absorption. It has also been observed after the 193 nm excitation to the $^1B_{1u}$ state.¹⁸

The decay of benzene from the S_2 state under collision-free condition has also been studied. J. P. Reilly and co-worker studied the nanosecond UV laser induced multiphoton ionization/fragmentation processes. The rate equation model was used for the simulation and the lifetime of the second excited singlet state was estimated to be 20 ps.¹⁹ More recently, the

lifetime of the first and second excited state of benzene has been determined directly by pump and probe measurement with 160 fs laser pulses.²⁰ Benzene in the S_2 state, produced by 200 nm excitation, was found to have fast internal conversion to S_0 and S_1 states with a lifetime of ~ 40 fs; the decay of highly vibrationally excited S_1 states produced from this internal conversion occurred within 5–10 ps. The lifetime of benzene excited by the 155 nm photon was measured to be 70 fs,²¹ and the decay was attributed to the internal conversion from the initial excited to lower electronic state. Though many decay rates of benzene have been measured, they were all assigned to the relaxation rate from initial excited to lower electronic state. No dissociation rate of benzene has been accurately measured.

The main photoproducts of benzene vapor at 184.9 nm were reported to be an isomer of benzene,^{15,16} subsequently identified as fulvene,^{22,23} and polymers. *Cis*- and *trans*-1,3-hexadien-5-yne^{17,24} and small amounts of methane, ethane, ethylene, hydrogen and acetylene were also observed.^{15,25} The other two isomers, benzvalene and Dewar benzene were obtained only in condensed phase, and the results were interpreted as due to the formation of benzvalene and Dewar benzene with excess energy which must be rapidly dissipated if they were to survive.^{26,27} The photoproducts of methane, ethane, ethylene and acetylene indicate the existence of ring opening photodissociation processes. Photodissociation of benzene at 193 nm and 248 nm has been investigated in a molecular beam.²⁸ The H atom elimination, H_2 elimination, and a ring-opening dissociation channel $C_6H_6 \rightarrow C_5H_3 + CH_3$ were observed. The branching ratios of these three channels were reported to be 0.8, 0.16 and 0.04, respectively. However, recent *ab initio* calculations²⁹ showed that the dissociation barrier of the ring-opening channel is very close to the 193 nm photon energy. Therefore the branching ratio of the ring-opening channel is expected to be negligible.

We have used multimass ion imaging technique to study the photodissociation of benzene at 248 nm and 193 nm.^{30,31} Figure 6(a) shows the ion images of $m/e = 80$ –85 obtained from the photodissociation of d_6 -benzene at 193 nm. The image of $m/e = 85$, and 84 were from the parent ions and the ^{13}C of the parent ions. The images of $m/e = 83$ and 81 corresponded to the 3% of the impurity C_6D_5H , and the fragment of D elimination from the impurity, respectively. The image of $m/e = 82$ and 80 corresponded to the fragment of D elimination, C_6D_5 , and the fragment of two D atom (or D_2) elimination, C_6D_4 , respectively. Both the images of $m/e = 80$ and 82 contained two components. A line-shape component was superimposed on a disk-like component. The width of the line-shape component changed

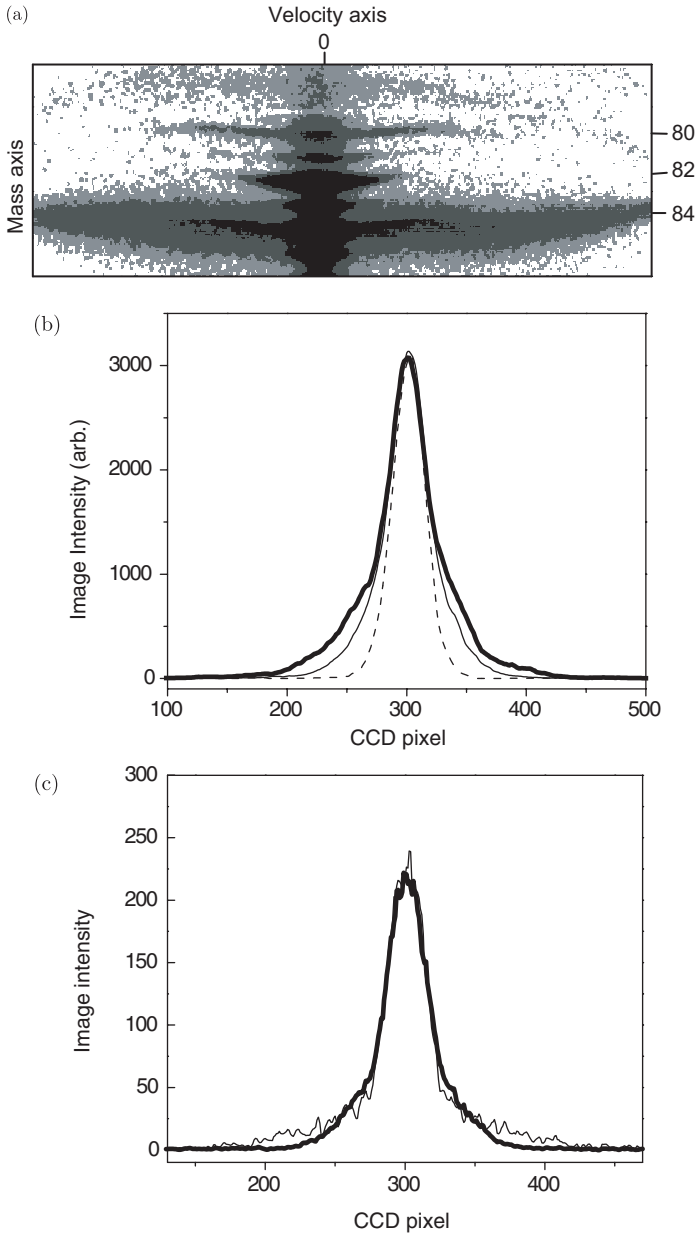


Fig. 6. (a) Image of $m/e = 80\text{--}85$. (b) Image intensity profiles of $m/e = 82$ at delay time $124\ \mu\text{s}$ (thick solid line), $94\ \mu\text{s}$ (thin solid line), and $43\ \mu\text{s}$ (dash line). (c) Image intensity profiles of $m/e = 80$ at delay time $19\ \mu\text{s}$ (thick solid line) and $43\ \mu\text{s}$ (thin solid line).

with the delay time, as illustrated on both wings of Figs. 6(b) and 6(c), corresponding to the neutral benzene dissociation. The width of the disk-like component did not change with the delay time, as shown in the center parts of Figs. 6(b) and 6(c), corresponding to the dissociation from benzene cations. These two components in the image of $m/e = 82$ cannot be easily distinguished. This is because the recoil velocity of the $m/e = 82$ fragment from neutral dissociation was very small. The relative intensity of these two

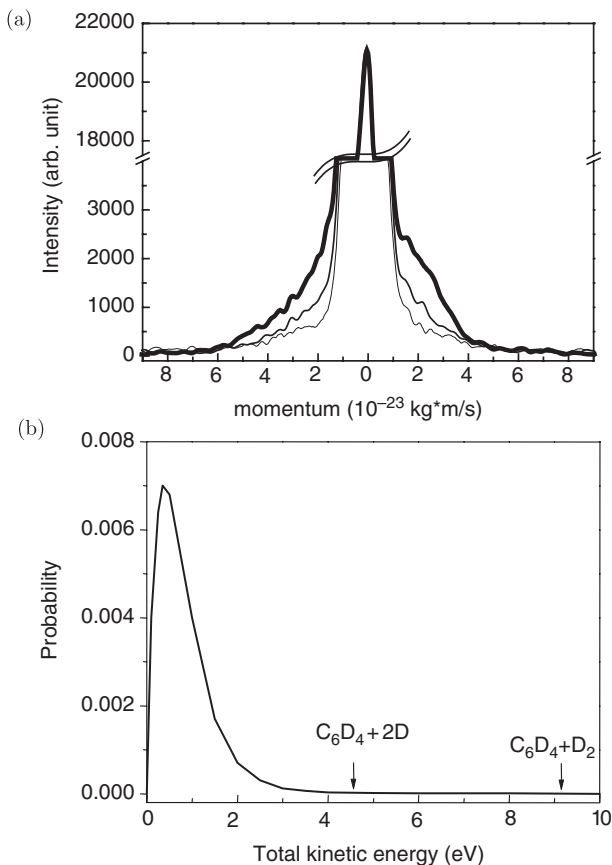


Fig. 7. (a) Momentum distribution of $m/e = 80$ at laser intensities: 8.0 mJ/cm^2 (thick solid line), 4.5 mJ/cm^2 (medium), 2.1 mJ/cm^2 (thin). (b) Translational energy distribution from the image line-shape component. The arrows indicate the maximum available translational energy for the reactions $C_6D_6 + 2 \times h\nu_{193\text{nm}} \rightarrow C_6D_4 + 2D$ and $C_6D_6 + 2 \times h\nu_{193\text{nm}} \rightarrow C_6D_4 + D_2$. (c) Image intensity profiles of $m/e = 82$ at laser intensities: 4.6 mJ/cm^2 (thick), 1.1 mJ/cm^2 (medium), 0.5 mJ/cm^2 (thin).

components in the image of $m/e = 80$ changes with the 193 nm photolysis laser intensity, as shown in Fig. 7(a). The disk-like component resulted from one-photon dissociation, but the two-photon dissociation has significant contribution to the line-shape component of fragment C_6D_4 . We did not detect the D atom or D_2 molecule due to their high ionization energies. However, the translational energy distribution calculated from the line-shape image of C_6D_4 , as shown in Fig. 7(b), suggests that the line-shape component of the fragments C_6D_4 are most likely from the elimination of two D atoms. On the other hand, the relative intensity of these two components in the image of $m/e = 82$ does not change with the photolysis laser fluence, and they both resulted from one-photon dissociation.

Figures 8(a) and 8(b) show the images of $m/e = 66$, 64 and 18, corresponding to C_5D_3 , C_5D_2 and CD_3 . At low photolysis laser fluence, the image of C_5D_3 was disk-like. The photolysis laser fluence dependence showed that the intensity of the disk-like image resulted from the one-photon absorption. However, a line-shape image superimposed on the disk-like image was observed at high photolysis laser fluence. The line-shape components of C_5D_3 and C_5D_2 had the same velocity distribution. It indicated that C_5D_2 was due to the fragment cracking of C_5D_3 by photoionization. On the other hand, only the line-shape component was observed in the CD_3 image. It totally resulted from the fragments of neutral benzene dissociation. The fragment momentum in the center-of-mass frame can be

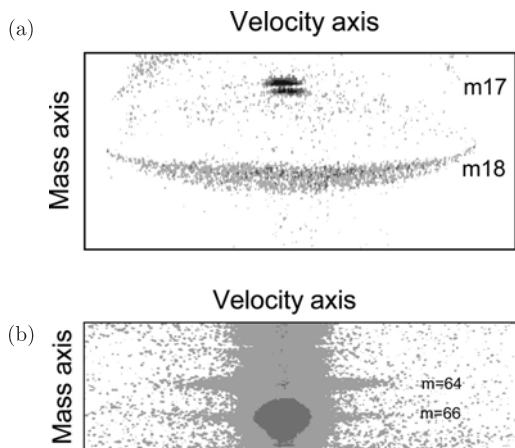


Fig. 8. (a) Image of $m/e = 18$. The image of $m/e = 17$, corresponding to NH_3 which was used as a mass indicator. (b) Image of $m/e = 66$ and 64.

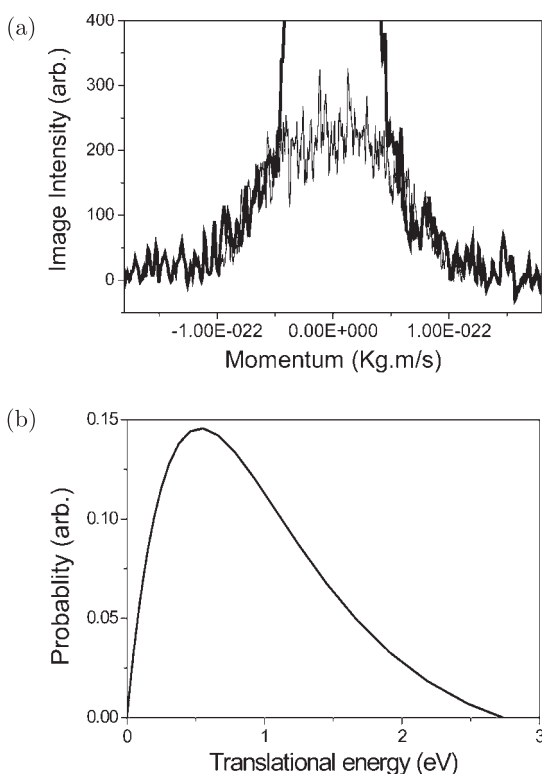


Fig. 9. (a) Momentum distributions of CD_3 and C_5D_3 . Momentum of these two fragments match very well, except the central part of C_5D_3 which was obscured by the disk-like image. (b) Translational energy distribution for the reaction $\text{C}_6\text{D}_6 + 2 \times h\nu_{193\text{nm}} \rightarrow \text{C}_5\text{D}_3 + \text{CD}_3$.

obtained directly from the ion image, i.e., the fragment displacement from the origin of the center-of-mass frame measured directly by CCD camera divided by flight time, and then multiplied by the mass of ion. The momentum of CD_3 and the line-shape component of C_5D_3 match very well, as shown in Fig. 9(a). It suggests that these two fragments resulted from the same dissociation channels. The fragment translational energy distribution obtained from velocity distribution multiplied by the Jacobian which transfers the velocity axis to energy axis is shown in Fig. 9(b). Since CD_3 resulted only from the neutral benzene dissociation, measurement of the total CD_3 ion intensity as a function of the photolysis laser fluence revealed the photon number dependence of this dissociation channel. Figure 10(a) shows that it resulted from the two-photon absorption.

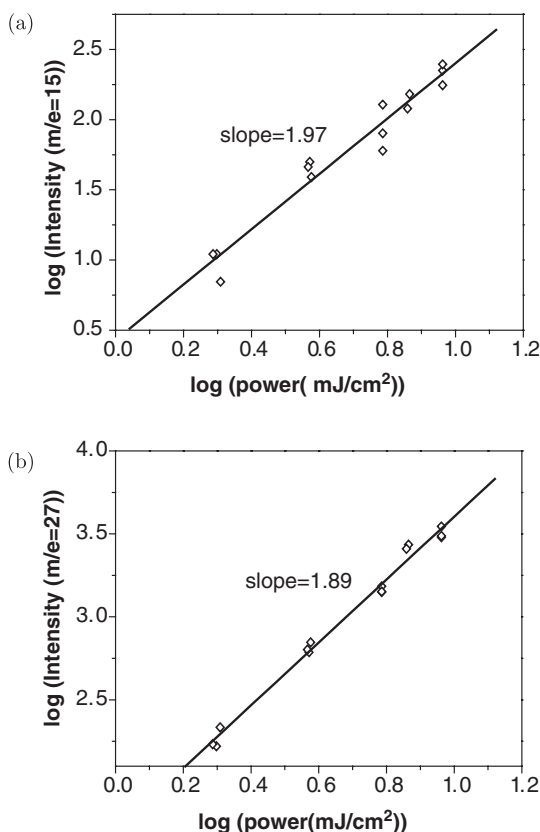


Fig. 10. (a) CH_3^+ (b) C_2H_3^+ signal intensities as a function of photolysis laser fluence. It shows that both the reactions are from two-photon dissociation.

Figures 11(a) and 11(b) show the images of masses $m/e = 52, 54, 56, 30$ and 32 , corresponding to $\text{C}_4\text{D}_2, \text{C}_4\text{D}_3, \text{C}_4\text{D}_4, \text{C}_2\text{D}_3$ and C_2D_4 , respectively. C_4D_4 and C_2D_4 had disk-like images and the width of the images did not change with the photolysis delay time. They resulted from the dissociative ionization of hot benzene. The image of $m/e = 52$ and 54 had two components. Each of them had a line-shape image superimposed on a disk-like image. On the other hand, the image of C_2D_3 only had the line-shape component, and it totally resulted from the fragments of neutral hot benzene dissociation. The line-shape components of C_4D_2 and C_4D_3 had the same velocity distribution. It indicates that C_4D_2 was produced from the fragment cracking of C_4D_3 by photoionization. C_4D_3 has a momentum

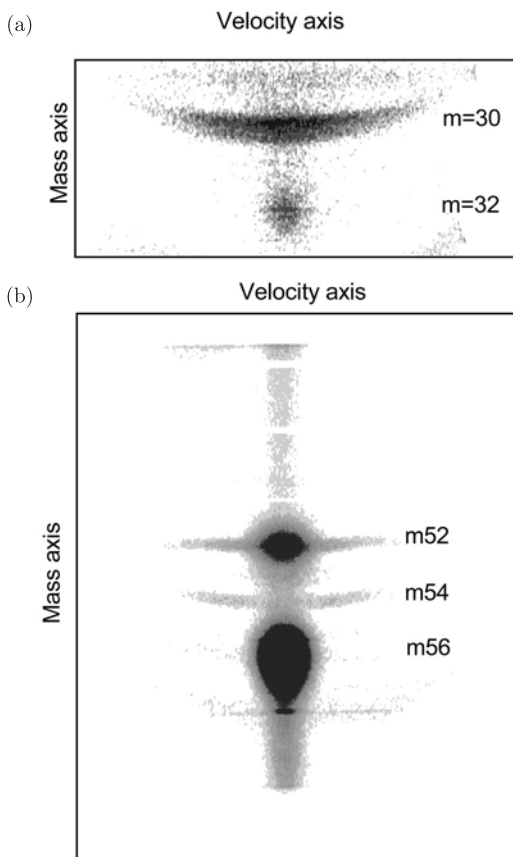


Fig. 11. (a) Image of $m/e = 32$ and 30. (b) Image of $m/e = 56$, 54 and 52.

distribution that matches the momentum distribution of the C_2D_3 primary photofragment, as shown in Fig. 12(a). This suggests that these two fragments resulted from the same dissociation channel. The translational energy distribution of this dissociation channel is shown in Fig. 12(b). Measurement of the C_2D_3 ion intensity as a function of photolysis laser fluence showed that this dissociation channel resulted from two-photon absorption, as illustrated in Fig. 10(b).

Figure 13 shows the images of masses $m/e = 42$, corresponding to C_3D_3 , at various delay times. The image of $m/e = 42$ was disk-like and its width did not change with the delay time. Therefore, it was totally from the dissociation of hot benzene after the ionization. Photolysis laser fluence dependence study showed that it was from one-photon absorption.

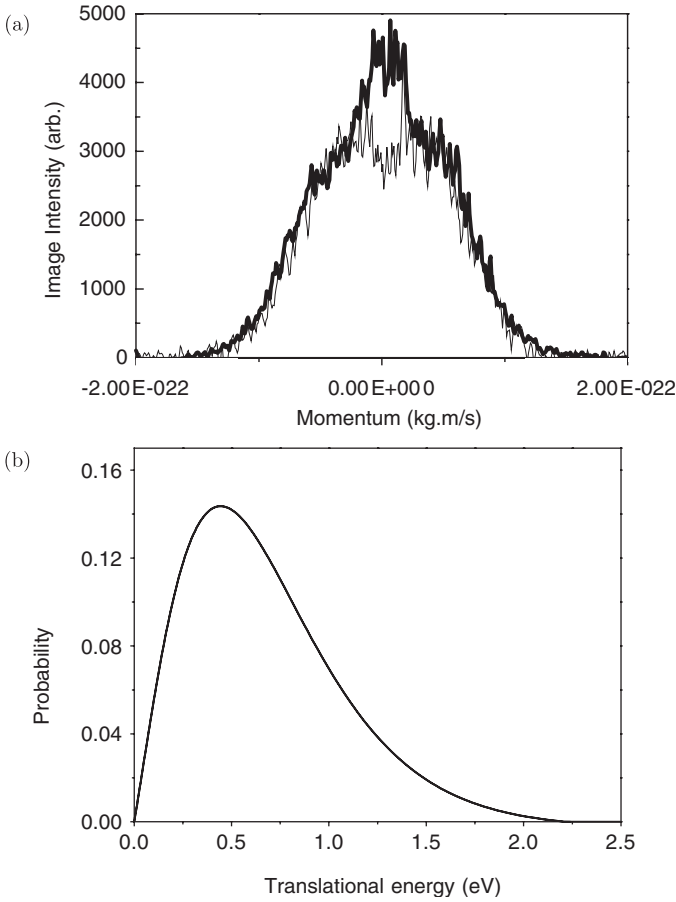
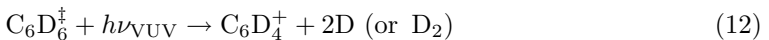
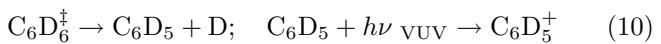


Fig. 12. (a) Momentum distributions of C_2D_3 and C_4D_3 . Momentum of these two fragments match very well, except the central part of C_4D_3 which had additional contribution from the disk-like image. (b) Translational energy distribution for reaction $C_6D_6 + 2 \times h\nu_{193nm} \rightarrow C_4D_3 + C_2D_3$.

The observed photofragment ion images can be described with the following reactions:



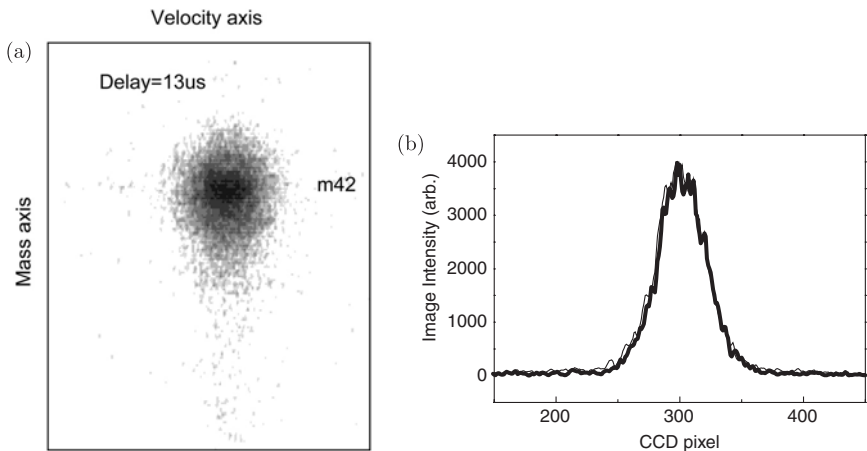
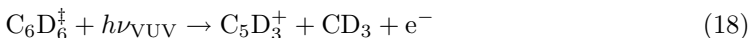
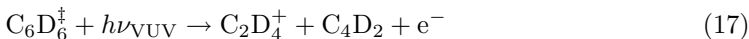
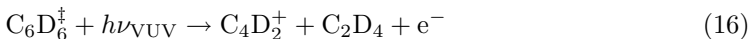
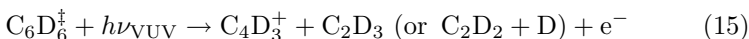
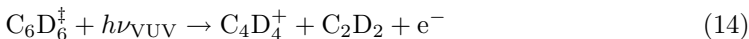
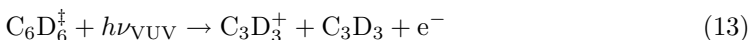
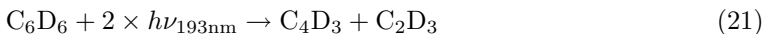
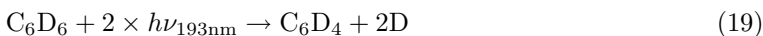


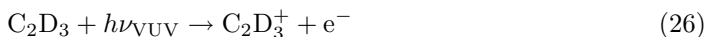
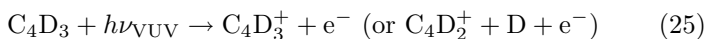
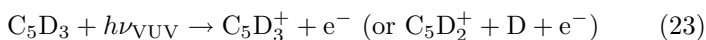
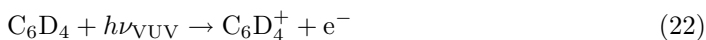
Fig. 13. (a) The disk-like image of $m/e = 42$ from C_6D_6 . (b) The image intensity profiles of the disk-like image at delay time $13\ \mu s$ and $32\ \mu s$.



Here $C_6D_6^*$ represents benzene in the second singlet electronic excited state, and $C_6D_6^\dagger$ represents the highly vibrationally excited ground electronic state of benzene. Reaction (10) represents the D atom elimination and the detection of the fragment C_6D_5 by VUV photoionization. Reactions (11)–(18) represent the various dissociative ionization processes of hot benzene. The disk-like images were all from the reactions (11)–(18). Most of these benzene cation dissociation channels have been found in previous studies.^{19–23}

The elimination of two D atoms and two ring-opening dissociation channels were observed from the two-photon dissociation.





Reactions (19)–(21) represent the dissociation of benzene and reactions (22)–(26) represent the detection of fragments by VUV laser photoionization. The line-shape images resulted from these reactions.

In the previous study, the ring-opening dissociation channel $\text{C}_6\text{H}_6 \rightarrow \text{C}_5\text{H}_3 + \text{CH}_3$ was observed.²⁸ In order to produce C_5H_3 and CH_3 , H atoms in benzene must migrate until one carbon gathers three H atoms and the CC bond breaks. This must involve successive H atom migration and benzene isomerization, and the dissociation mechanism must be very complicated. Recently, the potential energy surface calculated by Mebel *et al.* indicates that this ring-opening dissociation of benzene is indeed energetically allowed at 193 nm.²⁹ Part of the calculated results of the ring-opening dissociation mechanisms are shown in Fig. 14. However, the dissociation barrier is very close to the 193 nm photon energy, therefore, the branching ratio of

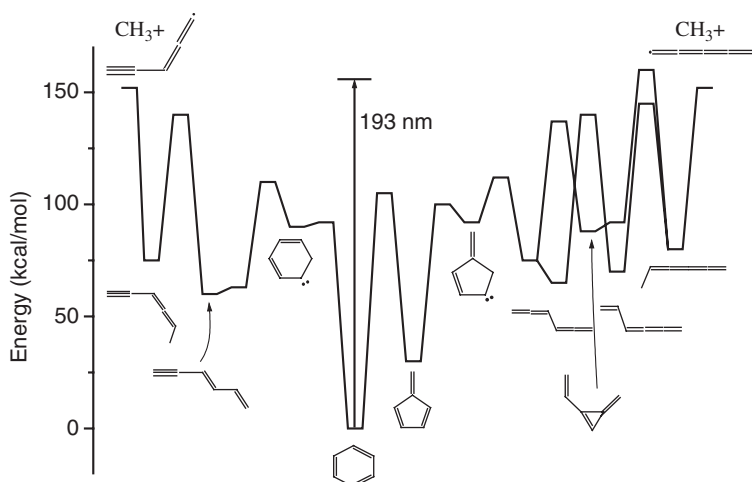


Fig. 14. Energy diagram of the ring-opening dissociation $\text{C}_6\text{D}_6 \rightarrow \text{C}_5\text{D}_3 + \text{CD}_3$ from *ab initio* results (Ref. 29). Note that there are many intermediates which can dissociate into $\text{C}_4\text{D}_3 + \text{C}_2\text{D}_3$ by a simple C–C bond fission.

the ring-opening channel from one-photon dissociation is expected to be negligible.

In our study, two ring-opening channels, $\text{C}_6\text{D}_6 \rightarrow \text{C}_5\text{D}_3 + \text{CD}_3$ and $\text{C}_6\text{D}_6 \rightarrow \text{C}_4\text{D}_3 + \text{C}_2\text{D}_3$, were observed and confirmed by the momentum match between the fragments in each channel. However, the photolysis laser fluence dependence showed that they were from two-photon dissociation. The observation of C_5D_3 and CD_3 fragments confirms the report of the ring-opening channel in the previous study.²⁸ Though various dissociation pathways to produce C_5D_3 and CD_3 have been performed by *ab initio* calculations, no calculation was performed for the $\text{C}_6\text{D}_6 \rightarrow \text{C}_4\text{D}_3 + \text{C}_2\text{D}_3$ dissociation channel. However, as shown in Fig. 14, most of the calculated dissociation pathways of $\text{C}_6\text{D}_6 \rightarrow \text{C}_5\text{D}_3 + \text{CD}_3$ have intermediates which can dissociate into C_4D_3 and C_2D_3 by a simple C–C bond fission. The dissociation of one of the C_6D_6 intermediates shown in Fig. 14 could thus also provide a route to branch to the $\text{C}_4\text{D}_3 + \text{C}_2\text{D}_3$ product channel. These are the possible dissociation pathways producing C_4D_3 and C_2D_3 . The observation of the fragments C_2D_3 and CD_3 from ring-opening dissociation provides a possible explanation of the photodissociation products of methane, ethane, ethylene and acetylene in benzene photolysis at 184.9 nm.

The dissociation rate of $\text{C}_6\text{D}_6^\ddagger$ with internal energy of 618 kJ/mol from the 193 nm photon excitation was measured from the intensity change of the disk-like image at various delay times. A dissociation rate of $5 \pm 1 \times 10^4 \text{ s}^{-1}$, corresponding to the lifetime of $20 \pm 4 \mu\text{s}$ was obtained from the disk-like image intensity change of $m/e = 42, 52, 56, 66$ and 80, as shown in Fig. 15. The dissociation rate of $\text{C}_6\text{H}_6^\ddagger$ with the same internal energy was measured from the disk-like image intensity change of $m/e = 52$ and 39. A dissociation rate of $1 \pm 0.2 \times 10^5 \text{ s}^{-1}$, corresponding to the lifetime of $10 \pm 3 \mu\text{s}$ was obtained. However, the intensity of $m/e = 52$ with internal energy of 483 kJ/mol from the 248 nm photon excitation did not change with the delay time, as shown in Fig. 15. This is because the lifetime is too long to be measured in our instrument. We estimated the upper limit of the dissociation rate of $\text{C}_6\text{H}_6^\ddagger$ with internal energy of 483 kJ/mol to be $3 \times 10^3 \text{ s}^{-1}$. Since the lifetimes measured from all the different products, reactions (11)–(18), are the same, these products must be from the same electronic state. It is most likely that $\text{C}_6\text{D}_6^\ddagger$ and $\text{C}_6\text{H}_6^\ddagger$ are in the ground electronic state. The dissociation rate of benzene at 193 nm and 211 nm have been calculated to be $3.6 \times 10^4 \text{ s}^{-1}$ and $6 \times 10^2 \text{ s}^{-1}$, respectively, by the RRKM model on the electronic ground state surface.²⁹ It shows that the

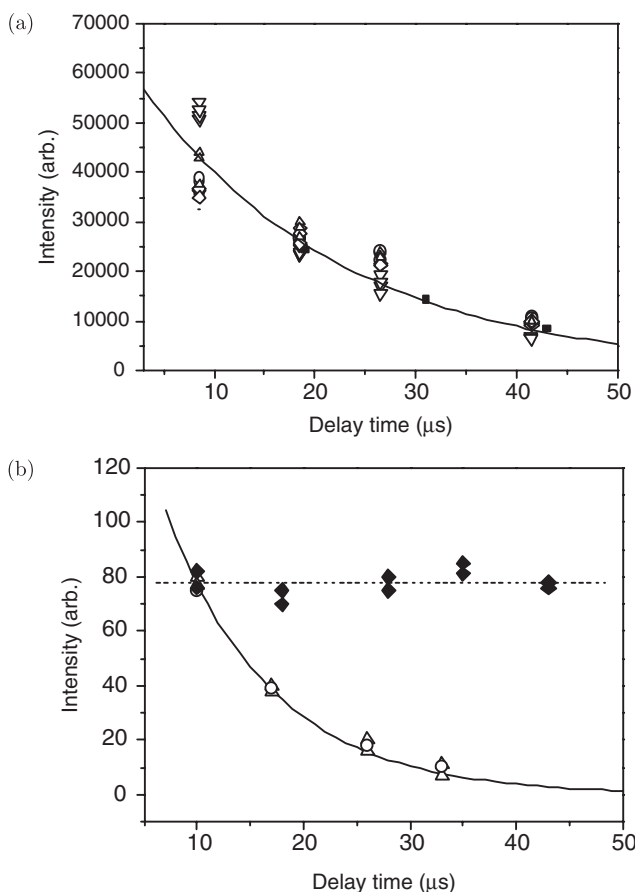


Fig. 15. (a) The change of disk-like image intensity of $m/e = 42$ (o), 52 (∇), 56 (\diamond), 66 (Δ), and 80 (\blacksquare) as a function of delay time from dissociative ionization of hot C_6D_6 after 193 nm excitation. The solid line shows the fit corresponding to a lifetime of 20 μs . (b) The change of disk-like image intensity of $m/e = 52$ (Δ), 39 (o) as a function of delay time from dissociative ionization of hot C_6H_6 after 193 nm excitation. The solid line shows the fit corresponding to a lifetime of 9.5 μs . Solid diamonds represent the disk-like imaging intensity change of $m/e = 52$ from the hot C_6H_6 after 248 nm excitation. The dashed line represents no intensity change of $m/e = 52$ with delay time.

dissociation rate from RRKM calculation is very close to our experimental measurement.

Comparison of C_6D_6^+ and C_6H_6^+ shows the isotope effect on the dissociation rates. This isotopic effect has also been observed in the dissociation rates of toluene, ethylbenzene, propylbenzene and butylbenzene.⁷ RRKM

calculation and experimental result also demonstrate that the dissociation rate of toluene is faster than that of D atom substituted toluene by a factor of two.³² Though the photon energy of 193 nm is higher than the channel-three threshold (244.5 nm) and the photon energy of 248 nm is lower than the threshold, the fast dissociation rate at 193 nm is not resulted from the channel-three effect. This is because the non-radiative decay rates above and below the channel three-threshold are much faster than the dissociation rates at 193 or 248 nm. The difference in dissociation rates at 193 nm and 248 nm simply reflects the internal energy dependence of the dissociation rate. This is also supported by the RRKM calculation.

3.2. Toluene

Toluene is the simplest alkyl derivative of benzene. The UV fluorescence quantum yield of toluene was found to be very similar to that of benzene. In the S_1 state, it decreases rapidly with the increase in photon energy, and no UV fluorescence is observed from the S_2 state.³³ The monomolecular reaction of toluene after excitation to the S_1 state is dominated by the isomerization after internal conversion to the ground electronic state. The isomerization of aromatic molecules has been studied extensively. In liquid solution, the most characteristic monomolecular process for alkylaromatic compounds is photoisomerization with formation of the derivatives of fulvenes, benzvalenes, Dewar benzenes, prismanes, as well as isomerization with a change in the alkyl substitute's position in the aromatic ring.^{34–38} The generally accepted view is that photoisomerization of this kind proceeds by the intermediary formation of isomers like fulvene, benzvalene, Dewar benzene with their further rearomatization. It has been suggested that all isomerization processes of benzene and its alkyl derivatives can be described in terms of ring permutation.³⁹ Figure 16 shows some of the ring permutation of benzene and xylene. The result from the ring permutation is that not only the position of the alkyl group can be changed during the ring permutation isomerization, but also the carbon atoms within the aromatic ring can be exchanged during the ring permutation. In addition, the carbon and hydrogen atoms belonging to the alkyl group are not involved in the exchange with those atoms in the aromatic ring. The ring permutation has also been observed in benzene and alkyl-substituted benzene in gas phase after excitation to the S_1 state.^{40–42}

Another monomolecular reaction that competes with the isomerization in collisionless condition is dissociation. Dissociation is found to be the

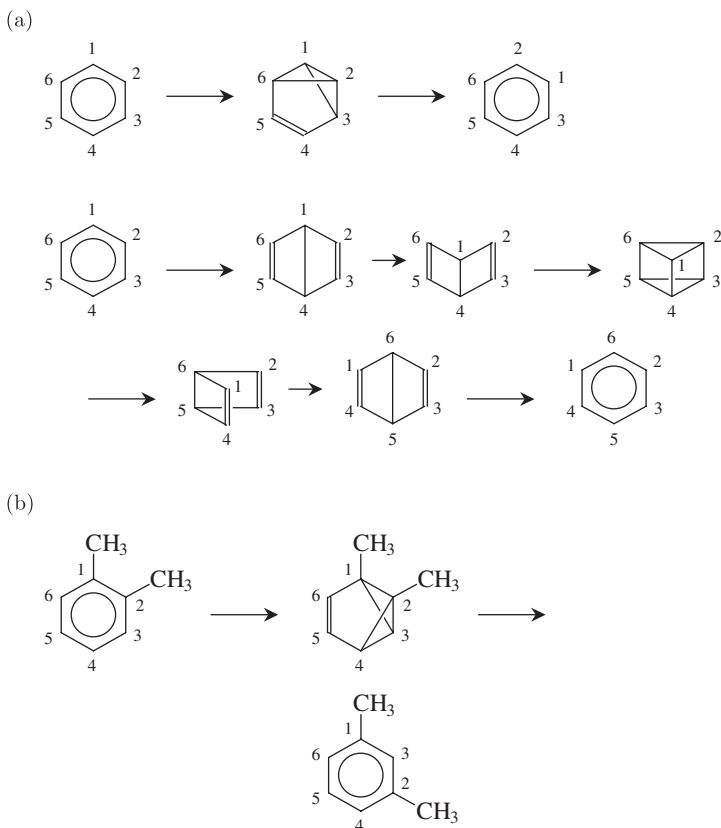


Fig. 16. Some of the isomerization pathways of benzene and xylene through ring permutation.

major channel in the S_2 state. Photodissociation of toluene in the gas phase at 193 nm showed that α -H atom elimination and CH_3 elimination are the major dissociation channels.^{32,43–48} The dissociation rates were found to be $2 \times 10^6 \text{ s}^{-1}$, and the proposed dissociation mechanism is *direct* C–H bond and C–C bond rupture, proceeding through the vibrationally excited ground electronic state. Recently, toluene in the S_2 state produced by 200 nm excitation was found to have a fast internal conversion to the S_0 and S_1 states with a lifetime of $\sim 50 \text{ fs}$.²⁰ The fast internal conversion from the initial excited state to lower electronic states and the slow dissociation rate of toluene supports the hot molecule reaction mechanism.

The photodissociation of isotope labelled toluene $\text{C}_6\text{H}_5\text{CD}_3$ and $\text{C}_6\text{H}_5^{13}\text{CH}_3$ at 193 nm and 248 nm under collision-free conditions were

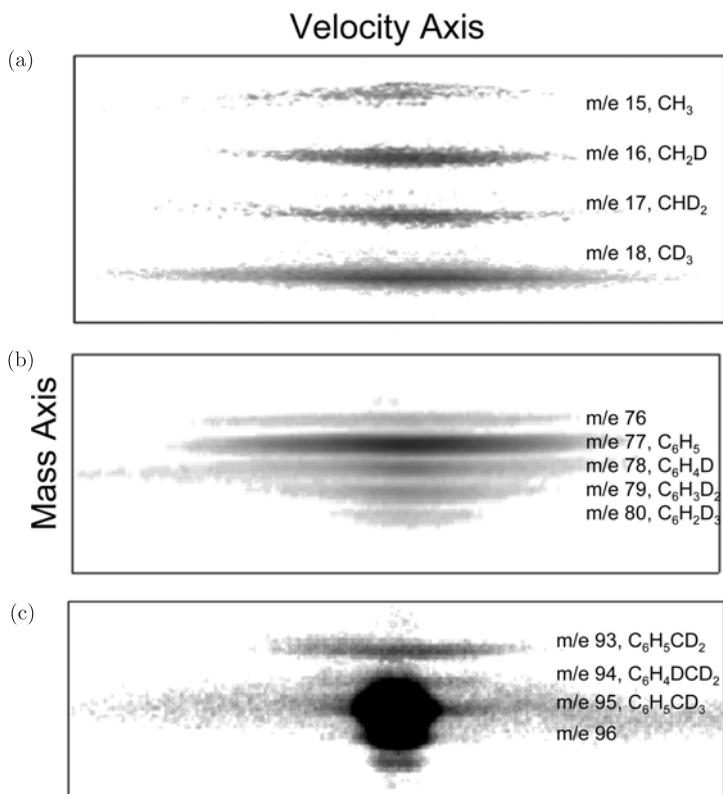


Fig. 17. Photofragment ion images of $\text{C}_6\text{H}_5\text{CD}_3$ in three different mass regions. Image of $m/e = 76$ in (b) resulted from two-photon dissociation. Image of parent molecule $m/e = 95$, and $m/e = 96, 97$ due to the ^{13}C natural abundance are shown in (c).

studied by multimass ion imaging technique and TOF mass spectrometer in our laboratory.⁴⁹ The photofragment ion images are shown in Fig. 17. In addition to the major fragments, $\text{C}_6\text{H}_5\text{CD}_2$, C_6H_5 and CD_3 from the *direct* dissociation of $\text{C}_6\text{H}_5\text{CD}_3 \rightarrow \text{C}_6\text{H}_5\text{CD}_2 + \text{D}$ and $\text{C}_6\text{H}_5\text{CD}_3 \rightarrow \text{C}_6\text{H}_5 + \text{CD}_3$, observations of the heavy fragments $\text{C}_7\text{H}_4\text{D}_3$, $\text{C}_6\text{H}_4\text{D}$, $\text{C}_6\text{H}_3\text{D}_2$, and $\text{C}_6\text{H}_2\text{D}_3$, and the corresponding light fragment partners, CD_2H , CDH_2 , and CH_3 , suggest the existence of the other dissociation channel, i.e., isotope exchange prior to dissociation. Momentum matches of two fragments in each dissociation channel, as shown in Fig. 18, further confirm that each fragment pair, C_6H_5 and CD_3 , $\text{C}_6\text{H}_4\text{D}$ and CD_2H , $\text{C}_6\text{H}_3\text{D}_2$ and CDH_2 , $\text{C}_6\text{H}_2\text{D}_3$ and CH_3 , is from the dissociation of $\text{C}_6\text{H}_5\text{CD}_3$. These momentum matches also

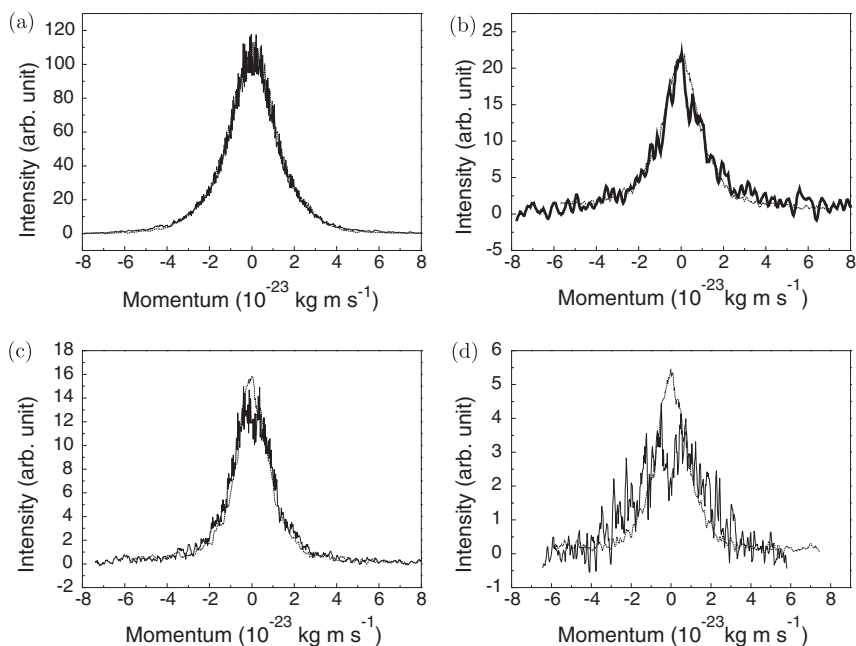


Fig. 18. The momentum matches of two fragments in each dissociation channel (a) $m/e = 77$ and 18, (b) $m/e = 78$ and 17, (c) $m/e = 79$ and 16, (d) $m/e = 80$ and 15. The thick lines represent light fragments, and the thin lines represent heavy fragments.

exclude the contribution from three-body dissociation, like the dissociation of clusters, or the contribution from cation dissociation. Measurements of the fragment intensities as a function of photolysis laser fluence in the region from 2 to 54 mJ/cm² show that all of these dissociation channels result from one-photon dissociation. The results from one-photon dissociation were also confirmed by the photofragment translational energy distribution. Figure 19 shows that the fragment maximum translational energy does not exceed the available energy (= photon energy – bond energy) from one 193 nm photon. The respective ratios between CD₂H, CDH₂ and CH₃, and those ratios between C₆H₄D, C₆H₃D₂, C₆H₂D₃ from experiment are very close to the statistical values. This suggests that a small fraction of parent molecules enter the other dissociation channel. The isotopic scrambling of D and H atoms between the methyl group and the aromatic group in this channel is almost complete before dissociation occurs.

The photofragment TOF mass spectra resulting from the dissociation of C₆H₅¹³CH₃ are shown in Fig. 20. In addition to the major dissociation

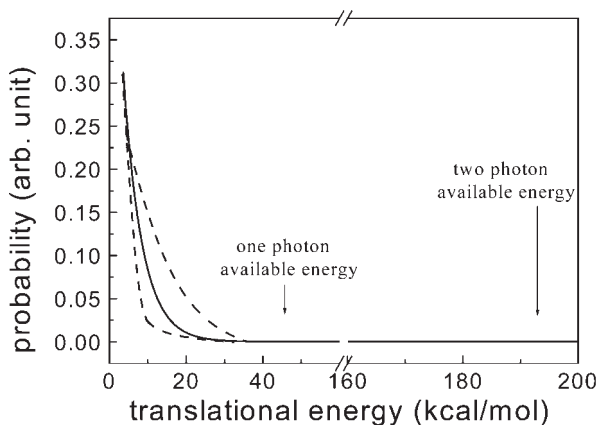


Fig. 19. Photofragment translational energy distribution from reactions (29b) and (34b). The translational energy distributions are the same for reactions (29b) and (34b) within the experimental uncertainty. The solid line represents the experimental measurement, and the dashed lines represent the upper and lower limits due to experimental uncertainty.

channel, $\text{C}_6\text{H}_5^{13}\text{CD}_3 \rightarrow \text{C}_6\text{H}_5 + ^{13}\text{CH}_3$, the observation of $^{13}\text{CC}_5\text{H}_5$ and CH_3 indicates that the methyl carbon atom is also involved in the exchange with aromatic carbon atoms prior to dissociation.

The results cannot be explained by the existing isomerization mechanisms for aromatic molecules, i.e., ring permutation, because ring permutation involves only hydrogen and carbon atom exchange within the aromatic group. A reasonable isomerization mechanism that explains the experimental results is the isomerization from a six-membered ring (toluene) to a seven-membered ring (cycloheptatriene). After isomerization to a seven-membered ring, isotopic scrambling of the H/D and carbon atoms occurs through H or D atom migration around the seven-membered ring. In the end, the rearomatization of cycloheptatriene to toluene and the subsequent dissociation through C–C bond cleavage results in the formation of the fragments CD_2H , CDH_2 and CH_3 , and their heavy fragment partners, $\text{C}_6\text{H}_4\text{D}$, $\text{C}_6\text{H}_3\text{D}_2$ and $\text{C}_6\text{H}_2\text{D}_3\text{CH}$. Hydrogen or D atom elimination can occur from cycloheptatriene, or occur after the rearomatization of cycloheptatriene to toluene. The same mechanism can be used to explain the formation of the respective photofragments CH_3 , $^{13}\text{CH}_3$, $\text{C}_6\text{H}_5\text{C}_5^{13}\text{CH}_5$ from the dissociation of $\text{C}_6\text{H}_5^{13}\text{CH}_3$.

This particular isomerization pathway is supported by *ab initio* calculations. The energies of isomers and various transition states along the

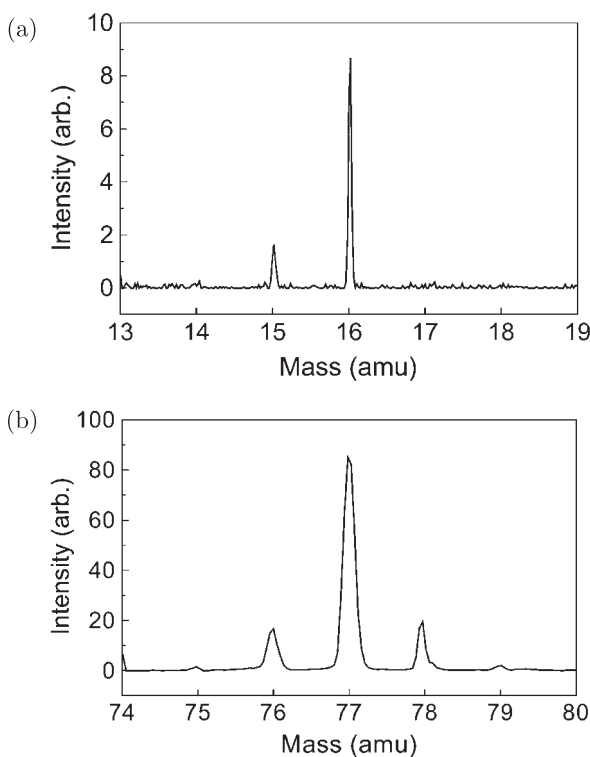


Fig. 20. The photofragment TOF mass spectrometry from the dissociation of $\text{C}_6\text{H}_5^{13}\text{CH}_3$ in two different mass regions. The fragment of $m/e = 76$ results from multiphoton dissociation.

isomerization pathway from *ab initio* calculation are shown in Fig. 21. The dissociation of toluene has barrier heights of 89.7 kcal/mol for C–H bond cleavage, and 103.8 kJ/mol for C–C bond cleavage. The six-membered ring to seven-membered ring isomerization has a barrier height of 84.9 kJ/mol. Since the barrier heights are all very close in energy, C–C bond and C–H bond dissociation competes with isomerization. Most of the toluene molecules dissociate directly through C–C and C–H bond cleavages after the internal conversion. However, a small fraction of toluene molecules isomerize to CHT. The migration of H or D atoms in CHT due to the low barrier height results in isotopic scrambling of D/H atoms and carbon atoms in CHT. Fast H and D atom scrambling in CHT is consistent with the complete isotopic scrambling of CHT excited by 248 nm photons in the previous study.³²

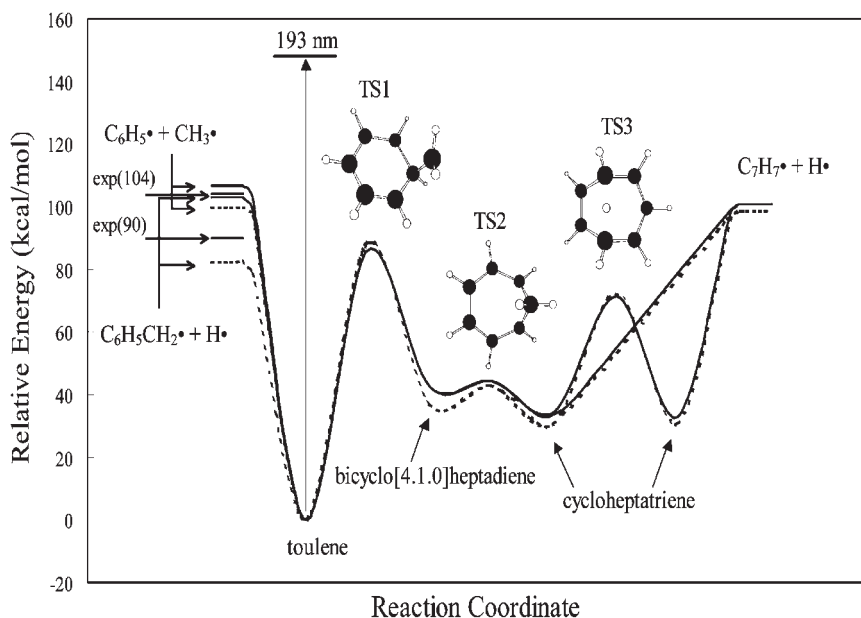
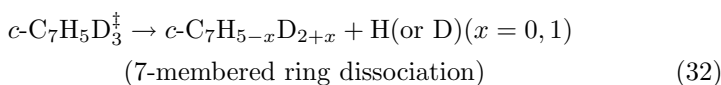
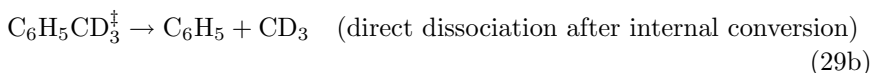
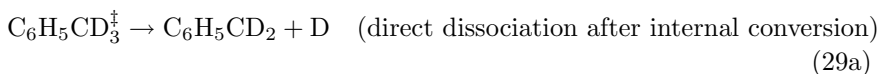
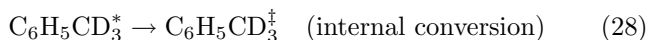
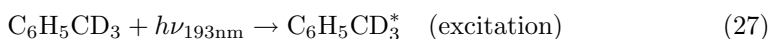
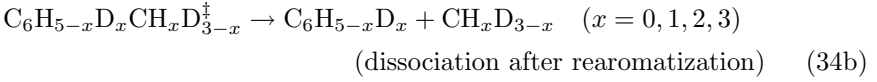
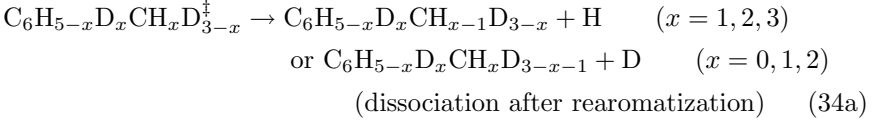
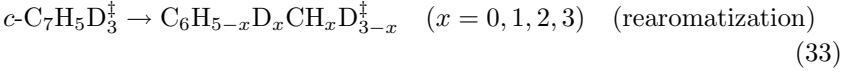


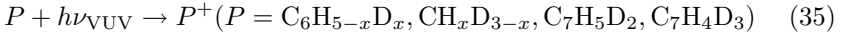
Fig. 21. Energy diagram for isomerization and dissociation reactions of toluene. The energies shown are computed at the B3LYP/aug-cc-pVTZ (solid line) and CCSD/6-311+G* (dashed line) at the geometry optimized by B3LYP/6-31+G*.

The results of the experiments can be described using the following reactions:

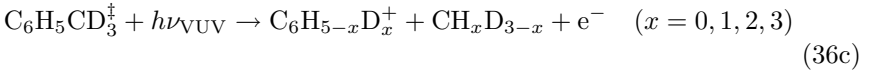
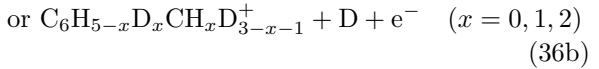
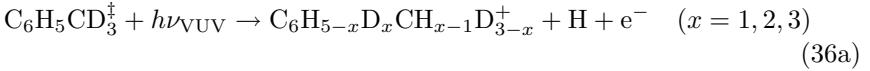




All of the dissociation products from reactions (29), (32) and (34) were ionized by VUV laser and detected by ion image detector. They can be represented by the following reaction:



However, at very short delay time, some of the hot toluene which has not dissociated into fragments could absorb the VUV photon and result in dissociative ionization.



The ions from the dissociative ionization channels produce the disk-like image at short delay time. However, at long delay time, most of the hot toluene dissociates into fragments, and this background decays to zero. The dissociation lifetime, $1/k_{29} (= 1/(k_{29a} + k_{29b})) = 850 \text{ ns}$ at 193 nm is very short compared to the delay time between pump and probe laser pulses ($\sim 30 \mu\text{s}$) in imaging experiments, therefore, most of the hot toluene molecules dissociate into fragments and only the line-shape images were observed.

The product buildup times of the respective photofragments C_6H_5 , $\text{C}_6\text{H}_4\text{D}$, $\text{C}_6\text{H}_3\text{D}_2$, $\text{C}_6\text{H}_2\text{D}_3$, $\text{C}_7\text{H}_5\text{D}_2$, and $\text{C}_7\text{H}_4\text{D}_3$, originating from $\text{C}_6\text{H}_5\text{CD}_3$, were measured by a TOF mass spectrometer. The results are shown in Fig. 22. The non-zero intensity at $t = 0$ and the intensity decay of $m/e = 94$ in Fig. 22 is due to the background from the dissociative ionization channels. Reactions (27)–(36) are used to simulate the apparent rate

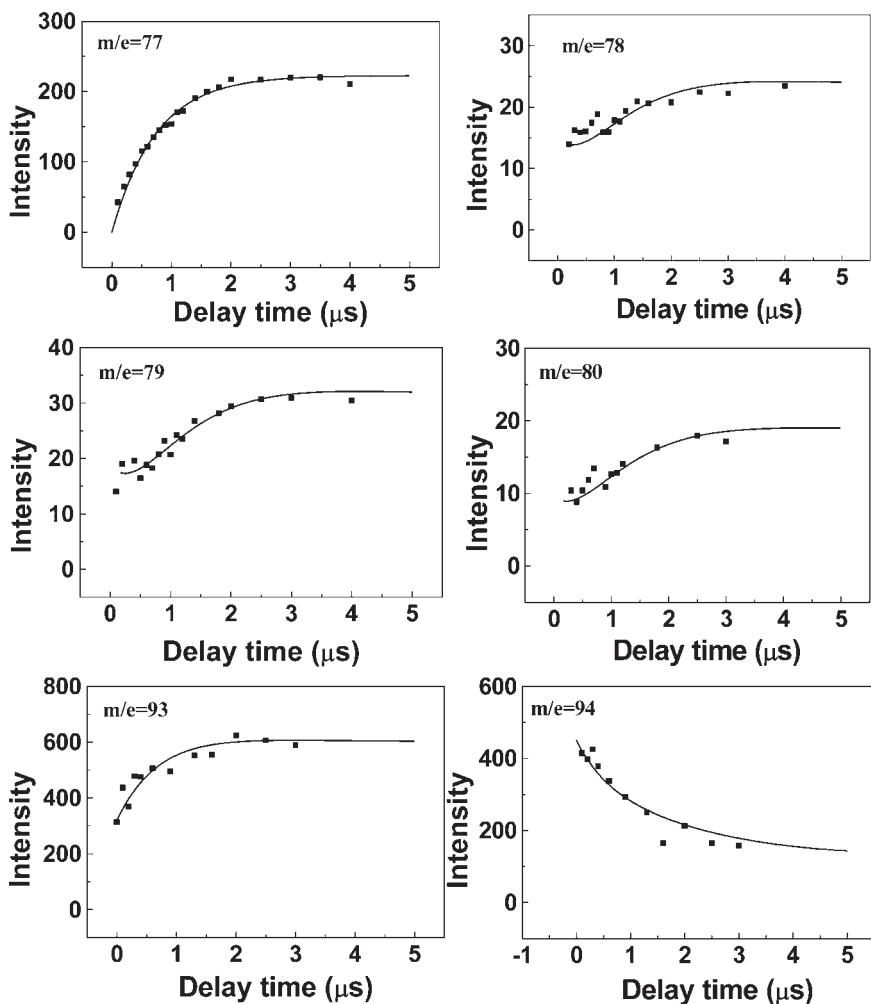


Fig. 22. The product buildup times. The solid line is the simulation from reactions (27)–(36). The non-zero intensity at $t = 0$ and the intensity decay of $m/e = 94$ is due to the dissociative ionization (reaction (36)).

and the relative intensity of the fragments. We neglect the reactions (27) and (28) since they are very fast compared to the other reactions. In addition, we neglect all the isotopic effects except those on the H and D atom elimination channels (reactions (29a) and (34a)), where the isotopic effect is expected to be large. We assume that $k_{30} = k_{-33}$, $k_{33} = k_{-30}$, $k_{31} = k_{-31}$, and $k_{29b} = k_{34b}$. The simulation result shows that $k_{29} (= k_{29a} + k_{29b})$

is very sensitive to the apparent rate of fragment $m/e = 77$. This is because most of the fragments of $m/e = 77$ come from reaction (29). However, the value of k_{31} is not sensitive with respect to the final results as long as its value is 5 times larger than that for k_{33} . This is because the result will not be changed by the increase in the scrambling rate after the isotopic scrambling is complete. On the other hand, the best value of k_{33} is $(1 \pm 0.3) \times 10^8 \text{ s}^{-1}$ in order to fit the apparent rate of fragments $m/e = 78, 79$, and 80. For the H or D atom elimination channel, they could result from the 7-membered ring dissociation (reaction (32)) or from the 6-membered ring dissociation (reactions (29a) and (34a)). However, our result is not sensitive to k_{32} when it is smaller than $1 \times 10^7 \text{ s}^{-1}$. As a result, the upper limit of k_{32} is $1 \times 10^7 \text{ s}^{-1}$. Although the upper limit of the dissociation rate from the 7-membered ring is larger than the dissociation rate from the 6-membered ring, the dissociation from 7-membered ring must compete with the rearomatic process. Since the rearomatic rate is at least 10 times larger than the upper limit of the 7-membered ring dissociation rate, it is not likely that the dissociation from 7-membered ring is important. The simulation results are shown in Fig. 22. From the simulation, we obtain $k_{29} (= k_{29a} + k_{29b}) = (1.17 \pm 0.08) \times 10^6 \text{ s}^{-1}$, $k_{30} = (3.4 \pm 0.3) \times 10^5 \text{ s}^{-1}$, $k_{31} > 5 \times 10^8 \text{ s}^{-1}$, $k_{32} < 1 \times 10^7 \text{ s}^{-1}$, and the ratio of H and D atom elimination from the methyl group of toluene is 1.6 ± 0.2 . Values for k_{29}, k_{31} , and k_{33} are very close to those from previous studies of toluene^{32,50,51} and CHT.^{32,43,52} The $k_{30}/(k_{29} + k_{30})$ ratio shows that about $25 \pm 4\%$ of hot toluene molecules isomerize to cycloheptatriene, followed by H and D atom exchange in cycloheptatriene, and subsequent rearomatization to toluene prior to dissociation. Although the percentage is small, it is clearly not negligible. This is the first time that this kind of isomerization was experimentally observed in aromatic molecules. The most significant difference of this particular isomerization channel from that of other aromatic isomerization pathways is that alkyl carbon and hydrogen atoms are involved in the exchange with those atoms in the aromatic ring during this isomerization process. This is unlike that found in ring permutation isomerization, in which only the hydrogen and carbon atoms of the aromatic ring are involved in the exchange.

3.3. Ethylbenzene and Propylbenzene

Since the ethyl and propyl groups are not the electronic chromophore at 248 nm and 193 nm, the photon absorption corresponds to the excitation

of the phenyl ring. Dissociation must occur indirectly either through the coupling between the stable and repulsive states, or after the internal conversion from the initial excited state to a lower electronic state. In contrast to benzene and toluene, the C–C bond in the alkyl group is the weakest chemical bond in both ethylbenzene and propylbenzene. Therefore, it is expected that the C–C bond cleavage plays an important role in the dissociation channel of these molecules. A CH_3 yield of $96 \pm 4\%$ and a dissociation rate of $2 \times 10^7 \text{ s}^{-1}$ were reported for the ethylbenzene photodissociation at 193 nm,^{32,43–47,50,53} although the dissociation channel due to the H atom elimination was also observed.³² For *n*-propylbenzene, ethyl radical elimination was found to be the major channel for the photodissociation at 193 nm, and the dissociation rate is $7 \times 10^6 \text{ s}^{-1}$.⁴⁵ A dissociation mechanism through internal conversion to S_0 was used to interpret the dissociation rates and branching ratios of ethylbenzene and propylbenzene in the S_2 state.^{43–47} No dissociation experiment has been performed for these molecules in the S_1 state. However, the onset and ultimate dominance of IVR in these molecules was found in the single vibronic level fluorescence spectra of the S_1 state.⁵⁴ More recent high resolution laser fluorescence excitation spectra near the band origin of the S_1 state showed that propylbenzene and butylbenzene exhibit the excess linewidths, but the source of the excess width remains elusive.⁵⁵

We have used the multimass ion imaging technique to study the photodissociation of ethylbenzene and propylbenzene at both 193 nm and 248 nm.^{56,57} Figure 23(a) depicts the photofragment ion images obtained from the photodissociation of ethylbenzene at 193 nm. Fragments of $m/e = 91$, 92 and 93 correspond to the phenyl radical and its ^{13}C isotopes due to the natural abundance. The fragment translational energy distribution obtained from the ion image is presented in Fig. 23(b). The monotonic decrease of the probability with the increasing translational energy is the typical characteristic of dissociation from a molecule undergoing internal conversion to the ground electronic state with no exit barrier. The similar phenomenon was also observed in the photodissociation of d_{10} -ethylbenzene and *n*-propylbenzene, as shown in Figs. 24 and 25.

However, the photofragment ion images of ethylbenzene obtained at 248 nm are significantly different from those obtained at 193 nm. Figures 26(a) and 26(b) illustrate the ion images of phenyl radicals obtained from the photodissociation of ethylbenzene at 248 nm at two different delay times. It clearly shows that the image of fragment $m/e = 91$ has three components. A component located on both wings and a line-shape component

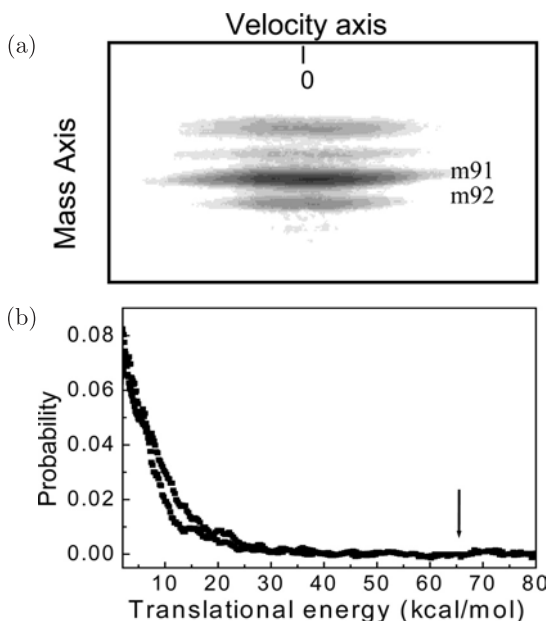


Fig. 23. (a) Photofragment ion images from the photodissociation of ethylbenzene at 193 nm. The total delay time between the pump laser and probe laser pulses is 22 μ s. Fragment $m/e = 92$ is the ^{13}C isotope of fragment $m/e = 91$, and $m/e = 90$ and 89 result from two-photon dissociation. (b) The fragment translational energy distribution for the reaction $\text{C}_6\text{H}_5\text{C}_2\text{H}_5 \rightarrow \text{C}_6\text{H}_5\text{CH}_2 + \text{CH}_3$. The arrow indicates the maximum available energy from one-photon dissociation.

superimposed on a disk-like component at the center. As the delay time between the pump and the probe laser pulses increased, the component on both wings moved rapidly towards the outside, and the length of the line-shape component at the center increased. On the other hand, the size of the disk-like image did not change, but the intensity decreased with the increase in the delay time. These three components can be assigned easily according to the relationship illustrated in Fig. 2. The component on the wings and the line-shape component are the phenyl radical fragments that resulted from the dissociation of ethylbenzene with large recoil velocity and small recoil velocity, respectively. The third component, the disk-like image, was from the dissociative ionization of undissociated hot ethylbenzene by VUV photoionization due to the slow dissociation rate at 248 nm.

Among these three components, the decay rate of the disk-like component was found to be $1.1 \times 10^5 \text{ s}^{-1}$, as illustrated in Fig. 26(c). The

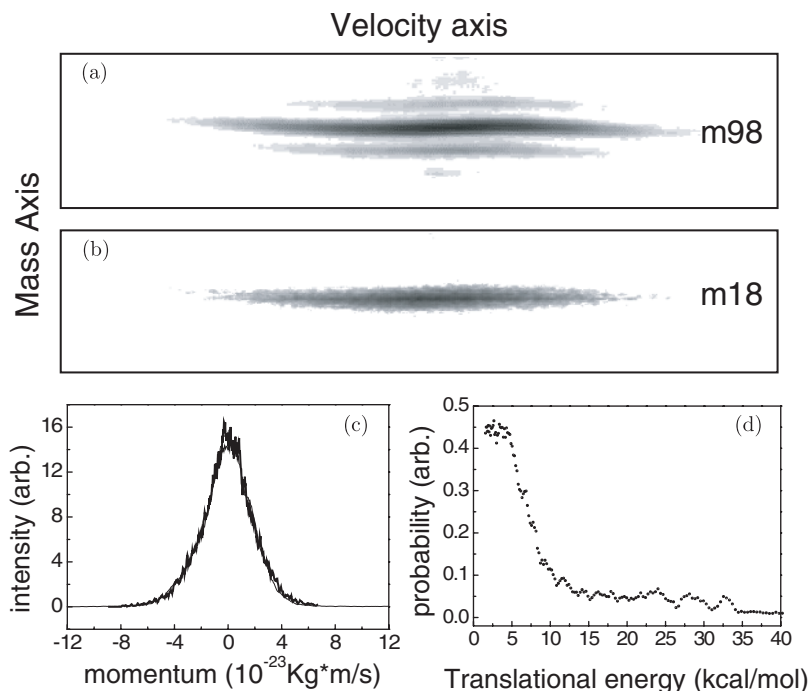


Fig. 24. Ion image of photofragment (a) $m/e = 98$, (b) $m/e = 18$ from photodissociation of d_{10} -ethylbenzene at 193 nm. The delay times between pump and probe laser pulses are 30 μs and 7 μs , respectively. (c) The translational momentum distributions of $m/e = 18$ (thin solid line) and 98 (thick solid line). (d) The fragment translational energy distribution for the reaction $\text{C}_6\text{D}_5\text{C}_2\text{D}_5 \rightarrow \text{C}_6\text{D}_5\text{CD}_2 + \text{CD}_3$.

product growth rates of the phenyl radical with large recoil velocity and small recoil velocity components were obtained by forward convolution simulation from the images at various delay times. It shows that the product growth rate of the large recoil velocity component is faster than $1 \times 10^6 \text{ s}^{-1}$, and that of the small velocity component is $1 \times 10^5 \text{ s}^{-1}$. The photofragment translational energy distribution obtained from the line-shape ion image by forward convolution is shown in Fig. 26(d). The different dissociation rates suggest that there are two mechanisms involved in the dissociation of ethylbenzene at 248 nm. For the component of small recoil velocity, the average translational energy release is small and the dissociation rate is slow. These are the characteristics of dissociation from the ground electronic state. In contrast, the dissociation rate for the component of large recoil velocity is fast, the average released translational energy is large, and the peak of the

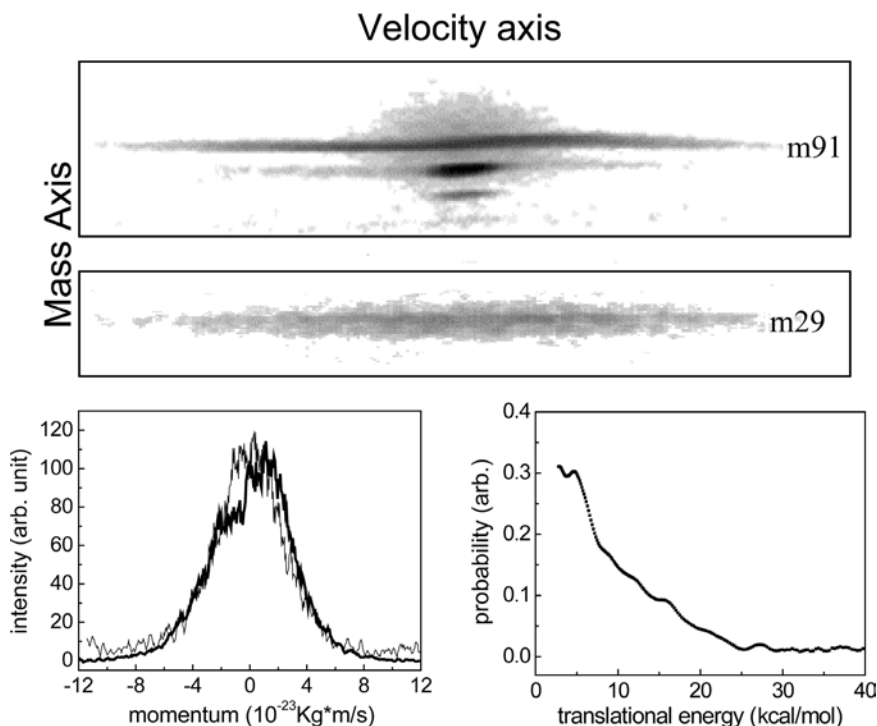


Fig. 25. Ion image of photofragment (a) $m/e = 91$, (b) $m/e = 29$, from photodissociation of *n*-propylbenzene at 193 nm. The delay times between pump and probe laser pulses are 28 μ s and 8 μ s, respectively. (c) The translational momentum distributions of $m/e = 29$ (thin solid line) and 91 (thick solid line). (d) The fragment translational energy distribution for the reaction $C_6H_5C_3H_7 \rightarrow C_6H_5CH_2 + C_2H_5$.

distribution is located at 18 kcal/mol. These are the characteristics of dissociation from a repulsive excited state, or dissociation from an electronic state with an exit barrier.

Similar results were obtained for the photodissociation of *d*₁₀-ethylbenzene and *n*-propylbenzene, as illustrated in Figs. 27 and 28. For *n*-propylbenzene, the intensity decay rate of the disk-like image was found to be $4.9 \times 10^4 \text{ s}^{-1}$, and the product growth rates obtained from simulation are $5 \times 10^4 \text{ s}^{-1}$ and larger than $5 \times 10^5 \text{ s}^{-1}$ for the slow velocity component and the fast recoil velocity component, respectively.

A photolysis laser fluence dependence measurement was carried out in the region of 0.7 to 10 mJ/cm² for 193 nm and 2.2 to 33 mJ/cm² for 248 nm. The shapes and the ratio of the components in the translational energy

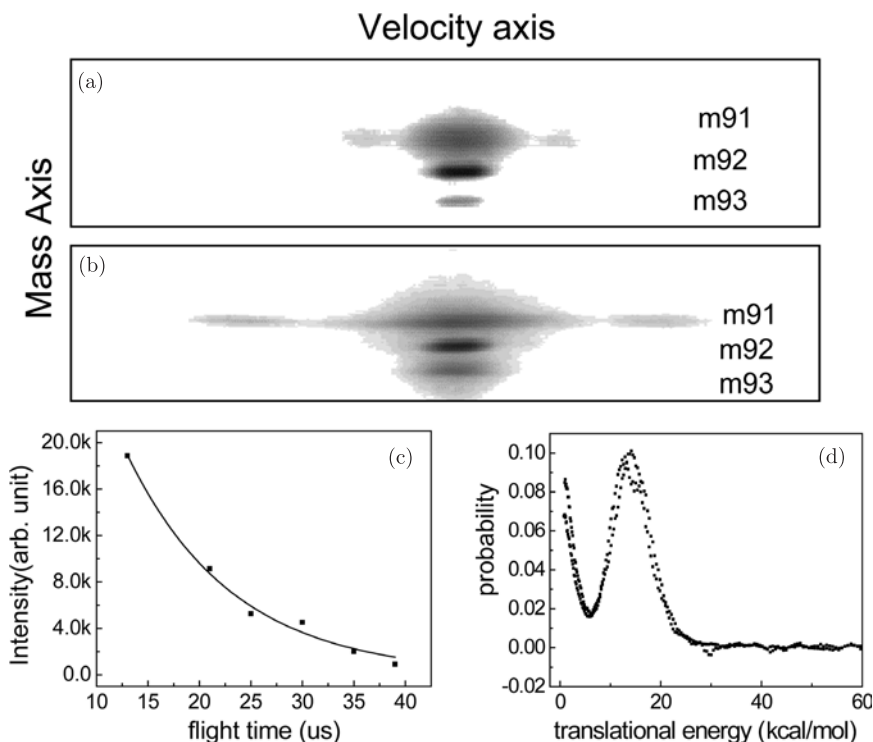


Fig. 26. Ion images of phenyl radical obtained from the photodissociation of ethylbenzene at 248 nm at two different delay times: (a) 15 μs , (b) 32 μs . (c) Intensity decay of the disk-like image as a function of delay times. A decay rate of 10^5 s^{-1} was obtained. (d) The fragment translational energy distribution for the reaction $\text{C}_6\text{H}_5\text{C}_2\text{H}_5 \rightarrow \text{C}_6\text{H}_5\text{CH}_2 + \text{CH}_3$.

distribution do not change with photolysis laser intensity and the maximum translational energies are less than the available energies from one-photon dissociation. The measurements suggest that they all result from one-photon dissociation.

Figure 29 shows the potential energy diagram of the reaction $\text{C}_6\text{H}_5\text{C}_2\text{H}_5 \rightarrow \text{C}_6\text{H}_5\text{CH}_2 + \text{CH}_3$ obtained from an *ab initio* calculation (B3LYP/6-31+G*). In the ground electronic state, the methyl group changes gradually from pyramidal geometry to planar geometry as the C–C bond length increases during the dissociation process. There is no exit barrier for the dissociation from the ground state. This indicates that the slow component in the translational energy distribution results from the ground state dissociation and the fast component did *not* result from the ground

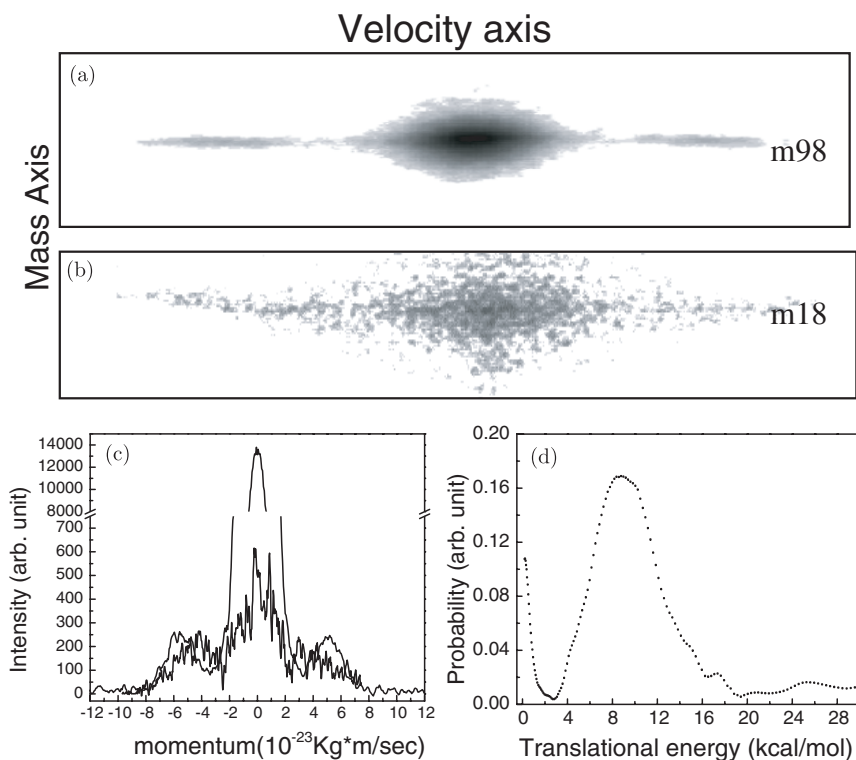


Fig. 27. Fragment ion images obtained from the photodissociation of d_{10} -ethylbenzene at 248 nm. (a) $m/e = 98$, delay time $30 \mu\text{s}$. (b) $m/e = 18$, delay time $7 \mu\text{s}$. (c) The translational momentum distributions of $m/e = 18$ (thin solid line) and 98 (thick solid line). (d) The fragment translational energy distribution for the reaction $\text{C}_6\text{D}_5\text{C}_2\text{D}_5 \rightarrow \text{C}_6\text{D}_5\text{CD}_2 + \text{CD}_3$.

state dissociation. The fast component must result from either through the coupling between the stable and repulsive states, or a lower electronic state with an exit barrier. Figure 29 also shows the potential energy diagram in the first triplet state for the same dissociation channel. The exit barrier height is about 31 kcal/mol. Similar potential energy diagrams were found in the photodissociation channel of n -propylbenzene; the corresponding calculated energies for n -propylbenzene are shown in parentheses in Fig. 29. The dissociation from the ground state is barrierless. However, the dissociation from the first triplet state has a barrier height of 32 kcal/mol. Although the other electronic states cannot be definitively excluded (no potential energy surfaces for the other excited states are available), the exit

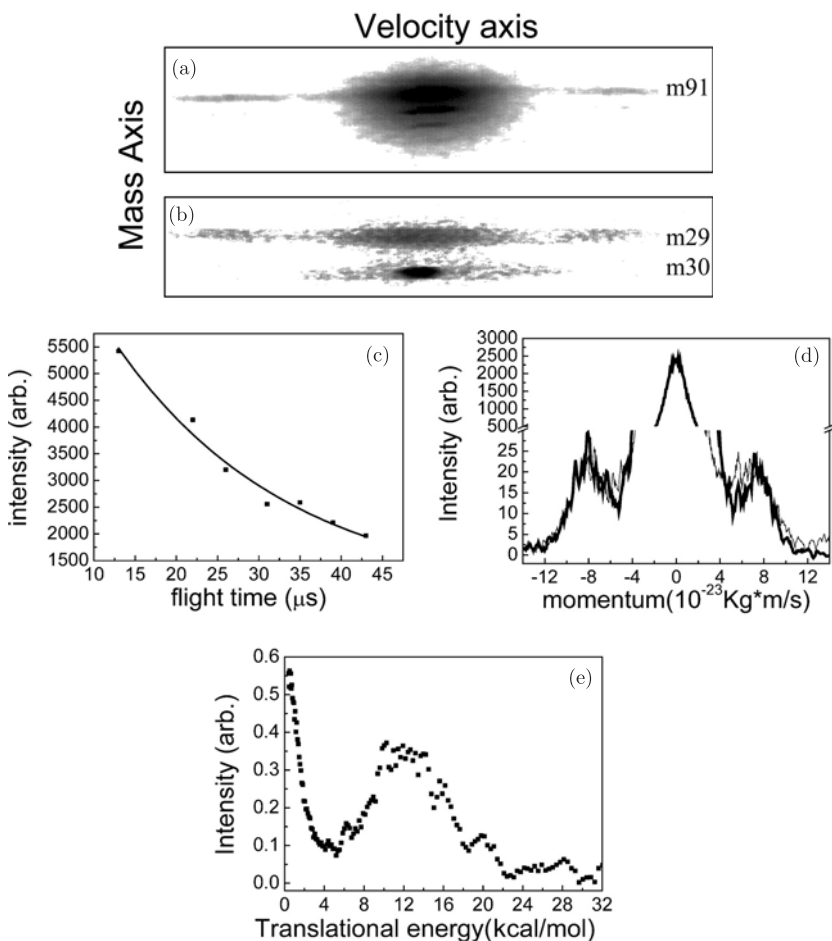


Fig. 28. Ion image of photofragment (a) $m/e = 91$, (b) $m/e = 29$, from photodissociation of *n*-propylbenzene at 248 nm. The delay times between the pump and probe laser pulses are 20 μs and 5 μs , respectively. The image of $m/e = 30$ is the mass indicator. (c) The intensity decay of the disk-like image, a dissociation rate of $4.9 \times 10^4 \text{ s}^{-1}$ was obtained. (d) The translational momentum distributions of $m/e = 29$ (thin solid line) and 91 (thick solid line). (e) The fragment translational energy distribution for the reaction $\text{C}_6\text{H}_5\text{C}_3\text{H}_7 \rightarrow \text{C}_6\text{H}_5\text{CH}_2 + \text{C}_2\text{H}_5$.

barrier in the first triplet state and the translational energy distribution of the fast component in both ethylbenzene and propylbenzene suggest that dissociation upon intersystem crossing to the first triplet state is a likely explanation for the fast component in the translational energy distribution of ethylbenzene and *n*-propylbenzene.

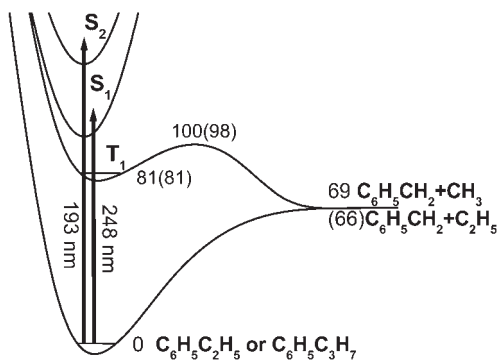


Fig. 29. The S_0 and T_1 energy diagrams of reactions of $C_6H_5C_2H_5 \rightarrow C_6H_5CH_2 + CH_3$ and $C_6H_5C_3H_7 \rightarrow C_6H_5CH_2 + C_2H_5$ obtained by an *ab initio* calculation. The numbers are the zero point energies for the S_0 and T_1 states, the transition states, and the products. The numbers in the parentheses are the energies of propylbenzene.

Two-color photoionization has been applied to the measurement of the time evolution of laser excited first singlet state of benzene, toluene, ethylbenzene, and xylene.^{58–60} The observed photoionization signals exhibited a bi-exponential dependence upon the time delay between the pump and ionization lasers. The fast exponential decay resulted from the relaxation of the S_1 state, and the slow exponential decay was interpreted as the decay of the T_1 state after the $S_1 \rightarrow T_1$ intersystem crossing. Although the triplet state was found to play an important role in the relaxation of the S_1 state in those molecules, the interpretation of the T_1 state decay was only attributed to the intersystem crossing from the T_1 state to the S_0 state. No dissociation from the T_1 state following the excitation of the first singlet state has been reported. In those studies, the decay rates were monitored as a function of vibrational energy and were found to increase with energy. For ethylbenzene, the decay rate of the triplet state was found to be $4 \times 10^5 \text{ s}^{-1}$ at the excitation wavelength of 266 nm.⁵⁸ In this work, the excitation energy is larger than the energy in the previous study, and the increase of the decay rate, therefore, is expected. However, additional channels may open as the energy increases and result in the competition with the intersystem crossing from the T_1 state to the S_0 state. Our experimental results demonstrate that the dissociation not only competes with the intersystem crossing but also becomes the dominant channel at the excitation wavelength of 248 nm.

The fragment translational energy distribution and dissociation rate measurements of ethylbenzene and *n*-propylbenzene suggest that the

dissociation mechanisms at 193 and 248 nm are different. For ethylbenzene and *n*-propylbenzene, molecules following 193 nm excitation dissociate through the hot molecule mechanism. It indicates that the coupling between the S_2 and S_0 states, or the coupling between the S_2 and S_0 states through some intermediate states is very strong at this energy level. As a result, ethylbenzene and *n*-propylbenzene excited by a 193 nm photon converts to ground electronic state prior to dissociation. On the other hand, most of the ethylbenzene and *n*-propylbenzene following 248 nm excitation dissociate from the first triplet state. The dissociation of ethylbenzene and *n*-propylbenzene from the S_0 state could result from the direct internal conversion $S_1 \rightarrow S_0$ or through the two-step intersystem crossing $S_1 \rightarrow T_1 \rightarrow S_0$. Therefore, the minimum values of 0.75 and 0.8 for the intersystem crossing quantum yield of ethylbenzene and propylbenzene, respectively, can be determined from the ratio of the fast and slow components in the translational energy distribution. The high intersystem crossing quantum yield indicates the strong coupling between the S_1 and T_1 states at this energy level. The results suggest that dissociation from the first triplet state may play a very important role in the photoexcitation of alkylbenzenes in the S_1 state.

4. Conclusions

The photodissociation studies of benzene and its alkyl derivatives demonstrated the capability of measuring photofragment translational spectroscopy using multimass ion imaging technique. Compared to the other methods in the translational spectroscopy measurement, these studies also illustrated several advantages of this technique. They are summarized as followings. (1) Many fragments' translational energy distributions can be measured simultaneously in the center-of-mass frame. (2) The fragment cracking in the ionization process is minimized due to the low VUV photon energy. (3) Neutral molecule dissociation can be investigated without the interference from dissociative ionization. (4) High detection sensitivity allows us to study the photodissociation under low photolysis laser fluence. As a result, one-photon dissociation can be easily distinguished from two-photon dissociation. (5) The range of dissociation rate that can be measured is large. These advantages become particularly important in the photodissociation studies of large molecules with multi-dissociation channels and slow dissociation rates.

Acknowledgments

This work was partly supported by the National Science Council under contract NSC 91-2113-M-001-023.

References

1. A. M. Wodtke and Y. T. Lee, "High resolution photofragmentation – Translational spectroscopy", in *Molecular Photodissociation Dynamics*, eds. M. N. R. Ashfold and J. E. Baggett, Royal Society of Chemistry, London, 1987.
2. D. W. Chandler and P. L. Houston, *J. Chem. Phys.* **87**, 1445, (1987).
3. A. T. J. B. Eppink and D. H. Parker, *Rev. Sci. Instrum.* **68**, 3477 (1997).
4. M. Ahmed, D. S. Peterka and A. G. Suits, *Chem. Phys. Lett.* **317**, 264 (2000).
5. M. Mons and I. Dimicoli, *Chem. Phys. Lett.* **131**, 298 (1986).
6. C. K. Ni and G. W. Flynn, *Chem. Phys. Lett.* **210**, 333 (1993).
7. N. Nakashima and K. Yoshihara, *J. Phys. Chem.* **93**, 7763 (1989).
8. Y. T. Lee, "Thirty years of Scattering", in *Modern Trends in Chemical Dynamics, An International Symposium*, Dec. 1996, Taipei, Taiwan.
9. S.-T. Tsai, C.-K. Lin, Y. T. Lee and C. K. Ni, *Rev. Sci. Instrum.* **72**, 1963 (2001).
10. J. H. Moore, C. C. Davis and M. A. Coplan, *Building Scientific Apparatus*, (Addison-Wesley, 1983).
11. C. E. Otis, J. L. Knee and P. M. Johnson, *J. Chem. Phys.* **78**, 2091 (1983).
12. N. Nakashima and K. Yoshihara, *J. Chem. Phys.* **77**, 6040 (1982).
13. M. Sumitani, D. V. Oconnor, Y. Takagi, N. Nakashima, K. Kamogawa, Y. Udagawa and K. Yoshihara, *Chem. Phys.* **93**, 359 (1985).
14. M. A. Duncan, T. G. Dietz, M. G. Liverman and R. E. Smalley, *J. Phys. Chem.* **85**, 7 (1981).
15. J. K. Foote, M. H. Mallon and J. N. Pitts, Jr., *J. Am. Chem. Soc.* **88**, 3698 (1966).
16. K. Shindo and S. Lipsky, *J. Chem. Phys.* **45**, 2292 (1966).
17. H. R. Ward and J. S. Wishnok, *J. Am. Chem. Soc.* **90**, 5353 (1968).
18. N. Nakashima and K. Yoshihara, *J. Chem. Phys.* **79**, 2727 (1983).
19. P. Reilly and K. L. Kompa, *J. Chem. Phys.* **73**, 5468 (1980).
20. W. Radloff, Th. Freudenberg, H.-H. Ritze, V. Stert, F. Noack and I. V. Hertel, *Chem. Phys. Lett.* **261**, 301 (1996).
21. P. Farmanara, O. Steinkellner, M. T. Wick, M. Wittmann, G. Korn, V. Stern and W. Radloff, *J. Chem. Phys.* **111**, 6264 (1999).
22. H. R. Ward, J. S. Wishnok and P. D. Sherman, Jr., *J. Am. Chem. Soc.* **89**, 162 (1967).
23. L. Kaplan and K. E. Wilzbach, *J. Am. Chem. Soc.* **89**, 1030 (1967).
24. L. Kaplan, S. P. Walch and K. E. Wilzbach, *J. Am. Chem. Soc.* **90**, 5646 (1968).
25. F. Mellows and S. Lipsky, *J. Phys. Chem.* **70**, 4076 (1966).
26. D. Bryce-Smith and A. Gilber, *Tetrahedron* **32**, 1309 (1976).

27. K. E. Wilzbach, J. S. Ritcher and L. Kaplan, *J. Am. Chem. Soc.* **89**, 1031 (1968).
28. A. Yokoyama, X. Zhao, E. J. Hintsa, R. E. Continetti and Y. T. Lee, *J. Chem. Phys.* **92**, 4222 (1990).
29. A. M. Mebel, S. H. Lin, X. M. Yang and Y. T. Lee, *J. Phys. Chem.* **101**, 6781 (1997).
30. S. T. Tsai, C. K. Lin, Y. T. Lee and C. K. Ni, *J. Chem. Phys.* **113**, 67 (2000).
31. S. T. Tsai, C. L. Huang, Y. T. Lee and C. K. Ni, *J. Chem. Phys.* **115**, 2449 (2001).
32. J. Park, R. Bersohn and I. Oref, *J. Chem. Phys.* **93**, 5700 (1990).
33. M. Suto, X. Wang, J. Shan and L. C. Lee, *J. Quant. Spectrosc. Radiat. Transfer* **48**, 79 (1992).
34. K. E. Wilzbach and L. Kaplan, *J. Am. Chem. Soc.* **86**, 2307 (1964).
35. A. W. Burgstahler and P. L. Chien, *J. Am. Chem. Soc.* **86**, 2940 (1964).
36. L. Kaplan, K. E. Wilzbach, W. G. Brown and Shu Shu Yang, *J. Am. Chem. Soc.* **87**, 675 (1965).
37. K. E. Wilzbach and L. Kaplan, *J. Am. Chem. Soc.* **87**, 4004 (1965).
38. I. E. Den Besten, L. Kaplan and K. E. Wilzbach, *J. Am. Chem. Soc.* **90**, 5868 (1968).
39. D. Bryce-Smith and A. Gilbert, *Rearrangement in Ground and Excited States*, ed. P. De Mayo (Academic Press, New York, 1980) Vol. 3.
40. A. H. Jackson, G. W. Kenner, G. McGillvray and G. S. Sach, *J. Am. Chem. Soc.* **87**, 675 (1965).
41. K. E. Wilzbach, A. L. Harkness and L. Kaplan, *J. Am. Chem. Soc.* **90**, 1116 (1968).
42. K. E. Wilzbach and L. Kaplan, *J. Am. Chem. Soc.* **86**, 2307 (1964).
43. H. Hippler, V. Schubert, J. Troe and H. Wendelken, *J. Chem. Phys. Lett.* **84**, 253 (1981).
44. R. Fröchtenicht, *J. Chem. Phys.* **102**, 4850 (1994).
45. N. Nakashima and K. Yoshihara, *J. Phys. Chem.* **93**, 7763 (1989).
46. K. Luther, J. Troe and K. L. Weitzel, *J. Phys. Chem.* **94**, 6316 (1990).
47. U. Brand, H. Hippler, L. Lindemann and J. Troe, *J. Phys. Chem.* **94**, 6305 (1990).
48. T. Shimada, Y. Ojima, N. Nakashima, Y. Izawa and C. Yamanaka, *J. Phys. Chem.* **96**, 6298 (1992).
49. C. K. Lin, C. L. Huang, J. C. Jiang, A. H. H. Chang, Y. T. Lee, S. H. Lin and C. K. Ni, *J. Am. Chem. Soc.* **124**, 4068 (2002).
50. Y. Kajii, K. Obi, I. Tanaka, N. Ikeda, N. Nakashima and K. Yoshihara, *J. Chem. Phys.* **86**, 6115 (1987).
51. N. Ikeda, N. Nakashima and K. Yoshihara, *J. Chem. Phys.* **82**, 5285 (1985).
52. J. Troe and W. Wieters, *J. Chem. Phys.* **71**, 3931 (1979).
53. S. Lange, K. Luther, T. Rech, A. M. Schmoltner and J. Troe, *J. Phys. Chem.* **98**, 6509 (1994).
54. J. B. Hopkins, D. E. Powers and R. E. Smalley, *J. Chem. Phys.* **72**, 2905 (1980); *ibid.* **72**, 5039 (1980); *ibid.* **73**, 683 (1980); J. B. Hopkins,

- D. E. Powers, S. Mukamel and R. E. Smalley, *ibid.* **72**, 5049 (1980); S. Mukamel and R. E. Smalley, *ibid.* **73**, 4156 (1980).
55. D. R. Borst and D. W. Pratt, *J. Chem. Phys.* **113**, 3658 (2000), D. R. Borst, P. W. Joireman, D. W. Pratt, E. G. Robertson and J. P. Simons, *ibid.* **116**, 7057 (2002).
56. C. L. Huang, J. C. Jiang, Y. T. Lee, S. H. Lin and C. K. Ni, *J. Chem. Phys.* **116**, 7779 (2002).
57. C. L. Huang, J. C. Jiang, Y. T. Lee and C. K. Ni, *J. Chem. Phys.* **117**, 7034 (2002).
58. M. A. Duncan, T. G. Dietz, M. G. Liverman and R. E. Smalley, *J. Phys. Chem.* **85**, 7 (1981).
59. T. G. Dietz, M. A. Duncan, M. G. Liverman and R. E. Smalley, *J. Chem. Phys.* **76**, 1227 (1982).
60. H. G. Lohmannsroben, K. Luther and M. Stuke, *J. Phys. Chem.* **91**, 3499 (1987).

This page intentionally left blank

CHAPTER 5

REACTIONS OF NEUTRAL TRANSITION METAL ATOMS WITH SMALL MOLECULES IN THE GAS PHASE

Jonathan J. Schroden and H. Floyd Davis

*Department of Chemistry and Chemical Biology,
Cornell University, Ithaca, NY 14853, USA*

Contents

1. Introduction	216
1.1. Previous Theoretical Work	216
1.2. Previous Experimental Work	220
1.2.1. M + Oxygen-Containing Molecules	220
1.2.2. M + Hydrocarbons	221
2. Experimental Details	226
2.1. Production of the Beams	227
2.2. Detection	228
2.3. Sample Data: Y(a^2D) + CH ₃ OH	229
3. Y(a^2D) + Cyclopropane and Propene	234
3.1. Yttrium + Cyclopropane: $E_{\text{coll}} = 18.5$ kcal/mol	236
3.2. Yttrium + Cyclopropane: Collision Energy Dependence	238
3.3. Yttrium + Propene: $E_{\text{coll}} = 25.2$ kcal/mol	240
3.4. Yttrium + Propene: Collision Energy Dependence	242
3.5. Non-Reactive Scattering in Cyclopropane and Propene Reactions	245
3.6. Yttrium + Cyclopropane \rightarrow YC ₃ H ₄ + H ₂	248
3.7. YCH ₂ + C ₂ H ₄ from the Cyclopropane Reaction	250
3.8. YC ₃ H ₄ + H ₂ and YH ₂ + C ₃ H ₄ from the Propene Reaction	251
3.9. YCH ₂ + C ₂ H ₄ Formation from the Propene Reaction	253
4. Y(a^2D) + Four Butene Isomers	255
4.1. Y + Butenes: $E_{\text{coll}} = 26.6$ kcal/mol	256
4.2. Y + Butenes: $E_{\text{coll}} = 11.0$ kcal/mol	260
4.3. Y + Butenes Reaction Mechanisms	260
5. Conclusions	266
6. Future Directions	268
6.1. The Role of Vibrational Excitation in Transition Metal Reactivity	268
6.2. Reaction Dynamics of Partially-Ligated Species	270

Acknowledgments

272

References

273

1. Introduction

Our lives would be very different without the advent of transition metal catalysts. An extraordinary number of chemical transformations and industrial processes require either homogeneous or heterogeneous catalysts in order to be commercially viable. Some examples include the production of polymers such as polyethylene (plastics), functionalization of abundant saturated hydrocarbons to produce more useful molecules, the epoxidation of ethene, and many more. Unfortunately, while chemical engineers have in some cases been able to make these processes commercially feasible, many of the fundamental factors that influence why certain transition metals form good catalysts while others do not are not well understood. Thus, there has in recent years been a strong research effort, both theoretically and experimentally, to better understand the fundamental aspects of transition metal chemistry. Such an understanding would be invaluable to the design of better catalysts, which should have many positive repercussions, including greater efficiency of chemical processes and less waste generation, both of which are beneficial to industry and to the average citizen.

One reason why many fundamental aspects of transition metal chemistry are not well understood is that the reactions can be very complex. The variations in electronic structure among transition metals, combined with the extremely large number of available ligands and solvents, hinder the ability to probe the most important fundamental principles governing this type of chemistry. Therefore, the majority of studies aimed at developing a molecular level of understanding have focused on simpler, model systems, usually concentrating on reactions of naked transition metal atoms (M) in the gas phase, for which solvent and ligand effects are absent. As will be described in detail in subsequent sections, this is the approach that our research group has adopted as well. We will begin with a brief review of neutral transition metal atom chemistry in the gas phase.

1.1. *Previous Theoretical Work*

Perhaps the most comprehensive body of theoretical work on the bonding and reactivity of neutral transition metal atoms with small molecules has been compiled by the Siegbahn group in Stockholm.^{1–40} It would be

impossible to describe all of their results here; instead only the most salient aspects will be presented.

The earliest studies by Siegbahn *et al.* focused on the binding and oxidative addition of small molecules to Ni,¹⁻¹³ Fe,^{3,8,14} Co,^{8,14} Cu,^{8,14} Cr,⁹ Nb,¹⁵ Rh,¹⁵ and Pd.^{1,16,17} Using the contracted configuration interaction (CCI) method,¹ binding energies and potential energy barrier heights for oxidative addition were determined. These calculations stressed the role of the electronic state of the metal in bonding; for example for Ni it was found that the active bonding state was always d^9s^1 , and not the d^8s^2 ground state, which was found to be repulsive towards ligands. Subsequently, their focus shifted from centering on a particular metal atom to investigating trends of binding and transition state energies for an entire row of transition metals. Because of the similar sizes of the $4d$ and $5s$ orbitals, and small relativistic effects (relative to the third row), the second transition metal row was chosen as the benchmark. Reactions of $M + CH_4$,¹⁸⁻²⁴ C_2H_2 ,²⁵ C_2H_4 ,^{22,26,27} C_2H_6 ,^{18,22,28} $c-C_3H_6$,^{22,28} $c-C_4H_8$,²⁸ H_2O ,²⁹ and NH_3 ,³⁰ as well as bonding of M to O ,³¹ O_2 ,³² CH_2 ,³¹ H ,^{33,34} F ,^{33,34} Cl ,^{33,34} CH_3 ,^{35,36} $CH_2(OH)$,³⁵ $CH_2(NH_2)$,³⁵ CH_2F ,³⁵ C_2H_3 ,³⁶ and C_2H_4 ,³⁶ and reactions involving insertion of a small molecule into a metal-ligand bond³⁷⁻³⁹ were investigated. These studies utilized the modified coupled pair functional (MCPF) method, with the accuracy of their later studies improved via the use of parametrized configuration interaction (PCI-80).⁴⁰ A number of interesting trends were elucidated through this approach, both with regard to bond strengths and to barrier heights for insertion of metals into covalent bonds. For insertion of M into the C-H bond of methane, it was found that the avoided crossing between the repulsive ground states of the metal atoms and attractive, low-spin excited states (diabatic curves) gave rise to adiabatic potential energy barriers for insertion (see Fig. 1).^{19,20,24} Atoms to the left of the second transition metal row (Y, Zr, Nb) had large potential energy barriers for insertion due to their repulsive $4d^n5s^2$ ground electronic states and large promotion energies to attractive excited states with $4d^{n+1}5s^1$ configurations, while the atoms in the middle of the row (Mo, Tc) had large barriers due to loss of exchange energy. The atoms on the right side of the second row had much lower barriers due to the presence of low-lying $4d^{n+1}5s^1$ and $4d^{n+2}5s^0$ states. The s^0 state allows for avoidance of repulsion to the σ -electron density of the C-H bond, while the s^1 state is desirable for formation of the two new bonds in the insertion intermediate.^{19,20,24} It was also discovered that the barrier heights for insertion into the C-H bond of methane or ethane were lower than for

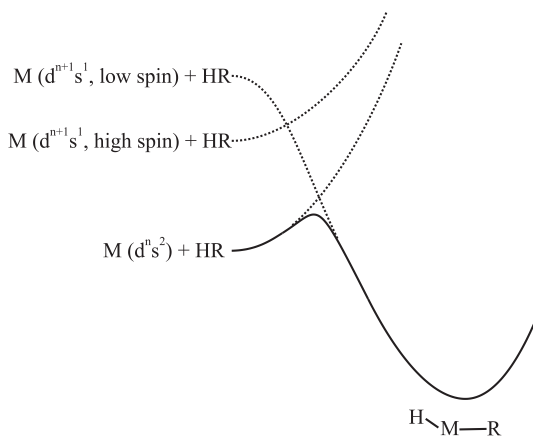


Fig. 1. Schematic potential energy curves for a neutral transition metal atom (M) inserting into the H-R bond of a hydrocarbon. Diabatic curves are shown as dashed lines, adiabatic curve shown as a solid line.

insertion into the C-C bond of ethane.^{2,18,22} This was explained by considering the initial bonding interactions between M and the hydrocarbon. For insertion into a C-H bond, there is an initial donation of electron density from the hydrocarbon σ orbital to the metal s orbital, and a concurrent back-donation of electron density from the metal d orbital to a high-lying σ^* orbital on the hydrocarbon (see Fig. 2). In both bonding interactions, because H atoms are spherically symmetric, there is only a minor distortion of the hydrocarbon during the insertion process. Furthermore, multicenter bonding at the transition state is favorable in reactions involving H atoms. For C-C insertion, on the other hand, in order to achieve the optimal orbital overlap for back-donation of electron density, the methyl groups must undergo a significant tilt, with the C-C bond nearly broken at the transition state. This, together with the directionality of the C-C bond which leads to much less favorable multicenter bonding, leads to larger potential energy barriers for C-C insertion than for C-H insertion.^{2,18,22}

For bonding to ligands with π -electrons, such as ethene, the Dewar-Chatt-Duncanson^{41,42} (DCD) model of bonding was found to be quite appropriate. This model describes the bonding as involving two processes: donation of π -electron density from the ligand to the metal, and back-donation of electron density from the metal d -orbitals into a high-lying π^* anti-bonding orbital of the ligand (see Fig. 3). This type of bonding interaction is strongest for atoms to the right of the transition metal row

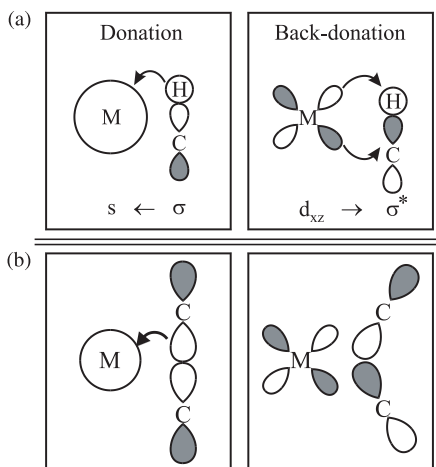


Fig. 2. Schematic bonding pictures for transition metal atom (M) insertion into (a) a C-H bond, or (b) a C-C bond of a hydrocarbon.

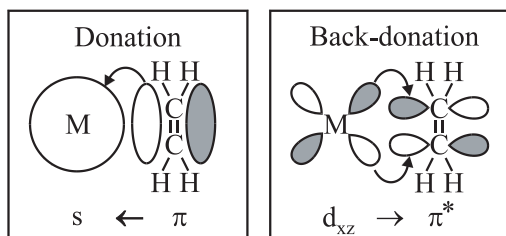


Fig. 3. Schematic bonding pictures for transition metal atoms (M) binding to C_2H_4 via the Dewar-Chat-Duncanson model.

because of their low-lying s^1 and s^0 states which are good for accepting electron density from the ligand. Their doubly-occupied d orbitals, which are good for back-donation of electron density to the π^* orbitals of the ligand, also play an important role in the bonding interaction.^{26,27} For binding to ligands with lone pairs of electrons, such as H_2O or NH_3 , it was found that the atoms to the left of the row had significantly larger bond strengths than those to the right because their relatively empty $4d$ orbitals allowed for less repulsion toward the electron lone pairs on the ligands.²⁹⁻³⁵ It should also be mentioned that several other groups have made important contributions to these ideas, most notably those of Bauschlicher⁴³ and Goddard.⁴⁴

Unfortunately, following their seminal paper on C–H bond insertion of methane for all three transition metal rows, Siegbahn *et al.* changed their focus to biological systems. However, several other groups have taken to studying these systems using newer, more advanced computational methods such as density functional theory (DFT) and coupled cluster theory. For example, in addition to performing experimental work which will be described in more detail shortly, Weisshaar *et al.* have looked quite extensively at the reactions of Y and Zr with C_2H_4 using DFT.^{45–47} They calculated the entire reaction coordinate for both systems, with special attention paid to the mechanisms for reaction and to the presence of entrance- and exit-channel barriers. For Zr, the role of the low-lying singlet excited state was also examined.⁴⁶ For both reactions, it was found that the previously-assumed stepwise mechanism, which proceeds via π -complex formation between the metal atom and ethene, followed by insertion into a C–H bond and H migration to the metal center with subsequent elimination of H_2 , contained a very large barrier in the exit-channel.^{46,47} In fact, the height of this barrier in each case was large enough to be inconsistent with their experimental finding that reaction occurred in flow cells at room temperature, so this stepwise mechanism was ruled out. Instead, an alternate mechanism, in which a H atom migrates to the H atom attached to the metal, followed by concerted H_2 loss over a multicentered transition state (MCTS) was proposed.^{46,47} This type of concerted mechanism has also been found to be the dominant one in theoretical studies of the $\text{Y} + \text{H}_2\text{CO}$ ⁴⁸ and $\text{Y} + \text{CH}_3\text{CHO}$ ⁴⁹ reactions performed by Bayse using coupled-cluster *ab initio* methods (CCSD(T)). Calculations of Y binding to acetylene and vinylidene,⁵⁰ and of the reaction $\text{Y} + \text{C}_2\text{H}_2$ ⁵¹ have also been performed recently by Glendenning.

1.2. Previous Experimental Work

1.2.1. M + Oxygen-Containing Molecules

Some of the earliest experimental studies of neutral transition metal atom reactions in the gas phase focused on reactions with oxidants ($\text{OX} = \text{O}_2$, NO , N_2O , SO_2 , etc.), using beam-gas,^{52,53} crossed molecular beam,^{54,55} and flow-tube techniques.⁵⁶ A few reactions with halides were also studied. Some of these studies were able to obtain product rovibrational state distributions that could be fairly well simulated using various statistical theories,^{52,54,55} while others focused on the spectroscopy of the MO products.⁵³ Subsequently, rate constants and activation energies for reactions of nearly all the transition metals and all the lanthanides with various oxidant molecules

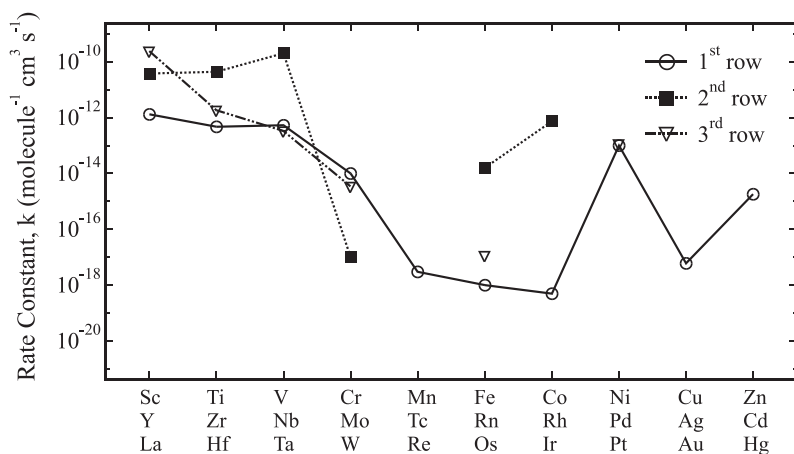


Fig. 4. Room temperature second-order rate constants for the $M + N_2O$ reaction for all three transition metal rows. Values taken from Refs. 73 and 76. Missing points were either not studied or exhibited no reaction with N_2O .

were measured by Campbell using a laser photolysis/laser-induced fluorescence (LIF) technique.^{57–81} Honma and co-workers,⁸² as well as several other groups,^{83,84} have also studied some of these systems using similar techniques. There were interesting aspects of the reactivity of each metal, and in addition, several overall trends were observed: the reactions with O_2 and N_2O were generally bimolecular, presumably forming MO as the oxygen-atom abstraction product (reactions with NO were termolecular, forming an MNO complex), $d^{n+1}s^1$ states were generally more reactive than $d^n s^2$ states for a given metal, and the trend in reactivity for the three rows followed the pattern $2^{nd} > 3^{rd} \approx 1^{st}$ (see Fig. 4).^{57–81}

Attempts were made at explaining the trends in reactivity through the use of both an electron-transfer model⁸⁵ and a resonance interaction model,^{86,87} but without success. It seems that the trends in reactivity on a fine scale cannot be easily explained by such simple models, but instead depend on a multitude of factors, which may include the ionization potential of the metal, the electron affinity of the oxidant molecule, the energy gap between $d^n s^2$ and $d^{n+1}s^1$ states, the $M-O$ bond strength, and the thermodynamics of the reaction.^{57–81}

1.2.2. $M + \text{Hydrocarbons}$

Reactions of neutral transition metal atoms with hydrocarbons have received considerable attention, most notably by Weisshaar's group at

the University of Wisconsin-Madison,^{88–95} and by Mitchell, Hackett and co-workers at the National Research Council in Canada.^{96–108} Campbell^{109–112} and Honma^{113,114} have also studied a few systems. Reactions of the majority of the transition metals were studied with small linear alkanes (methane, ethane, propane, *n*-butane) and cyclopropane.^{88–94,96,107,109–115} It was found that very few metal atoms reacted with methane at the thermal energies employed in these studies (typically only a few kcal/mol or less). In fact, only Rh,¹⁰⁹ Ir,¹¹⁰ Pd,¹¹⁵ and Pt^{93,94,112} were found to be reactive with CH₄, confirming the theoretical predictions²⁴ discussed in Sec. 1.1.¹¹⁶ It was also found that for Pt, the reactivity increased with the size of the alkane, i.e. *n*-butane > propane > ethane > methane.⁹³ This was attributed to several factors: an increased vibrational density of states that allowed the weakly-bound Pt-alkane complexes more time to cross from the repulsive triplet surface to the reactive singlet surface, and a weakening of C–H bonds as the size of the alkane increased.^{93,117,118}

The lack of reactivity between many transition metal atoms and alkanes is primarily due to large potential energy barriers attributable to the repulsive interaction between the alkane and the ground state electronic configuration of most metal atoms. For the first transition metal row, the 4*s* orbital is considerably larger than the 3*d* orbital (and lower in energy), so a 3*dⁿ4s²* configuration is common in the ground state. This configuration appears to be closed-shell to an incoming hydrocarbon molecule. Therefore, as the metal atom approaches an alkane, the 4*s* orbital is brought close to the σ -bonding orbital of the alkane and the result is a repulsive interaction. This brings about the idea of “promotion energy,” i.e. the activation energy (adiabatic potential energy barrier) for M + alkane reactions is related to the amount of energy needed to promote the metal atom from the repulsive ground state to the appropriate reactive excited state (see Fig. 1).⁹² For the second row of transition metals, the 4*d* orbital becomes much closer in size to the 5*s* orbital, allowing for greater *sd* hybridization. This reduces *d*–*d* electron repulsion on the metal atom, facilitates formation of stronger M–C and M–H bonds, and allows chemical bonding interactions to begin earlier in the approach of the hydrocarbon molecule to the metal atom.⁹¹ For the third row of metal atoms, the lanthanide contraction lowers the energy of the 6*s* orbital relative to the 5*d* orbital causing 5*dⁿ6s²* ground states to again be the norm.⁹⁴ Furthermore, some of the metals that have favorable *dⁿ⁺¹s¹* ground state electronic configurations are high-spin, and so are repulsive towards alkanes. This is because formation of the two new

bonds in the H–M–alkyl complex from a high spin metal atom requires a spin-flip, again leading to an adiabatic potential energy barrier for reaction (see Fig. 1).⁹⁴

The reactions of transition metals with small alkenes were also studied,^{45–47,94–96,98,102,103,105} and it was found that many metals from the second and third rows react with alkenes, including ethene. The measured reaction rates typically increased as the hydrocarbon was changed from ethene to propene, but levelled off for larger alkenes.⁹⁴ Among the first-row metals, only Ni reacted with ethene, but several of the other metals reacted with larger alkenes.⁹⁴ The observed trend in reactivity for alkene reactions was 2nd > 3rd > 1st, similar to what was observed for the M + N₂O reactions (see Fig. 5). This trend was explained in both cases by the pattern of electronic states in each row, as discussed above.

Transition metal atoms react much more readily with alkenes than with alkanes because the initial interaction between the metal atom and an alkene is much less repulsive than for M+alkanes. To insert into a C–H bond of an alkane, the metal atom has to break a C–H bond and form an M–C and an M–H bond. The first step in a reaction with an alkene, however, is formation of a π -complex in which the C=C bond is merely weakened, not broken.¹¹⁹ The availability of the DCD bonding scheme (Sec. 1.1) leads

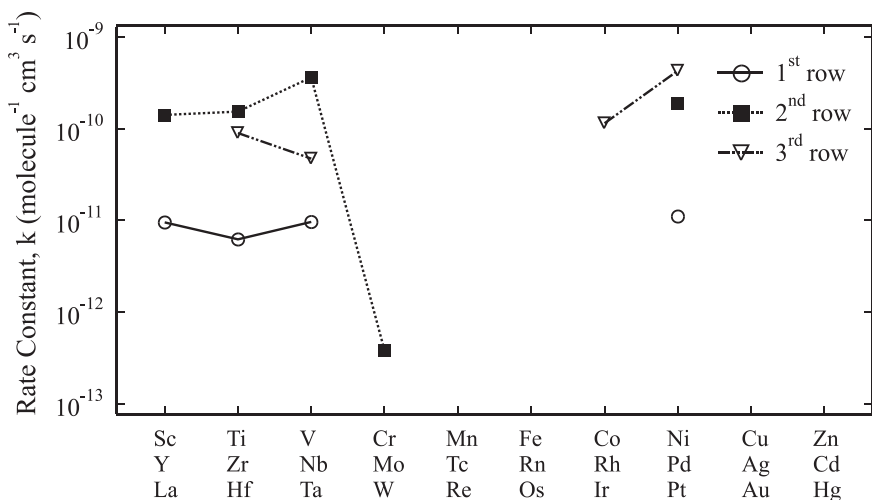


Fig. 5. Effective bimolecular rate constants at 300 K for the M + C₃H₆ reaction for all three transition metal rows. Values taken from Refs. 89, 91, and 94. Missing points were either not studied or exhibited no reaction with propene.

to a large capture cross-section for complex formation with unsaturated hydrocarbons. It is notable that even metal atoms with $d^n s^2$ ground states can efficiently react with alkenes (for example Y, Zr, Hf, and Ir), suggesting that barriers for formation of metal-alkene complexes, if present, must be relatively small.⁹⁴ Several subtler reasons also play a role in determining the trends of metal atom reactivity within a given row, as discussed in Refs. 92 and 94.

One rather unfortunate aspect of the $M + \text{hydrocarbon}$ (and $M + \text{OX}$) reactions mentioned thus far is that the products of the reactions were not detected directly, but were instead inferred via the pressure and temperature dependencies of the measured rate constants for metal reactant consumption and by comparison to *ab initio* calculations. Exceptions are the reactions of Y, Zr + C_2H_4 and C_3H_6 , for which the Weisshaar group employed the 157 nm photoionization/mass spectrometry technique to identify the products of the reaction as those resulting from bimolecular elimination of H_2 .^{45–47,95}

We have recently begun studying reactions of second-row neutral transition metal atoms in the gas phase using the technique of crossed molecular beams. There are several advantages of this technique over previous approaches. First, because of the relatively low concentrations of reactants in each beam, and because the reaction chamber is held under high-vacuum conditions, the reaction products are guaranteed to be the result of single, bimolecular collisions.^{120,121} Thus, observation of complexes stabilized by third-body collisions does not complicate the experimental results. Second, the ionization potentials (IPs) of most of the metal atoms from the second transition metal row (and their complexes) lie below the energy of a single 157 nm photon (7.9 eV, see Fig. 6), while the IPs of most molecules that may contribute to background signal are higher than this value.^{120,121} Thus, an F_2 excimer laser can be used as an ionization source for nearly all second-row transition metal reactions. The combination of this ionization source with a quadrupole mass filter gives an essentially zero-background technique.

Some of the earliest studies carried out in our laboratory were of ground state $\text{Zr}(a^3F)$, $\text{Nb}(a^6D)$ with C_2H_4 ¹²² and $\text{Y}(a^2D)$ with C_2H_2 ,¹²³ C_2H_6 ,¹²⁴ and H_2CO ,¹²⁵ as well as of excited state $\text{Mo}^*(a^5S_2)$ with CH_4 and C_2H_6 .^{126,127} For the $\text{Mo}^* + \text{CH}_4$, C_2H_6 reactions it was found that ground state $\text{Mo}(a^7S_3)$ atoms were quite ineffective at activating the C–H bonds of methane and ethane, while the excited state was found to be reactive even at very low collision energies. This confirmed the notion that low-spin

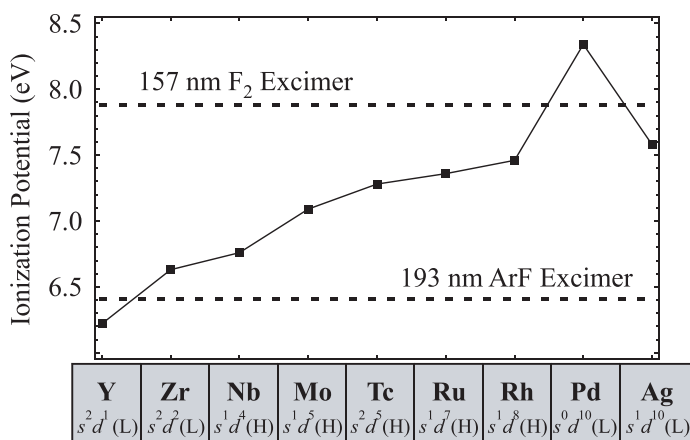


Fig. 6. The ionization potentials of the second transition metal row as a function of metal atom. The energies of a single 157 nm and 193 nm photon are indicated as dashed lines. L and H denote an atom with a low-spin or a high-spin ground electronic state, respectively.

states are generally more reactive than high-spin states. Also, for a given total energy (i.e. electronic + translational), it was observed that electronic energy was very effective at promoting reaction, while translational energy was not.^{126,127}

For Zr and Nb + C₂H₄, our experiments confirmed the observation of Weisshaar^{45,46,95} that the reaction products were ZrC₂H₂ + H₂ and NbC₂H₂ + H₂. However, the lack of wide-angle non-reactive scattering for Zr at collision energies below 9 kcal/mol (see Fig. 7) led to the suggestion that the initial step in the zirconium reaction may not be formation of a π -complex, but might instead be direct C–H insertion.¹²² Such a possibility was ruled out by subsequent isotopic-substitution experiments performed by Weisshaar.^{45,46} However, a suitable explanation for this result does not yet exist, as DFT calculations by Porembski *et al.* were unable to unambiguously determine whether or not there exists a barrier in the entrance channel for this reaction.⁴⁶

For the Y + C₂H₂¹²³ and Y + C₂H₆¹²⁴ reactions, competing product channels were directly observed for the first time. Elimination of H₂ was seen in both reactions, while a second product channel corresponding to elimination of H and C₂H₄ was observed for the Y + C₂H₂ and C₂H₆ reactions, respectively. For Y + C₂H₂, the endothermicity of the H elimination channel was measured, leading to the determination of the Y–CCH bond energy (110.2 ± 2.0 kcal/mol).¹²³ For the Y + C₂H₆ reaction, the height of

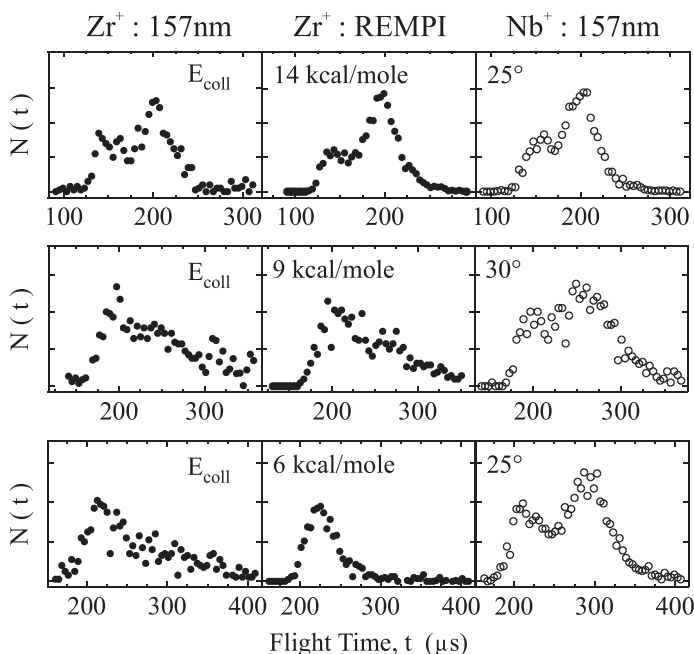


Fig. 7. Time-of-flight spectra for Zr and Nb+C₂H₄ at $E_{\text{coll}} = 14, 9$, and 6 kcal/mol from top to bottom, respectively. Note that at $E_{\text{coll}} = 6$ kcal/mol, the slower peak disappears in the Zr system. Reprinted with permission from Ref. 121.

the potential energy barrier for insertion into a C–H bond was measured to be 19.9 ± 3.0 kcal/mol,¹²⁴ in good agreement with Siegbahn’s predicted barrier height for insertion into a C–H bond of methane (20.7 kcal/mol).^{22,24} Three competing product channels were observed in the Y+H₂CO reaction, corresponding to elimination of H, H₂, and CO.^{125,128,129}

2. Experimental Details

All of the experiments described in this chapter were carried out at Cornell using a rotatable source crossed molecular beams apparatus. This apparatus has been described in detail previously,^{120,121} as have the methods used to produce and characterize the metal and molecular beams,¹³⁰ and the program used to fit the data (X-Beam).^{130,131} The apparatus consisted of two regions housed inside a main chamber: the metal source region and the molecular source region. These two regions were kept isolated from one another during the reaction to avoid pre-mixing of the reactants. The two

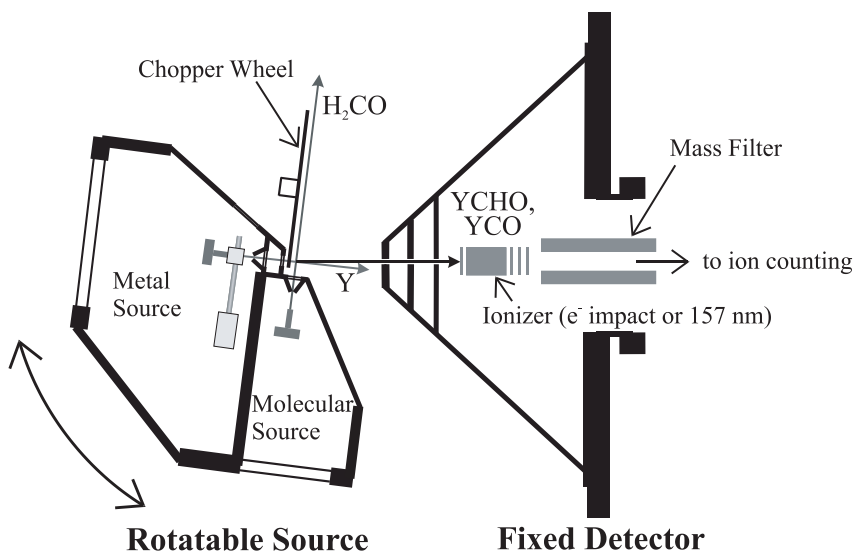


Fig. 8. Cross-sectional view of the apparatus in the plane of the two beams. Adapted from Ref. 120.

regions were held in a perpendicular geometry, and could be rotated with respect to the fixed detector (Fig. 8).

2.1. Production of the Beams

The atomic yttrium beam was generated by focusing the 532 nm output of a Nd:YAG laser (Continuum Surelite) onto a 0.25-inch diameter yttrium rod (Alfa Aesar, 99.9%) that was rotated and translated by a screw assembly.^{120,121} The ablated metal atoms were entrained in an inert gas¹³² (typically H_2 , He, Ne, Ar or mixtures of these) delivered by a piezoelectric pulsed valve.¹³³ The metal beam was collimated using a skimmer (0.5 mm diameter), then passed through a differentially-pumped region and through a defining aperture (2×2 mm). The beam was temporally refined through the use of a slotted chopper wheel (10.83 cm diameter, 0.5 mm slot width). The metal beam was crossed by a skimmed molecular beam. A 5% to 30% mixture of the reactant in H_2 or He was prepared in advance, and 5 psig of this mixture was delivered to a second pulsed valve housed in the molecular source region.

The velocity distributions of both the metal and molecular beams were measured using the same slotted chopper wheel described above by

monitoring their time-of-flight (TOF) to the detector using electron impact ionization.^{120,121} For beam velocity measurements, a pinhole aperture was placed in front of the detector to prevent a large gas load from entering the ionizer region. For reactive scattering, for which TOF spectra were taken at lab angles off-axis of the metal beam, a larger-diameter aperture was used to allow a larger solid angle of the product scattering sphere to be sampled.¹³⁰ Typical operating pressures in the metal and molecular source regions were 1×10^{-4} and 1×10^{-5} Torr, respectively. The pressure in the main chamber was usually less than 10^{-6} Torr, and the pressure in the ionization region of the detector was typically around 1×10^{-10} Torr.

Several characteristics of the metal beam have been studied in detail. It is well known that metal clusters and metal oxides are formed as a result of the ablation process. However, these potentially interfering species have been studied in detail¹³⁰ and it has been concluded that they do not introduce any doubt as to the validity of the experimental results. Much more important than cluster or oxide formation are the atomic electronic state populations of the metal beams. For each metal reactant, these have been characterized using laser-induced fluorescence (LIF) excitation spectroscopy. For Y, only the two spin-orbit states of the ground electronic state ($a^2D_{5/2}$ and $a^2D_{3/2}$) were observed.¹²³

2.2. Detection

For both reactive and non-reactive scattering, the metallic species drifted collision-free 24.1 cm to the triply-differentially pumped detector, where they were ionized at 157 nm using an F₂ excimer laser (LPX220i)^{120,121} and filtered by mass using a quadrupole mass spectrometer. The mass-selected ions were detected with a channeltron; the signal was amplified and integrated using a gated photon counter (Stanford Research Systems, SR-400). By scanning (Stanford Research Systems, Delay Generator DG-535) the delay time of the excimer trigger with respect to a time zero for reaction,¹³⁴ product TOF spectra were obtained at various lab angles. Integration of these spectra as a function of lab angle yielded the lab angular distribution, $N(\Theta)$.

Using a forward-convolution program¹³¹ with instrumental and experimental parameter inputs (aperture sizes, flight distances, beam velocities, etc.), along with two center-of-mass (CM) input functions (the translational energy release distribution, $P(E)$, and the CM angular distribution, $T(\theta)$), TOF spectra and lab angular distributions were calculated and compared

with experimental data. The two CM functions were iteratively adjusted until calculated angular distributions and TOF spectra matched those from experiment.

2.3. Sample Data: $\text{Y}(a^2D) + \text{CH}_3\text{OH}$

As an example to the reader, some sample data are presented here to illustrate some results common to many of the reactions studied recently. For this purpose, the $\text{Y} + \text{CH}_3\text{OH}$ reaction has been chosen because it exhibits some features that are fairly general and common to many transition metal reactions. The goal of this section is not to provide a complete description of this reaction, but merely to use it as an example of some basic principles involved in these experiments.

The first aspect of the $\text{Y} + \text{CH}_3\text{OH}$ reaction that will be discussed is that of non-reactive (NR) scattering, which is common to all reactions studied in our laboratory. Non-reactive TOF spectra for the $\text{Y} + \text{CH}_3\text{OH}$ reaction are shown in Fig. 9, recorded at m/e 89 (Y^+). The solid-line fits to the experimental data are actually the sum of two processes, represented by dotted and dashed lines. The dotted line corresponds to inelastically-scattered Y

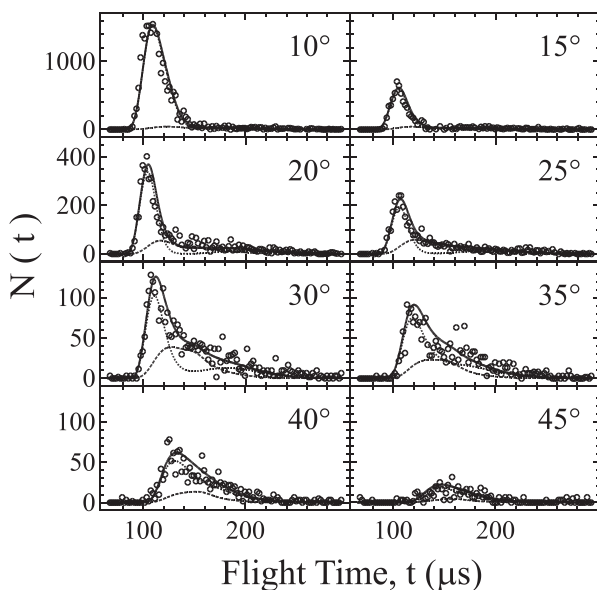


Fig. 9. Time-of-flight spectra for non-reactively scattered yttrium atoms at indicated lab angles for the $\text{Y} + \text{CH}_3\text{OH}$ reaction at $E_{\text{coll}} = 28.1$ kcal/mol. Fits data generated using the CM distributions shown in Fig. 10.

atoms that are a result of glancing collisions with methanol. Such collisions, which correspond to large impact parameters, only slightly modify the trajectory of the yttrium atoms, resulting in mostly forward-scattered atoms (i.e. near $\theta = 0^\circ$). This can be seen clearly in the CM angular distribution shown in Fig. 10. The dashed line corresponds to yttrium atoms that have formed a long-lived complex with methanol and have subsequently decayed back to reactants. Because these complexes live longer than their picosecond rotational lifetimes, they are scattered with a forward-backward symmetric angular distribution in the CM frame,¹³⁵ as shown in Fig. 10.

In looking at the CM translational energy distributions, it is evident that complex formation results in a greater transfer of the initial collision energy to the internal degrees of freedom of methanol than does large impact parameter (glancing) scattering. This is typically observed for metal

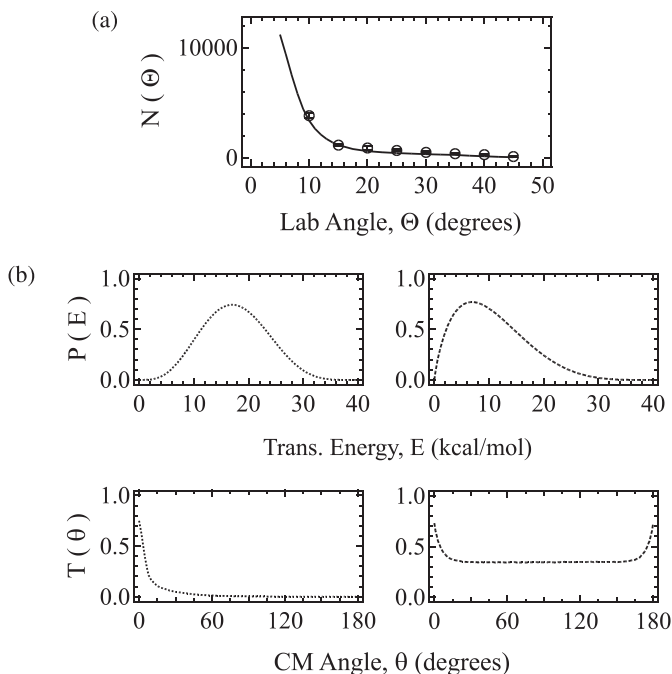


Fig. 10. (a) Lab angular distribution for non-reactively scattered yttrium atoms from the $\text{Y} + \text{CH}_3\text{OH}$ reaction at $E_{\text{coll}} = 28.1$ kcal/mol. (b) CM translational energy and angular distributions used to generate solid-line fits to the data in Fig. 9. Dotted lines correspond to yttrium atoms resulting from glancing collisions, while dashed lines correspond to those resulting from complex decay.

reactions. The actual percentage of energy transferred was 62% for complex formation and 37% for glancing collisions. We have found that formation of complexes that decay back to reactants is an important feature of transition metal reactions involving unsaturated hydrocarbons such as ethene¹²² or acetylene.¹²³ However, it should be noted that not all reactions have both of these non-reactive processes occurring. For reactions with saturated hydrocarbons (methane, ethane, propane, etc.), for example, only forward scattered metal atoms have been observed, indicating the absence of significant decay of complexes back to reactants.^{124,126,127} In these cases the non-reactive data could be adequately fit using only a forward-peaking CM angular distribution, similar to those used to fit data for metal atoms scattering from noble gases, for which the collisions are elastic.

A second feature of the $Y + \text{CH}_3\text{OH}$ reaction that is common to many metal reactions is the presence of competing reaction channels, in this case $\text{YH}_2 + \text{H}_2\text{CO}$ and $\text{YOCH}_3 + \text{H}$. Time-of-flight spectra for both these products are shown in Fig. 11. The corresponding lab angular distributions and CM distributions used to fit the TOF spectra are shown in Fig. 12.

The YH_2 products were scattered over a much wider range of lab angles than the YOCH_3 products, despite the fact that the latter had more available energy. This is due to the kinematics of each process. Because the YH_2 products recoiled from a relatively heavy counter-fragment (H_2CO), in order to conserve momentum they carried away a substantial fraction of the relative velocity. In contrast, the YOCH_3 products recoiled from a very light counter-fragment (H) and are thus formed with very low recoil velocities. These considerations can be easily seen via the construction of a Newton diagram,¹³⁵ which may be used to visualize the concepts just described (and also to convert between the lab and CM frames of reference). A Newton diagram for the $Y + \text{CH}_3\text{OH}$ reaction is shown in Fig. 13. The circles in this figure depict the maximum range of scattering angles for each product as determined through conservation of energy and linear momentum. If all of the available energy ($E_{\text{coll}} - \Delta E_{\text{rxn}}$) were channelled into product translational energy, the products would be scattered over this range. Of course, this is not usually the case and so the products are in actuality scattered over a smaller range of lab angles, as is evident in Fig. 12.^{136,137}

The translational energy release distributions shown in Fig. 12 are similar in shape for both products, with the major difference being how much of the available energy is channelled into product translation. For YH_2 , this amount is 28%, while for YOCH_3 it is considerably larger (40%). The CM angular distributions are strikingly different for these two product

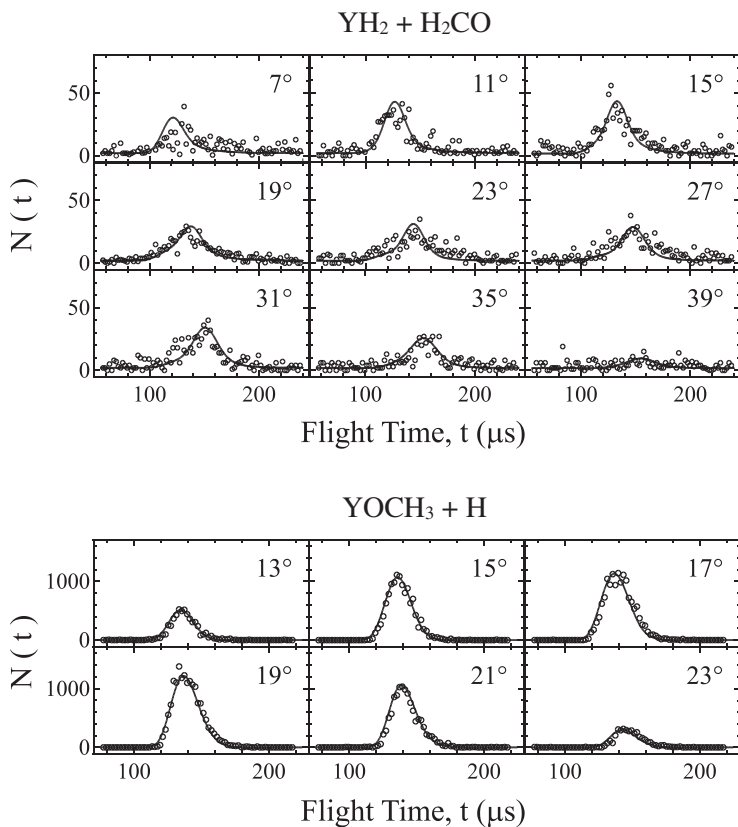


Fig. 11. Time-of-flight spectra for YH_2 and YOCH_3 products at indicated lab angles for the $\text{Y} + \text{CH}_3\text{OH}$ reaction at $E_{\text{coll}} = 28.1$ kcal/mol. TOFs have been scaled to the same number of scans. Solid-line fits generated using the CM distributions shown in Fig. 12.

channels, as the YH_2 $T(\theta)$ is quite sharply forward-backward peaking while the YOCH_3 $T(\theta)$ is isotropic (flat). The reasons for this are related to the kinematics of crossed-beam reactions and the geometry of the dissociating transition state.¹²⁸ Both CM angular distributions were symmetric about $\theta = 90^\circ$, indicating that both products result from reaction mechanisms involving long-lived intermediates.

The lab angular distributions shown in Fig. 12 contain information about the cross-section for each reaction. In practice, extraction of an absolute cross-section is difficult because of uncertainties in the number densities of the reactant beams and the ionization efficiencies of the products.^{130,135} However, in the determination of the product branching ratio, many of

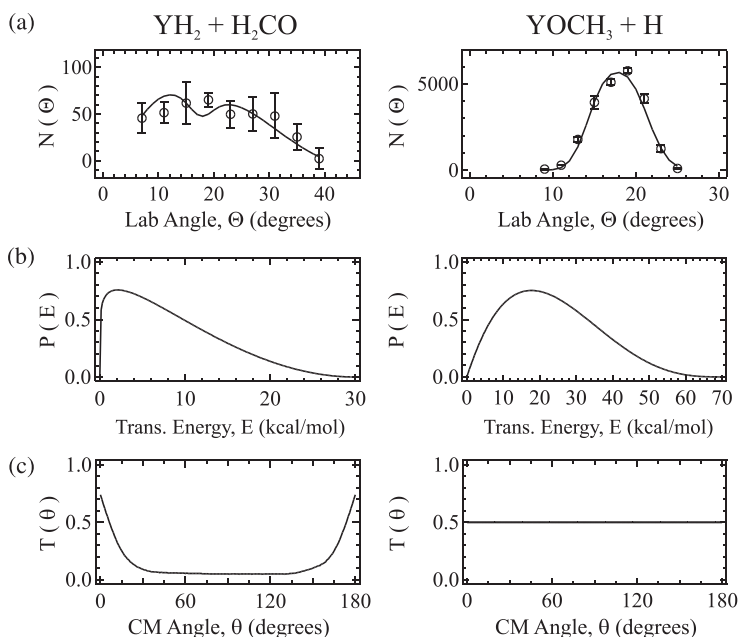


Fig. 12. (a) Lab angular distributions, (b) CM translational energy distributions, and (c) CM angular distributions, for YH_2 and YOCH_3 products from the $\text{Y} + \text{CH}_3\text{OH}$ reaction at $E_{\text{coll}} = 28.1$ kcal/mol. Solid-line fits in the lab angular distributions generated using the CM distributions.

these factors cancel out. In order to obtain the branching ratio, several issues need to be accounted for: Jacobian factors related to the transformation of data from the lab to the CM frame, product fragmentation patterns, and differences in the 157 nm photoionization cross-section for each product. The Jacobian factors are explicitly taken into consideration by the *X-Beam* data-fitting program, as described elsewhere.^{130,131} The product fragmentation patterns are measured by taking TOFs at the CM angle at the parent masses and at all possible fragmentation masses. The TOFs for the parent masses are then scaled to each of the TOFs for the fragmentation masses in order to determine the extent of fragmentation. Ideally (and sometimes necessarily) this process is repeated at several collision energies. Also, the 157 nm photoionization cross-sections have not been measured for any of the products that we have observed experimentally. A study was undertaken to measure the product branching ratio between YCH_2 and YC_3H_4 products from the $\text{Y} + \text{propene}$ reaction using electron impact,^{130,138} for which the ionization cross-sections can be calculated from the polarizabilities of each

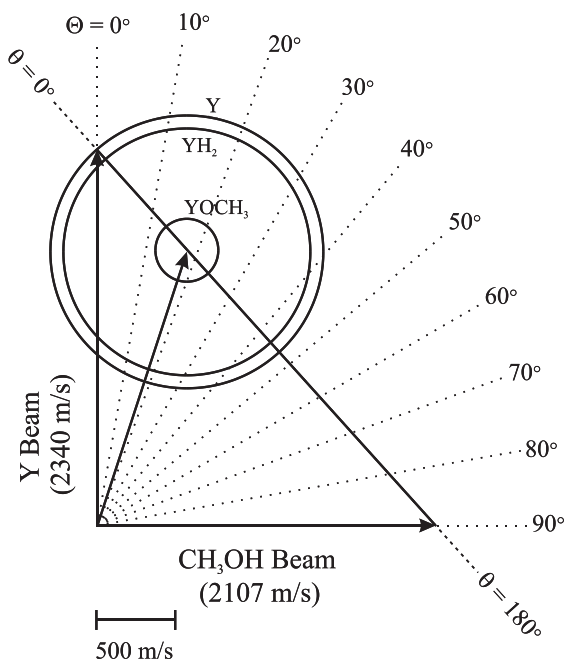


Fig. 13. Newton diagram in velocity space for the $\text{Y} + \text{CH}_3\text{OH}$ reaction at $E_{\text{coll}} = 28.1$ kcal/mol. See Ref. 136.

product.^{139,140} This study showed that the branching ratio measured using electron impact was nearly identical to those measured using 157 nm photoionization at similar collision energies, indicating that the ratio of 157 nm photoionization cross-sections for these two products was near unity.^{130,138}

3. $\text{Y}(a^2D)$ + Cyclopropane and Propene

One common feature of all $\text{M} + \text{hydrocarbon}$ systems mentioned in Sec. 1.2.2 is that none of the products resulted from cleavage of a C–C bond. This is a result of several factors. First, C–H bonds are less directional than C–C bonds (Sec. 1.1), allowing for multicentered bonding at the transition state, which tends to lower the barrier for C–H insertion relative to C–C insertion.^{2,18,22} Second, since M–H bonds are usually stronger than M–C bonds, intermediates resulting from insertion into a C–H bond are usually thermodynamically favored.¹⁴¹ Third, there are typically more C–H bonds in hydrocarbons than C–C bonds, so C–H insertion is also statistically favored. Finally, C–H bonds are more accessible to an incoming metal atom and are therefore more susceptible to insertion.

In certain cases, however, C–C insertion has been predicted to be competitive with C–H insertion. One notable example is cyclopropane, for which the relief of ring strain is a factor that significantly lowers the barrier for C–C insertion. In fact, Siegbahn has predicted that in reactions of Y, Mo, Rh, and Pd with cyclopropane, the C–C insertion barrier should actually lie lower than the C–H insertion barrier (see Fig. 14).²² We have recently studied the reactions of Y, Zr, Nb, and Mo* with cyclopropane at two collision energies (27 and 37 kcal/mol), and have observed products corresponding to both C–H and C–C bond cleavage for all four reactants. An analysis of the branching ratios between MCH_2 and MC_3H_4 products confirmed the predicted trends in relative insertion barrier heights for the cyclopropane reaction.¹⁴²

We have also observed competition between products resulting from C–C and C–H bond activation in reactions of Y with propene,¹³⁸ propyne,¹⁴³ 2-butyne,¹⁴³ four butene isomers,¹³⁸ acetaldehyde,¹²⁸ acetone,¹²⁸ ketene,¹⁴⁴ and two cyclohexadiene isomers,¹⁴⁵ as well as for Zr, Nb, Mo, and Mo* with 2-butyne.¹⁴³ In this chapter, we use the term “C–C activation” to describe any reaction leading to C–C bond fission in which the hydrocarbon reactant is broken into two smaller hydrocarbon products, with one hydrocarbon bound to the metal. It is important to note, however, that C–C activation does not necessarily require true C–C insertion. As will be shown in this chapter, the reaction of Y, the simplest second-row transition metal atom, with propene leads to formation of $\text{YCH}_2 + \text{C}_2\text{H}_4$. The mechanism involves addition to the $\text{C}=\text{C}$ bond followed by H atom migration and C–C bond fission, rather than by true C–C insertion.

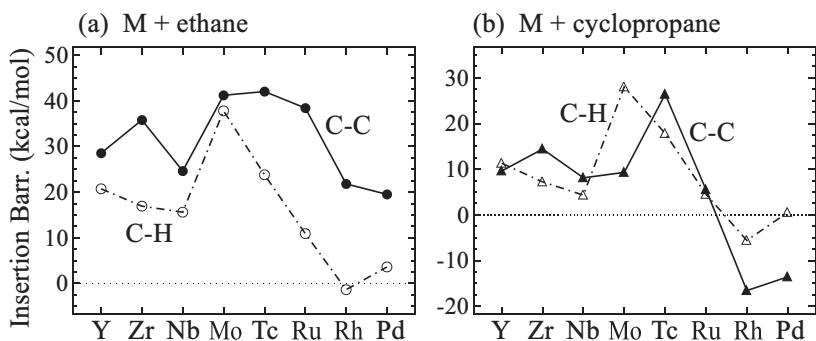


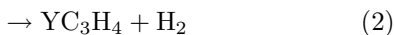
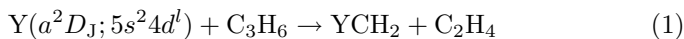
Fig. 14. Potential energy barrier heights as calculated using *ab initio* theory for insertion of transition metal atoms into a C–H or C–C bond of (a) ethane and (b) cyclopropane. Values taken from Ref. 22.

Several experimental and theoretical studies of the reactions of neutral transition metal atoms with propene have been reported. In a combined experimental and theoretical effort, Carroll and co-workers reported that both ethene and propene undergo bimolecular reaction with second-row transition metal atoms.²² In those early studies, products were not observed, but it was correctly hypothesized that they involved elimination of H₂. The rate of depletion of Y atoms in a fast-flow reactor was monitored as a function of reactant pressure, leading to effective room temperature bimolecular rate constants of $8.2 \times 10^{-12} \text{ cm}^3 \text{ s}^{-1}$ and $143 \times 10^{-12} \text{ cm}^3 \text{ s}^{-1}$ for ethene and propene, respectively.²² Although the very large difference in rate constants for the two molecules was quite notable, the origin of this difference was not determined. Porembski and Weisshaar also studied the reactions in a flow cell, and directly observed H₂ elimination in room temperature experiments, demonstrating that H₂ elimination occurs in reactions with ethene and propene even at a mean collision energy of 0.9 kcal/mol.⁴⁷

Reactions of second-row transition metal atoms (M) with alkenes are initiated by formation of a π -complex, which subsequently undergoes C–H insertion forming HMC₂H₃. Calculations indicated that the lowest pathway to H₂ elimination involved concerted molecular elimination over a multicenter transition state, rather than via a stepwise mechanism involving (H)(H)M(C₂H₂).^{45–47} Such multicenter transition states have also been shown to be important in H₂ elimination in Y + H₂CO reactions,⁴⁸ and are very likely to be generally important in many metal hydrocarbon systems leading to H₂ production.

3.1. Yttrium + Cyclopropane: $E_{\text{coll}} = 18.5 \text{ kcal/mol}$

Several competing product channels were observed from both C₃H₆ reactant isomers:



The reaction was studied over a range of collision energies, ranging from 9.4 to 36.8 kcal/mol (Table 1). The competition between YCH₂ + C₂H₄ and YC₃H₄ + H₂ was monitored at various laboratory angles by alternating scans at m/e 103 (YCH₂⁺) and 129 (YC₃H₄⁺). As illustrated in Fig. 15, the

Table 1. Experimental conditions for Y-atom beam.

$E_{\text{coll}}^{\text{a}}$	Carrier gas	Velocity ^b	FWHM ^b
<i>Y + Cyclopropane</i>			
11.6	pure Ne	1410	150
18.5	50% Ne/50% He	1690	190
29.5	pure He	2480	310
36.8	50% He/50% H ₂	2930	420
<i>Y + Propene</i>			
12.3	Pure Ne	1380	130
15.8	50% Ne/50% HE	1680	190
25.2	pure He	2430	310
28.8	50% He/50% H ₂	2570	350
43.2	pure H ₂	3290	470

^akcal/mol^bm/s

relationship between the lab and CM reference frames in velocity space may be represented by the Newton diagram.¹³⁵ The maximum allowed velocities (shown as Newton circles) are determined by reaction energetics and conservation of linear momentum. These circles are centered at the tip of the CM velocity vector, v_{CM} ; lab angular distributions for both product channels (Fig. 15) are thus centered about the CM lab angle (Θ_{CM}). The m/e 103 data have been corrected for a small contribution from fragmentation of YC_3H_4 . Representative TOF spectra are shown at indicated lab angles in Fig. 16.

The CM translational energy, $P(E)$, and angular, $T(\theta)$, distributions for the reaction, shown in Fig. 17, were used to generate the solid-line simulations included in Figs. 15 and 16. In Fig. 17, the maximum allowed translational energy for formation of the two possible YC_3H_4 isomers, Y-allene and Y-propyne, are denoted by arrows. Using the calculated energetics for Y-propyne²² formation, the fraction of available energy deposited as translational energy (f_{T}) was 0.34 on average. For the C–C activation channel leading to elimination of ethane, the $P(E)$ peaked closer to zero translational energy (Fig. 17), with $f_{\text{T}} = 0.18$. For both product channels, the best-fit CM angular distributions were symmetric about $\theta = 90^\circ$.^{135,146} The product branching ratio at $E_{\text{coll}} = 18.5$ kcal/mol, $\phi_{\text{YCH}_2} : \phi_{\text{YC}_3\text{H}_4}$, was determined to be 1.09 : 1.00.

The data for non-reactively scattered Y atoms recorded at m/e 89 (not shown) exhibit typical features for impulsive inelastic scattering without appreciable long-lived complex formation.^{124,127} In the CM reference frame,

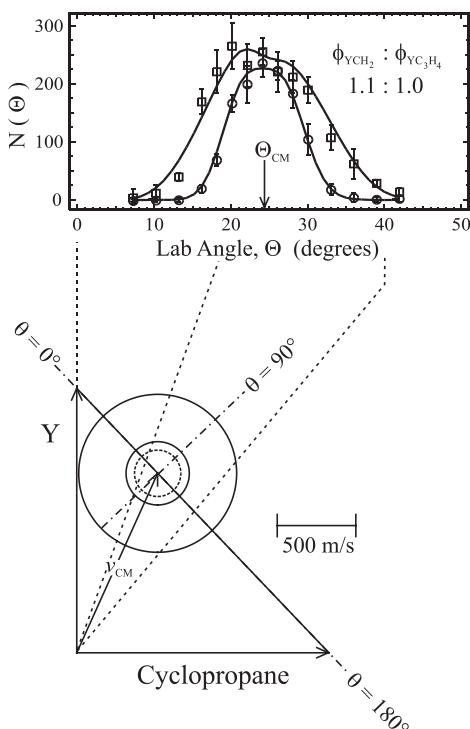


Fig. 15. Newton diagram in velocity space for Y+cyclopropane at $E_{\text{coll}} = 18.5$ kcal/mol. Larger solid circle corresponds to maximum velocities for YCH_2 products, while smaller solid circle and smaller dotted circle correspond to maximum velocities for Y-propyne and Y-allene products, respectively. Lab angular distributions for YCH_2 (open squares) and YC_3H_4 (open circles) recorded under identical collision conditions. Solid-line fits to lab angular distributions generated using CM distributions in Fig. 17.

the recoiling Y atoms were forward scattered as seen in the $T(\theta)$, with $\sim 31\%$ of the initial kinetic energy transformed into cyclopropane internal energy.

3.2. Yttrium + Cyclopropane: Collision Energy Dependence

Products at m/e 129 (YC_3H_4^+), resulting from H_2 elimination, were observed at E_{coll} as low as 9.4 kcal/mol in the reaction with cyclopropane. At $E_{\text{coll}} = 9.4$ kcal/mol, production of YCH_2 could not be confirmed because of background signal from YO mass overflow. However, with increasing collision energy, the strength of the YCH_2 signal increased strongly, and for $E_{\text{coll}} \geq 19$ kcal/mol, formation of YCH_2 became dominant (Fig. 18). The CM distributions for these two product channels

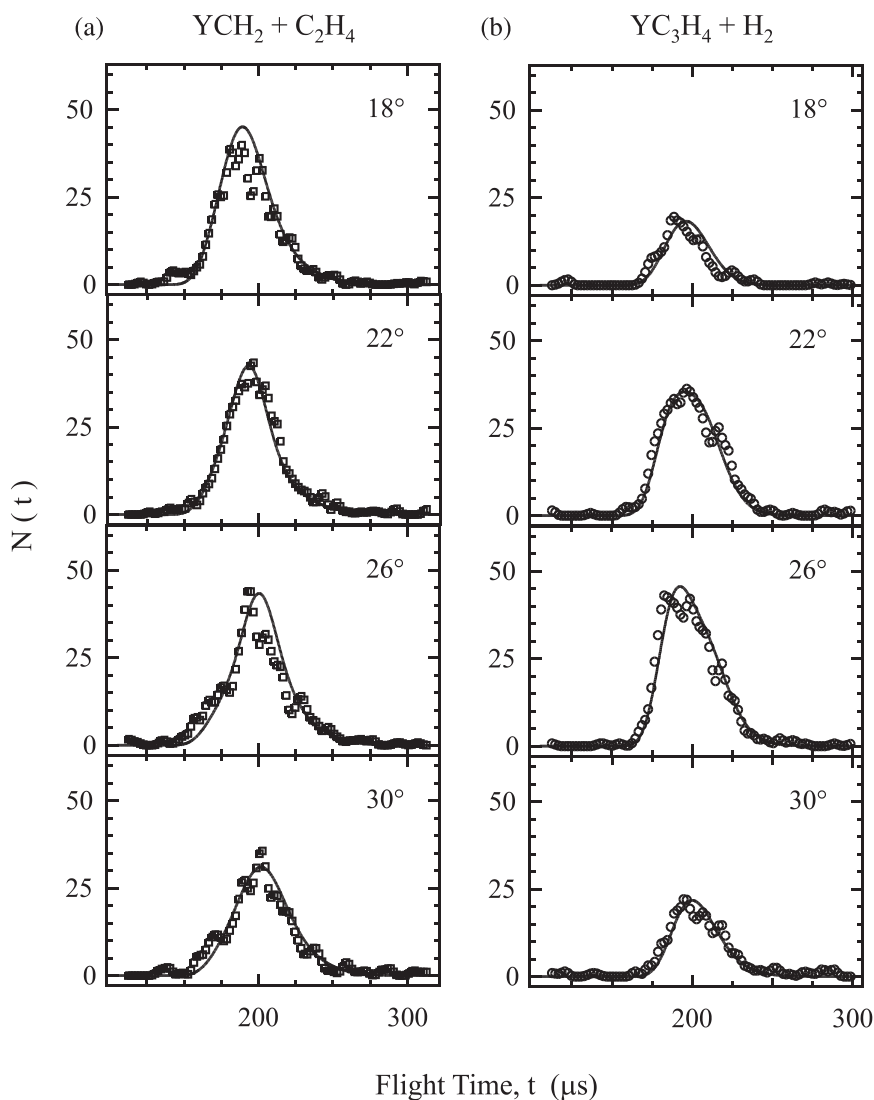


Fig. 16. Sample TOF spectra recorded at indicated lab angles for (a) YCH_2 and (b) YC_3H_4 products from collisions of $\text{Y} + \text{cyclopropane}$ at $E_{\text{coll}} = 18.5 \text{ kcal/mol}$ (open points). Solid-line fits generated using CM distributions in Fig. 17.

were found to be qualitatively similar at all E_{coll} studied. A third, minor product channel, $\text{YH}_2 + \text{C}_3\text{H}_4$ (recorded at m/e 91), was also observed at $E_{\text{coll}} = 36 \text{ kcal/mol}$. Assuming the YH_2 157 nm photoionization cross-section is the same as that for YC_3H_4 , the YH_2 signal was 25 times weaker

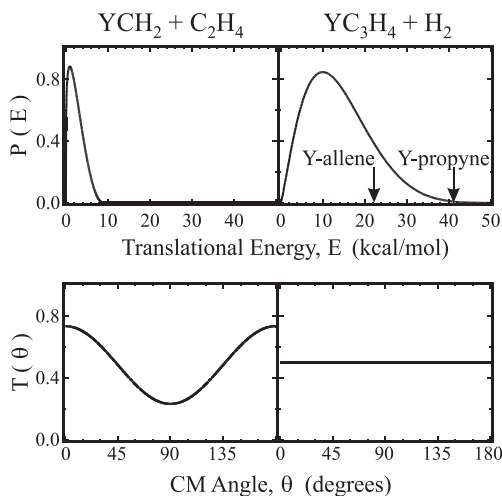


Fig. 17. CM translational energy distributions, $P(E)$, and angular distributions, $T(\theta)$, used to simulate data from collisions of Y + cyclopropane at $E_{\text{coll}} = 18.5$ kcal/mol. Arrows indicate maximum allowed translational energy for formation of two distinct product isomers.

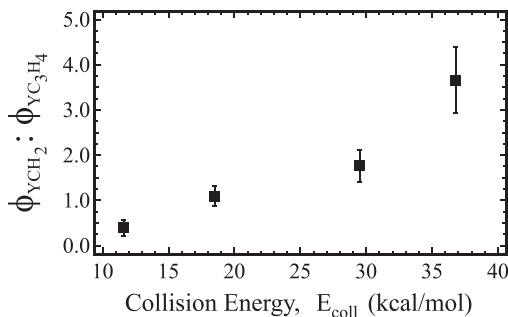


Fig. 18. Product branching ratio, $\phi_{YCH_2} : \phi_{YC_3H_4}$, for reactions of Y + cyclopropane as a function of E_{coll} .

than YC_3H_4 . Using the best-fit $P(E)$ with the energetics for YH_2 + allene formation, f_T was 0.15.

3.3. Yttrium + Propene: $E_{\text{coll}} = 25.2$ kcal/mol

In the propene reaction, both YCH_2 and YC_3H_4 were again observed. The YC_3H_4 data at $E_{\text{coll}} = 25.2$ kcal/mol were similar to those observed for the cyclopropane reaction at 18.5 kcal/mol. From the difference in enthalpies

of formation for propene and cyclopropane, these two data sets correspond to nearly the same total energy above the product asymptotes.²² The TOF spectra at m/e 103, corresponding to YCH_2^+ (Fig. 19), were recorded with a similar amount of averaging as those shown in Fig. 16.

The CM distributions shown in Fig. 20 were used to generate the solid-line fits shown in Fig. 19. For YCH_2 , $\langle P(E) \rangle = 3.18 \text{ kcal/mol}$, giving $f_T = 0.23$. The $T(\theta)$, however, was identical to that shown in Fig. 17 for the cyclopropane reaction. The product branching ratio, $\phi_{\text{YCH}_2} : \phi_{\text{YC}_3\text{H}_4}$, at $E_{\text{coll}} = 25.2 \text{ kcal/mol}$ was $0.48 : 1.00$.

The minor $\text{YH}_2 + \text{C}_3\text{H}_4$ channel was observed for the propene reaction at $E_{\text{coll}} = 28.8 \text{ kcal/mol}$, as shown in Fig. 21. For YH_2 , $\langle P(E) \rangle = 3.7 \text{ kcal/mol}$, which yields $f_T = 0.32$. The $T(\theta)$ was strongly polarized with $T(0^\circ)/T(90^\circ) = 12_{-4}^{+6}$. The YH_2 channel was 45 times weaker than for YC_3H_4 at $E_{\text{coll}} = 28.8 \text{ kcal/mol}$.

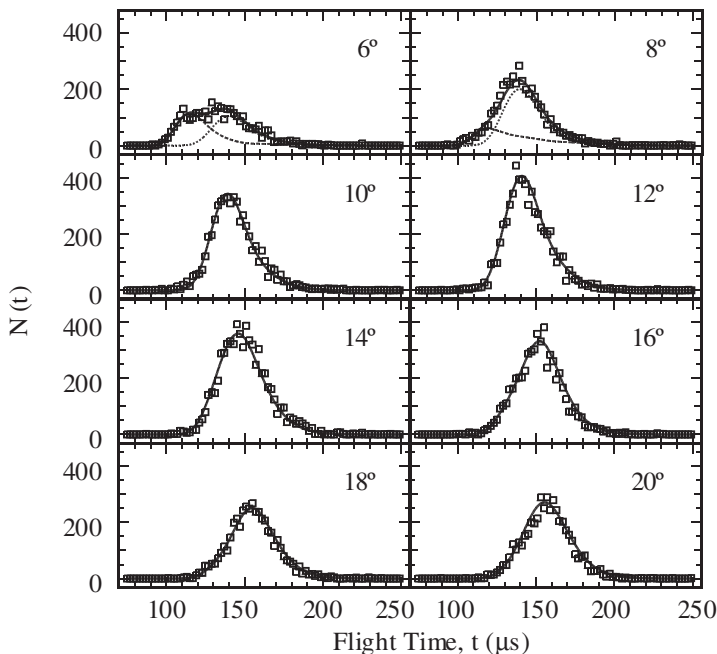


Fig. 19. Sample TOF spectra recorded at indicated lab angles for YCH_2 products from collisions of $\text{Y} + \text{propene}$ at $E_{\text{coll}} = 25.2 \text{ kcal/mol}$ (open points). Solid-line simulations generated from CM distributions shown in Fig. 20. Dashed line indicates overflow contribution from YO contamination in the Y atomic beam.

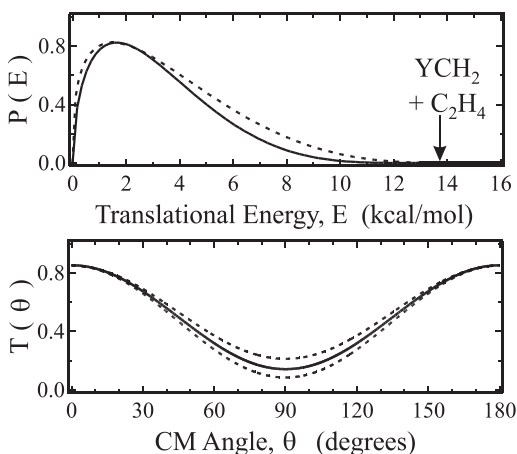


Fig. 20. CM distributions for $\text{YCH}_2 + \text{C}_2\text{H}_4$ from collisions of $\text{Y} + \text{propene}$ at $E_{\text{coll}} = 25.2 \text{ kcal/mol}$. Arrow in the $P(E)$ indicates maximum allowed translational energy. Dashed lines correspond to range of distributions that give acceptable fits to the data.

The signal recorded at m/e 89 (Fig. 22) corresponds to non-reactive $\text{Y} + \text{propene}$ collisions. These data are distinctly different from corresponding data obtained for cyclopropane. As in studies of reactions of transition metal atoms with C_2H_4 ,¹²² C_2H_2 ,¹²³ and carbonyl-containing species such as H_2CO ,^{125,128} the slower peak ($\sim 175 \mu\text{s}$) becomes more intense than the fast peak at increasing laboratory angles. This wide-angle scattering results from decay of π -complexes back to reactants. The data was simulated using two separate $P(E)$ and $T(\theta)$ combinations (Fig. 22). In one combination (shown on the right), $T(\theta)$ was constrained to forward-backward symmetry, representing long-lived complexes that survive many rotational periods prior to decay back to reactants.^{122,123} A second, forward-scattered $T(\theta)$ represents direct non-reactive collision events that do not persist for timescales longer than their rotational periods.

3.4. Yttrium + Propene: Collision Energy Dependence

At $E_{\text{coll}} = 12.3 \text{ kcal/mol}$, formation of $\text{YC}_3\text{H}_4 + \text{H}_2$ was observed (Fig. 23). Weak signal was also observed at m/e 103, the mass corresponding to YCH_2^+ , but comparison of the data recorded at m/e 103 to m/e 129 at this E_{coll} revealed that the weak m/e 103 signal originated primarily from fragmentation of YC_3H_4 during photoionization. The intensity of fragmentation signal at m/e 103 was 3.6% of the parent ion signal (m/e 129). The

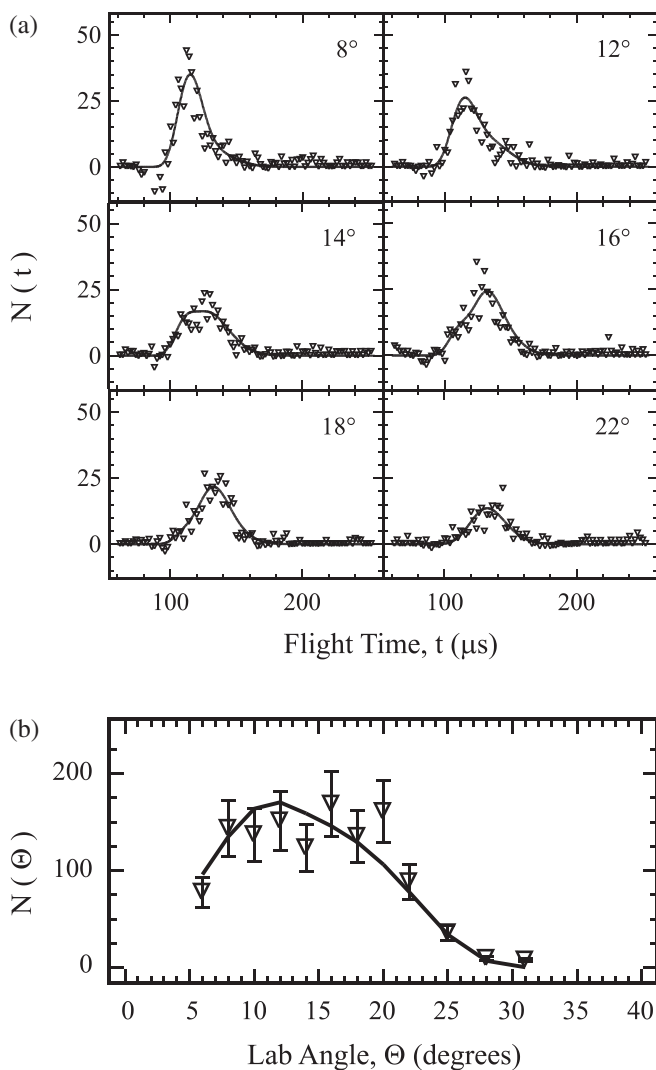


Fig. 21. (a) Sample TOF spectra recorded at indicated lab angles for YH_2 products from collisions of $\text{Y} + \text{propene}$ at $E_{\text{coll}} = 28.8 \text{ kcal/mol}$ (open points). (b) Lab angular distribution generated by integrating TOF spectra.

same value was obtained at $E_{\text{coll}} = 10.4 \text{ kcal/mol}$ and was used to correct the YCH_2 data at all E_{coll} . The best-fit $P(E)$ (Fig. 23(b)) indicated that $f_{\text{T}} = 0.46$. The product flux distributions for the two major product channels, YC_3H_4 and YCH_2 , are shown in Fig. 24.

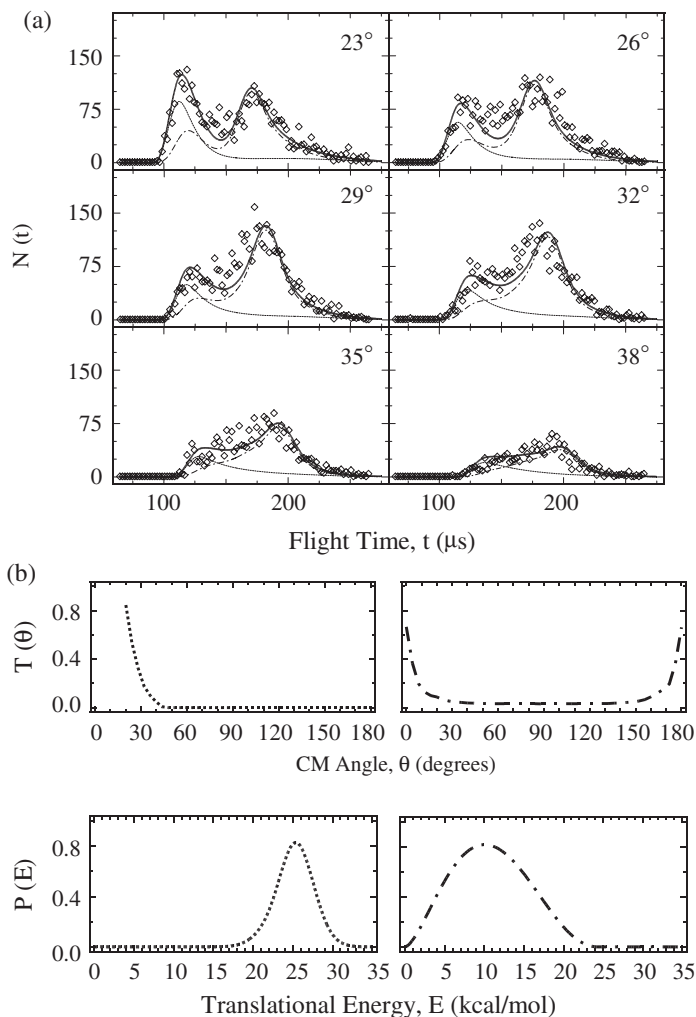


Fig. 22. (a) Sample TOF spectra recorded at indicated lab angles for non-reactive scattering of Y atoms from collisions with propene at $E_{\text{coll}} = 28.8$ kcal/mol (open points). (b) CM distributions used to generate simulations to the TOF data. Solid-line fits are the sum of the dashed and dash-dot lines. See text for details.

For the reaction with propene, the YCH_2 product signal was clearly observed at $E_{\text{coll}} \geq 15.8$ kcal/mol. The complete set of lab angular distributions recorded for reactions of Y + propene at different collision energies is shown in Fig. 25. Although an increase in the relative amount of YCH_2 formed was observed as E_{coll} increased (Fig. 26), YC_3H_4 formation was always the dominant process.

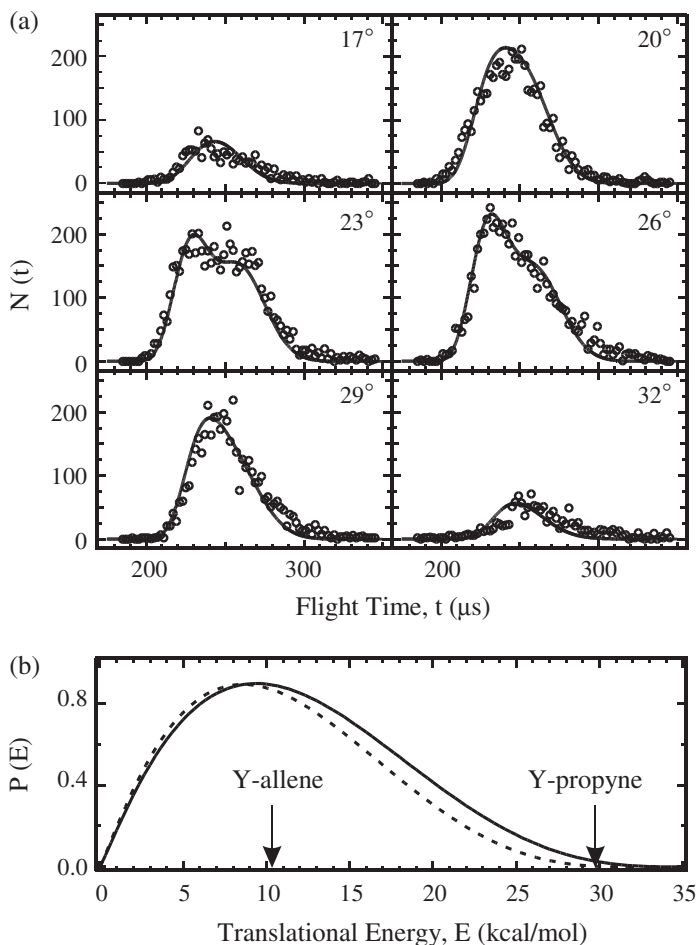


Fig. 23. (a) Sample TOF spectra recorded at indicated lab angles for YC_3H_4 products from collisions of $\text{Y} + \text{propene}$ at $E_{\text{coll}} = 12.3 \text{ kcal/mol}$ (open points). (b) $P(E)$ used to generate solid-line fits. Arrows indicate maximum translational energy for two distinct YC_3H_4 product isomers. Dashed lines correspond to range of distributions that give acceptable fits to the data.

3.5. Non-Reactive Scattering in Cyclopropane and Propene Reactions

In reactions involving cyclopropane, the forward-peaking of the Y angular distribution (not shown) is similar to that reported previously for saturated hydrocarbons such as ethane.^{124,127} The absence of a peak at large laboratory angles indicated that there is no significant contribution from formation of long-lived intermediates decaying back to reactants. For bare

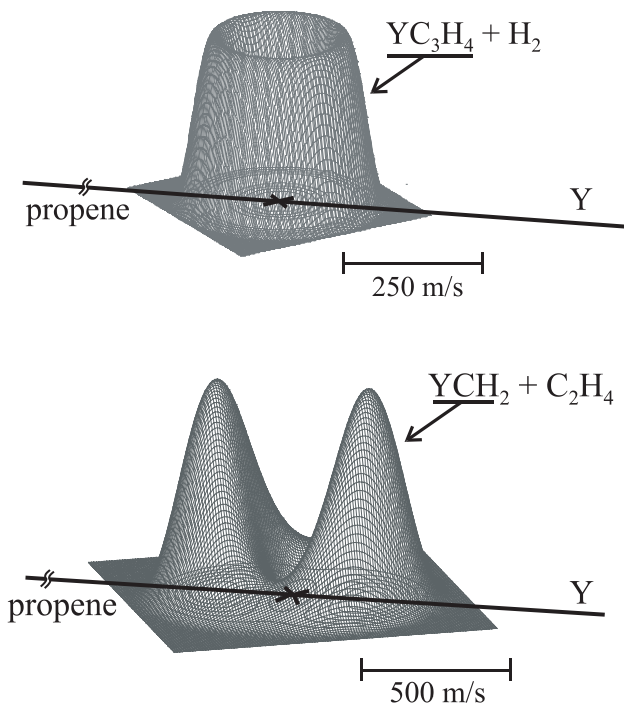


Fig. 24. YC_3H_4 and YCH_2 product flux distributions from collisions of $\text{Y} + \text{propene}$ at $E_{\text{coll}} = 12.3 \text{ kcal/mol}$ and 25.2 kcal/mol , respectively. Arrows represent the CM relative velocity vectors for the colliding reactants.

transition metal atom reactions with hydrocarbons like cyclopropane, the small local minimum corresponding to σ -bound complexes should be no deeper than several kcal/mol. At the relatively high collision energies of this experiment, the small binding energies, which are comparable to those in van der Waals species, do not support σ -bound complexes for timescales greater than their rotational periods. Therefore, for $\text{Y} + \text{cyclopropane}$, C–C and C–H bond insertion are direct processes, without initial σ -complex formation. Insertion into cyclopropane C–H and C–C bonds has been reported previously in reactions of transition metal complexes in solution,¹⁴¹ cation reactions in gas phase guided beam experiments,^{147,148} and neutral transition metal atoms in low temperature matrices.¹⁴⁹

The reaction dynamics are quite different for $\text{Y} + \text{propene}$. The wide angle scattering in the Y atom angular distribution (Fig. 22) indicates that a substantial fraction of initially-formed complexes decay back to reactants, rather than forming chemical products.^{122,123} Recent calculations on

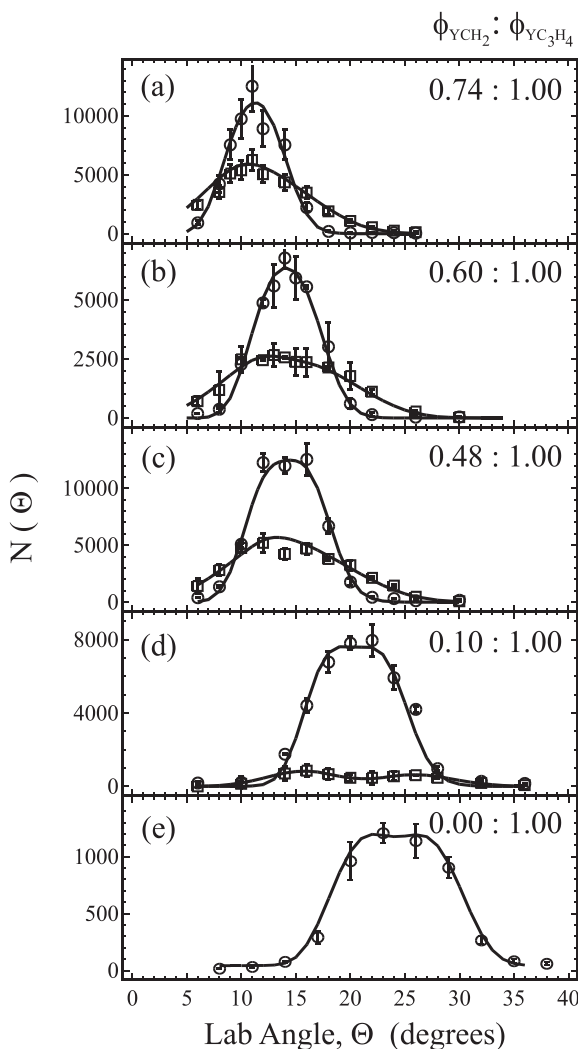


Fig. 25. Lab angular distributions for YC_3H_4 (open circles) and YCH_2 (open squares) from collisions of $\text{Y} + \text{propene}$ at $E_{\text{coll}} =$ (a) 43.2, (b) 28.8, (c) 25.2, (d) 15.8, and (e) 12.3 kcal/mol. Product branching ratio, $\phi_{\text{YCH}_2} : \phi_{\text{YC}_3\text{H}_4}$, included in top right corner.

the reaction of $\text{Y} + \text{C}_2\text{H}_4$ have found no barrier to formation of a YC_2H_4 π -complex,⁴⁷ which is expected to readily convert to a more stable doublet metallacyclopropane.^{22,47} This complex may go on to form products, or decay back to reactants, as in systems studied previously.^{122,123}

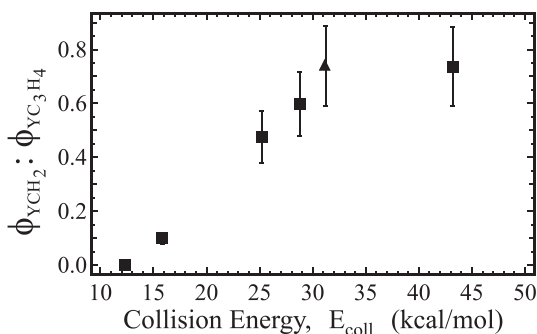


Fig. 26. Product branching ratio, $\phi_{\text{YCH}_2} : \phi_{\text{YC}_3\text{H}_4}$, from collisions of Y + propene as a function of E_{coll} obtained using 157 nm photoionization (squares) and electron impact ionization (triangle).

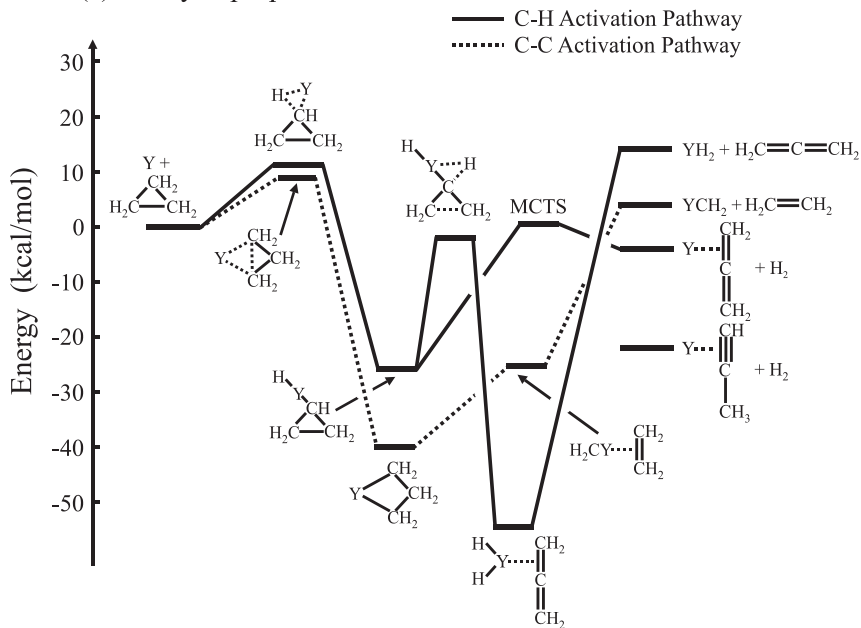
3.6. Yttrium + Cyclopropane \rightarrow YC_3H_4 + H_2

We found that H_2 elimination was significant at all collision energies for Y + cyclopropane. From the ground state reactants, a doublet C–H insertion transition state lying at +11.3 kcal/mol leads to an HYC_3H_5 insertion intermediate, lying 26.9 kcal/mol below the separated reactants (Fig. 27).²² We observed H_2 elimination at collision energies as low as 9.4 kcal/mol. Since spin-orbit excited $\text{Y}(a^2D_{5/2})$ atoms, which contribute 1.5 kcal/mol of electronic energy, are known to be present in our beam,¹²³ the calculated C–H insertion barrier of 11.3 kcal/mol must be a strict upper limit.

The observation of significant translational energy in the YC_3H_4 + H_2 products ($f_{\text{T}} = 0.34$) from Y + cyclopropane suggests the presence of a potential energy barrier along the exit channel reaction coordinate. Similar behavior has been observed in our laboratory for H_2 elimination in reactions of Y with acetylene,¹²³ ethene,¹²² ethane,¹²⁷ and formaldehyde,^{125,128} and is explained by the existence of a multicentered transition state (MCTS) just prior to H_2 elimination, lying slightly higher in energy than the product asymptote.^{46–48}

Like other metal reactions studied previously in our laboratory, H_2 elimination is initiated by insertion into one of the C–H bonds forming HMC_3H_5 . The reaction rate constant for Y + cyclopropane was found to be very small at room temperature, $0.7 \times 10^{-12} \text{ cm}^3 \text{ s}^{-1}$, and it was suggested that the reaction most likely involved termolecular stabilization of C–H or C–C insertion complexes, rather than molecular elimination.²² By analogy with other systems studied, the dynamically most favorable route to H_2 loss in this case is likely via H atom migration to the Y–H moiety, with concerted

(a) Y + cyclopropane



(b) Y + propene

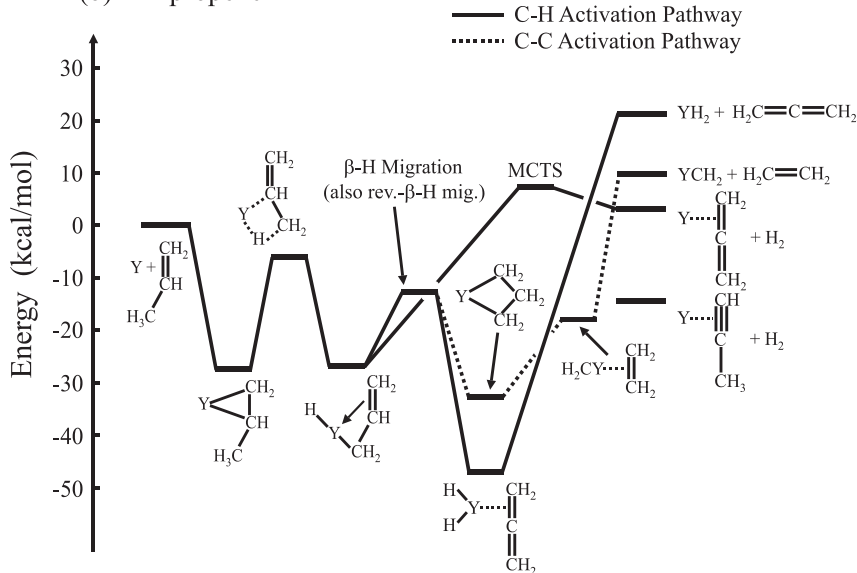


Fig. 27. Schematic potential energy diagrams for the reactions (a) Y + cyclopropane and (b) Y + propene (Ref. 22).

H₂ elimination over a multicenter transition state.^{46–48} This process may involve α -H atom migration (i.e., migration of the lone H atom from the metal-bound C atom), followed by ring opening with formation of allene. Elimination of propyne, which is thermodynamically more favorable than loss of allene,²² requires further H atom rearrangement. From the maximum translational energy distribution shown in Fig. 17, at least 30% of the C₃H₄ products are indeed propyne, indicating that H atom migration occurs during H₂ loss.

3.7. YCH₂ + C₂H₄ from the Cyclopropane Reaction

For the cyclopropane reaction, insertion of a Y atom into the C–C bond results in formation of a “metallacyclobutane” intermediate. This species derives its name from the fact that it involves a four-member ring consisting of the metal atom and 3 carbon atoms (Fig. 27). This complex, which lies 40.0 kcal/mol below the reactants,²² can decay to form YCH₂ + C₂H₄ products by simple electronic rearrangement with simultaneous fission of one C–C bond and one Y–C bond. Since no isomerization or H atom migration is necessary for this process, direct ethene elimination from the metallacyclobutane is expected to be dynamically favorable. There is extensive precedence in the organometallic chemistry literature for this process in both the forward and reverse direction.^{150,151} For example, in the olefin metathesis reaction, the step involving the addition of ethene to a metal carbene forming a metallacyclobutane is the exact reverse of the mechanism proposed here.^{150,151} The small translational energy release ($f_T = 0.18$) observed for ethene loss in the present reaction, and the large yield of YCH₂ products, is consistent with a loose transition state for loss of ethene from the metallacyclobutane complex.

Formation of YCH₂ + C₂H₄ is thermodynamically less favorable than production of YC₃H₄ + H₂. The fact that this channel becomes dominant relative to H₂ elimination at high collision energies is quite striking, and strongly suggests that these processes involve separate dynamical pathways without rapid interconversion to complexes that undergo H₂ elimination. Indeed, H₂ elimination from the cyclic metallacyclobutane complex would require 1,1- or 1,2-H₂ elimination from the sp^3 hybridized carbon atoms, a process that will likely involve large potential energy barriers. These considerations, as well as others,^{141,152} indicate that C₂H₄ rather than H₂ elimination is the dominant decay pathway for the metallacyclobutane. Conversely, C–H insertion in cyclopropane leads to H₂ elimination. Since the rate-limiting steps for both C–C and C–H activation reactions are the

initial insertion processes, and because interconversion between C–C and C–H insertion complexes is not likely to compete with molecular elimination forming products, the branching ratio between YCH_2 and YC_3H_4 production is a measure of the branching ratio for initial C–C to C–H insertion.

3.8. $\text{YC}_3\text{H}_4 + \text{H}_2$ and $\text{YH}_2 + \text{C}_3\text{H}_4$ from the Propene Reaction

In the propene reactions, H_2 elimination was observed at all collision energies studied. This is certainly not surprising in light of the fact that Porembski and Weisshaar observed H_2 elimination at a mean collision energy of only 0.9 kcal/mol.⁴⁷ We observe YC_3H_4 signal from the propene reaction to be 15 times more intense than from cyclopropane at $E_{\text{coll}} = 12$ kcal/mol. As already noted, the reactivity of propene results from the large capture cross-section for formation of π -complexes, a process that has been shown theoretically to proceed with no significant potential energy barrier for $\text{Y} + \text{ethene}$.⁴⁷ This contrasts the situation for reactions of alkanes that must be initiated by direct insertion over relatively tight transition states.²²

As already noted, it has been known for some time that the reaction rate constant is much larger for propene than for ethene at room temperature.²² To date, however, no definitive explanation for this behavior has been offered. We have previously studied the reactions of several second-row transition metal atoms, including Y , with ethene. To better understand why propene is more reactive than ethene, we have measured the branching ratio for decay of π -complexes to products, relative to that for decay back to reactants. This measurement was accomplished by including all reactive contributions, with explicit inclusion of fragmentation effects upon 157 nm photoionization. The non-reactive scattering channel was evaluated by monitoring wide-angle signal appearing at long flight times (Fig. 22) for each reactant system. We find that the ratio for propene and butene is larger than that for ethene by nearly an order of magnitude, indicating that the potential energy barrier for the rate-limiting step in the reaction must be substantially smaller for propene and butene than for ethene. Since the potential energy barriers for insertion of the metal center into the vinylic C–H bonds in each system should not differ appreciably, we conclude that the large difference in reactivity must result from the presence of methyl groups in the propene and butene reactants. These methyl groups apparently open up an important reaction pathway that was not available in the ethene reactions.

There is little doubt that reactions of ethene, propene, and butenes are initiated by formation of π -complexes. For ethene, reaction involves subsequent C–H insertion into one of the four relatively strong sp^2 hybridized C–H bonds. For propene and the butenes, owing to the presence of a methyl group, insertion into the weaker sp^3 hybridized methyl C–H bonds can also occur. The large barriers for insertion of ground state neutral transition metal atoms into the C–H bonds of saturated hydrocarbons are largely due to the inert gas-like s^2 repulsion of the ground state atomic configuration (e.g. s^2d^1 for Y, leading to a barrier height of 20.3 kcal/mol). However, formation of the ground state Y-propene π -complex leads to considerable electronic rearrangement at the metal center, with considerable rehybridization with s^1d^2 electronic character.²⁶ This will substantially decrease the barrier height for intramolecular β -C–H insertion into the methyl C–H bonds in propene. To date, there have been no calculations of the insertion barrier height for the sp^3 hybridized methyl group within the propene complex. However, the much greater reactivity of propene inferred from our experiments, as well as those seen by Carroll²² strongly suggest that this barrier height must be substantially smaller than for insertion into sp^2 hybridized vinylic C–H bonds.

The mechanism for C–H activation of propene is illustrated in Fig. 28. Formation of a π -complex is followed by insertion into a methyl C–H bond. The resulting species may be represented by several resonance structures; two involving a single Y–C bond with added stabilization resulting from donation of π -electron density into the unoccupied levels of the metal, as indicated by the arrow, and a third resonance contribution involving a symmetric allyl-type structure. Transfer of the single hydrogen atom from the central carbon atom is known as “ β -H migration” in the inorganic literature. This process is well known to be the primary decomposition pathway for transition metal alkyl complexes having β -H atoms; such complexes tend to be kinetically unstable.^{153,154} As indicated in Fig. 28(b), this H atom may be transferred to the H atom already present on the metal, leading to H_2 elimination via a multicenter transition state, forming the metal-allene complex. Alternatively, β -H migration to the metal (rather than to the H atom bound to the metal) can lead to production of a Y allyl dihydride complex, which can subsequently eliminate allene. This mechanism is completely analogous to those believed to play important roles in formation of YH_2 in reactions of Y with ethane¹²⁴ and formaldehyde.^{48,125,128}

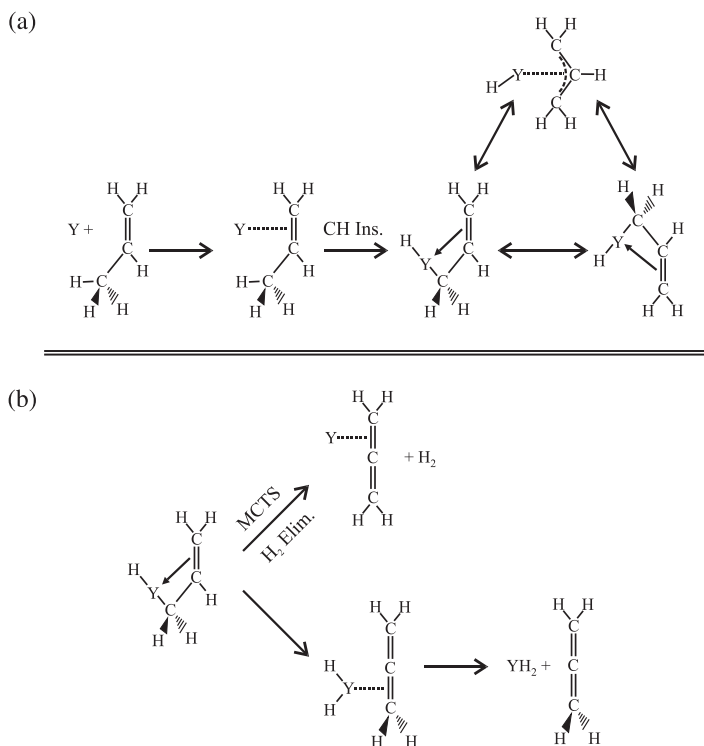


Fig. 28. (a) Proposed reaction mechanism for $Y + \text{propene}$. Addition to the $\text{C}=\text{C}$ bond leads to formation of a π -complex, followed by intramolecular insertion into a methyl $\text{C}-\text{H}$ bond. Three resonance structures may be written for the resulting allyl hydride complex. (b) Mechanism for $\text{C}-\text{H}$ activation of propene. Decay of the allyl hydride complex may proceed via migration of the lone vinyl H atom (β - H migration). Migration may proceed towards the $\text{Y}-\text{H}$ moiety via a MCTS, forming $\text{YC}_3\text{H}_4 + \text{H}_2$ or, alternatively, to Y forming $\text{H}_2\text{YC}_3\text{H}_4$, which subsequently decomposes by simple ligand loss to give $\text{YH}_2 + \text{C}_3\text{H}_4$.

3.9. $\text{YCH}_2 + \text{C}_2\text{H}_4$ Formation from the Propene Reaction

Formation of $\text{YCH}_2 + \text{ethene}$ from the $Y + \text{propene}$ reaction illustrates the cleavage of an unstrained $\text{C}-\text{C}$ bond in a neutral metal-hydrocarbon reaction. We were at first quite surprised that the YCH_2 yield is nearly as large as that for YC_3H_4 at high collision energies, despite the much less favorable thermodynamics for this channel (Fig. 27). We now consider possible mechanisms for rearrangement of the initially-formed Y -propene π -complex to $\text{YCH}_2 + \text{C}_2\text{H}_4$. Immediate insertion into the sp^2-sp^3 $\text{C}-\text{C}$ bond adjacent to the oxidized $\text{C}=\text{C}$ bond in the Y -propene complex, as shown in Fig. 29, is one possible mechanism. The resulting $\text{Y}(\text{CH}_3)$

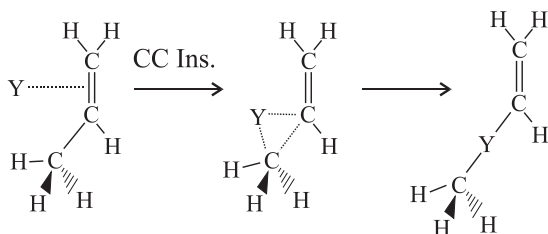


Fig. 29. Possible mechanism for C–C activation involving formation of a π -complex followed by direct sp^2 – sp^3 C–C insertion. This mechanism is ruled out based on the much larger potential energy barrier for C–C insertion relative to C–H insertion from the π -complex.

(CH=CH₂) intermediate could further rearrange via α -C–H insertion to form YCH₂(H)(CH=CH₂). Transfer of an H atom then gives CH₂YC₂H₄ which can decay to YCH₂ + C₂H₄ products. Assuming that all propene reactions originate from a common initially-formed π -complex, the product branching ratio $\phi_{\text{YCH}_2} : \phi_{\text{YC}_3\text{H}_4}$ is the ratio of the rates for C–C insertion (k_{CC}) to that for C–H insertion (k_{CH}) from the initial π -complex. We have thus used RRKM theory to calculate $k_{\text{CC}}(E)/k_{\text{CH}}(E)$.¹³⁰ From these calculations, it is clear that the large yields of YCH₂ + C₂H₄ require that the potential energy barrier for C–C insertion cannot significantly exceed that for C–H insertion. However, theoretical calculations^{22,28} and molecular orbital arguments¹⁵⁵ indicate that C–C insertion barriers are always significantly larger than C–H insertion barriers, except in systems containing ring strain. The observed branching ratios become nearly 1:1 at the highest collision energies, requiring a C–C insertion barrier in the RRKM calculations that is nearly identical to that for C–H insertion, which is not likely. We therefore conclude that the sp^2 – sp^3 C–C insertion mechanism shown in Fig. 29 cannot be an important mechanism for YCH₂ formation from Y + propene.

We believe that the large yield of YCH₂ + C₂H₄ involves a mechanism very similar to that already described for production of YH₂ + C₃H₄ and YC₃H₄ + H₂. Following π -complex formation, insertion of the metal center into one of the methyl C–H bonds leads to production of HYCH₂CHCH₂. As already discussed, YH₂ + C₃H₄ and YC₃H₄ + H₂ result from β -H migration to the metal or to the H atom, respectively. However, if the metal-bound H atom instead migrates to the β -carbon (i.e. to the central carbon in allyl), the *same* metallacyclobutane complex implicated in the cyclopropane reaction is formed through ring closure (Fig. 30). The metallacyclobutane

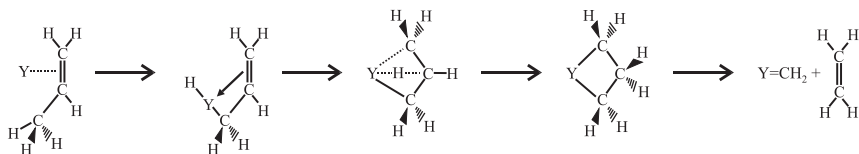


Fig. 30. Mechanism for C–C activation of propene. Decay of the allyl hydride complex may proceed via migration of the metal-bound H atom to the β -carbon atom in the allyl moiety (i.e. reverse β -H migration), leading to formation of the same metallacyclobutane complex implicated in the Y + cyclopropane reaction. The dynamically most favorable decay pathway is to $YCH_2 + C_2H_4$.

complex will preferentially decay to $YCH_2 + C_2H_4$ by simple electronic rearrangement, as in the cyclopropane reaction.

In the propene reaction, C–H insertion into the methyl group following π -complex formation is common to all three reaction pathways. The relative branching ratios for C–H to C–C activation depends on the competition between β -H migration *from* the allyl complex, relative to that involving motion *towards* the allyl complex. Successful synthesis of C–H activation complexes resistant to decomposition usually requires design strategies in which the presence of β -H atoms can be avoided.^{153,154} This is because decomposition via β -H migration to the metal is energetically favorable via a planar transition state. In the case of propene, only a single β -H atom is present in the insertion complex. This lone β -H atom is bonded to an sp^2 hybridized carbon atom (Fig. 28(a)), and is therefore rather strongly bound. This results in relatively small rate constants for C–H bond activation by β -H migration, so in this case, the channel leading to C–C activation can successfully compete.

4. $Y(a^2D)$ + Four Butene Isomers

In an effort to further support the proposed mechanisms for the Y + propene reaction, we have examined the reactions of Y with four isomeric butenes, which are essentially propene molecules with one additional methyl group (Fig. 31). Based on estimated potential energy barrier heights²² and thermodynamics (Fig. 32),^{22,31,34,156,157} it is expected that analogous product channels to those observed for propene should be seen for the butenes. Therefore, a comparison of reactions of butene isomers to reactions with propene should allow us to further test the validity of the proposed mechanisms. Here we briefly summarize our most notable conclusions from this work.

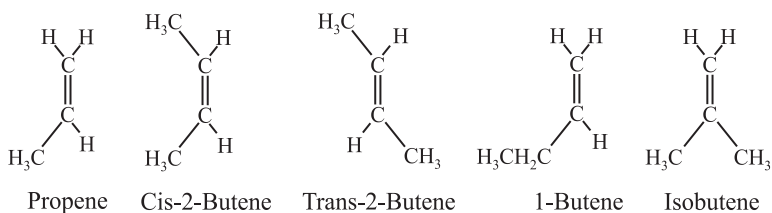


Fig. 31. Structures of propene and four butene isomers.

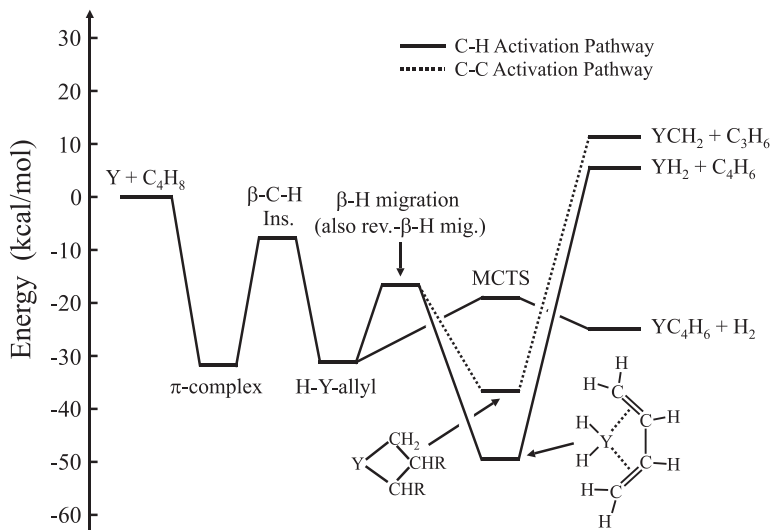


Fig. 32. Schematic potential energy diagram for the reaction of ground state $Y(a^2D)$ with *cis*-2-butene. Energies of stationary points estimated from calculations on $Y + C_2H_4$.²² Energies of product asymptotes calculated from known thermodynamic values and calculated bond dissociation energies.^{22,31,34,156,157}

4.1. $Y + \text{Butenes}$: $E_{\text{coll}} = 26.6 \text{ kcal/mol}$

The reactions of Y with four butene isomers, namely 1-butene, *cis*-2-butene, *trans*-2-butene, and isobutene, were studied at a collision energy (E_{coll}) of 26.6 kcal/mol (see Table 2). In reactions with 1-butene and *cis*- and *trans*-2-butene, four processes were observed:

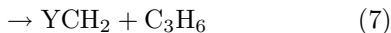
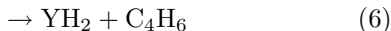
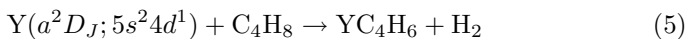


Table 2. Experimental conditions for Y + butene reactions.

$E_{\text{coll}}^{\text{a}}$	Y Carrier Gas	Y Beam Velocity ^b	Y Beam FWHM ^b	Butene Mixture	Butene Beam Velocity ^b	Butene Beam FWHM ^b
11.0	Ne	1100	150	8% in He	1275	116
26.6	He	2200	370	8% in He	1275	116

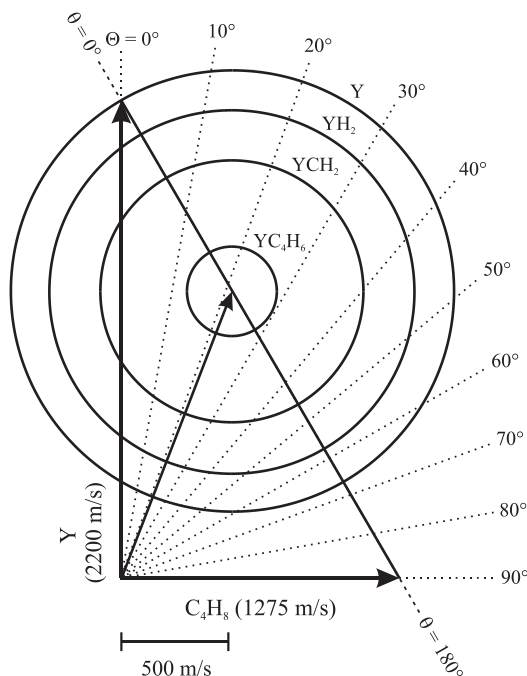
^acal/mol^bm/s

Fig. 33. Newton diagram in velocity space for the reaction Y + *cis*-2-butene at $E_{\text{coll}} = 26.6$ kcal/mol. Circles represent the maximum CM velocity constraints on the indicated metal-containing fragment from the various product channels based on reaction thermodynamics as shown in Fig. 32 and momentum conservation.

Reactions with isobutene led to channels (5), (7), and (8), but no evidence for process (6) was observed. Time-of-flight (TOF) spectra for all four isomers were similar, so only data for the Y + *cis*-2-butene reaction will be shown. A Newton diagram for this reaction is shown in Fig. 33.

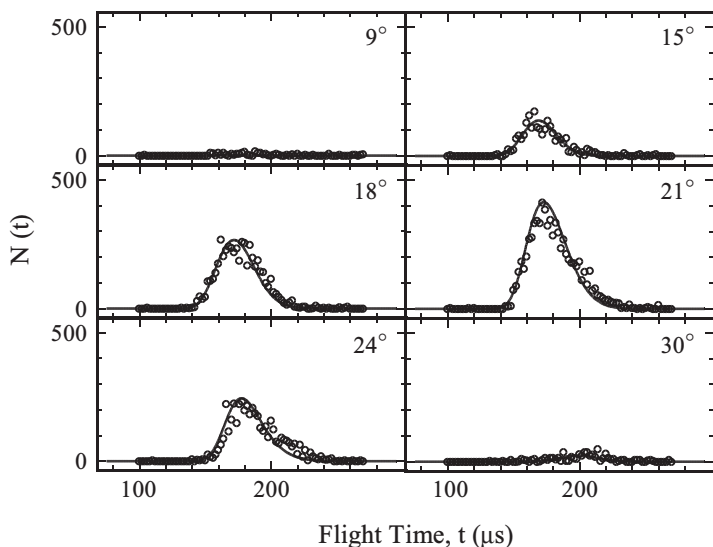


Fig. 34. Sample TOF spectra for YC_4H_6 products at indicated lab angles for the $\text{Y} + \text{cis-2-butene}$ reaction at $E_{\text{coll}} = 26.6$ kcal/mol (open circles). Solid-line fits generated using CM distributions shown in Fig. 38.

In Figs. 34, 35, and 36, the time-of-flight spectra for formation of YC_4H_6 , YH_2 , and YCH_2 respectively, are shown as open points for indicated lab angles. The corresponding lab angular distributions are shown in the second panel of Fig. 37, along with the lab angular distributions for the other three butene isomers. Solid-line fits to the data were generated using the CM distributions shown in Fig. 38. We found that the same CM distributions could be used to fit the data for each of the butene isomers, suggesting similar dynamics in each case. The translational energy distributions for YC_4H_6 and YH_2 were peaked well away from the zero of kinetic energy, with $\langle P(E) \rangle = 12.6$ and 5.6 kcal/mol, respectively, while for YCH_2 , $\langle P(E) \rangle = 2.8$ kcal/mol. From the thermodynamics shown in Fig. 32 for *cis*-2-butene, the average fraction of energy appearing in translation (f_{T}) for each channel was calculated. For YC_4H_6 , $f_{\text{T}} = 0.24$, which is typical for reactions of Y involving elimination of H_2 . For YCH_2 and YH_2 , $f_{\text{T}} = 0.18$ and 0.27 , respectively. Similar values were obtained for the other butene isomers. The CM angular distributions were symmetric about $\theta = 90^\circ$ for each product, indicating the presence of at least one long-lived intermediate along the reaction pathway. For YC_4H_6 , the CM angular distribution

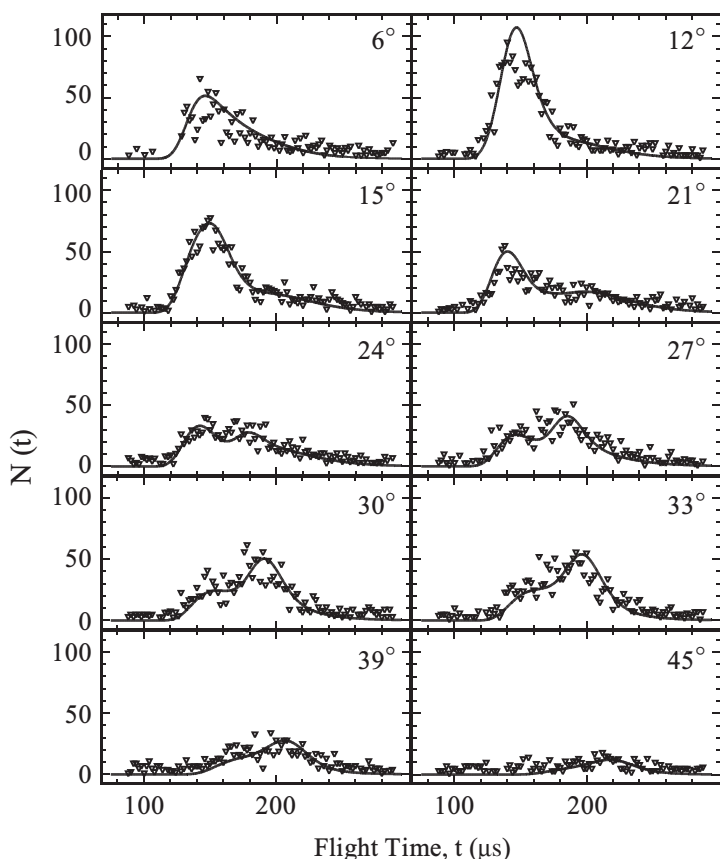


Fig. 35. Sample TOF spectra for YH_2 products at indicated lab angles for the $\text{Y} + \text{cis-2-butene}$ reaction at $E_{\text{coll}} = 26.6 \text{ kcal/mol}$ (open triangles). Solid-line fits generated using CM distributions shown in Fig. 38.

was isotropic, as expected based on angular momentum considerations.¹⁴⁶ The CM angular distributions for YCH_2 and YH_2 were forward-backward peaking, with $T(0^\circ)/T(90^\circ) = 2.8$ and 11.0 , respectively.

The product branching ratios between formation of YC_4H_6 , YCH_2 , and YH_2 were measured for each butene isomer. The values obtained were: for 1-butene, $\phi_{\text{YC}_4\text{H}_6} : \phi_{\text{YH}_2} : \phi_{\text{YCH}_2} = 1.00 : 0.52 : 0.016$, for *cis*-2-butene, $\phi_{\text{YC}_4\text{H}_6} : \phi_{\text{YH}_2} : \phi_{\text{YCH}_2} = 1.00 : 0.87 : 0.011$, for *trans*-2-butene, $\phi_{\text{YC}_4\text{H}_6} : \phi_{\text{YH}_2} : \phi_{\text{YCH}_2} = 1.00 : 0.68 : 0.014$, and for isobutene, $\phi_{\text{YC}_4\text{H}_6} : \phi_{\text{YH}_2} : \phi_{\text{YCH}_2} = 1.00 : 0.00 : 0.034$ (upper right corners of Fig. 37 graphs).¹³⁸

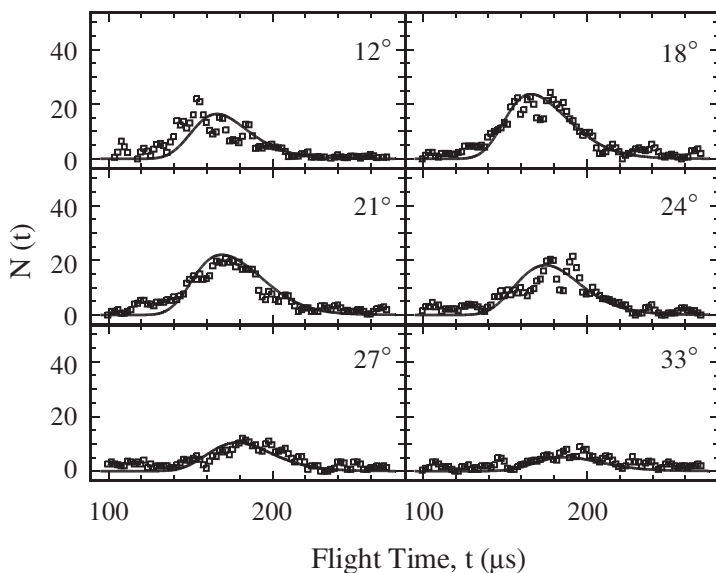


Fig. 36. Sample TOF spectra for YCH_2 products at indicated lab angles for the $\text{Y} + \text{cis-2-butene}$ reaction at $E_{\text{coll}} = 26.6 \text{ kcal/mol}$ (open squares). Solid-line fits generated using CM distributions shown in Fig. 38.

4.2. $\text{Y} + \text{Butenes}$: $E_{\text{coll}} = 11.0 \text{ kcal/mol}$

Data were also recorded for the reaction of Y with all four butene isomers at a lower collision energy of 11.0 kcal/mol . Time-of-flight spectra were taken at the CM angle for each isomer. As shown in Fig. 39 for $\text{Y} + \text{cis-2-butene}$, only YC_4H_6 products were observed. This collision energy corresponded to the thermodynamic threshold for YCH_2 formation, and was only slightly above threshold for the YH_2 channel (Fig. 32).

4.3. $\text{Y} + \text{Butenes}$ Reaction Mechanisms

Upon examining the data for the reactions of all four butene isomers (Fig. 37), the most striking observation is that the data for all four isomers are quite similar, except that there is no YH_2 formed from isobutene. In addition, the branching ratios for each isomer are similar, except that $\phi_{\text{YCH}_2} : \phi_{\text{YC}_4\text{H}_6}$ is approximately a factor of two greater for isobutene than for the other isomers, and for propene, YCH_2 is a much more important channel than is YH_2 (Fig. 40), a situation that is exactly the opposite to that for the butene reactions (Fig. 37).

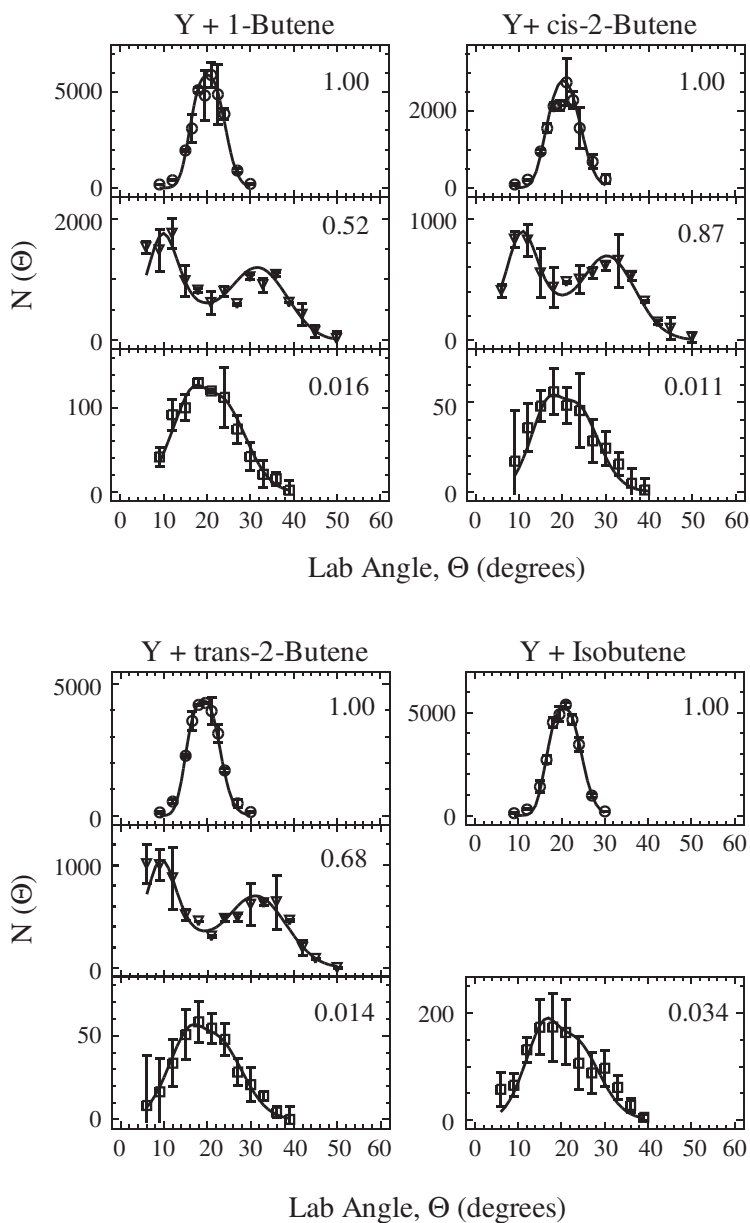


Fig. 37. Lab angular distributions for all reactive products from reactions of Y with four butene isomers at $E_{\text{coll}} = 26.6$ kcal/mol. Products are: YC_4H_6 (open circles), YH_2 (open triangles), and YCH_2 (open squares). Solid-line fits generated using CM distributions shown in Fig. 38. Corresponding product yields given in the upper right corner of each graph. Each distribution is scaled to the same number of scans (2).

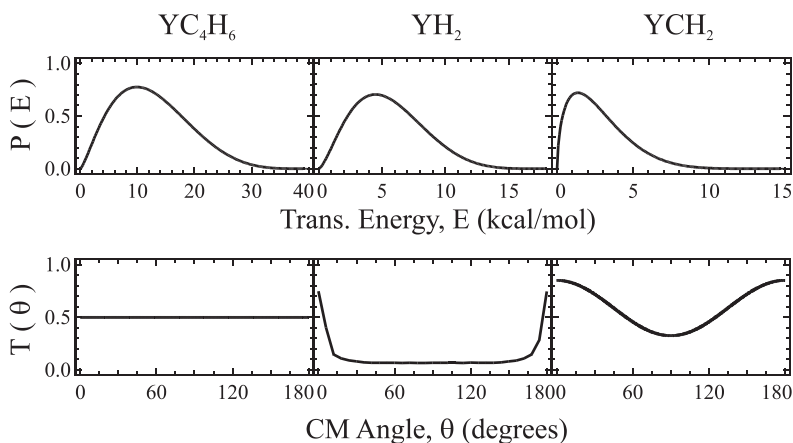


Fig. 38. Center-of-mass distributions used to fit the YC_4H_6 , YH_2 , and YCH_2 data shown in Figs. 34–37 at $E_{\text{coll}} = 26.6$ kcal/mol.

It was noted that the branching ratio for decay of π -complexes to products relative to that for decay back to reactants ($\phi_{\text{reactive}} : \phi_{\text{non-reactive}}$) was an order of magnitude greater for propene compared to ethene, indicating that insertion of Y into the β -C–H bonds of the methyl group in propene (forming H–Y-allyl) was an important reaction channel that was not available for ethene. The presence of an MCTS along the pathway to YC_3H_4 formation was postulated by analogy to calculations on H_2 elimination from $C_2H_4^{47}$ and H_2CO .⁴⁸ The step following H–Y-allyl formation on the pathway to formation of YH_2 is an example of intramolecular β -H migration, a process that is well known in solution-phase organometallic chemistry, where transition metal alkyl complexes containing β -H atoms have been observed to be kinetically much less stable than those complexes lacking β -H atoms.^{153,154} The mechanism for YCH_2 formation involving decomposition of a metallacyclobutane intermediate¹⁵⁰ allowed for C–C activation to occur without direct insertion of the metal atom into a C–C bond. For propene, the availability of a low energy pathway involving H atom migration for YCH_2 production facilitated effective competition with YC_3H_4 production. The YCH_2 product channel would be expected to be very minor if C–C bond insertion was required, since the barrier for that process should be significantly larger than that for C–H insertion.

Owing to the similarity in structures (Fig. 31) and the magnitude of $\phi_{\text{reactive}} : \phi_{\text{non-reactive}}$ for propene and the four butene isomers, the

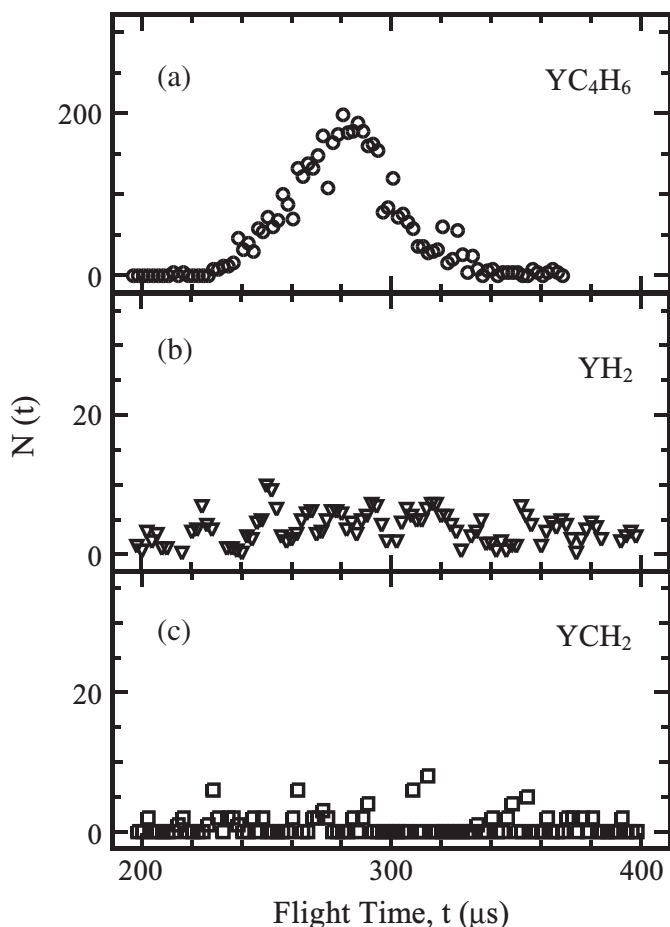


Fig. 39. Time-of-flight spectra for m/e values corresponding to (a) YC_4H_6 , (b) YH_2 , and (c) YCH_2 products from the $\text{Y} + \text{cis-2-butene}$ reaction at the CM angle for $E_{\text{coll}} = 11.0 \text{ kcal/mol}$.

mechanisms for the butenes are similar to those discussed for propene, as shown in Fig. 41. The first step is again formation of a π -complex, which should be bound by approximately 30 kcal/mol relative to reactants (Fig. 32). The next step is β -C-H bond insertion, forming a methyl-substituted H-Y-allyl intermediate that can subsequently decay by the three competing processes described above for propene.

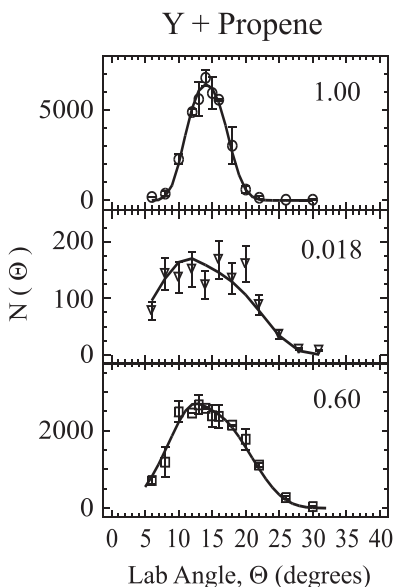


Fig. 40. Lab angular distributions for YC_3H_4 (open circles), YH_2 (open triangles), and YCH_2 (open squares) products from the $\text{Y} + \text{propene}$ reaction at $E_{\text{coll}} = 28.8 \text{ kcal/mol}$. Corresponding product yields are given in the upper right corner of each graph. Note that each distribution is scaled to the same number of scans (2).

Mechanisms for formation of $\text{YC}_4\text{H}_6 + \text{H}_2$ and $\text{YCH}_2 + \text{C}_3\text{H}_6$ in the butene reactions are similar to those for the analogous products from propene. However, there exists a significant difference between the reaction mechanisms for butene and propene for the β -H migration step on the pathway leading to YH_2 and H_2 elimination. For propene, there is only one β -H atom in the H-Y-allyl intermediate available to undergo migration, residing on the central sp^2 hybridized C atom (Fig. 41(a)). For *cis*- and *trans*-2-butene (Fig. 41(b)) and 1-butene (Fig. 41(c)), the extra methyl group presents three β -H atoms attached to an sp^3 hybridized carbon atom. Since $\text{C}(sp^3)\text{-H}$ bond strengths are smaller than those for $\text{C}(sp^2)\text{-H}$ bonds (86.7 kcal/mol for propene versus 109.7 kcal/mol for ethene, respectively¹³⁷), β -H migration for the butenes should be more thermodynamically favorable than for propene. There is also a statistical advantage for the butenes, since there are three β -H atoms available for migration, rather than one. Both of these factors should greatly enhance the rate of β -H migration leading to YH_2 and H_2 elimination products. These factors, combined with more favorable thermodynamics for YH_2 formation

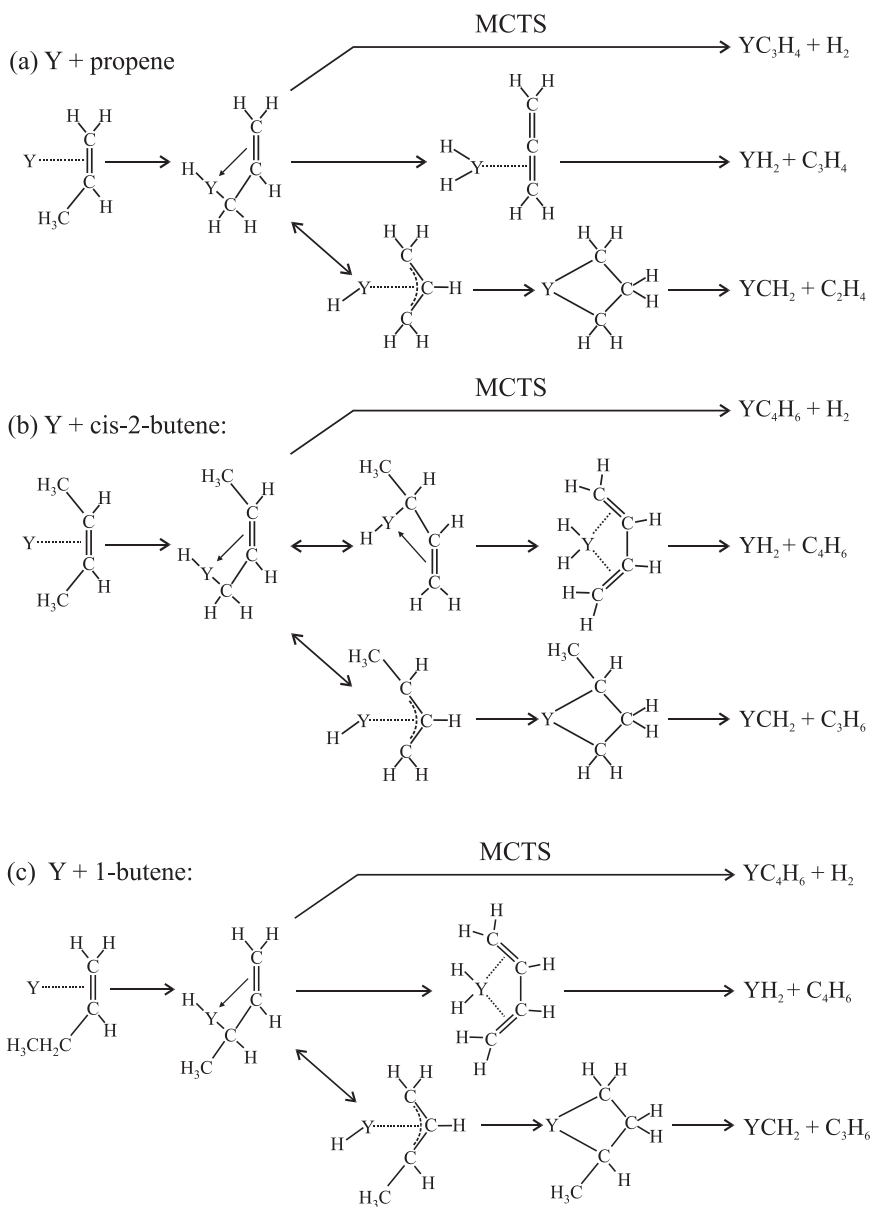


Fig. 41. Proposed mechanisms for the reactions: (a) Y + propene, (b) Y + *cis*-2-butene, (c) Y + 1-butene, (d) Y + isobutene. Note that the mechanism for Y + *trans*-2-butene is similar to that for Y + *cis*-2-butene and so is not shown. Double-sided arrows indicate resonance structures. See text for details.

(d) Y + isobutene:

MCTS

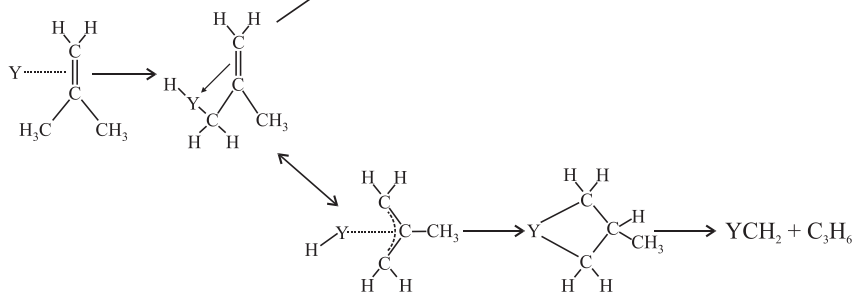


Fig. 41. (Continued)

from butene reactions than from propene, should cause YH₂ formation to be very important for the butene reactions. Indeed, the branching ratios for Y + *cis*- and *trans*-2-butene and 1-butene (Fig. 37) indicate that the YH₂ yield is much greater than that for YCH₂, exactly opposite to that observed for propene (Fig. 40).¹⁵⁸ Further evidence for the importance of β -H migration comes from the Y + isobutene reaction (Fig. 41(d)). In this case, the extra methyl group resides on the central carbon atom, so the methyl-substituted H-Y-allyl intermediate contains no β -H atoms. This is consistent with the lack of YH₂ products from the isobutene reaction (Fig. 37).

5. Conclusions

In this article, we have attempted to review the present state of knowledge pertaining to the chemistry of neutral gas-phase transition metal atoms. Taking into account work that has been performed in our lab and the work of others as described in Sec. 1, it is apparent that there is a large body of experimental data for the reactions of transition metal atoms (Y, Zr, Nb, and Mo in particular) with small molecules. As a result, there are beginning to emerge general trends pertaining to such reactions.

Among the early second-row transition metals, the chemistry is richest for yttrium. In our early studies of Y + C₂H₂¹²³ and C₂H₆,¹²⁴ several competing product channels were observed, while only H₂ elimination was observed for Zr, Nb, or Mo.¹²² Likewise, in reactions with larger molecules (containing three or more carbons for example), yttrium always led to the greatest number of unique product channels. A likely cause for this result is the presence of an exit-channel barrier for H₂ elimination in reactions with Y. Because H₂ elimination is usually the most thermodynamically

avored channel, it is ubiquitous in these metal-atom reactions (the only exception being $Y + \text{CH}_3\text{OH}$, see Sec. 2.3), and is quite often the most dominant product. However, in the case of Y , the exit-channel barrier for H_2 elimination is a tight transition state, acting as a kinetic restriction for formation of H_2 elimination products. Since the final steps for most of the other observed product channels correspond to simple bond fission (i.e. a loose transition state), these reactions are not kinetically restrained and can therefore become competitive at higher collision energies, despite being less thermodynamically favorable than H_2 elimination. A prime example of this was demonstrated for $Y + \text{CH}_3\text{CHO}$,¹⁵⁹ where at low collision energies H_2 elimination was dominant, but as the collision energy was raised, H elimination became competitive. The observation of a large amount of translational energy in H_2 elimination products from Y reactions (typically around 30% of the available energy) also is a strong indicator of a barrier. Recent calculations by Weisshaar and Bayse have confirmed the existence of such exit-channel barriers for the $Y + \text{C}_2\text{H}_4$ ⁴⁷ and $Y + \text{H}_2\text{CO}$ ⁴⁸ reactions, respectively.

Another trend obvious from our work is that the chemistry gets richer as the size of the molecular reactant increases. In particular, for molecules containing more than two carbon atoms, $\text{C}-\text{C}$ bond activation becomes competitive with $\text{C}-\text{H}$ activation. For example, in reactions of Y with both cyclopropane and propene (Sec. 3), YC_3H_4 and YH_2 products were observed along with YCH_2 . In this and most other cases, the $\text{C}-\text{C}$ bonds being cleaved were single bonds, but interestingly, in the $Y + \text{H}_2\text{CCO}$ reaction, products resulting from cleavage of the $\text{C}=\text{C}$ bond were observed to be quite important.¹⁴⁴ One important feature of these reactions is the availability of mechanisms other than direct insertion of the metal atom into $\text{C}-\text{C}$ bonds. For example, in the propene and butene reactions (Secs. 3 and 4), the reaction mechanism involves initial π -complex formation followed by insertion of Y into a $\beta\text{-C}-\text{H}$ bond. Subsequent competition between three H migration processes led to the three observed product channels.

The experimental techniques that have been used to study transition metal atom reactions (crossed molecular beams, flow tubes, etc.) are powerful ones. However, a complete interpretation of the mechanistic and dynamic aspects of these reactions is greatly facilitated through comparison of experimental results to theoretical predictions.¹⁵⁹ The early theoretical work by the group of Siegbahn led to a great number of testable predictions, many of which have been found to be remarkably precise. Our measurements of various thermodynamic quantities have shown these calculations to be generally accurate to within 5–6 kcal/mol. Unfortunately, due to the

limited capacity of the theoretical methods employed at that time, complete potential energy surfaces (or even complete reaction coordinates) were not calculated for most of the reactions they studied. Subsequent calculations by the Weisshaar group^{45–47} and by Bayse⁴⁸ have focused on computationally mapping out the entire reaction coordinate for a given reaction. These efforts, while time-intensive and computationally demanding, are extremely rewarding in the amount of knowledge they yield. And although the methods employed have yet to be shown to be of chemical accuracy (i.e. to within 1–2 kcal/mol) for these transition metal atom reactions,¹⁵⁹ they are nonetheless invaluable in the search for comprehensive descriptions of these reactions.

Clearly, the study of reactions of neutral transition metal atoms with small molecules in the gas-phase is a very active area of chemistry, and these reactions have proven to not only be reasonable models for important organometallic reactions, but to be very interesting both chemically and physically in their own right. The great wealth of theoretical and experimental data accumulated thus far has unlocked many of the secrets regarding trends in neutral transition metal atom chemistry both within a given row or column of the periodic table and between the rows and columns themselves. However, there are a great many subtler, and perhaps more interesting, factors governing the chemistry of metal atoms at the microscopic level that are only now beginning to be discovered.

6. Future Directions

6.1. *The Role of Vibrational Excitation in Transition Metal Reactivity*

To date, our studies have primarily focused on reactions of neutral transition metal atoms in their ground electronic states. Recent work, both by Weisshaar's group and by us, has confirmed that electronic excitation is quite effective in promoting transition metal-hydrocarbon reactivity. However, except in favorable cases,¹⁶⁰ the potential energy surfaces for reactions involving electronically excited transition metals are extremely complex. Consequently, we believe that the most important fundamental insight in transition metal chemistry will emerge from studies of reactions involving the ground electronic states.

The role of reactant vibrational energy in bimolecular reactions is one of the oldest and most fundamental topics in chemical reaction dynamics.^{161,162} For simple three-atom systems, the concept of “early” and

“late” transition states, first proposed by Polanyi,¹⁶² has been remarkably successful in its ability to predict the effects of reactant vibrational and translational energy, and the disposal of excess energy into the products’ degrees-of-freedom. For the reactions H and $\text{Cl} + \text{HOD}$ (and its isotopic variants),¹⁶³ the role of reactant vibrational energy has been elegantly studied, most notably by the groups of Crim^{164–166} and Zare.^{167–169} Mode and bond-specific effects in this family of reactions are now well-documented, and are examples in textbook chapters on reaction dynamics.¹⁷⁰ In all of the studies to date, the reactions have involved direct abstraction *without* formation of long-lived intermediates.

Crim and co-workers have also recently studied the direct abstraction reactions of chlorine atoms with symmetric and asymmetric vibrational levels of CH_4 produced by direct vibrational excitation using an OPO.¹⁷¹ Since the pure symmetric stretching mode (ν_1) is IR inactive, the mode near 6000 cm^{-1} involving the symmetric stretch-bend combination of CH_4 ($\nu_1 + \nu_4$) was compared to the antisymmetric stretch-bend combination ($\nu_3 + \nu_4$). Although both modes promoted chemical reactivity, the *symmetric* combination promoted reactivity by a factor of approximately twice that of the *asymmetric* mode. This behavior, which has also been predicted theoretically,^{172–174} is intriguing because it is somewhat counter-intuitive. For direct abstraction, to a first approximation, the reaction coordinate resembles asymmetric stretching more closely than symmetric stretching, so one would have initially anticipated that symmetric stretching should be less effective, rather than more effective, in promoting reaction.

An extensive review of the literature reveals that the only studies of vibrational effects in insertion chemistry have focused on reactions of $\text{O}(^1\text{D})$ ^{175–177} and $\text{C}(^1\text{D})$ ^{177,178} with H_2 . Since there is no potential energy barrier to insertion in these systems, reaction proceeds readily even for unexcited reactants.¹⁷⁹ Since the efficiency of vibrational excitation was $\approx 20\%$ in both studies, due to the large cross-sections for ground state reactions, only small changes were observed in the experimental signal. From an analysis of the product distributions, it was concluded that while $\text{H}_2(v = 0)$ primarily reacted via an insertion mechanism, direct abstraction seemed to become important for $\text{H}_2(v = 1)$. For $\text{O}(^1\text{D})$, this is similar to behavior at elevated collision energies.¹⁸⁰

In studies of vibrationally excited hydrocarbons with transition metal atoms to be carried out in our laboratory, reaction of the unpumped molecules cannot occur at collision energies below the C–H insertion barrier for $v = 0$. Thus, no background signal from unpumped molecules will be

present. Because the molecular reactants are polyatomic, different vibrational modes can be pumped, allowing us to compare their reactivity. For example, the same pair of modes studied by Crim's group, $\nu_1 + \nu_4$ and $\nu_3 + \nu_4$ for CH_4 , can be compared directly. Although the reactions do involve formation of long-lived C–H insertion complexes, since the initial step involves direct insertion over a substantial barrier, considerable mode specificity is likely to exist in the initial dynamics. Indeed, there is now good evidence for mode specificity in the dissociative adsorption of CH_4 at metal surfaces, which, like gas phase metal atom insertion, proceeds over a substantial barrier. In the studies of dissociation of CH_4 antisymmetric ($\nu_3 = 1$) levels on a metal surface, Utz¹⁸¹ finds reactivity is enhanced by a factor of up to 1600 for vibrationally excited molecules at low collision energies. However, these molecules are less reactive than if the same energy was put into relative translation. Furthermore, this pure vibrationally excited state was found to be less reactive than a thermal ensemble of molecules (prepared using a heated nozzle) having an average energy equal to that for $\nu_3 = 1$. This suggests that other vibrational modes populated in a thermal ensemble must be significantly more reactive than $\nu_3 = 1$. Results from recent experiments by Scoles¹⁸² group are consistent with these ideas.

6.2. Reaction Dynamics of Partially-Ligated Species

Our experiments so far have focused exclusively on reactions of isolated transition metal *atoms* with small molecules. Owing to their simplicity, these systems are attractive from a theoretical and experimental point of view. However, the absence of ligands makes these systems quite foreign to an inorganic chemist. In the near future, we plan to carry out studies of reactions involving partially-ligated species in crossed beams. We hope that this will provide an important link between reactions of isolated transition metal atoms and “real” transition metal complexes of interest to the inorganic and synthetic community.

Of course, commercially available transition metal complexes are stable at room temperature because they have achieved an 18-electron “noble gas-like” electronic configuration. Thus, molecules like iron pentacarbonyl $[\text{Fe}(\text{CO})_5]$, ferrocene $[\text{Fe}(\text{C}_5\text{H}_5)_2]$, as well as “piano-stool” complexes such as $\text{C}_5\text{H}_5\text{Co}(\text{CO})_2$ are chemically quite inert. In order to study bimolecular reactions, it is necessary to first prepare unsaturated complexes. For studies using molecular beams, one approach is through photolysis of a stable volatile precursor in a supersonic nozzle.

In the early 1980s, considerable excitement was generated by the finding that photolytically-produced 16-electron unsaturated complexes, $\text{Cp}^*\text{M}(\text{CO})$ [$\text{M} = \text{Ir}, \text{Rh}$; $\text{Cp}^* = \text{C}_5(\text{CH}_3)_5$] readily insert into unactivated alkane C–H bonds.¹⁸³ In homogeneous environments, these or related complexes might be useful as future catalysts for converting abundant volatile hydrocarbons into more useful liquid hydrocarbon fuels. The reactivity of these species has been subsequently studied by several groups using a number of techniques, most recently by Harris and co-workers using time-resolved femtosecond pump-probe methods.¹⁸⁴

We have begun to develop and characterize a source of jet-cooled $\text{C}_5\text{H}_5\text{Co}(\text{CO})$, produced by near UV photodissociation of $\text{C}_5\text{H}_5\text{Co}(\text{CO})_2$. A potential energy barrier around 10 kcal/mol is thought to exist for insertion of $\text{C}_5\text{H}_5\text{Co}(\text{CO})$ into the C–H bond of methane. Although the bond dissociation energies for the Co and Rh complexes have not been measured, M–CO bond strengths are 20–30 kcal/mol ($7,000\text{--}10,500\text{ cm}^{-1}$); the M– C_5H_5 binding energy is likely to be somewhat larger.¹⁸⁵

In preliminary studies carried out recently in our laboratory, we have found that UV excitation of $\text{C}_5\text{H}_5\text{Co}(\text{CO})_2$ at 355 nm leads primarily to CO bond fission, producing $\text{C}_5\text{H}_5\text{Co}(\text{CO})$.¹⁸⁶ In these experiments, the $\text{C}_5\text{H}_5\text{CoCO}$ products were detected in a photofragment translational energy spectroscopy experiment with very high signal to noise ratios (Fig. 42). Although some $\text{C}_5\text{H}_5\text{Co}$ products were also seen, the contribution increases with laser fluence, suggesting that it is a two-photon process. The signal to noise ratio was high, suggesting that parent compounds with lower volatility should also be amenable to this approach.

Photodissociation approximately 1–3 mm from the nozzle orifice at an appropriate wavelength will produce highly reactive jet-cooled unsaturated species. The bimolecular insertion and ligand exchange dynamics of these species with small hydrocarbons (CH_4 , C_2H_4 , etc.) can then be studied using the method of crossed molecular beams. Also, by adding several percent Xe or Kr to the metal complex carrier gas, jet-cooled noble gas adducts such as $\text{C}_5\text{H}_5\text{Rh}(\text{CO})\text{Xe}$ can also be produced, and the bimolecular exchange reactions from single collisions with hydrocarbon molecules can be studied. These experiments will facilitate measurements of reaction mechanisms, potential energy barrier heights, and energy disposal in prototype ligand exchange reactions and hydrocarbon C–H and C–C bond activation processes.

For example, single collisions of $\text{C}_5\text{H}_5\text{MCO}$ with hydrocarbons such as CH_4 are expected to lead to insertion forming $\text{C}_5\text{H}_5\text{M}(\text{CO})(\text{R})(\text{H})$. In the

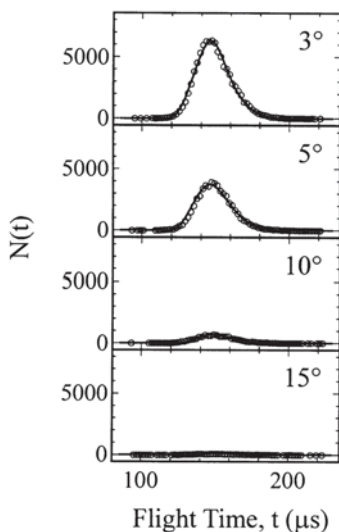
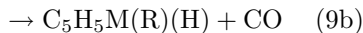
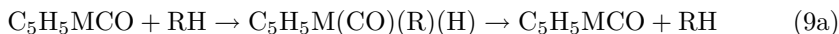


Fig. 42. $\text{Co}(\text{C}_5\text{H}_5)\text{CO}$ time-of-flight spectra at indicated laboratory angles from photodissociation of $\text{Co}(\text{C}_5\text{H}_5)(\text{CO})_2$ at 355 nm.

absence of collisions, this species cannot remain bound but must dissociate back to reactants or eliminate CO:



We plan to study the competition between RH and CO elimination as a function of collision energy. By measuring the branching ratio for competing decay channels as a function of collision energy, we can gain considerable insight into the nature of the potential energy surfaces governing reaction. Furthermore, molecular elimination (e.g. H_2) similar to that observed in our studies of transition metal atom reactions may be possible, particularly if a low-energy multicenter transition state or ring-slip mechanism facilitates H_2 formation via $\eta^3\text{-C}_5\text{H}_5\text{M}(\text{CO})(\text{CH}_2)(\text{H})(\text{H})$.

Acknowledgments

This work was supported by the National Science Foundation. J. J. S. thanks the Cornell Graduate School, Department of Education, and Franz Roessler Foundation for fellowships. The authors have benefited greatly from the detailed mechanistic insight provided through numerous discussions with Professor Paul Chirik.

References

1. M. Blomberg, U. Brandemark, L. Pettersson and P. Siegbahn, *Int. J. Quantum Chem.* **23**, 855 (1983).
2. M. R. A. Blomberg, U. Brandemark and P. E. M. Siegbahn, *J. Am. Chem. Soc.* **105**, 5557 (1983).
3. P. E. M. Siegbahn and M. R. A. Blomberg, *Chem. Phys.* **87**, 189 (1984).
4. M. R. A. Blomberg, U. B. Brandemark, P. E. M. Siegbahn, K. B. Mathisen and G. Karlstrom, *J. Phys. Chem.* **89**, 2171 (1985).
5. P. Widmark, B. O. Roos and P. E. M. Siegbahn, *J. Phys. Chem.* **89**, 2180 (1985).
6. M. R. A. Blomberg, P. E. M. Siegbahn and A. Strich, *Chem. Phys.* **97**, 287 (1985).
7. P. E. M. Siegbahn and U. B. Brandemark, *Theor. Chim. Acta* **69**, 119 (1986).
8. M. R. A. Blomberg, U. B. Brandemark and P. E. M. Siegbahn, *Chem. Phys. Lett.* **126**, 317 (1986).
9. C. W. Bauschlicher, Jr. and P. E. M. Siegbahn, *J. Chem. Phys.* **85**, 2802 (1986).
10. I. Panas, J. Schule, U. Brandemark, P. Siegbahn and U. Wahlgren, *J. Phys. Chem.* **92**, 3079 (1988).
11. M. Blomberg, U. Brandemark, J. Johansson, P. Siegbahn and J. Wennerberg, *J. Chem. Phys.* **88**, 4324 (1988).
12. M. R. A. Blomberg, U. B. Brandemark, P. E. M. Siegbahn, J. Wennerberg and C. W. Bauschlicher, Jr., *J. Am. Chem. Soc.* **110**, 6650 (1988).
13. S. A. Mitchell, M. A. Blitz, P. E. M. Siegbahn and M. Svensson, *J. Chem. Phys.* **100**, 423 (1994).
14. P. E. M. Siegbahn, M. R. A. Blomberg and C. W. Bauschlicher, Jr., *J. Chem. Phys.* **81**, 1373 (1984).
15. M. R. A. Blomberg, P. E. M. Siegbahn and M. Svensson, *J. Phys. Chem.* **95**, 4313 (1991).
16. J. E. Backvall, E. E. Bjorkman, L. Pettersson and P. Siegbahn, *J. Am. Chem. Soc.* **107**, 7265 (1985).
17. J. E. Backvall, E. E. Bjorkman, L. Pettersson, P. Siegbahn and A. Strich, *J. Am. Chem. Soc.* **107**, 7408 (1985).
18. M. R. A. Blomberg, P. E. M. Siegbahn, U. Nagashima and J. Wennerberg, *J. Am. Chem. Soc.* **113**, 424 (1991).
19. M. Svensson, M. R. A. Blomberg and P. E. M. Siegbahn, *J. Am. Chem. Soc.* **113**, 7076 (1991).
20. M. R. A. Blomberg, P. E. M. Siegbahn and M. Svensson, *J. Am. Chem. Soc.* **114**, 6095 (1992).
21. P. E. M. Siegbahn, *Organometallics* **13**, 2833 (1994).
22. J. J. Carroll, K. L. Haug, J. C. Weisshaar, M. R. A. Blomberg, P. E. M. Siegbahn and M. Svensson, *J. Phys. Chem.* **99**, 13955 (1995).
23. P. E. M. Siegbahn, M. R. A. Blomberg and M. Svensson, *J. Am. Chem. Soc.* **115**, 4191 (1993).

24. A. M. C. Wittborn, M. Costas, M. R. A. Blomberg and P. E. M. Siegbahn, *J. Chem. Phys.* **107**, 4318 (1997).
25. P. E. M. Siegbahn, *Theor. Chim. Acta* **87**, 277 (1994).
26. M. R. A. Blomberg, P. E. M. Siegbahn and M. Svensson, *J. Phys. Chem.* **96**, 9794 (1992).
27. P. E. M. Siegbahn, M. R. A. Blomberg and M. Svensson, *J. Am. Chem. Soc.* **115**, 1952 (1993).
28. P. E. M. Siegbahn and M. R. A. Blomberg, *J. Am. Chem. Soc.* **114**, 10548 (1992).
29. P. E. M. Siegbahn, M. R. A. Blomberg and M. Svensson, *J. Phys. Chem.* **97**, 2564 (1993).
30. M. R. A. Blomberg, P. E. M. Siegbahn and M. Svensson, *Inorg. Chem.* **32**, 4218 (1993).
31. P. E. M. Siegbahn, *Chem. Phys. Lett.* **201**, 15 (1993).
32. P. E. M. Siegbahn, *J. Phys. Chem.* **97**, 9096 (1993).
33. P. E. M. Siegbahn, *Theor. Chim. Acta* **86**, 219 (1993).
34. P. E. M. Siegbahn, *Theor. Chim. Acta* **87**, 441 (1994).
35. P. E. M. Siegbahn, *J. Am. Chem. Soc.* **116**, 7722 (1994).
36. P. E. M. Siegbahn, *J. Phys. Chem.* **99**, 12723 (1995).
37. M. R. A. Blomberg, C. A. M. Karlsson and P. E. M. Siegbahn, *J. Phys. Chem.* **97**, 9341 (1993).
38. P. E. M. Siegbahn, *J. Am. Chem. Soc.* **115**, 5803 (1993).
39. P. E. M. Siegbahn, *Chem. Phys. Lett.* **205**, 290 (1993).
40. P. E. M. Siegbahn, M. Svensson and P. J. E. Boussard, *J. Chem. Phys.* **102**, 5377 (1995).
41. M. J. S. Dewar, *Bull. Soc. Chim. Fr.* **18**, C71 (1951).
42. J. Chatt and L. A. Duncanson, *J. Chem. Soc.* 2939 (1953).
43. (a) C. W. Bauschlicher, Jr. and S. P. Walch, *J. Chem. Phys.* **76**, 4560 (1982); (b) P. S. Bagus, C. J. Nelin and C. W. Bauschlicher, Jr., *J. Vac. Sci. and Tech.* **A2**, 905 (1984); (c) P. S. Bagus, K. Hermann and C. W. Bauschlicher, Jr., *J. Chem. Phys.* **81**, 19866 (1984); (d) S. R. Langhoff, C. W. Bauschlicher, Jr. and H. Partridge, *J. Chem. Phys.* **89**, 396 (1988); (e) S. R. Langhoff and C. W. Bauschlicher, Jr., *J. Chem. Phys.* **89**, 2160 (1988); (f) S. R. Langhoff and C. W. Bauschlicher, Jr., *Ann. Rev. Phys. Chem.* **39**, 181 (1988); (g) L. A. Barnes and C. W. Bauschlicher, Jr., *J. Chem. Phys.* **91**, 314 (1989); (h) L. A. Barnes, M. Rosi and C. W. Bauschlicher, Jr., *J. Chem. Phys.* **94**, 2031 (1991); (i) C. W. Bauschlicher, Jr., *J. Chem. Phys.* **100**, 1215 (1994); (j) C. W. Bauschlicher, Jr. and P. Maitre, *Theo. Chim. Acta* **90**, 189 (1995).
44. (a) S. P. Walch and W. A. Goddard III, *J. Am. Chem. Soc.* **98**, 7908 (1976); (b) T. H. Upton and W. A. Goddard III, *J. Am. Chem. Soc.* **100**, 321 (1978); (c) S. P. Walch and W. A. Goddard III, *J. Am. Chem. Soc.* **100**, 1338 (1978); (d) J. J. Low and W. A. Goddard III, *J. Am. Chem. Soc.* **106**, 8321 (1984); (e) J. J. Low and W. A. Goddard III, *J. Am. Chem. Soc.* **106**, 6928 (1984); (f) J. J. Low and W. A. Goddard III, *Organometallics* **5**,

- 609 (1986); (g) J. J. Low and W. A. Goddard III, *J. Am. Chem. Soc.* **108**, 6115 (1986); (h) X. Xu, F. Faglioni and W. A. Goddard III, *J. Phys. Chem.* **A106**, 7171 (2002).
45. M. Porembski and J. C. Weisshaar, *J. Phys. Chem.* **A104**, 1524 (2000).
46. M. Porembski and J. C. Weisshaar, *J. Phys. Chem.* **A105**, 4851 (2001).
47. M. Porembski and J. C. Weisshaar, *J. Phys. Chem.* **A105**, 6655 (2001).
48. C. A. Bayse, *J. Phys. Chem.* **A106**, 4226 (2002).
49. J. J. Schroden, H. F. Davis and C. A. Bayse, in preparation.
50. E. D. Glendening and M. L. Strange, *J. Phys. Chem.* **A106**, 7338 (2002).
51. E. D. Glendening, personal communication.
52. K. Liu and J. M. Parson, (a) *J. Chem. Phys.* **67**, 1814 (1977); (b) *J. Chem. Phys.* **68**, 1794 (1978); (c) *J. Phys. Chem.* **83**, 970 (1979).
53. C. L. Chalek and J. L. Gole, (a) *J. Chem. Phys.* **65**, 2845 (1976); (b) *J. Chem. Phys.* **65**, 4384 (1976); (c) *Chem. Phys.* **19**, 59 (1977).
54. D. M. Manos and J. M. Parson, *J. Chem. Phys.* (a) **63**, 3575 (1975); (b) **69**, 231 (1978).
55. J. M. Parson, L. C. Geiger and T. J. Conway, *J. Chem. Phys.* **74**, 5595 (1981).
56. D. Ritter and J. C. Weisshaar, *J. Phys. Chem.* (a) **93**, 1576 (1989); (b) **94**, 4907 (1990).
57. M. Campbell, R. E. McClean, N. L. Garland and H. H. Nelson, *Chem. Phys. Lett.* **194**, 187 (1992).
58. R. E. McClean and L. Pasternack, *J. Phys. Chem.* **96**, 9828 (1992).
59. M. L. Campbell and R. E. McClean, *J. Phys. Chem.* **97**, 7942 (1993).
60. R. E. McClean, H. H. Nelson and M. L. Campbell, *J. Phys. Chem.* **97**, 9673 (1993).
61. M. L. Campbell, R. E. McClean and J. S. S. Harter, *Chem. Phys. Lett.* **235**, 497 (1995).
62. M. L. Campbell and R. E. McClean, *J. Chem. Soc. Farad. Trans.* **91**, 3787 (1995).
63. R. E. McClean, M. L. Campbell and R. H. Goodwin, *J. Phys. Chem.* **100**, 7502 (1996).
64. M. L. Campbell, *J. Chem. Phys.* **104**, 7515 (1996).
65. M. L. Campbell and J. R. Metzger, *Chem. Phys. Lett.* **253**, 158 (1996).
66. M. L. Campbell, *J. Phys. Chem.* **100**, 19430 (1996).
67. M. L. Campbell, *J. Chem. Soc. Farad. Trans.* **92**, 4377 (1996).
68. R. E. McClean, M. L. Campbell and E. J. Kolsch, *J. Phys. Chem.* **A101**, 3348 (1997).
69. J. S. S. Harter, M. L. Campbell and R. E. McClean, *Int. J. Chem. Kinet.* **29**, 367 (1997).
70. M. L. Campbell and K. L. Hooper, *J. Chem. Soc. Farad. Trans.* **93**, 2139 (1997).
71. M. L. Campbell, K. L. Hooper and E. J. Kolsch, *Chem. Phys. Lett.* **274**, 7 (1997).
72. M. L. Campbell, *J. Phys. Chem.* **A101**, 9377 (1997).
73. M. L. Campbell, *J. Chem. Soc. Farad. Trans.* **94**, 1687 (1998).

74. M. L. Campbell, *J. Phys. Chem.* **A102**, 892 (1998).
75. M. L. Campbell, *Chem. Phys. Lett.* **294**, 339 (1998).
76. M. L. Campbell, *J. Chem. Soc. Farad. Trans.* **94**, 353 (1998).
77. R. E. McClean, M. L. Campbell, M. D. Vorce and L. J. Medhurst, *J. Phys. Chem.* **A103**, 2659 (1999).
78. M. L. Campbell, *J. Chem. Phys.* **111**, 562 (1999).
79. M. L. Campbell, *Phys. Chem. Chem. Phys.* **1**, 3731 (1999).
80. M. L. Campbell, *J. Phys. Chem.* **A103**, 7274 (1999).
81. M. L. Campbell, E. J. Kolsch and K. L. Hooper, *J. Phys. Chem.* **A104**, 11147 (2000).
82. (a) D. E. Clemmer, K. Honma and I. Koyano, *J. Phys. Chem.* **97**, 11480 (1993); (b) K. Honma, M. Nakamura, D. E. Clemmer and I. Koyano, *J. Phys. Chem.* **98**, 13286 (1994); (c) R. Matsui, K. Senba and K. Honma, *Chem. Phys. Lett.* **250**, 560 (1996); (d) R. Matsui, K. Senba and K. Honma, *J. Phys. Chem.* **A101**, 179 (1997); (e) C. L. Haynes and K. Honma, *J. Chem. Soc. Farad. Trans.* **94**, 1171 (1998); (f) K. Honma, *J. Phys. Chem.* **A103**, 1809 (1999).
83. A. S. Narayan, P. M. Futerko and A. Fontijn, *J. Phys. Chem.* **96**, 290 (1992).
84. G. A. Raiche and J. L. Belbruno, *Chem. Phys. Lett.* **134**, 341 (1987).
85. D. R. Herschbach, *Adv. Chem. Phys.* **10**, 319 (1966).
86. P. M. Futerko and A. Fontijn, *J. Chem. Phys.* (a) **95**, 8065 (1991); (b) **97**, 3861 (1992); (c) **98**, 7004 (1993).
87. D. P. Belyung, P. M. Futerko and A. Fontijn, *J. Chem. Phys.* **102**, 155 (1995).
88. D. Ritter and J. C. Weisshaar, *J. Am. Chem. Soc.* **112**, 6425 (1990).
89. D. Ritter, J. J. Carroll and J. C. Weisshaar, *J. Phys. Chem.* **96**, 10636 (1992).
90. J. J. Carroll and J. C. Weisshaar, *J. Am. Chem. Soc.* **115**, 800 (1993).
91. J. J. Carroll, K. L. Haug and J. C. Weisshaar, *J. Am. Chem. Soc.* **115**, 6962 (1993).
92. J. C. Weisshaar, *Acc. Chem. Res.* **26**, 213 (1993).
93. J. J. Carroll, J. C. Weisshaar, P. E. M. Siegbahn, C. A. M. Wittborn and M. R. A. Blomberg, *J. Phys. Chem.* **99**, 14388 (1995).
94. J. J. Carroll and J. C. Weisshaar, *J. Phys. Chem.* **100**, 12355 (1996).
95. Y. Wen, M. Porembski, T. A. Ferrett and J. C. Weisshaar, *J. Phys. Chem.* **A102**, 8362 (1998).
96. S. A. Mitchell, P. A. Hackett, D. M. Rayner and M. Cantin, *J. Phys. Chem.* **90**, 6148 (1986).
97. J. M. Parnis, S. A. Mitchell and P. A. Hackett, *J. Phys. Chem.* **94**, 8152 (1990).
98. S. A. Mitchell and P. A. Hackett, *J. Chem. Phys.* **93**, 7822 (1990).
99. C. E. Brown, S. A. Mitchell and P. A. Hackett, *J. Phys. Chem.* **95**, 1062 (1991).
100. M. A. Blitz, S. A. Mitchell and P. A. Hackett, *J. Phys. Chem.* **95**, 8719 (1991).

101. M. A. Blitz, S. A. Mitchell and P. A. Hackett, *J. Phys. Chem.* **97**, 5305 (1993).
102. C. E. Brown, S. A. Mitchell and P. A. Hackett, *Chem. Phys. Lett.* **191**, 175 (1992).
103. S. A. Mitchell, *Int. J. Chem. Kin.* **26**, 97 (1994).
104. S. A. Mitchell, M. A. Blitz and R. Fournier, *Can. J. Chem.* **72**, 587 (1994).
105. L. Lian, S. A. Mitchell and D. M. Rayner, *J. Phys. Chem.* **98**, 11637 (1994).
106. J. M. Parnis, R. D. Lafleur and D. M. Rayner, *Chem. Phys. Lett.* **218**, 544 (1994).
107. J. M. Parnis, R. D. Lafleur and D. M. Rayner, *J. Phys. Chem.* **99**, 673 (1995).
108. D. B. Pederson, M. Z. Zgierski, S. Anderson, D. M. Rayner, B. Simard, S. Li and D. S. Yang, *J. Phys. Chem.* **A105**, 11462 (2001).
109. M. L. Campbell, *J. Am. Chem. Soc.* **119**, 5984 (1997).
110. M. L. Campbell, *J. Phys. Chem.* **A101**, 9377 (1997).
111. M. L. Campbell, *J. Phys. Chem.* **A102**, 892 (1998).
112. M. L. Campbell, *J. Chem. Soc. Farad. Trans.* **94**, 353 (1998).
113. K. Honma, *J. Chin. Chem. Soc.* **42**, 371 (1995).
114. K. Senba, R. Matsui and K. Honma, *J. Phys. Chem.* **99**, 13992 (1995).
115. M. L. Campbell, *Chem. Phys. Lett.* **365**, 361 (2002).
116. Note that although rate constants have been reported for the reactions of Zr, Nb, and Ta with CH₄, the values were below the minimum value for reliable measurement. See Ref. 107 for details.
117. J. Berkowitz, G. B. Ellison and D. Gutman, *J. Phys. Chem.* **98**, 2744 (1994).
118. H. Basch, *Inorg. Chim. Acta* **252**, 265 (1996).
119. Note that although it may be possible for metal atoms to form a σ -complex with an alkane prior to insertion into a C–H bond, such complexes would be bound by only a few kcal/mol (comparable to dispersion forces), while metal-alkene π -complexes are typically bound by 20–60 kcal/mol.
120. P. A. Willis, H. U. Stauffer, R. Z. Hinrichs and H. F. Davis, *Rev. Sci. Instrum.* **70**, 2606 (1999).
121. P. A. Willis, Ph.D. Thesis, Cornell University, 1999.
122. P. A. Willis, H. U. Stauffer, R. Z. Hinrichs and H. F. Davis, *J. Phys. Chem.* **A103**, 3706 (1999).
123. H. U. Stauffer, R. Z. Hinrichs, P. A. Willis and H. F. Davis, *J. Chem. Phys.* **111**, 4101 (1999).
124. H. U. Stauffer, R. Z. Hinrichs, J. J. Schroden and H. F. Davis, *J. Phys. Chem.* **A104**, 1107 (2000).
125. H. U. Stauffer, R. Z. Hinrichs, J. J. Schroden and H. F. Davis, *J. Chem. Phys.* **111**, 10758 (1999).
126. P. A. Willis, H. U. Stauffer, R. Z. Hinrichs and H. F. Davis, *J. Chem. Phys.* **108**, 2665 (1998).
127. R. Z. Hinrichs, P. A. Willis, H. U. Stauffer, J. J. Schroden and H. F. Davis, *J. Chem. Phys.* **112**, 4634 (2000).
128. J. J. Schroden, M. Teo and H. F. Davis, *J. Chem. Phys.* **117**, 9258 (2002).
129. J. J. Schroden, M. Teo, H. F. Davis and C. Bayse, to be submitted.

130. R. Z. Hinrichs, Ph.D. Thesis, Cornell University, 2001.
131. H. U. Stauffer, Ph.D. Thesis, Cornell University, 2000.
132. D. E. Powers, S. G. Hansen, M. E. Geusic, A. C. Pui, J. B. Hopkins, T. G. Dietz, M. A. Duncan, P. R. R. Langridge-Smith and R. E. Smalley, *J. Phys. Chem.* **86**, 2556 (1982).
133. D. Proch and T. Trickl, *Rev. Sci. Instrum.* **60**, 713 (1989).
134. The $t = 0$ trigger for the experiment was a signal generated every time one of the slots of the chopper wheel passed a photodiode. Since the chopper wheel was spun at 210 Hz, this resulted in a trigger signal at a frequency of 420 Hz (2 slots \times 210 Hz). However, the maximum repetition rate for the lasers employed in this experiment was 30 Hz, so the trigger signal was actually divided by a factor of 14 using a home-built "divide-by-box". The resulting 30 Hz trigger signal was sent to a delay box, which generated trigger signals for the lasers and pulsed valves used in the experiment.
135. R. D. Levine and R. B. Bernstein, *Molecular Reaction Dynamics and Chemical Reactivity* (Oxford University Press, Oxford, 1987).
136. Exoergicities of the YH_2 and YOCH_3 product channels were calculated to be -1.35 kcal/mol and -30 kcal/mol, respectively, using values from Refs. 33 and 137. $\text{Y}-\text{OCH}_3$ binding energy estimated to be 133 kcal/mol based on Ref. 31.
137. J. Berkowitz, G. B. Ellison and D. Gutman, *J. Phys. Chem.* **98**, 2744 (1994).
138. R. Z. Hinrichs, J. J. Schroden and H. F. Davis, *J. Phys. Chem.* **A**, submitted.
139. Y. T. Lee, in *Atomic and Molecular Beam Methods*, ed. G. Scoles (Oxford University Press, New York, 1988), Vol. 1, Chap. 22.
140. R. E. Center and A. Mandl, *J. Chem. Phys.* **57**, 4104 (1972).
141. B. Rybtchinski and D. Milstein, *Angew. Chem. Int. Ed.* **38**, 870 (1999).
142. R. Z. Hinrichs, J. J. Schroden and H. F. Davis, *J. Am. Chem. Soc.* **125**, 860 (2003).
143. R. Z. Hinrichs, J. J. Schroden and H. F. Davis, *J. Chem. Phys.*, submitted.
144. J. J. Schroden, M. Teo and H. F. Davis, *J. Phys. Chem.* **A106**, 11695 (2002).
145. J. J. Schroden and H. F. Davis, to be submitted.
146. W. B. Miller, S. A. Safron and D. R. Herschbach, *Discuss. Faraday Soc.* **44**, 108 (1967).
147. (a) Y.-M. Chen and P. B. Armentrout, *J. Am. Chem. Soc.* **117**, 9291 (1995); (b) L. S. Sunderlin and P. B. Armentrout, *Phys. Chem.* **94**, 3589 (1990); (c) E. R. Fisher and P. B. Armentrout, *J. Phys. Chem.* **94**, 1674 (1990); (d) Y.-M. Chen, M. R. Sievers and P. B. Armentrout, *Int. J. Mass Spec. Ion. Proc.* **167/168**, 195 (1997).
148. P. A. M. van Koppen, D. B. Jacobson, A. Illies, M. T. Bowers, A. Hanratty and J. L. Beauchamp, *J. Am. Chem. Soc.* **111**, 1991 (1989).
149. (a) C. J. Chu, Z. H. Kafafi, J. L. Margrave, R. H. Hauge and W. E. Billups, *Organometallics* **19**, 39 (2000); (b) E. S. Kline, R. H. Hauge, Z. H. Kafafi and J. L. Margrave, *Organometallics* **7**, 1512 (1988).
150. R. H. Crabtree, *The Organometallic Chemistry of the Transition Metals* (John Wiley & Sons, Inc., New York, 1994), p. 291.

151. (a) R. H. Grubbs, P. L. Burk and D. D. Carr, *J. Am. Chem. Soc.* **97**, 3265 (1975); (b) T. R. Cundari and M. S. Gordon, *Organometallics* **11**, 55 (1992); (c) A. K. Rappe and W. A. Goddard, *J. Am. Chem. Soc.* **104**, 448 (1982).
152. (a) R. Puddephatt, *Coord. Chem. Rev.* **22**, 149 (1980); (b) P. W. Jennings and L. L. Johnson, *Chem. Rev.* **94**, 2241 (1994).
153. G. O. Spessard and G. L. Miessler, *Organometallic Chemistry* (Prentice-Hall, Inc., Upper Saddle River, 1997), pp. 118–119.
154. D. M. P. Mingos, *Comprehensive Organometallic Chemistry*, eds. G. Wilkinson, F. G. A. Stone and E. A. Abel (Pergamon Press, Oxford, 1982), Vol. 3, p. 77.
155. J. J. Low and W. A. Goddard III, (a) *J. Am. Chem. Soc.* **106**, 8321 (1984); (b) *Organometallics* **5**, 609 (1986).
156. Thermodynamics Research Center, NIST Boulder Laboratories, M. Frenkel director. "Thermodynamics Source Database" in *NIST Chemistry WebBook, NIST Standard Reference Database Number 69*, eds. P. J. Linstrom and W. G. Mallard, July 2001, National Institute of Standards and Technology, Gaithersburg MD, 20899 (<http://webbook.nist.gov>).
157. The product asymptote for H₂ elimination was calculated assuming YC₄H₆ to be Y bound to both π -bonds of 1,3-butadiene; that for YCH₂ formation was calculated assuming C₃H₆ was propene; and that for YH₂ formation was calculated assuming C₄H₆ was 1,3-butadiene.
158. Note that the total product intensity for H₂ elimination was similar for the Y + propene and Y + butene reactions.
159. J. J. Schroden, Ph.D. Thesis, Cornell University, 2003.
160. For example, reactions of the electronically excited state of Cu, a pseudo-alkali, are amenable to detailed theory.
161. H. F. Davis and H. U. Stauffer, *Encyclopedia of Physical Science and Technology* (Academic Press, 2002).
162. J. C. Polanyi, *Accts. Chem. Res.* **5**, 161 (1972).
163. I. W. M. Smith and F. F. Crim, *Phys. Chem. Chem. Phys.* **4**, 3543 (2002).
164. (a) F. F. Crim, *Accts. Chem. Res.* **32**, 877 (1999); (b) F. F. Crim, *J. Phys. Chem.* **100**, 12725 (1996).
165. (a) J. D. Thoemke, J. M. Pfeiffer, R. B. Metz and F. F. Crim, *J. Phys. Chem.* **99**, 13748 (1995); (b) A. Sinha, J. D. Thoemke and F. F. Crim, *J. Chem. Phys.* **96**, 372 (1992).
166. M. C. Hsiao, A. Sinha and F. F. Crim, *J. Phys. Chem.* **95**, 8263 (1991).
167. R. N. Zare, *Science* **279**, 1875 (1998).
168. M. J. Bronikowski, W. R. Simpson and R. N. Zare, *J. Phys. Chem.* (a) **97**, 2204 (1993); (b) **97**, 2194 (1993).
169. M. J. Bronikowski, W. R. Simpson, B. Girard and R. N. Zare, *J. Chem. Phys.* **95**, 8647 (1991).
170. See, for example, P. Atkins and J. de Paula, in *Physical Chemistry*, 7th edn. (W. H. Freeman, New York, 2001), p. 964, Box 27.2.
171. S. Yoon, S. Henton, A. N. Zivkovic and F. F. Crim, *J. Chem. Phys.* **116**, 10744 (2002).
172. H.-G. Yu and G. Nyman, *Phys. Chem. Chem. Phys.* **1**, 1181 (1999).

173. J. C. Corchado, D. G. Truhlar and J. Espinosa-Garcia, *J. Chem. Phys.* **112**, 9375 (2000).
174. J. Palma and D. C. Clary, *Phys. Chem. Chem. Phys.* **2**, 4105 (2000).
175. P. A. Berg, J. J. Sloan and P. J. Kuntz, *J. Chem. Phys.* **95**, 8038 (1991).
176. K. M. Mikulecky and K.-H. Gericke, *J. Chem. Phys.* **96**, 7490 (1992).
177. K. M. Mikulecky and K.-H. Gericke, *Chem. Phys.* **175**, 13 (1993).
178. K. Mikulecky and K.-H. Gericke, *J. Chem. Phys.* **98**, 1244 (1993).
179. B. Bussery-Honvault, P. Honvault and J.-M. Launay, *J. Chem. Phys.* **115**, 10701 (2001).
180. F. J. Aoiz, L. Banares, J. F. Castillo, V. J. Herrero, B. Martinez-Haya, P. Honvault, J. M. Launay, X. Liu, J. J. Lin, S. A. Harich, C. C. Wang and X. Yang, *J. Chem. Phys.* **116**, 10692 (2002).
181. (a) L. B. F. Juulink, P. R. McCabe, R. R. Smith, C. L. DiCologero and A. L. Utz, *Phys. Rev. Lett.* **83**, 868 (1999); (b) L. B. F. Juulink, R. R. Smith and A. L. Utz, *Faraday Disc.* **117**, 133 (2000).
182. J. Higgins, A. Conjusteau, G. Scoles and S. L. Bernasek, *J. Chem. Phys.* **114**, 5277 (2001).
183. (a) E. P. Wasserman, C. B. Moore and R. G. Bergman, *Science* **255**, 315 (1992); (b) B. A. Arndtsen, R. G. Bergman, T. A. Mobley and T. H. Peterson, *Accts. Chem. Res.* **28**, 154 (1995); (c) A. A. Bengali, B. A. Arndtsen, P. M. Burger, R. H. Schultz, B. H. Weiller, K. R. Kyle, C. B. Moore and R. G. Bergman, *Pure & App. Chem.* **67**, 281 (1995).
184. (a) H. Yang, K. T. Kotz, M. C. Asplund, M. J. Wilkens and C. B. Harris, *Accts. Chem. Res.* **32**, 551 (1999); (b) S. E. Bromberg, T. Q. Lian and R. G. Bergman, *J. Am. Chem. Soc.* **118**, 2069 (1996); (c) J. B. Ashbury, K. Hang, J. S. Yeston, J. G. Cordaro, R. G. Bergman and T. Lian, *J. Am. Chem. Soc.* **122**, 12870 (2000).
185. N. Dunwoody, S.-S. Sun and A. J. Lees, *Inorg. Chem.* **39**, 4442 (2000).
186. J. J. Schroden and H. F. Davis, unpublished.

CHAPTER 6

PHOTODISSOCIATION DYNAMICS OF OZONE IN THE HARTLEY BAND

Paul L. Houston

*Department of Chemistry and Chemical Biology
Cornell University, Ithaca, NY 14853-1301, USA
plh2@cornell.edu*

An overview of work aimed at understanding the photodissociation dynamics of ozone in the Hartley band is presented, focusing on measurements of the vibrational and angular distributions for products of the triplet channel yielding $\text{O}(^3\text{P}) + \text{O}_2(^3\Sigma^-)$ and the singlet channel yielding $\text{O}(^1\text{D}) + \text{O}_2(^1\Delta_g)$. The vibrational distribution of $\text{O}_2(^1\Delta_g)$ in the singlet channel is unsurprising; for any dissociation wavelength, every vibrational level allowed by conservation of energy is observed in a distribution that peaks at $v = 0$ and falls off slowly to the highest vibrational level. The vibrational distribution of $\text{O}_2(^3\Sigma^-)$ in the triplet channel, is unusual. It consists of a broad peak near $v = 16$ for dissociation at 226 nm that shifts to lower vibrations as the wavelength increases. In addition, for wavelengths of 230 nm or shorter, there is a sharp additional peak in the distribution at $v \geq 26$. The angular distributions generally exhibit positive anisotropy parameters that increase with increasing recoil velocity.

Contents

1. Introduction	282
2. Experimental Techniques	284
2.1. The Singlet Channel	284
2.2. The Triplet Channel	286
3. Results and Discussion	288
3.1. The Singlet Channel: $\text{O}_3 + h\nu \rightarrow \text{O}(^1\text{D}_2) + \text{O}_2(^1\Delta_g)$	288
3.1.1. $\text{O}(^1\text{D}_2)$ Speed Distributions	288
3.1.2. $\text{O}(^1\text{D}_2)$ Angular Distributions	290
3.1.3. $\text{O}_2(^1\Delta_g)$ Angular Distributions	296

3.2. The Triplet Channel: $\text{O}_3 + h\nu \rightarrow \text{O}({}^3\text{P}) + \text{O}_2({}^3\Sigma)$	303
3.2.1. $\text{O}({}^3\text{P})$ Speed Distributions	303
3.2.2. $\text{O}({}^3\text{P})$ Angular Distributions	312
4. Conclusions and Remaining Questions	322
Acknowledgments	324
Note Added in Proof	324
References	325

1. Introduction

The purpose of this article is to summarize and synthesize work on photodissociation of ozone at wavelengths corresponding the Hartley band. It will focus primarily on the work of my own group, which has used the tools of product imaging to investigate the two main electronic channels of the dissociation.^{1–8} Of course, many others have contributed to our knowledge of this photodissociation. While many references to this literature are included here, the current article is not meant to be a comprehensive review of the field. In particular, while there have been many recent articles on the branching between various electronic channels in the dissociation, this article will be concerned primarily with the dynamics of only two of these, that producing both the O and O₂ in the triplet (ground) states, and that producing both in their singlet (first excited) states.

Chapman was the first to provide a clear picture of the formation of ozone in the stratosphere.⁹ Figure 1 summarizes the principal production

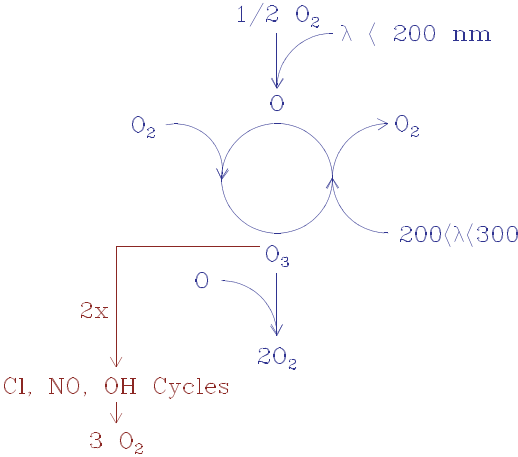


Fig. 1. Overview of production and destruction of ozone in the stratosphere.

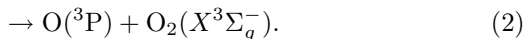
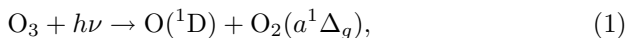
and destruction mechanisms for stratospheric ozone. Ozone is formed after sunlight with wavelengths less than about 200 nm dissociates O_2 to give oxygen atoms. The atoms then recombine with O_2 to form ozone, O_3 (a third body like N_2 may serve to take away the energy and stabilize the O_3). The fate of most ozone in the stratosphere is to be dissociated by light in the Hartley band, centered near 250 nm. However, since the products of this dissociation, after electronic relaxation, are $\text{O} + \text{O}_2$, the O atom can simply recombine with O_2 to reform ozone. Thus, the results of the cycle are that sunlight in the Hartley band is absorbed, and that heat is provided to the atmosphere. The former result is what prevents light near 250 nm from arriving at the surface of the earth, where it would damage the chromosomes of species living there, whereas the latter result is principally what accounts for the fact that the stratospheric temperature increases with altitude. Depending on the altitude, the central cycle of Fig. 1 may be traversed several hundred times for every O atom formed in the stratosphere by the dissociation of O_2 . The cycle then assures that the concentrations of "odd oxygen", O and O_3 , are in equilibrium with each other. Note also that an understanding of stratospheric ozone will be sensitively dependent on understanding its dissociation, since if there were even a minor channel in this dissociation not depicted in Fig. 1, its effect would be multiplied by the average number of cycles traversing the central loop of the diagram.

In order to calculate the steady-state concentration of ozone in the stratosphere, we need to balance the rate of production of odd oxygen with its rate of destruction. Chapman originally thought that the destruction was due to the reaction $\text{O} + \text{O}_3 \rightarrow 2\text{O}_2$, but we now know that this pathway is a minor sink compared to the catalytic destruction of O_3 by the trace species OH , NO , and Cl . The former two of these are natural constituents of the atmosphere, formed primarily in the photodissociation of water or nitric oxide, respectively. The Cl atoms are produced as the result of man-made chlorofluorocarbons, which are photodissociated by sunlight in the stratosphere to produce free chlorine atoms. It was Rowland and Molina who proposed in 1974 that the reactions $\text{Cl} + \text{O}_3 \rightarrow \text{ClO} + \text{O}_2$ followed by $\text{ClO} + \text{O} \rightarrow \text{Cl} + \text{O}_2$ could act to reduce the concentration of stratospheric ozone.¹⁰ The net result of all of these catalytic reactions is $2\text{O}_3 \rightarrow 3\text{O}_2$.

Even with our much-advanced understanding of the chemistry of the stratosphere, it appears that there are still some discrepancies between the calculated amount of ozone in the stratosphere and the amount measured. Toumi and Kerridge have summarized data showing that the range of calculated concentrations is some 10–15% below the range of measured

concentrations at an altitude of about 40 km.¹¹ However, Crutzen *et al.* have more recently argued that this discrepancy is due to an error in the measurements.¹² Whatever the situation, it is clear that a thorough understanding of ozone photodissociation will be necessary before we can have a deep and sufficiently comprehensive understanding of stratospheric chemistry. Our studies were undertaken to provide some steps towards that goal.

We have investigated the two principal channels in the dissociation of ozone at wavelengths corresponding to the Hartley band:



Channel (1) is the dominant dissociation pathway, accounting for roughly 90% of the product yield at wavelengths near the Hartley absorption maximum. The remaining 10% is dissociation through channel (2). In the remainder of this article, we will refer to (1) as the “singlet” channel, and to (2) as the “triplet” channel. Our objectives have been to measure the recoil velocity between the O and O₂ to learn about the internal (vibrational/rotational) energy of the O₂ fragment and to measure the recoil direction of the fragments relative to the polarization direction of the photolysis laser. Product imaging in conjunction with velocity mapping and ion counting has provided a sensitive means to achieve both measurements.^{13–15}

2. Experimental Techniques

2.1. The Singlet Channel

The technique of ion imaging has been described more fully elsewhere.^{4,14,15} A molecular beam of ozone was formed by flowing helium at about 810 torr over ozone trapped on silica gel at -78°C . The resulting mixture of less than 1% ozone was expanded through a pulsed, 250 mm diameter nozzle and collimated by a 500 mm diameter skimmer mounted about 5 mm away from the nozzle. Two counter-propagating laser beams intersect the molecular beam at right angles. One laser dissociates the ozone molecules, and the other ionizes the resulting O(¹D) fragments using the (2 + 1) REMPI processes at 203.7 and 205.4 nm.^{2,16} Due to the speed of the oxygen fragments, it was necessary to scan the ionization laser wavelength over the Doppler absorption profile to ensure equal detection of all the fragments.

The dissociation laser light between 230 and 305 nm was produced by frequency doubling the output of an optical parametric oscillator (Spectra-Physics MOPO-730) pumped by an injection-seeded Nd:YAG

laser (Spectra-Physics GCR-230). Typical powers were 1–3 mJ/pulse with a pulse width of 9 ns. The output polarization was rotated, if necessary, with a double Fresnel rhomb, and then cleaned up with a stack of fused silica plates held at Brewster's angle. The resultant polarization ratio was about 10 : 1. The light used to ionize the $O(^1D)$ fragments at 203 and 205 nm was generated by doubling the output of a Nd:YAG (Spectra-Physics GCR-230) pumped dye laser (Quanta Ray PDL1 with SR640 dye) in a KDP crystal, and then summing the fundamental with this doubled light in BBO. Typical powers achieved were 1 mJ/pulse with a pulse width of 9 ns. The polarization of the probe laser was rotated, if necessary, with a double Fresnel rhomb. The resultant polarization ratio was 10 : 1. Both lasers were operated at 10 Hz. The photolysis and probe lasers were directed into the vacuum chamber and focused onto the molecular beam with 25 and 7.5 cm focal length plano-convex lenses, respectively.

The imaging technique uses an electrostatic immersion lens which serves to extract the ionized $O(^1D)$ fragments from the interaction region and to focus ions with equal velocity vectors to the same point on the detector.¹⁴ The magnification factor of the lens was measured to be 1.17 ± 0.03 by dissociating O_2 and detecting the $O(^3P_2)$ fragment using $(2 + 1)$ REMPI at 225.65 nm.^{17,18} The ionized fragments were accelerated into a field-free flight tube mounted along the axis of the molecular beam. Ions were imaged when they hit a position-sensitive detector consisting of a chevron double micro-channel plate (MCP) assembly coupled to a fast phosphor screen (Galileo, P-47). The image on the phosphor screen was recorded by a 640×480 pixel CCD camera (Xybion Electronics, ISG-250U). Both the MCP and camera were electronically gated to collect only signal corresponding to the mass of the $O(^1D)$ fragment. Signal levels were kept below 300 ions per laser shot to avoid saturation of the MCP. The ion counting method was used to increase the spatial resolution of the images.¹⁵ About 100,000 total laser shots were added to generate the final image.

For the $O_2(^1\Delta_g)$ imaging the dissociation laser was a Kr-F excimer (248 nm) which was irised before entering a pile-of-plates polarizer. The polarized beam was then focused onto the ozone beam by a 400 mm focal length lens. Typical dissociation laser power was about 2 mJ/pulse, and this was sufficient to dissociate a significant fraction of the ozone in the beam, although no saturation effects were observed. The probe laser beam was produced by doubling the output of a dye laser (Spectra-Physics PDL-2) pumped by a doubled Nd-YAG laser. Using Rhodamine 640 or a mixture of Rhodamine 640 and DCM dyes, we obtained 10–15 mJ/pulse in the probe

region from 303–315 nm when pumping with 550 mJ/pulse at 532 nm. The probe laser beam was collimated using a telescope and directed through a double Fresnel rhomb polarization rotator, and then into the main chamber. The beam was then focussed by a 75 mm focal length lens mounted inside the chamber. Despite the high probe laser power, no evidence of space charge effects was observed. These “Coulomb explosion” effects are readily apparent as a strongly power-dependent distortion of the images. The probe laser was delayed 75 ns with respect to the dissociation laser, and master timing was obtained from the 30 Hz video board, divided to yield the 10 Hz repetition rate of the experiment. Velocity map imaging and ion counting were not used for the $\text{O}_2(^1\Delta_g)$ imaging experiments.

2.2. The Triplet Channel

A molecular beam of ozone was formed by flowing helium with about 810 Torr backing pressure over ozone maintained on silica gel at a temperature of -78°C . The subsequent mixture of $<1\%$ ozone was expanded through a pulsed 250 μm diameter nozzle and collimated by a 500 μm diameter skimmer mounted about 5 mm from the nozzle orifice. Further downstream, the molecular beam was crossed at right angles by two counter-propagating laser beams, one serving to dissociate the ozone and the other to probe the resulting $\text{O}(^3\text{P}_J)$ fragments using the $\text{O}(3p^3\text{P}_{2,1,0} \leftarrow\leftarrow 2p^3\text{P}_J)(2+1)$ REMPI scheme at 226.23, 226.06, and 225.65 nm for $J = 0, 1$, and 2 , respectively.^{17,18} Due to the large Doppler width of the $\text{O}(^3\text{P}_J)$ fragments it was necessary to scan the probe laser over the resonance to ensure that the images detect all product $\text{O}(^3\text{P}_J)$ atom velocities with equal sensitivity.

The dissociating laser radiation between 230 and 266 nm was produced by frequency doubling the output of an optical parametric oscillator (Spectra-Physics MOPO-730) pumped by an injection seeded Nd: YAG laser (Spectra Physics GCR-230). Typical laser powers were 1–3 mJ/pulse with a pulse duration of 8–10 ns. The tunable light needed to probe the $\text{O}(^3\text{P}_J)$ fragments at 226 nm was generated by frequency doubling the output of an injection-seeded, Nd: YAG-pumped dye laser and then summing the doubled light with the Nd: YAG laser fundamental; typical powers achieved were 1.0 mJ/pulse with a pulse duration of 8–10 ns. Both lasers were operated at 10 Hz. For studies of photodissociation at 226 nm, the laser at this wavelength served as both the photolysis and probe laser. Photolysis and probe beams were directed into the vacuum chamber and focused into

the interaction region by 25-cm and 7.5-cm focal length plano-convex lenses, respectively. The polarizations of both the photolysis and probe laser beams were perpendicular to the plane defined by the molecular and laser beams.

The velocity mapping-ion counting technique^{14,15} was used to obtain high resolution photofragment images. An electrostatic lens was employed that served both to extract the ionized $\text{O}(^3\text{P}_J)$ fragments from the interaction zone and to de-blur the image. The magnification factor of this electrostatic lens was measured to be 1.17 ± 0.02 by dissociating O_2 and detecting the oxygen atom fragment with the same REMPI scheme used in the ozone experiments. The ionized fragments were accelerated into a flight tube mounted along the axis of the molecular beam. The ions were imaged by a position-sensitive detector consisting of a chevron double micro-channel plate (MCP) assembly coupled to a fast phosphor screen. The image on the phosphor screen was recorded by a 640×480 pixel charge coupled device (CCD) camera. Both the MCP and CCD camera were electronically shuttered to collect signal corresponding to the mass of the oxygen atoms. Signal levels were kept below 200 ions per shot to avoid saturation of the MCP for images with bright central features. Data were accumulated typically for 100,000 total laser shots.

One experimental complication is the potential “contamination” of the images obtained in two-color experiments by signal due to dissociation by the 226 nm probe radiation. Careful adjustment of both the spatial and temporal overlap between the two laser pulses, coupled with the high power of the photolysis pulse and low ozone concentration in the molecular beam allowed images to be acquired with minimal probe contamination. In spite of these precautions, some of the images with photolysis wavelengths between 230 and 240 nm were contaminated with one-color 226 nm signal. This signal was removed by subtracting an appropriately-scaled amount of pure 226 nm signal from the image. A much smaller source of background contamination was also present due to the one-color signal from 230 to 240 nm radiation. Images of these background signals were collected and their contribution was subtracted from the two-color product images. The resulting data is a two-dimensional projection of the $\text{O}(^3\text{P}_J)$ photofragment’s three-dimensional velocity distribution. Because the projection is made perpendicular to the electric vectors of the dissociation and probe radiation, it is possible to reconstruct the original three-dimensional velocity distribution using the inverse Abel transform.^{19–21}

The branching ratios for the fine structure states of the $\text{O}(^3\text{P}_J)$ were measured by placing a 2-inch diameter active area photomultiplier tube

(Thorn EMI 9235QB) near the phosphor screen to collect all of the ion signal as the probe laser was tuned over the $O(^3P_J)$ Doppler profile at laser wavelengths of 226.23, 226.06 and 225.65 nm for $j = 0, 1$ and 2 , respectively. The output of the photomultiplier was sent to a boxcar averager gated at the appropriate arrival time. The probe laser power was simultaneously measured with a photodiode in order to normalize the $O(^3P_J)$ signal intensity for fluctuations in laser power.

3. Results and Discussion

3.1. The Singlet Channel: $O_3 + h\nu \rightarrow O(^1D_2) + O_2(^1\Delta_g)$

3.1.1. $O(^1D_2)$ Speed Distributions⁸

The imaging technique produces a two-dimensional projection of the three-dimensional fragment ion distribution. If the latter distribution is cylindrically symmetric about an axis in the plane of the detector, then it is possible mathematically to reconstruct the 3D distribution from the 2D projection using the inverse Abel transform.^{19–21} Once the 3D distribution is calculated, the speed distribution can be obtained by integrating over all angles at each speed, and the angular distribution can be obtained by integrating over all speeds at each angle. A simple transformation using conservation of linear momentum links the speed and translational energy distributions:

$$|m_o v_o| = |m_{o_2} v_{o_2}| \quad (3)$$

$$\begin{aligned} KE_{\text{total}} &= \frac{1}{2} m_o v_o^2 + \frac{1}{2} m_{o_2} v_{o_2}^2 \\ &= \frac{1}{2} m_o v_o^2 + \frac{1}{2} (2m_o) \left(\frac{m_o v_o}{2m_o} \right)^2 \\ &= \frac{3}{4} m_o v_o^2. \end{aligned} \quad (4)$$

The internal energy of the O_2 fragment is found from the total kinetic energy distribution using the energy conservation equation

$$KE_{\text{total}} = E_{h\nu} - D_0 (O_2(^1\Delta_g) + O(^1D)) - T(v)_{o_2} + ZPE_{o_2} - F_v(J)_{o_2} \quad (5)$$

where KE_{total} is the total kinetic energy, $E_{h\nu}$ is the laser energy, D_0 is the dissociation energy, $T(v)_{o_2}$ is the vibrational energy of the $O_2(^1\Delta_g)$ fragment, ZPE_{o_2} is the zero point energy of the $O_2(^1\Delta_g)$ fragment, and $F_v(J)_{o_2}$ is the rotational energy of the $O_2(^1\Delta_g)$ fragment.

Inverse Abel transformed images are shown in Fig. 2 for various dissociation wavelengths using the 205.4 nm REMPI scheme. The images that

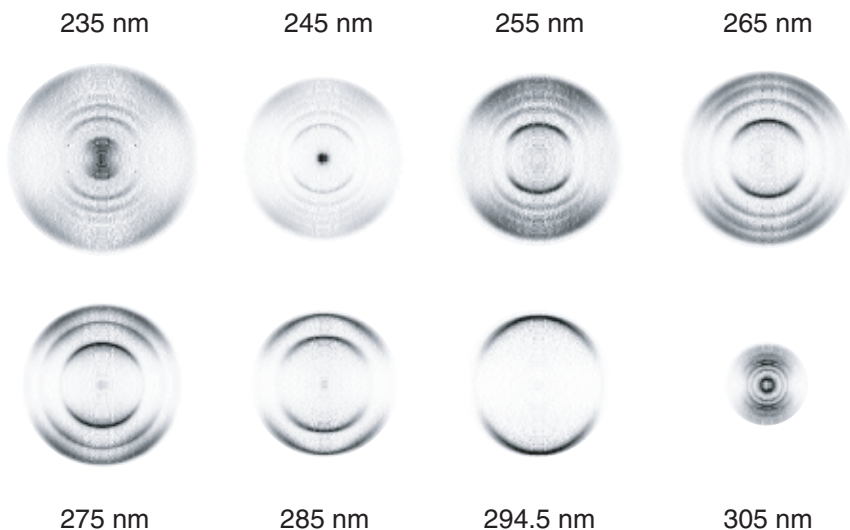


Fig. 2. The inverse Abel transform of the $\text{O}(^1\text{D}_2)$ photofragment images with both laser polarizations vertical and in the plane of the paper. The dissociation wavelength is shown for each image, but each image is arbitrarily scaled in size. The atoms were ionized via the 205.4 nm (2 + 1) REMPI process.

used the 203.7 nm probe had similar radial distributions but slightly different angular distributions from the ones shown here. It is important to note that the true nascent angular distribution of the $\text{O}(^1\text{D}_2)$ fragments has a shape characterized by $1 + \beta P_2(\cos \theta_d)$. Any deviation from that shape is due to the variation in ionization probability caused by the atomic alignment. Although it is possible for the atomic alignment and thus the integrated ionization probability to change with radius, we assumed that the overall effect of any changes in alignment on the vibrational populations was small. This assumption is justified by the small change in atomic alignment as a function of speed in our measurements. The corresponding energy distribution for each wavelength is shown in Fig. 3. Structure in the 305 nm dissociation result is due to individual rotational levels within the $v = 0$ level of the $\text{O}_2(^1\Delta_g)$ molecule. This structure can be used to determine the dissociation energy of O_3 to high accuracy, as discussed in Ref. 6.

In order to obtain the vibrational populations, Gaussian functions were fitted to each vibrational peak and then integrated to determine the relative population of that peak relative to the whole curve. We recognize that the Gaussians sometimes do not accurately represent the vibrational populations due to the tail on the high energy side of the vibrational peak

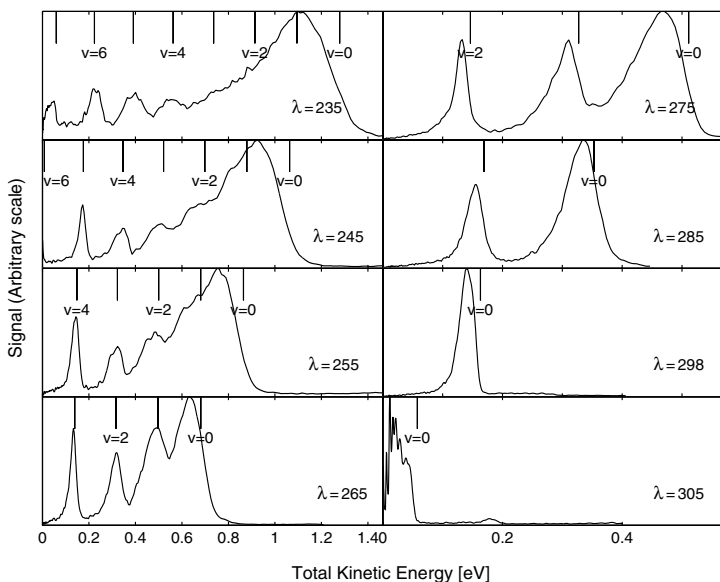


Fig. 3. Total kinetic energy distribution for $\text{O}_3 \rightarrow \text{O}_2(^1\Delta_g) + \text{O}(^1\text{D}_2)$. Also shown at each wavelength is a comb corresponding to each vibrational level with no rotational excitation. The peaks observed in the 305 nm image are due to rotational structure. The small peak at ~ 0.19 eV in the 305 nm image is due to an ozone “hot band”.

that sometimes extends beyond the energy corresponding to the lowest rotational energy state of the products. Some signal may extend to higher energies than the theoretical limit due to our finite experimental resolution and/or space charge effects, etc. For most peaks, the fit is sufficient. The vibrational populations are shown in Table 1 along with the populations reported by other research groups. Vibrational populations for $v = 0$ and 1 at 235 and 245 nm are only estimates due to our inability to properly separate the two vibrational modes.

3.1.2. $\text{O}(^1\text{D}_2)$ Angular Distributions⁸

Both the spatial anisotropy parameter and the $|m_j|$ distributions can change for the different vibrational modes of the $\text{O}_2(^1\Delta_g)$ fragment. To account for this we used a semi-continuous parameter method to find the best fit parameters. This method involved breaking the image up into 10-pixel wide rings concentric about the center of the image, and then fitting each region separately. The value of 10 pixels was chosen to approximately average over the rotational levels within one vibrational band.

Table 1. Vibrational populations of $\text{O}_2(^1\Delta_g)$ from the photodissociation of ozone with light of wavelength λ .

λ (nm)	$v = 0$	$v = 1$	$v = 2$	$v = 3$	$v = 4$	$v = 5$	$v = 6$	$v = 7$	Source
235	30%	24%	15%	7%	7%	7%	5%	6%	This work
240	64%	15%	8%	4%	5%	4%	2%		Ref. 24
245	34%	23%	20%	8%	8%	4%	0%		This work
248	49%	15%	15%	8%	8%	5%			Ref. 23
248	65%	18%	8%	5%	3%	4%			Ref. 24
255	39%	30%	14%	10%	8%				This work
265	44%	32%	14%	10%					This work
266	52%	27%	14%	7%					This work ^a
266	57%	24%	12%	7%					Ref. 22
266	59%	22%	12%	7%					Ref. 24
275	59%	26%	15%						This work
275	61%	27%	12%						Ref. 23
280	70%	30%							Ref. 23
280	70%	22%	8%						Ref. 24
285	71%	29%							This work
285	76%	24%							Ref. 23
293	76%	24%							Ref. 24

^aOnly one image was taken at this wavelength using the 205 nm ionization scheme.

Upon examining the data (shown in Fig. 2), it is immediately apparent that the $\text{O}(^1\text{D})$ fragment from the photodissociation of ozone does not display a $1 + \beta\text{P}_2(\cos\theta)$ angular distribution. The origin of the unusual shape of the images lies in the interaction of the ionization laser with the angular momentum of the oxygen atom. By ionizing with linearly-polarized light, it is possible to measure the spatial anisotropy parameter and also the relative populations of each $|m_j| = 0, 1$, or 2 projection. Two fully quantum mechanical methods of extracting the $|m_j|$ distributions of the atomic fragments are used.

In the first method, known as the diagonal density matrix method, we followed Mo and Suzuki's analysis²⁵ by assuming the ion angular distribution is of the form

$$I(\theta_d) = I_{\text{dissociation}}(\theta_d) \times I_{\text{detection}}(\theta_d), \quad (6)$$

with

$$I_{\text{dissociation}}(\theta_d) = I(v)[1 + \beta\text{P}_2(\cos\theta_d)], \quad (7)$$

while the detection distribution is more complex and depends on the angle between \mathbf{v} and \mathbf{J} of the atomic fragment. The angular variable θ_d is used

to denote the angle between the velocity of the fragment and the polarization of the *dissociation* laser. This method assumes that the angular momentum distribution is cylindrically symmetric about the velocity vector of the fragment, and thus it only considers the diagonal elements of the angular momentum density matrix in the molecular frame. Furthermore, the direction of \mathbf{J} is assumed to be independent of the specific direction \mathbf{v} in the lab frame. Under these assumptions, the detection probability equations are given as:²⁵

$$I_{\text{detection}}(\theta_d) \propto \sum_K P_K \rho_0^{(K)}(\text{probe}), \quad (8)$$

$$\rho_0^{(K)}(\text{molecular}) = \sum_m (-1)^{J-m} \sqrt{2K+1} \begin{pmatrix} J & K & J \\ -m & 0 & m \end{pmatrix} f_m, \quad (9)$$

where P_K are linestrength factors that depend on the specific ionization scheme used, K is the rank of the expansion term, and the f_m are the m_j fractional populations. The $\rho_0^{(K)}(\text{molecular})$ are the multipole moments in the molecular frame, and can easily be rotated to the probe frame multipole moments, denoted by $\rho_0^{(K)}(\text{probe})$. Since we are using a linearly-polarized, two-photon ionization process, all the odd rank linestrength factors are zero in the expansion. While it may not be possible to calculate the linestrength factors explicitly, Mo and Suzuki²⁶ have shown that the ratio $P_0 : P_2 : P_4$ can easily be calculated if the initial and final atomic angular momentum states are not equal, i.e., provided $J_i \neq J_f$. When using a two-photon probe, the linestrength factors are theoretically nonzero for $K \leq 4$. We calculated the P_K ratios $P_0 : P_2 : P_4 = 1 : 0.683 : -0.115$ for the 203.7 nm (2 + 1) REMPI scheme, and $1 : -0.598 : -1.07$ for the 205.4 nm (2 + 1) REMPI scheme. These ratios have been reported in other publications as well.^{25,27}

Using the previous equations and the calculated P_K ratios, we can determine the angular shapes of the $I_{\text{detection}}(\theta_d)$ distribution for $|m_j| = 0, 1$, or 2. The resulting distributions are shown in Fig. 4. Note that since the ratios of P_K were used, the absolute scale is arbitrary; only the relative shapes and magnitudes are important. We then fit the angular distribution data to a sum of these functions multiplied by the $I_{\text{dissociation}}$ term to obtain the relative $|m_j|$ populations and the β value:

$$I(\theta_d) = P(v)[1 + \beta P_2(\cos \theta_d)] I_{\text{detection}}(\theta_d), \quad (10)$$

with

$$I_{\text{detection}}(\theta_d) = [f_0 F_0(\theta_d) + f_1 F_1(\theta_d) + f_2 F_2(\theta_d)], \quad (11)$$

where f_0 , f_1 , and f_2 are the fractional populations of $\text{O}(^1\text{D})$ in $|m_j| = 0, 1$, and 2, respectively, and $F_0(\theta_d)$, $F_1(\theta_d)$ and $F_2(\theta_d)$ are the corresponding

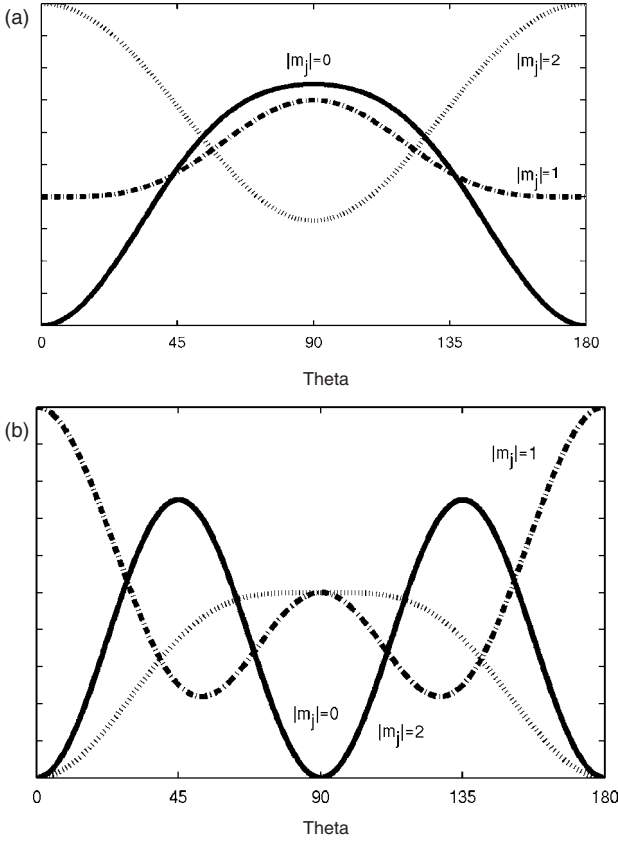


Fig. 4. Ionization probability for (a) the $O(^1F_3) \leftarrow\leftarrow O(^1D_2)$ ionization scheme at 203 nm, and (b) the $O(^1P_1) \leftarrow\leftarrow O(^1D_2)$ ionization scheme at 205 nm.

probe frame angular detectivity functions for each magnetic sublevel:

$$\begin{aligned}
 F_0^{203.7}(\theta_d) &= \frac{3}{4} - \frac{1}{3} \cos^2(\theta_d) - 0.45 \cos^4(\theta_d) \\
 F_1^{203.7}(\theta_d) &= \frac{3}{4} - 0.6 \cos^2(\theta_d) - \frac{1}{3} \cos^4(\theta_d) \\
 F_2^{203.7}(\theta_d) &= \frac{3}{8} + \frac{3}{4} \cos^2(\theta_d) - 0.075 \cos^4(\theta_d)
 \end{aligned} \tag{12}$$

$$\begin{aligned}
 F_0^{205.4}(\theta_d) &= 0 + 3 \cos^2(\theta_d) - 3 \cos^4(\theta_d) \\
 F_1^{205.4}(\theta_d) &= \frac{1}{2} - \frac{3}{2} \cos^2(\theta_d) + 2 \cos^4(\theta_d) \\
 F_2^{205.4}(\theta_d) &= \frac{1}{2} + 0 \cos^2(\theta_d) - \frac{1}{2} \cos^4(\theta_d)
 \end{aligned} \tag{13}$$

These detectivity functions were derived for each magnetic sublevel by setting the population of one sublevel equal to 1 while setting the others to zero in Eq. (12), and then solving for the angular shape $I_{\text{detection}}(\theta_d)$ by transforming the multipoles to the probe frame and summing over K .

Since we use the laser geometry where both lasers are parallel and in the plane of the detector, the resultant 3D distributions are cylindrically symmetric about the laser polarization, and thus the angular distribution can be characterized by the single variable q_d . When plotting the full angular distribution $I(\theta_d) = P(v)[1 + \beta P_2(\cos \theta_d)]I_{\text{detection}}(\theta_d)$, as seen in Fig. 5, we see that the difference between the shapes of the $|m_j| = 0$ and $|m_j| = 2$

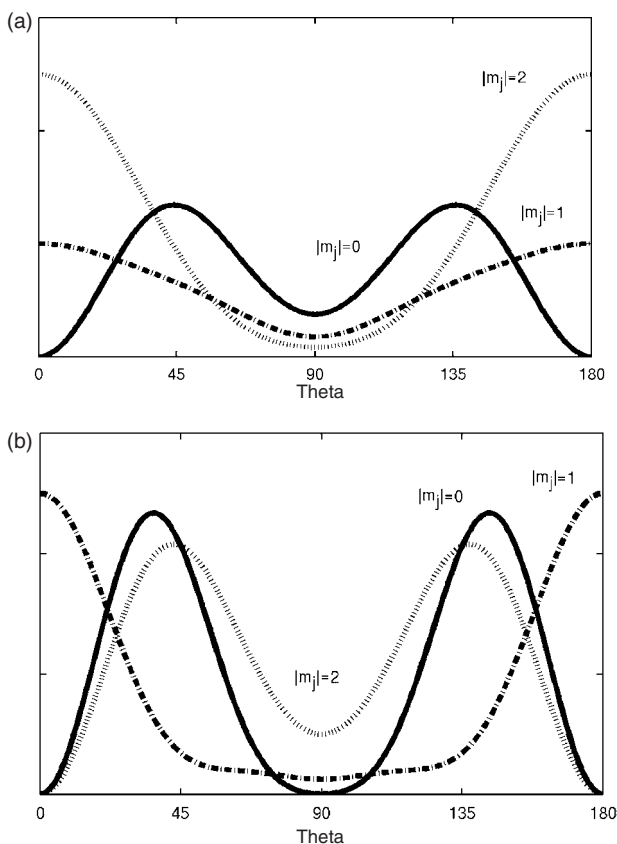


Fig. 5. Ionization probability for (a) the $O(^1F_3) \leftarrow O(^1D_2)$ ionization scheme at 203 nm, and (b) the $O(^1P_1) \leftarrow O(^1D_2)$ ionization scheme at 205 nm, including the $1 + \beta P_2(\cos \theta_d)$ term with $\beta = 1.5$.

curves is small for the 205.4 nm REMPI scheme. In order to resolve any possible ambiguity between the shapes of different $|m_j|$ curves, we used two different $O(^1D)$ REMPI schemes: one $\{O(^3F) \leftarrow O(^1D)\}$ at 203.7 and one $\{O(^1P) \leftarrow O(^1D)\}$ at 205.4 nm. The shapes of the 203.7 nm REMPI detectivity curves easily distinguish between the $|m_j| = 0$ and $|m_j| = 2$ levels. Thus, for each dissociation wavelength, we can take one image using each REMPI scheme, and then fit the spatial anisotropy parameter and the $|m_j|$ populations to the angular distributions of both images. This method is valuable because only one laser polarization geometry (both laser polarizations parallel, and in the plane of the detector) is needed in order to obtain the $|m_j|$ populations, β value, and speed distribution. In addition, fitting 1D angular functions is fast and easily done. We used this method at all wavelengths.

A full density matrix method was also used for analysis, following the method analysis pioneered by Bracker *et al.*, Siebbeles *et al.*, and Rakitzis and Zare.^{27–32} The model for the 3D angular momentum polarization functions when using linearly-polarized light assumes only that \mathbf{J} is cylindrically symmetric about \mathbf{v} . It does not neglect coherence effects, and thus allows for the determination of the full angular momentum density matrix as a function of the angle between the photolysis laser polarization and \mathbf{v} . Details for this method and its application to the singlet channel for ozone dissociation may be found in Ref. 8.

Angular distributions and fits at 265 nm are shown in Fig. 6 for the 203 and 205 nm schemes. The curves shown represent the angular distribution obtained at the maximum of the $v = 0$ and $v = 3$ peaks; the angular distributions at other energies have a similar signal-to-noise ratio, but different shapes. Since regions with low ion counts between the vibrational peaks contribute less to the total image signal and also contain more noise due to counting statistics, the best angular fit parameters for each vibrational level were determined at the peak of the fit for each vibrational level. The best angular fit parameters are listed in Table 2, which also displays results we obtained using the full density matrix method as well as any results previously published. Anisotropy parameter errors are assumed to be $\pm 10\%$.

$O(^1D_2)$ alignment results using the “diagonal matrix method” are shown in Table 3. The numbers reported as “average” were determined by calculating one speed-averaged angular distribution, and then finding the best fit to that data. Since the probe used a linearly-polarized $(2 + 1)$ REMPI technique, the experiment does not measure the sign of $|m_j|$. Orientation (+ versus $-m_j$) measurements would require a circularly-polarized beam.

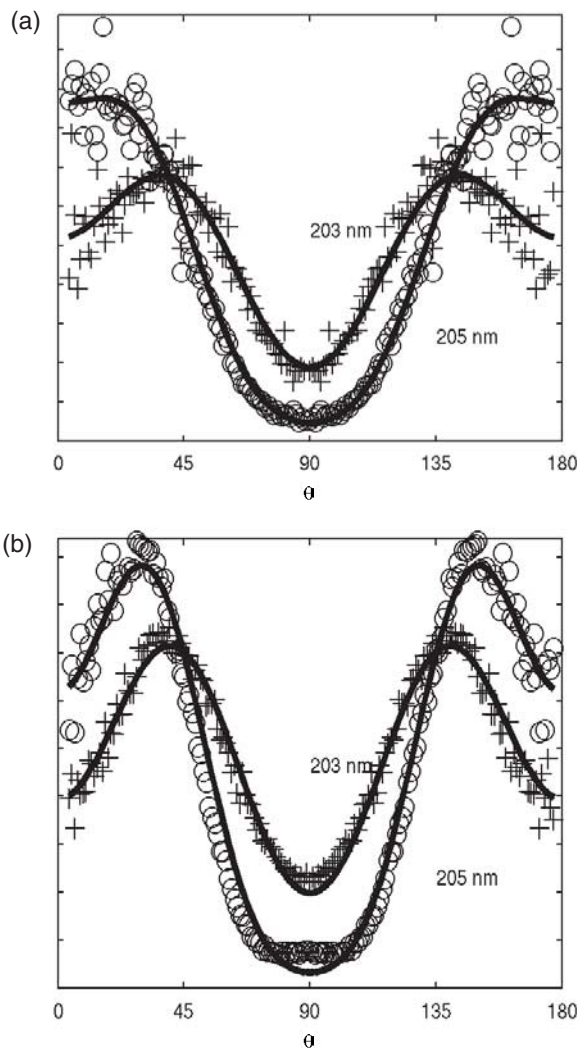


Fig. 6. Angular distribution and fits for the (a) $v = 3$ and (b) $v = 0$ peak, in the 255 nm energy distribution. The two curves in each figure represent angular distributions from different $O(^1D_2)$ ionization schemes.

3.1.3. $O_2(^1\Delta_g)$ Angular Distributions¹

Figure 7 shows an image of $O_2(a^1\Delta_g, v = 0)$ obtained via the 4-0 band of the $^1\Pi_g \leftarrow ^1\Delta_g$ transition at 303.19 nm, with both laser polarizations parallel to the plane of the image and in the vertical direction. The

Table 2. Singlet channel anisotropy parameter, β , results and comparison with results from other research groups.

λ (nm)	Beta								Avg.	Source	Comments
	$v = 0$	$v = 1$	$v = 2$	$v = 3$	$v = 4$	$v = 5$	$v = 6$	$v = 7$			
230									1.12	Ref. 33	
235	1.1	1.19	1.21	1.15	1.00	0.84	0.57	0.71	0.80		
245	1.3	1.28	1.23	1.15	1.08	1.03			1.16		
248	1.25	1.25	1.25	1.25	1.25	1.6				Ref. 23	
248									1.2	Ref. 1	Qualitative
255	1.2	1.33	1.28	1.35	1.32				1.03		
	1.2*	1.4*	1.4*	1.2*	1.1*						
265	1.5	1.46	1.27	1.37					1.39		
266									1.11	Ref. 33	
275	1.6	1.5	1.5						1.49		
270–300									1.6 ± 0.2	Ref. 23	
274–300									1.2 ± 0.2	Ref. 34	Effusive beam
285	1.8	1.6							1.46		
294.5	1.9								1.45		
298	1.9								1.71		
	1.7*										

*Full density matrix method.

image shown is for the 248 nm dissociation of O_3 . The probe laser alone produces detectable fragment flux, but proper timing and overlap renders this contribution negligible for the case in which dissociation and probe polarizations are parallel. A residual contribution from dissociation by the probe is present when the laser polarizations are perpendicular, but this is lower than the 248 nm contribution by several orders of magnitude. In addition, the probe laser signal is confined to the center of the image, owing to the reduced energy available following photolysis at the probe laser wavelength. This contribution was monitored, but no correction was found to be necessary. The absence of perfect four-fold symmetry in the image of Fig. 7 results largely from imperfect overlap of the focal regions of the photolysis and probe lasers, despite considerable care taken to optimize this. To facilitate comparison with the simulations, and to illustrate more clearly the underlying vector correlations, we have symmetrized the experimental images by combining them with their horizontal and vertical reflections. The symmetrized experimental images are shown in Fig. 8 for the 4 possible polarization cases on the 303.19 nm line of the 4–0 band. A REMPI spectrum of O_2 in this region shows clear rotational structure; the molecular constants for the Rydberg state are not available, however, so the specific rotational lines have not yet been assigned.

Table 3. $O(^1D_2)|m_j|$ populations using the diagonal matrix method corresponding to different vibrational states of $O_2(^1\Delta_g)$. The populations were found at the peak of the Gaussian fit for each vibrational level. The average $|m_j|$ populations for the whole image is shown in the right column.

λ (nm)	Populations								Avg.
	$v = 0$	$v = 1$	$v = 2$	$v = 3$	$v = 4$	$v = 5$	$v = 6$	$v = 7$	
235	$ m_j = 0$	71%	74%	74%	68%	56%	44%	31%	57%
	$ m_j = 1$	20%	18%	19%	24%	32%	45%	43%	30%
	$ m_j = 2$	9%	8%	7%	8%	12%	12%	26%	14%
245	$ m_j = 0$	65%	69%	63%	56%	48%	50%		60%
	$ m_j = 1$	29%	27%	33%	41%	47%	39%		34%
	$ m_j = 2$	6%	5%	4%	4%	5%	11%		6%
255	$ m_j = 0$	59%	65%	60%	51%	57%	57%		76%
	$ m_j = 1$	39%	34%	40%	43%	40%	20%		23%
	$ m_j = 2$	1%	1%	0%	6%	2%	2%		0%
265	$ m_j = 0$	62%	65%	62%	52%				60%
	$ m_j = 1$	34%	32%	31%	44%				35%
	$ m_j = 2$	4%	3%	8%	5%				5%
275	$ m_j = 0$	67%	70%	52%					63%
	$ m_j = 1$	32%	29%	47%					35%
	$ m_j = 2$	1%	1%	1%					1%
285	$ m_j = 0$	74%	79%						77%
	$ m_j = 1$	26%	21%						23%
	$ m_j = 2$	0%	0%						0%
294.5	$ m_j = 0$	52%	24%						42%
	$ m_j = 1$	47%	45%						46%
	$ m_j = 2$	1%	31%						12%
298	$ m_j = 0$	48%							45%
	$ m_j = 1$	49%							50%
	$ m_j = 2$	3%							6%
305	$ m_j = 0$								28%
	$ m_j = 1$								49%
	$ m_j = 2$								24%

The 4–1 band has not previously been observed, but a scan of the appropriate region of the spectrum, near 310 nm, yielded the anticipated series of rotational lines. An image recorded on one of these lines, at 310.70 nm, is shown in Fig. 9. These images are clearly smaller than those shown in Fig. 8, consistent with the reduced energy available for translation for this vibrationally-excited product. Striking differences also appear in the general shapes of these images, and in the effect of changing the probe laser polarization. These effects are a direct manifestation of $\mathbf{v}\text{--}\mathbf{J}$ correlation, as will be discussed below.

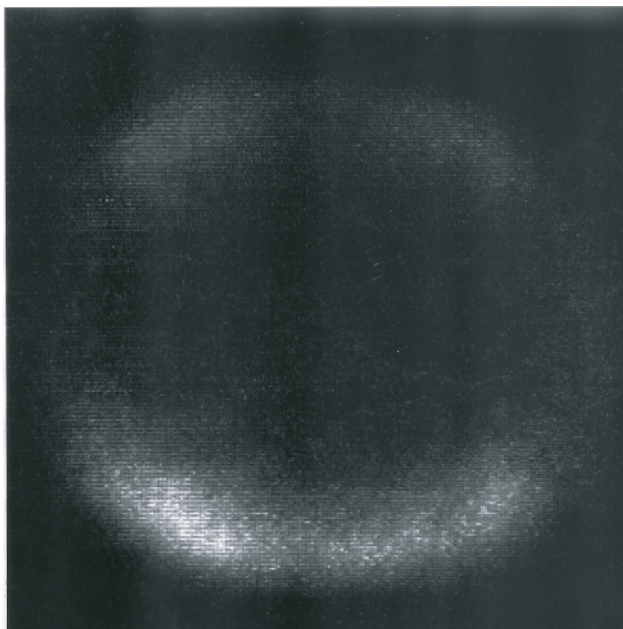


Fig. 7. Image of $\text{O}_2(a^1\Delta_g, v=0)$ recorded with both laser polarizations parallel to the image and in the vertical direction.

We recorded images (not shown) on many lines in these regions. In general the behavior resembled that displayed by one or the other of the two sets shown. Both types of polarization dependence were observed in the region of the 4–1 band. In addition, images corresponding to the 3–0 band were obtained at 312.13 nm. These images resembled those of Fig. 5, though with greater translational energy.

As mentioned above, the change in the appearance of the recorded image as the probe laser polarization is rotated immediately reveals the presence of some angular momentum polarization. Changing the probe laser polarization only changes the *detectivity*; it clearly has no effect on the product velocity distribution. The nature of this effect will in turn depend on the nature of the probe transition and the distribution of the laboratory projections of the total fragment angular momentum (the M_J distribution). In order to understand this effect we have modified a Monte Carlo based forward convolution program, described in detail elsewhere,³⁵ to simulate the experimental images shown in Figs. 8 and 9. The program uses Monte Carlo techniques to sample input distributions representing the various

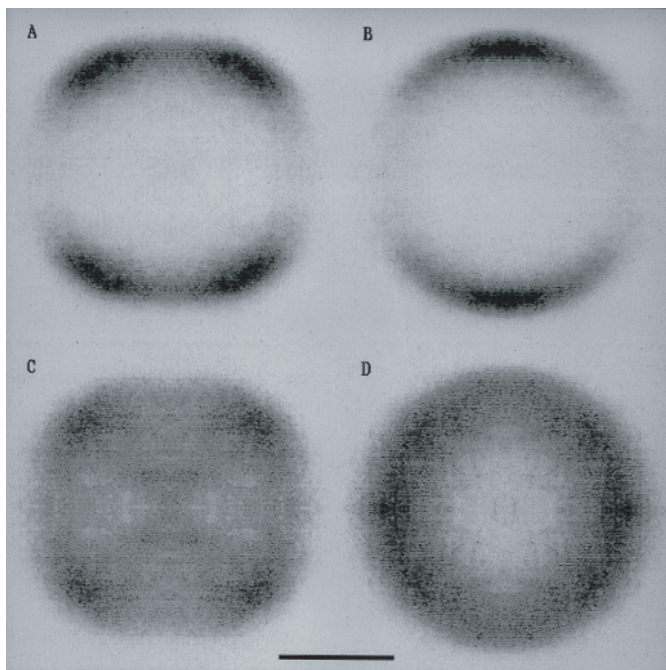


Fig. 8. Symmetrized images of $\text{O}_2(a^1\Delta_g)$ recorded on the 4 – 0 band. The four images (a) through (d) correspond to the following polarizations: (a) both E_d and E_p parallel to the image and vertical, (b) E_d parallel and vertical, E_p perpendicular, (c) E_d perpendicular, E_p parallel and vertical, (d) both perpendicular to the image. The bar represents 1000 m/s in the plane of the image.

experimental functions: beam velocity distribution, dissociation and probe laser volumes, the angular distribution (β), etc. For each “trajectory”, the scattering angles (θ, ϕ), defined with respect to the dissociation laser polarization, are rotated to the laboratory frame (if necessary) and used, in conjunction with the known available translational energy, to determine the laboratory velocity of the fragment. If the fragment occupies the probe laser volume it is “ionized” and its velocity components in the image plane are propagated through the measured product flight time ($5\mu\text{s}$), and scaled according to the measured number of pixels/mm in the experimental images. The trajectory is binned into the simulated image with a weight determined by its detection probability, obtained as described below. The simulation program requires an input angular distribution (β) and an input product rotational level to determine the laboratory distribution. We have used a simple impulsive model³⁴ to provide the angular distribution

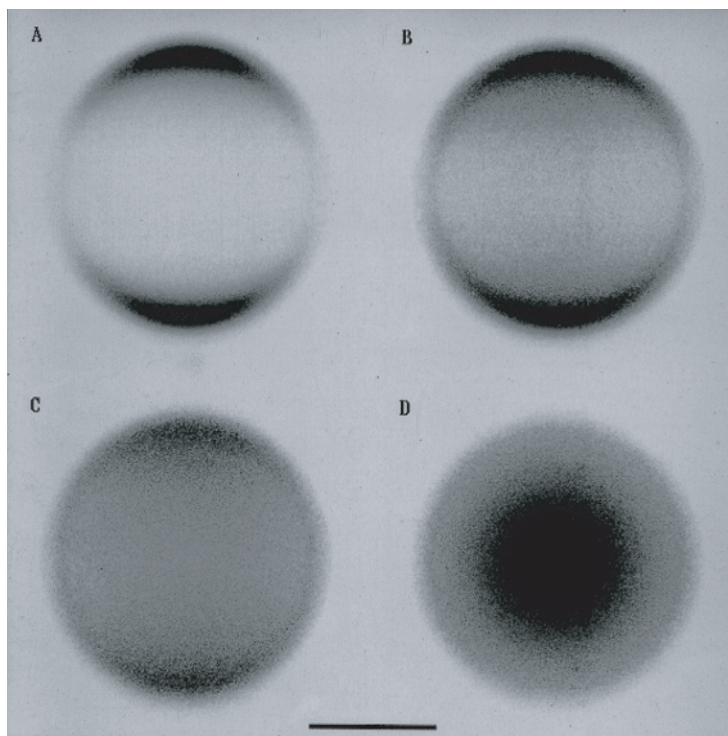


Fig. 9. Symmetrized images of $\text{O}_2(a^1\Delta_g)$ recorded on the 4-1 band. The four images (a) through (d) correspond to the polarizations indicated in the caption to Fig. 8. The bar represents 1000 m/s in the plane of the image.

and predict the M_J distribution used below, and we varied the rotational level to obtain the best fit to the images.

The Hartley band absorption is known to occur to the ($^1\text{B}_2$) excited state, with very rapid (40 fs) dissociation.³⁶ The singlet channel correlates with this excited surface, so singlet products dominate the fragment distribution. The ozone ground state is ($^1\text{A}_1$), so the transition moment lies in the ozone plane, perpendicular to the C_{2v} axis. The bond angle changes only slightly in going from the ground state (117°) to the excited state (108°). If dissociation occurs along the O-O bond axis immediately upon absorption, the angular distribution may be readily calculated.³⁶ A value of 1.18 is obtained for β , assuming direct dissociation from the ground state geometry. This impulsive picture also predicts substantial \mathbf{v} - \mathbf{J} correlation: for the high rotational levels anticipated, the classical limit of \mathbf{v} perpendicular to \mathbf{J} will be closely approached.

The detection probability for a given trajectory depends on the fragment orientation (its M_J value) and the nature of the probe transition. All of these images were obtained via the two-photon ($^1\Pi_g \leftarrow \leftarrow ^1\Delta_g$) transition. Five rotational branches are thus possible: O , P , Q , R and S . The amplitudes for each of these two-photon transitions can be obtained from a sum of paired, M_J -dependent, one-photon amplitudes.³⁷ The O branch, for example, consists of a contribution from a parallel P -type transition to a $^1\Delta_u$ virtual state, followed by a perpendicular P -type transition to the final $^1\Pi_g$ Rydberg (which is assumed to be ionized promptly). The product of those two transition amplitudes must be summed with another product in which the first transition is perpendicular and the second is parallel. The P and R branches consist of four contributions each and the Q branch has six such terms in its transition amplitude. The required one-photon amplitudes are taken from Ref. 37.

For each Monte Carlo trajectory an M_J value is obtained by making the following assumptions: \mathbf{J} is assumed to be perpendicular to \mathbf{v} , so the projection of \mathbf{J} on the probe laser direction may be obtained for a given angle between the \mathbf{J} vector and the Z - \mathbf{v} plane (ϕ') from the appropriate direction cosine matrix. Z in this case is the dissociation laser polarization direction. The angles ϕ' are assumed to be randomly distributed, i.e., there is no $\boldsymbol{\mu}$ - \mathbf{v} - \mathbf{J} correlation. This is necessarily incorrect, as will be indicated in the discussion, but not likely to lead to significant errors in this case. This projection of \mathbf{J} is then “quantized” to yield an M_J value for use in calculating the transition amplitudes. The trajectory is then weighted by the square of these transition amplitudes and binned into the simulated image as described above. Typically 4×10^6 trajectories are used to generate the simulations (10 minutes on an IBM RS/6000-550).

Three distinct types of simulations result: detection on an O or S line yields images resembling the data in Fig. 9. Detection on a P or R line produces images resembling the data of Fig. 8, and detection on a Q line produces images similar to Figs. 9(a) and 9(c), but which do not show a change on rotating the probe polarization by 90° . We have not yet observed images of this type. The resulting simulations are shown in Figs. 10 and 11, corresponding to the data in Figs. 8 and 9, respectively. The simulation in Fig. 10 was obtained for $\text{O}_2(a\ ^1\Delta_g v = 0, J = 38)$ detected via a P transition. The simulation in Fig. 11 was obtained for $\text{O}_2(a\ ^1\Delta_g v = 1, J = 34)$, detected via an O transition. All simulations were obtained using the calculated β value of 1.18.

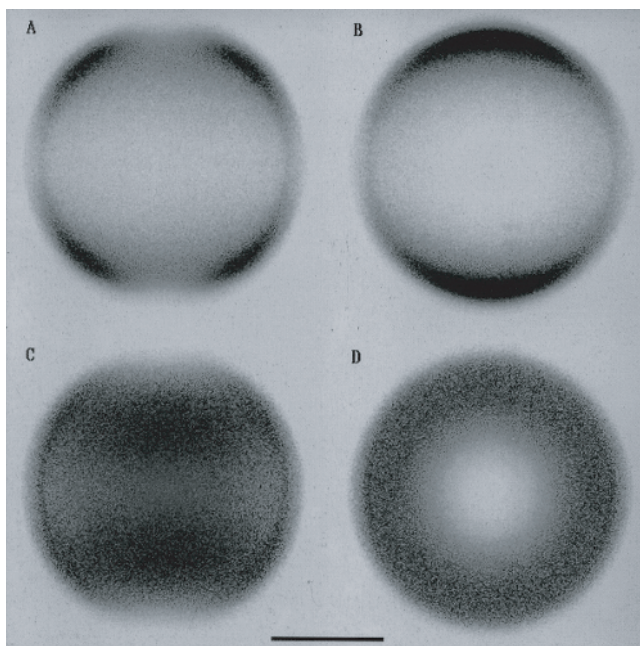


Fig. 10. Simulations of the results of Fig. 8 obtained as described in the text. The four images (a) through (d) correspond to the polarizations indicated in the caption to Fig. 8. The bar represents 1000 m/s in the plane of the image.

3.2. The Triplet Channel: $\text{O}_3 + h\nu \rightarrow \text{O}(^3\text{P}) + \text{O}_2(^3\Sigma)$

3.2.1. $\text{O}(^3\text{P})$ Speed Distributions⁷

Images of the $\text{O}(^3\text{P}_J)$ fragments formed in the minor photodissociation channel of ozone, probed through a $(2 + 1)$ REMPI scheme, were obtained at six photolysis wavelengths between 226 and 266 nm. Figure 12 displays the results for four of these wavelengths as slices through the Abel-reconstructed three-dimensional distributions of the $\text{O}(^3\text{P}_J)$ fragments. The electric vector of the dissociating light is parallel to the vertical direction in the plane of the image. The images have been altered slightly to correct for the inverse Abel-transform singularity along the vertical axis by fitting the angular distributions to a $A[1 + \beta P_2(\cos \theta)]$ distribution and interpolating across the middle 12 pixels for radii greater than 10 pixels. The recovered $\text{O}(^3\text{P}_J)$ velocity distributions from the inverse Abel-transformed slices can be separated into angular and speed components. Angular distributions are determined by integrating over the desired speed interval for each angle.⁵

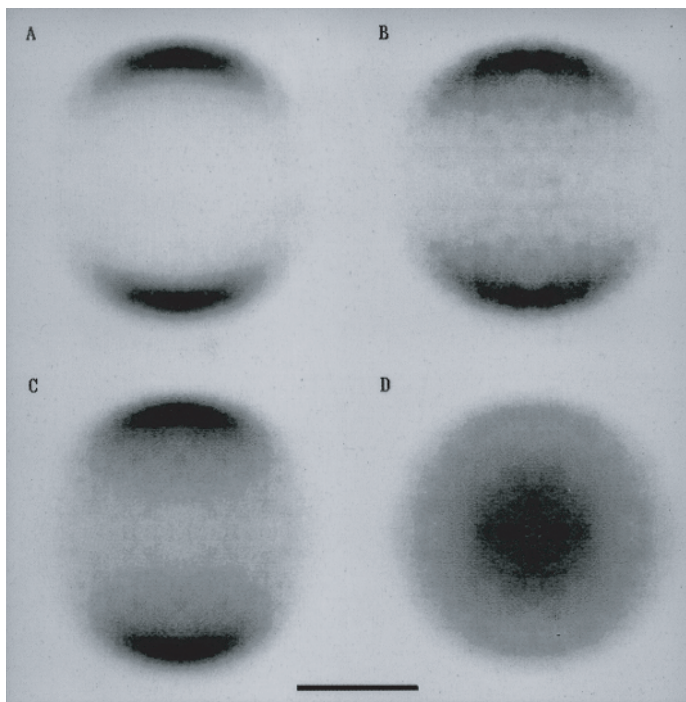


Fig. 11. Simulations of the results of Fig. 9 obtained as described in the text. The four images (a) through (d) correspond to the polarizations indicated in the caption to Fig. 8. The bar represents 1000 m/s in the plane of the image.

Extraction of the speed distribution is achieved in an analogous manner by integrating over all angles for each speed. The speed distributions can be further transformed, using the law of conservation of momentum, into total translational energy distributions for the $\text{O}_3 \rightarrow \text{O}_2(X^3\Sigma_g^-) + \text{O}(^3\text{P}_J)$ dissociation.

From pump-probe experiments detecting the LIF signal from $\text{O}_2(X^3\Sigma_g^-, v = 26)$, it is known that the imaged oxygen atoms are paired with ground electronic state O_2 molecules.² The vibrational distribution of the O_2 product can therefore be determined by imaging the atomic fragment and using conservation of energy,

$$KE = E_{h\nu} - D_0(\text{O}_2 - \text{O}) - T_{\text{O}_2}(v) + ZPE_{\text{O}_2} - F_{v,\text{O}_2}(J) - E_{\text{O}(^3\text{P}_J)}, \quad (14)$$

where $D_0(\text{O}_2 - \text{O})$ is the ozone dissociation of energy 1.0523 ± 0.0026 eV,³⁸ $T_{\text{O}_2}(v)$ is the vibrational term, $F_{v,\text{O}_2}(J)$ the rotational term calculated from the spectroscopic constants given by Laher and Gilmore,³⁹ ZPE_{O_2} is the

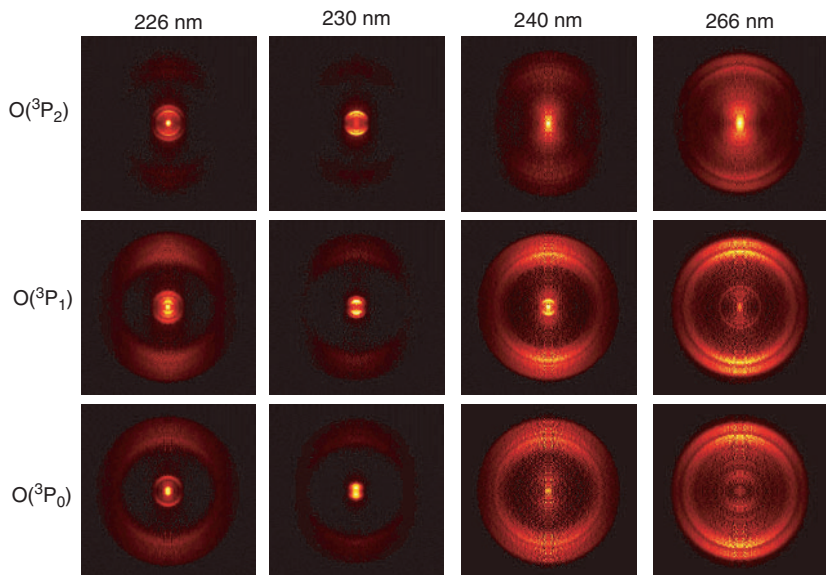


Fig. 12. Table of the images of the reconstructed 3D distributions of the $O(^3P_J)$ fragments from ozone photodissociated at 226, 230, 240 and 266 nm and for $O(^3P_2)$, $O(^3P_1)$, and $O(^3P_0)$.

zero point energy of the O_2 fragment, and $E_{O(^3P_J)}$ are the $O(^3P_J)$ energies obtained from Moore's table.⁴⁰ The energy distributions together with a comb indicating the energy of the vibrational states of the O_2 fragment formed in conjunction with $O(^3P_2)$ are shown in Fig. 13. It is interesting to note that virtually all of the oxygen molecules formed are vibrationally excited. The population of interest for the ozone deficit problem is that in $v \geq 26$. This population is determined from the images for each spin-orbit state as a function of wavelength and is shown in Table 4. The uncertainties reported in Table 4 take several factors into account. Uncertainty in the intensity of the image arises from counting statistics and from variation in the detector's efficiency in its different quadrants. There is uncertainty in the energy axis arising from uncertainty in the magnification factor and the flight time.

The branching ratios into the various $O(^3P_J)$ states were surprisingly difficult to measure. The power dependence of the ionizing laser at the center of the Doppler profile was measured before each scan of the Doppler profile to provide proper normalization of the power dependence. It was found that the combination of our laser power and sample concentration put

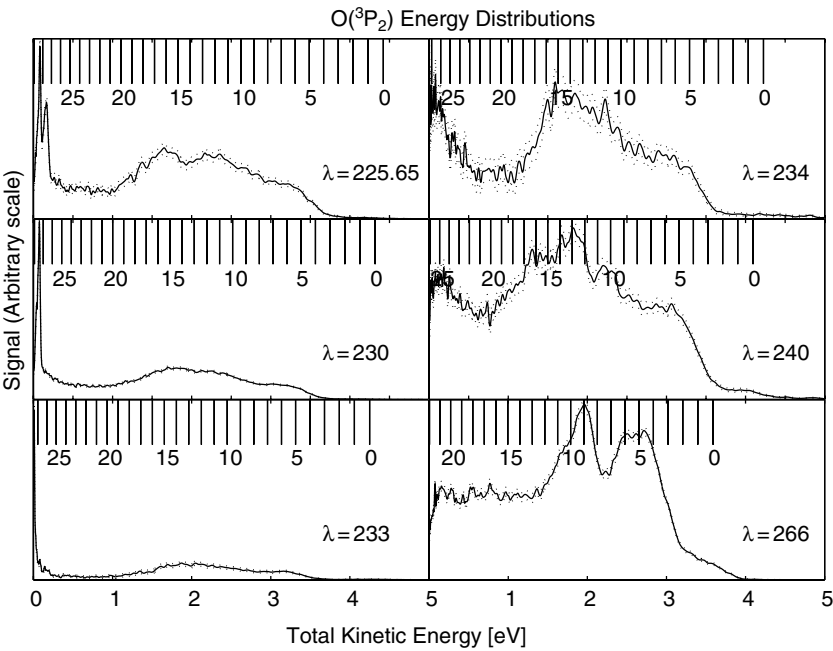


Fig. 13. The total translational energy distributions for the dissociation of O_3 to $O(^3P_j) + O_2(X^3\Sigma_g^-)$ at 226, 230, 233, 234, 240 and 266 nm. The vibrational levels of the $O_2(X^3\Sigma_g^-)$ fragment are indicated by the combs. The dotted curves represent the uncertainty in the signal intensity arising from counting statistics.

Table 4. The percent population of O_2 from the triplet channel in $v \geq 26$ as a function of photolysis wavelength and spin-orbit state of the counter fragment. Note that the thermodynamic threshold for the generation of $O_2(v = 26)$ is at 241.6 nm.

	226 nm	230 nm	233 nm	234 nm	240 nm
$O(^3P_2)$	14.5 ± 2.0 11 ± 3^a	16.8 ± 3.8	15.2 ± 0.2	6.9 ± 0.9	0.70 ± 0.10
$O(^3P_1)$	5.5 ± 0.5 5.9 ± 2.0^a	5.1 ± 0.7	0.7 ± 0.2	0.8 ± 0.2	0.30 ± 0.10
$O(^3P_0)$	3.6 ± 0.5 4.6 ± 2.0^a	4.1 ± 0.6	0.4 ± 0.2	0.6 ± 0.2	0.10 ± 0.05

^aRef. 41

us at an inconvenient place on the saturation curve, leading to dependencies ranging from quadratic to cubic. The laser power was measured during the scans, and the resulting profile was normalized for variations in this power. The data was also normalized by the two-photon line strength,¹⁸ but

Table 5. The branching ratios into the three spin-orbit states of the oxygen atom fragment as a function of photolysis wavelength in the Hartley band. Note that a statistical yield would give a branching ratio of 5:3:1, or as percentages, 55.5:33.3:11.1.

	O(³ P ₂)	O(³ P ₁)	O(³ P ₀)	
226 nm	69 ± 9	23 ± 3	7.7 ± 2.2	this work
	45	39	16	Ref. 47
	59 ± 4	30 ± 2	11	Ref. 2
	55	35	15	Ref. 43
	45 ± 10	36 ± 10	18 ± 10	Ref. 41
230 nm	55 ± 3	31 ± 4	14 ± 2	This work
240 nm	67 ± 5	25 ± 5	7.9 ± 0.4	This work
266	66 ± 3	26 ± 1	8.5 ± 2.6	This work
	55 ± 3	23 ± 3	12 ± 3	Ref. 42
308	66 ± 3	27 ± 3	9 ± 1	Ref. 42

this correction was small. The results are shown in Table 5. The reported uncertainties represent 2σ of 9, 4, 3 and 3 measurements at 226, 230, 240 and 266 nm respectively.

The total fraction of O₂($v \geq 26$) generated from the photodissociation of ozone at a particular wavelength is given by

$$F_{v \geq 26}(\lambda) = F_t(\lambda) R_{v \geq 26}(\lambda) \quad (15)$$

where $F_t(\lambda)$ is quantum yield of triplet channel and $R_{v \geq 26}(\lambda)$ is a fraction of the triplet channel product formed in $v \geq 26$ at that same wavelength. The photofragment product imaging data combined with the measured branching ratios allows the determination of the latter value as

$$R_{v \geq 26}(\lambda) = \frac{\sum_J F_{3P_J}(\lambda) F_{J, v \geq 26}(\lambda)}{\sum_J F_{3P_J}(\lambda)} \quad (16)$$

where $F_J, v \geq 26(\lambda)$ is the fraction of O₂ formed in coincidence with O(³P_{*J*}) that is in $v \geq 26$, shown in Table 4, and $F_{3P_J}(\lambda)$ is the branching ratio of minor channel product into O(³P_{*J*}), shown in Table 5. The branching ratio was not measured for 233 and 234 nm dissociation. At these wavelengths a statistical population was assumed with estimated uncertainties of 10%, 6% and 3% in the $J = 2, 1$, and 0 state respectively. The resulting populations are summarized in Table 6 and plotted in Fig. 14.

The velocity mapping-ion counting technique increases the resolution of imaging data. This is clearly seen when it is compared with the data from the conventional Wiley–McLaren imaging apparatus² or even the

Table 6. The total percentage of minor channel product created in $v \geq 26$ as a function of photolysis wavelength.

Wavelength (nm)	Percent population in $v \geq 26$	Assuming statistical
226	11.6 ± 1.9	10.3
230	11.4 ± 2.2	11.5
233	—	8.7
234	—	4.2
240	0.6 ± 0.1	0.5

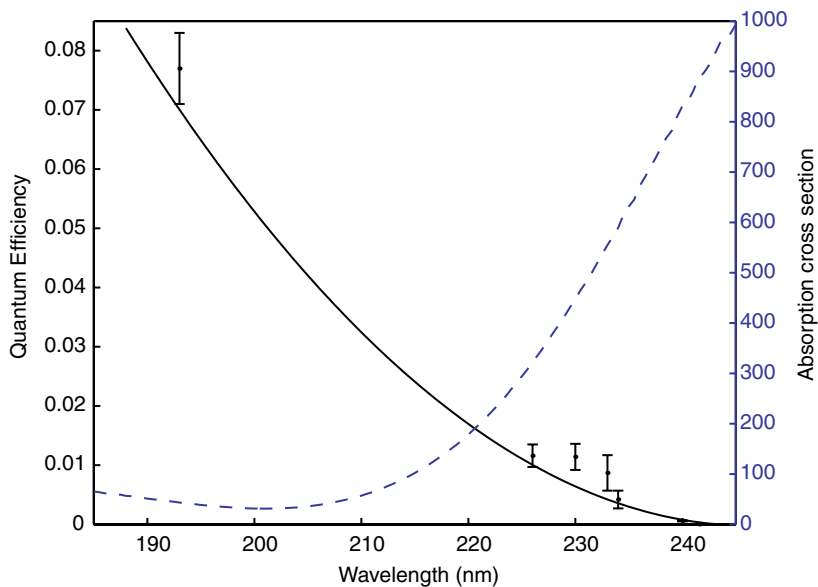


Fig. 14. Plot of the quantum efficiency for the formation of $\text{O}_2(v \leq 26)$ as a function of wavelength. The value at 193 nm is taken from Stranges *et al.*⁴⁴ A 10% branching ratio into the triplet channel is assumed. The absorption cross-section for ozone is plotted as the dashed curve on the right-hand axis.

more recent data employing solely the velocity mapping technique.¹⁴ This improvement allowed the observation of previously unresolved structure in all the photolysis images collected here. This structure spans multiple vibrational levels and is indicative that complicated photodissociation dynamics occurs in this three-atom system.

A further quantitative improvement over the previous imaging work was due to the discovery that the intense central feature of many of the

images was saturating the position-sensitive MCP, but only in those locations with high ion flux. Thus the relative intensities of faster fragments (lower vibrational energy in the O_2 fragment) were artificially augmented in previous work.^{2,5}

Takahashi *et al.*⁴⁵ have reported a measurement of the translational energy distribution for the $\text{O}(^3\text{P}_J)$ fragment from 266 nm photodissociation of ozone. The atomic fragment was detected using VUV-LIF. Although the resolution of this data is extremely low, it agrees qualitatively with that reported here, except for the strong minimum observed in their data at about 0.8 eV. We are unaware of any other measurements of the $\text{O}(^3\text{P}_J) + \text{O}_2(^3\Sigma)$ translational energy distributions at wavelengths of 230 to 240 nm.

Our measurements of the branching ratios are significantly different from many of those obtained in other laboratories. These data are shown in Table 5. There seems to be a wide range of scatter in the different measurements at 226 nm, and none of them quite agree with our values; for example, every measurement finds less $\text{O}(^3\text{P}_2)$ than we do. The closest value to ours is the measurement that was previously performed by this group. Also at 266 nm we find more population in $\text{O}(^3\text{P}_2)$ than the other measurement. Our values are fairly constant at all four wavelengths and agree more closely with the literature values at 308 nm, the exception being at 230 nm, where we found an essentially statistical distribution. It seems likely that our values are high. One possible contribution to this would be the presence of thermal oxygen atoms from the decomposition of ozone on the metal surfaces of the sample line.

One goal of these experiments was to measure the fraction of $\text{O}_2(v \geq 26)$ formed in the triplet channel. Our results are shown in Table 6. Given the concern with the measured branching ratios into the different spin-orbit states of $\text{O}(^3\text{P})$, we might ask how dependent these values are on the exact branching ratios used. The final column shows the fraction of $\text{O}_2(v \geq 26)$ calculated if a statistical distribution is assumed. These two sets of values represent what seems to be the two extremes of the branching ratio. The resulting fractions of $\text{O}_2(v \geq 26)$ formed are not significantly different.

Previous measurements of the fraction of $\text{O}_2(v \geq 26)$ formed in the minor channel for photodissociation at 226 nm were consistently lower than our current value, although they agree closely with each other. Miller *et al.*² measured 8.1% while Syage⁴⁶ found $7.9 \pm 2.0\%$ in $v \geq 26$. The results should be higher than the previous imaging measurement² because of the saturation effect discussed above, in which the relative intensities of slower fragments (higher vibrational energy in the O_2 fragment) were artificially

suppressed. Although our new measurement is not as close to that of Syage as the previous measurement, the new value is still within the error limit. Kinugawa *et al.*⁴⁷ show a translational energy distribution for the $\text{O}(^3\text{P}_1)$ fragment that agrees qualitatively with our data. However, their data seem to have more intensity in the lowest vibrational levels ($v = 0 - 3$).

One motivation for these particular experiments was to be able to evaluate possible implications for the ozone deficit problem. If a deficit exists and if $\text{O}_2(^3\Sigma_g^-, v \geq 26)$ leads to formation of two ozone molecules through, for example, the reactions $\text{O}_2(^3\Sigma_g^-, v \geq 26) + \text{O}_2 \rightarrow \text{O}_3 + \text{O}$, $\text{O} + \text{O}_2(+M) \rightarrow \text{O}_3(+M)$, then accurate values for the amount of vibrationally-excited O_2 formed as a function of wavelength would be needed for proper modelling. Previous data on the yield of $\text{O}_2(v \geq 26)$ were available only at 193 and 226 nm, and models assumed a yield as a function of wavelength that passed through these points and the energetic threshold for $\text{O}_2(v = 26)$ at 241.6 nm. The experiments reported here have added several points to the high wavelength end of this region. It is particularly important to characterize the yield in this wavelength region because the ozone absorption cross-section increases rapidly with wavelength as shown in Fig. 14. The wavelength dependence of the yield is tied to the altitude dependence of ozone concentration because the solar flux changes significantly with altitude; see e.g. Ref. 48.

The points in Fig. 14 give the wavelength dependence of the $\text{O}_2(v \geq 26)$ yield. Also shown is the original fit by Toumi *et al.* using only data at 193, 226, and 243 nm.³

$$Q = 1.49388 - 0.012125\lambda + 2.4599 \times 10^{-5}\lambda^2 \quad (17)$$

Although the fit does not capture the onset of $\text{O}_2(v \geq 26)$ near 234 nm, it does about as well as can be done using a quadratic polynomial.

Given the current state of the theoretical work on the $\text{O}_2(^3\Sigma_g^-, v \geq 26) + \text{O}_2 \rightarrow \text{O}_3 + \text{O}$ reaction, the model calculation³ represents an upper limit for ozone production because it assumes that all of the $\text{O}_2(v \geq 26)$ reacts to form ozone. Even if the $\text{O}_2(^3\Sigma_g^-, v \geq 26) + \text{O}_2 \rightarrow \text{O}_3 + \text{O}$ reaction occurs, it is unlikely that all of the excited oxygen molecules follow this reaction. The dependence of the $\text{O}_2(v \geq 26)$ yield on wavelength shown by the points in Fig. 14 is similar enough to that assumed previously that it appears likely that the new measurements will not change the previous results. We thus again come to the conclusion that, if there is a mechanism for generating ozone from the vibrationally-excited O_2 , then the production yield of $\text{O}_2(v \geq 26)$ from ozone photolysis partially accounts for the ozone

deficit problem, particularly at the lowest altitudes at which the problem is manifest. It does not account for the ozone deficit at higher altitudes.

Although it should eventually be possible to explain much of the structure in each of the individual images, more theoretical effort is first needed concerning the nature of the electronic states of ozone reached by these dissociation wavelengths. A few conclusions can nonetheless be made. First, the two regions in the bimodal distribution seen in the lower wavelength images arise from distinct processes. This is seen clearly by examining the angular distributions. For the slower fragments, there is a well defined β value, while for the fast fragments a $\mathbf{v}-\mathbf{J}$ correlation becomes pronounced, leading to a different yet less well-defined β value.⁵ This observation is strong evidence that two different processes lead to these products.

Second, there appears to be a distinct threshold for forming $\text{O}_2(v \geq 26)$. The photodissociation wavelengths corresponding to the energetic thresholds for forming $\text{O}_2(v)$ in association with the three spin-orbit states of the atomic product are shown in Table 7. The highly-excited fragments begin to be observed near 234.5 nm, a wavelength that corresponds to the formation of rotationally-excited molecules in $v = 27$. This is also clearly seen from the vibrational combs in Fig. 13.

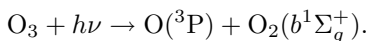
Third, there are clear differences in the images for dissociation at the same wavelength while probing different spin-orbit states. Two effects contribute to these differences. One is the slight difference in energy in the atomic states, most easily seen in the data at 234 nm where the $\text{O}(^3\text{P}_2)$ data clearly has the strong contribution from vibrationally-excited O_2 while the other spin-orbit states do not. In this case the threshold for the dynamical process that forms the vibrationally-excited products has been crossed by the 158.265 cm^{-1} of the spin-orbit excitation. The second effect is that due to the nature of the J -level. It is known that there is a $\mathbf{v}-\mathbf{J}$ correlation from the angular fits as well as from the fact that when the polarization of the

Table 7. Fitted β values obtained at photolysis wavelengths of 226, 230, 240 and 266 nm.

Dissociation wavelength (nm)	β	
	Fast	Slow
226	1.31 ± 0.20	0.67 ± 0.05
230	1.52 ± 0.30	0.80 ± 0.07
240	1.10 ± 0.30	0.56 ± 0.07
266	0.71 ± 0.15	

probe laser is rotated 90° , the image changes. The extent of this correlation can be different for different values of J . This is most evident for the case where $J = 0$, as in this instance there is no $\mathbf{v}-\mathbf{J}$ correlation.

The bimodal feature in the lower wavelength images is accounted for by the presence of the two processes for which evidence has been presented above. There is also a clear bimodality in the data from 266 nm dissociation. The energy distribution displays peaks at 2.7 and 3.6 eV. This distribution raises further questions since the process creating $\text{O}_2(v \geq 26)$ at lower wavelengths is no longer energetically accessible. One possibility is that it arises from a previously unobserved spin-forbidden process in the Hartley band. Energetically, the lower energy feature corresponds to the channel



This channel has recently been observed in the 335–352 nm region of the Huggins band.⁴⁹ Such a channel is not inconsistent with previously determined branching ratios in the Hartley band. These determinations typically rely on measuring the amount of $\text{O}(^3\text{P})$ as a function of time and inferring the channels present from the observed kinetics. Such a measurement accounts for the amount of $\text{O}(^1\text{D})$ versus $\text{O}(^3\text{P})$ formed but not which channels gives rise to these species.

We cannot say that the low energy feature is indeed due to this spin-forbidden channel without further corroboration, that is, direct measurement of the $\text{O}_2(b^1\Sigma_g^+)$ product, for example by a $(2+1)$ REMPI process.⁵⁰ There are several complications in this measurement. First, only one rovibrational state of the $\text{O}_2(b^1\Sigma_g^+)$ may be probed at a time. Thus, if this spin-forbidden process occurs, the amount of signal is dependent upon the nascent rovibrational distribution. Second, $\text{O}(^1\text{D})$ readily reacts with $\text{O}_2(X^3\Sigma_g^-)$ to form $\text{O}_2(b^1\Sigma_g^+)$.⁵¹ Because $\text{O}(^1\text{D})$ is readily formed in the UV photodissociation of ozone, this reaction is likely to give a significant background signal. However, if this channel does occur, it is pertinent to ask what its wavelength dependence might be. It is interesting to note that the images at other wavelengths have peaks or shoulders at the energetic threshold for this spin-forbidden channel.

3.2.2. $\text{O}(^3\text{P})$ Angular Distributions⁵

The $\text{O}(^3\text{P}_2)$ formed in the minor dissociation channel was probed through a $(2+1)$ REMPI scheme at photolysis wavelengths of 226, 230, 240 and 266 nm. Abel-transformed images similar to those used for this analysis

have been shown in Fig. 12. The electric vector of the dissociating light is parallel to the vertical direction in the plane of the image.

For photolysis at 226 and 230 nm the images exhibit a similar bimodal velocity distribution. However, the intensity ratios of the inner to outer portions of the images are different, with the ratio of slow (inner) to fast (outer) $O(^3P_2)$ fragments increasing for photolysis at 230 nm with respect to that at 226 nm. The velocity mapping technique increases the resolution of our data, allowing observation of structure within the inner portion of the 226 nm photolysis image; two rings are clearly apparent. The images obtained at dissociation wavelengths 240 and 266 nm display less marked bimodal velocity distributions; instead more continuous distributions are observed.

The recovered $O(^3P_2)$ velocity distributions from the Abel-transformed slices can be separated into an angular and speed component. Angular distributions are determined by integrating over all speeds for each angle. Extraction of the speed distribution is achieved in an analogous manner by integrating over all angles for each speed. The speed distributions can be further transformed, using the law of conservation of momentum, into total translational energy distributions for the $O_3 \rightarrow O(^3P_2) + O_2(X^3\Sigma_g^-)$ dissociation. As discussed above, the translational energy distributions obtained from our data at photolysis wavelengths of 226 and 230 nm are both strongly bimodal, peaking at energies of 0.1 and 1.7 eV with a minimum at 0.8 eV for both dissociation wavelengths.

The $O(^3P_2)$ angular distributions have been analyzed using two different methods. The first approach assumes the data for dissociation at 226, 230 and 240 nm to be well characterized by two β parameters, one fitted to the slow peak in the translational distribution and the other to the fast peak. Since data obtained for dissociation at 266 nm is not characterized by a clear separation between fast and slow translational speeds, the angular distribution was determined in this method by integrating over the entire speed profile of the 266 nm photolysis images. The second method of analysis makes fewer assumptions. Here the speed dependence of the $O(^3P_2)$ angular distributions is determined by examining the angular distributions obtained from a number of different speed regions of each image. This method was applied to data collected at all four dissociation wavelengths.

The angular distributions for the slow and fast $O(^3P_2)$ fragments have been determined separately. The division between slow and fast fragments corresponds to the relative minimum in the $O(^3P_2)$ speed

distribution, determined as 3315 m/s , 2972 m/s and 2572 m/s for dissociation at 226, 230 and 240 nm. Since no bimodal velocity distributions were obvious for dissociation at 266 nm, the entire $O(^3P_2)$ velocity profiles were considered.

The fitted β values are listed in Table 7. The angular distributions of the slow $O(^3P_2)$ fragments are well characterized by this equation, however the fast atom distributions we observe do not appear to be governed by a simple $\cos^2 \theta$ dependence, where θ is the angle between the polarization direction of the photolysis light and the direction of recoil. The fits to the fast fragments for all three wavelengths are therefore poor.

After careful testing of our data acquisition procedure and experimental setup, we have concluded that the flat bottoms observed in the angular distributions of the fast $O(^3P_2)$ fragments are real, possibly due to alignment effects between the angular momentum of the $O(^3P_2)$ atom and the recoil velocity of the fragment. This conclusion has been borne out by preliminary analysis of $O(^3P_0)$ images from the 226 nm dissociation of ozone where no $\mathbf{v}-\mathbf{J}$ correlations are possible. The angular distributions obtained from these images follow a $\cos^2 \theta$ dependence regardless of the fragment speed.

The exact nature of the $\mathbf{v}-\mathbf{J}$ correlations are the focus of further work. In this investigation no attempt has been made to model or account for the suspected $\mathbf{v}-\mathbf{J}$ correlations at high fragment speed velocities. Instead the breakdown of the assumptions that the angular distributions follow a $\cos^2 \theta$ distribution and that the probe laser does not affect the efficiency of fragment detection, at high $O(^3P_2)$ speeds, is reflected in the magnitude of the error quoted with the anisotropy parameters.

Table 7 shows that the anisotropy parameters fitted to the angular distributions of the slow oxygen atoms are considerably smaller than those characterizing the angular behavior of the fast product pathway. A wavelength dependence is also suggested, with decreasing β values being determined as the photolysis wavelength increases.

The considerable speed dependence of the anisotropy parameters characterizing the angular distributions for photolysis at 226, 230 and 240 nm prompted a more thorough investigation into the speed dependence of β for all the photolysis wavelengths considered in this work. The Abel-transformed images were split into concentric speed rings. The angular distributions of the $O(^3P_2)$ fragments were then determined for each speed ring separately, and a β value was extracted by fitting the distributions to the functional form given in Eq. (3) (see below). The anisotropy parameters

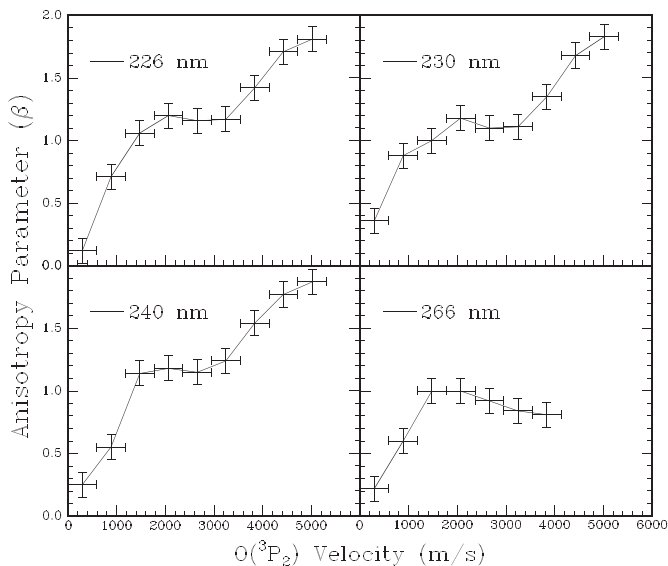


Fig. 15. β versus $\text{O}(^3\text{P}_2)$ speed for photolysis at 226, 230, 240 and 266 nm.

obtained are plotted in Fig. 15 as a function of the average $\text{O}(^3\text{P}_2)$ fragment speed for each ring.

The broad behavior of the anisotropy parameter versus speed curves is similar for all photolysis wavelengths. Unfortunately the 266 nm photolysis data at high $\text{O}(^3\text{P}_2)$ speeds was of insufficient quality to fit anisotropy parameters satisfactorily, so we cannot state with confidence whether the speed dependence of β changes at higher photolysis wavelengths. The overriding feature in Fig. 15 is the steady increase in β as the $\text{O}(^3\text{P}_2)$ fragments travel faster. Some structure is also apparent in the curves, with a plateau between approximately 1200 and 3700 m/s.

The angular distributions of the $\text{O}(^3\text{P}_2)$ fragments show the degree of correlation between the product recoil velocity (v) with the electric vector of the dissociating light and are typically characterized by the lab frame anisotropy parameter (β) given in the equation,^{52,53}

$$I(\theta) = [1 + \beta P_2(\cos \theta)]/4\pi \quad (18)$$

Here θ is the recoil angle relative to the electric vector of the dissociating light and P_2 is the second-order Legendre polynomial.

The anisotropy parameter is also sensitive to both the lifetime and geometry of the dissociating molecule. For an instantaneous dissociation, and

assuming that the recoil velocity is directed along the breaking bond, β can be related directly to the structure of the parent molecule by the expression

$$\beta = \frac{2(3\cos^2\chi - 1)}{2} \quad (19)$$

where χ is the angle between the transition dipole moment (μ) and the recoil velocity of the photofragment. The anisotropy parameter therefore ranges from $\beta = -1$, for a dissociation where χ is perpendicular to μ , to $\beta = 2$ where χ and μ are parallel. Since the transition moment for the $B\ ^1B_2 \leftarrow \tilde{X}\ ^1A_2$ electronic transition lies in the plane of the ozone molecule and perpendicular to the C_2 axis, the average O–O–O bond angle prior to dissociation is simply given by 180° minus 2χ .

If the photolysis process is not immediate, but instead has some finite lifetime τ , the parent molecule may have time to rotate during dissociation and so “wash out” the angular distribution. In this case a reduced effective anisotropy parameter (β_{eff}) is used to characterize the observed angular distribution. The relationship between β_{eff} and parent lifetime can be expressed as^{52,54}

$$\beta_{\text{eff}} = \beta \left[\frac{1 + \omega^2\tau^2}{1 + 4\omega^2\tau^2} \right] \quad (20)$$

where ω is the frequency of parent rotation.

Some idea of the expected lifetime of the parent molecule leading to the triplet products can be obtained by first considering experimental studies on the singlet channel.^{1,34,44,55,56} Generally, except for dissociation at 193 nm,⁴⁴ the measured (or inferred) value of β in these studies is close to the limiting anisotropy parameter of 1.18 for an instantaneous dissociation following a $B\ ^1B_2 \leftarrow \tilde{X}\ ^1A_1$ from the ground state equilibrium geometry of ozone. The close agreement between the measured values of β for a number of dissociation wavelengths and the limiting anisotropy parameter indicates the dissociation must be prompt, occurring on a timescale much shorter than the rotational period of the parent molecule. This conclusion has also been drawn from theoretical studies on the $B\ ^1B_2$ surface, where most of the molecules are found to dissociate within 40–60 fs.^{57,58}

In the absence of a long-lived intermediate, the time constants for product formation must be the same for the two branches of the parallel reactions giving triplet products or singlet products; each appearance time is given by the reciprocal of the sum of the rates for the two parallel channels. As discussed above the appearance time for the production of the singlet

channel is thought to be prompt and constant with wavelength. Thus, barring a long-lived intermediate, the appearance time of the channel giving triplets must also be prompt and independent of photolysis energy. In this case, any variation of β with dissociation wavelength cannot be caused by a variation in the lifetime, τ , but rather must be due to a variation in the prevalent geometrical structure of the molecule immediately prior to dissociation.

Table 7 shows that significantly different anisotropy parameters characterize the angular distributions of the fast and slow $\text{O}(^3\text{P}_2)$ fragments for photolysis at 226, 230 and 240 nm. A wavelength dependence is also suggested, with photolysis at 240 and 266 nm resulting in a more isotropic angular distribution. As discussed earlier, rotation of the excited parent molecule prior to dissociation cannot reasonably be the cause of the reduced anisotropy parameters characterizing the angular distributions of the slow oxygen atoms. Vibrational motion, however, can occur within the expected timescale for photolysis, so that the average geometry of the dissociating molecules may be different from that of the equilibrium ground state configuration.

For dissociation at 226 and 230 nm, the determined β values for the fast and slow oxygen atoms are $\sim 1.3/1.5$ and $\sim 0.7/0.8$, respectively. The former value corresponds to a bond angle of $\sim 120^\circ$, close to the ozone ground state equilibrium bond angle of 117° . The reduced anisotropy parameter of 0.8 implies a more strongly bent geometry with a bond angle of $\sim 100^\circ$.

The differing anisotropy parameters determined for the fast and slow $\text{O}(^3\text{P}_2)$ atoms strongly suggest that the two $\text{O}(^3\text{P}_2)$ velocity components sample either different potential energy surfaces or different regions of the same surface. The former situation might occur if excitation reaches more than one electronic state, whereas the latter situation might be due to multiple regions for crossing between electronic surfaces. Speed dependent anisotropy parameters reported in the dissociation of $\text{C}_2\text{F}_5\text{I}$ (Ref. 59) and iodobenzene (Ref. 60) have been rationalized by the existence of indirect photolysis channels via curve crossing. In the latter case, the photolysis lifetime also influences the relationship between the product translational energy and the angular distribution.

The bimodal velocity distribution of the $\text{O}(^3\text{P}_J)$ fragments produced via the triplet channel in the UV photodissociation of ozone has also been observed by Syage^{41,43,46} and Stranges *et al.*⁴⁴ at photolysis wavelengths of 226 and 193 nm, respectively. Both authors measured anisotropy parameters for the fast and slow product pathways separately.

Our determined anisotropy parameters for 226 nm photolysis agree favorably with the reported values of Syage, where a β value of 1.2 was measured for the fast $\text{O}(^3\text{P}_2)$ products. Syage observed a less anisotropic distribution for the slow $\text{O}(^3\text{P}_2)$ atoms, with a reported β value of 0.4. The β value of 1.2 for the high velocity component was rationalized by a prompt dissociation from the equilibrium ground state of ozone following an $B\ ^1\text{B}_2 \leftarrow \tilde{X}\ ^1\text{A}_1$ transition.

Syage speculated that a reduced anisotropy may be expected for the slow $\text{O}(^3\text{P}_J)$ fragments if a cyclic transition state were accessed, which would also allow the expulsion of the central oxygen atom. Such a mechanism would explain the production of vibrationally hot $\text{O}_2(^3\Sigma_g^-)$ fragments. Interestingly, theoretical calculations⁶¹ show an intersection between the repulsive \hat{R} (\tilde{C} in C_s symmetry) surface and the ground state surface very close to the transition state for abstraction of the central oxygen. This intersection would provide an alternate route to the ground state products via an equilateral geometry.

For photolysis at 193 nm, Stranges *et al.* determined β values of 0.09 and -0.33 for the fast and slow velocity components of the $\text{O}(^3\text{P}_2)$ fragments produced via the triplet channel. The considerable difference in excitation energy between the study by Stranges *et al.* and this work makes a direct comparison between our results and theirs less meaningful. However, a brief discussion is warranted. The very small β value reported for the angular distribution of the fast velocity component was rationalized by proposing a rapid decrease in bond angle during dissociation.⁵⁸ This effect is not generally consistent with our results, and we find no manifestation of this phenomenon in the angular distributions of the fast $\text{O}(^3\text{P}_2)$ fragments at longer photolysis wavelengths. Because of the increased yield of the slow $\text{O}(^3\text{P}_2)$ atoms for dissociation at 193 compared to that at 226 nm, Stranges inferred that the slow product pathway originated from optical excitation, not to the $B\ ^1\text{B}_2$ (\tilde{D} in C_s symmetry) surface but instead directly to the \hat{R} state (\tilde{C} in C_s symmetry). If two electronic states are responsible for the absorption in the 226–266 nm region we have investigated, then it is possible that the variation in β with speed may be related to differing absorptions and crossing probabilities involving these two states. However, because we do not observe negative β values for the slow oxygen atoms at photolysis wavelengths of 226 and 230 nm, and because we furthermore observe an increased yield at lower photolysis energies, it seems to us that this proposition is an unlikely explanation for our results.

At longer photolysis wavelengths, where no apparent bimodal velocity distribution is evident in our images, β decreases yielding a value of 0.7 for dissociation at 266 nm. This value agrees well with the work of Shamsuddin *et al.*⁶² where a β value of 0.81 was obtained for photolysis at 266 nm. Lower anisotropy parameters suggest that the prevalent transition state geometry alters as a function of photolysis wavelength, becoming increasingly bent as the dissociation energy decreases.

The results of the more thorough analysis carried out on the speed dependence of β are illustrated in Fig. 15. The main feature is the steady increase in anisotropy parameter as a function of increasing $O(^3P_2)$ fragment speed, as well as the similarity of the curves for dissociation at 226, 230, 240 and 266 nm. The β versus fragment speed plots also appear to have a plateau occurring at a value 0.8 with an onset at 1200 m/s, this structure is more prevalent in the 226 and 230 nm photolysis data. Although a speed dependent anisotropy parameter was expected and had been partially uncovered for the bimodal 226 and 230 nm photolysis images, the similarity and strength of the speed dependence for the β values extracted from the 240 and 266 nm data was not anticipated.

Figure 15 provides us with a more complete picture of the dissociation process with our results indicating the following points: (1) The $O(^3P_2)$ speed dependence of β is insensitive to the dissociation wavelength, yet the probability of an $O(^3P_2)$ fragment having a particular speed is a function of photolysis energy. (2) The excited ozone molecules do not photolyze immediately but do so instead on a timescale which allows the excited molecules to bend. The β values obtained correspond to bond angles varying from $\sim 80^\circ$ to $\sim 130^\circ$. (3) The structure of the dissociating state is directly correlated to the partitioning of available energy between the translational and internal energies of the resulting $O(^3P_2)$ and $O_2(^3\Sigma_g^-)$ photofragments. The increasingly bent parent molecules favor slow products and vibrationally hot $O_2(^3\Sigma_g^-)$ fragments, while those with more obtuse bond angles result in fast products in coincidence with vibrationally cooler $O_2(^3\Sigma_g^-)$ fragments.

The steady increase in β with fragment speed could possibly be explained if many different regions of the same potential surface were sampled by the dissociating molecules. The obvious manner for this sampling to occur would be along the crossing seam between the initially excited B^1B_2 surface and the repulsive \tilde{R} state correlating to the triplet products. A possible explanation which qualitatively accounts for the main features of

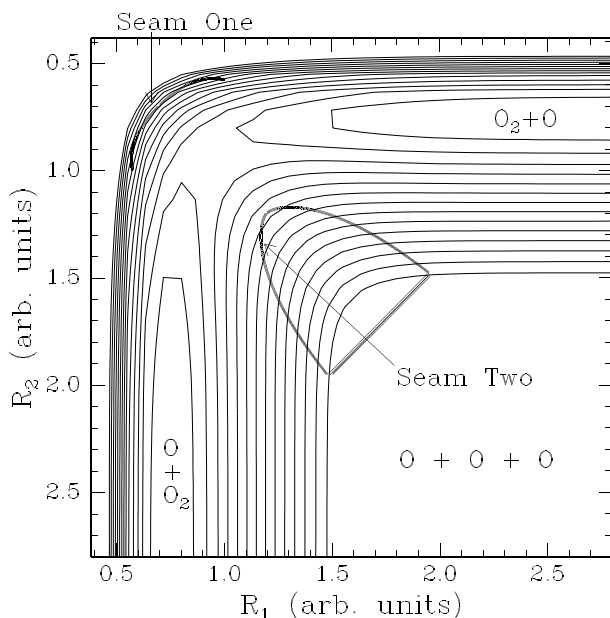


Fig. 16. Schematic of the repulsive surface correlating to the triplet products illustrating the two crossing regions of the initially excited $B\ ^1B_2$ surface.

our data trends comes from predicting the expected dynamics for molecules crossing at different points between these two surfaces.

First consider the expected crossing between the $B\ ^1B_2$ surface and repulsive \tilde{R} state along the symmetric stretch coordinate. We can plausibly expect the surfaces to interact in more than one region even though the asymptotes correlating to the dissociation products along the symmetric and asymmetric stretch coordinates of the $B\ ^1B_2$ state lie higher in energy than the corresponding asymptotic limits of the \tilde{R} state. This interaction is possible, providing the upper state surface is shallower along the symmetric stretch coordinate than the \tilde{R} state. Figure 16 is a two-dimensional schematic of the repulsive surface and illustrates how the intersection between the two states might appear.

We can now imagine two illustrative cases for nonadiabatic transitions between the $B\ ^1B_2$ and \tilde{R} states, one where the crossing takes place at a point along seam "one" and the second where the crossing point lies along seam "two". In the first case, the transition is made when the ozone bond lengths are little extended, and the molecules move onto the repulsive

surface at a point relatively close to the minimum energy pathway. Such a trajectory will impart energy into both the vibration of the oxygen diatomic and the translational of the fragments. If, however, the transition between the two surfaces is made when the ozone bond lengths are considerably extended, we can imagine a scenario where the molecules would move on to the repulsive surface at a point on the second crossing seam directly above (in energy) the valley leading to dissociation. As the molecules move down this hill and into the valley they are travelling more nearly perpendicular to the dissociation coordinate and so do not follow the minimum energy path. A trajectory such as this will “oscillate” up and down the valley walls (the bobsled effect) on its way to dissociation and impart energy to the vibrational coordinate of the $\text{O}_2(^3\Sigma_g^-)$ fragment at the expense of translation.

It is unclear exactly how the two potential surfaces, and hence the interaction regions between them, behave as the parent molecules bend. Our experimental results indicate that the more bent the ozone molecules are as they dissociate the more effectively is the available energy channelled into the $\text{O}_2(^3\Sigma_g^-)$ fragment vibration. It is possible that as the parent molecules bend, the crossing seams move to a region on the repulsive state that more strongly favors the production of vibrationally excited $\text{O}_2(^3\Sigma_g^-)$ fragments.

The dynamics of the two illustrative examples show how our results could be rationalized by considering the crossing points between the two surfaces. The scenarios presented would explain both the insensitivity of the $\text{O}(^3\text{P}_2)$ fragments’ speed-dependent angular distributions with regard to photolysis energy and also the correlation we observe between parent geometry and the degree of vibrational excitation in the $\text{O}_2(^3\Sigma_g^-)$ molecules. Our experimental results indicate that the probability of an $\text{O}(^3\text{P}_2)$ fragment being produced with a certain speed is dependent on excitation energy. This dependence could be incorporated into our conceptual model if the likelihood of crossing at a particular point on the seams is influenced by the excitation wavelength.

Although the above discussion seems reasonable, its difficult either to take it much further or even to ascertain the likelihood of the scenarios presented without more detailed three-dimensional calculations on the nonadiabatic crossing region between the $B\ ^1\text{B}_2$ and \tilde{R} surfaces.^{4,32,36–39} It should be stressed that the scenarios are not presented as an exact mechanism but rather as a speculative model which qualitatively explains the trends in our data.

4. Conclusions and Remaining Questions

For the singlet channel, $\text{O}(^1\text{D}_2) + \text{O}_2(^1\Delta_g)$, the vibrational populations of $\text{O}_2(^1\Delta_g)$ are peaked at $v = 0$ for all wavelengths in the 235–305 nm range and all vibrationally-accessible states are at least partially filled. Images of the two-dimensional projection of the nascent three-dimensional velocity distribution of $\text{O}_2(^1\Delta_g, v, J)$ from the 248 nm dissociation of ozone show strong evidence of $\mathbf{v}-\mathbf{J}$ correlation. The experimental results are accurately reproduced assuming an impulsive dissociation from the ground state geometry ($\beta = 1.18$). A diagonal density matrix method was used to study the alignment and spatial anisotropy of the $\text{O}(^1\text{D}_2)$ fragment. The value of β varied from about 1.2 at 235 nm to 1.7 at 298 nm. The $|m_j|$ populations were peaked at $|m_j| = 0$, with some population in $|m_j| = 1$, and very little in $|m_j| = 2$. These results were generally confirmed by the larger data sets taken at 255 nm and 298 nm, where four different laser polarization combinations were used in order to determine the full density matrix, albeit with only rank 0 and 2 terms. The $|m_j|$ distributions using this method were more peaked at $|m_j| = 1$, yet still maintained the lack of population in $|m_j| = 2$. The results also illustrated a clear preference for incoherent, parallel excitation. Dissociation of ozone to $\text{O}(^1\text{D}_2) + \text{O}_2(^1\Delta_g)$ takes place after excitation to a state of A' symmetry and after substantial bending of the parent molecule.

For the triplet channel, $\text{O}_3 + h\nu \rightarrow \text{O}(^3\text{P}_J) + \text{O}_2(^3\Sigma_g^-)$, we have studied the UV photodissociation at photolysis wavelengths of 226, 230, 233, 234, 240, and 266 nm. The imaging experiments, together with a measurement of the branching ratio into the different spin-orbit states of the O atom, allowed the determination of the yields of the O_2 product in vibrational states greater than or equal to 26 as a function of wavelength. At 226, 230, 233, 234, and 240 nm, the yields were $11.8 \pm 1.9\%$, $11.5 \pm 1.2\%$, 8.2 ± 2.0 , 4.7 ± 1.8 , and $0.6 \pm 0.1\%$, respectively. This yield may play an important role in analyzing the ozone deficit, the mismatch between measured ozone concentrations as a function of altitude and those predicted by modelling calculations. Two-dimensional product imaging has also been used to determine the speed dependence anisotropy of dissociation in the triplet channel. The anisotropy parameters determined for dissociation at 226, 230, 240, and 266 nm show a similar and marked dependence on $\text{O}(^3\text{P}_2)$ fragment speed: β increases with oxygen atom speed. This dependence translates to a strong correlation between the average ozone bond angle prior to dissociation and the partitioning of available energy between the translational and internal energies of the photofragments.

Perhaps the most intriguing remaining question is the cause for the bimodal vibrational distribution of $\text{O}_2(^3\Sigma)$ in the triplet channel. These distributions, calculated from the data of Figs. 12 and 13 is summarized in Table 8 and plotted in Fig. 17. Whether the high and low vibrational levels are due to two areas of surface crossing, as suggested in the discussion above, to the influence of a triangular form of ozone, or to some other cause is not yet known. Detailed *ab initio* calculations will be needed before we will have an explanation for this interesting experimental observation.

Table 8. Fractional population of $\text{O}_2(^3\Sigma)$ vibrational levels as a function of photolysis wavelength.

Vibrational level	226 nm	230 nm	240 nm	266 nm
0	0.13E-02	0.13E-02	0.37E-02	0.11E-01
1	0.16E-02	0.17E-02	0.44E-02	0.16E-01
2	0.31E-02	0.26E-02	0.80E-02	0.33E-01
3	0.85E-02	0.80E-02	0.20E-01	0.65E-01
4	0.23E-01	0.23E-01	0.40E-01	0.88E-01
5	0.39E-01	0.38E-01	0.52E-01	0.87E-01
6	0.45E-01	0.44E-01	0.53E-01	0.74E-01
7	0.46E-01	0.44E-01	0.53E-01	0.59E-01
8	0.52E-01	0.48E-01	0.58E-01	0.86E-01
9	0.58E-01	0.56E-01	0.63E-01	0.89E-01
10	0.61E-01	0.62E-01	0.69E-01	0.69E-01
11	0.64E-01	0.63E-01	0.60E-01	0.50E-01
12	0.64E-01	0.64E-01	0.75E-01	0.39E-01
13	0.60E-01	0.67E-01	0.76E-01	0.33E-01
14	0.64E-01	0.72E-01	0.63E-01	0.31E-01
15	0.68E-01	0.67E-01	0.53E-01	0.28E-01
16	0.61E-01	0.54E-01	0.48E-01	0.27E-01
17	0.50E-01	0.40E-01	0.35E-01	0.25E-01
18	0.36E-01	0.29E-01	0.26E-01	0.23E-01
19	0.27E-01	0.21E-01	0.22E-01	0.22E-01
20	0.18E-01	0.17E-01	0.18E-01	0.24E-01
21	0.16E-01	0.15E-01	0.18E-01	0.20E-01
22	0.13E-01	0.15E-01	0.18E-01	0.17E-02
23	0.14E-01	0.15E-01	0.18E-01	0
24	0.13E-01	0.14E-01	0.20E-01	0
25	0.12E-01	0.17E-01	0.20E-01	0
26	0.14E-01	0.21E-01	0.46E-02	0
27	0.28E-01	0.63E-01	0	0
28	0.37E-01	0.17E-01	0	0
29	0.37E-02	0	0	0
30	0	0	0	0

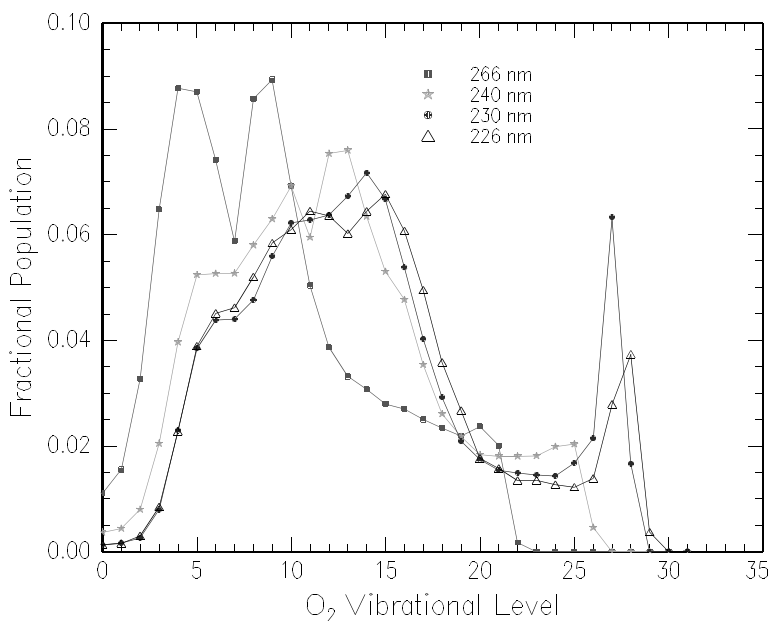


Fig. 17. Fractional population of $O_2(^3\Sigma)$ vibrational levels as a function of photolysis wavelength.

Acknowledgments

This work would not have been possible without the efforts of many graduate students, undergraduate students, and postdoctoral associates and other senior collaborators who have worked with me during the past several years. Most of all, I want to acknowledge those who prepared the original work published in primary journals: A. G. Suits, R. L. Miller, L. S. Bontuyan, R. Toumi, J. A. Mack, and A. M. Wodtke, R. J. Wilson, J. A. Mueller, N. Taniguchi, K. Takahashi, Y. Matsumi, S. Dylewski, and J. Geiser. This work was supported by the National Science Foundation under grants ATM-9528086, CHE-8920404, and CHE-9901065, and by the Research Institute of Innovative Technology for the Earth administered by the New Energy and Industrial Technology Development Organization of Japan.

Note Added in Proof

This article was submitted in September 2003. Other papers on this subject have been published since then, and are not referenced here.

References

1. A. G. Suits, R. L. Miller, L. S. Bontuyan and P. L. Houston, *J. Chem. Soc., Faraday Trans. II* **89**, 1443–1447 (1993).
2. R. L. Miller, A. G. Suits, P. L. Houston, R. Toumi, J. A. Mack and A. M. Wodtke, *Science* **265**, 1831–1838 (1994).
3. R. Toumi, P. L. Houston and A. M. Wodtke, *J. Chem. Phys.* **104**, 775–776 (1996).
4. P. L. Houston, A. G. Suits and R. Toumi, *J. Geophys. Res.* **101**, 18829–18834 (1996).
5. R. J. Wilson, J. A. Mueller and P. L. Houston, *J. Phys. Chem.* **A101**, 7593–7599 (1997).
6. N. Taniguchi, K. Takahashi, Y. Matsumi, S. Dylewski, J. Geiser and P. L. Houston, *J. Chem. Phys.* **111**, 6350–6355 (1999).
7. J. D. Geiser, S. M. Dylewski, J. A. Mueller, R. J. Wilson, P. L. Houston and R. Toumi, *J. Chem. Phys.* **112**, 1279–1286 (2000).
8. S. M. Dylewski, J. D. Geiser and P. L. Houston, *J. Chem. Phys.* **115**, 7460–7473 (2001).
9. S. Chapman, *J. R. Meteorol. Soc.* **3**, 103 (1930); S. Chapman, *Philos. Mag.* **10**, 345 (1930).
10. M. J. Molina and F. S. Rowland, *Nature* **249**, 810 (1974).
11. R. Toumi, B. J. Kerridge and J. A. Pyle, *Nature* **351**, 217–219 (1991).
12. P. J. Crutzen, J.-U. Groö, C. Brühl, R. Müller and J. M. Russell III, *Science* **268**, 705–708 (1995).
13. D. W. Chandler and P. L. Houston, *J. Chem. Phys.* **87**, 1445 (1987).
14. A. T. J. B. Eppink and D. H. Parker, *Rev. Sci. Instrum.* **68**, 3477–3484 (1997).
15. B.-Y. Chang, R. C. Hoetzlein, J. A. Mueller, J. D. Geiser and P. L. Houston, *Rev. Sci. Instrum.* **69**, 1665–1670 (1998).
16. S. T. Pratt, P. M. Dehmer and J. L. Dehmer, *Phys. Rev.* **A43**, 282–286 (1991).
17. D. J. Bamford, L. E. Jusinski and W. K. Bischel, *Phys. Rev.* **A34**, 185–198 (1986).
18. D. J. Bamford, M. J. Dyer and W. K. Bischel, *Phys. Rev.* **A36**, 3497–3500 (1987).
19. L. A. Shepp and B. F. Logan, *IEEE Trans. Nucl. Sci.* **NS-21**, 21–32 (1974).
20. L. M. Smith and D. R. Keefer, *J. Quant. Spectrosc. Radiat. Transfer* **39**, 367–373 (1988).
21. M. Kalal and K. A. Nugent, *Appl. Opt.* **27**, 1956–1959 (1988).
22. R. K. Sparks, L. R. Carlson, K. Shobatake, M. L. Kowalczyk and Y. T. Lee, *J. Chem. Phys.* **72**, 1401–1402 (1980).
23. M.-A. Thelen, T. Gejo, J. A. Harrison and J. R. Huber, *J. Chem. Phys.* **103**, 7946–7955 (1995).
24. J. M. Valentini, D. P. Gerrity, D. L. Phillips, J.-C. Nieh and K. D. Tabor, *J. Chem. Phys.* **86**, 6745–6756 (1987).
25. Y. Mo, H. Katayanagi, M. C. Heaven and T. Suzuki, *Phys. Rev. Lett.* **77**, 830–833 (1996).

26. Y. Mo and T. Suzuki, *J. Chem. Phys.* **108**, 6780–6789 (1998); Y. Mo and T. Suzuki, *J. Chem. Phys.* **109**, 4691–4692 (1998).
27. M. Ahmed, E. R. Wouters, D. S. Peterka, O. S. Vasyutinskii and A. G. Suits, *Faraday Discuss.* **113**, 425–436 (1999).
28. A. S. Bracker, Ph.D., University of California at Berkeley, 1997.
29. A. S. Bracker, E. R. Wouters, A. G. Suits, Y. T. Lee and O. S. Vasyutinskii, *Phys. Rev. Lett.* **80**, 1626–1629 (1998).
30. A. S. Bracker, E. R. Wouters, A. G. Suits and O. S. Vasyutinskii, *J. Chem. Phys.* **110**, 6749–6765 (1999).
31. L. D. A. Siebbeles, M. Glass-Maujean, O. S. Vasyutinskii, J. A. Beswick and O. Roncero, *J. Chem. Phys.* **100**, 3610–3623 (1994).
32. T. P. Rakitzis and R. N. Zare, *J. Chem. Phys.* **110**, 3341–3350 (1999).
33. K. Takahashi, N. Taniguchi, Y. Matsumi and M. Kawasaki, *Chem. Phys.* **231**, 171–182 (1998).
34. C. E. Fairchild, E. J. Stone and G. M. Lawrence, *J. Chem. Phys.* **69**, 3632–3638 (1978).
35. A. G. Suits, L. S. Bontuyan, P. L. Houston and B. J. Whitaker, *J. Chem. Phys.* **96**, 8618 (1992).
36. D. Chasman, D. J. Tannor and D. G. Imre, *J. Chem. Phys.* **89**, 6667 (1988).
37. R. G. Bray and R. M. Hochstrasser, *Mol. Phys.* **31**, 1199 (1976).
38. K. Takahashi, M. Kishigami, N. Taniguchi, Y. Matsumi and M. Kawasaki, *J. Chem. Phys.* **106**, 6390–6397 (1997).
39. R. R. Laher and F. R. Gilmore, *J. Phys. Chem. Ref. Data* **20**, 685–712 (1991).
40. C. E. Moore, *Tables of Spectra of Hydrogen, Carbon, Nitrogen, and Oxygen Atoms and Ions* (CRC Press, Boca Raton, 1993).
41. J. A. Syage, *J. Chem. Phys.* **105**, 1007–1022 (1996).
42. S. M. Shamsuddin, Y. Inagaki, Y. Matsumi and M. Kawasaki, *Can. J. Chem.* **72**, 637–642 (1994).
43. J. A. Syage, *J. Phys. Chem.* **99**, 16530–16533 (1995).
44. D. Stranges, X. Yang, J. D. Chesko and A. G. Suits, *J. Chem. Phys.* **102**, 6067–6077 (1995).
45. K. Takahashi, N. Taniguchi, Y. Matsumi and M. Kawasaki, *Chem. Phys.* **231**, 171–182 (1998).
46. J. A. Syage, *J. Phys. Chem.* **100**, 13885 (1996).
47. T. Kinugawa, T. Sato, T. Arikawa, Y. Matsumi and M. Kawasaki, *J. Chem. Phys.* **93**, 3289–3294 (1990).
48. J. H. Seinfeld and S. N. Pandis, *Atmospheric Chemistry and Physics: From Air Pollution to Climate Change* (John Wiley & Sons, New York, 1998).
49. P. O’Keeffe, T. Ridley, S. Wang, K. P. Lawley and R. Donovan, *Chem. Phys. Lett.* **298**, 368–374 (1998).
50. R. O. Loo, W. J. Marinelli, P. L. Houston, S. Arepalli, J. R. Wiesenfeld and R. W. Field, *J. Chem. Phys.* **91**, 5185–5200 (1989).
51. D. R. Snelling and M. Gauthier, *Chem. Phys. Lett.* **9**, 254–256 (1971).
52. G. E. Busch and K. R. Wilson, *J. Chem. Phys.* **56**, 3638 (1972).
53. R. N. Zare and D. R. Herschbach, *Proc. IEEE* **51**, 173 (1963).

- 54. C. Jonah, *J. Chem. Phys.* **55**, 1915 (1971).
- 55. M. A. Thelen, T. Gejo, J. A. Harrison and J. R. Huber, *J. Chem. Phys.* **103**, 7946 (1995).
- 56. H. B. Levene and J. J. Valentini, *J. Chem. Phys.* **87**, 2584 (1987).
- 57. D. Chasman, D. J. Tannor and D. G. Imre, *J. Chem. Phys.* **89**, 6667 (1988).
- 58. C. Leforestier, F. Le Quéré, K. Yamashita and K. Morokuma, *J. Chem. Phys.* **101**, 3806 (1994).
- 59. H. J. Hwang and M. A. El-Sayed, *Chem. Phys. Lett.* **170**, 161 (1990).
- 60. J. E. Freitas, H. J. Hwang and M. A. El-Sayed, *J. Phys. Chem.* **97**, 12481 (1993).
- 61. S. S. Xantheas, G. J. Atchity, S. T. Elbert and K. Ruedenberg, *J. Chem. Phys.* **94**, 8054 (1991).
- 62. S. M. Shamsuddin, Y. Inagaki, Y. Matsumi and M. Kawasaki, *Can. J. Chem.* **72**, 637 (1994).

This page intentionally left blank

CHAPTER 7

CROSSED MOLECULAR BEAM REACTIVE SCATTERING: TOWARDS *UNIVERSAL* PRODUCT DETECTION BY *SOFT* ELECTRON-IMPACT IONIZATION

Piergiorgio Casavecchia,* Giovanni Capozza and Enrico Segoloni

Dipartimento di Chimica, Università di Perugia, 06123 Perugia, Italy

**piero@dyn.unipg.it*

This chapter focuses on very recent progress in reactive scattering studies using the Crossed Molecular Beam (CMB) technique with mass spectrometric detection, as made possible by the successful implementation in our laboratory of the *soft* (i.e., low energy) electron-impact ionization method for product detection. Analogously to the approach of *soft* photoionization by tunable VUV synchrotron radiation, *soft* electron-impact ionization permits one to reduce or even eliminate the problem of dissociative ionization of reactants, products and residual background gases which may seriously interfere with product detection and which has severely undermined so far the “universality” of the mass spectrometric detection method in CMB experiments. In addition, in contrast to when using photoionization, it also permits one to more readily determine product branching ratios. All this opens up completely new opportunities in reaction dynamics.

To illustrate the capabilities of the new experimental approach based on *soft* electron-impact ionization, measurements of reactive differential cross-sections for some polyatomic multichannel reactions, which play a fundamental role for our basic understanding of reaction phenomena, are presented and discussed. The examples include reactions of ground state oxygen atom, O(³P), and carbon atom, C(³P), with unsaturated hydrocarbons (acetylene and ethylene), which are of great relevance in combustion and astrophysical chemistry. For these reactions the reactive differential cross-sections have been recently measured for each energetically allowed channel and the branching ratios derived, the results being discussed in the light of theoretical information on the relevant potential energy surfaces.

Another new twist in CMB reactive scattering which has very recently been implemented in our laboratory, will also be briefly discussed in this chapter. It consists in carrying out CMB experiments with a crossing angle of the reactant beams of 135°, rather than the

conventional 90° . The new geometrical arrangement is able to provide not only an increased collision energy, but also an increased angular and velocity resolution.

The future prospects opened up by *soft* electron-impact ionization for product detection in CMB studies of atom/radical reactions with polyatomic molecules/radicals are briefly examined.

Keywords: Reactive scattering; reaction dynamics; crossed molecular beams; elementary reactions.

Contents

1. Introduction	330
2. Experimental Considerations	335
2.1. "Hard" Electron-Impact Ionization	336
2.2. "Soft" Photoionization by Synchrotron Radiation	337
2.3. "Soft" Electron-Impact Ionization by Low-Energy Electrons	337
2.4. Mass Spectra	340
2.5. Measurements of Product Angular and TOF Distributions	343
2.6. Electron-Impact Efficiency Curves	343
2.7. CMB Experiments with Variable Beam Crossing Angle	346
3. Examples: $\text{O}(^3\text{P}) + \text{Unsaturated Hydrocarbons}$	348
3.1. $\text{O}(^3\text{P}) + \text{C}_2\text{H}_2$	348
3.1.1. Product Angular and TOF Distributions Using "Soft" EI Ionization	350
3.1.2. Product Angular and TOF Distributions with Beam Crossing Angle $\gamma = 135^\circ$	354
3.1.3. CMB Determination of the Branching Ratios	355
3.2. $\text{O}(^3\text{P}) + \text{C}_2\text{H}_4$	358
3.2.1. Observation of all Product Channels	361
4. Examples: $\text{C}(^3\text{P}) + \text{Unsaturated Hydrocarbons}$	364
4.1. $\text{C}(^3\text{P}) + \text{C}_2\text{H}_4$	365
4.1.1. Observation of the C–C Bond Fission Channel	368
4.2. $\text{C}(^3\text{P}) + \text{C}_2\text{H}_2$	371
5. Conclusions and Future Prospects	373
Acknowledgments	377
References	377

1. Introduction

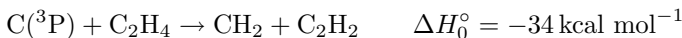
Tremendous advances, both experimental and theoretical, in our fundamental understanding of elementary chemical reactions have occurred during the past decade. This is especially true for simple three-atom (such as $\text{H} + \text{H}_2$, $\text{F} + \text{H}_2$, $\text{Cl} + \text{H}_2$) and some four-atom (such as $\text{OH} + \text{H}_2$) bimolecular reactions, which all involve only one product channel with one of the

two co-products being an atom. Indeed, for such systems it has been possible to carry out very detailed measurements of state-to-state integral and differential cross-sections, and these experimental quantities have been the subject of very detailed comparisons with theoretical predictions based on both exact quantum and quasiclassical trajectory scattering calculations on *ab initio* potential energy surfaces (PESs).^{1–5}

However, more common reactions in chemistry encompass polyatomic molecules or radicals as reactants, and these reactions usually involve several energetically allowed product channels. One of the most basic goals of chemistry is to determine (a) the products of multichannel reactions, (b) the relative importance of the various channels, and (c) their reaction dynamics. This goal is very difficult (if not impossible) to achieve by using any of the several, powerful and sensitive laser-based spectroscopic techniques commonly used nowadays, for reaction dynamics studies at the state-resolved level, such as LIF (laser-induced-fluorescence) and REMPI (resonant-enhanced-multi-photon-ionization), especially when products include polyatomic radicals or molecules, whose spectroscopy is not known or for which not suitable LIF or REMPI schemes or laser sources are available.¹ Noteworthy is the very recent experimental development, based on crossed beam experiments which couple a novel time-sliced ion velocity imaging technique to measure the velocity distribution of a state-selected product by REMPI, which permits one to determine for a polyatomic reaction giving two molecular products, $F + CH_4 \rightarrow CH_3(\nu) + HF(v)$ (and its isotopomers), both integral and double differential cross-sections at the state-resolved level, analogously to what was previously obtained for a three-atom system such as $F + H_2 \rightarrow H + HF(v)$, but with the additional feature of pair-correlated information on the differential cross-sections for the two product partners, thus providing unprecedented, detailed insight on a polyatomic reaction.^{6–8}

Undoubtedly, the technique most suited to tackle polyatomic multichannel reactions is the crossed molecular beam (CMB) scattering technique with mass spectrometric detection and time-of-flight (TOF) analysis. This technique, based on “universal” electron-impact (EI) ionization coupled with a quadrupole mass filter for mass selection, has been central in the investigation of the dynamics of bimolecular reactions during the past 35 years.^{1,9–11} EI ionization affords, in principle, a “universal” detection method for all possible reaction products of even a complex reaction exhibiting multiple reaction pathways. Although the technique is not usually able to provide state-resolved information, especially on a polyatomic

reaction, it does permit one, in principle, to identify the primary products, to determine the product energy partitioning between translation and internal degrees-of-freedom, to derive the product angular distributions in the center-of-mass system and to obtain information on the micro-mechanism (direct or via a long-lived complex) of the reaction, to derive information on the relation between the dynamics and features of the underlying PES, thus providing a global picture of the reaction dynamics. However, since the introduction of the CMB technique in 1969,⁹ its “universality” has essentially remained only “in principle” up to date, because the mass spectroscopic detection method encounters considerable difficulties when applied to CMB experiments. These difficulties reside in (a) the very low number density of products to be detected (as low as 10^{-15} mbar partial pressure), (b) the presence of background gas, and (c) the high energy of the ionizing electrons, being the typical energies used in CMB instruments of the order of 60–200 eV. Point (c) in particular leads to the problem of “dissociative ionization”, which constitutes the most serious problem with the technique. While in analytical chemistry, for instance, this phenomenon is often exploited to recognize complex molecules from their fragmentation patterns, in CMB reactive scattering experiments (as well as photodissociation experiments) ion fragmentation in the ionizer represents a very serious complication which makes very difficult, and often prohibits, the identification of reaction products, particularly when several reaction channels occur simultaneously, as in complex, multichannel reactions, especially involving hydrocarbon molecules or radicals. One of the reasons is that, in general, the reaction products are internally hot, and consequently their fragmentation scheme can be quite different from that of the ground state molecule. Although it is, in some cases, possible to distinguish whether a product at a given mass originates from several species by exploiting energy and momentum conservation (ion fragments coming from the same product species will exhibit identical angular and velocity distributions),¹¹ in general the “dissociative ionization” constitutes “the problem”. For instance, it would be impossible to detect any of the two possible products corresponding to the reaction pathway:



which is an energetically allowed channel of the reaction between atomic carbon and the ethylene molecule.¹² In fact, reactive scattering signal at the mass-to-charge ratio $m/e = 14$ (CH_2) or 26 (C_2H_2) would be overwhelmed, when using 60–200 eV electrons, by the much more intense signal

(by nearly two orders of magnitude) at these masses originating from dissociative ionization of *elastically*-scattered C_2H_4 (see Sec. 4.1). Similarly, it would be impossible to detect the C_3H_7 radical product from the reaction $\text{Cl} + \text{C}_3\text{H}_8 \rightarrow \text{C}_3\text{H}_7 + \text{HCl}$ for analogous reasons.

The problem of dissociative ionization prompted Nobel Laureate Y. T. Lee to introduce during the mid-1990s the concept of *soft* (i.e., non-dissociative) ionization by tunable VUV radiation from a third generation synchrotron (as the Advanced Light Source (ALS) in Berkeley), the only one capable of delivering the 10^{16} photons s^{-1} mandatory for reactive scattering experiments.¹³ Recently, this approach has also been implemented in Taiwan.^{14–16} By using quasicontinuous VUV synchrotron radiation, tunable in a broad energy range (5–30 eV), and by tuning the photon energy below the threshold for dissociative ionization of interfering species, i.e. using *soft* (nondissociative) photoionization (PI), one can often eliminate background signal that would normally prohibit experiments using classic, i.e., *hard*, EI ionization, and so detection of a species of mass m at the parent m/e mass ratio is possible. In general, *soft* PI by synchrotron radiation is also able to solve other shortcomings of *hard* EI ionization, such as background problems, space charge effects, and time resolution.¹³ In fact, the residual background at critical masses can be kept to a minimum because of the negligible amount of heat generated. The tunability of the radiation adds selectivity in the internal energy of the detected species, in addition to universality: this makes it possible to distinguish among possible isomer products by properly tuning the frequency of the ionizing radiation. Since no space charge effects accompany the PI process, by spatially focusing the photons it is possible to attain high time-resolution for TOF measurements. A remaining problem is the low ionization efficiency, as photoionization cross-sections are typically about two orders of magnitude smaller than EI ionization cross-sections; however, the higher the VUV flux, the higher the sensitivity.

Many photodissociation studies in recent years have demonstrated the power of the *soft* photoionization approach by synchrotron radiation.^{13–20} However, there have been only a very few (two) examples of reactive scattering studies.^{21,22} For instance, the reaction $\text{Cl} + \text{propane}$ was investigated²¹ by detecting the propyl radical product using 9.5 eV PI radiation, which is below the threshold for dissociative ionization of C_3H_8 to C_3H_7^+ (the ionization energy (IE) of C_3H_8 is 10.9 eV). The detection of C_3H_7 radicals with virtually zero background would not have been possible using *hard* EI ionization detection because of the huge background signal at

$m/e = 43$ (C_3H_7^+) arising from heavy fragmentation of the C_3H_8 reagent. Analogously, the pentyl radical was detected as a product from the reaction $\text{Cl} + n\text{-C}_5\text{H}_{12}$.²² Recently, single photon PI by a 157-nm F_2 laser (7.9 eV radiation) has been successfully used in reactive scattering studies of transition metals exploiting the low ionization potentials of these metals and their compounds.^{23–29} Obviously the latter detection approach remains confined, beyond transition metal compounds, to a limited number of large polyatomic radicals having an IE somewhat below 7.9 eV. Higher photon energies may be generated by nonlinear four-wave mixing in inert gases or metal vapors. Although the currently available table-top VUV radiation sources relying on nonlinear frequency conversion of pulsed laser light cannot offer the quasicontinuous 10^{16} photons s^{-1} of synchrotrons, up to 10^{14} photons/pulse at 125 nm (9.91 eV) can be obtained by using resonant mixing schemes and this should be sufficient for pulsed CMB experiments. Of course, VUV lasers cannot match the broad tunability of a synchrotron source.

However, a shortcoming with the VUV photoionization approach is that absolute PI cross-sections are very often not known, and therefore branching ratios cannot be estimated. As matter of fact, studies of photodissociation processes by *soft* PI using synchrotron light are usually accompanied by measurements carried out using classic (*hard*) EI ionization, where much data have to be taken at all possible fragment masses in order to estimate branching ratios.^{14–16,20}

Obviously, it would be desirable to perform product ionization by *soft* electron impact, that is by using electrons with low, tunable energy, a concept analogous to that of *soft* PI with tunable VUV photons. Besides offering similar advantages as *soft* PI with respect to the dissociative ionization problem, the *soft* EI ionization approach would give the bonus of the possibility of determining branching ratios, since EI absolute ionization cross-sections are often known or can be reliably estimated.^{20,30} Unfortunately, this approach has never been applied (nor envisaged) in CMB experiments, prior to our recent work,^{31–34} mainly for sensitivity reasons. In fact, it implies that the energy of the ionizing electrons should be varied down to low values, and it is well known that ionization cross-sections decrease dramatically towards threshold, leaving no sufficient signal for carrying out product angular and velocity distribution measurements in CMB experiments.

Very recently, however, in our laboratory we have implemented successfully the method of *soft* EI ionization for product detection in CMB reactive

scattering experiments. In this chapter, we will outline the application of this simple and, yet, very powerful method. It will be shown how this simple approach, well known to mass spectroscopists, permits one to achieve practically “universality” of detection in CMB experiments, thus permitting the identification of all primary reaction products of multichannel, polyatomic elementary reactions, the determination of their branching ratios, and the characterization of the reaction dynamics for each single channel. These goals have represented one of the most important “holy grails” in the field of reaction dynamics since the introduction of the technique, more than 35 years ago. Some reactions between ground state oxygen atoms, $O(^3P)$, and carbon atoms, $C(^3P)$, with unsaturated hydrocarbons (acetylene and ethylene), of great relevance in combustion- and astro-chemistry, will be used as examples to illustrate the capability and the power of the *soft* EI ionization method, undoubtedly an attractive alternative to the use of PI by synchrotron radiation.

2. Experimental Considerations

The principles and the outcome of CMB reactive scattering experiments with mass spectrometric detection and TOF analysis have been discussed at length in reviews and book chapters.^{1,11} Briefly, in a typical experiment, beams of atoms/radicals and molecules with known, narrow, angular and velocity distributions are crossed, typically at 90° , in a large vacuum chamber kept at 10^{-6} – 10^{-7} mbar and the total angular distribution as well as TOF spectra of all reaction products are recorded as a function of laboratory recoil angle for single and well-defined collision events, using the rotatable mass spectrometer detector and pseudo-random TOF system. Such a detector is usually composed of an ionizer, a quadrupole or magnetic sector mass filter, and an ion counting device, such as a secondary electron multiplier^{23,35} or a Daly detector.^{9,36}

The measurements are carried out in the laboratory (lab) system of coordinates, but for the physical interpretation of the scattering process it is necessary to transform the data (angular, $N(\Theta)$, and velocity, $N(\Theta, v)$ distributions) to a coordinate system which moves with the center-of-mass (CM) of the collision partners.¹¹ This transformation is fairly straightforward, and the relation between lab and CM fluxes is given by $I_{\text{lab}}(\Theta, v) = I_{\text{CM}}(\theta, u)v^2/u^2$, (where Θ and v are lab angle and velocity, respectively, and θ and u are the corresponding CM quantities), i.e. the scattering intensity observed in the laboratory is distorted by the transformation Jacobian v^2/u^2 from that in the CM system. The velocity vector (so called “Newton”)

diagram, which illustrates the nature of the lab–CM transformation, is generally used for interpreting and discussing scattering results.^{11,35} Because of the finite resolution of experimental conditions, i.e. finite angular and velocity spread of the reactant beams and finite angular resolution of the detector, the lab–CM transformation is not single-valued. Therefore, analysis of the laboratory data is usually carried out by forward convolution procedures, over the experimental conditions, of trial CM distributions (i.e. CM angular and velocity distributions are assumed, averaged and transformed to the laboratory frame for comparison with the observed data). The final outcome of a reactive scattering experiment is often the generation of velocity flux contour maps of the reaction products, i.e. the plot of intensity as a function of angle and velocity in the CM system, $I_{\text{CM}}(\theta, u)$. The product contour map can be regarded as an *image* of the reaction in angle-velocity space.

2.1. “Hard” *Electron-Impact Ionization*

The typical detection method in CMB instruments is by *hard* EI ionization with electrons having energies in the range 60–200 eV,^{9,23,35,36} which correspond to the maximum of the ionization cross-section for most molecular species. Electron-impact mass spectrometry provides “universal” detection and is also extremely sensitive: a product flux smaller than 10^4 molecules $\text{cm}^{-2}\text{s}^{-1}$ (0.1 molecule cm^{-3} at a velocity of 10^5 cm s^{-1}) can be detected, provided the background is maintained sufficiently low. It is usually said that the detection efficiency of the CMB method is limited by (a) the low ionization efficiency ($<10^{-4}$) and (b) the high background in the ultra-high-vacuum (UHV) detection region, determined by the hot filament used in EI sources, of many species, and some of these may be of interest. While little can be done about problem (a), because of the limited residence time of travelling molecules within the ionization detector region (number density detector), the S/N (signal-to-noise) limitations due to point (b) can be, to some extent, overcome by reducing the overall detector background, especially at some particular masses. Indeed, modern UHV technology based on hydrocarbon-free, magnetically-suspended turbomolecular pumps and close-circuit Helium-refrigerators capable of cooling cryo-panels to temperatures ≤ 6 K, can be used to significantly lower the overall background in the detector to values $\leq 10^{-12}$ mbar. As an example, a new CMB apparatus has been recently constructed in Taiwan with an improved detection efficiency, obtained as described above and by further enhancing it with the use of larger diameter rods of the

quadrupole mass filter to increase ion transmission.³⁶ With this apparatus, exploiting isotopically-labelled ^{18}O atoms, the dynamics of a series of multichannel reactions of electronically-excited oxygen atoms, $\text{O}(^1\text{D})$, with saturated hydrocarbons (CH_4 , C_2H_6 , C_3H_8 , $c\text{-C}_3\text{H}_6$)^{37–40} and other molecules (NH_3 , CH_3F , SiH_4)^{41–43} have been characterized in detail.

Electron-impact ionization remains, however, plagued by the problem of the dissociative ionization of the neutral reaction products when using 60–200 eV electrons in the ionization source of the mass spectrometer. Actually, dissociative ionization of also parent beam species (or impurities) and of residual background gases may also greatly complicate the identification of reaction products, because of strong elastic scattering signals overlapping in mass and time with the reactive signal of interest and of high background at the product mass, respectively.

2.2. “Soft” Photoionization by Synchrotron Radiation

As mentioned in the Introduction, all the disadvantages of *hard* EI ionization can be overcome by using *soft* PI with tunable synchrotron radiation.^{13,14} In fact, dissociative ionization can be avoided by tuning the radiation below the dissociative ionization potential of a molecule or radical, and so detection of a species of mass m at the parent m/e mass ratio is possible. The residual background at critical masses can be kept to a minimum because of the negligible amount of heat generated. The current third generation synchrotron sources, able to provide 10^{16} photons s^{-1} , allow a satisfactory detection efficiency for single photon ionization, comparable to that of EI ionization.^{13,14} Although, as remarked in the Introduction, *soft* PI has been mainly exploited in photodissociation experiments, it is analogously suitable for reactive scattering experiments, despite the fact that reactive signals are much smaller than photodissociation signals. However, a serious shortcoming, besides the fact that a dedicated CMB machine and a synchrotron source are needed, is the difficulty, both in photodissociation and reactive scattering, of deriving branching ratios between competing channels, because absolute PI cross-sections are often not known.^{14–16,20}

2.3. “Soft” Electron-Impact Ionization by Low-Energy Electrons

It would be advantageous to be able to lower the electron energy in the electron impact source of CMB instruments sufficiently to reduce strongly, or even eliminate, the problem of dissociative ionization from interfering

species, either reactants, products, or background gases, while still leaving enough intensity to readily carry our product angular and velocity distribution measurements.

In our laboratory we have recently implemented this detection method, that we call *soft* EI ionization.^{31–34} It is analogous to *soft* PI by synchrotron radiation, but has the bonus that one can also derive branching ratios, a very important piece of information when studying multichannel reactions, and this affords an attractive alternative to the use of PI by a synchrotron source.

In applying the method of *soft* EI ionization using tunable, low-energy electrons, in order to attain a good S/N in a reasonable counting time, it was first mandatory to increase the sensitivity of our classic CMB instrument. This was achieved (a) by lowering the inherent detector background as much as possible, and (b) by increasing the number density of the reactants at the collision region. The first goal was reached to a satisfactory extent by the use of all magnetically-suspended turbomolecular pumps in the triply differentially pumped detector regions, in addition to the usual liquid nitrogen cooling of the second and third (containing the ionizer) detector chambers. Further gain is expected in the near future with the installation in the ionizer region of a powerful 6 K He close-circuit refrigerator and with the use of a thoriated iridium filament, rather than a tungsten filament, which will require only about one half of the power to produce the same electron emission current. The second goal was achieved by simply moving closer to the collision region the two reactant beam sources, which permitted the gain of more than a factor of 20 in signal intensity with respect to the original configuration characterized by two doubly differentially pumped beam sources.^{35,44,45} In the new arrangement, depicted in Fig. 1, the differential pumping chambers of the two beam sources have been removed, while still maintaining the presence of a defining slit, located in the main chamber, after the skimmer on each beam source, in order to control the beam sizes and their angular divergence. We exploit the high pumping speed of the main chamber (more than 6.000 l s^{-1} for air, and more than 18.000 l s^{-1} for condensable species) to maintain a base pressure of about $1\text{--}2 \times 10^{-6}$ mbar under operating conditions with two continuous beams. In addition, a cryo-panel, attached to a close-circuit He refrigerator, with two holes slightly larger than the beam defining slits, surrounds the collision region, so that the detector sees most of the time a 20 K cold surface, which is able to pump effectively molecules that otherwise would fly straight through all the detector slits until the ionizer, upon favorable geometrical reflections.

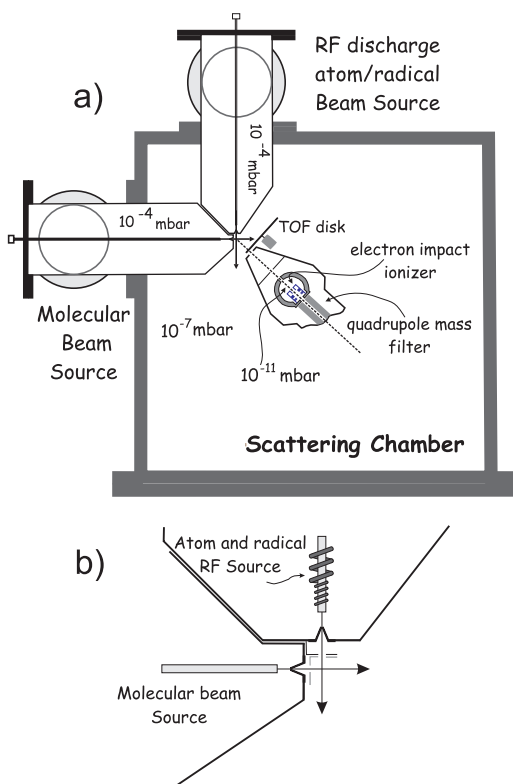


Fig. 1. (a) New setup of Perugia “classic” crossed molecular beam instrument with fixed, singly differentially pumped beam sources at 90° and rotating TOF mass spectrometer detector. (b) Enlargement of the beam source fronts with skimmers and defining slits.

A further gain in sensitivity (by about another factor of three) will still be possible in the future by installing a larger quadrupole mass filter (see, for instance, Refs. 37–40).

The S/N attainable with the above setup is often enhanced by the dramatic reduction in background that one often achieves when reducing the electron energy (see below). In fact, the use of ionizing electrons with tunable energy permits one to also obviate, at least in some cases, the usual problem connected with the hot filament used in EI sources, whereby the background partial pressure of many species in the detector chamber are significantly high, and some of these maybe of interest. In particular, the masses (H , H_2 , CH_4 , H_2O , CO , CO_2) that are usually at an inherently

high background level when using 60–200 eV electrons because of the out-gassing of the heated metal surfaces of the ionizer and of the universality of EI ionization, may constitute a serious limitation for product detection at that mass. However, by tuning, for instance, the electron energy below 14.0 eV (the IE of CO), one can reduce the background at $m/e = 28$ practically to zero, and therefore be able to detect a possible ethylene (C_2H_4) product (IE = 10.5 eV) with essentially zero background. The only problems that in principle cannot be eliminated using electrons, with respect to photons, are those connected with space-charge effects which limit the time and energy resolution of an electron-impact source. But this is not a serious limitation in many practical cases. For instance, the TOF resolution is mainly limited by the reactant beam velocity distributions, which are usually of the order of 10–30%, and not by the finite length of the ionizer (typically 10 mm) over typical flight lengths of 250 mm (ensuing $\Delta l/l$, and then $\Delta t/t$ resolution of 4%).¹ Furthermore, although the energy spread of the electrons is that connected with a hot tungsten filament at about 2000 K (about 0.7–1 eV, against a typical $\Delta E/E$ bandwidth of 2.5–3% for synchrotron radiation^{13,14}), which does not permit one to be selective with species having very similar ionization energies, yet, the tunability of the electron energy can still add, analogously to PI, selectivity in addition to universality provided the ionization energies of two isomer products differ by more than 1–2 eV. It should be noted, however, that the identification of a given species on the basis of its ionization energy remains very problematic with both EI ionization and PI because the products to be detected in photodissociation or reactive scattering studies usually have a large internal energy content which may red-shift significantly their IE.^{13,14}

Another noteworthy aspect of *soft* EI ionization is that the reduction of dissociative ionization of the species to be detected, which accompanies the lowering of the electron energy, often determines a significant gain back in the intensity of the parent ion. Finally, the *soft* EI ionization approach requires, with respect to *hard* EI ionization, a reduced effort in terms of data collection for determining branching ratios, since at low electron energies data at only a few m/e ratios need to be taken, because of the strongly reduced dissociative ionization pattern of the reaction product species (usually polyatomic radical products) at low electron energy.

2.4. Mass Spectra

We will first examine the effect of *soft* EI ionization on the mass spectra of the background (detector closed) and during an experiment (detector open

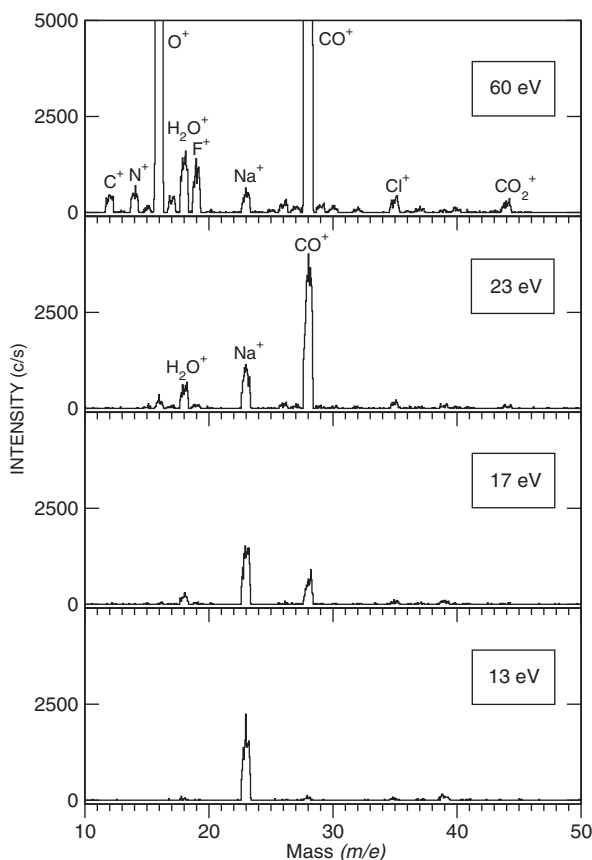


Fig. 2. Detector background mass spectra at an electron energy of 60, 23, 17, and 13 eV (see text).

and beams on). Figure 2 shows the detector background mass spectrum at different energies of the ionizing electrons: 60 eV, 23 eV, 17 eV, and 13 eV (all the other parameters being the same: emission current typically 1–2 mA, extraction voltage, ion energy, lens voltages, and electron multiplier voltage). At 60 eV, the most intense background peaks (besides $m/e = 2$ corresponding to H_2 , which fall outside the mass range shown) are due to residual CO, H_2O , and CO_2 . Note that the intense peak at $m/e = 16$ is not due to methane (in fact $m/e = 15$ is very low), but to dissociative ionization of CO, H_2O , O_2 and CO_2 to O^+ . Analogously, the $m/e = 12$ peak is due to dissociative ionization of CO and CO_2 to C^+ , and the $m/e = 14$ peak to dissociative ionization of residual N_2 to N^+ . Note the peaks due to halogen (F, Cl) and alkali (Na) atoms contained in the stainless steel of the

ionizer. By lowering the electron energy to 23 eV, the dissociative ionization processes leading to C^+ ($m/e = 12$), to N^+ ($m/e = 14$), and O^+ ($m/e = 16$), have been nearly suppressed, the main remaining peaks being those of CO, H_2O , and Na. At 17 eV (see also Fig. 3(a)), the latter are practically the only discernable peaks, with traces of Cl^+ ($m/e = 35$) and K^+ ($m/e = 39$); note the absence of $m/e = 17$, being the dissociative ionization of water to OH^+ (appearance energy, AE = 18.1 eV) suppressed. Finally, at 13 eV

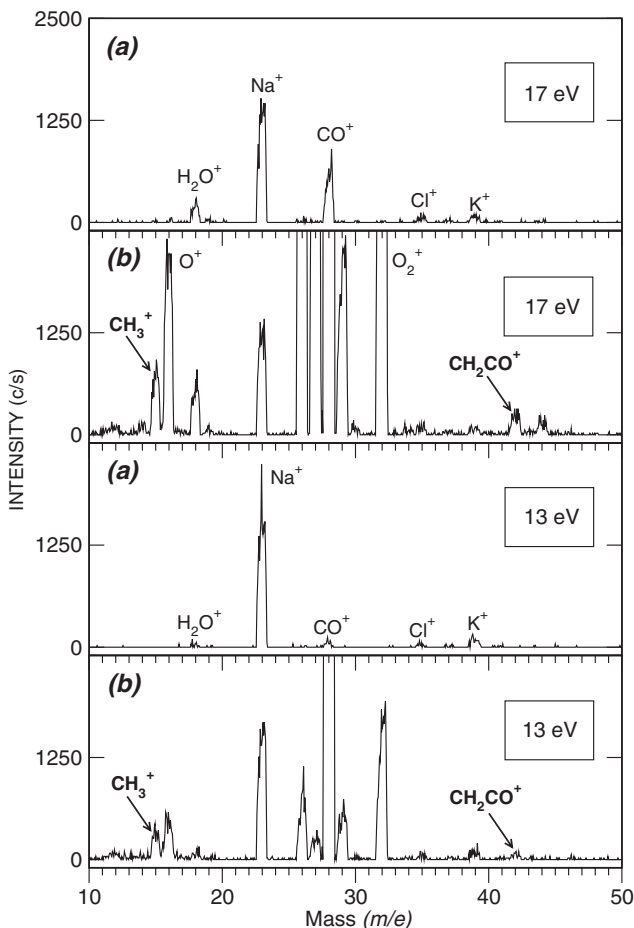


Fig. 3. (a) Enlargement of the spectra at 17 and 13 eV electron energy shown in Fig. 2 (detector closed). (b) Mass spectra during the experiment $\text{O}(^3\text{P}) + \text{C}_2\text{H}_4$ at the lab angle of 30° (detector open) with an electron energy of 17 and 13 eV (see text).

(see also Fig. 3(a)), the main peak is due to Na^+ , followed by K^+ (much smaller); at this energy, CO is nearly zero, being the IE of CO 14.0 eV. Of course, the parent peaks at $m/e = 18$ (H_2O) and $m/e = 28$ (CO) are quite small at 17 eV because the ionization cross-sections are quite small for those species at that energy, so, one may wonder if there is sensitivity left for carrying out product detection in CMB reactive scattering experiments.

Shown in Fig. 3(b) are the corresponding mass spectra at 17 eV during an experiment, namely the study of the $\text{O} + \text{C}_2\text{H}_4$ reaction at a collision energy of $12.9 \text{ kcal mol}^{-1}$ (see Sec. 3.2), at a laboratory angle of 30° (close to the center-of-mass angle). The following features can be noted: strong peaks at $m/e = 16$ (due to the elastically/inelastically-scattered atomic oxygen beam), at $m/e = 32$ (due to the elastically/inelastically-scattered undissociated O_2 contained in the oxygen beam), and at $m/e = 28$ (due to the elastically/inelastically-scattered C_2H_4 beam) (the peaks at $m/e = 27$ and 26 are due to dissociative ionization of C_2H_4 to C_2H_3^+ and C_2H_2^+ , and that at $m/e = 29$ to $^{13}\text{C}_2\text{H}_4^+$). The peaks at $m/e = 18$ and $m/e = 44$ are due to residual H_2O and CO_2 in the main chamber effusing into the detector when the detector gate valve is open for scattering measurements. There is, of course, also a strong peak at $m/e = 4$ (outside of the mass range shown in Fig. 3) due to elastically-scattered helium, which is the seeding gas in the atomic oxygen beam. Besides all the above peaks, mainly connected with the two reactant beams, one can notice strong peaks at $m/e = 15$ (CH_3^+) and $m/e = 42$ (CH_2CO^+) which arise from reactive scattering signals; notice also the small peak at $m/e = 14$ (CH_2^+) and the absence of a peak at $m/e = 43$ (CH_2CHO^+) (see Sec. 3.2). By tuning the quadrupole mass filter on these masses it is possible to readily measure product angular and TOF distributions. Peaks due to reactive scattering signals at $m/e = 15$ and 42 are still visible when using 13 eV electron energy (see Fig. 3(b)).

2.5. *Measurements of Product Angular and TOF Distributions*

Measurements of product angular and TOF distributions using *soft* EI ionization will be discussed with reference to some multichannel reactions of $\text{O}(^3\text{P})$ and $\text{C}(^3\text{P})$ with unsaturated hydrocarbons (see Secs. 3 and 4).

2.6. *Electron-Impact Efficiency Curves*

We now briefly discuss the new capability gained by using a variable energy electron beam source, that of measuring the EI efficiency curves of reactants

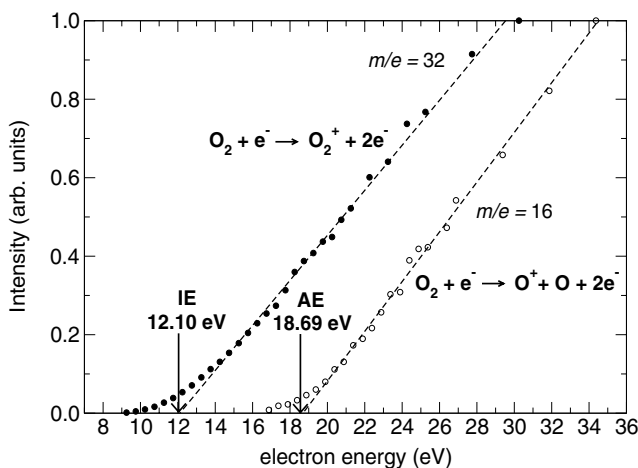


Fig. 4. Electron-impact efficiency curves at $m/e = 32$ and $m/e = 16$ for a supersonic beam of O_2 . Arrows indicate the literature values⁷² of the ionization energy of O_2 and of the appearance energy of O^+ .

and also products down to their thresholds. One important aspect is to know the absolute electron energy scale. This has been calibrated by using beams of pure rare gases (He, Ne, Ar) and of O_2 to cover an energy range from about 12 to 25 eV (see, for instance, Fig. 4). The energy scale has been obtained by assuming the threshold for ionization to be given by a simple straight-line extrapolation. This is only an approximation. A more accurate analysis in terms of Wannier's law^{46,47} is currently under way in collaboration with the group of Märk at Innsbruck. Figure 4 shows the EI efficiency curve for an O_2 beam at $m/e = 32$ and 16: the results clearly indicate that it would be possible to detect O atoms (for instance in an elastic scattering experiments of O with a rare gas, where the O atoms are produced from partial dissociation of O_2 in a radio-frequency discharge source^{35,45,48}) with no interference from dissociative ionization of residual O_2 in the beam (and also in the detector) by simply setting the electron energy at a value ≤ 18 eV.

Figure 5 shows the EI efficiency curve of the signal at $m/e = 41$, 14, and 13 from the reaction $\text{O}(^3\text{P}) + \text{C}_2\text{H}_2$ at an angle close to the center-of-mass angle and for $E_c = 9.5 \text{ kcal mol}^{-1}$ (see Sec. 3.1). The threshold of 11.2 eV derived for $m/e = 41$ (corresponding to the HCCO product) by straight-line extrapolation will not change, within an uncertainty of ± 0.2 eV, from the threshold derived when using Wannier's law. Interestingly, from these

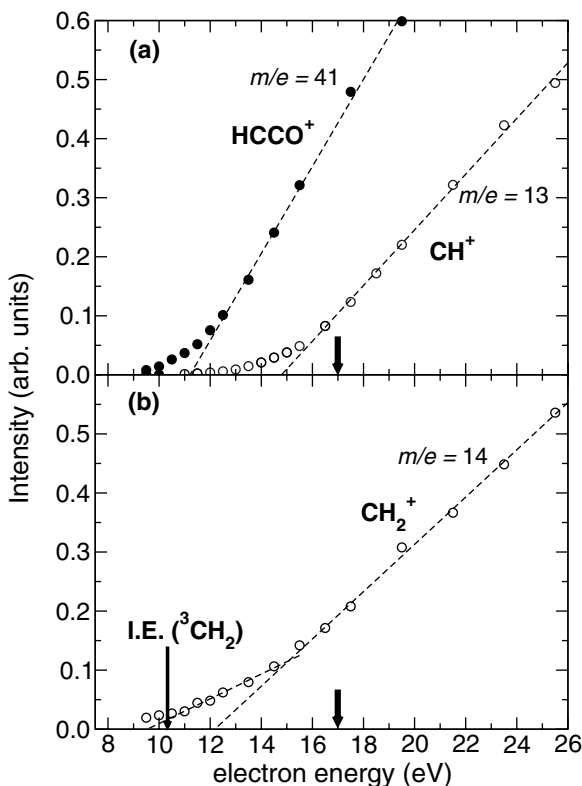


Fig. 5. Electron-impact efficiency curves at (a) $m/e = 41$ and $m/e = 13$, and (b) $m/e = 14$, recorded at a lab angle of 30° during the CMB study of the reaction $\text{O}(^3\text{P}) + \text{C}_2\text{H}_2$ at $E_c = 12.6 \text{ kcal mol}^{-1}$. The thick arrow marks the electron energy (17 eV) used for product angular and TOF distribution measurements. In (b) the thin arrow marks the literature value⁵⁰ of the IE of triplet methylene (see text).

measurements it is possible to obtain information on the ionization energy of a radical species, such as the ketyl radical, one of the main products of the $\text{O}(^3\text{P}) + \text{C}_2\text{H}_2$ reaction (see Sec. 3.1), with a well-defined internal energy content. Notably, no previous direct experimental information existed on the IE of the ketyl (HCCO) radical.⁴⁹

Looking at the signal at $m/e = 14$ (Fig. 5(b)), which corresponds to the methylene radical produced in the same reaction, we notice that its threshold is at around 9.5 eV, which is somewhat red-shifted with respect to the adiabatic IE of triplet CH_2 (IE = 10.386 eV).⁵⁰ This is not surprising since the CH_2 radical product is internally hot, but it could also

be that some singlet methylene is actually being formed from the reaction $\text{O}(^3\text{P}) + \text{C}_2\text{H}_2$. It can be noted that at around 15 eV the EI efficiency curve becomes steeper; this is due to the onset of the contribution from $^{13}\text{CH}^+$ coming from dissociative ionization of the dominant reaction product HCCO (see Fig. 5(a)) and also of the elastically-scattered C_2H_2 reagent beam.

2.7. CMB Experiments with Variable Beam Crossing Angle

The relative collision energy in a CMB experiment is given by $E_c = \frac{1}{2}\mu v_r^2$, where μ is the reduced mass of the system and v_r is the relative velocity. In general

$$v_r^2 = v_1^2 + v_2^2 - 2v_1v_2 \cos \gamma$$

where v_1 and v_2 are the two reactant beam velocities in the lab frame and γ the beam crossing angle.^{12,51,52} All “universal” CMB instruments built to date feature a 90° crossing geometry for the two molecular beams; in this case $v_r^2 = v_1^2 + v_2^2$. Usually, in order to increase the collision energy one increases the velocity of one or both beams, and this leads to a loss in angular and velocity resolution, because the CM velocity increases as well and consequently the Newton circle within which the product is confined to be scattered on the basis of energy and linear momentum conservation, moves away from the CM and consequently (a) the product velocities become larger (to which correspond TOF spectra distributed over a smaller number of channels) and (b) the product angular distribution is distributed over a narrower lab angular range.

One can, however, increase the collision energy by crossing the reactant beams at an angle larger than 90° ; this arrangement will give the simultaneous extra bonus of also an increased angular and velocity resolution. In fact, it can be readily shown that the CM velocity decreases with increasing crossing angle γ according to the relation:

$$v_{\text{CM}} = \left(\frac{1}{m_A m_{\text{BC}}} \right) [(m_A v_A)^2 + (m_{\text{BC}} v_{\text{BC}})^2 + 2m_A v_A m_{\text{BC}} v_{\text{BC}} \cos \gamma]^{1/2}$$

where v_{CM} is the center-of-mass velocity, v_A and v_{BC} the beam reactant velocities, and m_A and m_{BC} the reactant masses. This dependence is shown graphically in Fig. 6 for the case of the $\text{O}(^3\text{P}) + \text{C}_2\text{H}_2$ system with the indicated beam velocities; there, the corresponding Newton diagrams for $\gamma = 45^\circ$, 90° , and 135° with the maximum Newton circles for HCCO

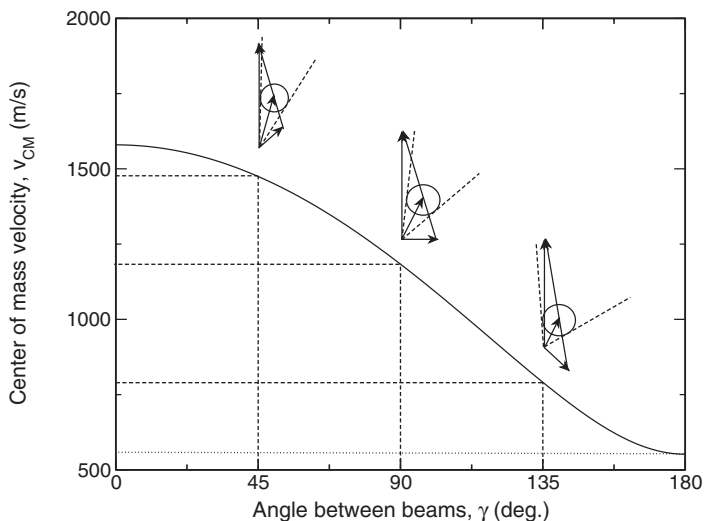


Fig. 6. Variation of the center-of-mass velocity with beam crossing angle, γ , for the reaction $\text{O}(^3\text{P}) + \text{C}_2\text{H}_2$ with the $\text{O}(^3\text{P})$ and C_2H_2 beam velocities of 2798 m s^{-1} and 827 m s^{-1} , respectively. The Newton diagrams for $\gamma = 45^\circ$, 90° , and 135° are shown (see text).

formation are also depicted. For instance, because of the lower CM velocity and the higher collision energy resulting from $\gamma = 135^\circ$, the Newton circle within which the products are energetically confined will consequently move closer to the lab velocity origin and become larger, that is, the product angular distribution in the lab frame will extend over a broader angular range and the product TOF distributions will be slower and extend over a larger number of channels (see Sec. 3.1.2).

Recently, we have built a new beam source for the molecular species which allows us to cross the two beams in our CMB apparatus either at $\gamma = 135^\circ$ or $\gamma = 45^\circ$ (by a simple rotation of 180° of the terminal part of the source). Figure 7 depicts the new arrangement. In Sec. 3.1.2 we will discuss the advantages obtained for the $\text{O}(^3\text{P}) + \text{C}_2\text{H}_2$ reaction when using $\gamma = 135^\circ$ with respect to $\gamma = 90^\circ$. The 45° arrangement is instead intended for reaching very low collision energies, which is of interest when studying barrierless reactions, as those of $\text{C}(^3\text{P})$ with unsaturated hydrocarbons (see Sec. 4).^{12,52} In this case, however, one loses angular and velocity resolution with respect to $\gamma = 90^\circ$, as can be inferred from the corresponding Newton diagram in Fig. 6.

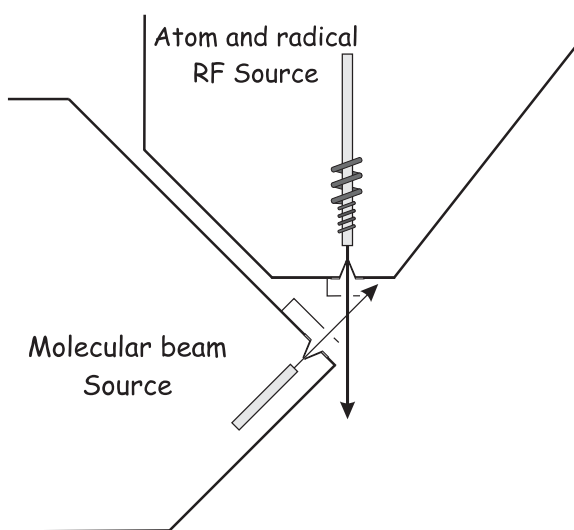


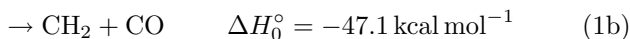
Fig. 7. CMB setup with beam intersection angle of $\gamma = 135^\circ$.

3. Examples: $O(^3P) + \text{Unsaturated Hydrocarbons}$

We will now discuss some very recent applications of the *soft* EI ionization method for product detection in CMB experiments. We will first deal with two polyatomic reactions of ground state oxygen atoms with unsaturated hydrocarbons (acetylene and ethylene); these reactions are characterized by multiple reaction pathways and are of great relevance, besides being from a fundamental point of view, in combustion and atmospheric chemistry.

3.1. $O(^3P) + C_2H_2$

The reaction $O(^3P) + C_2H_2$ plays a key role not only in the combustion of acetylene itself,⁵³ but also in the overall mechanism for hydrocarbon combustion, since acetylene is an important intermediate in the combustion of methane, larger aliphatic hydrocarbons, and aromatics.^{54–57} There are two energetically-allowed channels:



Acetylene also plays an important role as intermediate in soot formation in flames, because the reverse of reaction (1a) forms singlet methylene,

$\text{CH}_2(^1\text{A}_1)$,⁵⁸ which in turn undergoes a fast reaction with C_2H_2 itself⁵⁹ to form propargyl, CH_2CCH , which by dimerization is responsible for the formation of the first aromatic ring (benzene),⁶⁰ and then of PAH's, made up ultimately of soot.⁶¹ Reaction (1) is also thought to be responsible for the "prompt" CO_2 formation in acetylene flames via the reaction $\text{HCCO} + \text{O}_2$.⁶² For the theoretical modelling of combustion systems it is very important to know accurately the branching ratio of reaction (1).

Because of its paramount practical relevance, the reaction has been studied very extensively from the kinetic standpoint using a variety of experimental techniques,⁶³ starting from the 1960s.⁶⁴ While its overall rate constant has been well established, the question of the identity of the primary reaction products and their relative importance has been a subject of considerable controversy over the years (see Ref. 65 for a critical survey until 1989). The most recent, accurate kinetic determinations at room temperature have given $k(1a)/[k(1a) + k(1b)] = 0.83 \pm 0.08$ ^{66,67} and $k(1b)/[k(1a) + k(1b)] = 0.17 \pm 0.08$,⁶⁶ in good agreement with theoretical predictions based on *ab initio* calculations of the triplet potential energy surface and RRKM computations.⁶⁸ Both experiment and theory indicate that the branching ratio is essentially temperature independent,^{68–70} because the barrier to H-loss and to isomerization of the initial triplet HCCHO diradical to triplet ketene, which will give $\text{CH}_2 + \text{CO}$ by C–C bond cleavage, are both well below the reactant asymptote.

There have been two previous CMB studies^{65,71} of this reaction, both conducted at a collision energy of about 6 kcal mol^{-1} , but the reaction dynamics derived from the laboratory data, which were of limited resolution, did not fully agree. Specifically, Clemon *et al.*⁷¹ derived for the HCCO channel a CM angular distribution significantly sideways-peaked with slightly more intensity in the backward direction (with respect to the direction of the O beam) and a product translational energy distribution peaked at very high energy and ending abruptly at the limit of energy conservation. In contrast, for the same channel Schmoltner *et al.*⁶⁵ derived a CM angular distribution backward-forward symmetric with some degree of polarization (the intensity at $\theta = 90^\circ$ being 0.75 of that at 0° and 180°) and a product translational energy distribution peaking at 10 kcal mol^{-1} and dying off at the limit of energy conservation, with a shape significantly different from that of the previous study.

The only previous estimate of the branching ratio under truly single-collision conditions is that carried out in one of these CMB studies: Schmoltner *et al.*⁶⁵ used a beam of ^{18}O in order to be able to detect, in

addition to HCCO, also ^{18}CO at $m/e = 30$. A branching ratio of cross-sections $\sigma(1a)/[\sigma(1a)+\sigma(1b)] = 0.58 \pm 0.21$ was derived, which is somewhat lower than the value obtained from kinetic studies.^{66,67,70}

In the light of the importance of this reactive system, once we (a) increased the sensitivity of the apparatus, (b) improved the resolution with which to measure product angular and TOF distributions, especially using a beam crossing angle of 135° , and (c) developed the ability to also detect the CH_2 radical from this reaction by using *soft* EI ionization, we thought that it would have been useful and interesting to explore further the reaction dynamics and the branching ratio under single-collision conditions. Here we discuss some of the results obtained in very recent CMB studies.³³

3.1.1. *Product Angular and TOF Distributions Using “Soft” EI Ionization*

In the study of the reaction $\text{O}(^3\text{P}) + \text{C}_2\text{H}_2$ with the CMB technique it is very easy to detect the heavy HCCO (ketenyl) fragment corresponding to the $\text{HCCO} + \text{H}$ channel, because HCCO is kinematically constrained in a narrow angular region around the center-of-mass. The detection of any of the two products from the $\text{CH}_2 + \text{CO}$ forming channel is much more problematic. In particular, detection of CO is plagued by the high inherent detector background at $m/e = 28$ due to residual CO in any UHV chamber. To overcome this difficulty, after a first CMB study⁷¹ in which only the $\text{HCCO} + \text{H}$ channel could be detected, Lee and co-workers⁶⁵ used a beam of isotopically labelled ^{18}O in order to be able to detect the CO product as C^{18}O^+ at $m/e = 30$, which is a much cleaner mass than $m/e = 28$. Still, this could not avoid the fact that at $m/e = 30$ dissociative ionization of HCC^{18}O also contributes; in fact, the TOF spectra at $m/e = 30$ were exhibiting two peaks corresponding to the two possible reaction channels (1a) and (1b), $\text{H} + \text{HCCO}$ and $\text{CH}_2 + \text{CO}$. Because of this, it was not possible to measure directly the angular distribution of the CO product in the usual way that is possible in CMB experiments with continuous beams: that is, by modulating one of the two beams for background subtraction. Information on the laboratory angular distribution of the CO product could only be inferred from integration of a few TOF spectra at $m/e = 30$, which led to considerable uncertainty in the estimate of the branching ratio between the two competing channels (see above).

Detection of the CH_2 counter-fragment at $m/e = 14$ is also problematic in classic CMB experiments employing *hard* EI ionization, because of the

high inherent background at this mass (though lower than at $m/e = 28$) due to dissociative ionization of residual CH_4 to CH_2^+ , of residual N_2 to N^+ , but especially due to the interference from the dissociative ionization to $^{13}\text{CH}^+$ of the intense HCCO product and of the elastically-scattered, intense C_2H_2 beam. Although ^{13}C represents only about 2% of the total C in HCCO and C_2H_2 , the $^{13}\text{CH}^+$ signal is comparable to the reactive scattering signal due to CH_2 product formation. For all these reasons, detection of CH_2 from reaction (1b) was never attempted in the past.

In our laboratory, after having reduced to a very low value the partial pressure of methane in the detector (and consequently its contribution to $m/e = 14$ via dissociative ionization), we were ready to also tackle all the other contributions to $m/e = 14$. To get rid of the contribution arising from dissociative ionization of residual N_2 it is sufficient to reduce the electron energy below the appearance energy (AE) of N^+ from N_2 , which is 24.3 eV.⁷² To eliminate the contribution from elastically-scattered C_2H_2 to $^{13}\text{CH}^+$ it would be sufficient to lower the electron energy below 20.9 eV which is the AE of CH^+ from C_2H_2 .⁷² Finally, to eliminate the contribution from dissociative ionization of HCCO it would be required to lower the electron energy below about 14 eV, on the basis of our measurements (see Fig. 5), but actually it is not necessary to go so low, because only a small fraction of CH^+ appears at $m/e = 14$, so that an electron energy of 17 eV is already sufficient. All this is exemplified in Fig. 8, which shows the TOF spectra recorded at $m/e = 14$ at the lab angle of 30° from the reaction $\text{O}(^3\text{P}) + \text{C}_2\text{H}_2$ using three different electron energies: 60, 23 and 17 eV. As can be seen, at 60 eV the TOF spectrum exhibits a fast peak due to the CH_2 product and a large, slow peak arising from contribution from dissociative ionization of HCCO and C_2H_2 , the latter also influencing the fast peak of the CH_2 product. At 23 eV, practically all the C_2H_2 contribution has been suppressed, with the slow peak essentially due only to dissociative ionization of HCCO and with the fast peak due to CH_2 more clearly emerging. Finally, at 17 eV the HCCO contribution is also suppressed. This clearly indicates that operating at 17 eV electron energy it is possible to measure in a clean way the angular distribution of the CH_2 product from the $\text{CH}_2 + \text{CO}$ channel by modulating the acetylene beam at 160 Hz for background subtraction. The resulting CH_2 angular distribution is shown in Fig. 9, together with that of the HCCO product for an $E_c = 9.5$ kcal/mol. Figure 10 shows the TOF spectra of HCCO ($m/e = 41$) and CH_2 ($m/e = 14$) radical products at the angle $\Theta = 22^\circ$. As can be seen the heavy HCCO product, left by the very light H counterpart, is confined

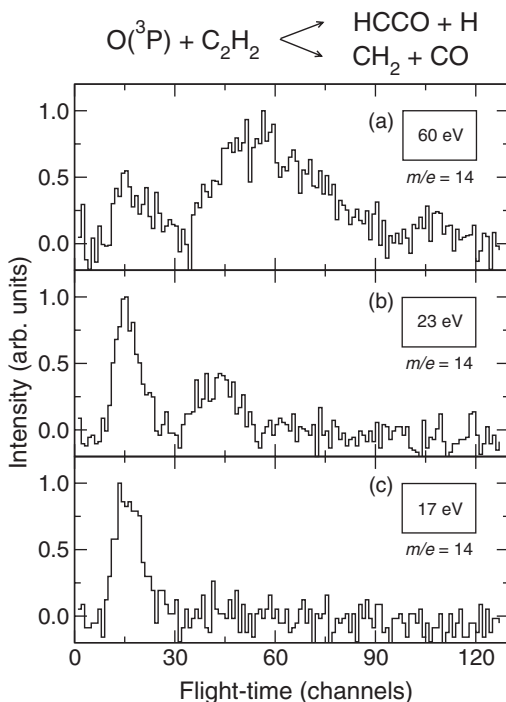


Fig. 8. $m/e = 14$ pseudo-random TOF spectra at the lab angle of 30° during the CMB study of the reaction $\text{O}(^3\text{P}) + \text{C}_2\text{H}_2$ at $E_c = 9.5 \text{ kcal mol}^{-1}$ using an electron energy of (a) 60 eV, (b) 23 eV, and (c) 17 eV. Accumulation time 900 s.

in a narrow angular range around the CM and is quite slow in the lab frame, while the light CH_2 product, left by the heavy CO counterfragment, has a very broad angular distribution and is very fast in the lab frame. Regarding signal intensities, at $m/e = 41$ (HCCO), S/N is about 600 in 50 s when using 60 eV electrons, and TOF spectra could be recorded using the single-shot method at $2 \mu\text{s/channel}$ with very small error bars in very short time (~ 15 min). With 17 eV electrons the fragmentation of HCCO is strongly reduced and this permits still $\text{S/N} \sim 200$ in 50 s. At $m/e = 14$ $\text{S/N} = 35$ in 100 s, and TOF spectra were recorded at $5 \mu\text{s/channel}$ using either the pseudo random or even the single-shot TOF method (the latter being possible because of the near absence of background at $m/e = 14$ when using 17 eV electrons). TOF spectra were measured at nine lab angles for HCCO and at eleven lab angles for CH_2 . From product angular and TOF distributions in the lab, product angular and translational energy

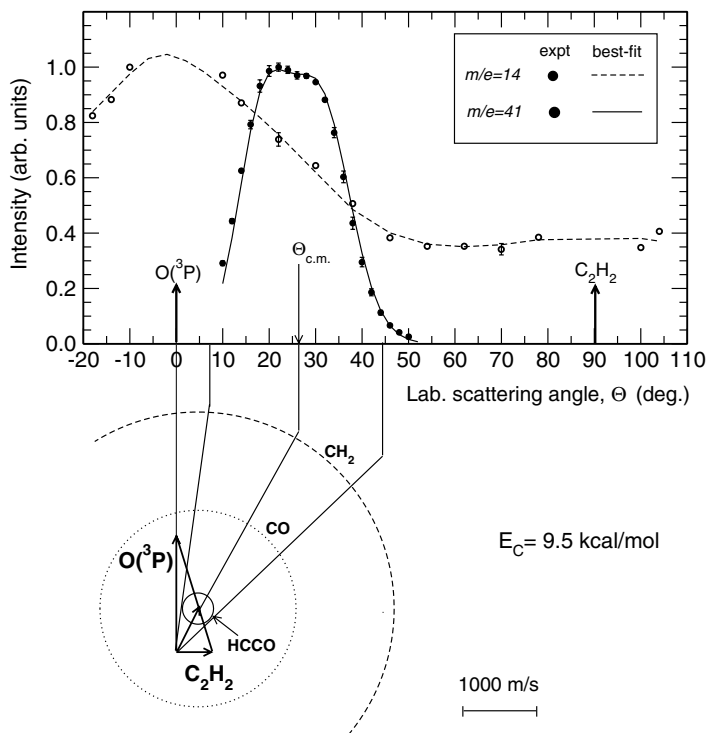


Fig. 9. HCCO and CH₂ product lab angular distributions from the O(³P) + C₂H₂ reaction at $E_c = 9.5 \text{ kcal mol}^{-1}$. Solid lines are best-fit curves obtained from the best-fit product angular and translational energy distributions (adapted from Ref. 33). The Newton diagram of the experiment is also shown; there the Newton circles delimit the maximum velocity that the indicated products can attain assuming that all the available energy is channelled into translation.

distributions in the center-of-mass were derived for both channels (1a) and (1b) with relatively small uncertainties, especially for the HCCO channel.³³ Indeed, these measurements permitted one to unravel some sideways scattering of the HCCO product in this system, which reflects the detailed geometry of the decomposing HCCHO transition state.³³ The sideways-scattered shape of the HCCO angular distribution in the CM is well depicted in Fig. 11, where the product flux (velocity-angle) contour map is reported.

More detailed information about the dynamics of ketylenyl formation was obtained at the higher E_c of $12.6 \text{ kcal mol}^{-1}$, which was reached by crossing the same reactant beams at 135° .

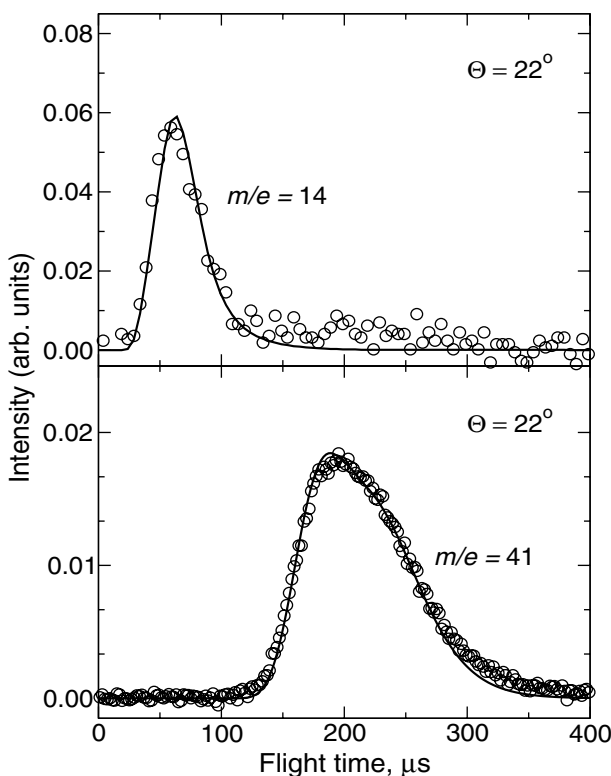


Fig. 10. Exemplary TOF spectra of HCCO ($m/e = 41$) and CH_2 ($m/e = 14$) products at the lab angle of 22° from the $\text{O}(^3\text{P}) + \text{C}_2\text{H}_2$ reaction at $E_c = 9.5 \text{ kcal mol}^{-1}$. Solid lines are best-fit curves obtained from the best-fit product angular and translational energy distributions (see Ref. 33).

3.1.2. Product Angular and TOF Distributions with Beam Crossing Angle $\gamma = 135^\circ$

Figure 12 compares the lab angular distribution and the TOF spectrum (at $\Theta = 22^\circ$) of the HCCO product from the $\text{O}(^3\text{P}) + \text{C}_2\text{H}_2$ reaction as obtained by crossing the two reactants, beams at a geometry of 90° and of 135° (the corresponding Newton diagrams are also shown). As the two beam velocities are the same in the two cases, E_c increases from 9.5 to 12.6 kcal/mol in going from $\gamma = 90^\circ$ to $\gamma = 135^\circ$. The higher angular and TOF resolution afforded by the $\gamma = 135^\circ$ arrangement, with respect to the 90° case, is clearly witnessed by the wider (i.e. extended over a much broader angular range) product angular distribution and by the slower and wider (i.e. extended

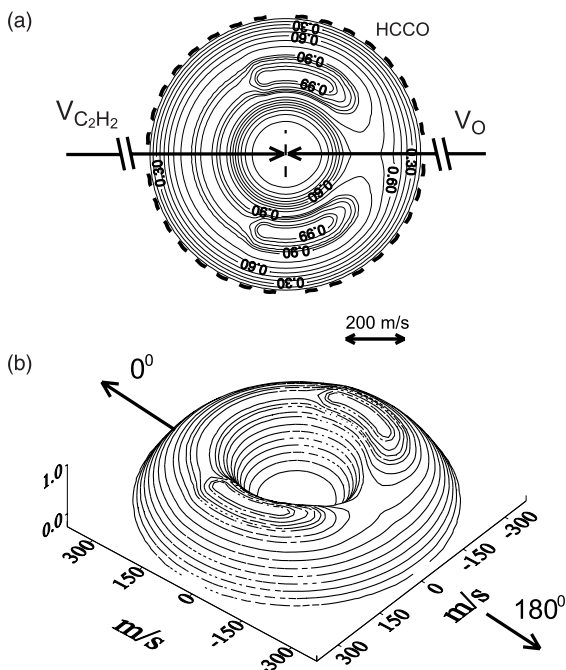


Fig. 11. HCCO product flux (velocity-angle) contour map from the $\text{O}(^3\text{P}) + \text{C}_2\text{H}_2$ reaction at $E_c = 9.5 \text{ kcal mol}^{-1}$ (a). 3D perspective (b).

over a much larger number of channels) TOF distribution, resulting as a consequence of a maximum Newton circle closer to the CM and a lower CM velocity (i.e. slower products in the lab frame) in the 135° case (see Newton diagrams in Fig. 12). As can be seen, some bimodal structure starts appearing in the TOF spectrum, corresponding to the fast and slow side (with respect to the CM velocity) of the product velocity distribution. In this particular case, the bimodality reflects a product translational energy distribution peaking well away from zero, which indicates that a large fraction of the total available energy is released as product recoil energy. Also the lab angular distribution for $\gamma = 135^\circ$ reveals more details around the CM angle than when $\gamma = 90^\circ$, and this contains more information about the shape of the angular distribution in the CM system.³³

3.1.3. CMB Determination of the Branching Ratios

Although the absolute beam intensities, the exact size of the collision volume, and the detection efficiency are not known in a CMB experiment, they

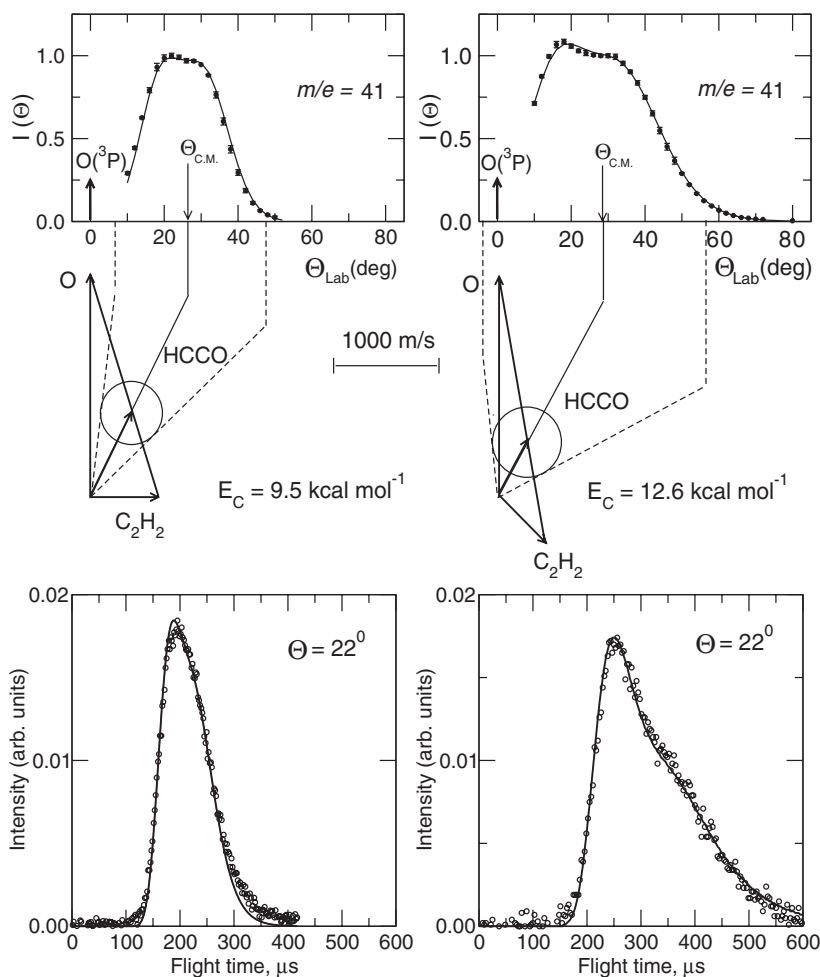


Fig. 12. Comparison of HCCO product lab angular distributions and TOF spectra at $\Theta = 22^\circ$ from the $\text{O}(^3\text{P}) + \text{C}_2\text{H}_2$ reaction for a beam crossing angle of $\gamma = 90^\circ$ ($E_c = 9.5 \text{ kcal mol}^{-1}$, setup of Fig. 1) and of $\gamma = 135^\circ$ ($E_c = 12.6 \text{ kcal mol}^{-1}$, setup of Fig. 7). The corresponding Newton diagrams are also shown. Note the higher angular and TOF resolution obtained when $\gamma = 135^\circ$, as witnessed by the wider HCCO lab angular distribution and slower (and wider) TOF spectrum.

are however constant, and this permits one to determine relative reaction cross-sections. We follow the procedure outlined by Schmoltner *et al.*⁶⁵ in which we exploit the advantages of using *soft* EI ionization. From the laboratory angular and velocity distributions of the reaction products and from

the fitting procedure one obtains the apparent total cross-sections for CH_2 and HCCO formation, $\sigma^0(\text{CH}_2)$ and $\sigma^0(\text{HCCO})$. By correcting the apparent cross-sections for the ionization cross-sections, fragmentation patterns and quadrupole mass filter transmission, one obtains the relative reaction cross-sections, $\sigma(\text{CH}_2)$ and $\sigma(\text{HCCO})$.

In order to estimate more accurately the ratio of CH_2 and HCCO signals, it is advantageous to measure TOF spectra at $m/e = 14$ not at 17 eV electron energy, where only the CH_2 channel contribution is present, but rather at a somewhat higher electron energy, such as 23 eV (see Fig. 13), at which the HCCO product still fragments significantly to CH^+ , giving a measurable contribution at $m/e = 14$ because of the natural abundance of ^{13}C . The ionization cross-sections at their maximum can be estimated according to the method of Fitch and Sauter,³⁰ which is based on the addition of atomic ionization cross-sections, and then scaled to the electron energy at which the TOF spectrum has been measured (23 eV) by

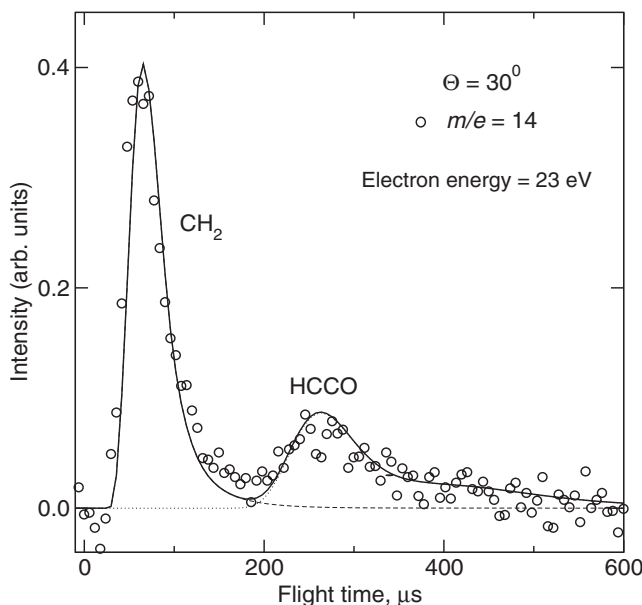
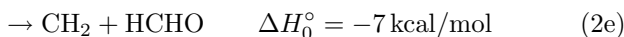
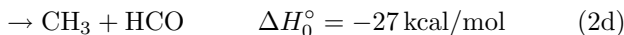
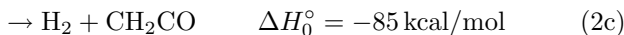
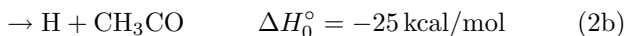


Fig. 13. $m/e = 14$ TOF spectrum at $\Theta = 30^\circ$ for the $\text{O}(^3\text{P}) + \text{C}_2\text{H}_2$ reaction ($E_c = 12.6 \text{ kcal mol}^{-1}$), obtained using an electron energy of 23 eV. Note the fast peak coming from the CH_2 forming channel and the slow peak coming from dissociative ionization of the HCCO product. Solid line is obtained from the best-fit product angular and translational energy distributions (see Ref. 33).

using the measured total ionization cross-section curve at $m/e = 14$. The quadrupole transmission can be calibrated with a known compound at 70 eV electron energy, measuring by TOF the relative intensity of the various fragments. With this procedure, we obtained³³ the following branching ratios at the $E_c = 12.6 \text{ kcal mol}^{-1}$, $\sigma(1a)/[\sigma(1a) + \sigma(1b)] = 0.81 \pm 0.15$ and $\sigma(1b)/[\sigma(1a) + \sigma(1b)] = 0.19 \pm 0.04$, which are in excellent agreement with the accurate kinetic determinations of Peeters *et al.*^{66,67} (see above). The present estimate of the branching ratio is thought to be more accurate than the previous CMB estimate (at $E_c = 6 \text{ kcal mol}^{-1}$)⁶⁵ because of the higher data quality, and consequently more accurate determination of the CM differential cross-sections for the two competing channels, and of the better determination of the fragmentation pattern of the HCCO product (at 23 eV electron energy HCCO fragments much less than at 200 eV, the value used in the previous study).

3.2. $\text{O}(^3\text{P}) + \text{C}_2\text{H}_4$

The reaction $\text{O}(^3\text{P}) + \text{C}_2\text{H}_4$ also plays a key role, besides in the combustion of ethylene itself,^{54,72,73} in the overall mechanism for hydrocarbon combustion.^{54,57,74,75} There are five exoergic channels:



Since the pioneering work of Cvetanović,⁷⁶ many research groups have investigated this reaction, employing a variety of experimental techniques under different conditions of pressure and temperature, identifying only some of the possible products, which has given rise to uncertainties and controversy.^{77–86} Some theoretical work has also been carried out on this reaction.^{87,88} While its overall rate constant has been well established,^{77,86} the question of the identity of the primary reaction products and their relative importance has been, and still is, a subject of considerable controversy. On the other hand, for modelling combustion systems, detailed knowledge of all primary reaction products, their rate coefficients, and their branching ratios are needed.

Of course, it would be desirable to investigate the reaction using a technique sensitive to all energetically possible product channels. The most

suitable, and perhaps the only technique is the CMB technique with mass spectrometric detection. Two different previous CMB studies^{71,89} of this reaction at $E_c \approx 6 \text{ kcal mol}^{-1}$ found evidence of only channel (1a), the easiest to detect for kinematics reasons, which confine the heavy CH_2CHO product in a narrow angular range around the center-of-mass. Channels (2c)–(2e) are much more difficult to detect due to unfavorable kinematics and to the fact that, for mass spectrometric detection, the expected ion signal from products of channel (2c) at $m/e = 42$, of channel (2d) at $m/e = 15$ or 29 (or 28), and of channel (2e) at $m/e = 14$ or 30, coincide with major background peaks and/or with peaks coming from dissociative ionization of the most intense signal corresponding to CH_2CHO formation and of the elastically-scattered ethylene reagent.

Only the problem connected with channel (2d) was partly overcome in a previous CMB study⁷⁸ by using a beam of isotopically labelled ^{18}O , which permitted one to detect the HC^{18}O product of channel (2d) at $m/e = 31$ (HC^{18}O^+) and 30 (C^{18}O^+), and to obtain an estimate of the branching ratio between channels (2a) and (2d) of 0.71 ± 0.26 , a value which is somewhat larger than any previous kinetic estimate, which gave values ranging from 0.44 to 0.55.^{81,85,86}

Channel (2b) is difficult to detect with the CMB technique because CH_3CO is an isomer of CH_2CHO and has therefore the same parent mass. The detection of channel (2c) requires high TOF resolution to be able to distinguish the $m/e = 42$ signal coming from ketene from the $\text{CH}_2\text{CO} + \text{H}_2$ channel and the $m/e = 42$ signal coming from dissociative ionization of vinoxy (CH_2CHO) from the $\text{CH}_2\text{CHO} + \text{H}$ channel. Finally, channel (2e) is very difficult to detect because it is kinematically very unfavorable and it is expected to have a small cross-section being the less exoergic channel. In addition, detection of formaldehyde at $m/e = 30$ is adverse because of some background interference arising from the ^{13}C in the ethylene beam and in the HCO product (from channel (2d)); but especially because the H_2CO product, internally excited, is not expected to give a strong parent peak at $m/e = 30$. Indeed, H_2CO formed from the reaction $\text{O}(^1\text{D}) + \text{CH}_3\text{F}$ was not observed at $m/e = 30$, but at $m/e = 29$, as HCO^+ .⁴¹ On the other hand, detection at $m/e = 29$ is practically impossible in the present case because the $m/e = 29$ TOF signal is contaminated by elastically-scattered ethylene, $^{13}\text{C}_2\text{H}_4$, which would fall in the same flight-time region of the product, and by the intense HCO signal from channel (2d). The alternative would be to detect the methylene radical from the $\text{CH}_2 + \text{HCHO}$ channel, but this is really impossible when using *hard* EI ionization, because the TOF spectrum

of the methylene product at $m/e = 14$ would be completely overwhelmed by the $m/e = 14$ signal due to dissociative ionization to CH_2^+ of elastically-scattered C_2H_4 , as can be seen from Figs. 14(a) and 14(b), where the TOF spectrum at $m/e = 27$ (which is identical to the spectrum at the parent peak of $m/e = 28$) is compared with the TOF spectrum at $m/e = 14$ at the same lab angle when using 60 eV electron energy. This complication is completely removed when using tunable electrons for product ionization (see below).

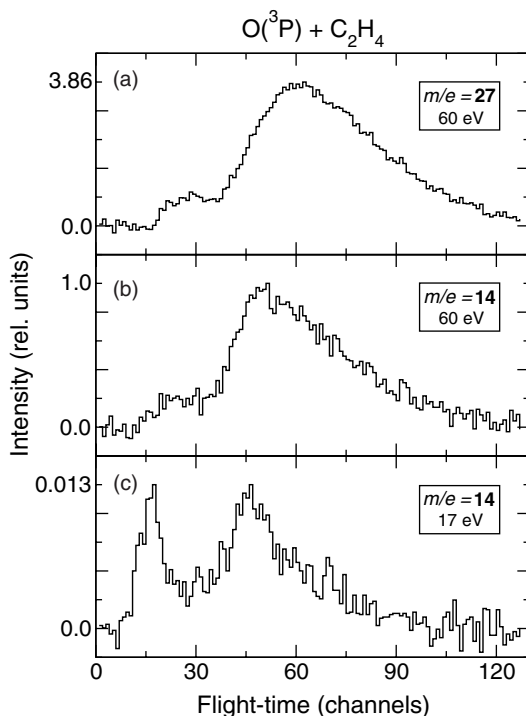


Fig. 14. TOF spectra for the $\text{O}(^3\text{P}) + \text{C}_2\text{H}_4$ reaction ($E_c = 12.9 \text{ kcal mol}^{-1}$) at (a) $m/e = 27$ and 60 eV electron energy, reflecting elastically-scattered C_2H_4 (detected at $m/e = 27$ as C_2H_3^+) from O (slow peak) and O_2 (fast peak); (b) $m/e = 14$ and 60 eV electron energy, reflecting elastically-scattered C_2H_4 (detected at $m/e = 14$ as CH_2^+); (c) $m/e = 14$ and 17 eV electron energy, reflecting only reactive scattering signals since the elastic scattering has been completely suppressed (see text for details). Note the relative scale of the three spectra: the reactive signal at $m/e = 14$ (and 17 eV) is of the order of 1% of the elastic signal at $m/e = 14$ (and 60 eV).

3.2.1. Observation of all Product Channels

Indeed, by using *soft* EI ionization, we have been able to unambiguously detect products from all five reaction pathways (2a)–(2e), determine their branching ratio and characterize their dynamics.³⁴ Here we discuss some of the results that we have obtained on this reaction, which well exemplify the power of *soft* EI ionization. First of all, from measurements of the EI efficiency curves at various m/e ratios (15, 42, and 43), we have found that the parent ion at $m/e = 43$ (CH_2CHO^+ , corresponding to one of the main reaction channels, the vinoxy radical,) is not stable, so measurements of angular and TOF distributions were carried out at $m/e = 42$. Incidentally, from the EI ionization efficiency curve at $m/e = 42$ we have obtained some direct information on the IE of the vinoxy radical, for which no such information was available till now. The IE should be ≤ 11 eV.

Figure 15 shows the TOF spectra recorded at $m/e = 42$, 15 and 14 with an electron energy of 17 eV at the lab angle $\Theta = 34^\circ$, for the reaction $\text{O}(^3\text{P}) + \text{C}_2\text{H}_4$ at $E_c = 12.9 \text{ kcal mol}^{-1}$; the configuration with $\gamma = 135^\circ$ was used for higher TOF resolution. Angular distributions were also measured at $m/e = 42$ and 15. As derived from the data analysis, and as clearly shown in Fig. 15, those three TOF spectra already carry the fingerprints of all five possible product channels (2a)–(2e). Specifically, the $m/e = 15$ TOF spectrum exhibits a fast peak which is unambiguously due to the CH_3 from the $\text{CH}_3 + \text{HCO}$ channel (reaction (2d)), and a slower, more intense peak, due to dissociative ionization in the ionizer of the vinoxy radical, corresponding to the $\text{CH}_2\text{CHO} + \text{H}$ channel (reaction (2a)). The $m/e = 42$ TOF spectrum exhibits (a) a dominant peak, analogous to the main peak observed at $m/e = 15$, and which is due to dissociative ionization in the ionizer of the vinoxy radical (reaction (2a)), (b) a fast peak, which appears as a shoulder on the main peak, which is unambiguously attributed, on the basis of energy and linear momentum conservation, to the ketene product from the channel $\text{CH}_2\text{CO} + \text{H}_2$ (reaction (2c)), (c) a small component, peaked at the CM velocity, which is attributed to formation of the acetyl radical from the channel $\text{CH}_3\text{CO} + \text{H}$ (reaction (2b)) with a very small recoil energy. Note that the small peak of acetyl does not appear visible in the TOF spectrum at $m/e = 15$, presumably because of a different fragmentation pattern of hot vinoxy and hot acetyl. The $m/e = 14$ TOF spectrum exhibits contributions from fragmentation of the ketene, vinoxy, and acetyl products, and very clearly also a fast peak which can only correspond to methylene formation from the channel $\text{CH}_2 + \text{HCHO}$ (formaldehyde). A small contribution

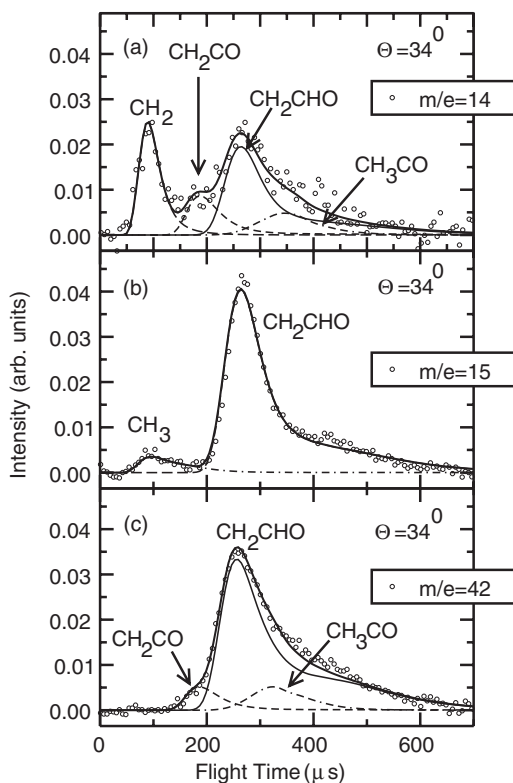


Fig. 15. TOF spectra at $\Theta = 34^\circ$ for the $\text{O}(^3\text{P}) + \text{C}_2\text{H}_4$ reaction ($E_c = 12.9 \text{ kcal mol}^{-1}$) recorded at (a) $m/e = 14$, (b) $m/e = 15$, and (c) $m/e = 42$, using an electron energy of 17 eV. The fingerprints of all five energetically-allowed channels (formation of methylene, ketene, vinoxy, acetyl, and methyl) from the $\text{O}(^3\text{P}) + \text{C}_2\text{H}_4$ reaction are indicated (see text). Relative intensities at the TOF peak for $m/e = 14$, 15, and 42 are 0.23, 3.0, and 1, respectively.

to this fast peak from also fragmentation of the CH_3 radical product from channel (2d) cannot be ruled out, but this is expected to be small, considering that the appearance energy of CH_2^+ from CH_3 dissociative ionization is $\text{AE} = 15.1 \text{ eV}$.⁹⁰ Measurement of a TOF spectrum at lower electron energies ($\leq 15 \text{ eV}$) is, however, needed to clarify the extent of the contribution to CH_2^+ from dissociative ionization of “hot” CH_3 from the $\text{CH}_3 + \text{HCO}$ channel and to determine a more reliable branching ratio.

We would like to stress how, for instance, the detection of methylene from the reaction channel (2e) was only possible because of the use of *soft* EI ionization. In fact, because the AE of CH_2^+ from C_2H_4 is 18 eV,⁷² by using an electron energy of 17 eV it was possible to remove completely the

elastic contribution due to C_2H_4 in the TOF spectrum, as can be seen in Fig. 14(c). There, the fast peak can be unambiguously assigned to CH_2 from reaction channel (2e), while the slow peak and some intensity in between the two peaks is due to dissociative ionization at $m/e = 14$ (CH_2^+) of CH_2CHO , CH_3CO , and CH_2CO from the reaction channels (2a), (2b) and (2c), respectively, as indicated by the best-fit curves obtained from the best-fit CM product angular and translational energy distributions discussed above.³⁴ Note the dramatic change of scale in Figs. 14(b) and 14(c), corresponding to the TOF spectra at 60 and 17 eV, respectively: it shows clearly how much smaller the reactive scattering signals are with respect to the elastic signals.

From a detailed series of angular and velocity distribution measurements at $m/e = 42$, 15, and 14 using different electron energies, and from measurements of fragmentation patterns, it was possible to characterize the reaction dynamics of all five competing channels and determine their branching ratios.³⁴ Subtle dynamical features, such as sideways scattering in the formation of vinoxy, attributable to the geometry of the decomposing transition state and angular momentum partitioning, were observed for the first time in this reaction, analogously to what was previously observed in the analogous reaction of $\text{F} + \text{C}_2\text{H}_4$.^{91,92} For the first time it was also firmly established that formation of molecular products, $\text{CH}_2\text{CO} + \text{H}_2$, is a sizeable channel in the reaction $\text{O}(^3\text{P}) + \text{ethylene}$, accounting for about 10% of the yield, contrary to what was concluded from the most recent and reliable kinetic studies,⁸⁶ but in qualitative agreement with the early, pioneering suggestion of Cvetanović in the early 1950s.⁷⁶ For the first time, it was also shown that a small fraction of acetyl radicals is formed in this reaction. The spatial and velocity distributions of vinoxy, acetyl, and ketene products at $E_c = 12.9 \text{ kcal mol}^{-1}$ are depicted comparatively in the 3D product flux (velocity-angle) contour maps shown in Fig. 16. And, finally, for the first time we have observed unambiguously, under truly single collision conditions, the formation of methylene + formaldehyde in this reaction, corroborating two of the most recent kinetic investigations^{85,86} which, by using different detection techniques, had reached the conclusion that this channel was also occurring in the $\text{O}(^3\text{P}) + \text{C}_2\text{H}_4$ reaction.

All this indicates that ISC (inter-system-crossing) plays an important role in the reaction, since the occurrence of channels (2b), (2c), and (2d), which account for about 2/3 of the overall reaction yield, can only be rationalized assuming that ISC between triplet and singlet PESs is occurring very efficiently. Theoretical work on both triplet and singlet PESs of $\text{C}_2\text{H}_4\text{O}$, with inclusion on nonadiabatic couplings, is desirable and would

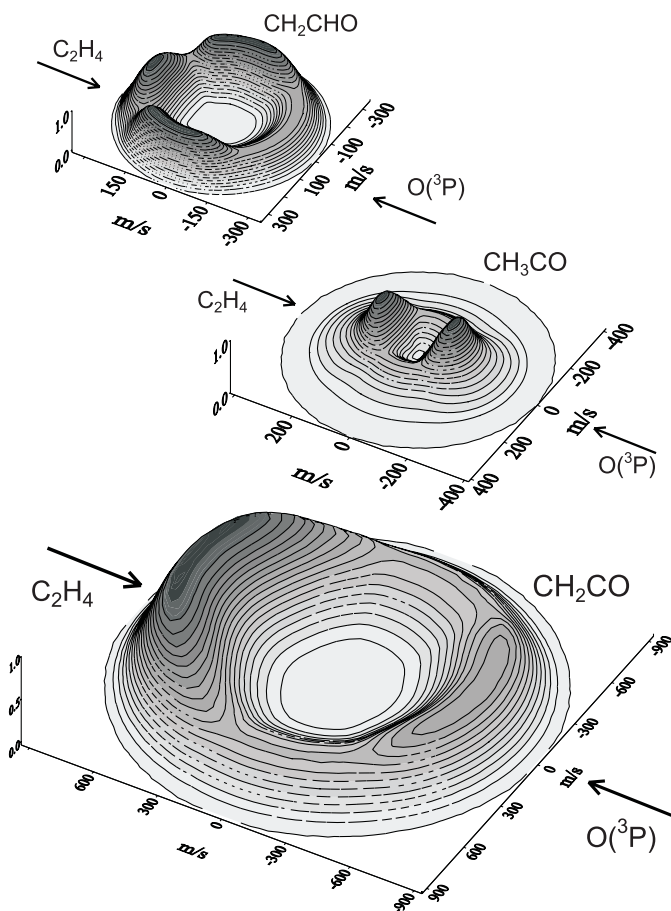


Fig. 16. Flux (velocity-angle) contour maps of the vinoxy (CH_2CHO), acetyl (CH_3CO), and ketene (CH_2CO) products from the $\text{O}(^3\text{P}) + \text{C}_2\text{H}_4$ reaction at $E_c = 12.9 \text{ kcal mol}^{-1}$.

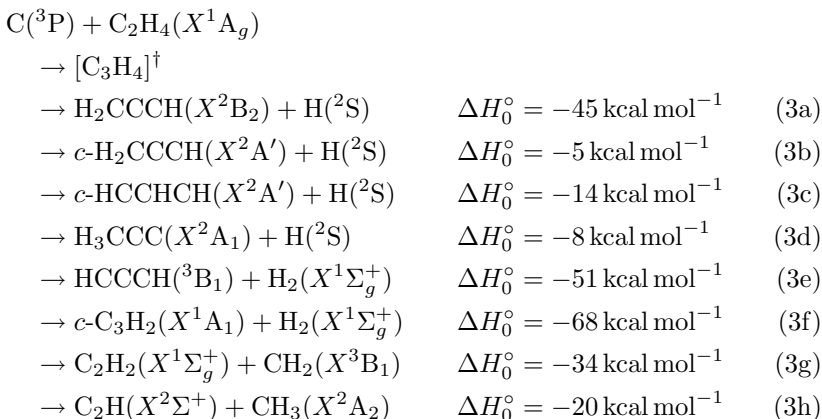
contribute to our understanding of the detailed, complex dynamics of this important and fascinating reactive system.

4. Examples: $\text{C}(^3\text{P}) + \text{Unsaturated Hydrocarbons}$

The reactions of ground state atomic carbon, $\text{C}(^3\text{P}_J)$, with unsaturated hydrocarbons are another important class of reactions characterized by multiple pathways. These reactions, besides being of fundamental interest, are of great relevance in the chemistry of the interstellar medium and also in combustion.^{12,93–95}

4.1. $C(^3P) + C_2H_4$

The reaction of $C(^3P)$ with ethylene has many energetically-allowed channels:



A pioneering CMB study⁹⁶ of this reaction at two E_c (4.1 and 9.2 kcal mol⁻¹) was able to identify only channel (3a), leading to propargyl + H formation, as the sole reaction pathway. A more recent, higher resolution study from our laboratory,¹² at three different E_c (2.2, 4.1, and 7.4 kcal mol⁻¹) was able to detect the formation of another C_3H_3 isomer, although it could not specify which of the other three energetically-allowed ones (channels (3b)–(3d)). However, on the basis of theoretical information on the PES for reaction, this other C_3H_3 isomer is presumably *c*-propenyl (channel (3c)) and/or propyn-1-yl (channel (3d)).

Our high-resolution CMB study was also able to show that the H_2 -elimination channels (channels (3e) and (3f)) leading to *l*- $C_3H_2 + H_2$ and *c*- $C_3H_2 + H_2$, respectively, were not occurring to a measurable extent in the investigated collision energy range. This is in strong contrast to the reaction $C(^3P) + C_2H_2$, where the H_2 -elimination channel leading to $C_3 + H_2$ formation was found, at comparable E_c , to account for more than one third of the overall reaction, with formation of $C_3H + H$ being the main channel.^{93,94,97} This is consistent with a study of these reactions in bulk conditions at 300 K which has given a branching ratio of 92% for the H-elimination channel in $C(^3P) + C_2H_4$, but 53% in $C(^3P) + C_2H_2$.⁹⁸ Theoretical calculations^{99,100} indeed indicate that H_2 elimination from triplet propyne to $HCCCH(^3B_1) + H_2$ (channel (3e)) has a very high energy barrier and that the only remaining possibility requires ISC from triplet to singlet PESs with formation of *c*- $C_3H_2(^1A_1) + H_2$ (channel (3f)). Our differential

cross-section results indicate that ISC in the C_3H_4 system is not an efficient process, to the contrary of the C_3H_2 system. It can be put forward that the H-elimination channel is strongly exoergic in the $\text{C}(^3\text{P}) + \text{C}_2\text{H}_4$ system, while nearly thermoneutral in $\text{C}(^3\text{P}) + \text{C}_2\text{H}_2$. Therefore, the C_3H_4 complex is likely to spend a time in the triplet allene potential well significantly shorter than C_3H_2 does in the triplet propargylene potential well. This should determine a lower probability of ISC from triplet to singlet PES in C_3H_4 .

The above results are exemplified in Figs. 17 and 18. Figure 17 shows the angular distribution of the products detected at $m/e = 38$ together with the Netwon diagram of the experiment at $E_c = 7.4 \text{ kcal mol}^{-1}$. Figure 18 shows five TOF spectra, also at $m/e = 38$. The corresponding distributions recorded at $m/e = 39$ (the parent peak of C_3H_3) were found¹² to be superimposable to those at $m/e = 38$, and this indicates unambiguously that the $m/e = 38$ signal is coming from dissociative ionization of the C_3H_3 product in the ionizer, and not from a dynamically different channel corresponding to H_2 elimination. As can be seen, the angular and TOF distributions exhibit features attributable to the formation of two energetically and also dynamically different C_3H_3 isomer products. This finding was fully supported by concurrent CMB experiments¹² in which the excitation function (i.e. the collision energy dependence of the integral cross-section) for H production was measured in Bordeaux down to very low collision energies in CMB experiments with pulsed beams and LIF detection of the H-atoms; these experiments also gave evidence of the presence of two H-forming channels. In addition, our study¹² was also able to provide very detailed information about the reaction dynamics of propargyl formation as a function of collision energy, giving also the branching ratio between formation of propargyl and the less stable C_3H_3 isomer(s), and this represents a significant improvement with respect to the previous study.

However, our study was not able to tell anything about the occurrence of the C–C bond breaking channel (3g) leading to the formation of $\text{C}_2\text{H}_2 + \text{CH}_2$ (acetylene + methylene). On the other hand, this channel is only 11 kcal mol^{-1} less exoergic than the most important channel (3a), and is much more exoergic than the channels (3b)–(3d), corresponding to the formation of the less stable C_3H_3 isomers, which were found to contribute to about 14% of the overall H-formation pathways at $E_c = 7.4 \text{ kcal mol}^{-1}$.¹² It is also worth noting that a recent kinetic study at room temperature (i.e. corresponding to an average collision energy of about 1 kcal mol^{-1}) has estimated an absolute H branching ratio of the $\text{C}(^3\text{P}) + \text{C}_2\text{H}_4$ reaction to

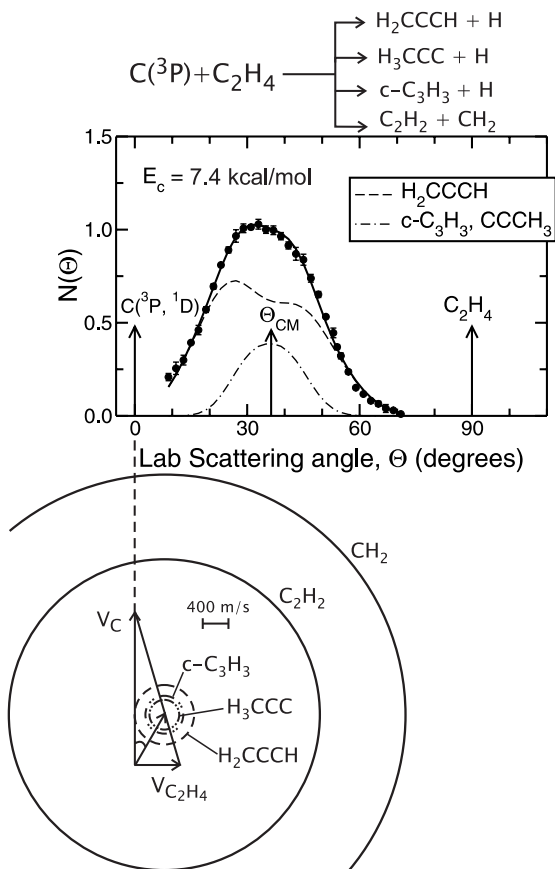


Fig. 17. Laboratory angular distribution of the C_3H_3 products at $m/e = 38$ from the reaction $\text{C}(^3\text{P}) + \text{C}_2\text{H}_4$ at $E_c = 7.4 \text{ kcal mol}^{-1}$, together with the Newton diagram of the experiment. The circles in the diagram delimit the maximum velocity that the various, indicated C_3H_3 isomer products from channels (3a), (3c), and (3d) and the C_2H_2 and CH_2 products from channel (3g) can attain on the basis of energy and linear momentum conservation if all the available energy goes into product translational energy. The solid line is the total angular distribution calculated from the best-fit product CM translational energy and angular distributions; the separate contributions from the propargyl (H_2CCCH) and the less stable C_3H_3 isomers are shown with dashed and dashed-dotted lines, respectively. (Adapted from Ref. 12.)

be 0.92 ± 0.04 .⁹⁸ All this strongly suggests that the C–C bond cleavage pathway (3g) should be quite relevant, especially at high collision energies. In regard, also some contribution from the less exoergic channel (3h) leading to $\text{C}_2\text{H} + \text{CH}_3$ cannot be ruled out.

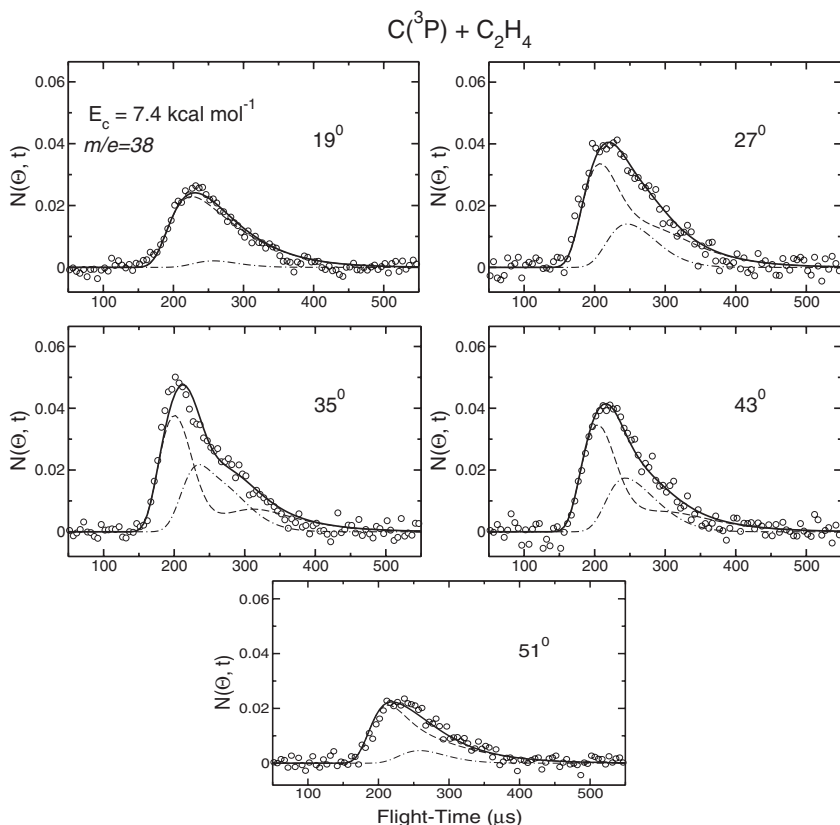


Fig. 18. TOF distributions of the $m/e = 38$ product from the reaction $\text{C}(^3\text{P}) + \text{C}_2\text{H}_4$ at $E_c = 7.4 \text{ kcal mol}^{-1}$ at the indicated laboratory angles. Lines are as in Fig. 17. (Adapted from Ref. 12.)

4.1.1. Observation of the C–C Bond Fission Channel

One reason for the difficulty in detecting the products of the C–C bond-rupture channel, is due to the fact that two heavy fragments are produced in the process and, because of energy and linear momentum conservation, they are expected to be scattered over a wide angular range, as indicated in Fig. 17, where the maximum Newton circles within which the two co-products can be scattered are indicated, and this decreases strongly the signal intensity in the laboratory frame. But again, there is an additional, much more severe complication which actually prevented the detection of the expectedly weak (in the lab frame) reactive scattering signal at $m/e = 26$ or 14. As mentioned in the Introduction,

it is indeed impossible to detect any of the two products corresponding to the reaction pathway (3g) by using 60–200 eV electrons, because the reactive scattering signal at $m/e = 14$ (CH_2) or 26 (C_2H_2) is overwhelmed by the much more intense signal at these masses originating from dissociative ionization of *elastically-scattered* C_2H_4 . This can be seen in Fig. 19 which shows the TOF spectrum of $m/e = 28$ (Fig. 19(a)) and $m/e = 14$ (Fig. 19(b)) when using 60 eV electrons. As can be seen, the

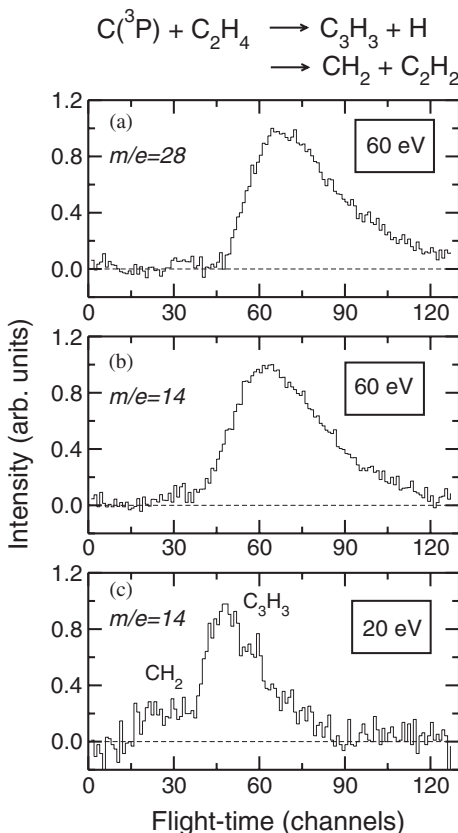


Fig. 19. TOF distributions of (a) $m/e = 28$ and (b) $m/e = 14$, at $\Theta = 36^\circ$ and 60 eV electron energy from the reaction $\text{C}(^3\text{P}) + \text{C}_2\text{H}_4$ at $E_c = 7.4 \text{ kcal mol}^{-1}$. The $m/e = 28$ signal is due to elastically-scattered C_2H_4 , while the $m/e = 14$ signal comes from dissociative ionization of elastically-scattered C_2H_4 (see text). (c) TOF distributions of $m/e = 14$ at 20 eV electron energy; here the fast peak reflects CH_2 from channel (3g) while the slow peak reflects the dissociative ionization of the C_3H_3 main product (channel (3a)).

two distributions are identical, except for a small shift due to the different ion-flight-time of the two ions. Clearly, the $m/e = 28$ (C_2H_4^+) distribution is due to elastically/inelastically-scattered C_2H_4 , and the $m/e = 14$ (CH_2^+) distribution also reflects elastically/inelastically-scattered C_2H_4 detected via the fragment CH_2^+ produced by dissociative ionization of C_2H_4 . Since the reactive scattering signal at $m/e = 14$ due to the formation of CH_2 (channel (3g)) is expected to be about two order of magnitude smaller than the $m/e = 14$ signal coming from elastically-scattered C_2H_4 , there is no hope of being able to discern it. However, by using *soft* EI ionization it has recently become possible to overcome this problem, as demonstrated by the following preliminary experiments.

Since the formation of CH_2^+ from C_2H_4 has an appearance energy $\text{AE} = 18 \text{ eV}$,⁹¹ it is sufficient to lower the electron energy close to this value to suppress practically completely the elastic scattering contribution, as well as to reduce to zero any background at $m/e = 14$ due to dissociative ionization of residual N_2 . A TOF spectrum recorded using 20 eV electron energy at the same laboratory angle is shown in Fig. 19(c). As can be seen, the spectrum is very different from that in Fig. 19(b); it exhibits a main, slow peak, and a fast shoulder. While the fast peak can be attributed to methylene from the $\text{CH}_2 + \text{C}_2\text{H}_2$ channel, the slow peak is due to dissociative ionization of the main propargyl product (C_3H_3) to CH_2^+ , as can be seen in Fig. 20, where TOF spectra at $m/e = 14$ and $m/e = 38$ are compared. The observation of both product channels at the same $m/e = 14$ will permit one to determine accurately the branching ratio, once the fragmentation patterns of C_3H_3 and CH_2 at 20 eV electron energy have been determined.

Although these data are only preliminary, and clearly more work is needed to determine the dynamics of the $\text{CH}_2 + \text{C}_2\text{H}_2$ channel and its relative importance, it is clear that this is the way to disentangle the detailed dynamics of this multichannel reaction. Finally, measurements at $m/e = 15$ using low electron energy should also be able to reveal the possible occurrence of channel (3h) leading to $\text{CH}_3 + \text{C}_2\text{H}$. Such measurements are being planned for the near future.

Because of the acquired capability of measuring EI efficiency curves, it will also be interesting to perform such measurements at $m/e = 39$, 38, 14, and 15. This should provide some information on the various C_3H_3 isomer products, since the IE of propargyl (CH_2CCH), cyclopropenyl (*c*- HCCHCH), and propyn-1-yl (CH_3CC) are quite different (8.7 eV, 6.6 eV, and 10.8 eV, respectively).⁹¹ Also, the dissociative ionization patterns of propargyl and propyn-1-yl are expected to be quite different as a function of electron energy. In fact, as the propargyl ion is considerably more stable

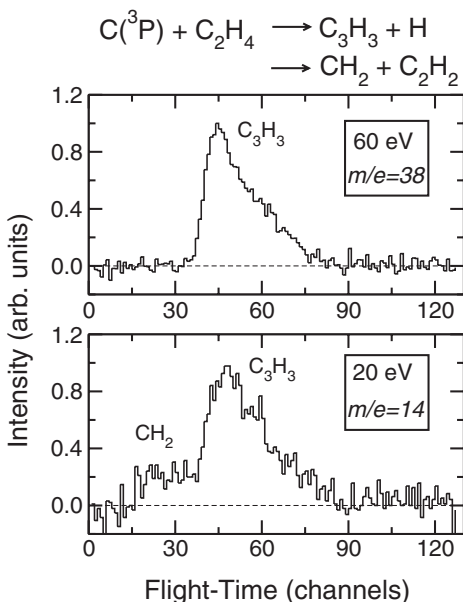
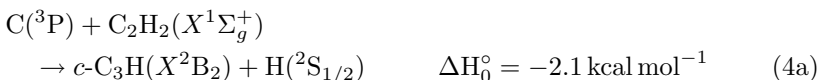


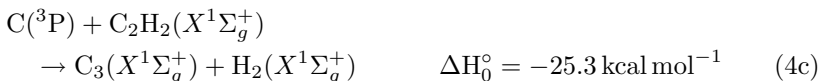
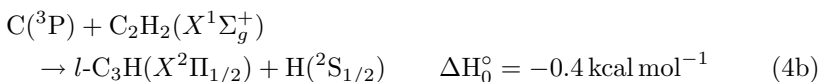
Fig. 20. Comparison of TOF spectra of $m/e = 38$ at 60 eV electron energy, exhibiting a peak due to the C_3H_3 forming channels (see text, and Ref. 12), and of $m/e = 14$ at 20 eV electron energy (see Fig. 19), exhibiting a fast peak due to CH_2 formation and a slow peak due to C_3H_3 dissociative ionization.

than the propynyl ion, it implies that the propargyl cation would have, at high electron energy (such as 60 eV), a considerable contribution to the $m/e = 39$ signal, while the propynyl cation predominantly dissociates to the $m/e = 38$ ion (see also Ref. 101). However, the relative contribution to $m/e = 38$ of propargyl and propynyl products may change significantly at low electron energy. Finally, because of the recently increased instrument sensitivity, it should also be possible to revisit the H_2 -forming channel, which may become detectable if not smaller than a few percent; and this would permit one to explore more deeply the possible occurrence of ISC in the C_3H_4 system.

4.2. $\text{C}(^3\text{P}) + \text{C}_2\text{H}_2$

The reaction of $\text{C}(^3\text{P})$ with acetylene also exhibits chemical branching, with competing exit channels:





Again, a pioneering CMB study¹⁰² at three E_c (2.1, 6.7, and 10.8 kcal mol⁻¹) using pulsed C(³P) beams obtained by laser ablation of graphite identified C₃H + H as the sole reaction products, and explained the change in dynamics observed as a function of E_c by invoking two competing microscopic channels leading to the cyclic *c*-C₃H and linear *l*-C₃H isomers (reactions (4a) and (4b)), with the formation of *c*-C₃H occurring at low E_c and the contribution of *l*-C₃H taking place at higher kinetic energies. A recent quantum study gives, however, the opposite result, *l*-C₃H being preferentially formed at low E_c .¹⁰³

A more recent CMB study⁹⁷ carried out in our laboratory using a continuous carbon beam has clearly demonstrated that, in addition to the H-elimination channel, the strongly exoergic, spin-forbidden H₂-elimination pathway (4c) leading to C₃(X¹Σ_g⁺) + H₂(X¹Σ_g⁺) also plays an important role through ISC between the triplet and the singlet PESs, the branching ratio of integral cross-sections $\sigma(\text{C}_3 + \text{H}_2)/[\sigma(\text{C}_3 + \text{H}_2) + \sigma(\text{C}_3\text{H} + \text{H})]$ being *ca* 0.37 at $E_c = 7.0$ kcal mol⁻¹. This result is consistent with those of a recent experimental investigation⁹⁸ of the detailed kinetics of C(³P) + C₂H₂(X¹Σ_g⁺) at 300 K, which has found a branching ratio for H-production, i.e. $k_{(4a+4b)}/k_4$, of only 0.53 suggesting that the pathway (4c) should account for the rest. In addition, *ab initio* electronic structure calculations of the triplet and singlet PESs fully support this finding by having located the triplet-singlet seam of crossing where ISC is facile.⁹⁹

There are, however, still some unsolved, important questions¹⁰³ about this fundamental reaction, of great relevance in dense interstellar clouds, where it could well be the source of the C₃H and C₃ species detected there. These unsolved questions are: (a) what is the branching ratio for formation of the two isomeric C₃H species, *l*-C₃H and *c*-C₃H, and how does it vary with E_c ? (b) How do the detailed reaction dynamics and the branching ratio for C₃H and C₃ formation vary with E_c ?

These unsolved problems can be addressed by detailed CMB experiments, which use *soft* EI ionization for product detection and possibly also very low collision energies. In fact, by measuring the EI efficiency curves for the C₃H products it may be possible to obtain some information on which isomer is actually formed, because the IE of *c*-C₃H is expected to be

significantly lower (by several eVs) than that of *l*-C₃H (2-propynylidene). Furthermore, by using low electron energies it should also be possible to detect the parent peak of the C₃ product at $m/e = 36$, free, or nearly free, of the contribution from dissociative ionization of C₃H (which can be cleanly studied at the parent $m/e = 37$ peak) and measure its angular and velocity distributions without significant contribution from the C₃H + H channel (the AE of C₃⁺ from *l*-C₃H is 17.1 eV).⁹¹ Finally, by using neon as seeding gas in the C atom beam source, it is possible to lower the collision energy to about 2 kcal mol⁻¹, and by crossing the same two beams at 45°, using the same beam source described in Sec. 3.1.2 for obtaining the crossing configuration at 135°, but rotated by 180°, it will be possible to lower the collision energy below 1 kcal mol⁻¹, which corresponds to a temperature of about 300 K. At such low E_c it may become possible to disentangle the relative contributions of the two C₃H isomer products also on the basis of their translational energy release, provided the theoretical exoergicities reported in Eqs. (4a) and (4b) are accurate. Of course, if the difference in stability of *c*-C₃H and *l*-C₃H is much smaller than the current theoretical estimates, the only way to distinguish between the two isomer species in this type of experiments would be to discriminate them via their different ionization energy. In this regard, this is a case where the higher energy resolution afforded by the synchrotron radiation could turn very useful.

Because of the higher sensitivity and the advantages that one can obtain in terms of less fragmentation and lower interfering backgrounds, measurements of angular and TOF distributions of reaction products when using low electron energy remain still quite easy, even when using a C beam seeded in neon, which is about 5 times less intense than the C beam seeded in helium, used for the $E_c = 7.0$ kcal mol⁻¹ experiment. A preliminary angular distribution of the C₃H product recorded at $m/e = 37$ at $E_c = 2.0$ kcal mol⁻¹ using 24 eV electron energy was measured with a $S/N \approx 150$ in 50 s counting time.¹⁰⁴ More work on this system is being planned.

5. Conclusions and Future Prospects

In this chapter we have discussed the successful implementation in our laboratory, for the first time, of the *soft* (i.e. low energy) electron-impact ionization method for product detection in crossed molecular beams reactive scattering experiments with mass spectrometric detection. Analogous to the approach of *soft* photoionization by tunable VUV synchrotron radiation,

soft electron-impact ionization permits one to reduce or even eliminate the problem of dissociative ionization of reactants, products and residual background gases which may seriously interfere with product detection and which has severely undermined so far the “universality” of the mass spectrometric detection method in CMB experiments. Moreover, *soft* EI ionization permits one to determine more readily product branching ratios, in contrast to photoionization. Because of this, and considering the simplicity of the experimental requirements, it may well represent an attractive alternative to the use of synchrotron radiation.

The capabilities and the opportunities offered by the *soft* electron-impact ionization method have been illustrated with reference to very recent CMB studies of some polyatomic multichannel reactions of ground state oxygen atoms, $O(^3P)$, and carbon atoms, $C(^3P)$, with unsaturated hydrocarbons (acetylene and ethylene), which are of great relevance in combustion and astrophysical chemistry. For these reactions, *soft* EI ionization has permitted (or is permitting) one to measure the reactive differential cross-sections for each energetically-allowed channel and to derive the branching ratios, the reaction dynamics being discussed in the light of theoretical information on the relevant potential energy surfaces.

It appears that the use of *soft* EI ionization is enabling us to really reach the so-called “universal” detection in CMB reactive scattering experiments. Of course, *soft* photoionization by tunable synchrotron radiation can permit that too. In this regard, very recent experiments in Taiwan¹⁶ on the photodissociation of propene at 157.6 nm using VUV ionization with synchrotron radiation have permitted one to successfully detect eleven photofragments ascribed to eight (five binary and three triple) dissociation channels; branching ratios were also estimated. Basically, all photofragments could be detected and the universal detection could be achieved. All this is very promising for the approach to be extended successfully also to reactive scattering in the near future. In this regard, it should be noted the new method proposed in Berkeley¹⁰⁵ for determining absolute PI cross-sections of radicals, which is based on photofragment translational spectroscopy of suitable radical precursors employing tunable VUV synchrotron radiation. This kind of work aims at building up a database of absolute PI cross-sections for radical species, which is the required information for estimating branching ratios when using *soft* PI by synchrotron light, both in photodissociation and reactive scattering experiments.

We have also discussed the implementation, for the first time, of CMB experiments with mass spectrometric detection using a beam intersection

angle of 135° rather than the conventional 90° . It has been shown that this new geometrical arrangement is able to provide not only an increased collision energy, but also an increased angular and velocity resolution.

What are the future opportunities in CMB reactive scattering studies opened up by the *soft* electron-impact ionization?

We will examine here only the area where the largest contribution of *soft* EI ionization (and also photoionization) can be expected, and this is the area of polyatomic multichannel reactions, involving atoms + polyatomic molecules, radicals + polyatomic molecules, and atoms/radicals + polyatomic radicals. What we can expect, in general, in the field of reaction dynamics relative to simple, fundamental reactions involving three or four atoms, for which experiments at the state-resolved level are possible, has been discussed in recent reviews.¹⁻⁵ The rate of progress that can be envisioned in the study, also at the state-resolved level, of polyatomic reactions which produce triatomic and larger products will depend in a critical manner on the development of laser or other techniques for detecting polyatomic species state-specifically. These are badly needed and justify the amount of work currently underway, although fundamental limitations may remain. However, extension of dynamical studies to polyatomic reaction products by using spectroscopic detection is expected over the next few years, encouraged by the recent example of efficient state-selective detection of CH_3 radicals by REMPI in the $\text{F} + \text{CH}_4 \rightarrow \text{CH}_3 + \text{HF}$ reaction.⁶⁻⁸

Regarding atom-polyatom reactions exhibiting multiple channels and radical-molecule reactions, so far there have been a limited number of studies on the detailed dynamics. This attests to the difficulty of these studies, and indicates an area in reaction dynamics where effort should be diverted during the coming years. Indeed, given the intense interest in radical chemistry and also on polyatomic reactions on the part of the chemical community, including astrochemists, atmospheric chemists, plasma chemists and combustion chemists, and considering how rapidly experimental techniques are improving and how quickly theoreticians become motivated to tackle more complex problems, one can believe that sufficient microscopic experiments and more detailed theoretical work will be undertaken to bring about a better understanding of complex radical reaction dynamics. Undoubtedly, in the near future it will be possible to explore the detailed dynamics of a variety of atom-polyatom multichannel reactions, as those of $\text{O}(^3\text{P})$, $\text{N}(^2\text{D})$ and $\text{C}(^3\text{P})$ with unsaturated hydrocarbons, of great practical relevance, by using the *soft* EI ionization method, as demonstrated by the recent detailed

work on some $O(^3P)$ reactions discussed here. It should also be possible to extend the investigation to radical-polyatom multichannel reactions as those of OH and CN with unsaturated hydrocarbons.

Besides radical-molecule reactions, of great practical and fundamental interest are also atom/radical-radical reactions. While their kinetics have been studied extensively over the past two decades, very few dynamical studies of reactions between two "unstable" radicals have been reported to date, and these have been confined to the measurement of the product vibrational energy distribution in flow systems. Very recently, the dynamics of OH formation from the $O(^3P)$ reaction with allyl radicals have been investigated by LIF in pulsed CMB experiments.¹⁰⁶ Measurements of differential cross-sections for atom/radical-radical reactions are hampered, in general, by the technical difficulty of generating two beams of radicals (not counting NO, NO₂ and O₂) of sufficient intensity. However, the pioneering successful efforts on the reaction of $C(^3P)$ with the propargyl radical using pulsed beams have shown that such studies are technically feasible.¹⁰⁷ Important reactions such as $O(^3P)$, $C(^3P)$, and $N(^4S, ^2D) + \text{methyl, ethyl, propargyl, and allyl}$ are expected to become amenable to CMB studies using continuous beams in our laboratory and, again, *soft* EI ionization will turn extremely useful to disentangle the dynamics of competing pathways and determine their branching ratios.

There is no doubt that the classic CMB technique with mass spectrometric detection, using *soft* electron-impact ionization or *soft* photoionization by VUV laser and synchrotron radiation, will play a central role in the near future in the dynamic investigation of elementary multichannel reactions, since these *soft* ionization techniques will permit a new generation of CMB experiments, as those discussed in this chapter. In fact, low-energy EI ionization or photoionization mass spectrometry may readily detect most hydrocarbon radicals and many small open-shell species, which represent the products of many important reactions and which are not amenable to LIF or REMPI detection. This possibility of enlarging the scope of CMB studies to complex reactions of great practical interest is one factor that has spurred the development of new CMB machines in recent years. The limit to CMB work will lie only in our ability to generate beams of the desired reactants. This is an area in which significant progress has recently been made, as discussed in a recent review,¹ and much more can be expected during the coming years.

We conclude by emphasizing that the detection of all reaction channels in a reaction like $O(^3P) + C_2H_4$ reaction, the characterization of their

dynamics, and the determination of the branching ratios were not possible prior to the introduction of the *soft* EI ionization in CMB experiments, and therefore these studies represent a milestone not only in CMB reactive scattering, but also in the entire field of reaction dynamics and chemical kinetics, since they contribute to establish a much closer link between the dynamics and kinetics of polyatomic reactions.

Acknowledgments

We wish to thank undergraduate Francesca Leonori for her valuable contribution to some of the experiments using *soft* EI ionization. Special thanks to Emeritus Professor G. G. Volpi for continuous inspiration and support over the years: he has always believed that *soft* EI ionization could one day be applied in CMB experiments. We also thank other, present and past, group members (N. Balucani, R. Bobbenkamp, and L. Cartechini) and visitors (A. Russo) for their contribution to some aspects of the work discussed here. We acknowledge financial support from the Italian “Ministero Istruzione, Università e Ricerca — MIUR — (COFIN 2001 and 2002)” and the European Commission through the Research Training Network “REACTION DYNAMICS” (contract No. HPRN-CT-1999-00007).

References

1. P. Casavecchia, *Rep. Prog. Phys.* **63**, 355 (2000), and references therein.
2. P. Casavecchia, N. Balucani and G. G. Volpi, *Annu. Rev. Phys. Chem.* **50**, 347 (1999), and references therein.
3. K. Liu, *Annu. Rev. Phys. Chem.* **52**, 139 (2001), and references therein.
4. F. Fernandez-Alonso and R. N. Zare, *Annu. Rev. Phys. Chem.* **53**, 67 (2002), and references therein.
5. S. C. Althorpe and D. C. Clary, *Annu. Rev. Phys. Chem.* **54**, 493 (2003), and references therein.
6. J. J. Lin, J. Zhou, W. Shiu and K. Liu, *Rev. Sci. Instrum.* **74**, 2495 (2003).
7. J. J. Lin, J. Zhou, W. Shiu and K. Liu, *Science* **300**, 966 (2003).
8. J. Zhou, J. J. Lin, W. Shiu, S.-C. Pu and K. Liu, *J. Chem. Phys.* **119**, 2538 (2003); J. Zhou, J. J. Lin, W. Shiu and K. Liu, *J. Chem. Phys.* **119**, 4997 (2003).
9. Y. T. Lee, J. D. McDonald, P. R. Le Breton and D. R. Herschbach, *Rev. Sci. Instrum.* **40**, 1402 (1969).
10. Y. T. Lee, *Science* **236**, 793 (1987).
11. Y. T. Lee, in *Atomic and Molecular Beam Methods*, ed. G. Scoles, (Oxford University Press, New York, 1987), Vol. 1, pp. 553–568.
12. W. D. Geppert, C. Naulin, M. Costes, G. Capozza, L. Cartechini, P. Casavecchia and G. G. Volpi, *J. Chem. Phys.* **119**, 10607 (2003).

13. X. Yang, J. Lin, Y. T. Lee, D. A. Blank, A. G. Suits and A. M. Wodtke, *Rev. Sci. Instrum.* **68**, 3317 (1997).
14. C. C. Wang, J. Shu, J. J. Lin, Y. T. Lee and X. Yang, *J. Chem. Phys.* **117**, 153 (2002).
15. J. J. Lin, Y. Chen, Y. Y. Lee, Y. T. Lee and X. Yang, *Chem. Phys. Lett.* **361**, 374 (2002).
16. S.-H. Lee, Y.-Y. Lee, Y. T. Lee and X. Yang, *J. Chem. Phys.* **119**, 827 (2003).
17. D. A. Blank, W. Sun, A. G. Suits, Y. T. Lee, S. W. North and G. E. Hall, *J. Chem. Phys.* **108**, 5414 (1998).
18. W. Sun, K. Yokoyama, J. C. Robinson, A. G. Suits and D. M. Neumark, *J. Chem. Phys.* **110**, 4363 (1999), and references therein.
19. J. A. Mueller, B. F. Parsons, L. J. Butler, F. Qi, O. Sorkhabi and A. G. Suits, *J. Chem. Phys.* **114**, 4505 (2001).
20. J. C. Robinson, S. A. Harris, W. Sun, N. E. Sveum and D. M. Neumark, *J. Am. Chem. Soc.* **124**, 10211 (2002).
21. D. A. Blank, N. Hemmi, A. G. Suits and Y. T. Lee, *Chem. Phys.* **231**, 261 (1998).
22. N. Hemmi and A. G. Suits, *J. Chem. Phys.* **109**, 5338 (1998).
23. P. A. Willis, H. U. Stauffer, R. Z. Hinrichs and H. F. Davis, *Rev. Sci. Instrum.* **70**, 2606 (1999).
24. H. U. Stauffer, R. Z. Hinrichs, J. J. Schroden and H. F. Davis, *J. Chem. Phys.* **111**, 10758 (1999).
25. P. A. Willis, H. U. Stauffer, R. Z. Hinrichs and H. F. Davis, *J. Phys. Chem.* **A103**, 3706 (1999).
26. H. U. Stauffer, R. Z. Hinrichs, P. A. Willis and H. F. Davis, *J. Chem. Phys.* **111**, 4101 (1999).
27. R. Z. Hinrichs, P. A. Willis, H. U. Stauffer and H. F. Davis, *J. Chem. Phys.* **112**, 4634 (2000).
28. J. J. Schroden, M. Teo and H. F. Davis, *J. Chem. Phys.* **117**, 9258 (2002).
29. R. Z. Hinrichs, J. J. Schroden and H. F. Davis, *J. Am. Chem. Soc.* **125**, 860 (2003), and references therein.
30. W. L. Fitch and A. D. Sauter, *Anal. Chem.* **55**, 832 (1983).
31. P. Casavecchia, in *XX International Symposium on Molecular Beams* (Lisbon, Portugal, 8–13 June 2003), Book of Abstracts (Invited Lecture), p. 18.
32. G. Capozza, E. Segoloni, F. Leonori, A. Russo, G. G. Volpi and P. Casavecchia, in *XX International Symposium on Molecular Beams* (Lisbon, Portugal, 8–13 June 2003), Book of Abstracts, p. 151.
33. G. Capozza, E. Segoloni, F. Leonori, G. G. Volpi and P. Casavecchia, *J. Chem. Phys.* **120**, 4557 (2004).
34. G. Capozza, E. Segoloni and P. Casavecchia, to be published.
35. M. Alagia, N. Balucani, P. Casavecchia, D. Stranges and G. G. Volpi, *J. Chem. Soc., Faraday Trans.* **91**, 575 (1995).
36. J. J. Lin, S. Harich, Y. T. Lee and X. Yang, *Rev. Sci. Instrum.* **69**, 1642 (1998).

37. J. J. Lin, J. Shu, Y. T. Lee and X. Yang, *J. Chem. Phys.* **113**, 5287 (2000).
38. J. Shu, J. J. Lin, Y. T. Lee and X. Yang, *J. Chem. Phys.* **115**, 849 (2001).
39. J. Shu, J. J. Lin, Y. T. Lee and X. Yang, *J. Am. Chem. Soc.* **123**, 322 (2001).
40. C. C. Wang, J. Shu, J. J. Lin, Y. T. Lee and X. Yang, *J. Chem. Phys.* **116**, 8292 (2002).
41. J. Shu, J. J. Lin, Y. T. Lee and X. Yang, *J. Chem. Phys.* **113**, 9678 (2000).
42. J. J. Lin, Y. T. Lee and X. Yang, *J. Chem. Phys.* **113**, 1831 (2000).
43. J. Shu, J. J. Lin, C. C. Wang, Y. T. Lee and X. Yang, *J. Chem. Phys.* **115**, 842 (2001).
44. L. Beneventi, P. Casavecchia and G. G. Volpi, *J. Chem. Phys.* **85**, 7011 (1986).
45. N. Balucani, L. Beneventi, P. Casavecchia and G. G. Volpi, *Chem. Phys. Lett.* **180**, 34 (1991); N. Balucani, L. Beneventi, P. Casavecchia, D. Stranges and G. G. Volpi, *J. Chem. Phys.* **94**, 8611 (1991).
46. G. H. Wannier, *Phys. Rev.* **90**, 817 (1953). See also: T. Fiegele, G. Hanel, I. Torres, M. Lezius and T. D. Märk, *J. Phys. B: At. Mol. Opt. Phys.* **33**, 4263 (2000).
47. H. Deutsch, K. Becker, S. Matt and T. D. Märk, *Int. J. Mass Spectrom.* **197**, 37 (2000).
48. S. J. Sibener, R. J. Buss, C. Y. Ng and Y. T. Lee, *Rev. Sci. Instrum.* **51**, 167 (1980).
49. S. G. Lias, J. E. Bartmess, J. F. Liebman, J. L. Holmes, R. D. Levin and W. G. Mallard, *J. Phys. Chem. Ref. Data, Suppl.* **1**, **17**, 1–861 (1988).
50. S. Willitsch, L. L. Imbach and F. Merkt, *J. Chem. Phys.* **117**, 1939 (2002).
51. K. Liu, *Int. Rev. Phys. Chem.* **20**, 189 (2001).
52. L. Cartechini, A. Bergeat, G. Capozza, P. Casavecchia, G. G. Volpi, W. D. Geppert, C. Naulin and M. Costes, *J. Chem. Phys.* **116**, 5603 (2002).
53. A. Miller, R. E. Mitchell, M. D. Smooke and R. J. Kee, *Proceedings of the 19th International Symposium on Combustion* (The Combustion Institute, Pittsburgh, 1982), p. 181; A. Garo, P. R. Westmoreland, J. B. Howard and J. P. Longwell, *Combust. Flame* **72**, 271 (1988).
54. J. Warnatz, H. Bockhorn, A. Moser and H. W. Wenz, *Proceedings of the 19th International Symposium on Combustion* (The Combustion Institute, Pittsburgh, 1982), p. 197.
55. D. J. Hucknall, *Chemistry of Hydrocarbon Combustion* (Chapman Hall, New York, 1985), p. 199.
56. P. R. Westmoreland, J. B. Howard and P. J. Longwell, *Proceedings of the 21st International Symposium on Combustion* (The Combustion Institute, Pittsburgh, 1988), p. 773.
57. C. K. Westbrook and F. L. Dryer, *Proceedings of the 18th International Symposium on Combustion* (The Combustion Institute, Pittsburgh, 1981), p. 749; J. Warnatz, *ibid.* p. 369.
58. J. Peeters, S. Vanhaelemeersch, J. Van Hoeymissen, R. Borms and D. J. Vermeulen, *J. Phys. Chem.* **93**, 3892 (1989).

59. C. E. Canosa-Mas, M. Ellis, H. M. Frey and R. Walsh, *Int. J. Chem. Kinet.* **16**, 1103 (1984); W. Hack, M. Koch, H. Gg. Wagner and H. Wilms, *Ber. Bunsen-Ges. Phys. Chem.* **92**, 674 (1988).
60. U. Alkemade and K. H. Homann, *Z. Phys. Chem.* (Munich) **19**, 161 (1989).
61. C. H. Wu and R. D. Kerr, *J. Phys. Chem.* **91**, 6291 (1987); P. R. Westmoreland, A. M. Dean, J. B. Howard and P. J. Longwell, *J. Phys. Chem.* **93**, 8171 (1989); J. A. Miller, J. V. Volponi, J. L. Durant, Jr., J. E. M. Goldschmidt, G. A. Fisk and R. J. Kee, *Proceedings of the 23rd International Symposium on Combustion* (The Combustion Institute, Pittsburgh, 1990), p. 187.
62. D. L. Osborn, *J. Phys. Chem.* **A107**, 3728 (2003).
63. K. Mahmud and A. Fontijn, *J. Phys. Chem.* **91**, 1918 (1987), and references therein.
64. C. P. Fenimore and G. W. Jones, *J. Chem. Phys.* **39**, 1514 (1963).
65. A. M. Schmoltner, P. M. Chu and Y. T. Lee, *J. Chem. Phys.* **91**, 5365 (1989).
66. J. Peeters, W. Boullart and I. Langhans, *Int. J. Chem. Kinet.* **26**, 869 (1994).
67. W. Boullart and J. Peeters, *J. Phys. Chem.* **96**, 9810 (1992).
68. L. B. Harding and A. F. Wagner, *J. Phys. Chem.* **90**, 2974 (1986).
69. J. Peeters, M. Schaekers and C. Vinckier, *J. Phys. Chem.* **90**, 6552 (1986).
70. J. V. Michael and A. F. Wagner, *J. Phys. Chem.* **A94**, 2453 (1990).
71. A. R. Clemo, G. L. Duncan and R. Grice, *J. Chem. Soc., Faraday Trans. 2*, **78**, 1231 (1982).
72. NIST Chemistry WebBook, 2002.
73. C. P. Fenimore and G. W. Jones, *Proceedings of the 9th International Symposium on Combustion* (The Combustion Institute, Pittsburgh, 1963), p. 597; C. K. Westbrook, F. L. Dryer and K. P. Schug, *Proceedings of the 19th International Symposium on Combustion* (The Combustion Institute, Pittsburgh, 1982), p. 153.
74. J. N. White and W. C. Gardiner, Jr., *J. Phys. Chem.* **83**, 562 (1979).
75. K. Brezinsky, *Prog. Energy Combust. Sci.* **12**, 1 (1986).
76. R. J. Cvetanović, *J. Chem. Phys.* **23**, 1375 (1955). See also Ref. 78.
77. K. Mahmud, P. Marshall and A. Fontijn, *J. Phys. Chem.* **91**, 1568 (1987); R. B. Klemm, F. L. Nesbitt, E. G. Skolnik, J. H. Lee and J. F. Smalley, *J. Phys. Chem.* **91**, 1574 (1987), and references therein.
78. R. J. Cvetanović and D. L. Singleton, *Reviews Chem. Int.* **5**, 183 (1984), and references therein.
79. A. M. Schmoltner, P. M. Chu, R. J. Brudzynski and Y. T. Lee, *J. Chem. Phys.* **91**, 6926 (1989).
80. J. R. Kanofsky and D. Gutman, *Chem. Phys. Lett.* **15**, 236 (1972).
81. H. E. Hunzinger, H. Knepe and H. R. Wendt, *J. Photochem.* **17**, 377 (1981).
82. U. C. Sridharan and F. Kaufman, *Chem. Phys. Lett.* **102**, 45 (1983).
83. J. F. Smalley, F. L. Nesbitt and R. B. Klemm, *J. Phys. Chem.* **90**, 491 (1986).

84. K. Kleinermauns and A. C. Luntz, *J. Phys. Chem.* **85**, 1966 (1981).
85. Y. Endo, S. Tsuchiya, C. Yamada, E. Hirota and S. Koda, *J. Chem. Phys.* **85**, 4446 (1986).
86. U. Bley, P. Dransfeld, B. Himme, M. Koch, F. Temps and H. Gg. Wagner, *22nd Symposium (International) on Combustion* (The Combustion Institute, Pittsburgh, 1988), p. 997
87. K. Yamaguchi, S. Yabushita, T. Fueno, S. Kato and K. Morokuma, *Chem. Phys. Lett.* **70**, 27 (1980).
88. M. Dupuis, J. J. Wendoloski, T. Takada and W. A. Lester, Jr., *J. Chem. Phys.* **76**, 481 (1982).
89. R. J. Buss, R. J. Baseman, G. He and Y. T. Lee, *J. Photochem.* **17**, 389 (1981).
90. M. Litorja and B. Ruscic, *J. Chem. Phys.* **108**, 6748 (1998).
91. J. M. Parson, K. Shobatake, Y. T. Lee and S. A. Rice, *Faraday Discuss. Chem. Soc.* **55**, 344 (1973).
92. G. N. Robinson, R. E. Continetti and Y. T. Lee, *J. Chem. Phys.* **92**, 275 (1990).
93. D. C. Clary, E. Buonomo, I. R. Sims, I. W. M. Smith, W. D. Geppert, C. Naulin, M. Costes, L. Cartechini and P. Casavecchia, *J. Phys. Chem.* **A106**, 5541 (2002) (Feature Article).
94. P. Casavecchia, N. Balucani, L. Cartechini, G. Capozza, A. Bergeat and G. G. Volpi, *Faraday Discuss.* **119**, 27 (2001).
95. R. I. Kaiser, *Chem. Rev.* **102**, 1309 (2002).
96. R. I. Kaiser, Y. T. Lee and A. G. Suits, *J. Chem. Phys.* **105**, 8705 (1996).
97. L. Cartechini, A. Bergeat, G. Capozza, P. Casavecchia, G. G. Volpi, W. D. Geppert, C. Naulin and M. Costes, *J. Chem. Phys.* **116**, 5603 (2003).
98. A. Bergeat and J.-C. Loison, *Phys. Chem. Chem. Phys.* **3**, 2038 (2001).
99. A. M. Mebel, W. M. Jackson, A. H. H. Chang and S. H. Lin, *J. Am. Chem. Soc.* **120**, 5751 (1998).
100. T. N. Le, H.-Y. Lee, A. M. Mebel and R. I. Kaiser, *J. Phys. Chem.* **A105**, 1847 (2001).
101. S. Harich, J. J. Lin, Y. T. Lee and X. Yang, *J. Chem. Phys.* **112**, 6656 (2000).
102. R. I. Kaiser, C. Ochsenfeld, M. Head-Gordon, Y. T. Lee and A. G. Suits, *J. Chem. Phys.* **106**, 1729 (1997).
103. E. Buonomo and D. C. Clary, *J. Phys. Chem.* **A105**, 2694 (2001).
104. G. Capozza, E. Segoloni and P. Casavecchia, unpublished results.
105. J. C. Robinson, N. E. Sveum and D. M. Neumark, *J. Chem. Phys.* **119**, 5311 (2003).
106. J.-H. Park, H. Lee, H.-C. Kwon, H.-K. Kim and Y.-S. Choi, *J. Chem. Phys.* **117**, 2017 (2002).
107. R. I. Kaiser, W. Sun, A. G. Suits and Y. T. Lee, *J. Chem. Phys.* **107**, 8713 (1997).

This page intentionally left blank

CHAPTER 8

INTERACTIONS OF VIBRATIONALLY-EXCITED MOLECULES AT SURFACES: A PROBE FOR ELECTRONICALLY NONADIABATIC EFFECTS IN HETEROGENEOUS CHEMISTRY

Alec M. Wodtke

*Department of Chemistry and Biochemistry,
University of California, Santa Barbara, California 93106, USA*

When molecules with low levels of vibrational excitation collide at metal surfaces, vibrational coupling to electron-hole pairs is not found to be strong unless incidence energies are high. However, there is accumulating evidence that coupling of large amplitude molecular vibration to metallic-electron degrees-of-freedom can be much stronger even at the lowest accessible incidence energies. As reaching a chemical transition state also involves large amplitude vibrational motion, we pose the basic question: are electronically nonadiabatic couplings important at transition states of reactions at metal surfaces? We have indirect evidence in at least one example that the dynamics and rates of chemical reactions at metal surfaces may be strongly influenced by electronically nonadiabatic coupling. This implies that theoretical approaches relying on the Born–Oppenheimer approximation may not accurately reflect the nature of transition-state traversal in reactions of catalytic importance. Developing a predictive understanding of surface reactivity beyond the Born–Oppenheimer approximation represents one of the most important challenges to current research in physical chemistry. This paper reviews the experimental evidence concerning these and related topics.

Contents

1. Introduction	384
2. First Evidence of Born–Oppenheimer Breakdown	386
3. Born–Oppenheimer Breakdown in Surface Reactions	392
4. “Scattering the Transition State” from a Metal Surface	396
5. Measurements of Chemicurrent	403

6. Conclusions	405
Acknowledgments and Dedications	406
References	406

1. Introduction

The theory of chemical reactivity was written down in a modern form at least as early as 1936 by the late Henry Eyring and his co-workers.¹ Eyring recognized that all of the properties of a chemical reaction could be predicted by understanding the potential energy (hyper)-surface (potential energy surface) governing the atomic motion. Although the technology of quantum computation was still primitive, Eyring not only carried out some of the first calculations of a reactive potential energy surface,² discovering along the way the pitfalls of calculations near the transition states,^a he was one of the first to attempt classical trajectory calculations as a means to determine reaction probabilities³ (see Fig. 1). His insights came to fruition in his landmark work on the absolute theory of reaction rates.⁴

During the intervening decades, computational methodologies have advanced further than even the visionary young Eyring could have foreseen. *Ab initio* electronic structure calculations^{5,6} have become so sophisticated that one may now even carry them out over the Internet.⁷ Highly efficient methods of calculating either quantum or classical dynamics on potential hyper-surfaces are now available and widely used.⁸ Indeed, Eyring and the legacy he left have provided us with a way of looking at the chemical reaction that has endured and is likely to endure without substantive modification into the foreseeable future.

The topic of this review, reactions at metal surfaces, has been in general treated in a similar way to gas-phase reactivity. High level *ab initio* electronic structure methods are used to construct potential energy surfaces of catalytically important surface reactions in reduced dimensions. Once a “chemically accurate” potential surface is available, quantum or classical dynamics may be carried out in order to more deeply understand the microscopic nature of the reaction.

Central to the modern approach to chemical reactivity as dynamics on a potential energy surface, is the Born–Oppenheimer approximation.⁹

^aEyring’s earliest attempts were on the prototypical hydrogen exchange reaction and produced a well near the transition state that was later found to be an artifact, reflecting the difficulty of accurate electronic structure calculations in those days. This well is still fondly known as Lake Eyring!

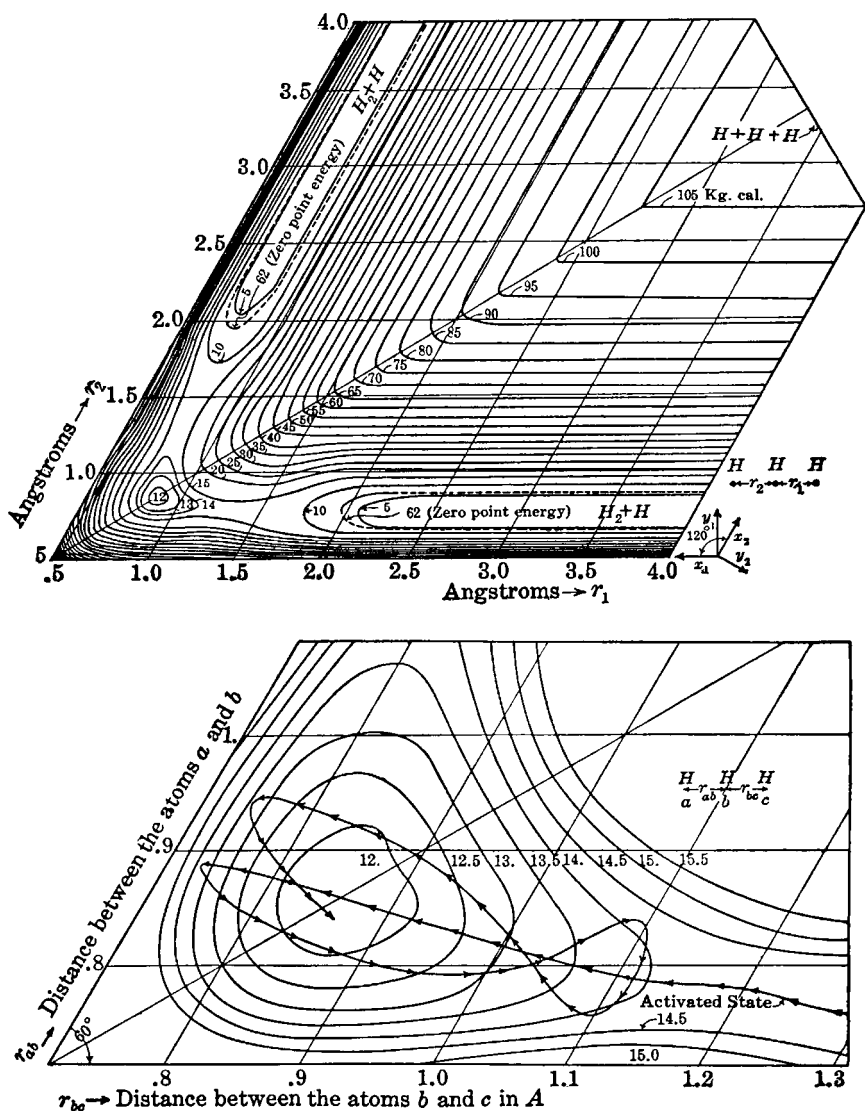


Fig. 1. Potential energy surface and classical trajectory calculations on the $\text{H} + \text{H}_2$ hydrogen exchange reaction. Note the orbiting trajectory in the vicinity of "Lake Eyring". Despite the unrealistic nature of a well near the transition state of this reaction, many of the modern ideas of chemical reaction theory can be seen in action already in this work. (See Ref. 1.)

According to this very powerful idea the average motion of the electrons re-adjusts instantaneously as heavy nuclei progress through chemical rearrangement. The validity of this approximation stems from the dramatic contrast in timescales for electron motion in comparison to nuclear motion. This is reflected in the quantum state energy spectrum. For example, in an isolated molecule or a gas-phase reactive system, electronic state energy separations are often very large compared to the energy separations of rovibrational-quantum levels, particularly if the reaction takes place on the ground electronic state. It is under these conditions that the Born–Oppenheimer approximation is most valid. In systems where electronic states approach or cross one another in energy space, transitions between electronic states may become possible and lead to a breakdown of the Born–Oppenheimer approximation.

Chemical reactions of molecules at metal surfaces represent a fascinating test of the validity of the Born–Oppenheimer approximation in chemical reactivity. Metals are characterized by a continuum of electronic states with many possible low energy excitations. If metallic electrons are transferred between electronic states as a result of the interactions they make with molecular adsorbates undergoing reaction at the surface, the Born–Oppenheimer approximation is breaking down.

How important the breakdown of the Born–Oppenheimer approximation is in limiting our ability to carry out *ab initio* simulations of chemical reactivity at metal surfaces is the central topic of this review. Stated more provocatively, do we have the correct theoretical picture of heterogeneous catalysis. This review will restrict itself to a consideration of experiments that have begun to shed light on this important question. The reader is directed to other recent review articles, where aspects of this field of research not mentioned in this article are more fully addressed.^{10–16}

2. First Evidence of Born–Oppenheimer Breakdown

Perhaps the first evidence for the breakdown of the Born–Oppenheimer approximation for adsorbates at metal surfaces arose from the study of infrared reflection–absorption line-widths of adsorbates on metals, a topic that has been reviewed by Hoffmann.¹⁷ In the simplest case, one considers the mechanism of vibrational relaxation operative for a diatomic molecule that has absorbed an infrared photon exciting it to its first vibrationally-excited state. Although the interpretation of spectral line-broadening experiments is always fraught with problems associated with distinguishing

homogeneous from inhomogeneous effects, some simple adsorbate systems appear to exhibit sufficiently rapid vibrational relaxation that the line-width is dominated by the relaxation of the adsorbate to the surface.

Persson and Persson suggested a simple model for understanding the line-broadening of CO on metals.¹⁸ Here it was recognized that CO binds to many metals by “back-bonding” where electron density from the metal flows into the π^* C–O anti-bonding orbital, creating a strong coupling between the M–CO bond and the C–O motion. Thus, as the CO bond vibrates, one expects electron-charge to oscillate in and out of the π^* orbital. This temporal and spatial oscillation of charge can be treated as a short range vibrational damping mechanism for CO vibration resulting in the excitation of metallic electrons. This model makes predictions that line-widths increase with degree of back-bonding, something that has been borne out at least qualitatively by experiment.¹⁷

More recently the application of sub-picosecond, time-resolved pump-probe methods revealed the timescale for vibrational relaxation of a diatomic molecule at a metal surface directly. See for example Refs. 19–21. In comparison to vibrational relaxation on NaCl salts,²² which occurs on the millisecond timescale, another relaxation mechanism is clearly at play. Theory of vibrational relaxation based on excitation of electron-hole pairs gave agreement with observed ps timescales for CO on copper.²³

Gas-surface scattering experiments have long played an important role in the investigation of the nature of the interactions of molecules with metal surfaces. One of the most significant experimental findings was also one of the simplest.^{24,25} Here, a molecular beam of nitric oxide (NO) was allowed to collide with a crystalline Ag(111) metal surface. The NO was seeded in a light carrier gas to control the incidence energy of the sample and the surface temperature could also be varied. A pulsed laser beam was used to probe population in selected quantum states of the scattered NO molecules. By varying the surface temperature and incidence energy while probing the scattered population in selected rotational levels of NO($v = 1$), the nature of the vibrational coupling to the metal surface could be observed.

Observed angular distributions were quasi-specular and scattered rotational distributions were strongly dependent upon the incidence energy, both observations indicating the direct nature of the interaction. The most important observation of the work was the approximately Arrhenius surface temperature dependence of the vibrational excitation probability, exhibiting an effective activation energy close to the vibrational excitation energy of the scattered molecule (see Fig. 2). The authors also showed that the

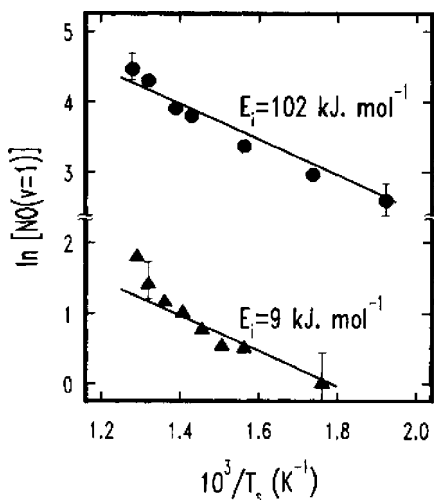


Fig. 2. Surface temperature dependence of the vibrational excitation of $\text{NO}(v = 0 \rightarrow 1)$ in collisions with a clean $\text{Ag}(111)$ surface. The observed thermal activation was attributed to hot electron-hole-pair recombination transferring energy to NO vibration. This work provided some of the first strong evidence that metal electrons can interact with an adsorbate molecule strongly enough to change its vibrational quantum numbers. (See Ref. 24.)

population of excited electron-hole pairs at an energy resonant with the $\text{NO}(0-1)$ vibrational spacing exhibited the same temperature dependence as that observed in the experiment. While still indirect, the implication was obvious: recombination of hot electron-hole pairs was responsible for vibrational excitation of the scattered molecules. This was the strongest evidence available at the time that thermally-excited electrons could interact strongly enough with nuclear motion to induce vibrational excitation in a molecule at the metal surface.

Much theoretical work went into trying to understand these results more completely. Newns constructed a simple 1D model that incorporated the idea of electrons hopping in and out of the π^* anti-bonding orbital of NO as the means by which hot electron-hole pairs could transfer energy to the NO molecule.²⁶ Using reasonable assumption, he was able to quantitatively reproduce the experimentally-observed surface temperature and incidence energy dependence.

However, others reached more ambiguous conclusions. Gates *et al.* developed a 2D model based on coupling NO vibration to surface phonons, but ignoring the possible role of electron-hole pairs, and successfully captured

the essential experimental results.^{27,28} Gross and Brenig also showed that it was not necessary to invoke hot electron-hole pairs to reproduce these experimental observations.²⁹⁻³¹ In these models, the potential energy surface was important in coupling NO vibration to surface phonon motion. Taking into account the softening of the NO bond upon bonding to Ag, model calculations could account for most of the characteristics of the vibrational exchange.

In the meantime other experiments have also improved our range of observational results. For example, Watts *et al.* carried out experiments very similar to the NO/Ag(111) experiments described above.³² A critical difference in this work was the substitution of Cu(110) in place of the Ag(111). Despite the chemically distinct metal surface, nearly identical results were obtained as those in Refs. 24 and 25, including surface temperature and incidence energy dependence. While it is not unlikely that the bond softening of NO is similar on Ag(111) and Cu(110), there is no *a priori* reason to believe that these two metals would exhibit the same incidence energy and surface temperature dependence in vibrational excitation experiments. More importantly, there has not been a theoretical attempt to explain why these two chemically distinct systems behave so similarly within the context of electronically adiabatic models.

On the other hand, the similarity between metals is a characteristic of the electron-mediated vibrational energy transfer models. Here one must only calculate the population of excited electron-hole pairs at the energy of vibrational excitation, a quantity that is quite similar for many metals.^b

Theoretical advances were also forthcoming. By comparing different models, some involving electron-hole pairs and others without, Gross and Brenig were able to make predictions about the incidence energy dependence of vibrational de-excitation,²⁹ a characteristic of the interactions that had not yet been experimentally investigated. According to their work, observation of a strong incidence energy dependence to the vibrational de-excitation probability would be an expected characteristic of electron-mediated vibrational energy transfer.

Experiments to measure the vibrational de-excitation of NO at a metal surface are much more challenging than those already described. One needs both a source of vibrationally-excited molecules as well as means of detecting the results of the scattering interaction, necessitating the use

^bUnless one includes the role of surface electronic states, only differences in the density of electronic states near the Fermi level is expected to distinguish one metal from another.

of at least two lasers. Furthermore, one might think that simply exciting $\text{NO}(v = 0 \rightarrow 1)$ would suffice to produce a vibrationally-excited sample. This approach fails however, due to a trivial background problem. When one attempts to detect the vibrationally-relaxed sample in $v = 0$, ambient NO in the experimental chamber obscures the results.

These problems were recently overcome. By using overtone excitation of $\text{NO}(v = 0 \rightarrow 2)$ as the means of preparing a sample of vibrationally-excited molecules, both excitation to $v = 3$ and de-excitation to $v = 1$ resulting from collisions with a Au(111) surface could be observed without difficulty.³³ The authors systematically investigated the incidence energy and surface temperature dependence of vibrational excitation and de-excitation. A strong incidence energy dependence to the vibrational de-excitation was indeed observed providing additional evidence as to the importance of electron-mediated vibrational energy transfer.

In the light of the accumulated evidence, it appears quite likely that the scattering of nitric oxide from metals does induce electronic transitions which represents a fundamental breakdown of the Born–Oppenheimer approximation. Clearly this falls in the category of electronically nonadiabatic phenomena that we set out to understand. But there is a broader question. Is the Born–Oppenheimer breakdown significant within a broader chemical context?

This question has been the subject of theoretical study, in particular by Tully and Head-Gordon. They developed one of the few methods that has the ability to go beyond the Born–Oppenheimer approximation, a method called “Molecular Dynamics with Electron Friction”.^{34–37} This approach assumes that electronic excitations that may be induced by molecular interactions are highly delocalized, so that the continuum of electronic potential energy surfaces on which nuclear motion occurs are all of similar shape, and can be replaced by a single, effective potential. Nonadiabatic energy exchange between nuclear and electronic degrees-of-freedom is then represented by frictional and fluctuating forces on the nuclei, and no explicit electronic dynamics are required.

Using this model they have tried to look at important chemical processes at metal surfaces to deduce the role of electronic nonadiabaticity. In particular, they have tried to evaluate the importance of electron-hole-pair excitation in scattering, sticking and surface mobility of CO on a Cu(100) surface.^{36,37} Those studies indicated that the magnitude of energy transferred by coupling to the electron bath was significantly less than that coupled to phonons. Thus the role of electron-hole-pair excitation in

determining the sticking probability was found to be small in this work.³⁶ In a similar way, coupling of electron-hole pairs to molecular rotation and translation was likewise found to be weak and the dominant interactions controlling exchange of these degrees-of-freedom with the surface were associated with phonons. These results are also not inconsistent with the results presented above. Indeed, the largest interaction of electron-hole pairs was with the molecular vibrations.³⁷

So, it might appear that electronically nonadiabatic interactions are important for vibrational energy transfer, but perhaps for little else. This alone might be of some significance to chemistry. The rate at which vibrational energy contained in molecular adsorbates comes to thermal equilibrium with the metal surface is undoubtedly of importance to an understanding of surface reactions. But there are more fundamental questions that we have up until now ignored. Up to this point we have taken for granted that vibrational exchange with electronic degrees-of-freedom is a good indicator of Born–Oppenheimer breakdown. Specifically, we assume that observation of vibrational transitions in NO from $v = 0$ to $v = 1$ tells us something about the validity of the Born–Oppenheimer approximation in surface chemistry.

Clearly, this view can provide only a general guide to this important question. There are fundamental differences between the nuclear motion associated with a surface reaction when compared to molecules making transitions between their lowest vibrational states. Surface chemical reactions, indeed all reactions, are characterized by large amplitude nuclear motion. An obvious example is the dissociative adsorption of a diatomic, which requires vibrational excursions comparable to, indeed greater than the equilibrium bond length. Thermally activated dissociative adsorption must be characterized by “multiple assaults on the summit” involving large amplitude nuclear motion that might be differently coupled to the electron bath than molecules that remain near their equilibrium geometries.

Furthermore, large amplitude “vibrational” motions are characterized by fundamental changes in the nature of the electronic structure of the system. Dissociation of many closed shell molecules, for example HCl, transforms two atoms cohabitating in a fashion that repels electrons into a non-interacting pair of “electron-attractors”.^c This picture suggests that molecules subjected to the rigors of large amplitude vibrational motion

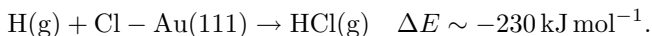
^cThe electron affinity of HCl is indeed negative, whereas the combined electron affinity of H and Cl atom exceed three eV.

typical of reacting systems might undergo the kind of electron hopping envisioned by Newns (see Ref. 26) with much greater alacrity than molecules residing near their equilibrium structures.

3. Born–Oppenheimer Breakdown in Surface Reactions

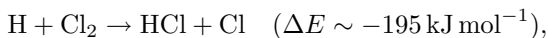
Experimental probes of Born–Oppenheimer breakdown under conditions where large amplitude vibrational motion can occur are now becoming available. One approach to this problem is to compare theoretical predictions and experimental observations for reactive properties that are sensitive to the Born–Oppenheimer potential energy surface. Particularly useful for this endeavor are recombinative desorption and Eley–Rideal reactions. In both cases, gas-phase reaction products may be probed by modern state-specific detection methods, providing detailed characterization of the product reaction dynamics. Theoretical predictions based on Born–Oppenheimer potential energy surfaces should be capable of reproducing experiment. Observed deviations between experiment and theory may be attributed to Born–Oppenheimer breakdown.

An interesting body of work merits the reader’s attention concerning the Eley–Rideal reaction of H-atom abstraction of chlorine atoms adsorbed on gold^{38–41}:



The energetics of the Eley–Rideal reaction ($\Delta E \sim -230 \text{ kJ mol}^{-1}$) are well established.⁴² Here, the highly exoergic reaction forming gas-phase HCl was probed by time-of-flight velocity measurements,^{39,41} scattering angular distributions,^{39,41} and state-selective laser spectroscopy.^{39–41}

Despite the large exoergicity, less than about 100 kJ mol^{-1} appears as HCl translation, rotation or vibration. On average, 60 kJ mol^{-1} appears as HCl translation, 30 kJ mol^{-1} appears as HCl vibration (peaks at $v = 1$) and 10 kJ mol^{-1} as rotation.³⁹ It was argued in Ref. 39 that despite possessing similar energetics, the Eley–Rideal reaction is qualitatively different than the gas-phase reaction:



where the vibrational population distribution of HCl peaks at $v = 3$.⁴³ Strong coupling of HCl vibration to metal electronic motion was mentioned as the most likely explanation of the apparent absence of HCl product vibrational excitation.³⁹ It should also be noted that at least for low coverage, Cl bound to Au will possess an excess negative charge (Cl^-), which must

be transferred to the metal surface when HCl departs,³⁹ clearly indicating that electronically nonadiabatic effects may be important in this system.

It should also be mentioned that a theoretical model using an empirical LEPS potential energy surface has successfully been used to reproduce the vibrational population distribution of the products of this surface reaction.⁴⁰ This approach confines itself to the assumptions of the Born–Oppenheimer approximation and underscores one of the major questions remaining in this field: do we just need better Born–Oppenheimer potential surfaces or do we need a different theoretical approach?

Luntz and co-workers have recently carried out an impressive study that follows in the spirit of the Eley–Rideal work.⁴⁴ Specifically, laser-assisted recombination of N-atoms desorbing to form gas-phase N₂ on Ru(0001) was investigated. Experimental measurements of state-selectively detected N₂ recoiling from the surface recombination event were obtained using resonance enhanced multiphoton ionization and ion time-of-flight methods. In this way translational energy distributions of individual rovibrational states could be obtained experimentally. In addition, N₂-vibrational population distributions could be derived.

This reaction is an interesting test of the modern approach to chemical reactivity. DFT calculations have been used to construct a potential energy surface for this reaction, which is reproduced in Fig. 3(c).⁴⁵ One can see that the transition state for this reaction occurs at an N–N separation of $\sim 1.85X$. Furthermore the energy release from the transition state to products is very large (250 kJ mol^{-1}).

From the point of view of associative desorption, this reaction is an early barrier reaction. That is, the transition state resembles the reactants.⁴⁶ Early barrier reactions are well known to channel large amounts of the reaction exoergicity into product vibration. For example, the famous chemical-laser reaction, $\text{F} + \text{H}_2 \rightarrow \text{HF}(v) + \text{H}$, is such a reaction producing a highly inverted HF vibrational distribution.^{47–50} Luntz and co-workers carried out classical trajectory calculation on the Born–Oppenheimer potential energy surface of Fig. 3(c) and found indeed that the properties of this early barrier reaction do include an inverted N₂ vibrational distribution that peaks near $v = 6$ and extends to $v = 11$ (see Fig. 3(a)). In marked contrast to these theoretical predictions, the experimentally observed N₂ vibrational distribution shown in Fig. 3(d) is skewed towards low values of v . The authors of Ref. 44 also employed the electronic friction theory of Tully and Head-Gordon³⁵ in an attempt to model electronically nonadiabatic influences to the reaction. The results of these calculations are shown in

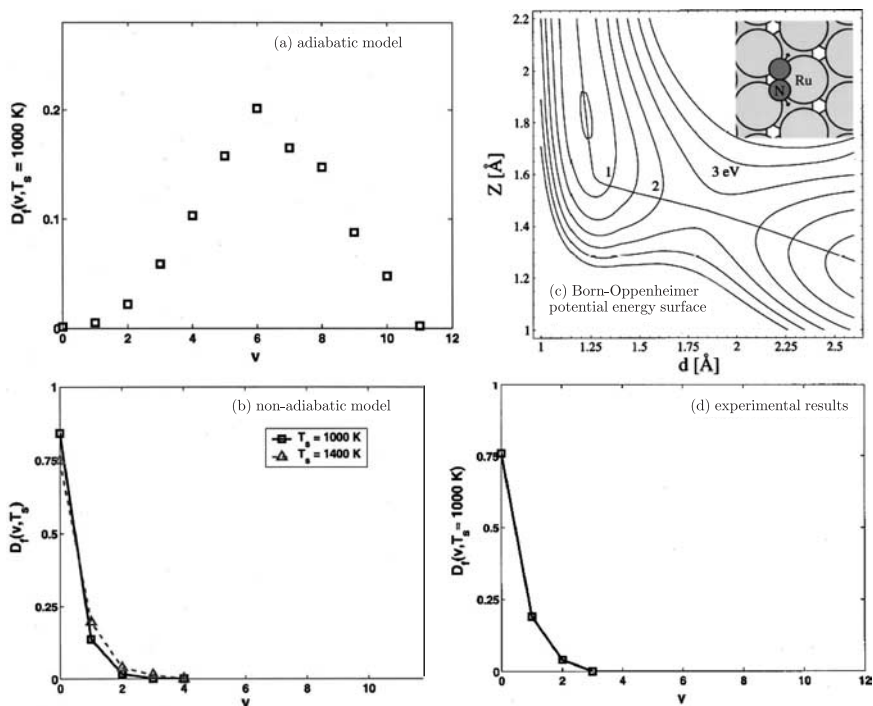


Fig. 3. Vibrational population distributions of N_2 formed in associative desorption of N-atoms from ruthenium. (a) Predictions of a classical trajectory based theory adhering to the Born–Oppenheimer approximation. (b) Predictions of a “molecular dynamics with electron friction” theory taking into account interactions of the reacting molecule with the electron bath. (c) Born–Oppenheimer potential energy surface. (d) Experimentally-observed distribution. The qualitative failure of the electronically adiabatic approach provides some of the best available evidence that chemical reactions at metal surfaces are subject to strong electronically nonadiabatic influences. (See Refs. 44 and 45.)

Fig. 3(b). The stunning agreement between experiment and theory suggests that electronically nonadiabatic effects strongly influence this reaction.

One of the most significant recent insights in surface chemical dynamics is the idea that the principle of detailed balance may be used to infer the properties of a dissociative adsorption reaction from measurements on an associative desorption reaction.^{51,52} This means, for example, that the observation of vibrationally-excited desorption products is an indicator that the dissociative adsorption reaction must be vibrationally activated, or vice versa; the observation of vibrationally-cold desorption products indicates little vibrational promotion of dissociative adsorption. In this spirit, it is

valuable to think carefully about the Luntz work from the point of view of detailed balance.

The picture of the reaction that emerges is quite interesting, suggesting that the newly-forming diatomic molecule whose bond is still dramatically stretched exhibits a tendency to release enormous amounts of vibrational energy into metal-electron degrees-of-freedom during vanishingly short times (see Fig. 4). This explains, at least qualitatively, the observation that the reaction probability for dissociative adsorption of N_2 to Ruthenium approaches only about 1% even when the available energy significantly exceeds the Born–Oppenheimer predicted reaction barrier.⁵³ Apparently, in the course of approaching the transition state, the reaction is subject to strong energy transfer phenomena from vibrational to metal-electron motion, an energy drain which naturally suppresses reaction. If this picture is correct, one must pity the N_2 molecule as it confronts the ruthenium surface. Not only does it have an uphill battle to reach the transition state, but upon its approach it is confronted with unprecedented energy loss channels that rob it of its reactive energy!

The nitrogen on ruthenium work is consistent with the observation made on the H/Cl/Au Eley–Rideal chemistry and, taken together, the implications of these two pieces of work are quite profound, suggesting that an accurate theory of surface reactions cannot be constructed without accounting for strong coupling between the reaction coordinate and the metals electron

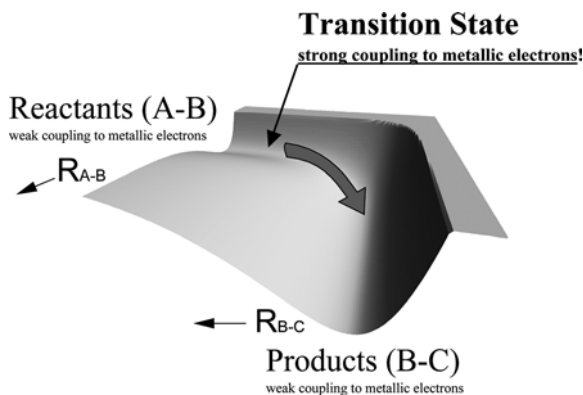


Fig. 4. Accumulating evidence is starting to show that molecules which undergo large amplitude vibration can interact strongly with metallic electrons in collisions and reactions at metal surfaces. This suggests that the Born–Oppenheimer approximation may be suspect near transition states of reactions at metal surfaces.

bath. These experiments provide some of the clearest indications that electronically nonadiabatic theories of chemical reactivity need to be developed before we will truly have an accurate theory of heterogeneous catalysis.

4. “Scattering the Transition State” from a Metal Surface

The work we have reviewed so far suggests that molecules that undergo large amplitude vibrational motion typical of passing through a transition state may interact much more strongly with metallic electrons than do vibrational ground-state molecules. Yet studies of the sort so far described are admittedly indirect. A proper theoretical treatment of surface chemistry involves many degrees-of-freedom and with technology available in the foreseeable future, it will remain necessary to carry out reduced dimensionality calculations. The Born–Oppenheimer approximation, is in fact an example of one way to reduce the number of (electronic) degrees-of-freedom. Thus, in some sense we should not be surprised when energy transfer to and from the “missing degrees-of-freedom” turns out to be important. However, there are other missing degrees-of-freedom, in particular phonons. Do molecules passing over transition states interact with phonons in important ways that have yet to be fully understood? In addition to the class of questions associated with ignoring certain degrees-of-freedom, we must also ask more mundane questions about the work described in the last section. Specifically is the Born–Oppenheimer potential energy surface accurate enough. In the light of these considerations, it is clearly useful to attempt more direct kinds of experiments that test the important ideas emerging from the study of surface chemistry.

One implication of the N_2/Ru work is that molecules in high states of vibrational excitation, that is in the process of bond formation, exchange energy with metallic electrons in a remarkable way. Recombining N-atoms that are expected to form N_2 in vibrational states as high as $v = 11$ (with more than 200 kJ mol^{-1} of vibrational energy) are observed primarily in $v = 0$. The time available for this to take place is on the order of tens of fs. Can we find evidence of such remarkable energy transfer events?

Experiments designed to probe these ideas have been carried out for NO colliding in high vibrational states on Au(111). Before considering the results of these experiment, let us first look at how vibration might lead to unusual interactions with metal electrons. Molecules in vibrational states as high as $\text{NO}(v = 15)$ undergo nuclear excursions that influence their

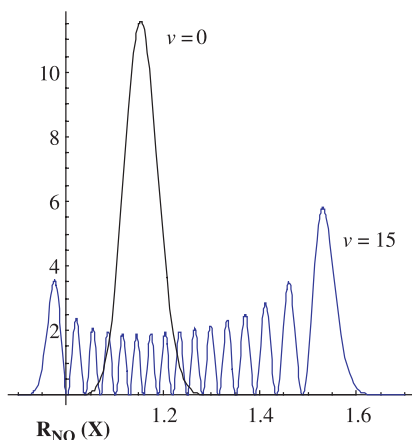


Fig. 5. Square of the vibrational wavefunction of NO for $v = 0$ and $v = 15$. Vibrational amplitude in $v = 15$ induces large changes in the electronic structure of the molecule, when one compares the molecule at its outer turning point, where it is already beginning to resemble separated atoms.

electronic properties. Figure 5 shows the square of the vibrational wave functions for NO($v = 0$) and NO($v = 15$). In contrast to the $v = 0$ state whose vibrational amplitude is in the order of $0.1X$, the $v = 15$ state exhibits vibrational amplitudes close to the magnitude of the bond length, that is greater than $1X$. To get a feeling for the kind of phenomena that can be important for large amplitude vibrational motion, consider the *ab initio* quantum chemical calculations shown in Fig. 6.⁵⁴ Here one sees the relative energies of the NO molecule compared to one with an electron attached, as a function of internuclear separation. In Fig. 6(b), one can see that the energy difference between the two potential curves (denoted as the vertical electron binding energy) is a strong function of the internuclear separation.^d This indicates that with respect to electron transfer, highly vibrationally-excited NO is a “schizophrenic” molecule. Near its outer turning point, it may attach an electron releasing more than 2 eV of energy. Near the inner turning point, the molecule exhibits a repulsion energy towards electrons of a similar magnitude.

^dThis idea harkens back to ideas originally put forward by Dennis Jacobs when considering the scattering of NO⁺ and NO⁻ from metal surfaces. See for example J. W. Qian, D. C. Jacobs and D. J. Tannor, *J. Chem. Phys. (USA)* **103**, 10764–10778 (1995) and references therein.

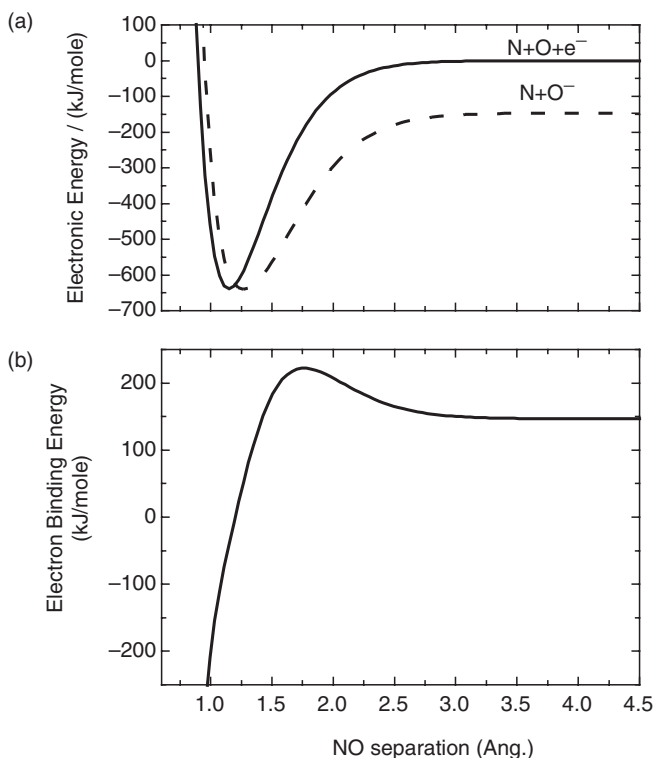


Fig. 6. *Ab initio* calculation on large amplitude NO electron transfer. More detailed information on the change in the chemical nature of a molecule, subject to large amplitude vibrational motion. In the upper panel, one sees the quantum chemical calculation of the NO molecule undergoing dissociation compared to the NO^- molecule. The energy difference between the two potential curves, called the vertical electron binding energy, varies strongly with internuclear separation. This NO is a schizophrenic molecule with respect to electron transfer: at its outer turning point, strongly desiring attachment, whereas at its inner turning point, behaving repulsively. (From Refs. 54 and 59.)

This insight has important implications for the electron hopping induced vibrational energy transfer picture put forward by Newns.²⁶ Figure 7(b) reproduces the Newns model of electron-mediated vibrational energy transfer of NO at Ag(111) described above. Two electronic states of the system are important in this model. The ground state represents the interaction of a neutral NO molecule with the metal surface. This interaction is relatively weak, resulting in a shallow physisorption well. The excited electronic state of the system is formed by removing an electron from the Fermi level of the metal and attaching it to the NO molecule. The interaction of the ion

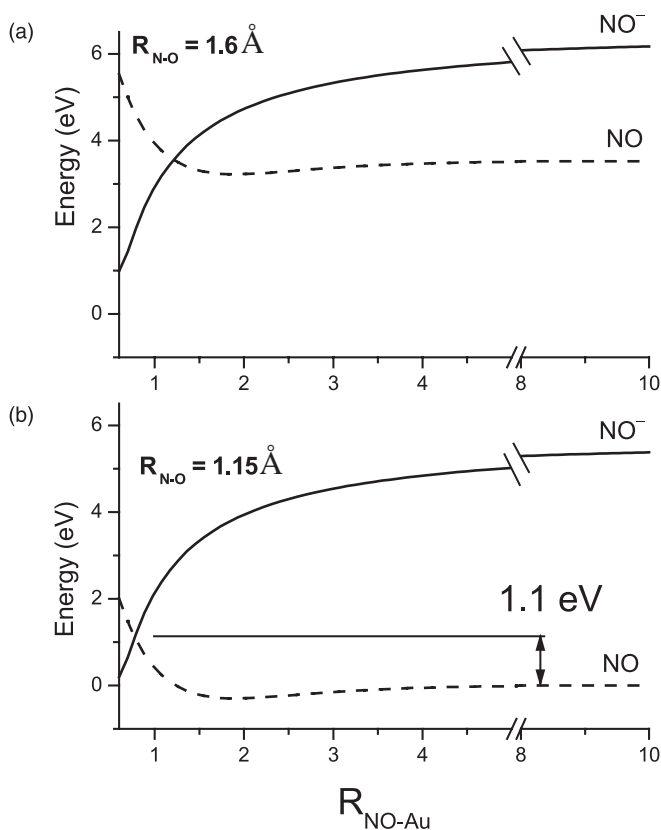


Fig. 7. The application of the Newns model with stretched molecules. (a) When the NO bond is stretched the incoming molecule behaves as if it exhibits a larger electron binding energy. This has the effect of removing the barrier to electron transfer. (b) The interaction of the neutral and anionic molecules with a metal surface results in a barrier to electron transfer of about 1.1 eV.

with its image charge lowers this state's energy as the molecule approaches the surface. The point at which the two curves cross is influenced strongly by the work function of the metal and the electron binding energy to the molecule. For NO near its equilibrium bond length ($R_{\text{NO}} = 1.15 \text{ \AA}$), the electron binding energy is very small and a barrier to the crossing associated with electron hopping results. By comparison, when the molecule is stretched, approaching the outer turning point of a high vibrational state ($R_{\text{NO}} = 1.6 \text{ \AA}$), the much larger electron binding energy eliminates the Newns-like barrier.

These considerations suggest a possible mechanism for energy transfer between metallic electrons and large amplitude vibration. First of all, it is clear that at low incidence energies, only molecules near the outer turning point to vibration may accept an electron. When, for example, an electron near the Fermi level is transferred to the NO molecule near its outer turning point, the compression of the NO bond has the effect of raising the potential energy of the electron far above the Fermi level. How far above the Fermi level it may go is dictated by the change in vertical electron binding energy with internuclear separation. The electron may now detach from the NO^- and enter unoccupied energy levels of the metal far above the Fermi level.

This model, which is a 2D extension of the 1D Newns picture, predicts several important things. First, it predicts that vibrational energy exchange will be possible at low incidence energies, in stark contrast to electron-mediated vibrational energy transfer in low vibrational states. Second, it implies that large amounts of vibrational energy may be converted to metallic electron excitation as the range of electronic excitation depends so strongly on internuclear vibration.

Figure 8 shows the results of an experiment designed to observe these effects. Employing stimulated emission pumping,^{55–57} highly vibrationally-excited NO was prepared in states as high as $v = 15$ and state-to-state scattering experiments were carried out on a Au(111) surface.^{58–62} By seeding the NO in a heavier carrier gas, it was possible to lower the incidence energy to 5 kJ mol^{-1} . State-selective laser detection methods were used to make measurements from which the scattered vibrational state distribution could be derived.

The scattered vibrational population distribution is remarkable. First of all, only a small fraction of the prepared population remains in the initial vibrational state, indicating that the survival probability is at most a few percent. At this low incidence energy, similar experiments carried out with $\text{NO}(v = 2)$ scattering from Au(111) were unable to detect vibrationally-inelastic processes, that is the vibrational survival probability is near unity.³³

Even more remarkable, vibrational relaxation of $\text{NO}(v = 15)$ on Au(111) is characterized by profound multi-quantum vibrational relaxation. Specifically, the most probable vibrational scattering channel releases more than 150 kJ mol^{-1} . Vibrational relaxation events exchanging as many as 10 vibrational quanta are observed. It appears likely that even more vibrational quanta can be exchanged with significant efficiency, but background problems prevented the observation of these channels. Thus the reported

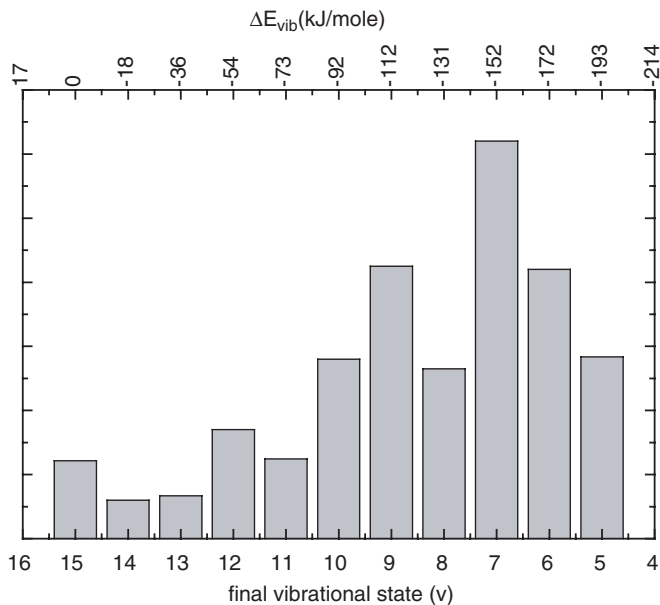


Fig. 8. Scattering the transition state from the surface. Measured vibrational distribution of NO resulting from scattering of laser-prepared NO($v = 15$) from Au (111) at $E_{\text{incidence}} = 5 \text{ kJ mol}^{-1}$. Only a small fraction of the laser-prepared population of $v = 15$ remains in the initial vibrational state. The most probable scattered vibrational level is more than 150 kJ mol^{-1} lower in energy than the initial state. Vibrational states below $v = 5$ could not be detected due to background problems. These experiments provide direct evidence that the remarkable coupling of vibrational motion to metallic electrons postulated by Luntz *et al.* can in fact occur. (See Refs. 44 and 59.)

vibrational population distribution terminates at below $v = 5$. Recently, Monte-Carlo wavepacket calculations employing the electron transfer mechanism described above have been able to reproduce the experimental results of Fig. 8.⁶³

Angular distributions of the scattered products were also measured in this work by translating the probe laser in front of the Au(111) surface. These were found to be sharply peaked and rotational distributions were strongly dependent upon incidence energy. These observations indicate a specular scattering mechanism. The timescale of interaction for specular scattering events is similar to that of surface chemical reactions N-atom recombination on Ru. In the light of these observations, the interpretations of Luntz and co-workers regarding the electronically nonadiabatic effects in Haber–Bosch chemistry appear to be supported.⁴⁴

Further evidence for strong coupling between large amplitude vibration and metallic electrons was found by carrying out similar experiments with an insulator surface where one expects and sees that these remarkable vibrational relaxation processes shut down.^{58,59} In this work vibrational relaxation of $\text{NO}(v = 12)$ was investigated on a LiF crystalline surface. Incidence energy and surface temperature were varied to help reveal the nature of the energy transfer mechanism. The results at two surface temperatures and incidence energies between 5 and 75 kJ mol^{-1} are presented in Fig. 9. Notice the large survival probability for the initially prepared state under all conditions. In dramatic contrast to the results on a metallic surface, here little vibrational energy transfer is observed. Also different from electron-mediated processes operative in

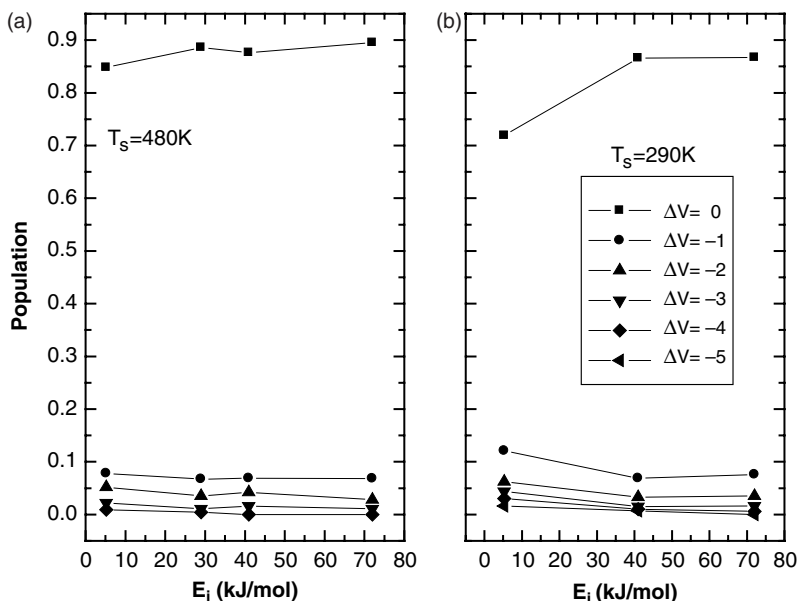


Fig. 9. Incidence energy dependence of the vibrational state population distribution resulting when $\text{NO}(v = 12)$ is scattered from LiF(001) at a surface temperature of (a) 480 K, and (b) 290 K. Relaxation of large amplitude vibrational motion to phonons is weak compared to what is possible on metals. Increased relaxation at the lowest incidence energies and surface temperatures are indicators of a trapping/desorption mechanism for vibrational energy transfer. Angular and rotational population distributions support this conclusion. Estimations of the residence times suggest that coupling to phonons is significant when residence times are only as long as ps. (See Ref. 58.)

collisions at metals, here one sees little or no dependence on incidence energy.

Despite the lack of vibrational energy transfer observed on the insulator surface in comparison to metals, these experiments do suggest that vibrational energy transfer to phonons may be substantially more efficient for molecules in large amplitude states of vibrational motion than present theory is capable of explaining. Examination of all of the data show in Fig. 9 does reveal that at the lowest incidence energies and surface temperatures, substantial (30%) loss of the population from the initial vibrational state is observed. Furthermore, under these conditions of surface temperature and incidence energy, angular distributions of scattered molecules approach a $\text{Cos}(\theta)$ -form, typical of trapping/desorption. Furthermore, rotational distributions of scattered molecules were found to be pseudo-Boltzmann with rotational temperatures approaching that of the surface.

Based on a knowledge of the binding energy of NO to LiF, one may estimate the residence time of the $\text{NO}(v = 12)$ molecules on the surface under these conditions to be in the ps range.⁵⁸ Observing 30% population loss in a few ps represents a rate of vibrational relaxation that is many orders of magnitude faster than has been reported for diatomic molecules relaxing from $v = 1$ on salt crystals, suggesting further theoretical and experimental work is needed to fully understand how large amplitude vibrational motion couples to solid phonons.

Figure 10 summarizes the basic picture emerging from these experiments. Transition from the ground electronic state to an anionic state which is strongly attractive to the metal surface can be accomplished by high translational energy when vibrational excitation is low, shown as a black trajectory with yellow peaks. When vibrational motion is highly excited, even low translational energies allow transition to the anionic state, shown as the red trajectory.

5. Measurements of Chemicurrent

Although it falls somewhat out of the scope of this paper and has furthermore been reviewed comprehensively recently,¹⁶ it would be remiss to overlook the exciting new work on chemicurrents. As we have seen for vibrational energy transfer, it is also observed that dissipation of chemical energy released in exothermic reactions at metal surfaces may happen adiabatically by creation of excited phonons or nonadiabatically by excitation of

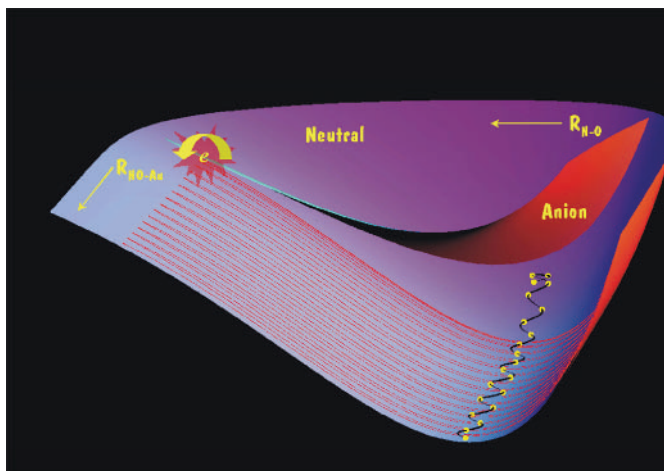


Fig. 10. The emerging picture of electronically nonadiabatic interactions of NO molecule scattering at a metal surfaces. Transition from the ground electronic state to an anionic state which is strongly attractive to the metal surface can be accomplished by high translational energy when vibrational excitation is low (black trajectory). When vibrational motion is highly excited, even low translational energies allow transition of the anionic state (red trajectory). Recently, Monte-Carlo wavepacket calculations have been carried out which tend to support this picture.⁶³

the electronic system of the metal or the reactants. In the past decades, the only direct experimental evidence for such nonadiabatic reactions has been exoelectron emission into vacuum and surface chemiluminescence which are observed in a special class of very exothermic reactions.

Recently a novel experimental approach using Schottky diodes with ultra-thin metal films (see Fig. 11) makes direct measurement of reaction-induced hot electrons and holes possible. See for example Refs. 64 and 65. The chemical reaction creates hot charge carriers which travel ballistically from the metal film towards the Schottky interface and are detected as a chemicurrent in the diode. By now, such currents have been observed during adsorption of atomic hydrogen and deuterium on Ag, Cu and Fe surfaces as well as chemisorption of atomic and molecular oxygen, of NO and NO₂ molecules and of certain hydrocarbons on Ag. Similar results have been found with metal-insulator-metal (MIM) devices, which also show chemi-currents for many exothermic surface reactions.^{64–68}

Interestingly, the efficiency for producing hot electrons scales with the reaction exoergicity.⁶⁴ A recent theoretical treatment of such devices has shown that the efficiency with which H-atom adsorption on Cu(111)

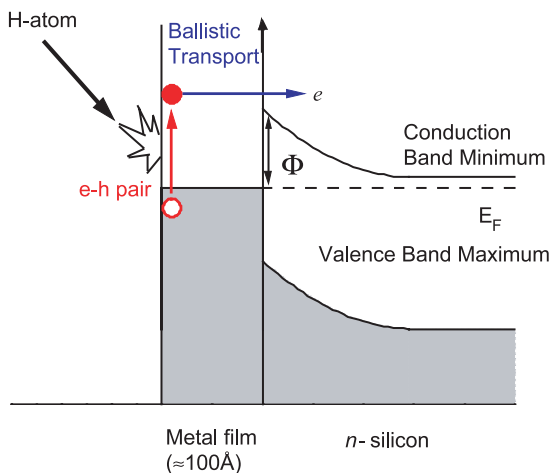


Fig. 11. Schottky diode device used for measurement of chemicurrents. Highly exoergic surface reactions like adsorption of an atom to the surface produce excited electrons and holes. Some of these electrons are able to surmount the Schottky barrier Φ and arrive at the semiconductor conduction band. This results in a detectable chemicurrent. (From Ref. 64.)

produced excited metallic electrons with energies above 100 kJ mol^{-1} is near unity.⁶⁹ A new theoretical approach based on analogies with theories of X-ray core-level spectroscopy has given qualitatively similar results.⁷⁰

6. Conclusions

There is an accumulating and persuasive body of evidence suggesting the validity of the Born–Oppenheimer approximation may be suspect for large amplitude vibrational motion including motion over chemical transition states in reactions at metal surfaces. It is now clear that at least for some reactions at metals including reactions of significant catalytic importance, theories of chemical reactivity that go beyond the Born–Oppenheimer approximation are required. It is perhaps too early to say whether the evidence that has been found so far represents an interesting conversation-piece within the field of heterogeneous catalysis or whether, they are just a hint of a more general chemical reality. The future will surely lead to studies similar in method to those presented here, applied to a wider variety of chemical reactions. New experimental methods designed to probe more electronically nonadiabatic effects in heterogeneous reactions will surely be

developed. Initial forays into the theory of non-Born–Oppenheimer chemical reactivity have already met with some success. Doubtless, more successes await the dedicated theorist. At the root of this field of research lies the fundamental question: “Do we have a correct picture of heterogeneous reactivity?” Improving our understanding of chemical reactivity at metal surfaces represents one of the great remaining challenges in physical chemistry.

Acknowledgments and Dedications

I would like to dedicate this chapter to the memory of Prof. Henry Eyring for the inspiration that his life in chemistry provided to me personally. I was fortunate enough to have an advanced quantum mechanics class from him in 1981. That experience left a lasting impression. Thanks also to Alan Luntz, Dan Auerbach and Eric McFarland who provided figures and were kind enough to review the paper in advance of its publication. Some of the work described came from my laboratory and would not have been possible without the support of the Airforce Office of Scientific Research and the Department of Energy. Nor could it have been accomplished without the dedicated efforts of many individuals who worked at various times in my lab including: Michael Murphy, Jason White, Hong-Tao Hou, Huang Yuhui and Steven Gulding.

References

1. H. Eyring, J. Walter and G. E. Kimball, *Quantum Chemistry* (John Wiley and Sons, New York, 1944).
2. H. Eyring, H. Gershinowitz and C. E. Sun, *J. Chem. Phys.* **3**, 786 (1935).
3. J. Hirschfelder, H. Eyring and B. Topely, *J. Chem. Phys.* **4**, 170 (1936).
4. S. Glasstone, K. Laidler and H. Eyring, *The Theory of Rate Processes* (McGraw-Hill Book Company, 1941).
5. J. A. Pople, *Angew. Chem.-Int. Edit.* **38**, 1894–1902 (1999).
6. W. Kohn, *Rev. Mod. Phys.* **71**, 1253–1266 (1999).
7. H. Metiu, private communication.
8. J. M. Bowman and G. C. Schatz, *Annu. Rev. Phys. Chem.* **46**, 169–195 (1995).
9. M. Born and E. Oppenheimer, *Ann. Physik* **84**, 457 (1927).
10. A. Gross, *Surf. Sci.* **500**, 347–367 (2002).
11. A. Gross, *Surf. Sci. Rep.* **32**, 291–340 (1998).
12. J. Greeley, J. K. Norskov and M. Mavrikakis, *Annu. Rev. Phys. Chem.* **53**, 319–348 (2002).
13. F. Zaera, *Prog. Surf. Sci.* **69**, 1–98 (2001).
14. J. C. Tully, *Annu. Rev. Phys. Chem.* **51**, 153–178 (2000).

15. G. O. Sitz, *Rep. Prog. Phys.* **65**, 1165–1193 (2002).
16. H. Nienhaus, *Surf. Sci. Rep.* **45**, 3–78 (2002).
17. F. M. Hoffmann, *Surf. Sci. Rep.* **3**, 107–192 (1983).
18. B. N. J. Persson and M. Persson, *Solid State Commun.* **36**, 175–179 (1980).
19. J. D. Beckerle, R. R. Cavanagh, M. P. Casassa, E. J. Heilweil and J. C. Stephenson, *J. Chem. Phys. (USA)* **95**, 5403–5418 (1991).
20. M. Morin, N. J. Levinos and A. L. Harris, *J. Chem. Phys. (USA)* **96**, 3950–3956 (1992).
21. R. R. Cavanagh, T. A. Germer and J. C. Stephenson, *Vib. Spectrosc.* **9**, 77–83 (1995).
22. C. Huan-Cheng and G. E. Ewing, *Phys. Rev. Lett.* **65**, 2125–2128 (1990).
23. M. Head-Gordon and J. C. Tully, *J. Chem. Phys. (USA)* **96**, 3938–3949 (1992).
24. C. T. Rettner, F. Fabre, J. Kimman and D. J. Auerbach, *Phys. Rev. Lett.* **55**, 1904–1907 (1985).
25. C. T. Rettner, J. Kimman, F. Fabre, D. J. Auerbach and H. Morawitz, *Surf. Sci.* **192**, 107–130 (1987).
26. D. M. Newns, *Surf. Sci.* **171**, 600–614 (1986).
27. G. A. Gates and S. Holloway, *Surf. Sci.* **309**, 132–137 (1994).
28. G. A. Gates, G. R. Darling and S. Holloway, *J. Chem. Phys. (USA)* **101**, 6281–6288 (1994).
29. A. Gross and W. Brenig, *Surf. Sci.* **289**, 335–339 (1993).
30. A. Gross and W. Brenig, *Chem. Phys. (Netherlands)* **177**, 497–508 (1993).
31. A. Gross, Y. Chiba and W. Brenig, *Prog. Theor. Phys. Suppl.* 335–340 (1991).
32. E. K. Watts, J. L. W. Siders and G. O. Sitz, *Surf. Sci.* **374**, 191–196 (1997).
33. Y. Huang, A. M. Wodtke, H. Hou, C. T. Rettner and D. J. Auerbach, *Phys. Rev. Lett.* **84**, 2985–2988 (2000).
34. C. Springer, M. Head-Gordon and J. C. Tully, *Surf. Sci.* **320**, L57–L62 (1994).
35. M. Head-Gordon and J. C. Tully, *J. Chem. Phys. (USA)* **103**, 10137–10145 (1995).
36. J. T. Kindt, J. C. Tully, M. Head-Gordon and M. A. Gomez, *J. Chem. Phys. (USA)* **109**, 3629–3636 (1998).
37. J. C. Tully, M. Gomez and M. Head-Gordon, *J. Vac. Sci. Technol. A — Vac. Surf. Films* **11**, 1914–1920 (1993).
38. C. T. Rettner, D. J. Auerbach, J. C. Tully and A. W. Kleyn, *J. Phys. Chem. (USA)* **100**, 13021–13033 (1996).
39. C. T. Rettner, *J. Chem. Phys. (USA)* **101**, 1529–1546 (1994).
40. B. Jackson, M. Persson and B. D. Kay, *J. Chem. Phys. (USA)* **100**, 7687–7695 (1994).
41. C. T. Rettner and D. J. Auerbach, *Science (USA)* **263**, 365–367 (1994).
42. G. N. Kastanas and B. E. Koel, *Appl. Surf. Sci.* **64**, 235–249 (1993).
43. K. G. Anlauf, J. C. Polanyi, K. B. Woodall, Macdonal.Rg and D. S. Horne, *J. Chem. Phys. (USA)* **57**, 1561–1574 (1972).
44. L. Diekhoner, L. Hornekaer, H. Mortensen, E. Jensen, A. Baurichter, V. V. Petrunin and A. C. Luntz, *J. Chem. Phys. (USA)* **117**, 5018–5030 (2002).

45. M. J. Murphy, J. F. Skelly, A. Hodgson and B. Hammer, *J. Chem. Phys.* (USA) **110**, 6954–6962 (1999).
46. J. C. Polanyi, *Acc. Chem. Res.* **5**, 161–192 (1972).
47. J. C. Polanyi and D. C. Tardy, *J. Chem. Phys.* (USA) **51**, 5717–5719 (1969).
48. J. H. Parker and G. C. Pimentel, *J. Chem. Phys.* (USA) **51**, 91–96 (1969).
49. T. P. Schafer, P. E. Siska, J. M. Parson, F. P. Tully, Y. C. Wong and Y. T. Lee, *J. Chem. Phys.* (USA) **53**, 3385–3387 (1970).
50. W. B. Chapman, B. W. Blackmon, S. Nizkorodov and D. J. Nesbitt, *J. Chem. Phys.* (USA) **109**, 9306–9317 (1998).
51. C. T. Rettner, H. A. Michelsen, D. J. Auerbach and C. B. Mullins, *J. Chem. Phys.* (USA) **94**, 7499–7501 (1991).
52. H. A. Michelsen, C. T. Rettner, D. J. Auerbach and R. N. Zare, *J. Chem. Phys.* (USA) **98**, 8294–9307 (1993).
53. L. Diekhoner, H. Mortensen, A. Baurichter, E. Jensen, V. V. Petrunin and A. C. Luntz, *J. Chem. Phys.* (USA) **115**, 9028–9035 (2001).
54. M. Cornelius McCarthy, J. W. R. Allington and K. S. Griffith, *Chem. Phys. Lett.* **289**, 156–159 (1998).
55. M. Silva, R. Jongma, R. W. Field and A. M. Wodtke, *Annu. Rev. Phys. Chem.* **52**, 811–852 (2001).
56. X. Yang, J. M. Price, J. A. Mack, C. G. Morgan, C. A. Rogaski, D. McGuire, E. H. Kim and A. M. Wodtke, *J. Phys. Chem.* (USA) **97**, 3944–3955 (1993).
57. C. E. Hamilton, J. L. Kinsey and R. W. Field, *Annu. Rev. Phys. Chem.* **37**, 493–524 (1986).
58. A. M. Wodtke, Y. Huang and D. J. Auerbach, *J. Chem. Phys.*, submitted (2002).
59. Y. H. Huang, C. T. Rettner, D. J. Auerbach and A. M. Wodtke, *Science* (USA) **290**, 111–114 (2000).
60. H. Hou, C. T. Rettner, D. J. Auerbach, Y. Huang, S. J. Gulding and A. M. Wodtke, *Faraday Discuss.* 181–200 (1999).
61. H. Hou, Y. Huang, S. J. Gulding, C. T. Rettner, D. J. Auerbach and A. M. Wodtke, *Science* (USA) **284**, 1647–1650 (1999).
62. H. Hou, Y. Huang, S. J. Gulding, C. T. Rettner, D. J. Auerbach and A. M. Wodtke, *J. Chem. Phys.* (USA) **110**, 10660–10663 (1999).
63. S. M. Li and H. Guo, *J. Chem. Phys.* (USA) **117**, 4499–4508 (2002).
64. B. Gergen, H. Nienhaus, W. H. Weinberg and E. W. McFarland, *Science* (USA) **294**, 2521–2523 (2001).
65. H. Nienhaus, H. S. Bergh, B. Gergen, A. Majumdar, W. H. Weinberg and E. W. McFarland, *Phys. Rev. Lett.* **82**, 446–449 (1999).
66. H. Nienhaus, H. S. Bergh, B. Gergen, A. Majumdar, W. H. Weinberg and E. W. McFarland, *Appl. Phys. Lett.* **74**, 4046–4048 (1999).
67. B. Gergen, S. J. Weyers, H. Nienhaus, W. H. Weinberg and E. W. McFarland, *Surf. Sci.* **488**, 123–132 (2001).
68. H. Nienhaus, H. S. Bergh, B. Gergen, A. Majumdar, W. H. Weinberg and E. W. McFarland, *Surf. Sci.* **445**, 335–342 (2000).
69. J. R. Trail, M. C. Graham, D. M. Bird, M. Persson and S. Holloway, *Phys. Rev. Lett.* **88**, art. no.-166802 (2002).
70. J. W. Gadzuk, *J. Phys. Chem.* **B106**, 8265–8270 (2002).

CHAPTER 9

FIRST PRINCIPLES QUANTUM DYNAMICAL STUDY OF FOUR-ATOM REACTIONS

Dong H. Zhang and Minghui Yang
*Department of Computational Science,
National University of Singapore,
Singapore 119260*

Soo-Y. Lee
*Department of Chemistry,
National University of Singapore,
Singapore 119260*

Michael A. Collins
*Research School of Chemistry,
Australian National University,
ACT 0200, Australia*

Over the last decade, advances in quantum dynamics, notably the development of the initial state selected time-dependent wavepacket method, coupled with advances in constructing *ab initio* potential energy surfaces, have made it possible for some four-atom reactions to be addressed from first principles, in their full six internal degrees-of-freedom. Given an accurate potential energy surface for a four-atom reaction, dynamics calculations should be able to provide quantitative descriptions of the reaction. We are able to calculate state-to-state reaction probabilities for $J \geq 0$, state-to-state integral cross-sections, and thermal rate constants to compare with experiments, notably for the $\text{H}_2 + \text{OH} \leftrightarrow \text{H} + \text{H}_2\text{O}$ reaction and its isotopic analogs. This chapter presents an overview of (a) the time-dependent quantum wavepacket method for four-atom reactions, (b) the method of constructing a potential energy surface by interpolation of *ab initio* data and evaluating it for quantum reaction dynamics, and (c) highlights of theoretical calculations in comparison with experimental results for the benchmark $\text{H} + \text{H}_2\text{O}$ abstraction and exchange reactions, the reverse $\text{H}_2 + \text{OH}$ reaction, and their isotopic analogs, and,

finally, the photoelectron and photodetachment spectroscopy of H_3O^- as a further test of the potential energy surfaces.

Contents

1. Introduction	410
2. Theory	413
2.1. Hamiltonian for AB + CD Reaction and Basis Set Expansion	413
2.2. Wavepacket Propagation for AB + CD Reaction	417
2.3. Hamiltonian for ABC + D Reaction and Basis Set Expansion	417
2.4. Wavepacket Propagation for ABC + D Reaction	420
2.5. Reaction Probability, Cross-Section, and Rate Constant	420
3. <i>Ab Initio</i> Potential Energy Surfaces	421
3.1. The PES Construction Method	422
3.2. Proof and Improvement of Accuracy	427
3.3. Computational Considerations	432
4. Results for Some AB + CD and ABC + D Reactions	437
4.1. Reactions of $\text{H}_2 + \text{OH}$, $\text{HD} + \text{OH}$, and $\text{D}_2 + \text{OH}$	437
4.2. Reactions of $\text{H} + \text{H}_2\text{O}$, $\text{H} + \text{D}_2\text{O}$	445
4.3. Photoelectron and Photodetachment Spectroscopy of H_3O^-	455
5. Conclusions	459
Acknowledgments	460
References	460

1. Introduction

The goal of quantum reaction theory is the accurate first principles prediction of the outcome of a chemical reaction based on calculations of accurate *ab initio* potential energy surfaces (PESs) for the reaction, followed by applying quantum scattering theory or quantum dynamics to calculate the reaction probabilities on the PESs, the reaction cross-sections, the detailed state-to-state cross-sections, and the thermal rate constants.¹ These calculated quantities not only allow us to compare theory with experiments, but they also give us a detailed picture of the reaction mechanism, and how energy is selectively consumed and how it is discharged in a specific manner in the reaction. When this knowledge is extended to include the excited state PESs and coupled with coherent spectroscopy, we can also study the quantum control of molecular processes.²

Accurate quantum reaction theory has been achieved for the simplest possible chemical reaction system: atom-diatom reactions $\text{A} + \text{BC} \rightarrow \text{AB} + \text{C}$, $\text{AC} + \text{B}$.³⁻⁵ In particular, for three decades, rigorous and detailed quantum calculations in three-dimensions have been carried out for the

$\text{H} + \text{H}_2$ reaction and its isotopically substituted analogs as the benchmark for testing exact and approximate theories of atom–diatom reactions.⁶ For example, the calculated rate constants for the $\text{H} + \text{H}_2$ reaction,⁷ and the converged quantum scattering calculations for the $\text{H} + \text{D}_2(v = 0, j = 0) \rightarrow \text{HD}(v', j') + \text{D}$ reaction⁸ at a collision energy of 1.28 eV agree very well with experiments. More recently, in a fully state- and angle-resolved study of the $\text{H} + \text{HD} \rightarrow \text{H}_2 + \text{D}$ reaction, it was found that the theoretical state-to-state differential cross-sections are in quantitative agreement with experiments at collision energies of 0.498 and 1.200 eV.⁹ The mechanism for the observed forward scattering was elucidated.¹⁰ Other reactions that were successfully studied include $\text{F} + \text{H}_2 \rightarrow \text{HF} + \text{H}$ where calculations are in agreement with molecular beam experiments,¹¹ the $\text{Cl} + \text{H}_2$ reaction¹² and $\text{Cl} + \text{HD}$ reaction¹³ even though the PESs for these two reactions were less accurate.

Atom–diatom reactions were well addressed by two general time-independent (TI) methods: the hyperspherical coordinate (HC) approach¹⁴ and the algebraic variational (AV) approach.¹⁵ The HC approach transforms the reactive scattering problem into a nonreactive-like scattering problem which then allows the use of standard inelastic computational techniques. This is deemed a hard approach not least because the Schrödinger equation is rather complicated in hyperspherical coordinates. The AV approach is preferred as it is physically intuitive in its multi-arrangement expansion of the full scattering wavefunction, similar to the idea of taking a linear combination of atomic orbitals to form molecular orbitals which is the basis of modern electronic structure calculations. The atom–diatom reactions have become a formally solved problem today and so it is natural to try to extend the theory and calculations to four-atom reactions as well as larger polyatomics. The development of new approaches always seeks generality for extension to larger systems. However, TI methods scale as N^3 , where N is the number of basis functions, which poses a serious limitation in dealing with polyatomic systems with four or more atoms where more than 10^4 basis functions are needed for convergence.

The progression from accurate quantum scattering calculations of atom–diatom reactions to four-atom and larger polyatomics by TI methods proved formidable. Approximations in the form of reduced dimensionality were necessary. In the rotating bond approximation (RBA) for a diatom–diatom reaction with a nonlinear geometry,^{16,17} two radial coordinates and one bending angle are explicitly treated while the remaining three coordinates are frozen in the scattering calculation; the first such quantum reactive scattering calculation was reported for $\text{OH} + \text{H}_2 \rightarrow \text{H}_2\text{O} + \text{H}$ in 1991.¹⁶

In the adiabatic bend approximation (ABA) for the same reaction,¹⁸ the three radial coordinates are explicitly treated while an adiabatic approximation was used for the three angles. These reduced dimensional studies are dynamically approximate in nature, but nevertheless can provide important information characterizing polyatomic reactions, and they have been reviewed extensively by Clary,¹⁹ and Bowman and Schatz.²⁰ However, quantitative determination of reaction probabilities, cross-sections and thermal reaction rates, and their relation to the internal states of the reactants would require explicit treatment of five or the full six degrees-of-freedom in these four-atom reactions, which TI methods could not handle. Other approximate quantum approaches such as the negative imaginary potential method^{16,21} and mixed classical and quantum time-dependent method have also been used.²²

The time-dependent (TD) quantum wavepacket approach has emerged as an important computational approach for studying complex chemical dynamics problems with more than three degrees-of-freedom.^{23,24} The main advantage over TI methods is its slower computational scaling with the number of basis functions, typically $\leq N^2$ versus N^3 in the coupled-channel TI approaches. In the TD method, the reactant or product Jacobi coordinates are used in defining the basis set expansion which simplifies the wavepacket propagation and makes the calculation similar to that for non-reactive problems. The development of the time-dependent wavepacket method coupled with advances in constructing potential energy surfaces and the rise in computational power has made possible accurate *ab initio* quantum dynamics calculation on four-atom systems. With the initial state-selected time-dependent wavepacket method,²⁵ we can now calculate fully converged integral cross-sections,^{26–28} full-dimensional state-to-state reaction probabilities for total angular momentum $J \geq 0$ without any dynamical approximations,^{29,30} as well as accurate cumulative reaction probabilities and thermal rate constants for some four-atom systems. Any remaining discrepancies between theoretical calculations and experiments are likely due to deficiencies in generating the potential energy surface(s) for the reaction rather than the quantum scattering or dynamics calculations in full (six) dimensions for four-atom reactions. We have reached a stage where some four-atom (diatom–diatom and atom–triatom) reactions can be addressed from first principles.

This chapter presents an overview of first principles theory for diatom–diatom and atom–triatom reactions in comparison with experiments. It is applied to the prototype $\text{H}_2 + \text{OH}$ and $\text{H} + \text{H}_2\text{O}$ reactions and their

isotopically substituted analogs in much the same way that the $\text{H} + \text{H}_2$ reaction served as the prototype for triatomic reactions. The $\text{H}_2 + \text{OH}$ reaction plays a significant role in atmospheric chemistry and in combustion,^{31,32} while the $\text{H} + \text{H}_2\text{O}$ reaction is the simplest system in which different vibrational modes in the reactants can play an important role in reaction dynamics.³³ Having three of the four atoms as hydrogen, also makes them ideal candidates for high quality *ab initio* quantum chemistry calculations of the PES as well as for accurate quantum reactive scattering studies. Numerous experiments^{34–38} have been carried out to measure the absolute reaction cross-section and the thermal rate constants of these reactions, and to study the influence of initial vibrational excitation, translational kinetic energy, and isotopic substitution on the reaction dynamics. Section 2 outlines the theoretical methodology of the initial state selected wavepacket approach to diatom–diatom and atom–triatom reactions. Construction of accurate PESs for these reactions are covered in Sec. 3. Highlights of important results for prototype benchmark four-atom reactions are presented in Sec. 4, including calculations of the spectrum for the photoelectron and photodetachment spectroscopy of H_3O^- , a process that accesses and tests the $\text{H}_2 + \text{OH} \leftrightarrow \text{H} + \text{H}_2\text{O}$ surface, which show remarkable agreement with experiment.^{39,40} We conclude in Sec. 5.

2. Theory

2.1. Hamiltonian for $\text{AB} + \text{CD}$ Reaction and Basis Set Expansion

The Jacobi coordinates $(R, r_1, r_2, \theta_1, \theta_2, \phi)$ for a diatom–diatom reaction $\text{AB} + \text{CD}$ are shown in Fig. 1.

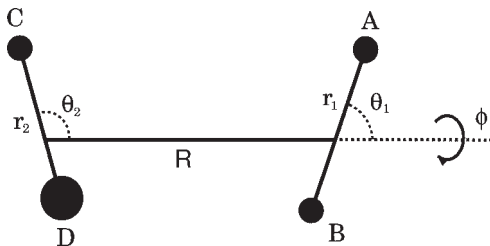


Fig. 1. Jacobi coordinates for a diatom–diatom reaction $\text{AB} + \text{CD}$. The angle ϕ is the out-of-plane torsion angle between the (r_1, R) plane and the (r_2, R) plane.

The Hamiltonian for the “internal motion” of the AB + CD system can be written as¹⁶

$$H = -\frac{\hbar^2}{2\mu} \frac{\partial^2}{\partial R^2} + h_1(r_1) + h_2(r_2) + \frac{(\mathbf{J} - \mathbf{j}_{12})^2}{2\mu R^2} + \frac{\mathbf{j}_1^2}{2\mu_1 r_1^2} + \frac{\mathbf{j}_2^2}{2\mu_2 r_2^2} + V(R, r_1, r_2, \theta_1, \theta_2, \phi), \quad (1)$$

where μ is the reduced mass between the centers-of-mass of AB and CD; \mathbf{J} is the total angular momentum operator; \mathbf{j}_1 and \mathbf{j}_2 are the rotational angular momentum operators of AB and CD, respectively, which are coupled to give $\mathbf{j}_{12} = \mathbf{j}_1 + \mathbf{j}_2$; $h_1(r_1)$ and $h_2(r_2)$ are the vibrational Hamiltonians for free AB and CD, respectively. $V(R, r_1, r_2, \theta_1, \theta_2, \phi)$, the interaction potential, is the difference between the total potential of the system and $V_1(r_1) + V_2(r_2)$, which are the vibrational potentials in $h_1(r_1)$ and $h_2(r_2)$.

The TD wavefunction satisfying the Schrödinger equation $i\hbar(\partial/\partial t)\Psi(t) = H\Psi(t)$ can be expanded in a basis set whose elements are the product of the translational basis of R , vibrational wavefunctions for r_1 , r_2 , and the body-fixed (BF) total angular momentum eigenfunctions as⁴¹

$$\begin{aligned} \Psi_{v_0 j_0 K_0}^{JM\varepsilon}(\mathbf{R}, \mathbf{r}_1, \mathbf{r}_2, t) &= \sum_{n,v,j,K} F_{nvjK,v_0 j_0 K_0}^{JM\varepsilon}(t) u_n^{v_1}(R) \phi_{v_1}(r_1) \phi_{v_2}(r_2) \\ &\times Y_{jK}^{JM\varepsilon}(\hat{\mathbf{R}}, \hat{\mathbf{r}}_1, \hat{\mathbf{r}}_2), \end{aligned} \quad (2)$$

where n is the translational basis label; v denotes (v_1, v_2) ; j denotes (j_1, j_2, j_{12}) ; K is the projection of \mathbf{J} along the BF z -axis, chosen to be \mathbf{R} , with values $0 \leq K \leq \min(J, j_{12})$; (v_0, j_0, K_0) denotes the quantum numbers for the initial rovibrational state; J and M are the quantum numbers for the total angular momentum and its space-fixed (SF) Z component, respectively; and $\varepsilon = (-1)^{j_1+j_2+L}$ is the parity of the TD wavefunction under inversion of the SF nuclear coordinates, with L being the quantum number for the orbital angular momentum, $\mathbf{L} = \mathbf{J} - \mathbf{j}_{12}$. The good quantum numbers for the TD wavefunction are J , M , and ε . The objective is to solve for the TD coefficients $F_{nvjK,v_0 j_0 K_0}^{JM\varepsilon}(t)$. In order to save computational time, the configuration space for the reaction $\text{AB} + \text{CD} \rightarrow \text{A} + \text{BCD}$ is partitioned into an interaction region **I** and an asymptotic region **II**, as shown in Fig. 2, with the v_1 dependent translational basis $u_n^{v_1}(R)$ defined as

$$u_n^{v_1}(R) = \begin{cases} \sqrt{\frac{2}{R_4 - R_1}} \sin \frac{n\pi(R - R_1)}{R_4 - R_1}, & v_1 \leq v_{\text{asy}}, \\ \sqrt{\frac{2}{R_2 - R_1}} \sin \frac{n\pi(R - R_1)}{R_2 - R_1}, & v_1 > v_{\text{asy}}, \end{cases} \quad (3)$$

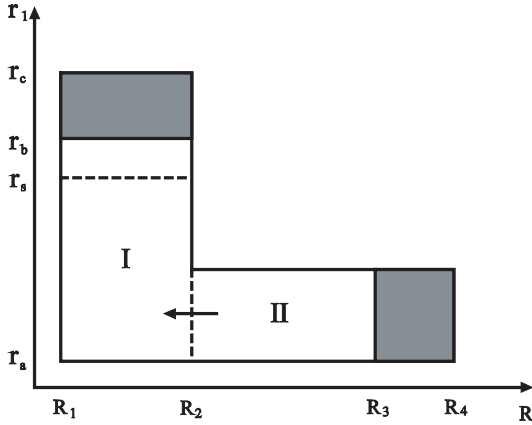


Fig. 2. Schematic configuration space for the reaction $AB + CD \rightarrow A + BCD$. R is the radial coordinate between the center-of-mass of the two diatoms, and r is the vibrational coordinate of the reactive AB diatom. I denotes the interaction region and II denotes the asymptotic region. The shaded regions are the absorption zones for the time-dependent wavefunction to avoid boundary reflections. The reactive flux is evaluated at the $r = r_s$ surface.

where v_{asy} is chosen to be the number of energetically open vibrational channels plus one or two closed vibrational channels of the reactive AB molecule.

The vibrational wavefunctions $\phi_{v_1}(r_1)$, $\phi_{v_2}(r_2)$ satisfy

$$h_i(r_i)\phi_{v_i}(r_i) = \left[-\frac{\hbar^2}{2\mu_i} \frac{\partial^2}{\partial r_i^2} + V_i(r_i) \right] \phi_{v_i}(r_i) = \varepsilon_{v_i} \phi_{v_i}(r_i), \quad (i = 1, 2). \quad (4)$$

The BF parity-adapted total angular momentum basis functions $Y_{jK}^{JM\varepsilon}(\hat{\mathbf{R}}, \hat{\mathbf{r}}_1, \hat{\mathbf{r}}_2)$ in Eq. (2) are the eigenfunctions for \mathbf{J} , \mathbf{j}_1 , \mathbf{j}_2 , \mathbf{j}_{12} , K , and the parity operator, and can be written as

$$Y_{jK}^{JM\varepsilon} = (1 + \delta_{K0})^{-1/2} \sqrt{\frac{2J+1}{8\pi}} \times [D_{K,M}^J Y_{j_1 j_2}^{j_{12} K} + \varepsilon(-1)^{j_1+j_2+j_{12}+J} D_{-K,M}^J Y_{j_1 j_2}^{j_{12}-K}], \quad (5)$$

where $D_{K,M}^J$ is the Wigner rotation matrix which relates the BF and SF coordinate systems; $0 \leq K \leq \min(J, j_{12})$ is the projection of the total angular momentum on the BF axis; and $Y_{j_1 j_2}^{j_{12} K}$ is an internal angular momentum

eigenfunction of \mathbf{j}_1 , \mathbf{j}_2 , and \mathbf{j}_{12}

$$Y_{j_1 j_2}^{j_{12} K} = \sum_{m_1} \langle j_1 m_1 j_2 K - m_1 | j_{12} K \rangle y_{j_1 m_1}(\theta_1, 0) y_{j_2 K - m_1}(\theta_2, \phi), \quad (6)$$

where $\langle j_1 m_1 j_2 K - m_1 | j_{12} K \rangle$ is a Clebsch–Gordon coefficient, and y_{jm} is a spherical harmonic. In Eq. (5), the restriction $\varepsilon(-1)^{j_1+j_2+j_{12}+J} = 1$ for $K = 0$ partitions the rotational basis set into even and odd parities. Thus a $K = 0$ initial state can only appear in one of these two parity blocks. For $K > 0$, however, there is no such restriction and the basis set is the same for even and odd parities; hence a $K > 0$ initial state can appear in both parities.

The potential matrix elements in the BF angular momentum basis $Y_{jK}^{JM\varepsilon}(\hat{\mathbf{R}}, \hat{\mathbf{r}}_1, \hat{\mathbf{r}}_2)$ for a fixed (R, r_1, r_2) is given by

$$\langle Y_{jK}^{JM\varepsilon} | V(R, r_1, r_2, \theta_1, \theta_2, \phi) | Y_{j'K'}^{JM\varepsilon} \rangle = 2\pi \delta_{KK'} \langle Y_{j_{12}K}^{j_{12}K} | V | Y_{j'_{12}K'}^{j'_{12}K} \rangle. \quad (7)$$

Thus the potential matrix for even parity is identical to that for odd parity for $K \neq 0$. The centrifugal potential with the $(\mathbf{J} - \mathbf{j}_{12})^2$ term in Eq. (1), which is not diagonal in K in the BF representation, has matrix elements

$$\begin{aligned} \langle Y_{jK}^{JM\varepsilon} | (\mathbf{J} - \mathbf{j}_{12})^2 | Y_{j'K'}^{JM\varepsilon} \rangle &= \delta_{jj'} \{ [J(J+1) + j_{12}(j_{12}+1) - 2K^2] \delta_{KK'} \\ &\quad - \lambda_{JK}^+ \lambda_{j_{12}K}^+ (1 + \delta_{K0})^{1/2} \delta_{K+1, K'} \\ &\quad - \lambda_{JK}^- \lambda_{j_{12}K}^- (1 + \delta_{K1})^{1/2} \delta_{K-1, K'} \} \end{aligned} \quad (8)$$

and λ_{AB}^\pm is defined as

$$\lambda_{AB}^\pm = [A(A+1) - B(B \pm 1)]^{1/2}. \quad (9)$$

The exact close-coupling calculations for $J > 0$ states are extremely expensive to compute. In the centrifugal sudden (CS) approximation, K is viewed as a good quantum number and conserved in the reaction, and thus the coupling between different K in Eq. (8) is neglected. For a given quantum number J and parity ε , there are $J+1$ manifolds of K states when the total parity is even, and J manifolds of K states when the total parity is odd. The CS approximation decouples these K states for total angular momentum $J > 0$, and thereby significantly reduces computational time in the diagonalization of the Hamiltonian matrix.

2.2. Wavepacket Propagation for AB + CD Reaction

The initial wavefunction is a product of a specific rovibrational eigenfunction for the reactants and a localized translational wavepacket for R :

$$\Psi_i(\mathbf{R}, \mathbf{r}_1, \mathbf{r}_2, t = 0) = \varphi_{k_0}(R) \phi_{v_{10}j_{10}}(r_1) \phi_{v_{20}j_{20}}(r_2) \times Y_{j_{10}j_{20}j_{120}}^{JM\varepsilon}(\hat{\mathbf{R}}, \hat{\mathbf{r}}_1, \hat{\mathbf{r}}_2), \quad (10)$$

where the translational wavepacket $\varphi_{k_0}(R)$ is chosen to be a Gaussian function

$$\varphi_{k_0}(R) = \left(\frac{1}{\pi\delta^2} \right)^{1/4} \exp \left[\frac{-(R - R_0)^2}{2\delta^2} \right] e^{-ik_0R}, \quad (11)$$

with average translational kinetic energy

$$E_t(k_0) = \frac{\hbar^2}{2\mu} \left(k_0^2 + \frac{1}{2\delta^2} \right). \quad (12)$$

The initial wavefunction is then expanded as in Eq. (2), and the wavepacket is propagated using the split operator method⁴²:

$$\Psi(\mathbf{R}, \mathbf{r}_1, \mathbf{r}_2, t + \Delta) = e^{-iH_0\Delta/2} e^{-iU\Delta/2} e^{-iV\Delta} e^{-iU\Delta/2} e^{-iH_0\Delta/2} \times \Psi(\mathbf{R}, \mathbf{r}_1, \mathbf{r}_2, t), \quad (13)$$

with the reference Hamiltonian H_0 and the centrifugal potential U defined, with reference to Eq. (1), as

$$H_0 = -\frac{\hbar^2}{2\mu} \frac{\partial^2}{\partial R^2} + h_1(r_1) + h_2(r_2), \quad (14)$$

$$U = \frac{(\mathbf{J} - \mathbf{j}_{12})^2}{2\mu R^2} + \frac{\mathbf{j}_1^2}{2\mu_1 r_1^2} + \frac{\mathbf{j}_2^2}{2\mu_2 r_2^2}.$$

A mixed DVR (discrete variable representation)⁴³ for all the radial coordinates and basis set representations for the angular coordinates are used in the wavepacket propagation.⁴⁴

2.3. Hamiltonian for ABC + D Reaction and Basis Set Expansion

The Jacobi coordinates $(R, r, \rho, \theta, \gamma, \phi)$ for a triatom-atom reaction ABC + D are shown in Fig. 3.

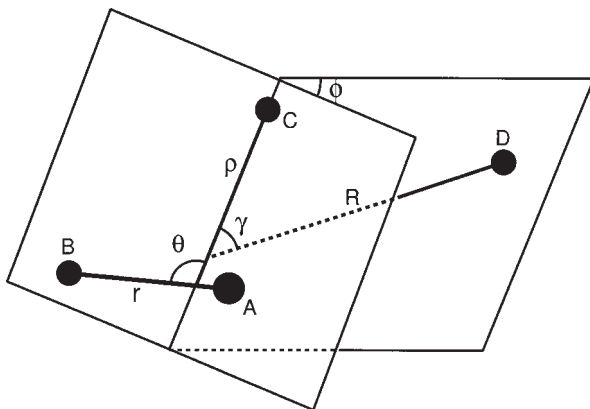


Fig. 3. Jacobi coordinates for a triatom-atom reaction $ABC + D$.

Similar to the diatom-diatom system and Eq. (1), the Hamiltonian for the “internal motion” of the $ABC + D$ system can be written as⁴⁵

$$H = -\frac{\hbar^2}{2\mu} \frac{\partial^2}{\partial R^2} + h_r(r) + h_\rho(\rho) + \frac{(\mathbf{J} - \mathbf{L})^2}{2\mu R^2} + \frac{\mathbf{j}^2}{2\mu_r r^2} + \frac{\mathbf{l}^2}{2\mu_\rho \rho^2} + V(R, r, \rho, \theta, \gamma, \phi), \quad (15)$$

where μ is the reduced mass of ABC and D ; μ_r is the reduced mass of AB ; μ_ρ is the reduced mass of AB and C ; R is the distance from the center-of-mass of ABC to D ; r is the bond length of AB ; ρ is the distance from the center-of-mass of AB to C ; \mathbf{J} is the total angular momentum operator; \mathbf{j} is the rotational angular momentum operator for AB ; \mathbf{l} is the orbital momentum operator of C with respect to AB ; and $\mathbf{L} = \mathbf{j} + \mathbf{l}$ is the coupled total angular momentum operator for ABC . The one-dimensional Hamiltonians $h_r(r)$ and $h_\rho(\rho)$ are defined as

$$h_r(r) = -\frac{\hbar^2}{2\mu_r} \frac{\partial^2}{\partial r^2} + V_r(r), \quad (16)$$

$$h_\rho(\rho) = -\frac{\hbar^2}{2\mu_\rho} \frac{\partial^2}{\partial \rho^2} + V_\rho(\rho), \quad (17)$$

where $V_r(r)$ and $V_\rho(\rho)$ are one-dimensional reference potentials obtained from the total potential $\mathbf{V}(R, r, \rho, \theta, \gamma, \phi)$ with other degrees-of-freedom fixed as follows:

$$V_r(r) = \mathbf{V}(R \rightarrow \infty, r, \rho = \rho_0, \theta = \theta_0, \gamma, \phi), \quad (18)$$

$$V_\rho(\rho) = \mathbf{V}(R \rightarrow \infty, r = r_0, \rho, \theta = \theta_0, \gamma, \phi), \quad (19)$$

and (r_0, ρ_0, θ_0) denotes the equilibrium Jacobi coordinates for the isolated triatomic ABC molecule. The interaction potential $V(R, r, \rho, \theta, \gamma, \phi)$ in Eq. (15) is thus given by

$$V(R, r, \rho, \theta, \gamma, \phi) = \mathbf{V}(R, r, \rho, \theta, \gamma, \phi) - V_r(r) - V_\rho(\rho). \quad (20)$$

Similar to Eq. (2), the time-dependent wavefunction is expanded in terms of the BF parity-adapted rotational basis functions:

$$\begin{aligned} \Psi_{v_0 L_0 \Omega_0}^{JM\varepsilon}(\mathbf{R}, \mathbf{r}, \boldsymbol{\rho}, t) = & \sum_{n, v_1, v_2, j, l, L, \Omega} F_{nv_1 v_2 j l L \Omega}^{JM\varepsilon}(t) u_n^{v_2}(R) \\ & \times \varphi_{v_1}(r) \varphi_{v_2}(\rho) \mathbf{Y}_{j l L \Omega}^{JM\varepsilon}(\hat{R}, \hat{r}, \hat{\rho}), \end{aligned} \quad (21)$$

where (v_0, L_0, Ω_0) denotes the initial rovibrational state of the triatom ABC, where L and $0 \leq \Omega \leq \min[J, L]$ are the total angular momentum and the modulus of its projection on the BF z -axis (along the vector \mathbf{R} in Fig. 3), respectively, for the triatom. The translational basis function $u_n^{v_2}(R)$ is defined in the same manner as in Eq. (3), and $\varphi_{v_1}(r)$, $\varphi_{v_2}(\rho)$ are the vibrational wavefunctions for $h_r(r)$, $h_\rho(\rho)$, respectively. The parity-adapted rotational basis functions are given by

$$\begin{aligned} \mathbf{Y}_{j l L \Omega}^{JM\varepsilon}(\hat{R}, \hat{r}, \hat{\rho}) = & [2(1 + \delta_{\Omega 0})]^{-1/2} \\ & \times [\mathbf{Y}_{j l L \Omega}^{JM}(\hat{R}, \hat{r}, \hat{\rho}) + \varepsilon(-1)^{j+l+L+J} \mathbf{Y}_{j l L -\Omega}^{JM}(\hat{R}, \hat{r}, \hat{\rho})], \end{aligned} \quad (22)$$

where the overall rotational basis function for the atom–triatom system in the BF frame is

$$\mathbf{Y}_{j l L \Omega}^{JM}(\hat{R}, \hat{r}, \hat{\rho}) = Y_{j l}^{L\Omega}(\hat{r}, \hat{\rho}) N_{M, \Omega}^J(\hat{R}), \quad (23)$$

with the eigenfunctions of \mathbf{J}^2 given by

$$N_{M, \Omega}^J(\hat{R}) = \sqrt{\frac{2J+1}{4\pi}} D_{M\Omega}^{J*}(\alpha, \beta, 0), \quad (24)$$

which depend on the angles which rotate the SF axes on to the BF axes. The rotational basis for diatom AB and atom C is given by

$$Y_{j l}^{L\Omega}(\hat{r}, \hat{\rho}) = \sum_K D_{\Omega K}^{L*}(\chi, \gamma, \phi) \sqrt{\frac{2l+1}{4\pi}} \langle j K l 0 | L K \rangle y_{j K}(\theta, 0), \quad (25)$$

where L and Ω are as defined above; $\langle j K l 0 | L K \rangle$ is a Clebsch–Gordon coefficient, and $y_{j K}(\theta, 0)$ is a spherical harmonic. The functions $D_{M\Omega}^{J*}(\alpha, \beta, 0)$ and $D_{\Omega K}^{L*}(\chi, \gamma, \phi)$ are elements of the Wigner rotation matrix.

2.4. Wavepacket Propagation for ABC + D Reaction

Similar to the diatom–diatom reaction, the initial wavefunction is chosen as the direct product of a localized translational wavepacket for R and a specific ($JM\varepsilon$) state for the atom–triatom system with a specific rovibrational eigenstate (ν_0, L_0, Ω_0) for the triatom ABC:

$$\Psi_{\nu_0 L_0 \Omega_0}^{JM\varepsilon}(\mathbf{R}, \mathbf{r}, \boldsymbol{\rho}, t = 0) = \varphi_{k_0}(r) \psi_{\nu_0 L_0 \Omega_0}^{JM\varepsilon}(\hat{\mathbf{R}}, \mathbf{r}, \boldsymbol{\rho}), \quad (26)$$

where the wavepacket is the same as in Eq. (11), and $\psi_{\nu_0 L_0 \Omega_0}^{JM\varepsilon}(\hat{\mathbf{R}}, \mathbf{r}, \boldsymbol{\rho})$ is the eigenfunction of the triatom ABC Hamiltonian

$$H_{\text{ABC}} = h_r(r) + h_\rho(\rho) + \frac{\mathbf{j}^2}{2\mu_r r^2} + \frac{\mathbf{l}^2}{2\mu_\rho \rho^2} + V(R \rightarrow \infty, r, \rho, \theta, \gamma, \phi), \quad (27)$$

with ν_0, L_0, Ω_0 representing the triatom ABC's initial vibrational state, total angular momentum, and its projection on the BF z -axis of the atom–triatom system, respectively. The initial wavefunction, Eq. (26), can be expanded as in Eq. (21) and the wavepacket is propagated using the split operator method similar to Eq. (13), with reference Hamiltonian

$$H_0 = -\frac{\hbar^2}{2\mu} \frac{\partial^2}{\partial R^2} + h_r(r) + h_\rho(\rho), \quad (28)$$

and the centrifugal potential U is defined by

$$U = \frac{(\mathbf{J} - \mathbf{L})^2}{2\mu R^2} + \frac{\mathbf{j}^2}{2\mu_r r^2} + \frac{\mathbf{l}^2}{2\mu_\rho \rho^2}. \quad (29)$$

2.5. Reaction Probability, Cross-Section, and Rate Constant⁴¹

In both the diatom–diatom and atom–triatom reactions, the energy-dependent scattering wavefunction is obtained by a Fourier transform of the propagated wavepacket:

$$|\psi_{iE}^+\rangle = \frac{1}{a_i(E)} \int_{-\infty}^{\infty} e^{iEt/\hbar} e^{-iHt/\hbar} |\Psi_i(0)\rangle dt, \quad (30)$$

where the subscript i denotes the initial rovibrational quantum state of the reactants, the coefficient $a_i(E)$ is given by

$$a_i(E) = \langle \psi_{iE}^+ | \Psi_i(0) \rangle = \langle \phi_{iE} | \Psi_i(0) \rangle, \quad (31)$$

and where ϕ_{iE} is the free or asymptotic stationary wavefunction.

With the stationary solution ψ_{iE}^+ , one can use asymptotic boundary conditions to extract the scattering matrix. However, for the total reaction

probability P_i the calculation can be simplified by evaluating the reactive flux through any dividing surface which separates the reactant from products, e.g. at a hypersurface close to the transition state, without the need to compute the state-to-state S matrix:

$$P_i = \sum_f |S_{fi}|^2 = \langle \psi_{iE}^+ | \hat{F} | \psi_{iE}^+ \rangle, \quad (32)$$

where the flux operator is

$$\hat{F} = \frac{1}{2} [\delta(\hat{s} - s_0) \hat{v}_s + \hat{v}_s \delta(\hat{s} - s_0)], \quad (33)$$

with s being the coordinate perpendicular to a surface located at s_0 for the flux evaluation, and \hat{v}_s is the velocity operator.

For a diatom–diatom reaction, the reaction cross-section from a specific initial state (v_1, v_2, j_1, j_2) is obtained by summing the reaction probabilities over all the partial waves with total angular momentum J^{46} :

$$\sigma_{v_1 v_2 j_1 j_2}(E) = \frac{1}{(2j_1 + 1)(2j_2 + 1)} \times \sum_{j_{12} K_0 \varepsilon} \left\{ \frac{\pi}{k_E^2} \sum_{J \geq K_0} (2J + 1) P_{v_1 v_2 j_1 j_2 j_{12} K_0}^{J \varepsilon}(E) \right\}, \quad (34a)$$

while for an atom–triatom reaction from an initial state (v_0, j_0, τ) it is given by²⁹

$$\sigma_{v_0 j_0 \tau}(E) = \frac{1}{(2j_0 + 1)} \sum_{K_0 \varepsilon} \left\{ \frac{\pi}{k_E^2} \sum_{J \geq K_0} (2J + 1) P_{v_0 j_0 \tau K_0}^{J \varepsilon}(E) \right\}, \quad (34b)$$

where $k_E = \sqrt{2\mu E}$ is the translational wave-vector.

The initial state-specific reaction rate constant for both diatom–diatom and atom–triatom reactions is calculated by averaging the corresponding cross-section over a Boltzmann distribution of translational energy:

$$k(T) = \left(\frac{8k_B T}{\pi \mu} \right)^{1/2} (k_B T)^{-2} \int_0^\infty E_t e^{-E_t/k_B T} \sigma(E_t) dE_t \quad (35)$$

where E_t is the translational energy, and k_B is the Boltzmann constant.

3. *Ab Initio* Potential Energy Surfaces

The method which has been developed to construct a potential energy surface (PES) by interpolation of *ab initio* data has been reviewed in some

detail.⁴⁷ Here we present a brief summary of the basic method and dwell at more length on the aspects most relevant to evaluating a PES for quantum reaction dynamics.

3.1. The PES Construction Method

The PES is only a function of the shape of the molecule, as described by the “internal” coordinates (there are $3N - 6$ of them for a non-collinear molecule of N atoms). There are many possible choices of internal coordinates, including atom–atom distances (bond lengths), bond angles, dihedral or out-of-plane angles, or some combination of these. However, the PES can be expressed solely in terms of the atom–atom distances (a result that follows from the group theory of functions like the PES which are invariant to rotation).^{48,49} For N atoms there are ${}^NC_2 = N(N - 1)/2$ such distances, which are easily calculated from the Cartesian coordinates. Rather than use these atom–atom distances, R_n , we actually use the reciprocal distances, Z_n :

$$Z_n = \frac{1}{R_n}. \quad (36)$$

The PES is not an analytic function of the atomic coordinates, because it diverges to infinity when any two atoms are at the same position. Using the $\{Z_n\}$ to describe the PES means that these singularities are banished to infinity, $Z_n \rightarrow \infty$, resulting in a much better behaved description of the PES.^{50,51}

When $N > 4$ there appears to be too many Z_n , since $N(N - 1)/2 > 3N - 6$. However, the $\{Z_n\}$ are *not globally redundant*. All Z_n are needed for a global description of molecular shape, and no subset of $3N - 6$ $\{Z_n\}$ will be adequate everywhere.⁴⁹ The space of molecular coordinates which defines the shape of a molecule is not a rectilinear or Euclidean space, it is a curved manifold. It is well known in the mathematical literature that you cannot find a single global set of coordinates for such curved spaces.

However, the *local* shape of a PES is given by $3N - 6$ locally independent coordinates. From the argument above, we must make different choices for local coordinates in different locales. How this can be accomplished is detailed elsewhere.⁵² Very briefly, the local changes in the $\{Z_n\}$ relative to changes in the Cartesian coordinates $\{X_i\}$, are given by the matrix \mathbf{B} (a variant of the Wilson \mathbf{B} matrix⁵³):

$$B_{ni} = \frac{\partial Z_n}{\partial X_i}, \quad n = 1, \dots, N(N - 1)/2; \quad i = 1, \dots, 3N. \quad (37)$$

Any matrix can be written in the form of a *singular value decomposition*^{54,55}

$$\mathbf{B} = \mathbf{U}\mathbf{\Lambda}\mathbf{V}^T, \quad (38)$$

where \mathbf{U} is an $N(N-1)/2 \times N(N-1)/2$ unitary matrix, \mathbf{V} is a $3N \times 3N$ unitary matrix, and $\mathbf{\Lambda}$ is a diagonal $N(N-1)/2 \times 3N$ matrix (only the Λ_{ii} elements can be nonzero). Only $3N-6$ of the Λ_{ii} are not zero. For these nonzero singular values, we define

$$\begin{aligned} \xi &= \mathbf{U}^T \mathbf{Z}, \\ \mathbf{Y} &= \mathbf{V}^T \mathbf{X}, \end{aligned} \quad (39)$$

so that

$$\delta\xi_i = \Lambda_{ii}\delta\mathbf{Y}_i. \quad (40)$$

As \mathbf{V} is a unitary matrix, $\mathbf{Y} = \mathbf{V}^T \mathbf{X}$ is just an equivalent set of Cartesian coordinates, and $\xi = \mathbf{U}^T \mathbf{Z}$ is just an equivalent set of internal coordinates, simply linear combinations of the $\{Z_n\}$. The ξ_1, \dots, ξ_{3N-6} , change independently, in proportion to changes in linear combinations of the Cartesian coordinates. So, locally, we have defined $3N-6$ independent internal coordinates. Every different configuration of the molecule, \mathbf{X} , will have a different \mathbf{B} matrix, and hence a different definition of local internal coordinates, defined automatically.

If we calculate, *ab initio*, the Cartesian gradients and second derivatives of the PES, this data can be transformed into internal coordinate derivatives by solving the following linear equations which follow from a change of variables:

$$\frac{\partial E}{\partial X_i} = \sum_{n=1}^{3N-6} \frac{\partial E}{\partial \xi_n} \frac{\partial \xi_n}{\partial X_i}, \quad i = 1, \dots, 3N; \quad (41a)$$

$$\frac{\partial^2 E}{\partial X_i \partial X_j} = \sum_{n=1}^{3N-6} \sum_{m=1}^{3N-6} \frac{\partial^2 E}{\partial \xi_n \partial \xi_m} \frac{\partial \xi_n}{\partial X_i} \frac{\partial \xi_m}{\partial X_j} + \sum_{n=1}^{3N-6} \frac{\partial E}{\partial \xi_n} \frac{\partial^2 \xi_n}{\partial X_i \partial X_j}. \quad (41b)$$

Problems arise in two situations: firstly, if the molecule is linear, no complete set of $3N-6$ internal coordinates is possible. For this case, a method for constructing PES in terms of Cartesian coordinates could be used.⁵⁶ Secondly, if the molecule is planar, atom-atom distances (or their reciprocals) cannot provide a complete set of internal coordinates, since they cannot describe out-of-plane motion. However, we have found the coordinates $\{Z_n\}$ so useful that we retain these coordinates and avoid planar geometries (except for three atoms, when only linear geometries are taboo). That is,

we will never evaluate the *ab initio* energy and derivatives at a perfectly planar molecular geometry (if necessary, it is “buckled”). In our experience, *ab initio* “data” can be evaluated sufficiently close to planar geometries that the PES described below is sufficiently accurate at these planar geometries.

Once the internal coordinate derivatives of the energy are known, the PES can be approximated in the vicinity of some configuration $\xi(i) = \xi[\mathbf{X}(i)]$ as a Taylor expansion, $T_i(\xi)$:

$$\begin{aligned} E(\xi) \approx T_i(\xi) = E[\xi(i)] &+ \sum_{n=1}^{3N-6} [\xi_n - \xi_n(i)] \left. \frac{\partial E}{\partial \xi_n} \right|_{\mathbf{X}(i)} \\ &+ \frac{1}{2} \sum_{n=1}^{3N-6} \sum_{m=1}^{3N-6} [\xi_n - \xi_n(i)] [\xi_m - \xi_m(i)] \left. \frac{\partial^2 E}{\partial \xi_n \partial \xi_m} \right|_{\mathbf{X}(i)} + \cdots \end{aligned} \quad (42)$$

This expansion can be continued beyond the terms which are second order in deviations of ξ from $\xi(i)$, but only at the cost of calculating the corresponding higher order *ab initio* Cartesian derivatives (which is not sufficiently efficient at present⁵⁷).

Equation (42) provides an accurate PES only in the vicinity of $\xi(i)$. Many different reference configurations, which we call “data points”, are needed. Suppose we have N_{data} such data points. Then, a modified Shepard interpolation⁵⁸ gives the PES as a weighted average of these Taylor expansions:

$$E(\mathbf{Z}) = \sum_{i=1}^{N_{\text{data}}} w_i(\mathbf{Z}) T_i(\mathbf{Z}). \quad (43)$$

Given the limited accuracy of Eq. (42), data points which are “closer” to the configuration in question, \mathbf{Z} , should have larger weights than data points which are “far” from \mathbf{Z} . The distance between a data point and any arbitrary configuration can be taken as $\|\mathbf{Z} - \mathbf{Z}(i)\|$:

$$\|\mathbf{Z} - \mathbf{Z}(i)\| = \left\{ \sum_{k=1}^{N(N-1)/2} [Z_k - Z_k(i)]^2 \right\}^{\frac{1}{2}}. \quad (44)$$

The weights in Eq. (43) are normalized functions of such distances:

$$\sum_{i=1}^{N_{\text{data}}} w_i = 1. \quad (45)$$

Normalization is ensured by defining the w_i in terms of a “primitive weight”, v_i :

$$w_i = \frac{v_i}{\sum_{j=1}^{N_{\text{data}}} v_j}. \quad (46)$$

Equation (43) is an interpolation, i.e., the value and derivatives of $E(\mathbf{Z})$, up to n th order, agree with the corresponding values of T_i as $\mathbf{Z} \rightarrow \mathbf{Z}(i)$, if

$$v_i \propto \|\mathbf{Z} - \mathbf{Z}(i)\|^{-(n+1)} \quad \text{as} \quad \|\mathbf{Z} - \mathbf{Z}(i)\| \rightarrow 0. \quad (47)$$

For our second order Taylor expansions, $n = 2$. Moreover, Eq. (43) becomes exact as $N_{\text{data}} \rightarrow \infty$, if⁵⁹

$$v_i \propto \|\mathbf{Z} - \mathbf{Z}(i)\|^{-(3N-3)} \quad \text{as} \quad \|\mathbf{Z} - \mathbf{Z}(i)\| \rightarrow \infty. \quad (48)$$

Rapid decay of the weight function at large distance ensures that data points far from the configuration \mathbf{Z} make no significant contribution to the energy. A simple implementation of Eq. (43) for the PES uses Eq. (46) with

$$v_i = \|\mathbf{Z} - \mathbf{Z}(i)\|^{-p}, \quad p > 3N - 3. \quad (49)$$

This type of weight was used in the first implementation of modified Shepard interpolation in the construction of PES.

Equation (43) requires the locations of the data points. A data point could be any molecular configuration and these occupy a $3N - 6$ dimensional space. It is not feasible to simply place data points on a uniform or nearly regular grid in $3N - 6$ dimensional space, a more efficient approach is required. The simplest picture of the reaction process is that of motion along a “reaction path” or “minimum energy path” (MEP) linking reactants, the saddle point (barrier), and products. Given the gradients and second derivatives of locations along such a path, one can estimate the reaction rates with variational transition state theory.⁶⁰ Following this picture, we choose a set of molecular configurations on such a reaction path as an *initial* data set to describe the PES via Eq. (43). To progress, an automated approach is used to choose additional data points. This automation is based on the idea that the value of the PES at configurations which the molecule passes through during the reaction dynamics must play some role in determining the observed dynamics. It is only at these configurations where the PES must be known, *not* throughout the whole space. It is very easy to discover which configurations are involved in the classical dynamics, but it is very difficult to discover which configurations are involved in the quantum dynamics of the reaction.

Given data points on the MEP for the reaction, the PES of Eq. (43) is defined, albeit inaccurately. We simulate the chemical reaction by solving the classical (Newtonian) equations of motion with initial conditions corresponding to the collision of the reacting molecules. The choice of initial conditions should reflect the observable properties we wish to simulate; for example, the initial vibration–rotation–translational energies or temperature should be at least as high as the values appropriate to any relevant experiments. Several (say 10) trajectories are calculated while the molecular configuration is periodically written to a file. This set of configurations N_{traj} represents a sample of the dynamically important region of configuration space. One of these configurations is chosen to be a new data point. Two criteria have been used. A quantity $h(k)$ is evaluated at each of the N_{traj} configurations:

$$h(k) = \frac{\sum_{\substack{m=1 \\ m \neq k}}^{N_{\text{traj}}} v_m[\mathbf{Z}(k)]}{\sum_{i=1}^{N_{\text{data}}} v_i[\mathbf{Z}(k)]}. \quad (50)$$

The ratio $h(k)$ is largest when $\mathbf{Z}(k)$ is near other sampled trajectory configurations, but is far from the existing data points. The trajectory configuration with the largest value of h is chosen to be a new data point. Alternatively, the accuracy of the PES might best be improved if a new data point were added where the PES is most inaccurate. Unfortunately, the accuracy of the PES is not known. However, the uncertainty in the interpolated PES at each of the N_{traj} configurations can easily be evaluated as $\sigma(k)$:

$$\sigma^2(k) = \sum_{i=1}^{N_{\text{data}}} w_i[\mathbf{Z}(k)] \{T_i[\mathbf{Z}(k)] - E[\mathbf{Z}(k)]\}^2, \quad (51)$$

where $E[\mathbf{Z}(k)]$ is the interpolated (averaged) energy of Eq. (43). The variance associated with the average is an estimate of the uncertainty in the average. The $\mathbf{Z}(k)$ with the largest value of $\sigma(k)$ is chosen as a new data point.

The *ab initio* calculations for the energy and derivatives at the chosen $\mathbf{Z}(k)$ are carried out, and $\mathbf{Z}(k)$ is added to the data set. The cycle of evaluating a small set of trajectories to generate a sample of configurations, choosing one of these as a new data point, and evaluating the *ab initio* data at this configuration to increment the data set, is repeated again and again. As the data set “grows”, say after every 100 data points are added, large

numbers of classical trajectories are evaluated to simulate the reaction and measure some relevant observables, e.g. the reaction cross-section or thermal rate coefficient. When the values of these observables do not change with increasing N_{data} , the PES is “converged” to sufficient accuracy.

A molecular PES has a definite symmetry. It is invariant to translation, rotation and inversion of the molecule. These properties are satisfied by Eq. (43) because the PES is expressed purely in terms of atom–atom distances. A molecular PES is also invariant to the permutation or exchange of indistinguishable nuclei. These operations form a group called the complete nuclear permutation (CNP) group. If we evaluate the *ab initio* energy and its Cartesian derivatives at \mathbf{X} , then the energy at a permuted configuration, $P\mathbf{X}$, is the same as at \mathbf{X} , the vector of first derivatives at $P\mathbf{X}$ is the same as at \mathbf{X} , except that the corresponding derivatives are permuted. Moreover, the matrix of second derivatives at $P\mathbf{X}$ is the same as at \mathbf{X} except that the corresponding rows and columns are permuted. So, for the computational cost of these calculations at \mathbf{X} , the energy, gradient and second derivatives are known at $|\text{CNP}|$ configurations. So, it is trivially easy to include all $|\text{CNP}|$ versions of each calculated data point in the data set. The data set is thus an invariant of the CNP group and therefore the PES is also an invariant of the CNP group. To make it clear that this symmetry is incorporated in the PES, we usually write the interpolation formula as

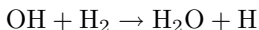
$$E(\mathbf{Z}) = \sum_{g \in G} \sum_{i=1}^{N_{\text{data}}} w_{g \circ i}(\mathbf{Z}) T_{g \circ i}(\mathbf{Z}), \quad (52)$$

where G represents the symmetry group and $g \circ i$ denotes that every permutation of each data point is also in the data set.

The complete process for iteratively “growing” the data set, for calculating the internal coordinates at each data point, and for implementing the correct CNP symmetry in the PES has been automated in a package of FORTRAN programs and Unix scripts called *Grow*. These programs also allow the user to generate classical simulations of the reactions and to calculate reaction cross-sections. The package is freely available to non-commercial researchers.⁶¹

3.2. Proof and Improvement of Accuracy

To show that this method is sufficiently accurate, a PES for the reaction



was constructed, not from *ab initio* calculations, but from the analytic PES of Schatz and Elgersma (SE).²¹ That is, the energy, energy gradient and

second derivatives were evaluated from a version of the SE surface. The interpolated PES is therefore an approximation to a known surface, and the reaction dynamics on both the SE surface and its interpolated approximation could be directly compared. Originally, classical mechanics was used to evaluate the reaction cross-section on both surfaces. The simple weight function of Eq. (49) was employed with the two methods for choosing the location of data points described above (and another method similar to the maximum variance option). For each method of choosing data point locations, this basic approach was sufficiently accurate to produce interpolated PES which gave accurate classical reaction cross-sections and energy and angular momentum distributions in the products. The detailed results have been presented elsewhere.⁶²

Subsequently, new PESs were constructed using *ab initio* calculations of the electronic energy for reactions in the CH_3^+ , BeH_3 and NH_3^+ systems. In each case, classical mechanics was used to examine the apparent convergence of the reaction cross-sections as a function of the size of the data set. In each case convergence was demonstrated.

In order to test whether this type of interpolated PES was sufficiently accurate for *quantum* dynamics calculations, the quantum reaction probability (for $J = 0$) was evaluated for the reaction $\text{BeH} + \text{H}_2 \rightarrow \text{BeH}_2 + \text{H}$, using an interpolated PES.⁶³ Unfortunately, as suggested by Fig. 4, the convergence of the quantum reaction probability was disappointing. The apparent cause of this effect is that the interpolated PES is not sufficiently “smooth”. The problem arises because the simple weight function of Eq. (49) varies too rapidly. The exponent p in Eq. (49) must exceed $3N - 3$. This means that if two data points have large and nearly equal weights, a small change in the geometry, \mathbf{Z} , produces a large change in the relative weights. Thus, in regions which are nearly equidistant from two or more data points, sharp changes can occur in the PES. The error in the gradient of the PES is relatively large.

This shortcoming can be largely rectified by the use of “more intelligent” weights. The simple weight function of Eq. (49) varies much more rapidly near $\mathbf{Z}(i)$ than is necessary for the PES to be an interpolation of the data at $\mathbf{Z}(i)$ [see Eq. (47)]. A form of weight function which obeys both the limiting restrictions of Eqs. (47) and (48) would be⁵²

$$v_i = \left\{ \left[\frac{\|\mathbf{Z} - \mathbf{Z}(i)\|}{\text{rad}(i)} \right]^q + \left[\frac{\|\mathbf{Z} - \mathbf{Z}(i)\|}{\text{rad}(i)} \right]^p \right\}^{-1}, \quad (53)$$

where $p > 3N - 3$, and $q > 2$, but $q \ll p$. In Eq. (53), $\text{rad}(i)$ is a “confidence radius”. If $\|\mathbf{Z} - \mathbf{Z}(i)\| < \text{rad}(i)$, then v_i falls relatively slowly as $\|\mathbf{Z} - \mathbf{Z}(i)\|$

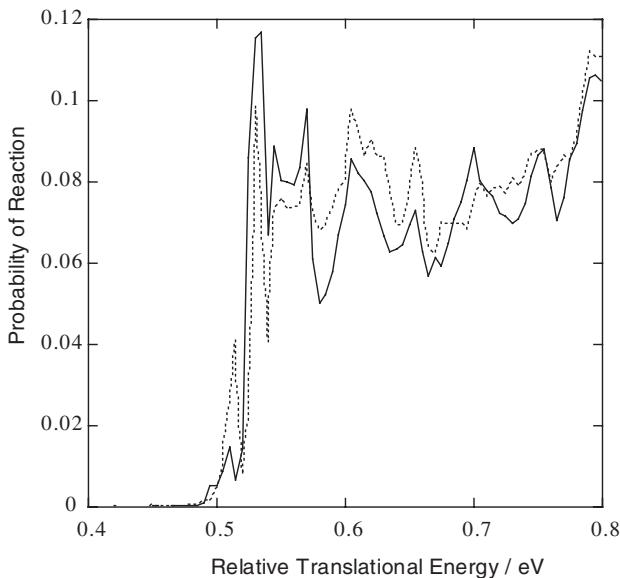


Fig. 4. The quantum reaction probability for $\text{BeH} + \text{H}_2 \rightarrow \text{BeH}_2 + \text{H}$ at $J = 0$ is shown as a function of the relative translational energy. The PES was evaluated using the simple weight function of Eq. (49) with a data set of 926 (\cdots) and 1110 ($—$) data points.

increases, while if $\|\mathbf{Z} - \mathbf{Z}(i)\| > \text{rad}(i)$, then v_i falls to zero very rapidly as $\|\mathbf{Z} - \mathbf{Z}(i)\|$ increases. Hence, the relative weights of two or more data points “near” \mathbf{Z} vary only slowly with varying \mathbf{Z} ; reducing the unphysically sharp changes in the PES caused by the simpler weight function. The values of $\text{rad}(i)$ are determined by a Bayesian analysis of the errors in the second order Taylor expansions as follows.⁶⁴

From the position of any one data point, $\mathbf{Z}(i)$, the remaining data points appear scattered around it in the $3N - 6$ dimensional space. The error in the Taylor expansion T_i , $E[\mathbf{Z}(j)] - T_i[\mathbf{Z}(j)]$, can be measured at each neighboring data point, $j \neq i$. If the data density is sufficiently high, there are a set of M points (typically $M \approx 20\text{--}100$) which are close enough to $\mathbf{Z}(i)$ that the error in T_i is dominated by the first term neglected in the Taylor expansion. Then

$$E[\mathbf{Z}(j)] - T_i[\mathbf{Z}(j)] \propto \|\mathbf{Z}(j) - \mathbf{Z}(i)\|^3. \quad (54)$$

If these M points are randomly scattered near $\mathbf{Z}(i)$, then the average error is near zero (positive and negative errors are equally likely), but the average square error is nonzero. An accurate Taylor expansion could be defined as one for which the root-mean-square error is less than some tolerance, E_{tol} ,

and a Bayesian analysis of the errors gives the distance, $\text{rad}(i)$, over which this accuracy should hold⁶⁴:

$$\text{rad}(i)^{-6} = \frac{1}{M} \sum_{j=1}^M \frac{\{E[\mathbf{Z}(j)] - T_i[\mathbf{Z}(j)]\}^2}{E_{\text{tol}}^2 \|\mathbf{Z}(j) - \mathbf{Z}(i)\|^6}. \quad (55)$$

To derive this result we only have to rely on Eq. (54) and the idea that the distribution of errors is a normal distribution. Of course, the error in the Taylor expansions is not just a function of distance, it is also a function of direction. Hence, a better model would assign each Taylor expansion “confidence lengths” for each direction in space. For various reasons, it is much simpler to associate a confidence length with each element of \mathbf{Z} , and to define the weight function as

$$v_i = \left\{ \left[\sum_{n=1}^{N(N-1)/2} \left(\frac{Z_n - Z_n(i)}{d_n(i)} \right)^2 \right]^{\frac{q}{2}} + \left[\sum_{n=1}^{N(N-1)/2} \left(\frac{Z_n - Z_n(i)}{d_n(i)} \right)^2 \right]^{\frac{p}{2}} \right\}^{-1}. \quad (56)$$

The confidence lengths, $d_n(i)$, have been derived from a Bayesian analysis of the errors in the gradients⁶⁴:

$$d_n(i)^{-6} = \frac{1}{M} \sum_{j=1}^M \frac{\left\{ \left[\left. \frac{\partial E}{\partial Z_n} \right|_{\mathbf{Z}(j)} - \left. \frac{\partial T_i}{\partial Z_n} \right|_{\mathbf{Z}(j)} \right] [Z_n(j) - Z_n(i)] \right\}^2}{E_{\text{tol}}^2 \|\mathbf{Z}(j) - \mathbf{Z}(i)\|^6}. \quad (57)$$

If there are sufficient data points available for the underlying statistical assumptions to be valid, the most accurate interpolation is given by Eq. (52) with the weight function defined by Eqs. (46), (56) and (57).

Figure 5 presents the quantum reaction probability of Fig. 4, recalculated on the same PES data for BeH_3 , but with the Bayesian weight function of Eq. (56). The improvement in the convergence of the reaction probability, compared to that in Fig. 4, is clearly dramatic. A calculation of the *ab initio* energy and gradient at configurations encountered in classical trajectories for this reaction shows that the average absolute error in the PES (based on 1300 data points) is reduced by about 15% if the Bayesian weight function is employed. More significantly, the average relative gradient error⁶² is reduced by half, from about 12% to 6%. Similar analysis of the interpolation errors for several systems showed that the use of Bayesian confidence lengths in the weight function produced significantly more accurate interpolation in every case.⁶⁴

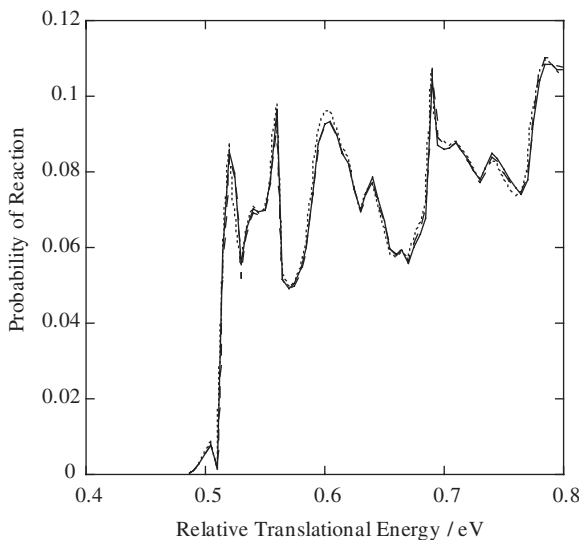


Fig. 5. Same as for Fig. 4, but here the PES was evaluated using the Bayesian weight function of Eq. (56) with a data set of 960 (\cdots), 1110 ($---$) and 1300 ($—$) data points.

To prove that the Bayesian weights give convergence of the PES to the correct surface, we again considered the interpolated approximation to a known analytic PES, a modified form of the SE surface for $\text{OH} + \text{H}_2$.⁶⁵ The quantum reaction probability, as a function of the relative translational energy of the reactants (for $J = 0$), was evaluated for the SE surface and interpolated approximations. Figure 6 shows that the interpolated PES is sufficiently accurate that the quantum reaction probability, $P(E)$, converges to the correct value as the size of the data set increases. Figure 7 displays, on an expanded scale, a small resonance feature in the reaction probability at low translational energy. The average absolute error in $P(E)$ over the energy range of Fig. 6 is just 0.00016 for a PES based on 391 data points. Not surprisingly then, the resonance feature, which occurs on a similar scale, is not *quantitatively* reproduced by the interpolated PES. Nevertheless, as Figs. 6 and 7 indicate, the interpolated PES can reasonably be described as sufficiently accurate for the practical calculation of quantum reaction dynamics. Hence, we can be confident that when the quantum reaction probability converges with increasing data set size, as shown in Fig. 5 for BeH_3 , then it converges to the correct result. Of course, the quantum probability we calculate is only the correct result for the level of *ab initio* theory employed in constructing the PES.

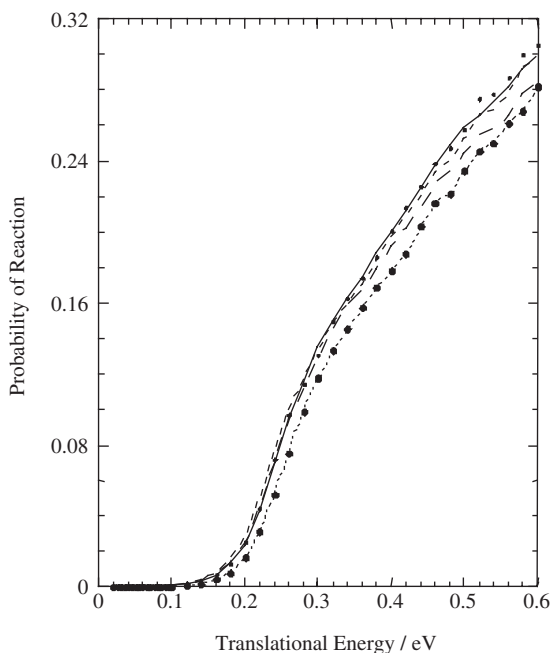


Fig. 6. The reaction probability for $\text{OH}(v=0, j=0) + \text{H}_2(v=0, j=0) \rightarrow \text{H}_2\text{O} + \text{H}$, with $J=0$, on a modified SE surface versus the relative translational energy of the reactants. The exact result (—) is compared with values given by the interpolated PES with 30 ($\cdots \bullet \cdots \bullet \cdots$), 191 (---), 291 (-.-), and 391 (\bullet) data points.

3.3. Computational Considerations

There are two computational hurdles which must be reduced in magnitude to ensure that this type of PES can be implemented. The construction of the PES requires a large number of *ab initio* quantum chemistry calculations. Once the PES has been constructed, the right-hand side of Eq. (52) has to be evaluated. For classical mechanics, both the value and gradient of the PES must be calculated at the very large number of molecular configurations which are encountered during a trajectory simulation. For quantum dynamics, only the energy is required, but the number of molecular configurations required is very large indeed. As a practical matter, it is important to minimize the computational time needed to evaluate Eq. (52).

Let us consider the *ab initio* task first. At each data point, we require the *ab initio* energy, gradient and second derivatives. Up to now, PESs have been constructed for about a dozen reactions involving four atoms, two involving five atoms and two involving six atoms. Roughly speaking, several

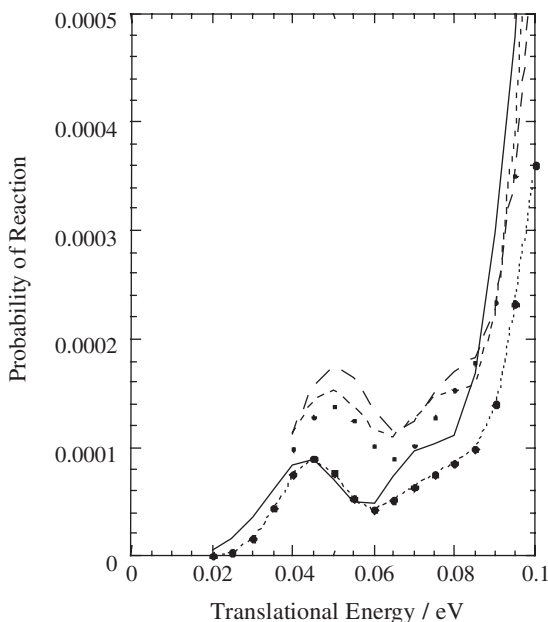


Fig. 7. An enlargement of the low energy portion of Fig. 6.

hundred data points have been required to achieve convergence for systems of four atoms, 800–1300 data points for five atoms, and 2000–3000 data points for six atoms. The level of *ab initio* theory required varies a great deal from one reaction to another. The first task in any implementation of this approach is a standard investigation of the convergence of the molecular energy with respect to the size of the basis set and the level at which electron correlation is treated. The usual practice is to identify the relevant stationary points on the PES (to the extent this is possible) and test convergence with respect to basis set and electron correlation at each of them. For some systems, second order Moller–Plesset perturbation theory (MP2) or even density functional theories like BLYP and B3LYP have proved to be adequate. Not only are such levels of theory relatively inexpensive, but analytic gradients and second derivatives are available. When a higher level of electron correlation is necessary, some quantum chemistry programs provide analytic gradients for methods like quadratic configuration interaction with single and double excitations (QCISD) or even coupled cluster configuration interaction with single and double excitations and perturbative treatment of triple excitations [CCSD(T)]. However, analytic

second derivatives are generally not available, or not very efficient, for high level methods like CCSD(T). In that case, the second derivatives, or even gradients, must be evaluated by numerical finite difference. The program package, *Grow*, can be used with electronic structure methods which provide analytic second derivatives, or only analytic gradients or only energies. When finite difference calculations are required, *Grow* performs this task more efficiently than some quantum chemistry programs, since the finite steps are evaluated in the robust internal coordinates, ξ , rather than in Cartesian coordinates. The *ab initio* computation time can also be reduced if a basis set correction method is sufficiently accurate. For example, the effect on the electron correlation energy of increasing the basis set size, might be adequately described at the MP2 level, even though the relative energy of stationary points on the PES might only be accurately given by a CCSD(T) calculation. Then, one can approximate the energy at CCSD(T) with a large basis set by

$$\begin{aligned} E[\text{CCSD(T)/large basis set}] &\approx E[\text{CCSD(T)/small basis set}] \\ &\quad + E[\text{MP2/large basis set}] \\ &\quad - E[\text{MP2/small basis set}]. \end{aligned} \quad (58)$$

Since analytic second derivatives are available for MP2 calculations, numerical difference calculations of CCSD(T) energies are only required for a relatively small basis set. This type of basis set correction approximation is also available in *Grow*. It is not possible to use some “composite” methods which, like the G2 and G3 schemes,⁶⁶ involve adding non-differentiable corrections to the estimated electronic energy. However, there are other recently developed composite methods which might be effectively employed to construct this type of interpolated PES.⁶⁷

Another type of approximation has been employed to minimize the time expended on *ab initio* calculations. The accuracy of any PES does not depend on the absolute electronic energy, but on the relative energies of the molecular configurations which are relevant for the reaction studied. Sometimes a low level of electron correlation and/or a relatively small basis set results in relative energies that are almost quantitatively accurate. For example, the reaction exothermicity and important barrier heights may be given to within a few kJ mol^{-1} of the most reliable high level values (which may be of the order of 10^2 kJ mol^{-1}). Since the computational time rises very rapidly with basis set size and level of electron correlation, these last few kJ mol^{-1} of accuracy are very expensive to obtain. Moreover, one

often finds that second derivatives evaluated at say the MP2 or even B3LYP levels of theory are often quite accurate in comparison with large basis set CCSD(T) values. Hence, it has proved possible in four cases (to date) to adopt the following approximation. An interpolated PES is constructed to fair accuracy at a computationally affordable level of *ab initio* theory. The energy (only) of each data point is then replaced with the value calculated at a much higher, more quantitatively accurate, level of theory. The gradient and second derivatives at each data point retain the values from the lower level of theory.

The second major hurdle to be minimized is the evaluation of the PES. Obviously from Eq. (52) there are two tasks, calculating the weights and the Taylor series. The total number of data points in the PES may be very large because of symmetry. For example, a PES for CH₅ with 2,500 symmetry-distinct data points has $2,500 \times 5! = 300,000$ data points in total. In some circumstances, the size of the symmetry group could be reduced without loss of accuracy by employing only the subset of feasible permutations, the molecular symmetry group,⁶⁸ rather than the CNP group.

In any case, at any particular configuration, **Z**, where the PES is evaluated, only a relatively small number of data points will have a significant weight. If we first evaluate the weights, then we can simply not evaluate the Taylor expansion for any data point for which the weight falls below some tolerance, w_{tol} . Typically, w_{tol} is taken in the range 10^{-6} to 10^{-5} without introducing a chemically significant error in the interpolation. For typical cases to date, only about 20 to 30 data points (on average) have weights above w_{tol} for a four-atom system, while this range rises to (roughly) 50 to 70 for six-atom systems. The actual number of significant data points for some **Z** can vary from a few to several hundred, and all $N_{\text{data}} \times |\text{CNP}|$ data points may make a non-negligible contribution somewhere. Nevertheless, very substantial computational saving results from only evaluating a small number of Taylor expansions. Note also that the local internal coordinates used in the Taylor expansions are only evaluated for the small number of significant data points.

In order to find the data points of significant relative weight, it would appear that the primitive weight of Eq. (56) needs to be evaluated for all the data points. However, this substantial task can be greatly reduced in the following way. For classical mechanics, the PES and its gradient are evaluated for a sequence of molecular configurations which evolve from one to the next along a trajectory. The molecular configuration changes gradually so that the significant data points for one configuration are also

significant for the next. We use the idea of a “neighbor list”. If we identify the “neighboring data points” (those with significant weight) at one time step in a classical trajectory, the weights at say 10 subsequent time steps need only be re-evaluated for data points on this neighbor list (containing perhaps less than 100 data points), rather than the whole data set. The entire data set is only reconsidered every 10 time steps (say) and the computational task is reduced by about an order of magnitude. In practice, we keep track of an inner neighbor list (for which the weight exceeded w_{tol} at some step) and an outer neighbor list (containing more data points of lower weight) and periodically update the outer list from the whole data set while the inner list is updated more frequently but only considering the outer list. In this way the task of determining the significant data points is vastly reduced in magnitude without loss of accuracy.

For quantum dynamics calculations, the PES may be needed on a regular grid in the $3N - 6$ dimensional space. Clearly, in six or more dimensions, the number of grid points, N_{grid} , can be large, and the relevant Taylor expansions must be evaluated at each one. Two simple steps can be taken to reduce the task of calculating the weights and the energies. First, in each grid direction, every third grid point has two unique nearest neighbors. There is a unique set of 3^{3N-6} grid points centered at each of $N_{\text{center}} = N_{\text{grid}}/3^{3N-6}$ grid points. We can evaluate a data point neighbor list for each of these N_{center} points and only calculate the weights at the local 3^{3N-6} grid points using this neighbor list rather than the full data set. The weight calculation is reduced in magnitude by a factor of nearly 3^{3N-6} . Another substantial time reduction is also possible. The full grid is usually chosen to be regularly spaced in the coordinates which are used to integrate the Schrödinger equation. This normally means that the grid extends to large regions of molecular configurations which are energetically unfeasible; that is, the quantum wavefunction is negligible in magnitude in such regions. It does not matter what the value of the PES is in such regions, so long as it is much larger than the energy available to the system. Hence, if we evaluate the PES at one of the N_{center} locations and find that its value far exceeds the available energy, we can put the value of the PES to be some large value at each of the associated 3^{3N-6} grid points without actually evaluating the PES more than once (at the local center). The time required to evaluate the PES at virtually all of these very high-energy locations is therefore eliminated. For high dimensional “quantum grids”, the computational task of evaluating the PES is nevertheless an onerous one.

4. Results for Some $\text{AB} + \text{CD}$ and $\text{ABC} + \text{D}$ Reactions

4.1. Reactions of $\text{H}_2 + \text{OH}$, $\text{HD} + \text{OH}$, and $\text{D}_2 + \text{OH}$

The $\text{H}_2 + \text{OH}$ reaction is the prototype for four-atom reactions in much the same way that the $\text{H} + \text{H}_2$ reaction has been for three-atom reactions. Many theoretical and experimental studies have been carried out on the $\text{H}_2 + \text{OH}$ reaction and its isotopic analogs. The approximate, analytic Walch–Dunning–Schatz–Elgersma (WDSE) PES^{69,21} featured prominently in facilitating the development of classical and quantum dynamical methods to study the $\text{H}_2 + \text{OH} \rightarrow \text{H} + \text{H}_2\text{O}$ reaction. Recently, high-level interpolated *ab initio* PESs were reported for the reverse reaction $\text{H} + \text{H}_2\text{O} \rightarrow \text{H}_2 + \text{OH}$ and its isotopic analogs.^{70,71} The so-called QCISD(T)/6-311++G(3df, 2pd) *ab initio* PES is not defined in the region of the $\text{H}_2 + \text{OH}$ entrance channel, due to the presence of a second low-lying electronic state, and so cannot be used to evaluate the final state distribution of $\text{H}_2 + \text{OH}$ products from the $\text{H} + \text{H}_2\text{O}$ reaction, or to study the $\text{H}_2 + \text{OH}$ reaction.

The near degeneracy of the ground and first excited electronic states in the $\text{H}_2 + \text{OH}$ entrance channel has recently been addressed by employing the CASSCF/CMRI+Q/aug-cc-pVQZ level of theory, using the MOLPRO package,⁷² in a substantial part of the $\text{H}_2 + \text{OH}$ entrance channel, while elsewhere the QCISD(T)/6-311++G(3df, 2pd) level of theory was used. Two new *ab initio* Yang–Zhang–Collins–Lee global PES — YZCL1 and YZCL2 — resulted.⁷³ They were constructed using the procedure outlined in Sec. 3 above. The YZCL1 surface has 1,600 data points. The energy of each of these data points was then evaluated at the UCCSD(T)/aug-cc-pVQZ level of theory to produce the YZCL2 surface, considered the best global PES for H_3O today.

Figure 8 compares the fully converged integral cross-sections for the $\text{H}_2(j_1 = 0) + \text{OH}(j_2 = 0)$ reaction as a function of translational energy for the WDSE, YZCL1, and YZCL2 PESs. There is a shift of ~ 0.035 eV between the cross-sections obtained on the YZCL1 and YZCL2 PESs in the higher energy region, which is larger than the difference in the barrier heights for these two surfaces of 0.014 eV. Thus the overall effect of the energy correction from QCISD(T)/6-311++G(3df, 2pd) in YZCL1 to UCCSD(T)/aug-cc-pVQZ in YZCL2 is not just the energy reduction in barrier height, but rather the energy shift of most data points in the general region of the barrier by 0.03–0.04 eV. The WDSE cross-section, by comparison, is too large at low energies and too small at high energies.

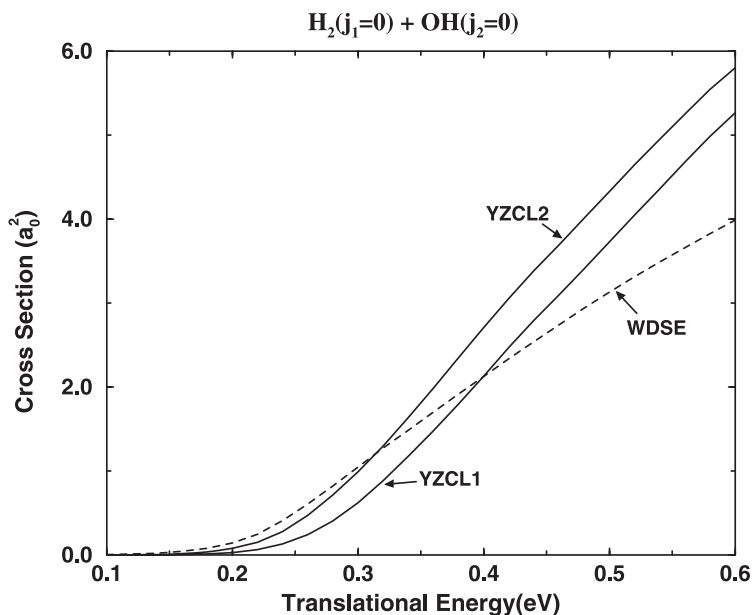


Fig. 8. Comparison of fully converged integral cross-sections as a function of the translational energy for the $\text{H}_2(j_1 = 0) + \text{OH}(j_2 = 0) \rightarrow \text{H}_2\text{O} + \text{H}$ reaction on the WDSE, YZCL1, and YZCL2 surfaces.

On the YZCL2 surface, the $\text{H}_2 + \text{OH} \rightarrow \text{H} + \text{H}_2\text{O}$ reaction is exothermic by 66.3 kJ mol^{-1} with a near L-shape geometry for the transition state, where $\text{H} \cdots \text{O}$ is one arm and an almost linear $\text{O} \cdots \text{H} \cdots \text{H}$ for the other arm, with a barrier to reaction of 22.2 kJ mol^{-1} . Thermal rate coefficients for the $\text{H}_2 + \text{OH} \rightarrow \text{H} + \text{H}_2\text{O}$ reaction in the temperature range from 238 to 1050 K have been measured.^{74,75} In Fig. 9, we compare the rate coefficients obtained on the three surfaces — WDSE, YZCL1 and YZCL2 — with the latest experimental results⁷⁴ for the temperature range 238–400 K. We took into account the electronic partition function for the OH reactant; the reactant population on the adiabatic ground state PES is that of the lower spin-orbit state of OH (assuming a splitting of 140 cm^{-1}). We assumed that the OH rotational excitation has a negligible effect on the rate coefficient at low temperatures and used a thermal averaging of the rate coefficient for the $(j_1 = 0, j_2 = 0)$ and $(j_1 = 2, j_2 = 0)$ states of $\text{H}_2(j_1) + \text{OH}(j_2)$, because in the low temperature region the contribution to the thermal rate coefficient from *para*- H_2 should be equal to that from *ortho*- H_2 . Clearly, Fig. 9 shows that the thermal rate coefficient obtained from the YZCL2 PES agrees best

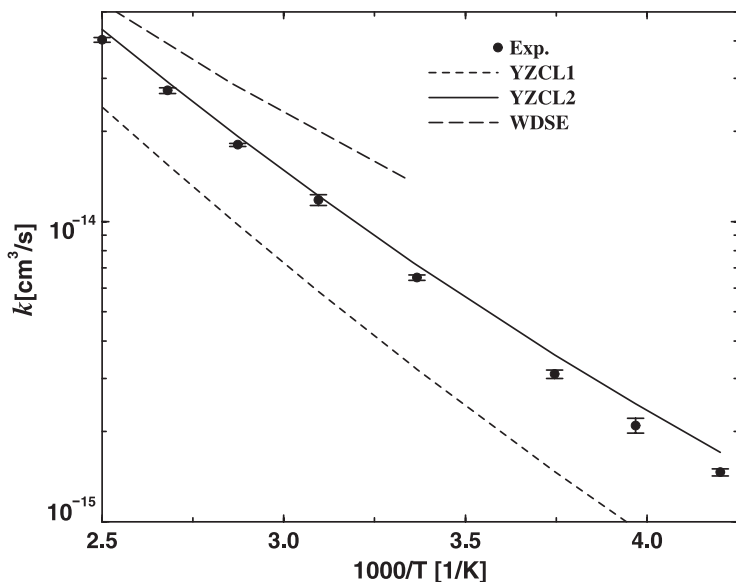


Fig. 9. The thermal rate coefficient for $\text{H}_2 + \text{OH} \rightarrow \text{H} + \text{H}_2\text{O}$ on the WDSE, YZCL1, and YZCL2 surfaces are compared with experimental results.⁷⁴

with the experimental data across the whole temperature range considered. On the other hand, the YCL1 PES rate is lower throughout, differing from the experimental data by a factor of 2 at 297 K, while the WDSE PES rate is larger by a similar factor. In Fig. 10, the rate coefficient for the ground rovibrational state of $\text{H}_2 + \text{OH}$ is compared with the experimental results over a wider temperature range, 238–1050 K. In principle, many rovibrational states would be required for the higher temperatures, but it is too computationally demanding at the moment. Nevertheless, the results show that the YZCL2 PES rate is in good agreement with experiment, while the YZCL1 PES only gives the correct trend and the WDSE PES rises too slowly as the temperature increases.

A full-dimensional (six degrees-of-freedom) study was also carried out on the $\text{HD} + \text{OH} \rightarrow \text{H}_2\text{O} + \text{D}$, $\text{HOD} + \text{H}$ reaction, on the most accurate YZCL2 PES as found for the $\text{H}_2 + \text{OH}$ reaction above.⁷⁶ This reaction allows us to look at the branching ratio and the effect of reagent rotation on the rate coefficient which can be compared to experiments. The initial state selected time-dependent wavepacket method was employed to calculate the fully converged integral cross-section for two sets of reagent angular momenta: the $\text{HD}(j_1 = 0-3) + \text{OH}(j_2 = 0)$, and $(j_1 = 0, j_2 = 0, 2, 4)$ initial states. The

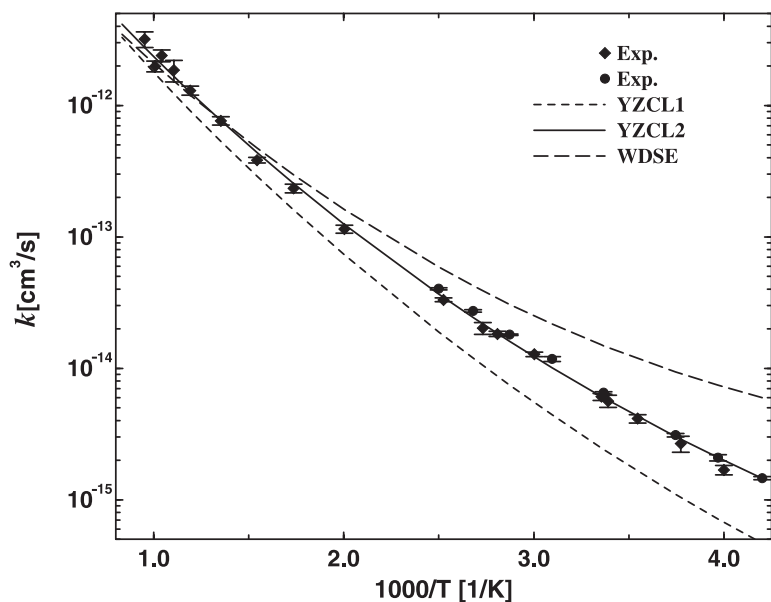


Fig. 10. The initial state selected rate coefficient for $\text{H}_2(j_1 = 0) + \text{OH}(j_2 = 0) \rightarrow \text{H} + \text{H}_2\text{O}$ calculated on the WDSE, YZCL1, and YZCL2 PESs are compared with experimental results: \bullet (Ref. 74); \blacklozenge (Ref. 75).

fully converged integral cross-sections for the first set as a function of translational energy are shown in Fig. 11(a). The cross-section for the $\text{HOD} + \text{H}$ product increases substantially faster than the $\text{H}_2\text{O} + \text{D}$ product as translational energy increases. However, for the (0, 0) state, the D-atom product is larger than for the H-atom product for translational energy below 0.226 eV, as shown in Fig. 11(b), which is close to the barrier height of the YZCL2 PES of 0.234 eV. In that energy region, quantum tunnelling plays a dominant role in determining the reactivity. As the HD reagent gets increasingly excited rotationally from $j_1 = 0$ to $j_1 = 3$ at a given translational energy, the cross-section for the H-atom product remains approximately the same in the low energy region, but in the high energy region the cross-section shows a monotonic decrease. On the other hand, the cross-section for the D-atom product increases with j_1 . Hence rotational excitation of the HD reagent substantially enhances the rate coefficient for forming the $\text{H}_2\text{O} + \text{D}$ product, and plays an important role in determining the branching ratios at low temperatures.

The influence of OH rotational excitation on the products is shown in Fig. 12, which plots the fully converged integral cross-sections for the

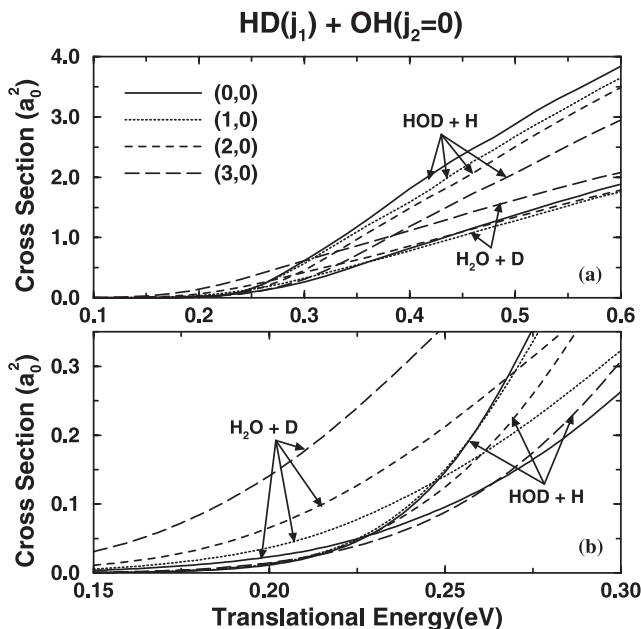


Fig. 11. Fully converged integral cross-section for the $\text{HD}(j_1 = 0-3) + \text{OH}(j_2 = 0) \rightarrow \text{H}_2\text{O} + \text{D}$, $\text{HOD} + \text{H}$ reaction, (a) for translational energy up to 0.6 eV; (b) in the low translational energy region.

$\text{HD}(j_1 = 0) + \text{OH}(j_2 = 0, 2, 4)$ reaction. In the high energy region, the cross-sections for both products decrease as j_2 increases. In the low energy region, as shown in Fig. 12(b), the rotational excitation of the OH has negligible effect on the cross-section for the H-atom product, but increasingly enhances the cross-section for the D-atom product.

Volpp *et al.*⁷⁷ have measured the absolute reaction cross-section to be $0.14 \pm 0.05 \text{ \AA}^2$ and the H/D branching ratio to be 1.2 ± 0.2 at a translational energy of 0.24 eV (with a half-width of 0.13 eV) for the $\text{HD} + \text{OH} \rightarrow \text{H}_2\text{O} + \text{D}$, $\text{HOD} + \text{H}$ reaction. The reagent OH in the experiment is highly excited rotationally, with an average $j_2 \approx 7$. It is not feasible at present to calculate the integral cross-sections for OH in such a high rotational state, and HD is thermally excited (300 K), also in a high rotational state. Nevertheless, we can use the theoretical results to make a rough comparison. First, we note that for such a broad reagent translational energy distribution, the main contribution to the measured absolute cross-section comes from the medium to high energy region, Fig. 12(a). The cross-sections for both products in

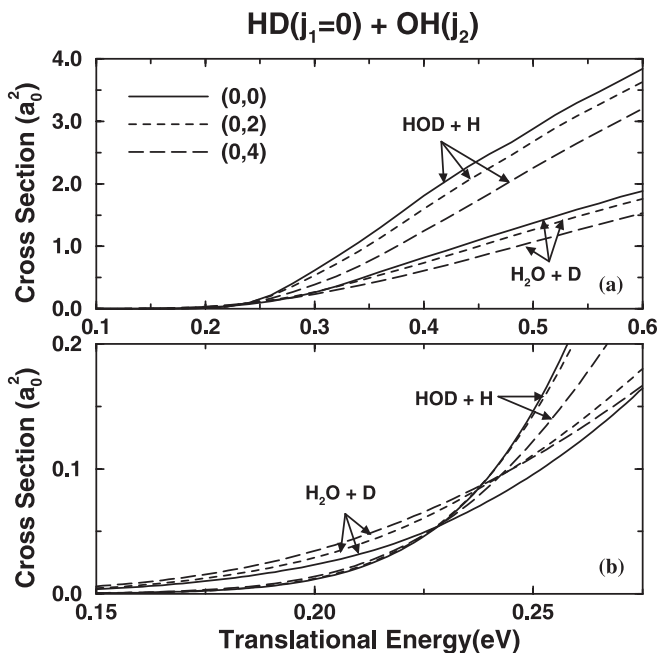


Fig. 12. Same as in Fig. 11, but for initial states HD($j_1 = 0$) + OH($j_2 = 0, 2, 4$).

that energy region decrease as j_2 increases, so we may assume that the branching ratio is not too sensitive to the OH rotational excitation. Therefore we can estimate the branching ratio from the integral cross-sections for these two products thermally averaged over the HD rotation. The resulting H/D branching ratio is 1.5, and since Fig. 12 shows that the cross-section for the H-atom product actually decreases faster than for the D-atom product as j_2 increases, the result obtained is likely to be an upper limit, and in agreement with experiment. Similarly, the upper limit absolute cross-section is estimated to be 0.12 \AA^2 , also in agreement with experiment.

We can calculate the thermal rate constants at low temperatures with the cross-sections for the HD and OH rotationally excited states, using Eqs. (34) and (35), and with the assumption that simultaneous OH and HD rotational excitation does not have a strong correlated effect on the dynamics as found in the previous quantum and classical trajectory calculations for the OH + H₂ reaction on the WDSE PES.^{69,78} In Fig. 13, we compare the theoretical thermal rate coefficient with the experimental values from 248 to 418 K of Ravishankara *et al.*⁷⁴ On average, the theoretical result

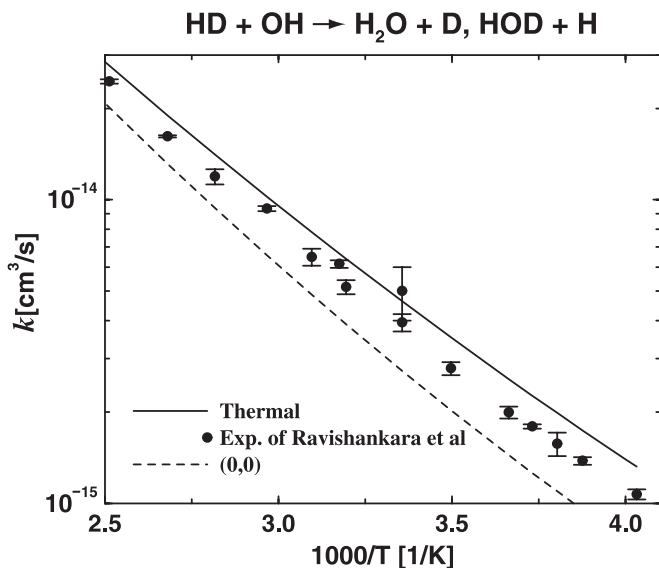


Fig. 13. Comparison of theoretical rate coefficients with experimental results of Ravishankara *et al.*⁷⁴

is larger than the experimental result by about 20%, which demonstrates again the quality of the YZCL2 PES. Also shown in Fig. 13 is the initial state selected rate coefficient for the ground rovibrational state, which is about 20–30% below the experimental result, indicating that the rotational excitations of the reagents are not very important for the measured rate coefficient of this reaction at low temperature.

Fully converged integral cross-sections for the $D_2(j_1 = 0, 2, 4) + OH(j_2 = 0, 2, 4) \rightarrow HOD + D$ reaction have been calculated on the YZCL2 PES. It is found that the effect of reagent rotational excitation on the reaction is relatively mild, particularly in the low translational energy region, compared with that of the D_2 vibrational excitation. However, this effect is fairly important to the thermal rate constant at low temperature. In general, the OH rotational excitation tends to hinder the reaction, while the D_2 rotational excitation tends to enhance it. The D_2 and OH rotational excitation has some correlated effect on the reaction. It is found that the reaction is strongly dependent on j_{12} (the coupled angular momentum between j_1 and j_2), K_0 (the projection of the reagent rotation on the body fixed axis), and the parity of the system. Figure 14 shows the initial state selected rate coefficients in the temperature range of 240–401 K for all the

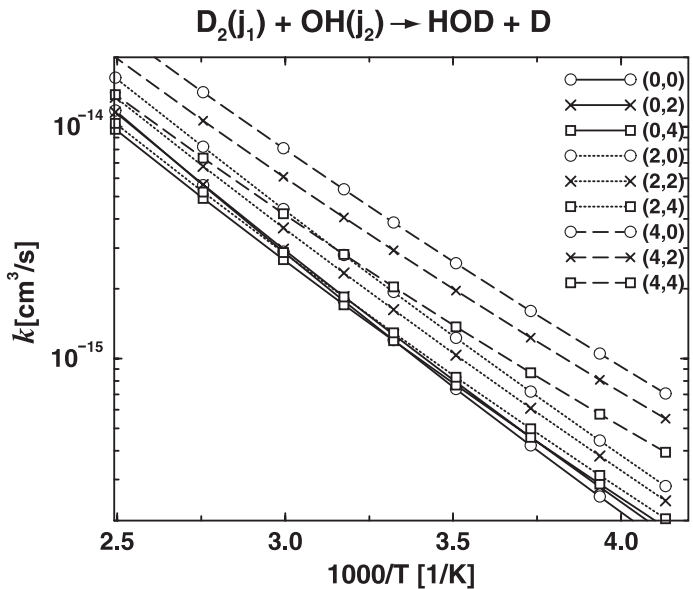


Fig. 14. Initial state selected rate coefficients for the reaction $D_2(j_1) + OH(j_2) \rightarrow HOD + D$, with $(j_1 = 0, 2, 4; j_2 = 0, 2, 4)$.

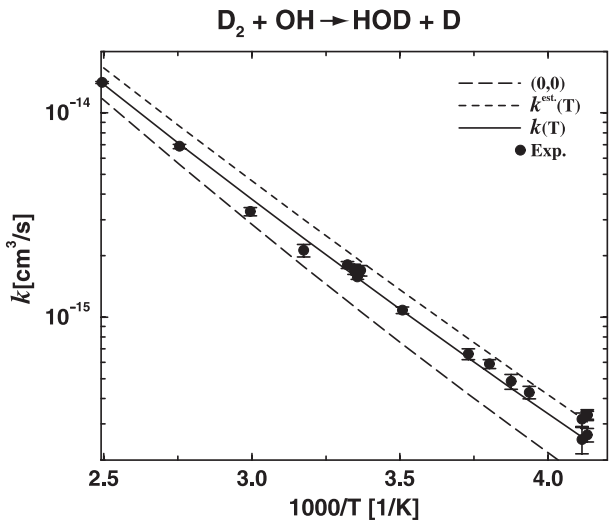
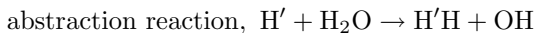


Fig. 15. Comparison of the theoretical thermal rate, $k(T)$, with experimental results.⁷⁴ Also shown are the initial state selected rate coefficient for the $(0,0)$ state, and an approximate theoretical thermal rate coefficient, $k^{\text{est}}(T)$.

states considered. In this temperature range, the rate coefficients are largely determined by the integral cross-section at low translational energies. At a given temperature, the rates increase as j_1 increases, and decreases as j_2 increases. Figure 15 compares the thermal rate coefficients, calculated from the initial state selected rate constants shown in Fig. 14, with the experimental results by Ravishankara *et al.*⁷⁴ Also shown in the figure are the rate coefficients for the (0,0) state, and the approximate rate coefficients $k^{\text{Est}}(T)$ calculated based on the assumption that simultaneous rotational excitation of the reagents does not have a correlated effect on the dynamics. The agreement between theory and experiment is quite remarkable, which again shows that the YZCL2 PES is of good quality.

4.2. Reactions of $\text{H} + \text{H}_2\text{O}$, $\text{H} + \text{D}_2\text{O}$

The reverse reaction to the above diatom–diatom reaction leads to the following possibilities:



The abstraction reaction has a saddle point with $\text{O} \cdots \text{H} \cdots \text{H}'$ close to a collinear geometry; hence the H' atom should collide with the H_2O molecule at totally different angles in order to abstract one H-atom or the other. As a result, one may treat one OH bond as a spectator bond in the abstraction reaction. On the other hand, the exchange reaction has a saddle point with OH_3 close to a C_{3v} geometry, and the H' atom can exchange with either of the two H atoms with equal probability. Thus, it would not be accurate to treat one of the OH bonds as a spectator bond; both OH bonds in the H_2O molecule will have to be treated as reactive bonds, even though only one of them is cleaved during the reaction. The saddle point for the abstraction and C_{3v} minimum for the exchange reactions are illustrated in Fig. 16, for the isotopic reaction, $\text{H} + \text{D}_2\text{O}$.

To illustrate the first point concerning a spectator bond for the abstraction reaction, Fig. 17 shows the total reaction probability for the abstraction reaction as a function of the translational energy for total angular momentum $J = 0$ on the YZCL2 PES with the H_2O reactant in the ground rovibrational state [the (00)(0) state in the local mode notation], where the uncleaved bond OH_b is treated in various ways. Using a limited number of one or five vibrational basis functions, $\text{VBF}(\text{OH}_b) = 1$ or 5, means that the OH_b bond is unreactive, a spectator. The abstraction reaction probability

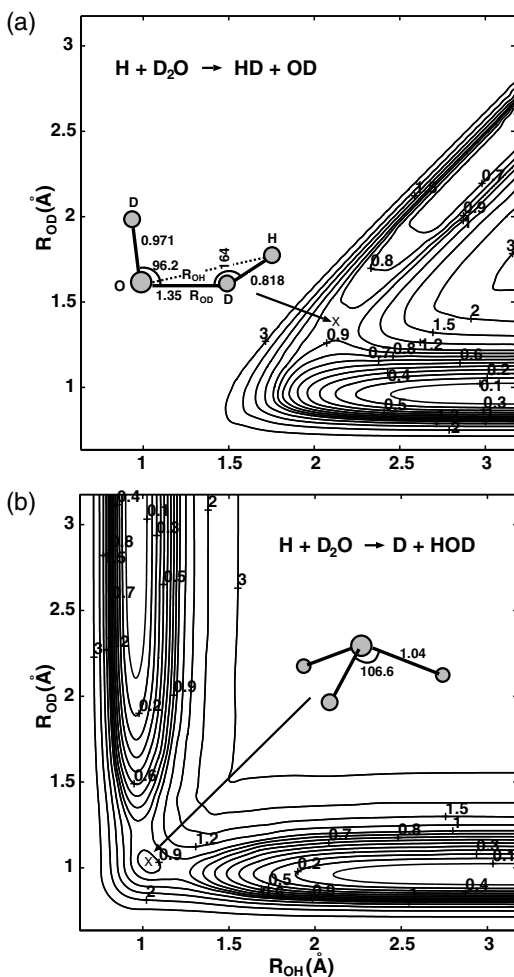


Fig. 16. Potential energy contours for the $\text{H} + \text{D}_2\text{O}$ system as a function of the OH and one OD bond length. In each panel, the energy has been minimized with respect to the remaining degrees-of-freedom in the vicinity of the minimum energy paths. In (a) the saddle point for the abstraction reaction, and in (b) the shallow C_{3v} minimum for the exchange reaction are marked with X.

is very small, due to the small reaction cone, but, more importantly, the results are almost identical whether the OH_b bond is treated as a spectator or as a reactive bond. It should be noted that when the OH_b bond is a spectator, then the reaction probability from OH_a alone is multiplied by two for comparison with the probability for two reactive bonds. Similar

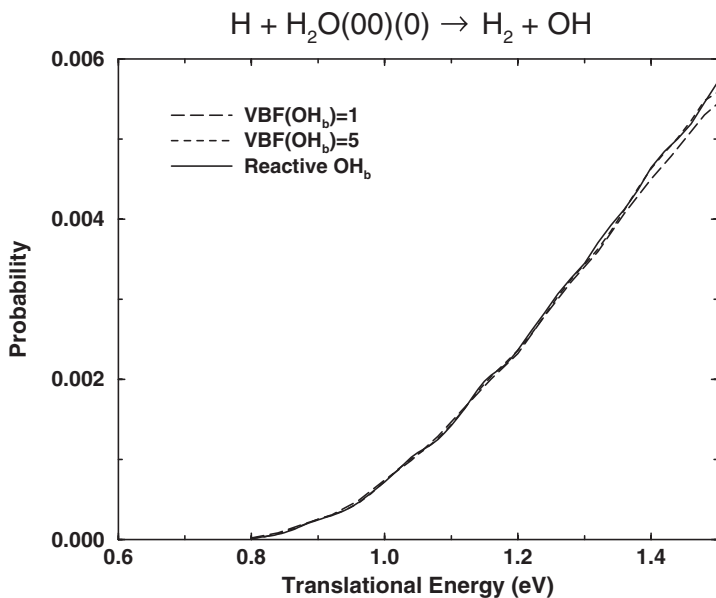


Fig. 17. Total reaction probability for the $\text{H} + \text{H}_2\text{O}(00)(0) \rightarrow \text{H}_2 + \text{OH}$ abstraction reaction as a function of the translational energy on the YZCL2 PES for $J = 0$.

results, shown in Fig. 18, are obtained for $J = 0$ with the H_2O reactant in the vibrationally excited symmetric or antisymmetric $(01)^\pm(0)$ stretching states. For comparison, we also show the small abstraction probability for the ground state in Fig. 18. Clearly, the OH stretching excitation enhances the reaction a great deal because the abstraction reaction has a later barrier which can be surmounted with the vibrational excitation energy.

To illustrate the second point that a spectator bond cannot be used for the exchange reaction, Fig. 19 shows results for the exchange reaction from the ground vibrational state for total angular momentum $J = 0$, similar to Fig. 17 for the abstraction reaction. The exchange reaction is much more favorable than the abstraction reaction. The three different curves in Fig. 19 clearly show that the way the OH_b bond is treated is important in studying the exchange process. The solid curve is the total reaction probability obtained with two reactive bonds for the realistic exchange reaction in full dimension by using over 220×10^6 basis functions. It is rather smooth with one prominent resonance peak just above the threshold, one around $E = 1.1$ eV, and some other broader resonances higher up in energy. These resonance structures are believed to be associated with the shallow C_{3v}

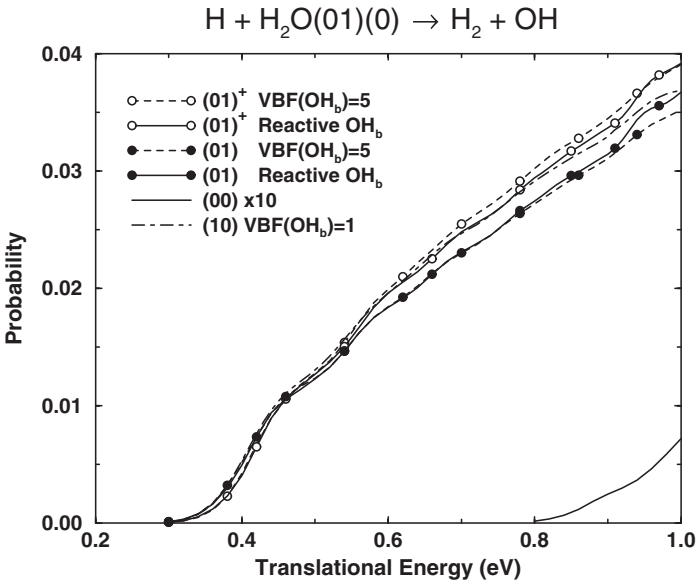


Fig. 18. Same as Fig. 17, but for the $\text{H}_2\text{O}(01)^\pm(0)$ initial states.

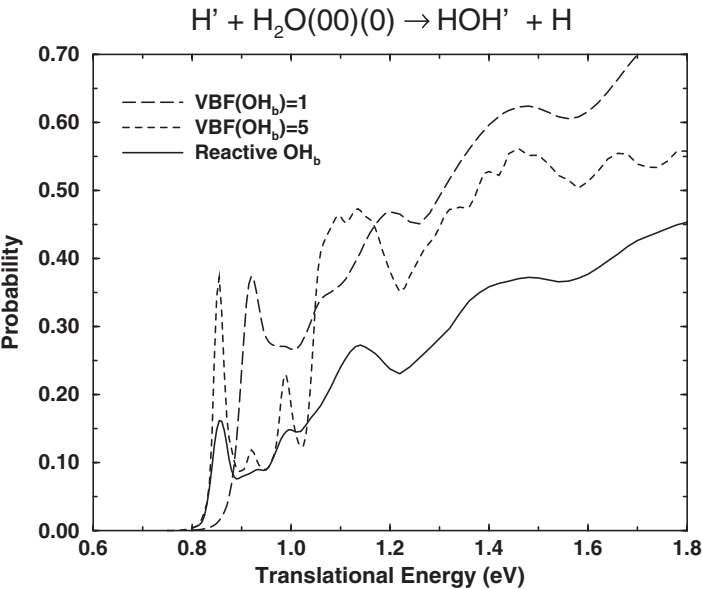


Fig. 19. Total reaction probability for the $\text{H}' + \text{H}_2\text{O}(00)(0) \rightarrow \text{H}'\text{OH} + \text{H}$ exchange reaction as a function of the translational energy on the YZCL2 PES for $J = 0$.

minimum on the reaction path. The total exchange probability with the OH_b bond frozen vibrationally [$\text{VBF}(\text{OH}_b) = 1$] is similar in behavior to that of the accurate exchange probability except for a shift in all the resonance peaks by roughly 0.07 eV, and is about 60–80% larger than the exact result. When the OH_b bond is nonreactive, but not frozen vibrationally [$\text{VBF}(\text{OH}_b) = 5$], the resonance structure appears richer, and the overall exchange probability is still larger than the exact result. In Fig. 20, the accurate exchange probabilities for the vibrationally excited $(01)^\pm(0)$ states together with those for $\text{VBF}(\text{OH}_b) = 5$ are shown. Clearly, the nonreactive treatment of the OH_b bond affects the exchange reaction probabilities considerably. For comparison, the exchange probability for the ground state is also plotted, and it shows that the enhancement of the exchange reaction by excitation of the stretching vibration is milder than that on the abstraction reaction (compare Fig. 20 with Fig. 18).

An earlier set of calculations⁷¹ on the $\text{H} + \text{H}_2\text{O}$, D_2O abstraction reactions had taken advantage of restricting one of the OH (OD) bonds in the $\text{H}_2\text{O}(\text{D}_2\text{O})$ reactant from being cleaved, leaving just 5 degrees-of-freedom, to reduce the computational time. A global YZCL1 PES, in hindsight, was used. The results showed that for the $\text{H} + \text{H}_2\text{O} \rightarrow \text{H}_2 + \text{OH}$ reaction there

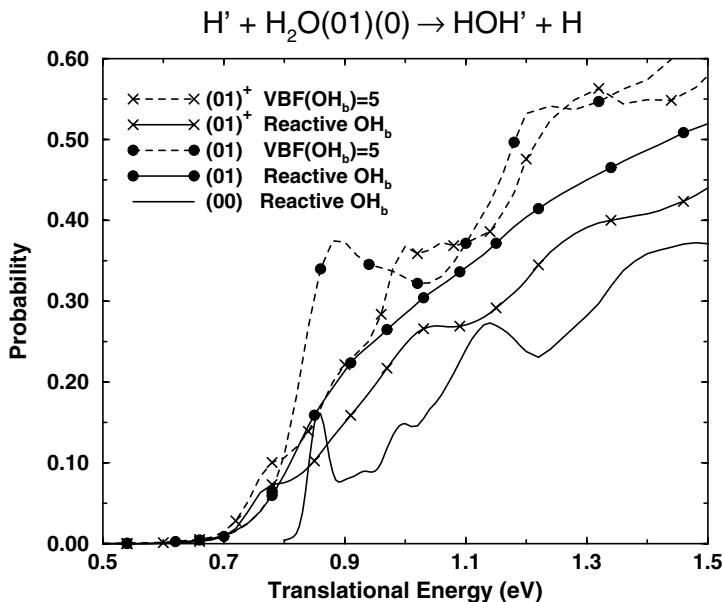


Fig. 20. Same as Fig. 19 but for the $\text{H}_2\text{O}(01)^\pm(0)$ state.

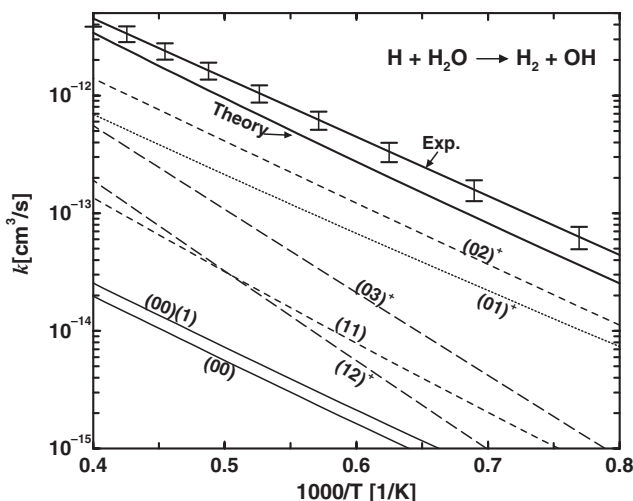


Fig. 21. Comparison of theory and experiment for the thermal rate constant of the $\text{H} + \text{H}_2\text{O} \rightarrow \text{H}_2 + \text{OH}$ reaction and the calculated contributions from individual vibrational states of H_2O .

is agreement between experiment³¹ and theory for the thermal rate constant, as shown in Fig. 21. In the low temperature region, the thermal rate coefficient is dominated by contributions from the excited OH stretching states $(02)^\pm$ and $(01)^\pm$, and in the high temperature region contributions from $(03)^\pm$ also become important. In contrast, there was disagreement between the calculations and the measured integral cross-sections⁷⁹ for the $\text{H} + \text{H}_2\text{O} \rightarrow \text{H}_2 + \text{OH}$ and $\text{H} + \text{D}_2\text{O} \rightarrow \text{HD} + \text{OD}$ abstraction reactions, as shown in Fig. 22. The measured cross-sections are larger than the theoretical results by a factor of 10 to 20. It seemed necessary to re-examine either the experiments or the calculations (the assumptions made and the PES) or both.

We had earlier vindicated treating one of the OH bonds in the H_2O molecule as a spectator bond in studying the abstraction reaction. Another key assumption that needed to be checked was the centrifugal sudden (CS) approximation which was invoked to reduce the number of rotational basis functions used in the computations.²⁸ Under the CS approximation and using only the $K = 0$ rotational basis functions, there was a total of 220 million basis functions for $J = 15$ alone. Relaxing the CS approximation, for example, with $K = 0, 1$ and $J = 15$ led to 650 million basis functions. To approach the fully coupled-channel (CC) results, i.e. without

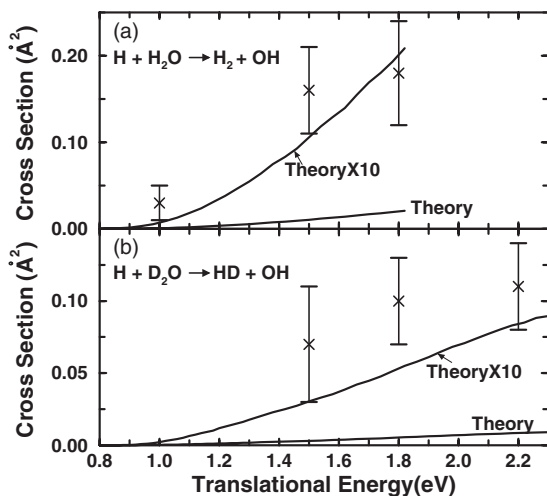


Fig. 22. Comparison between experimental (crosses with error bars indicating 1σ statistical uncertainty) and theoretical integral cross-sections for (a) the $\text{H} + \text{H}_2\text{O} \rightarrow \text{H}_2 + \text{OH}$ and (b) the $\text{H} + \text{D}_2\text{O} \rightarrow \text{HD} + \text{OH}$ reactions. The theoretical cross-sections are also shown enlarged by a factor of 10.

the CS approximation, we had to use three K -blocks for $J = 5, 10, 15, 20, 25$, and four K -blocks for $J = 30, 35, 40$, resulting in many-fold more rotational basis functions. The integral cross-sections, comparing the CS versus CC for the $\text{H} + \text{H}_2\text{O}(00)(0) \rightarrow \text{H}_2 + \text{OH}$ reaction on the more accurate YZCL2 PES, are shown in Fig. 23, and those for the $\text{H} + \text{H}_2\text{O}(01)(0) \rightarrow \text{H}_2 + \text{OH}$ reaction are shown in Fig. 24. Figure 23 also presents the quasi-classical trajectory (QCT) integral cross-section at $E = 1.4$ eV, reported on the same surface.⁸⁰ Clearly, the CS approximation does not work well for the abstraction reaction from the ground rovibrational state. The CC cross-section is larger than the CS cross-section, by about 60% for the ground rovibrational state of H_2O , and by about 15% for the first excited rovibrational state. In Ref. 71, we found that the experimental cross-sections for the abstraction reaction was more than 10 times larger than the CS integral cross-section; so, even if we used the larger CC cross-section the experimental cross-section would still be significantly higher. The experiment for the abstraction reaction has been re-examined recently,⁸¹ and the new value for the cross-section at collision energies close to 2.46 eV was found to be $0.041 \pm 0.018 \text{ Å}^2$, which is about a factor of 6 lower than previously reported,³¹ and is now just a factor of 2 lower than calculations, as shown in Fig. 25. Also shown are the quasi-classical trajectory (QCT) results of Schatz *et al.*⁸² on the WSLFH PES.⁸³

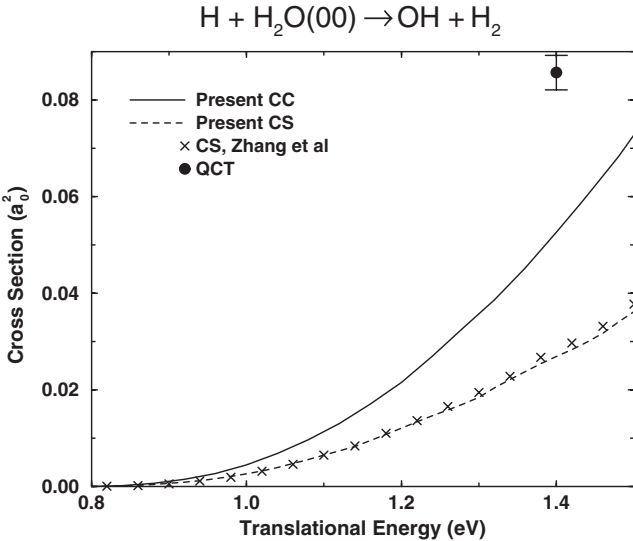


Fig. 23. The CC and CS integral cross-section for the $\text{H} + \text{H}_2\text{O}(00)(0)$ abstraction reaction. Other results: \times CS, Ref. 71; \bullet , Ref. 80.

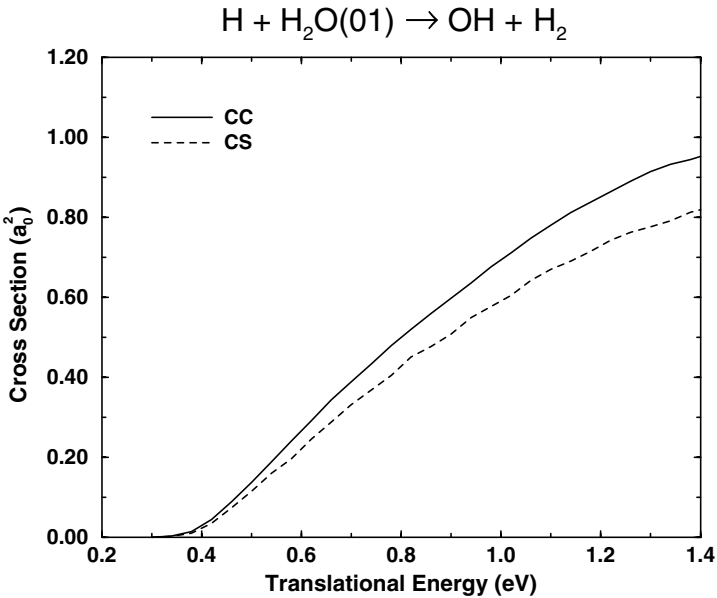


Fig. 24. Same as Fig. 23, but for the $\text{H} + \text{H}_2\text{O}(01)(0)$ reaction.

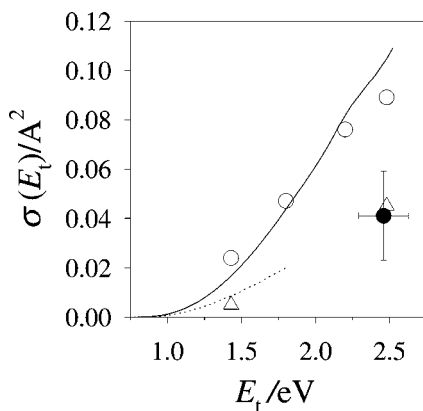


Fig. 25. Comparison between the experimental abstraction reaction $\text{H} + \text{H}_2\text{O}(00)(0)$ cross-section (solid point with error bars), and the 5D QM calculations (solid line). The 6D QM cross-sections with the CS approximation (dotted line), and the QCT data using normal (\circ) and Gaussian (Δ) binning procedures are shown.

The 5D QM results, which treat one OH bond as spectator, corresponds to the CC cross-section. Potential reasons for the discrepancy between experiment and theory include the presence of a close-lying excited electronic state. At the abstraction barrier, this state is only ~ 2 eV above the equilibrium energy of the reactants, and could play a role at the energies sampled by the experiment.

We are now able to calculate the state-to-state integral cross-section (ICS) for the $\text{H} + \text{H}_2\text{O}(00)(0) \rightarrow \text{H}_2(v_1, j_1) + \text{OH}(j_2)$ abstraction reaction which is very demanding as it requires state-to-state reaction probabilities for $J > 0$. A 5D calculation, with one OH bond as spectator, on the YZCL2 surface has been performed.³⁰ Figure 26 shows the total cross-section and the ICS for both H_2 and OH products in the ground rovibrational state, as a function of the translational energy. From the state-to-state ICS, we can calculate the fractions of energy going into the internal motions of the products, and these are shown in Fig. 27. It was found that (a) the H_2 molecule is produced vibrationally cold for collision energy up to 1.6 eV, (b) the OH rotation takes away about 4% of the total available energy in the products, and (c) the fraction of energy going into H_2 rotation increases with collision energy to about 20% at 1.6 eV. Sometimes, the fractions obtained for the $J = 0$ reaction probabilities are used to approximately study the distribution of the total available energy among the products, and are shown in Fig. 27 for comparison.

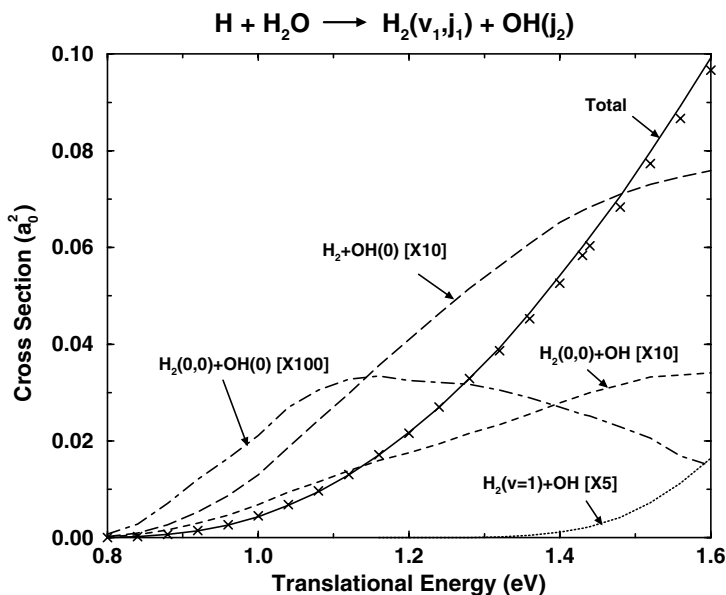


Fig. 26. Total and final rovibrational state specific integral cross-sections for the $\text{H} + \text{H}_2\text{O}(00)(0) \rightarrow \text{H}_2(v_1, j_1) + \text{OH}(j_2)$ reaction as a function of translational energy. The total cross-sections in crosses were calculated in the atom-triatom coordinates.

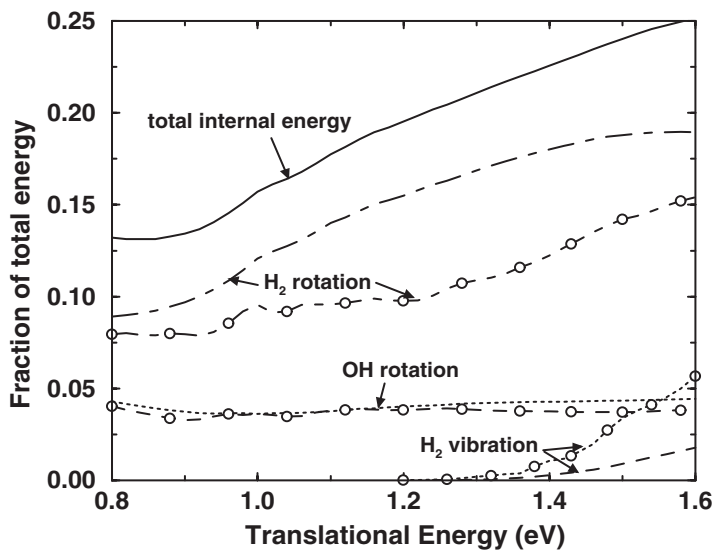


Fig. 27. The fraction of the total available energy in the product channel going into rovibration of H_2 and rotation of OH as a function of the translational energy. Curves without open circles were calculated from the $J = 0$ state-to-state reaction probability.

4.3. Photoelectron and Photodetachment Spectroscopy of H_3O^-

Experimentalists and theoreticians are also interested in probing the dynamics of the critical transition state that separates the reactants from the products. For several molecules, the stable anion has an equilibrium geometry that resembles the geometry of the transition state for a reaction involving the corresponding neutral molecule, e.g. FH_2^- and the transition state for the reaction $\text{F} + \text{H}_2 \rightarrow \text{FH} + \text{H}$. According to the Franck–Condon principle, photoemission of an electron from the anion creates the neutral molecule in the vicinity of the transition state. The kinetic energy distribution of the ejected electron can therefore provide information about the molecular states in the transition state region. The combination of such experiments with accurate *ab initio* calculation of the PESs of the neutral species and anion and exact quantum scattering calculations of the nuclear motion have provided quantitative understanding of the transition-state dynamics for the $\text{F} + \text{H}_2$ reaction.⁸⁴

Photoelectron spectroscopy of the polyatomic anion H_3O^- probes the transition state for the $\text{H}_2 + \text{OH} \leftrightarrow \text{H}_2\text{O} + \text{H}$ reaction.³⁹ A highly accurate *ab initio* PES for H_3O is available; so, constructing an accurate PES for the anion allowed us to study the photoelectron and photodetachment spectroscopy of H_3O^- .⁴⁰ The photoelectron spectrum has been reported,³⁹ while, thus far, the photodetachment spectrum has not. The photoelectron spectrum associated with the photoproduct state n can be simulated by calculating the Franck–Condon factor

$$P_{n \leftarrow i}(E) = \left| \langle \psi_n^{(-)}(E) | \Phi_i \rangle \right|^2 \quad (59)$$

where $|\Phi_i\rangle$ is the initial rovibrational state of H_3O^- which evolves into a scattering wavefunction on the dissociative H_3O surface with components $|\psi_n^{(-)}(E)\rangle$ corresponding to eigenstates of the asymptotic dissociated fragments with channel basis functions $|\phi_n\rangle$. The probability $P_{n \leftarrow i}(E)$ is calculated using the time-dependent wavepacket method where the propagated wavepacket is projected onto $|\phi_n\rangle$ in the asymptotic region with the reaction coordinate $R = R_L$ ^{85,86}:

$$|\Psi_i(E)\rangle = \int_0^\infty dt e^{i(E - \hat{H})t/\hbar} |\Phi_i\rangle = \sum_n C_{n \leftarrow i}(R_L, E) |\phi_n\rangle, \quad (60)$$

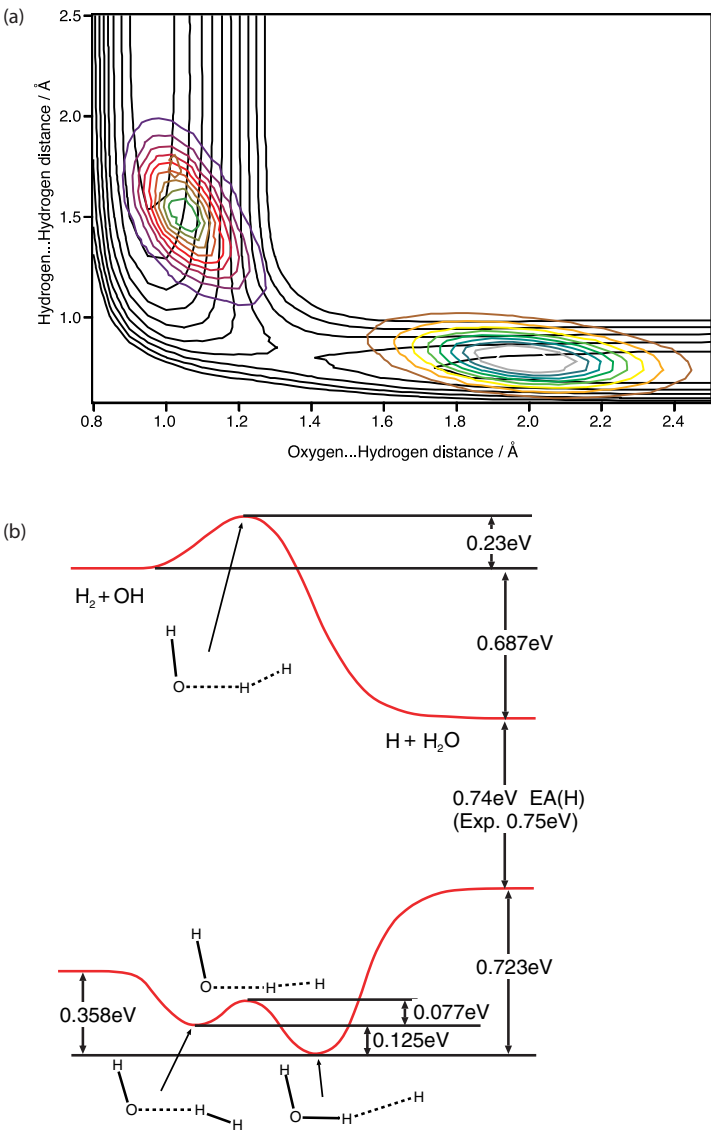


Fig. 28. (a) Contour plot of the minimum potential energy for OH + H₂, shown in the vicinity of the saddle point as a function of the forming O...H and breaking H...H bond lengths. Contour plots of the probability distribution for these two bond lengths area also shown for the ground state of H₃O⁻ (centered at H...H distance of 1.5 Å) and the excited initial state (centered at O...H distance of 2.0 Å). (b) Schematic representation of the relative energies of some features on the PES for H₃O and H₃O⁻.

and it can be shown⁸⁶ that

$$P_{n \leftarrow i}(E) = \frac{\hbar^2}{2\pi\mu} \text{Im} \left[C_{n \leftarrow i}^* \frac{d}{dR} C_{n \leftarrow i} \right]_{R=R_L}, \quad (61)$$

where μ is the corresponding reduced mass for the reaction coordinate R .

A contour plot of the minimum potential energy surface of the $\text{H}_2 + \text{OH} \leftrightarrow \text{H}_2\text{O} + \text{H}$ reaction in the vicinity of the saddle point is shown in Fig. 28(a), and a schematic of some features of the PESs for H_3O and H_3O^- is shown in Fig. 28(b).

Figure 29 compares the calculated⁴⁰ and experimental photoelectron spectra. Figure 29(a) compares the calculated spectrum from the ground state of H_3O^- with the experimental spectrum that was obtained with a zero angle between the laser polarization and direction of electron detection,

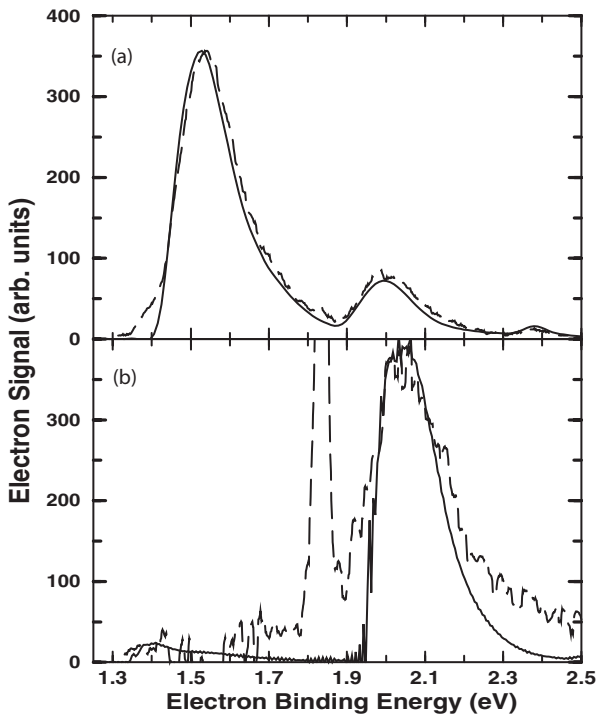


Fig. 29. (a) Photoelectron intensity calculated (solid line) for the ground state of H_3O^- , compared with the observed intensity (dashed line) of photoelectrons at $\Theta = 0$. (b) Same as (a), but for the excited initial state of H_3O^- , and compared with the observed intensity at $\Theta = 90$.

$\Theta = 0$. Figure 29(b) compares the calculated spectrum from an excited initial state of H_3O^- , which corresponds to $\text{H}_2 \cdots \text{OH}^-$, with the experimental spectrum that was obtained for $\Theta = 90$. The sharp intense experimental feature at about 1.83 eV in Fig. 29(b) is due to OH^- and is ignored here. There has been no adjustment to the energy scale for the theoretical results, so the coincidence of the peaks in the spectra is a measure of the agreement between theory and experiment and attests to the quality of the PESs.

Figure 30 presents a prediction for the photoelectron-photodetachment spectrum of ground state H_3O^- . The spectrum is dominated by the production of H_2O in a distribution of rotational levels of the ground vibrational state. For a given photoelectron kinetic energy, this spectrum directly measures the partitioning of the energy available to the photofragment into internal (rovibrational) excitation versus relative kinetic energy. Since the binding energy is about 1.29 eV, the distributions in Fig. 30 show that the average energy available to the $\text{H} + \text{H}_2\text{O}$ product is about 0.37 eV, and that about 25% of this energy is in relative translation of the products.

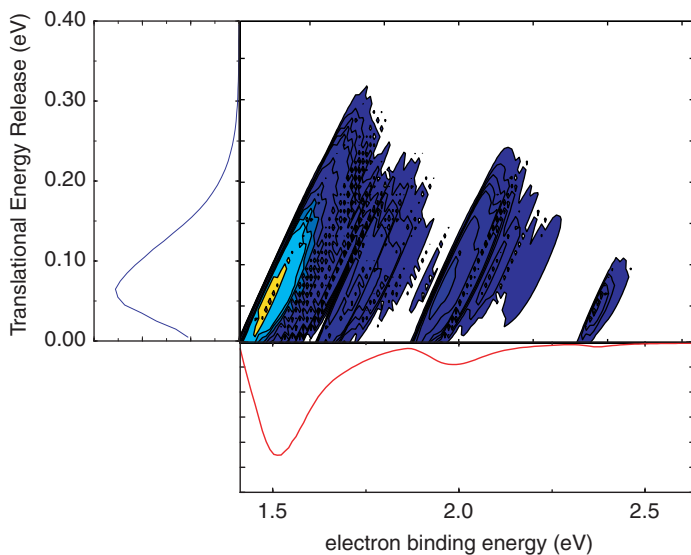


Fig. 30. Contour plot of photoelectron-photodissociation coincidence spectrum as a distribution of photoelectron intensity (dark shade = low, light shade = high) against the electron binding energy and relative translational energy of the photofragments. Also shown on the left and at the bottom are the partially averaged distributions for the translational energy release and the electron binding energy, respectively.

5. Conclusions

An overview of the time-dependent wavepacket propagation approach for four-atom reactions together with the construction of *ab initio* potential energy surfaces sufficiently accurate for quantum dynamics calculations has been presented. Today, we are able to perform the full-dimensional (six degrees-of-freedom) quantum dynamics calculations for four-atom reactions. With the most accurate YZCL2 surface for the benchmark four-atom reaction $\text{H}_2 + \text{OH} \leftrightarrow \text{H} + \text{H}_2\text{O}$ and its isotopic analogs, we were able to show the following:

- (a) There is good agreement between theory and experiment for the thermal rate coefficients for the $\text{H}_2 + \text{OH} \rightarrow \text{H}_2\text{O} + \text{H}$, $\text{D}_2 + \text{OH} \rightarrow \text{HOD} + \text{D}$, and $\text{HD} + \text{OH} \rightarrow [\text{H}_2\text{O} + \text{D}, \text{HOD} + \text{H}]$ reactions in the temperature range 238–1050 K using the initial state selected rate coefficient for the ground rovibrational state of the reactants. In these diatom–diatom reactions, the effect of reagent rotational excitation on reactivity is relatively mild compared to that of H_2 , D_2 or HD vibrational excitation. The estimated branching ratio for the $\text{HD} + \text{OH}$ reaction was also in agreement with experiments.
- (b) In the abstraction reaction $\text{H}' + \text{H}_2\text{O} \rightarrow \text{H}'\text{H} + \text{OH}$, we may treat the uncleaved OH bond as a spectator bond, reducing the dimensionality by one. However, for the exchange reaction $\text{H}' + \text{H}_2\text{O} \rightarrow \text{H} + \text{H}'\text{OH}$ this would not be a good assumption, and the full-dimensional calculation is necessary.
- (c) There remains a disagreement between theory and experiment in the integral cross-sections for both the $\text{H} + \text{H}_2\text{O} \rightarrow \text{H}_2 + \text{OH}$ and $\text{H} + \text{D}_2\text{O} \rightarrow \text{HD} + \text{OD}$ abstraction reactions. The latest experimental results for the former reaction indicate that it is about a factor of 2 lower than the theoretical results.
- (d) We are able to calculate the state-to-state integral cross-sections for the $\text{H} + \text{H}_2\text{O} \rightarrow \text{H}_2(v_1, j_1) + \text{OH}(j_2)$ abstraction reaction with H_2O in the ground rovibrational state, with the valid assumption of treating the uncleaved OH bond as a spectator. It is shown that both H_2 and OH are produced vibrationally cold for collision energy up to 1.6 eV.

Clearly, the difficult first principles theoretical study of four-atom reactions, particularly the prototype benchmark $\text{H}_2 + \text{OH} \leftrightarrow \text{H} + \text{H}_2\text{O}$ reaction and its isotopic analogs, has reached as exciting a level as when the first report of

three-dimensional quantum calculations for the three-atom $\text{H} + \text{H}_2$ reaction on the empirical PK2 PES was made in 1976.³

Like the three-atom case, it will take another decade or more to fully develop general and powerful numerical methods to compute other four-atom reactions. At the same time, the push to solve five-atom reactions and larger systems by *ab initio* or first-principles approach has started. It is believed that the TD approach provides the best hope for accurate quantum dynamics studies of polyatomic reactions, due to its relatively slow scaling of computational effort with the number of basis functions. To be computationally feasible, this needs to be coupled with a clever or fortuitous choice of reduced dimensionality by freezing out nonreactive or spectator coordinates without much loss of dynamical information. There is also the challenge of constructing *ab initio* global PESs, most likely by an interpolation method as described above, that can lead to accurate quantum reaction dynamics. Last, but not least, we need experiments that can produce reliable and detailed state-to-state dynamical measures for four-atom or more reactions to compare, to guide, and most likely to synergize with theoretical calculations and method development at the frontiers.

Acknowledgments

This work is supported in part by the Ministry of Education and Agency for Science and Technology Research, Republic of Singapore. M. A. C. gratefully acknowledges computational resources provided by the Australian University Supercomputer Facility and the Australian Partnership for Advanced Computing.

References

1. R. D. Levine and R. B. Bernstein, *Molecular Reaction Dynamics and Chemical Reactivity* (Oxford University Press, New York, 1987).
2. M. Shapiro and P. Brumer, *Principles of Quantum Control of Molecular Processes* (Wiley, Hoboken, 2003).
3. G. C. Schatz and A. Kuppermann, *J. Chem. Phys.* **65**, 4642 (1976).
4. W. H. Miller, *Annu. Rev. Phys. Chem.* **41**, 245 (1990), and references therein.
5. D. E. Manolopoulos and D. C. Clary, *Ann. Rep. R. Soc. Chem.* **86**, 95 (1989).
6. G. C. Schatz, in *The Theory of Chemical Reaction Dynamics*, ed. D. C. Clary and D. Reidel (Dordrecht, 1985), pp. 1–26.
7. T. J. Park and J. C. Light, *J. Chem. Phys.* **91**, 974 (1989).
8. L. Schneider, K. Seekamprahn, J. Borkowski, E. Wrede, K. H. Welge, F. J. Aoiz, L. Banares, M. J. D'Mello, V. J. Herrero, V. S. Rabanos and R. E. Wyatt, *Science* **269**, 207 (1995).

9. (a) S. D. Chao, S. A. Harich, D. X. Dai, C. C. Wang, X. M. Yang and R. T. Skodje, *J. Chem. Phys.* **117**, 8341 (2002); (b) S. A. Harich, D. Dai, X. M. Yang, S. D. Chao and R. T. Skodje, *J. Chem. Phys.* **116**, 4769 (2002).
10. (a) S. A. Harich, D. X. Dai, C. C. Wang, X. N. Yang, S. D. Chao and R. T. Skodje, *Nature* **419**, 281 (2002); (b) S. C. Althorpe, F. Fernandez-Alonso, B. D. Bean, J. D. Ayers, A. E. Pomerantz, R. N. Zare and E. Werde, *Nature* **416**, 67 (2002).
11. D. E. Neumark, A. M. Wodtke, G. N. Robinson, C. Hayden and Y. T. Lee, *J. Chem. Phys.* **82**, 3045 (1985).
12. M. Alagia, N. Balucani, L. Cartechimi, P. Casavecchia, E. H. Vankleeft, G. G. Volpi, F. J. Aoiz, L. Banares, D. W. Schwenke, T. C. Allison, S. L. Mielke and D. G. Truhlar, *Science* **273**, 1519 (1996).
13. D. Skouteris, D. E. Manolopoulos, W. S. Bian, H. J. Werner, L. H. Lai and K. P. Liu, *Science* **286**, 1713 (1999).
14. A. Kuppermann, *Chem. Phys. Lett.* **32**, 374 (1975).
15. J. Z. H. Zhang and W. H. Miller, (a) *Chem. Phys. Lett.* **153**, 465 (1988); (b) *Chem. Phys. Lett.* **159**, 130 (1989); (c) *J. Chem. Phys.* **91**, 1528 (1989).
16. D. C. Clary, *J. Chem. Phys.* **95**, 7298 (1991).
17. D. C. Clary, *Chem. Phys. Lett.* **192**, 34 (1992).
18. D. Wang and J. M. Bowman, *J. Chem. Phys.* **96**, 8906 (1992).
19. (a) D. C. Clary, *J. Phys. Chem.* **98**, 10678 (1994); (b) J. Palma and D. C. Clary, *Phys. Chem. Chem. Phys.* **2**, 4105 (2000); (c) J. Palma and D. C. Clary, *J. Chem. Phys.* **115**, 2188 (2001).
20. J. M. Bowman and G. C. Schatz, *Annu. Rev. Phys. Chem.* **46**, 169 (1995).
21. G. C. Schatz and H. Elgersma, *Chem. Phys. Lett.* **73**, 21 (1980).
22. A. Aguado, M. Paniagua, M. Lara and O. Roncero, *J. Chem. Phys.* **107**, 10085 (1997).
23. D. J. Kouri and R. C. Mowrey, *J. Chem. Phys.* **86**, 2087 (1987); (b) Y. Sun, R. C. Mowrey and D. J. Kouri, *J. Chem. Phys.* **87**, 339 (1987); (c) Y. Sun, R. S. Judson and D. J. Kouri, *J. Chem. Phys.* **90**, 241 (1989); D. Neuhauser, M. Baer, R. S. Judson and D. J. Kouri, *Comput. Phys. Commun.* **63**, 460 (1991).
24. See K. C. Kulander (ed.), Time-dependent methods for quantum dynamics, *Comput. Phys. Commun.* **63** (1991).
25. D. H. Zhang and J. Z. H. Zhang, *J. Chem. Phys.* (a) **99**, 5615 (1993); (b) **100**, 2697 (1994).
26. M. Yang, D. H. Zhang, M. A. Collins and S. Y. Lee, *J. Chem. Phys.* **114**, 4759 (2001).
27. D. H. Zhang, M. Yang and S. Y. Lee, *J. Chem. Phys.* **116**, 2388 (2002).
28. D. H. Zhang, M. Yang and S. Y. Lee, *J. Chem. Phys.* **117**, 10067 (2002).
29. D. H. Zhang and J. C. Light, *J. Chem. Phys.* (a) **104**, 4544 (1996); (b) **105**, 1291 (1996).
30. D. H. Zhang, D. Xie, M. Yang and S. Y. Lee, *Phys. Rev. Lett.* **89**, 283203 (2002).
31. J. V. Michael and J. W. Sutherland, *J. Phys. Chem.* **92**, 3853 (1988), and references therein.

32. J. N. Bradley, *Flame and Combustion Phenomena* (Methuen, London, 1969), p. 77.
33. I. W. M. Smith and F. F. Crim, *Phys. Chem. Chem. Phys.* **4**, 3543 (2002), and references therein.
34. M. J. Bronikowski, W. R. Simpson and R. N. Zare, *J. Phys. Chem.* **97**, 2194 (1993).
35. F. F. Crim, *J. Phys. Chem.* **100**, 12725 (1996).
36. M. Aligalia, N. Balucani, P. Casavecchia, D. Stranges, G. G. Volpi, D. C. Clary, A. Kleisch and H.-J. Werner, *Chem. Phys.* **207**, 389 (1996).
37. A. Jacobs, H.-R. Volpp and J. Wolfrum, *J. Phys. Chem.* **100**, 1936 (1994).
38. M. Brouard, I. Burak, S. Marinakis, D. Minayev, P. O'Keeffe, C. Vallance, F. J. Aoiz, L. Banares, J. F. Castillo, D. H. Zhang, D. Xie, M. Yang, S. Y. Lee and M. A. Collins, *Phys. Rev. Lett.* **90**, 93201 (2003).
39. E. de Beer, E. H. Kim, D. M. Neumark, R. F. Gunion and W. C. Lineberger, *J. Phys. Chem.* **99**, 13627 (1995).
40. D. H. Zhang, M. Yang, M. A. Collins and S. Y. Lee, *Proc. Natl. Acad. Sci. USA* **99**, 11579 (2002).
41. D. H. Zhang and J. Z. H. Zhang, *J. Chem. Phys.* **101**, 1146 (1994).
42. J. A. Fleck, Jr., J. R. Morris and M. D. Feit, *Appl. Phys.* **10**, 129 (1976).
43. (a) J. V. Lill, G. A. Parker and J. C. Light, *Chem. Phys. Lett.* **89**, 483 (1982); (b) J. C. Light, I. P. Hamilton and J. V. Lill, *J. Chem. Phys.* **82**, 1400 (1985).
44. (a) J. Z. H. Zhang and D. H. Zhang, *Chem. Phys. Lett.* **232**, 370 (1995); (b) D. H. Zhang, J. Z. H. Zhang, Y. C. Zhang, D. Wang and Q. Zhang, *J. Chem. Phys.* **102**, 7400 (1995); (c) D. H. Zhang and J. Z. H. Zhang, *J. Chem. Phys.* **103**, 6512 (1995).
45. D. H. Zhang, M. Yang and S. Y. Lee, *J. Chem. Phys.* **117**, 10067 (2002).
46. D. H. Zhang and S. Y. Lee, *J. Chem. Phys.* **110**, 4435 (1999).
47. M. A. Collins, *Theor. Chem. Acc.* **108**, 313 (2002).
48. M. A. Collins and D. F. Parsons, *J. Chem. Phys.* **99**, 6756 (1993).
49. M. A. Collins and K. C. Thompson, in *Chemical Group Theory: Techniques and Applications*, eds. D. Bonchev and D. H. Rouvray (Gordon and Breach, Reading, 1995), p. 191.
50. R. G. Parr and R. J. White, *J. Chem. Phys.* **49**, 1059 (1968).
51. G. Simons, R. G. Parr and J. M. Finlan, *J. Chem. Phys.* **59**, 3229 (1973).
52. K. C. Thompson, M. J. T. Jordan and M. A. Collins, *J. Chem. Phys.* **108**, 8302 (1998).
53. E. B. Wilson, J. C. Decius and P. C. Cross, *Molecular Vibrations* (Dover, New York, 1955).
54. A. Ben-Israel and T. N. Greville, *Generalised Inverses: Theory and Applications* (Wiley-Interscience, 1974).
55. W. H. Press, S. A. Teukolsky, W. T. Vetterling and B. P. Flannery, *Numerical Recipes in Fortran: The Art of Scientific Computing*, 2nd edn. (Cambridge University Press, Cambridge, 1992).
56. K. C. Thompson, M. J. T. Jordan and M. A. Collins, *J. Chem. Phys.* **108**, 564 (1998).

57. M. J. T. Jordan, K. C. Thompson and M. A. Collins, *J. Chem. Phys.* **103**, 9669 (1995).
58. R. Farwig, (a) *Math. Comput.* **46**, 577 (1986); (b) in *Algorithms For Approximation*, ed. J. C. Mason and M. G. Cox (Clarendon Press, Oxford, 1987), p. 194.
59. J. Ischtwan and M. A. Collins, *J. Chem. Phys.* **100**, 8080 (1994).
60. (a) D. G. Truhlar and M. S. Gordon, *Science* **249**, 491 (1990); (b) D. M. Wardlaw and R. A. Marcus, *Adv. Chem. Phys.* **70**, 231 (1991).
61. Details from one of the authors, M. A. Collins.
62. K. C. Thompson and M. A. Collins, *J. Chem. Soc., Faraday Trans.* **93**, 871 (1997).
63. M. A. Collins and R. P. A. Bettens, *Phys. Chem. Chem. Phys.* **1**, 939 (1999).
64. R. P. A. Bettens and M. A. Collins, *J. Chem. Phys.* **111**, 816 (1999).
65. M. A. Collins and D. H. Zhang, *J. Chem. Phys.* **111**, 9924 (1999).
66. M. J. Frisch, G. W. Trucks, H. B. Schlegel, G. E. Scuseria, M. A. Robb, J. R. Cheeseman, V. G. Zakrzewski, J. A. Montgomery, Jr., R. E. Stratmann, J. C. Burant, S. Dapprich, J. M. Millam, A. D. Daniels, K. N. Kudin, M. C. Strain, O. Farkas, J. Tomasi, V. Barone, M. Cossi, R. Cammi, B. Mennucci, C. Pomelli, C. Adamo, S. Clifford, J. Ochterski, G. A. Petersson, P. Y. Ayala, Q. Cui, K. Morokuma, D. K. Malick, A. D. Rabuck, K. Raghavachari, J. B. Foresman, J. Cioslowski, J. V. Ortiz, B. B. Stefanov, G. Liu, A. Liashenko, P. Piskorz, I. Komaromi, R. Gomperts, R. L. Martin, D. J. Fox, T. Keith, M. A. Al-Laham, C. Y. Peng, A. Nanayakkara, C. Gonzalez, M. Challacombe, P. M. W. Gill, B. Johnson, W. Chen, M. W. Wong, J. L. Andres, C. Gonzalez, M. Head-Gordon, E. S. Replogle and J. A. Pople, Revision A. 6th edn. (Gaussian Inc., Pittsburgh, PA, 1998).
67. J. Pu and D. G. Truhlar, *J. Chem. Phys.* **116**, 1468 (2002).
68. P. R. Bunker, *Molecular Symmetry and Spectroscopy* (Academic Press, New York, 1979).
69. (a) S. P. Walch and T. H. Dunning, *J. Chem. Phys.* **72**, 1303 (1980); (b) G. C. Schatz, *J. Chem. Phys.* **74**, 1133 (1981); (c) H. Elgersma and G. C. Schatz, *Intl. J. Quantum Chem., Quantum Chem. Symp.* **15**, 611 (1981).
70. R. P. Bettens, M. A. Collins, M. J. T. Jordan and D. H. Zhang, *J. Chem. Phys.* **112**, 10162 (2000).
71. D. H. Zhang, M. A. Collins and S. Y. Lee, *Science* **290**, 961 (2000).
72. MOLPRO is a suite of *ab initio* programs written by H.-J. Werner and P. J. Knowles, with contributions from J. Almlöf, R. D. Amos, A. Berning *et al.*
73. M. Yang, D. H. Zhang, M. A. Collins and S. Y. Lee, *J. Chem. Phys.* (a) **114**, 4759 (2001); (b) **115**, 174 (2001).
74. R. K. Talukdar, T. Gierczak, L. Goldfarb, Y. Rudich, B. S. M. Rao and A. R. Ravishankara, *J. Phys. Chem.* **100**, 3037 (1996).
75. (a) F. P. Tully and A. R. Ravishankara, *J. Phys. Chem.* **84**, 3126 (1980); (b) A. R. Ravishankara, J. M. Nicovich, R. L. Thompson and F. P. Tully, *J. Phys. Chem.* **85**, 2496 (1981).

- 76. D. H. Zhang, M. Yang and S. Y. Lee, *J. Chem. Phys.* **114**, 8733 (2001).
- 77. R. A. Brownsword, M. Hillenkamp, P. Schmiechen, H. R. Volpp and W. Wolfrum, *Chem. Phys. Lett.* **275**, 325 (1997).
- 78. D. H. Zhang and S. Y. Lee, *J. Chem. Phys.* **109**, 2708 (1998).
- 79. (a) K. Kleinermanns and J. Wolfrum, *Appl. Phys.* **B34**, 5 (1984); (b) S. Koppe, T. Laurent, P. D. Naik, H. Volpp and J. Wolfrum, *Can. J. Chem.* **72**, 615 (1994); (c) A. Jacobs, H. R. Volpp and J. Wolfrum, *J. Chem. Phys.* **100**, 1936 (1994).
- 80. J. F. Castillo, F. J. Aoiz and L. Banares, *Chem. Phys. Lett.* **356**, 120 (2002).
- 81. M. Brouard, I. Burak, S. Marinakis, D. Minayev, P. O'Keefe, C. Vallance, F. J. Aoiz, L. Banares, J. F. Castillo, D. H. Zhang, D. Xie, M. Yang, S. Y. Lee and M. A. Collins, *Phys. Rev. Lett.* **90**, 93201 (2003).
- 82. D. Troya, M. Gonzalez and G. C. Schatz, *J. Chem. Phys.* **114**, 8397 (2001).
- 83. G. Wu, G. C. Schatz, G. Lendvay, D. C. Fang and L. B. Harding, *J. Chem. Phys.* (a) **113**, 3150 (2000); (b) **113**, 7712 (2000).
- 84. D. E. Manolopoulos, K. Stark, H.-J. Werner, D. W. Arnold, S. E. Bradford and D. M. Neumark, *Science* **262**, 1852 (1993).
- 85. S. Y. Lee and E. J. Heller, *J. Chem. Phys.* **76**, 3035 (1982).
- 86. D. H. Zhang, Q. Wu and J. Z. H. Zhang, *J. Chem. Phys.* **102**, 124 (1995).

CHAPTER 10

PHOTODISSOCIATION DYNAMICS OF FREE RADICALS

Jingsong Zhang

*Department of Chemistry and Air Pollution Research Center
University of California at Riverside
Riverside, CA 92521-0403, USA*

Contents

1. Introduction	466
2. Experimental Approaches	467
2.1. Generation of Free Radical Beams	467
2.1.1. Pyrolysis	468
2.1.2. Photolysis	469
2.1.3. Electric Discharge	470
2.1.4. Negative Ion Photodetachment	471
2.2. Detection of Free Radicals	472
2.3. Experimental Techniques of Photodissociation Dynamics	474
3. Photodissociation of Free Radicals	475
3.1. Diatomic Radicals	475
3.1.1. OH and OD	475
3.1.2. ClO and BrO	481
3.2. Alkyl Radicals	484
3.2.1. Methyl (CH_3)	484
3.2.2. Chloromethyl (CH_2Cl)	487
3.2.3. Ethyl (C_2H_5)	489
3.3. Unsaturated Aliphatic Radicals	493
3.3.1. Vinyl (C_2H_3)	493
3.3.2. Propargyl (C_3H_3)	495
3.3.3. The C_3H_5 System: Allyl, 1-Propenyl, and 2-Propenyl	497
3.4. Alkoxy Radicals	501
3.4.1. Methoxy (CH_3O) and the Related Systems, Thiomethoxy (CH_3S) and Hydroxymethyl (CH_2OH)	501
3.4.2. Ethoxy ($\text{CH}_3\text{CH}_2\text{O}$)	506

3.4.3. Vinyloxy (CH_2CHO)	508
3.4.4. Cyclic Alkoxy	513
3.5. Others	513
4. Conclusions	514
Acknowledgments	514
References	515

1. Introduction

Free radicals are short-lived, highly-reactive transient species that have one or more unpaired electrons. Free radicals are common in a wide range of reactive chemical environments, such as combustion, plasmas, atmosphere, and interstellar environment, and they play important roles in these chemistries. For example, complex atmospheric and combustion chemistries are composed of, and governed by, many elementary processes involving free radicals. Studies of these elementary processes are pivotal to assessing reaction mechanisms in atmospheric and combustion chemistry, and to probing potential energy surfaces (PESs) and chemical reactivity.

As in the photochemical studies of closed-shell molecules, the studies of free radical photodissociation can provide important information about multiple PESs and their interactions, dissociation pathways, energetics, and thermodynamics. Free radicals are open-shell systems and they typically possess multiple low-lying electronic states, and these states, along with their nonadiabatic processes, complicate the photochemical dynamics. The structure, energetics, and photochemical reactivity are fundamental and inseparable. Sophisticated theories are required. Experimentally, it is difficult to study the photochemistry of gaseous free radicals due to the difficulty of their preparation and their highly-reactive nature, and sensitive and selective techniques are needed to detect radicals and their reaction products. In the studies of photodissociation of free radicals, the typical questions include: What are the detailed mechanisms? How do the open-shell structures and multiple PESs of free radicals govern their dissociation and unimolecular reactions? What are the product energy partitioning and the competing branching pathways? What are the electronic states, thermodynamics and energetics of free radicals? How does the photodissociation of free radicals compare with that of stable molecules?

The scope of this review focuses on photodissociation dynamics of free radicals in supersonic beam. The review concentrates on the new studies since the last review of this subject by Whitehead in 1996.¹ Due to the recent advances in high-intensity lasers and product detection schemes, as

well as methods of producing intense and clean supersonic beams of radicals (by flash pyrolysis, photolysis, electric discharge, and negative-ion photodetachment), significant progress has been made in the studies of photochemistry of free radicals. Compared with the number of systems included in the previous review, a larger number of free radical systems have been studied during the last couple of years, indicating significant advances in this field.

Although the spectroscopy of free radicals and their photochemistry are intimately related, this review does not specifically address the spectroscopy of free radicals. Several comprehensive reviews on spectroscopy of free radicals in supersonic jets have been made available recently,²⁻⁵ and more information can be obtained from these articles.

In the following, an overview of the experimental approaches is presented, including the production and detection methods of free radicals and the techniques for studying free radical photodissociation in the molecular beam. The photochemistry of the free radical systems investigated recently will then be discussed in detail.

2. Experimental Approaches

2.1. Generation of Free Radical Beams

The ideal free radical molecular beam sources for photodissociation dynamics studies should have the following features.

- (1) High intensity, with a high number density of radicals. This requirement is more desirable in the photodissociation study than in the spectroscopy study, as typically only a small fraction of the photoproducts of the radicals are detected, while in the spectroscopy study, the free radicals themselves are probed.
- (2) Clean, free of or with minimum amount of interfering species. In addition, the selection of the precursor molecules that are used to generate free radicals and the design of the experiments should minimize the contribution from the precursor photochemistry. At low photolysis photon energy (visible and near-UV), residual precursors generally do not interfere with the spectroscopy and photochemistry of the free radicals, as the radicals tend to absorb more strongly than the precursors in this spectral region. At higher photon energy, the contribution from the precursor photochemistry can be examined and removed with the radical production process turned on and off, and different precursors or radical generation techniques can be explored. If the free radicals have well-characterized absorption features, the spectroscopic selection

could help separate the free radical photochemistry from that of the precursors and their by-products; furthermore, the product kinetic and internal energy distributions can be very different due to the different dissociation energetics.

- (3) Cold, with well-defined internal energy. This is normally ensured with supersonic cooling. This requirement is important for high resolution and state-resolved studies, and it can remove the spectroscopy congestion of the radicals and enhance the interpretation of the results in photochemistry experiments.

2.1.1. *Pyrolysis*

Pyrolysis method involves thermal decomposition of suitable precursors to produce free radicals. Pyrolysis sources based on continuous molecular beam nozzles are well developed (for example, methyl⁶⁻⁸ and benzyl⁹). Recently, Chen and co-workers have pioneered a flash pyrolysis/supersonic jet technique to produce free radical beams (Fig. 1).¹⁰ In this radical

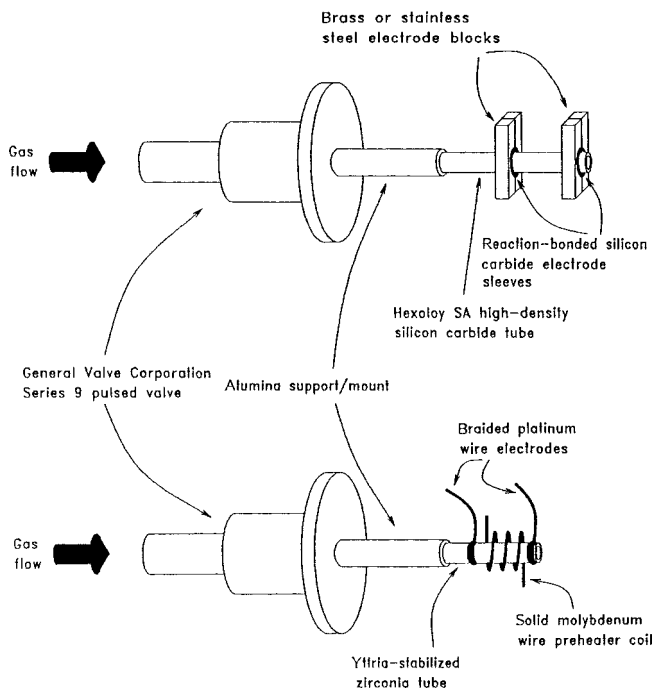


Fig. 1. Supersonic jet flash pyrolysis nozzles by Chen and co-workers. (From Kohn *et al.*¹⁰)

source, a silicon carbide or yttria-stabilized zirconia tube is attached to the front of a pulsed nozzle, and the front portion of the tube is resistively heated to a high temperature to achieve efficient conversion of the precursor molecules. The suitable radical precursor molecules and inert carrier gas pass through the tube in a subsonic flow in a short residence time (tens of μs), minimizing recombination of the free radicals in the source. The radicals produced are subsequently cooled by supersonic expansion. This radical source is intense ($>10^{14} \text{ cm}^{-3}$ at the nozzle), clean (with high conversion of the appropriate precursors in an excess amount of inert gas and minimized residence time and secondary reactions), and cold (with low $T_{\text{rot}} \sim 10\text{--}50 \text{ K}$ and $T_{\text{vib}} < 100 \text{ K}$ after supersonic cooling).^{5,10} Other pulsed free radical sources based on the same or similar designs have also been developed.^{11–14} A list of the free radicals that can be generated by this technique includes methyl (CH_3),^{14,15} ethynyl (C_2H),¹⁶ vinyl (C_2H_3),^{16,17} C_3H_2 ,^{18,19} propargyl (C_3H_3),²⁰ allyl (C_3H_5),²¹ cyclobutadiene ($c\text{-C}_4\text{H}_4$),¹⁰ benzyne ($o\text{-C}_6\text{H}_4$),²² benzyl,¹² phenyl,²¹ and NO_3 .^{23,24} Additional list and references of organic radicals produced by thermal dissociation can be found in Ref. 21. In general, the flash pyrolysis method works well for generating hydrocarbon free radicals.

2.1.2. Photolysis

Photolysis of suitable precursor molecules followed by supersonic expansion has been extensively used to produce free radical beams. A pulsed laser radiation (typically from an ArF or KrF excimer laser) is used as the photolysis light, which matches well with the pulsed molecular beam and the pulsed photolysis and probe laser radiation in the subsequent photodissociation of free radicals. The photolysis for radical production is typically carried out directly at the throat of the jet just in front of the pulsed nozzle,^{25–27} or through a nozzle extender,^{28–32} where the gas density and precursor concentrations are the highest. A typical photolysis radical source is shown in Fig. 2. The free radicals produced in the photolysis are cooled by subsequent supersonic expansion. Detailed knowledge of the photochemistry of the selected precursors is helpful. An appropriate precursor should have high quantum yield for producing the free radical of interest, with minimum internal energy deposited in the radical product; it should have large absorption cross-sections at the radical production photolysis wavelength for high conversion, but small or negligible absorption at the wavelength where the photolysis of the free radicals is carried out. Many free radical beams have been generated by the photolysis method: for example, OH ,^{29,30}

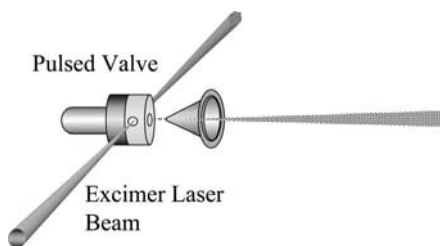


Fig. 2. Photolysis radical source with a nozzle extension piece.

SH,²⁶ ClO,³³ HCO,³⁴ CH₃O,^{28,35,36} C₂H₃,^{37,38} C₂H₅,^{31,39} C₃H₅ (allyl),³¹ and CH₂CHO (vinoy) radical.⁴⁰

2.1.3. Electric Discharge

Electric discharge of appropriate precursors with subsequent supersonic cooling has also been used to produce free radical beams. This is a commonly used method for spectroscopy study, and it has also been implemented in photodissociation and crossed beam experiments.^{41–43} A pulsed supersonic expansion coupled with a pulsed high voltage discharge across a needle electrode to the grounded pulse valve body or across two needle electrodes has been used for generating radical beams.^{44–46} Recently, the more common approach is to combine the pulsed supersonic expansion with a DC or pulsed high voltage discharge through a ring electrode to the grounded pulse valve body or through two ring electrodes. In the DC discharge source, the gas pulse passing through the electrodes starts and terminates the gas discharge,^{46–49} while in a pulsed voltage discharge source, the high voltage pulse strikes during the gas pulse to initiate the radical production.^{50–57} An example of the pulsed discharge free radical source based on the ring electrode design is shown in Fig. 3. In this source, two ring electrodes are mounted with electric insulator spacers in the front of a commercial pulsed valve. The pulsed valve and the first electrode are biased at ground, and when the precursor and carrier gas mixture pulses through the central channel, a negative high voltage pulse (~ -1 kV, tens to hundreds of μ s pulse width) is applied to the second electrode and initiates the discharge. The electric discharge radical sources tend to work well for making small, particularly diatomic, radicals (besides molecular ions). An example list of the free radicals that can be generated by the discharge sources include OH,^{46,49–51,57} CCl,⁴⁴ ClO,⁵⁸ CN,⁴⁷ NH,⁴⁷ CH₃,⁵² NH₂,⁵⁶ small Si- and Ge-containing species,⁵⁴ and unsaturated carbon chain species.⁵⁵

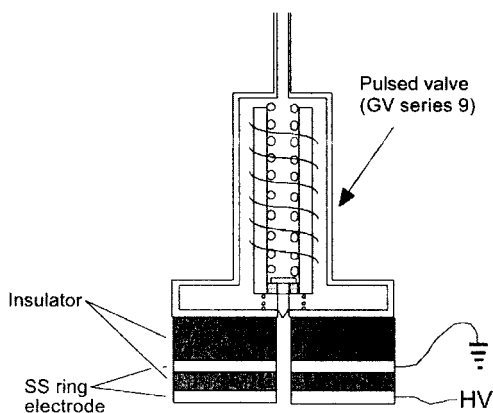


Fig. 3. Pulsed discharge radical source with two ring electrodes and pulsed high voltage. (From Xin *et al.*⁵⁶)

2.1.4. Negative Ion Photodetachment

A fast radical beam photofragment translational spectrometer based on negative ion photodetachment has been developed by Neumark and co-workers.^{59,60} In this approach, a fast beam of anions of the radical is produced by discharge and mass selected. The fast radical beam is generated by photodetachment of anions in the beam and the radicals are photodissociated by a second laser downstream (Fig. 4). The recoiled photofragments, with the initial high laboratory-frame kinetic energy of the radical beam (keV), are readily detected by a position sensitive detector. Another similar experimental setup involves dissociative photodetachment, in which the anions in the fast beam are photodetached to a repulsive excited state or above the dissociation barriers of the neutral radical, and the fragments are

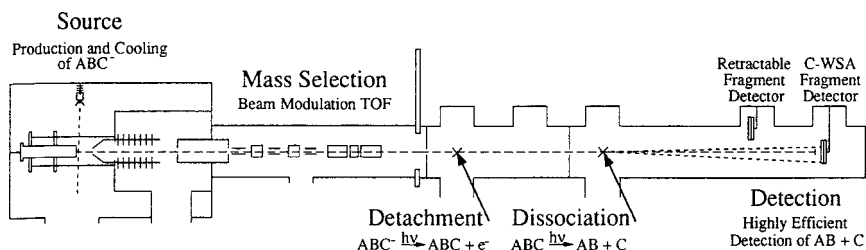


Fig. 4. Fast radical beam photofragment translational spectrometer. A fast free radical beam is produced from photodetachment of anions in a mass selected beam. The free radicals are then photodissociated in the downstream. (From Cyr *et al.*⁵⁹)

measured in a coincidence experiment with a position sensitive detector.⁶¹ In these two approaches, a clean radical beam is ensured by the mass selection of the anions, while the number density of the radicals is small, and subsequently the fast beam (which has a large laboratory-frame kinetic energy) is needed for sensitive detection of the photofragments of the radicals. The radical systems studied in the fast radical beams include, for example, N_3 ,⁶⁰ NCO ,⁵⁹ HCCO ,⁶² HOCO ,⁶³ HCO_2 ,⁶⁴ CH_3O ,⁶⁵ $\text{C}_2\text{H}_5\text{O}$,⁶⁶ CH_2CHO ,⁶⁷ etc.

2.2. Detection of Free Radicals

The general principle of detection of free radicals is based on the spectroscopy (absorption and emission) and mass spectrometry (ionization) or combination of both. An early review has summarized various techniques to detect small free radicals, particularly diatomic and triatomic species.⁶⁸ Essentially, the spectroscopy of free radicals provides basic knowledge for the detection of radicals, and the spectroscopy of numerous free radicals has been well characterized (see recent reviews²⁻⁴). Two experimental techniques are most popular for spectroscopy studies and thus for detection of radicals: laser-induced fluorescence (LIF) and resonance-enhanced multiphoton ionization (REMPI). In the photochemistry studies of free radicals, the intense, tunable and narrow-bandwidth lasers are essential for both the detection (via spectroscopy and photoionization) and the photodissociation of free radicals.

LIF is a highly sensitive technique for free radical detection.⁴ LIF involves exciting a radical with a tunable laser from a low vibrational and rotational level in the ground electronic state to a rovibrational level in an excited electronic state that subsequently fluoresces back to a lower state. The application of LIF requires that the radicals have suitable electronically excited states that have significant fluorescence quantum yield, i.e. they do not undergo significant non-radiative decay via dissociative processes such as predissociation. The LIF spectra, the total fluorescence intensity versus excitation wavelength, typically have rotational and fine-structure resolution, and can be used to identify the free radicals and to determine the initial relative state populations of the radicals in the beam.

REMPI provides high detection sensitivity for free radicals similar to that of LIF.⁴ In the REMPI method, one or more photons typically from a focused laser radiation initially excite the free radicals to an intermediate excited electronic state. The radicals are further excited and ionized by another photon in the same laser pulse (one-color REMPI) or by a photon of different wavelength from another laser beam overlapping in space and time

(two-color REMPI).⁶⁹ The REMPI spectra are obtained by recording the total ion signal, often mass selected by a time-of-flight mass spectrometer (TOF MS), as a function of the excitation energy of the intermediate state. The REMPI spectra also have the rotational resolution, and are utilized to characterize the free radicals and their initial state distributions in the beam. The applicability of REMPI detection of free radicals is still limited by the availability of the suitable intermediate state that has a reasonable lifetime. The REMPI technique has the advantage over LIF in that the intermediate state does not need to have a significant lifetime and a measurable fluorescence quantum yield. This is because the up-pumping from the intermediate state to the ionization continuum by the intense excitation laser radiation could compete efficiently with the intrinsic dissociative processes such as predissociation of the intermediate state.

Absorption spectroscopy is universal and is not affected by the dissociative lifetime of the excited electronic states as in the cases of LIF and REMPI, but the traditional absorption technique does not have enough sensitivity to probe the small number of free radicals in the molecular beam. A recent laser absorption method, cavity ring-down spectroscopy (CRDS), has developed into a powerful tool for spectroscopic study and for detection of the low-concentration free radicals. CRDS is based on measuring the rate (rather than the magnitude) of absorption, and it is insensitive to the light source instability and can increase sensitivity by orders of magnitude.^{70,71} Tunable laser pulses are injected into an optical cavity with two highly reflective mirrors ($R > 99.9\%$) and make $\sim 10^4$ round trips in the cavity, with a small amount transmitting through the mirrors with each pass. The decay rate (reciprocal of the ring-down time) due to the sample absorption as a function of laser wavelength yields an absorption spectrum. The multipass nature greatly enhances the absorption path and sensitivity. Recently, direct absorption of free radicals in the molecular beam has been demonstrated.⁵⁵

Photoelectron spectroscopy of free radicals has been utilized for detection of radicals. It can be via resonance photoexcitation and photoionization (e.g. ZEKE) or non-resonance photoionization (e.g. single-photon VUV photoionization). The photoelectron spectroscopy of free radicals has been reviewed in 1994 by Chen.⁵ A recent review on mass spectrometry, photoelectron spectroscopy, and photoionization of free radicals by Sablier and Fujii is available.⁷² It is worthwhile to point out that mass spectrometry by photoionization offers some advantage for the detection of radicals, in comparison with the conventional mass spectroscopy by electron-impact

ionization. Despite its simplicity, the electron-impact ionization tends to impact a large amount of internal energy in the ions produced and thus induces extensive fragmentation upon ionization. This could cause ambiguity in the identification of the free radicals, due to the likely ionization fragmentation of the precursor molecules producing the same ion masses of the radicals. The photoionization mass spectrometry, particularly with the VUV photon energy, has minimum ionization fragmentation and can readily differentiate the mass signals of the radicals from those of the parent precursor molecules.^{73,74} This is due to the fact that the ionization potentials of the free radicals are generally lower than those of the stable molecules.^{5,72}

2.3. *Experimental Techniques of Photodissociation Dynamics*

The experimental techniques used in the photodissociation studies of free radicals in molecular beam are essentially the same as those utilized in the studies of stable molecules.¹ Many reviews on the experimental techniques of photodissociation dynamics are available (for example, by Ashfold *et al.*,⁷⁵ and by Sato⁷⁶). As in the cases of stable molecules, the experimental techniques for studying photochemistry of free radicals should have: (i) high sensitivity for probing the photoproducts from the small number of radicals in the beam; (ii) high energy (state) resolution for revealing the details of the dissociation mechanisms; and (iii) generality in the detection of various photoproducts. Due to the small number density of the radicals and the potential interferences from the precursor molecules and by-products in the radical production processes, the experimental techniques that have particularly small background and high sensitivity are more successful in the free radical photochemistry. The common techniques used include spectroscopy methods (such as REMPI and LIF), and various photofragment translational energy spectroscopy methods (such as universal molecular beam machine, ion imaging, Rydberg atom tagging, fast radical beam photodissociation).^{1,75,76} The application of the various techniques will be discussed in more detail along with the specific free radical systems investigated in the next section.

The spectroscopy methods such as LIF and REMPI are utilized not only to detect the free radicals as discussed above, but also to directly measure the internal state distributions of the photoproducts in the photodissociation of free radicals. In this approach, the photochemistry is carried out in the free radical beam under single-collision conditions with well-defined

initial energy, and the photoproducts are detected by REMPI or LIF in a state-selected fashion; modest amount of information about the product translational energy could be obtained by the ion TOF profiles and Doppler spectroscopy.^{75,76}

Photofragment translational spectroscopy is another important tool in the study of photodissociation dynamics. Velocity distributions of the photoproduct fragments are measured using the TOF technique or imaging method, and the photoproduct translational energy and angular distributions are derived. Conventional molecular-beam machine with electron-impact ionization mass spectrometry has been utilized for photodissociation dynamics.⁷⁷ Ion imaging coupled with REMPI is also a popular method for the photodissociation dynamics studies.⁷⁸ More information about this technique can be found in several references.^{79–81} The high- n Rydberg atom time-of-flight (HRTOF) technique has high translational energy resolution and detection sensitivity^{75,82} and has been used in free radical photochemistry,^{39,83} although this technique is largely limited to the detection of H/D atom product. In the HRTOF method, the H/D atoms produced from the photodissociation of radicals are excited to a metastable high- n Rydberg state via two-photon excitation (Lyman- α + UV). The metastable Rydberg H atoms drift with their nascent velocities to a detector where they are field-ionized and detected. The H-atom product TOF spectra yield product translational energy distributions, corresponding to rovibronic states of the counterfragment by conservation of energy.

3. Photodissociation of Free Radicals

3.1. *Diatomic Radicals*

3.1.1. OH and OD

Hydroxyl radical (OH) is a key reactive intermediate in combustion and atmospheric chemistry, and it also serves as a prototypic open-shell diatomic system for investigating photodissociation involving multiple potential energy curves and nonadiabatic interactions. Previous theoretical and experimental studies have focused on electronic structures and spectroscopy of OH, especially the $A^2\Sigma^+ - X^2\Pi$ band system and the predissociation of rovibrational levels of the $A^2\Sigma^+$ state,^{84–93} while there was no experimental work on the photodissociation dynamics to characterize the atomic products. The $A^2\Sigma^+$ state [asymptotically correlating with the excited-state products $O(^1D) + H(^2S)$] crosses with three repulsive states [$^4\Sigma^-$, $^2\Sigma^-$, and $^4\Pi$, correlating with the ground-state fragments $O(^3P_J) + H(^2S)$] in

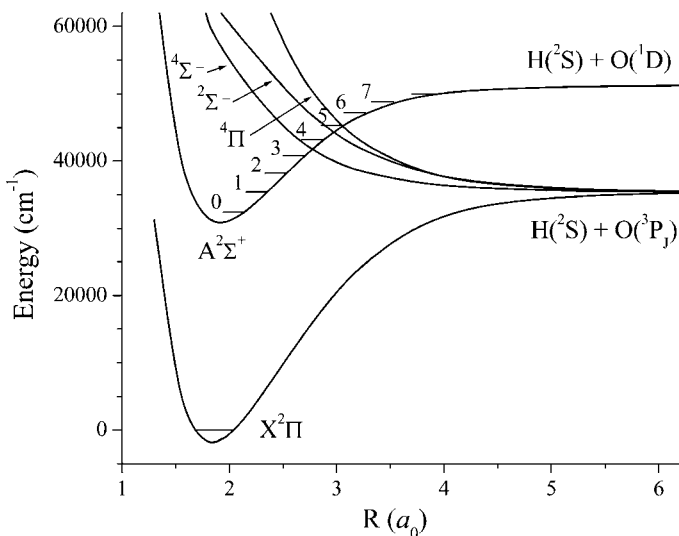


Fig. 5. Potential energy curves for the $X^2\Pi$, $A^2\Sigma^+$, $^4\Sigma^-$, $^2\Sigma^-$, and $^4\Pi$ states of OH. The vibrational levels $v' = 0-7$ of the $A^2\Sigma^+$ state are labelled. The information is from Refs. 83, 92 and 93.

the Franck–Condon (FC) region, and predissociates via spin-orbit induced couplings with the three repulsive states (Fig. 5).^{89–93} The high rotational states in $v' = 0$ ($N' \geq 24$) and in $v' = 1$ ($N' \geq 15$) of OH $A^2\Sigma^+$ and all rotational levels in $v' = 2$ (lifetime $\tau < 150$ ns) and $v' = 3$ ($\tau < 300$ ps) predissociate primarily via the $^4\Sigma^-$ state,^{84–87,89,90,92,93} while those in $v' = 4$ ($\tau < 20$ ps) decompose via the $^4\Sigma^-$, $^2\Sigma^-$, and $^4\Pi$ states.^{88,92,93} At larger internuclear distances ($R \sim 5.5-7$ a_0 , in the recoupling zone), where the separations between the molecular states are comparable to their spin-orbit and Coriolis interactions, the dissociative $^4\Sigma^-$, $^2\Sigma^-$, and $^4\Pi$ states can couple via the intrashell nonadiabatic interactions, which could alter the adiabatic fine-structure distributions established in the crossing region.^{93,94} At the largest separations (the asymptotic or atomic region), asymptotic spin-orbit interactions (through frame transformation, i.e. projection of molecular wavefunctions onto atomic basis states) also affect the $O(^3P_J)$ product spin-orbit branching fractions.^{93,94} Thus, the photo-predissociation dynamics of OH and the $O(^3P_J)$ spin-orbit branching fractions are affected by: (i) intersystem crossing (predissociation) from $A^2\Sigma^+$ and initial partitioning of the dissociation flux onto the $^4\Sigma^-$, $^2\Sigma^-$, and $^4\Pi$ states in the crossing region; (ii) spin-orbit and Coriolis couplings of the three repulsive

states in the recoupling zone; and (iii) asymptotic spin-orbit interaction at the large interunclear distance.^{90,93} The theoretical treatments of the $O(^3P_J)$ fine-structure distributions have to correctly describe OH potential energy curves, spin-orbit couplings between the bound and dissociative states and among the dissociative states, Coriolis interactions in the recoupling zone, asymptotic spin-orbit interactions, and multichannel quantum scattering/photodissociation.^{90,93}

Recently, Zhou *et al.* have investigated the state-to-state photopredissociation dynamics of the rotational states (N') of OH ($A^2\Sigma^+$, $v' = 3$ and 4), $OH(X^2\Pi, v'', N'', F_1) + h\nu \rightarrow OH(A^2\Sigma^+, v' = 3 \text{ and } 4, N', F_1) \rightarrow O(^3P_J) + H(^2S)$, using high- n Rydberg atom time-of-flight technique (HRTOF), and have experimentally measured the $O(^3P_J)$ product spin-orbit branching fractions.⁸³ Figure 6 shows the center-of-mass $O(^3P_J) + H(^2S)$ product translational energy distribution, $P(E_T)$, from the predissociation of OH ($A^2\Sigma^+$, $v' = 3$, $N' = 0$, $J' = 0.5$, F_1) and ($A^2\Sigma^+$, $v' = 4$, $N' = 0$, $J' = 0.5$, F_1), respectively. Isotropic angular distributions (with anisotropy parameter $\beta \approx 0$) are observed for both cases. Spin-orbit branching fractions of the $O(^3P_2) : O(^3P_1) : O(^3P_0)$ products are obtained from the $P(E_T)$'s: (i) $0.676 \pm 0.010 : 0.138 \pm 0.013 : 0.186 \pm 0.017$ for $N' = 0$ in $v' = 3$, in excellent agreement with a recent full quantum calculation ($0.675 : 0.141 : 0.184$)⁹³; and (ii) $0.873 \pm 0.026 : 0.102 \pm 0.028 : 0.025 \pm 0.005$ for $N' = 0$ in $v' = 4$, also in excellent agreement with the theory ($0.888 : 0.091 : 0.021$).⁹³

The $v' = 3$, $N' = 0$ level of the $A^2\Sigma^+$ state is below the first crossing (with $^4\Sigma^-$) and decays predominantly via this state ($^4\Sigma^-$).^{89,92,93,95} In a statistical (strong coupling) limit, the $O(^3P_{J=2,1,0})$ branching fractions are $0.556 : 0.333 : 0.111$. In the sudden (diabatic) limit, the fragments separate rapidly, and the $O(^3P_J)$ branching fractions are solely determined by the frame transformation (ignoring the intrashell nonadiabatic interactions in the recoupling zone), i.e. by the probabilities of projecting the molecular wavefunctions onto the asymptotic atomic basis set⁹⁴; for $^4\Sigma^-$, the sudden-limit single-state branching fractions are $O(^3P_{2,1,0}) = 0.611 : 0.167 : 0.222$.^{90,93} The experimental results do not match the simple models, but they agree very well with the values of $0.675 : 0.141 : 0.184$ by the full quantum calculation (multichannel scattering including all the nonadiabatic interactions from the FC to asymptotic region).⁹³ Comparisons among the experimental, full quantum, and single-state frame transformation $O(^3P_J)$ branching fractions indicate that the spin-orbit and Coriolis interactions in the recoupling zone are visible but do not significantly redistribute

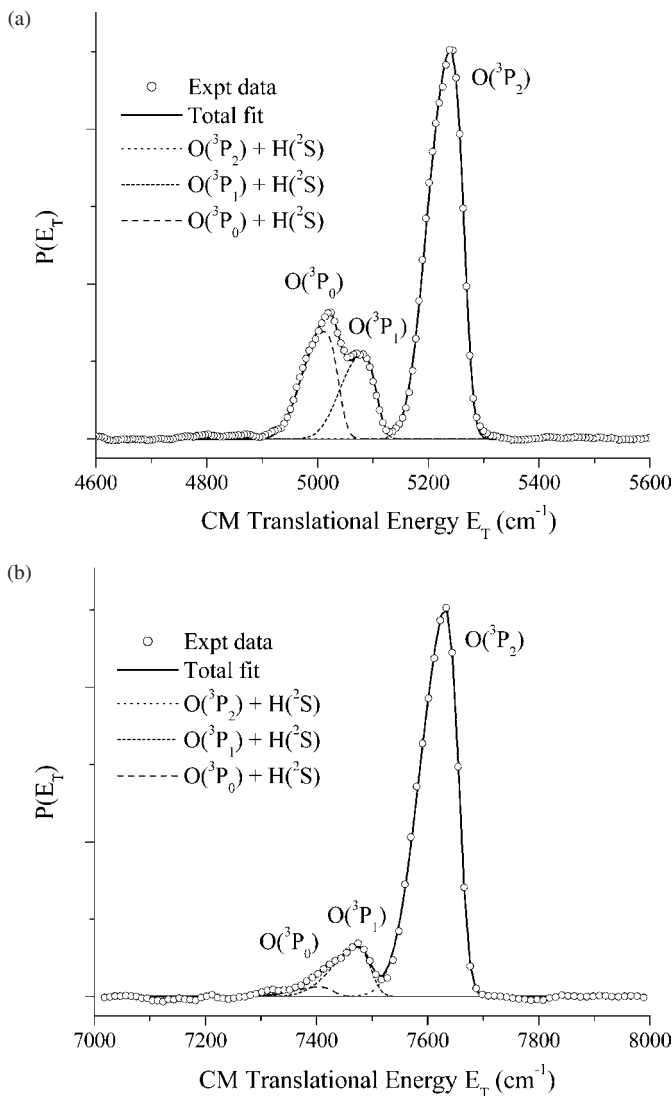


Fig. 6. (a) Center-of-mass $O(^3P_J) + H(^2S)$ product translational energy distribution, $P(E_T)$, from predissociation of OH ($A^2\Sigma^+$, $v' = 3$, $N' = 0$, $J' = 0.5$, F_1) via the $P_1(1.5)$ transition. The $P(E_T)$ is converted from the magic angle ($\theta = 54.7^\circ$) H-atom TOF spectrum. The spin-orbit $O(^3P_{J=2,1,0})$ sublevels are shown and are deconvoluted. (b) $P(E_T)$ for the $O(^3P_J) + H(^2S)$ products from predissociation of OH ($A^2\Sigma^+$, $v' = 4$, $N' = 0$, $J' = 0.5$, F_1) via the $P_1(1.5)$ transition. The $P(E_T)$ is at the magic angle. The spin-orbit $O(^3P_{J=2,1,0})$ sublevels are deconvoluted. (From Zhou *et al.*⁸³)

the initial dissociation flux on the $^4\Sigma^-$ state, and the asymptotic spin-orbit interactions (by frame transformation) are important in determining the $O(^3P_J)$ fine-structure distribution.⁹³ This is consistent with the small intrashell nonadiabatic interactions and the comparatively large product kinetic energy release and the light H-atom mass that lead to a short traversal time on the $^4\Sigma^-$ curve in the recoupling zone.^{93,94}

The $v' = 4$, $N' = 0$ level of the $A^2\Sigma^+$ state locates between the crossing points of $^4\Sigma^-$ and $^2\Sigma^-$ with $A^2\Sigma^+$, and the predissociation rate studies indicate that all three repulsive states contribute to the predissociation of $A^2\Sigma^+$, in the order of $^2\Sigma^-$ ($\sim 7\%$), $^4\Pi$ ($\sim 21\%$), and $^4\Sigma^-$ ($\sim 72\%$).^{93,95} The full quantum calculation predicts $O(^3P_{2,1,0}) = 0.888 : 0.091 : 0.021$, and a coherent average approximation (ignoring only the spin-orbit and Coriolis interactions in the recoupling zone) gives similar values ($0.873:0.094:0.033$), while a noncoherent average approximation (ignoring the spin-orbit and Coriolis interactions *and* the interferences of $^4\Sigma^-$, $^2\Sigma^-$, and $^4\Pi$) produces different fractions ($0.542:0.196:0.263$).⁹³ The experimental values agree well with the full quantum branching fractions and confirm that $A^2\Sigma^+ v' = 4$ predissociates via multiple repulsive states. Comparisons of the experimental results with the exact and approximate models (the coherent average approximation, noncoherent average approximation, and single-state frame transformations) indicate that the spin-orbit and Coriolis interactions in the recoupling zone are not very significant. More importantly, the comparisons reveal the quantum interferences among the three dissociative states. These interferences, through frame transformations in the asymptotic region and/or by mixing via $A^2\Sigma^+$ in the crossing region, redistribute the dissociation flux and strongly affect the $O(^3P_J)$ fine-structure distribution, e.g. enhancing the $O(^3P_2)$ population.⁸³

With the translational energies of the $O(^3P_2)$ peak in the $P(E_T)$'s (for $A^2\Sigma^+ v' = 3$ and 4) and the well-defined photolysis energies and internal energies of OH and $O(^3P_2)$, OH bond dissociation energy can be directly determined: $D_0(O-H) = 35565 \pm 30 \text{ cm}^{-1}$, compared favorably with the recent literature value ($35593 \pm 24 \text{ cm}^{-1}$).⁹⁶

The photodissociation dynamics of vibrationally-excited OD radical in the $X^2\Pi$ ground state has been examined at 243 and 226 nm using velocity map imaging to probe the angle-speed distributions of the $D(^2S)$ and $O(^3P_2)$ products by Radenovic and co-workers.⁹⁷ The OD radical is generated by electric discharge in a D_2O/Ar mixture,⁴⁹ and the OD radical is state-selected and focused in the $X^2\Pi_{3/2}, J = 3/2$, f lambda double level by a hexapole electrostatic lens. The angular distributions of the

D and O atom photoproducts are anisotropic (with $\beta = -1.0 \pm 0.2$ for the D atom), indicating a perpendicular transition (such as $^2\Sigma^{+,-} \leftarrow ^2\Pi$ or $^2\Delta \leftarrow ^2\Pi$, Fig. 5) and a rapid dissociation. With the conservation of energy $\text{TKER} = h\nu + E(\text{vib})_{\text{OD}} - D_0(\text{OD})$ and the known bond energy of OD, the peaks in the product kinetic energy distributions (TKER distributions, Fig. 7) are assigned to one-photon dissociation of OD in high vibrational levels of the ground electronic state $X^2\Pi$. The two main peaks in the $\text{O}(^3\text{P}_2)$ spectrum at 226 nm are attributed to photodissociation of OD in $v = 3$ and $v = 4$, and the three main peaks in the D spectrum at 243 nm are due to dissociation of OD ($v = 3, 4$, and 5). Furthermore, the relative intensity of these peaks are in good agreement with the photodissociation cross-sections from various vibrational states of $\text{OD}(X^2\Pi)$ that are computed by *ab initio* methods (the predicted yields are shown in the bar graphs of Fig. 7). An $\text{OD}(X^2\Pi)$ vibrational temperature of $\sim 1700\text{ K}$ (assuming a Boltzmann vibrational distribution) is estimated by modelling the experimental TKER distributions, and is supported by an independent measurement of the $v = 1$ population of OD in the beam using LIF from the $A-X$ transition. Both the experimental results and *ab initio* calculation conclude that the photodissociation occurs by excitation of OD from high

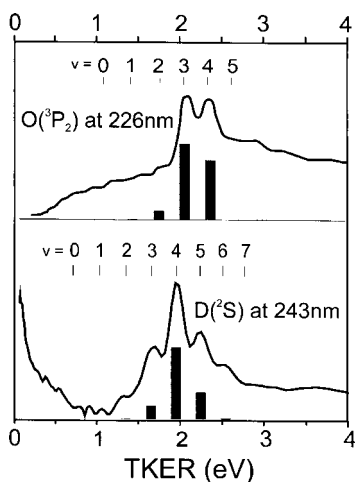
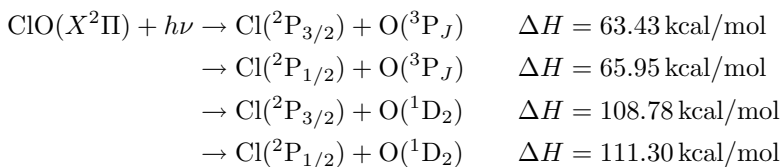


Fig. 7. Total kinetic energy release derived from velocity map images of $\text{O}(^3\text{P}_2)$ and $\text{D}(^2\text{S})$ fragment atoms following photodissociation of OD at 226 and 243 nm, respectively. The initial vibrational state of OD is determined from energy balance with $\text{TKER} = h\nu + E(\text{vib})_{\text{OD}} - D_0(\text{OD})$. The bar graphs show the calculated photodissociation yields for $\text{OD } X^2\Pi(v)$ at a vibrational temperature of 1700 K. (From Radenovic *et al.*⁹⁷)

vibrational levels of the ground $X^2\Pi$ to $1^2\Sigma^-$ state.⁹⁷ The repulsive $1^2\Sigma^-$ state is not accessible from the ground vibrational level of $OD(X^2\Pi)$; but the vibrationally-excited states of $OD(X^2\Pi)$, in spite of their small populations in the discharge radical beam (e.g. 3×10^{-5} for $v = 5$ at 1700 K), can be promoted to the $1^2\Sigma^-$ state, due to their higher initial internal energies and enhanced UV absorption cross-sections.

3.1.2. ClO and BrO

Halogen oxide radicals such as ClO and BrO are important reactive intermediates in the catalytic cycles of ozone destruction in the middle and upper stratosphere. The first absorption band $\text{ClO}(A^2\Pi \leftarrow X^2\Pi)$ starts from 318 nm and has a series of vibronic bands that converge to a broad continuum at wavelengths shorter than 264 nm (Fig. 8).^{98–101} In this continuum region four dissociation pathways are thermodynamically possible,³³



At photolysis wavelength $\lambda \geq 264$ nm, only the $\text{Cl}(^2\text{P}_J) + \text{O}(^3\text{P}_J)$ channels are possible. The series vibrational bands of $\text{ClO}(A^2\Pi)$ in this

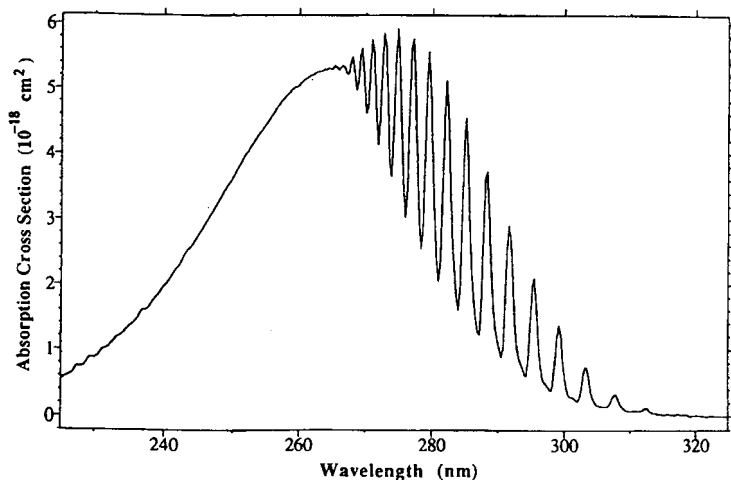


Fig. 8. UV absorption spectrum of ClO. (From Troler *et al.*¹⁰⁰)

region are broad; their rotational line-widths indicate that these states predissociate on a picosecond time scale.^{98,99,101} High level *ab initio* calculations on the potential energy curves have revealed that several repulsive states [which correlate with $\text{Cl}(^2\text{P}_J) + \text{O}(^3\text{P}_J)$ asymptotically] cross with the $\text{ClO}(A^2\Pi)$ state [asymptotically correlating with $\text{Cl}(^2\text{P}_J) + \text{O}(^1\text{D}_2)$] (Fig. 9),^{102,103} and the $1^4\Sigma^+$, $2^4\Sigma^-$, $3^2\Pi$, and $1^2\Delta$ states contribute most to the predissociation of $\text{ClO}(A^2\Pi)$. Schmidt *et al.* have observed the $\text{O}(^3\text{P})$ product in the structured region at $\lambda \geq 264\text{ nm}$.¹⁰⁴ Flesch and co-workers utilized vacuum ultraviolet (VUV) single-photon ionization to detect the photofragments of ClO , and they also confirm that $\text{O}(^3\text{P})$ is the exclusive product at $\lambda \geq 264\text{ nm}$.¹⁰⁵ In this pump-probe experiment, the tunable VUV radiation generated from the laser-produced plasma ionizes the laser-generated atomic photoproducts of ClO ; autoionization resonances of the atomic photoproducts are used to establish the quantum states of the photoproducts and to enhance the detection sensitivity.

In the continuum region above the threshold of $\text{O}(^1\text{D}_2)$ formation, there are several direct photodissociation studies of ClO .^{33,58,104–106} The threshold of the $\text{O}(^1\text{D}_2)$ production in the photodissociation of ClO is determined to be $37920 \pm 2\text{ cm}^{-1}$ in the VUV photoionization experiment by Flesch *et al.* and $37965 \pm 29\text{ cm}^{-1}$ with REMPI by Schmidt *et al.*,¹⁰⁴ downward shifted from the early values of 38052 cm^{-1} and $38026 \pm 7\text{ cm}^{-1}$ based on the analysis of the vibrational progression in the absorption spectrum.^{99,107} Davis and Lee have studied the photodissociation of ClO produced in a molecular beam at 248 nm using photofragment translational energy spectroscopy.³³ The $\text{Cl}(^2\text{P}_{3/2}) + \text{O}(^1\text{D}_2)$ production is the dominant channel (quantum yield $\phi \approx 0.97 \pm 0.01$) at 248 nm , with a negligible ($\phi < 0.005$) production of $\text{Cl}(^2\text{P}_{1/2}) + \text{O}(^1\text{D}_2)$ and a minor ($\phi < 0.03 \pm 0.01$) production of $\text{Cl}(^2\text{P}_{1/2}) + \text{O}(^3\text{P}_J)$. The photofragment anisotropy parameter β of the dominant channel $\text{Cl}(^2\text{P}_{3/2}) + \text{O}(^1\text{D}_2)$ is 1.2 ± 0.2 , less than the limiting value of 2.0 expected for the parallel ($\Delta\Omega = 0$) $\text{ClO}(A^2\Pi \leftarrow X^2\Pi)$ transition, indicating that a perpendicular transition ($\Delta\Omega = \pm 1$) to a state of $^2\Sigma$ or $^2\Delta$ symmetry also contributes to the absorption of ClO at 248 nm . Schmidt *et al.* have measured the kinetic energy distributions (with lower energy resolution) of the $\text{O}(^1\text{D}_2)$ product in the region of $237\text{--}270\text{ nm}$ using REMPI, and confirmed that the $\text{O}(^1\text{D}_2) + \text{Cl}(^2\text{P}_J)$ channels have a quantum yield of unity at $\lambda < 264\text{ nm}$.¹⁰⁴ Zou *et al.* have studied the photodissociation of jet-cooled ClO at 235 nm using REMPI with TOF mass spectrometry.⁵⁸ The product quantum yields of ClO photodissociation at 235 nm are 0.96 ± 0.02 for $\text{Cl}(^2\text{P}_{3/2}) + \text{O}(^1\text{D}_2)$, 0.02 ± 0.01 for

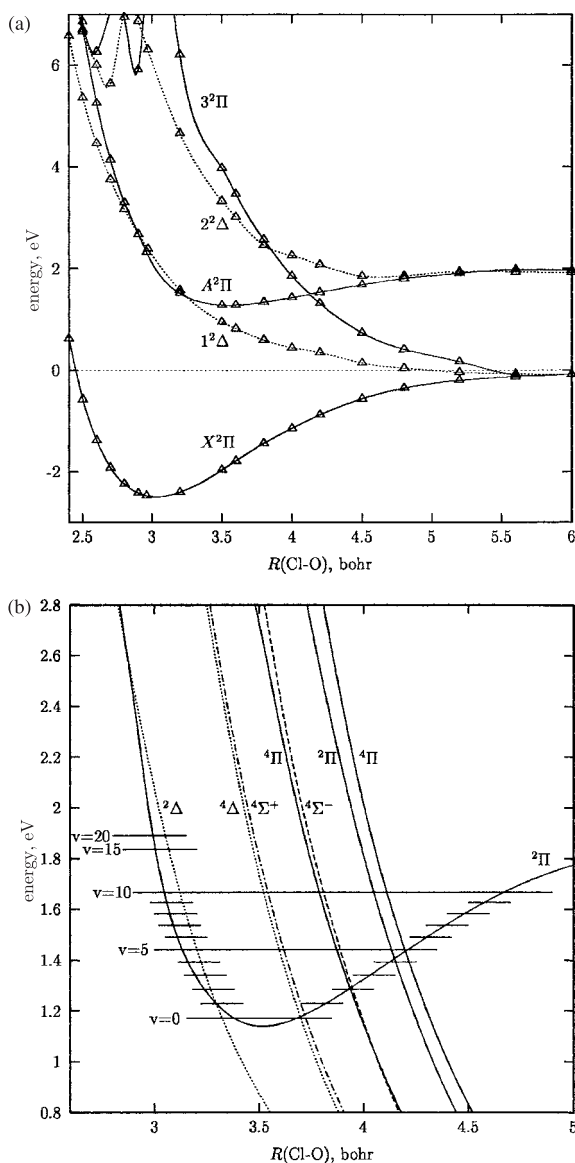


Fig. 9. (a) Calculated potential energy curves of $^2\Pi$ and $^2\Delta$ states of ClO; $^2\Sigma^+$, $^2\Sigma^-$, and quartet states of ClO are also calculated in Ref. 103 (not shown here). (b) Details of the potential energy curves of ClO on which the treatment of predissociation of $A^2\Pi$ is based. States with $\Omega = 3/2$. Some of the vibrational levels in the $A^2\Pi_{3/2}$ potential are also shown. (From Toniolo *et al.*¹⁰³ Similar calculation results are obtained by Lane *et al.*¹⁰²)

$\text{Cl}(^2\text{P}_{1/2}) + \text{O}(^1\text{D}_2)$, and 0.02 ± 0.01 for $\text{Cl}(^2\text{P}_{1/2}) + \text{O}(^3\text{P}_J)$,⁵⁸ essentially the same as those at 248 nm. The anisotropy parameter of the dominant channel $\text{Cl}(^2\text{P}_{3/2}) + \text{O}(^1\text{D}_2)$ at 235 nm photodissociation is $\beta = 1.2 \pm 0.2$, the same value at 248 nm; while β is 1.1 ± 0.3 for the minor channel $\text{Cl}(^2\text{P}_{1/2}) + \text{O}(^3\text{P}_J)$. As in the study at 248 nm, the nonlimiting β value of $\text{Cl}(^2\text{P}_{3/2}) + \text{O}(^1\text{D}_2)$ indicates that, besides the strong parallel $\text{ClO}(A^2\Pi \leftarrow X^2\Pi)$ transition, a perpendicular transition ($\Delta\Omega = \pm 1$) to a $^2\Sigma$ or $^2\Delta$ state also contributes to the ClO absorption at 235 nm. This $^2\Sigma$ or $^2\Delta$ state should correlate with the excited product channel $\text{Cl}(^2\text{P}_{3/2}) + \text{O}(^1\text{D}_2)$; the most likely candidate is $2^2\Sigma^+$,^{33,102,103} although the theoretical calculation indicates only a minor contribution of ~ 0.02 from this state at ~ 240 nm,¹⁰³ inconsistent with the large fraction of ~ 0.3 observed at 248 nm.³³

Zou *et al.* have also investigated the photodissociation of jet-cooled BrO at 335 nm.⁵⁸ Both of the thermodynamically accessible pathways are observed, with a quantum yield of 0.83 ± 0.10 for $\text{Br}(^2\text{P}_{3/2}) + \text{O}(^3\text{P}_2)$ and 0.17 ± 0.10 for $\text{Br}(^2\text{P}_{1/2}) + \text{O}(^3\text{P}_2)$. Both channels have an anisotropy parameter $\beta = 1.5 \pm 0.1$. The $\text{BrO}(A^2\Pi)$ state located in this near UV region is predissociative; the predissociation lifetime of the $v' = 4$ level of $\text{BrO}(A^2\Pi)$ at 355 nm is estimated to have an upper limit of 1.1 ps based on the anisotropy parameter.⁵⁸

3.2. Alkyl Radicals

3.2.1. Methyl (CH_3)

The methyl radical is considered to be one of the simplest organic free radicals and is important in combustion. The first absorption band of methyl is a strong, broad and diffuse band originating at 216 nm in the UV region, and is assigned to the $\tilde{B}^2A'_1 \leftarrow \tilde{X}^2A'_2$ transition of the planar radical.^{108,109} This transition is due to the excitation of the unpaired $2p_z$ electron on the radical-center carbon atom to the $3s$ Rydberg orbital. This absorption band has diffusive structures, indicating rapid predissociation of the excited state by tunnelling.¹⁰⁹ Orbital correlation consideration and theoretical calculations suggest that the excited $\tilde{B}^2A'_1$ state predissociates into the singlet $\text{CH}_2(\tilde{a}^1A_1) + \text{H}(^2\text{S})$,¹¹⁰ with a barrier to dissociation of 6.3 kcal/mol^{110,111}; while the ground $\tilde{X}^2A'_2$ state correlates with two asymptotic dissociation channels: $\text{CH}_2(\tilde{X}^3B_1) + \text{H}(^2\text{S})$ and $\text{CH}(X^2\Pi) + \text{H}_2(^1\Sigma_g^+)$ (Fig. 10).¹¹²

The photodissociation dynamics of jet-cooled methyl radical produced in a pyrolysis radical beam have been investigated at 193.3 nm using photofragment translational spectroscopy by North and co-workers.¹¹² Only

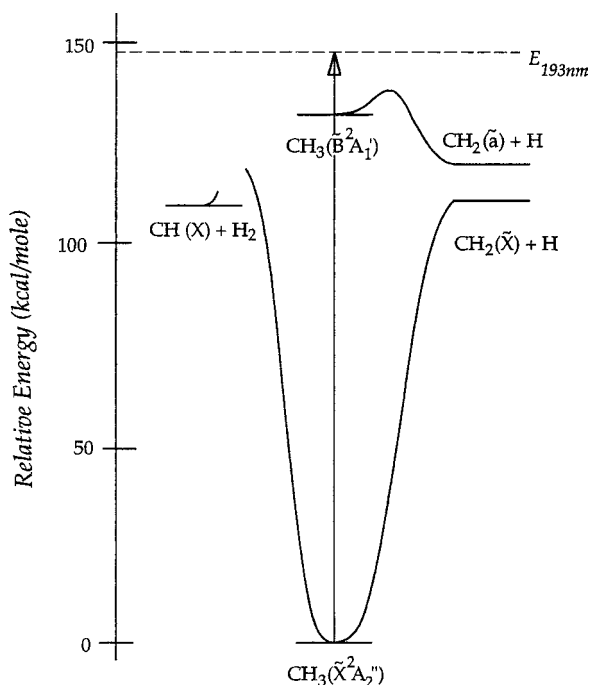


Fig. 10. Energy level diagram for methyl radical. The energetically accessible dissociation channels in the UV photolysis at 193 nm are shown. (From North *et al.*¹¹²)

the $\text{CH}_2 + \text{H}(^2S)$ dissociation pathway is observed and there is no evidence for the molecular elimination channel $\text{CH}(X^2\Pi) + \text{H}_2(^1\Sigma_g^+)$. The translational energy distribution of the products starts at the expected threshold of the singlet $\text{CH}_2(\tilde{a}^1A_1) + \text{H}$ channel, strongly suggesting that methylene is produced predominately in the \tilde{a}^1A_1 excited state (Fig. 11).¹¹² The breadth of the distribution suggests that the methyl radical dissociates from a wide range of geometries. The photofragment has an anisotropic angular distribution with $\beta = -0.9 \pm 0.1$, consistent with the perpendicular $\tilde{B}^2A_1' \leftarrow \tilde{X}^2A_2''$ transition and a fast dissociation.¹¹²

The photodissociation of jet-cooled methyl from a flash pyrolysis source has also been studied at 216.3 nm using the high- n Rydberg atom time-of-flight technique by Wilson and co-workers.¹¹³ The H-atom time-of-flight spectrum indicates that predissociation of $\text{CH}_3(\tilde{B}^2A_1')$ at 216.3 nm predominantly produces the vibrationless level of the low-lying \tilde{a}^1A_1 excited state of CH_2 , as shown in the internal energy spectrum of the CH_2 fragment derived from the measured product translational energy distribution (Fig. 12). This

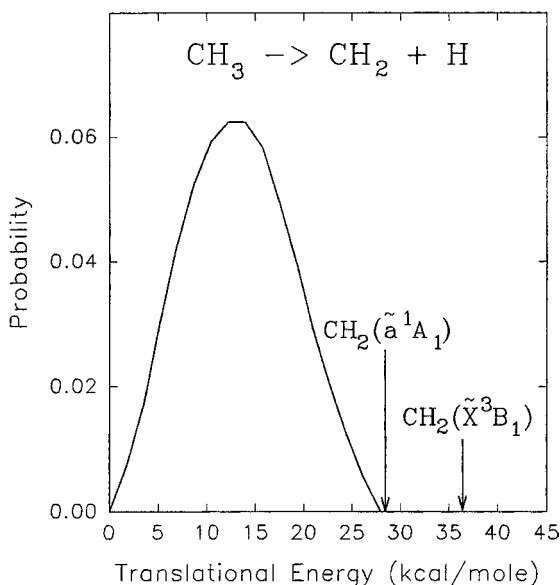


Fig. 11. Center-of-mass translational energy distribution of the $\text{CH}_2 + \text{H}$ product channel of CH_3 photodissociation at 193 nm. Arrows indicate the thermodynamic maximum available energies for formation of singlet and triplet methylene. (From North *et al.*¹¹²)

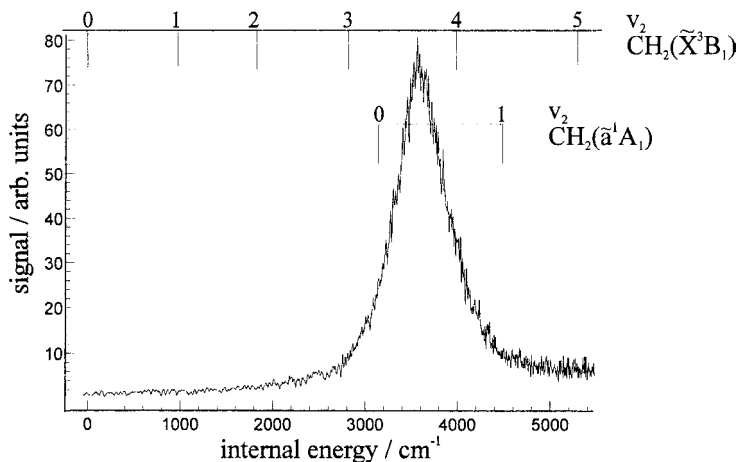
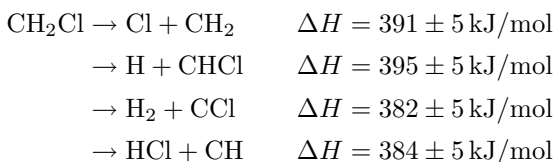


Fig. 12. Internal energy spectrum of the CH_2 fragment from photolysis of the CH_3 radical at 216.3 nm. The combs above the figure indicate the expected TOFs of H atoms formed, in association with triplet methylene $\text{CH}_2(\tilde{\text{X}}^3\text{B}_1)$ or singlet $\text{CH}_2(\tilde{\text{a}}^1\text{A}_1)$ respectively as a function of v_2 , the vibrational quantum number for their respective bending mode. (From Wilson *et al.*¹¹³)

result is consistent with that at 193 nm, although higher vibrational excitation in the $\text{CH}_2(\tilde{a}^1\text{A}_1)$ fragment is observed at 193 nm.

3.2.2. Chloromethyl (CH_2Cl)

Electronic states and photodissociation dynamics of chloromethyl radical have been studied recently.^{114–117} Because of the chlorine substitution, there are several low-lying valence excited states (such as 1^2A_1 and 2^2B_1 , which mainly involve the orbitals on the CCl bond) in addition to the 3s Rydberg state (2^2A_1), and more dissociation channels are available.



The energetics and correlation diagram for the dissociation of CH_2Cl to $\text{Cl} + \text{CH}_2$ are shown in Fig. 13.^{114,115}

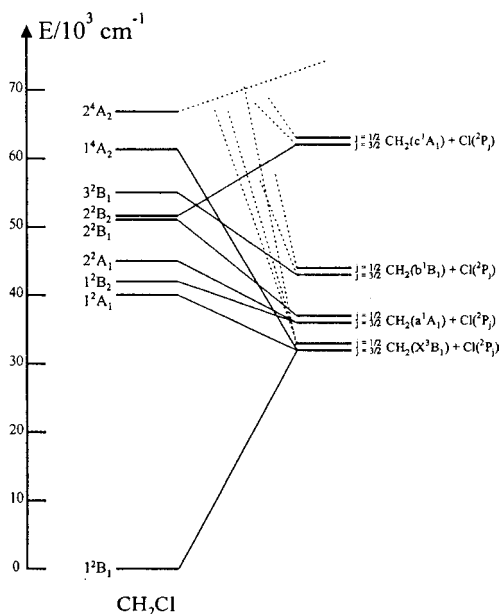


Fig. 13. Diabatic correlation diagram for the dissociation of CH_2Cl to $\text{CH}_2 + \text{Cl}$. The vertical energies and assignments of the excited electronic states of CH_2Cl are from Ref. 115. (From Dribinski *et al.*¹¹⁴)

Dribinski and co-workers have investigated the photodissociation of jet-cooled CH_2Cl radical (produced in a pyrolysis radical beam source) in the region of 312–214 nm.¹¹⁴ The Cl and CH_2 products are detected by REMPI and their velocity and angular distributions are measured by using the ion imaging technique. The experimental results show that the Cl + CH_2 production is the major channel in the region of 312–214 nm.¹¹⁴ In the long wavelength region of 312–247 nm, the product velocity and angular distributions and the *ab initio* calculations indicate that CH_2Cl excitation is mainly due to the perpendicular $1^2\text{A}_1 \leftarrow 1^2\text{B}_1$ transition (with a vertical maximum at ~ 252 nm), and the major dissociation product channel is $\text{CH}_2(\tilde{\text{X}}^3\text{B}_1) + \text{Cl}(^2\text{P}_{3/2})$ (which correlates with the lowest electronic excited state 1^2A_1). The substantial translational energy release and anisotropic angular distribution ($\beta = -0.7$) of the $\text{CH}_2(\tilde{\text{X}}^3\text{B}_1) + \text{Cl}(^2\text{P}_{3/2})$ products indicate a repulsive dissociation, and are consistent with the fact that the $1^2\text{A}_1 \leftarrow 1^2\text{B}_1$ transition promotes an electron from the singly occupied π_{CCl}^* orbital to an antibonding σ_{CCl}^* orbital.^{114,115} At shorter photolysis wavelength $\lambda \leq 220$ nm, the strong, parallel $2^2\text{B}_1 \leftarrow 1^2\text{B}_1$ transition becomes dominant, and the main product channel is $\text{CH}_2(\tilde{\text{a}}^1\text{A}_1) + \text{Cl}(^2\text{P}_{1/2,3/2})$ (which correlates with the 2^2B_1 state) and has a $\beta \sim 1.2$. The 2^2B_1 state is also repulsive due to the promotion of a bonding electron in π_{CCl} to the antibonding π_{CCl}^* orbital,^{114,115} thus generating Cl as the dominant dissociation product.

In the intermediate region of 235–243 nm, both the perpendicular $1^2\text{A}_1 \leftarrow 1^2\text{B}_1$ and parallel $2^2\text{B}_1 \leftarrow 1^2\text{B}_1$ transitions contribute to the photolysis of CH_2Cl to form the major product channel $\text{CH}_2 + \text{Cl}$ ^{114,116}; thus the fractions of the electronic and spin-orbit states of the products change with excitation wavelength. A minor H-atom product channel is observed at 243.1 nm.¹¹⁶ It is exclusively from a perpendicular transition (with $\beta = -0.5 \pm 0.1$). Its translational energy distribution is quite different from the corresponding perpendicular component of the Cl distribution at the same photolysis wavelength, but instead, its angular and energy distributions are qualitatively similar to those of the methyl radical from the 3s Rydberg state at 193 nm.¹¹² Potter and co-worker suggest that the H-atom channel might be due to the 3s (2^2A_1) $\leftarrow 1^2\text{B}_1$ Rydberg excitation of CH_2Cl in this wavelength region.^{115,116}

Some Cl product signals from “hot band” transitions due to the enhanced absorption of the vibrationally excited CH_2Cl radical are observed, particularly for excitation to the lowest 1^2A_1 state in the wavelength region longer than 247 nm.^{114,116} A recent theoretical study has

revealed that the valence 1^2A_1 state and the Rydberg 2^2A_1 state of CH_2Cl interact and have an avoided crossing at $r_{CCl} = 1.62 \text{ \AA}$ near the Franck–Condon region, and the subsequent change of the shape of the 1^2A_1 potential energy curve results in a large increase in the Franck–Condon factors for absorption from the vibrationally excited CH_2Cl in the 1^2B_1 ground electronic state.¹¹⁷

3.2.3. Ethyl (C_2H_5)

The UV absorption spectrum of ethyl (C_2H_5) radical has two broad and structureless (thus predissociative or dissociative) absorption bands.^{118,119} The first band in the range of 230–265 nm peaks around 245 nm and corresponds to the $2p_z \rightarrow 3s$ excitation on the radical-center carbon atom, while the second band in 190–230 nm peaks around 206 nm and is assigned to the $2p_z \rightarrow 3p$ transition.¹²⁰ Both excited states are predominantly Rydberg in character and thus can be envisaged as an ethyl cation core with an electron in the outer orbital.^{121,122} As the nonclassical H-bridged structure of the ethyl cation is more stable than the classical one (with a C_s equilibrium geometry similar to that of the ground-state C_2H_5), the nonclassical structures (in C_{2v}) of the $3s$ and $3p$ Rydberg states of ethyl are lower in energy than the classical ones (in C_s) (Fig. 14).^{121–123} The theoretical studies suggest that, upon vertical excitation to the $\tilde{A}^2A'(3s)$ state, a β H atom in the classical structure slides to the center to form the lower-energy bridged C_{2v} structure (the $\tilde{A}^2A_1(3s)$ state); this bridged \tilde{A}^2A_1 state is unstable and dissociates on a repulsive surface (without a barrier) to $H + C_2H_4(\tilde{X}^1A_g)$, and thus there is no local minimum on the $3s$ state (Fig. 15).^{121–123} The $H + C_2H_4(\tilde{X}^1A_g)$ products correlate adiabatically with the \tilde{A}^2A_1 state of ethyl in C_{2v} , but with the ground-state ethyl \tilde{X}^2A' in C_s (Fig. 14). Therefore, the $\tilde{A}^2A'(3s)$ state, via the formation of the nonclassical bridged structure, could undergo fast dissociation into H and ground-state ethylene adiabatically, with a large translational energy release. The $3p$ states are stable relative to the H splitting.¹²³ While the three $3p$ states do not correlate adiabatically with $H + C_2H_4(\tilde{X}^1A_g)$ in neither C_s nor C_{2v} , the lowest $3p$ state could dissociate without a barrier to $CH_3(\tilde{X}^2A''_2) + CH_2(\tilde{b}^1B_1)$.¹²⁴

Kopplitz and co-workers have studied the photolysis of C_2H_5 via the $\tilde{A}^2A'(3s)$ state by using 248-nm photolysis radiation and hot ethyl radicals generated from photolysis of ethyl halides.^{125,126} Chen and co-workers have investigated the photodissociation of jet-cooled ethyl (produced by flash pyrolysis of ethyl iodide and *n*-propyl nitrite) in the region of 245–264 nm

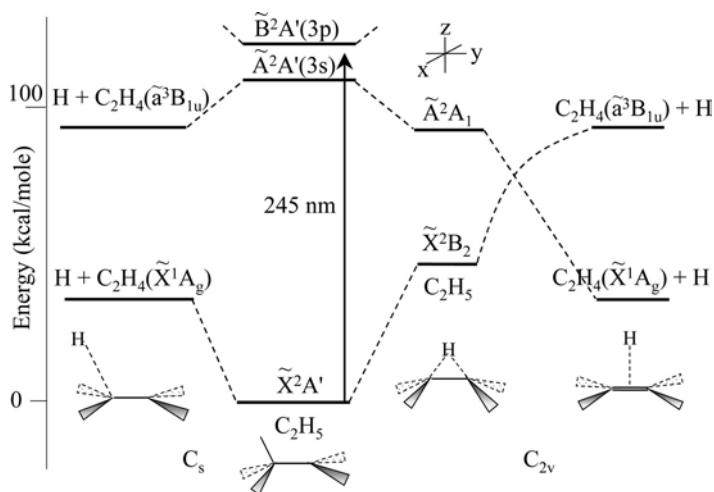


Fig. 14. Energy level and correlation diagram of the C_2H_5 photodissociation system in C_s and C_{2v} symmetry. Upper limits of the adiabatic energies of the $\tilde{A}^2A'(3s)$ and $\tilde{B}^2A'(3p)$ states are based on absorption spectra. The crossing of the 2B_2 and 2A_1 states in C_{2v} symmetry becomes an avoided intersection in C_s . The B_{1u} state of C_2H_4 is reduced to B_2 in C_{2v} when the z axis is chosen to be perpendicular to the C_2H_4 plane. (From Amaral *et al.*³⁹)

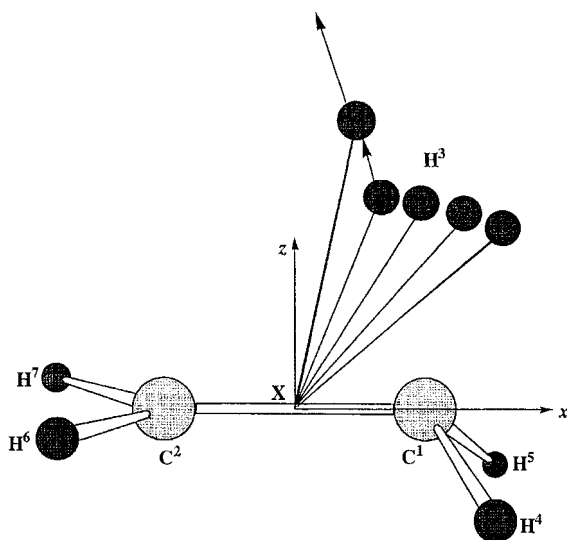


Fig. 15. Minimal energy path for hydrogen motion in the $\tilde{A}^2A'(3s)$ electronic state of C_2H_5 . (From Zyubin *et al.*¹²³)

by using H-atom REMPI TOFMS.¹²⁷ Site selectivity and exclusive loss of the β H atom have been observed in the isotopic studies, indicating no isotopic scrambling in the ethyl photodissociation via the $3s$ state.^{125–127} Small microcanonical dissociation rates (in the order of 10^7 s^{-1}) and product translational energy release ($\langle f_T \rangle \sim 0.27$) of the $\text{H} + \text{C}_2\text{H}_4$ channel have been measured by Chen and co-workers (Fig. 16).¹²⁷ The small kinetic energy release is consistent with unimolecular decomposition of the radical on the ground state, presumably after a fast internal conversion (IC) of the $3s$ excited state to the ground state.^{127,128}

Amaral *et al.* have examined the photodissociation of jet-cooled ethyl radical (produced by 193 nm photolysis of $\text{C}_2\text{H}_5\text{NO}_2$ (nitroethane), $\text{CH}_3\text{CD}_2\text{NO}_2$, and ethyl vinyl ether) via the $\tilde{A}^2A'(3s)$ state near 245 nm by using the high- n Rydberg-atom time-of-flight technique.³⁹ Bimodal product translational energy release and energy-dependent angular distribution are observed, suggesting two dissociation pathways (Fig. 17). A slow ($\langle f_T \rangle \sim 0.35$) and isotropic channel corresponds to unimolecular dissociation of the radical after internal conversion, which is similar to the results in Chen and co-workers' study. A fast ($\langle f_T \rangle \sim 0.78$) and anisotropic ($\beta = 0.5 \pm 0.1$) channel is consistent with direct and repulsive H-atom dissociation via a nonclassical H-bridged transition state from the $3s$ state to yield $\text{H} + \text{C}_2\text{H}_4(\tilde{X}^1A_g)$ in C_{2v} symmetry (Fig. 14). This fast process has been described by the theoretical studies (Fig. 15).^{121–123} The anisotropy parameter ($\beta = 0.5 \pm 0.1$) suggests a 45° angle between the transition dipole μ of the $\tilde{X}^2A' \rightarrow \tilde{A}^2A'$ transition (via the $2p_z \rightarrow 3s$ excitation)

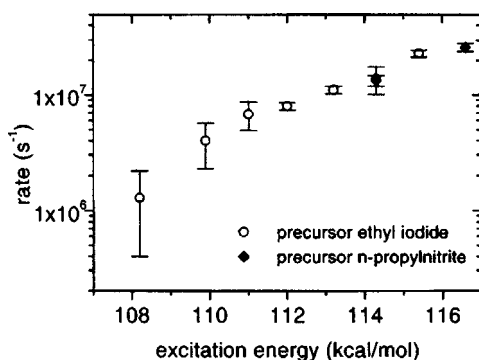


Fig. 16. The dissociation rate of ethyl radical as a function of excitation energy. The open circles correspond to data obtained with ethyl iodide used as the precursor, while the closed diamonds correspond to data obtained with n -propylnitrite used as precursor. (From Gilbert *et al.*¹²⁷)

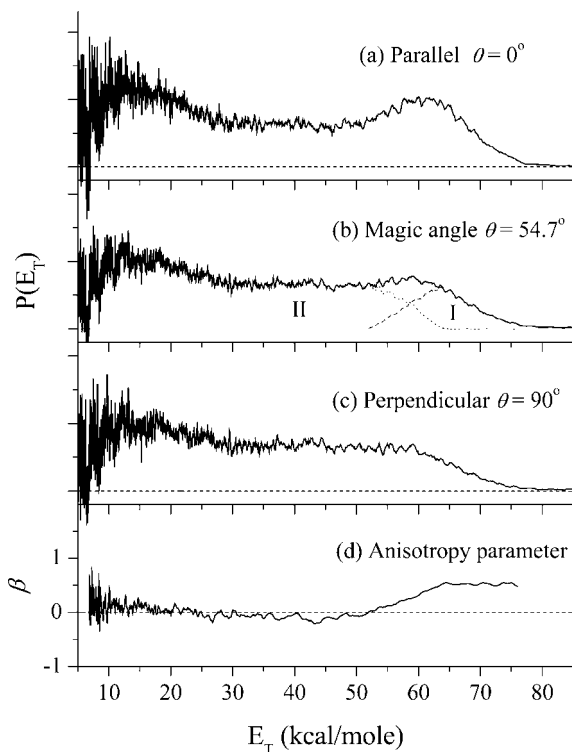


Fig. 17. H-atom product channel translational energy distributions of the ethyl photodissociation, with the 245-nm photolysis radiation polarization: (a) parallel to the TOF axis; (b) at magic angle; and (c) perpendicular to the TOF axis, and (d) anisotropy parameter $\beta(E_T)$. In (b), the de-convoluted fast component, $P_I(E_T)$, and slow-component, $P_{II}(E_T)$, are plotted in dashed and dotted lines, respectively. (From Amaral *et al.*³⁹)

and the velocity direction of the recoiling H atom,³⁹ in agreement with the calculated value of $\sim 50^\circ$ departing angle as the H atom approaches the C_{2v} bridged structure.¹²³ The fast/slow branching ratio is measured to be ~ 0.2 .

Site-selective loss of the β hydrogen atom is also confirmed by using the partially-deuterated CH_3CD_2 radical, consistent with a rapid internal conversion to the ground-state surface and the prompt dissociation in C_{2v} .³⁹ As shown in Fig. 14, the 2A_1 and 2B_2 surfaces cross with a conical intersection. In the C_s point group, however, this crossing becomes an avoided intersection in the A' symmetry. The migration of the β H atom to the bridged position on the excited surface serves to funnel the dissociating trajectories to the $\tilde{X}^2B_2/\tilde{A}^2A_1$ (or $\tilde{X}^2A'/\tilde{A}^2A'$) conical intersection region.

The prompt dissociation of the fast H atom in the C_{2v} pathway, for which character change and collapse of the 3s Rydberg orbital on the ethyl radical to the 1s orbital of the H product are required,^{121–123} could be assisted by the conical intersection. Also, relaxation and internal conversion from the 3s state to the ground state ethyl can be facilitated by this conical intersection, in addition to other possible vibronic couplings in the A' symmetry.³⁹

Photodissociation of C_2H_5 via the $3p$ state has also been studied via secondary photodissociation of hot ethyl radicals by Koplitz and co-workers (at 193 nm)¹²⁶ and by Bersohn and co-workers (at 205 nm).¹²⁹ At the high excitation energy, isotopic scrambling in ethyl has been observed in the H-product channel. The significant translational energy release ($\langle f_T \rangle \sim 0.34$) infers that the dissociation involves crossing from the Rydberg state to a repulsive region of the ground state surface near the center of the C–C bond.¹²⁹

3.3. Unsaturated Aliphatic Radicals

3.3.1. Vinyl (C_2H_3)

Vinyl radical (C_2H_3) is a prototype unsaturated hydrocarbon radical, and is an important reactive intermediate in many hydrocarbon reaction systems such as combustion and planetary atmospheres, due to its high reactivity and its decomposition into H and C_2H_2 . The first absorption band of C_2H_3 (via the $\tilde{A}^2A'' \leftarrow \tilde{X}^2A'$ transition), with resolved vibrational progressions, was identified by Hunziker *et al.* in the region 360–500 nm.¹³⁰ High-resolution \tilde{A} -band absorption spectra between 530 and 415 nm and 530 and 385 nm, with partially resolved rotational structure (of $\sim 1 \text{ cm}^{-1}$ line-width and thus pico-second excited \tilde{A} state lifetime near the band origin 20042 cm^{-1} or 499 nm), were obtained recently by Pibel and co-workers.^{131,132} The high-resolution spectra of the $\tilde{A}^2A'' \leftarrow \tilde{X}^2A'$ electronic transition of jet-cooled C_2H_3 and its partially deuterated isotopomer, CD_2CH , were obtained via action spectroscopy of the H/D-atom photoproduct of the vinyl radical by Pushkarsky and co-workers.¹³³ In the shorter wavelength region of 225 to 238 nm, a strong, broad and featureless UV absorption band of C_2H_3 , was reported by Fahr and co-workers.¹³⁴ This UV band is assigned to the allowed in-plane $\tilde{C}^2A' \leftarrow \tilde{X}^2A'$ transition via the $\pi^*(2a'') \leftarrow \pi(1a'')$ excitation. However, as the \tilde{B} state ($T_0 = 33530 \text{ cm}^{-1}$, 298 nm) and \tilde{C} state ($T_0 = 37700 \text{ cm}^{-1}$, 265 nm) of vinyl are close in energy,¹³⁵ it is unclear whether the initial excitation in this UV absorption band is to the \tilde{B} or \tilde{C} state or both.

The structures and energetics of the ground and several electronically excited states of C_2H_3 have been calculated by Wang *et al.*¹³⁶ and by Mebel *et al.*¹³⁵ Energetics of C–H bond rupture and H-atom migration pathways in the ground and excited states of vinyl have been studied theoretically by Sevin *et al.*: direct C_{2v} adiabatic pathways (via the bridged structures and high barriers) that take the excited-state vinyl to $\text{C}_2\text{H}_2 + \text{H}$ are suggested.¹²¹ Isomerization of methylene H atoms in the first excited state has also been studied theoretically by Paddon-Row and Pople, and an internal out-of-plane rotation mechanism, involving a twisted non-planar C_s structure (A' symmetry, with a pyramidalized CH_2 group), is proposed.¹³⁷ Recently, two more theoretical studies have treated the dissociation dynamics of vinyl from its \tilde{A} state in greater detail.^{132,138} Several internal conversion and intersystem crossing channels, which bring the excited vinyl radical to the ground state potential energy surface leading to dissociation on the ground state, have been identified within planar C_s , twisted C_s and C_{2v} symmetry. The most likely reaction channel is the direct internal conversion from \tilde{A} to the ground state within planar C_s symmetry, through a minimum of seam of crossing (conical intersection) at an energy of ~ 80 kcal/mol (with respect to the ground-state equilibrium geometry).^{132,138} The energy levels of the C_2H_3 electronic states and their correlations with the dissociation products are shown in Fig. 18.

The first direct experimental study of jet-cooled vinyl photodissociation was carried out at 243.2 nm using the velocity map imaging technique by Ahmed *et al.*³⁷ In this case, a primary product channel $\text{H}_2\text{CC}(\tilde{X}^1\text{A}_1) + \text{H}$ and a minor channel $\text{HCCH}(\tilde{a}^3\text{B}_2) + \text{H}$ were suggested, and an out-of-plane motion mechanism was proposed to explain how the A'' -symmetry excited states led to the A' -symmetry ground state and then to the vinylidene product. The photodissociation of vinyl radical via its first excited \tilde{A}^2A'' state was studied at 327.4 and 366.2 nm by using the HRTOF technique by Xu and co-worker.³⁸ The $\text{HCCH}(\tilde{X}^1\Sigma_g^+) + \text{H}$ product channel was observed, with two well-resolved vibrational progressions of $\text{C}_2\text{H}_2(\tilde{X}^1\Sigma_g^+)$. The anisotropic H-atom angular distributions indicate a short \tilde{A}^2A'' excited state lifetime with respect to dissociation. Moore and co-workers have reported H and D atom velocity and angular distributions for the photodissociation of C_2H_3 and CD_2CH from several vibrational levels in the lowest 2500 cm^{-1} of the \tilde{A}^2A'' state.¹³⁹ About 26–29% of the available energy is channelled into H-atom product translation. An upper bound of $1.3 \times 10^{11}\text{ s}^{-1}$ is given for the rate of H-atom scrambling between the α and β carbon atoms.

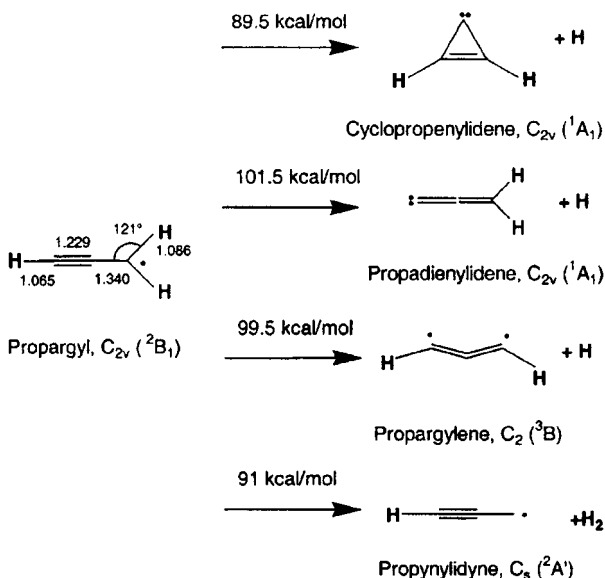


Fig. 19. The unimolecular reaction channels for the propargyl radical together with the heats of reaction. Assuming that H₂ loss is associated with a substantial reverse barrier, formation of cyclopropenylidene, *c*-C₃H₂, is the most likely channel. (From Deyerl *et al.*¹⁴³)

a prior distribution, indicating a dissociation proceeding through a loose transition state. The pump-probe time delay measurements of the H-atom production as a function of the excess energy by varying the excitation energy between 265 and 240 nm provide microcanonical rates for the loss of a hydrogen atom. These rates are in the order of 10^7 s^{-1} and in good agreement with RRKM calculations. A complete isotopic scrambling is observed in the photolysis of the partially deuterated propargyl radical, H₂CCCD; this implies that the *c*-C₃H₂ formation proceeds via a 1, 2 H-shift with either concurrent or subsequent cyclization and loss of a hydrogen atom as the final step in the sequence.

The photodissociation of propargyl radical at photon energies of 193 and 242 nm has also been investigated theoretically.¹⁴⁴ In this study, it is assumed that after UV photon excitation, a fast nonradiative decay to the electronic ground state produces vibrationally hot propargyl radical, which subsequently undergoes unimolecular dissociation on the ground state to various products. Product branching ratios calculated for 242 nm photodissociation are 90.2% for the HCCCH(3B) + H channel, 5.1% for

$c\text{-C}_3\text{H}_2(^1\text{A}_1) + \text{H}$, 3.0% for $\text{HCCC}(^2\text{A}') + \text{H}_2$, 1.6% for $\text{H}_2\text{CCC}(^1\text{A}_1) + \text{H}$, and 0.1% for $\text{CH}(^2\Pi) + \text{C}_2\text{H}_2$.¹⁴⁴ According to the theory, the $\text{HCCCH}(^3\text{B}) + \text{H}$ are the major products, and $c\text{-C}_3\text{H}_2(^1\text{A}_1) + \text{H}$ channel plays only a minor role; this is in contrast to the experimental data and their interpretation.¹⁴³ In addition, the theoretical H-loss rates are much higher than the experimental measurements, although the theoretical rates could be lowered by 2–3 orders magnitude to the $10^7\text{--}10^8\text{ s}^{-1}$ range by adjusting the reaction energies and by scaling the vibrational frequencies (to take into account anharmonicity).¹⁴⁴

3.3.3. The C_3H_5 System: Allyl, 1-Propenyl, and 2-Propenyl

The spectroscopy, structure, photochemistry, and unimolecular reactions of allyl radical have been studied extensively and reviewed recently.¹⁴⁵ Possible dissociation channels of allyl radical, their energetics, and the potential energy barriers of the C_3H_5 system are shown in Figs. 20 and 21.^{145,146}

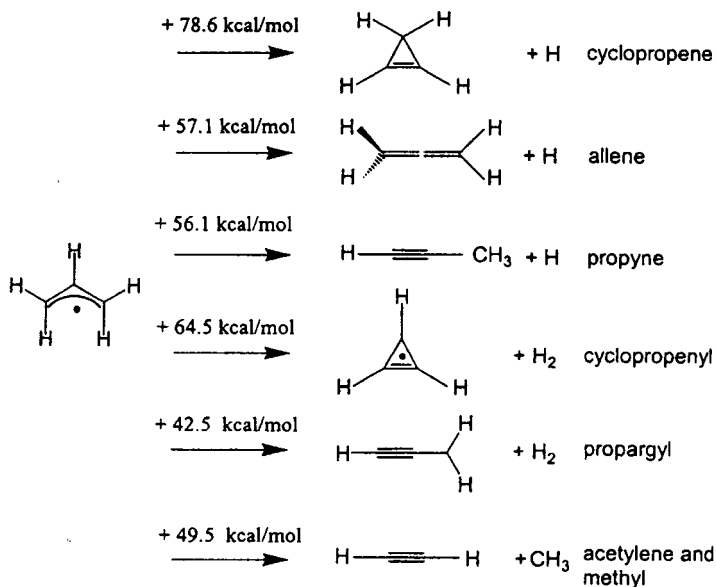


Fig. 20. Possible dissociation channels of allyl radical and their standard heats of formation relative to allyl. The loss of H_2 generally proceeds via a high activation barrier and is thus considered unlikely. (From Fischer *et al.*¹⁴⁵)

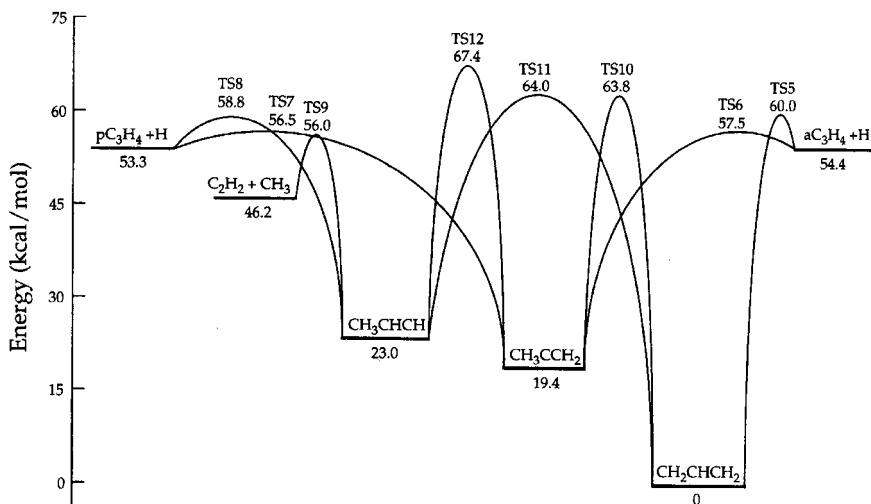


Fig. 21. Reaction energetics and potential energy barriers of the C_3H_5 system, determined at the G2(B3LYP) level of theory. aC_3H_4 stands for allene and pC_3H_4 for propyne. (From Davis *et al.*¹⁴⁶)

The loss of H_2 generally proceeds via a high activation barrier and is thus considered unlikely.

Stranges and co-workers have utilized photofragment translational spectroscopy and investigated the photodissociation dynamics of jet-cooled allyl radical generated through a flash pyrolysis source.¹⁴⁷ The allyl radical is excited at 248 and 351 nm to the $\tilde{C}(2^2B_1)$ and $\tilde{A}(1^2B_1)$ excited state,¹⁴⁷ which then relax to the ground electronic state via internal conversion.¹⁴⁵ Two primary photodissociation channels of the \tilde{C} state are observed at 248 nm: H-atom loss (84%) and CH_3 elimination (16%).¹⁴⁷ RRKM calculations (using an experimentally determined 48.6 kcal/mol allyl to 2-propenyl radical isomerization barrier) predict that $\sim 50\%$ of allyl radicals directly dissociate to allene ($CH_2=C=CH_2$) + H, and 50% isomerize to 1- and 2-propenyl radicals before dissociating to either allene or propyne ($CH_3CH\equiv CH$) + H. The production of the $CH_3 + C_2H_2$ might proceed through a four-center transition state of the allyl radical. For the lower excited \tilde{A} state at 351 nm, only the H-atom loss channel is observed. It is believed that the \tilde{A} state decays to the ground electronic state via isomerization to the ground-state cyclopropyl radical followed by ring opening.

Deyerl and co-workers have also studied the photodissociation of the jet-cooled allyl radical produced in a flash pyrolysis source.^{148,149} The allyl radical is excited near 250 nm and H-atom product is detected by

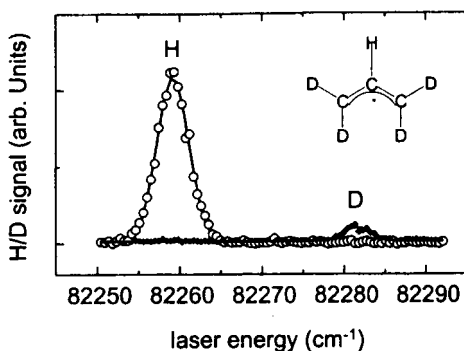
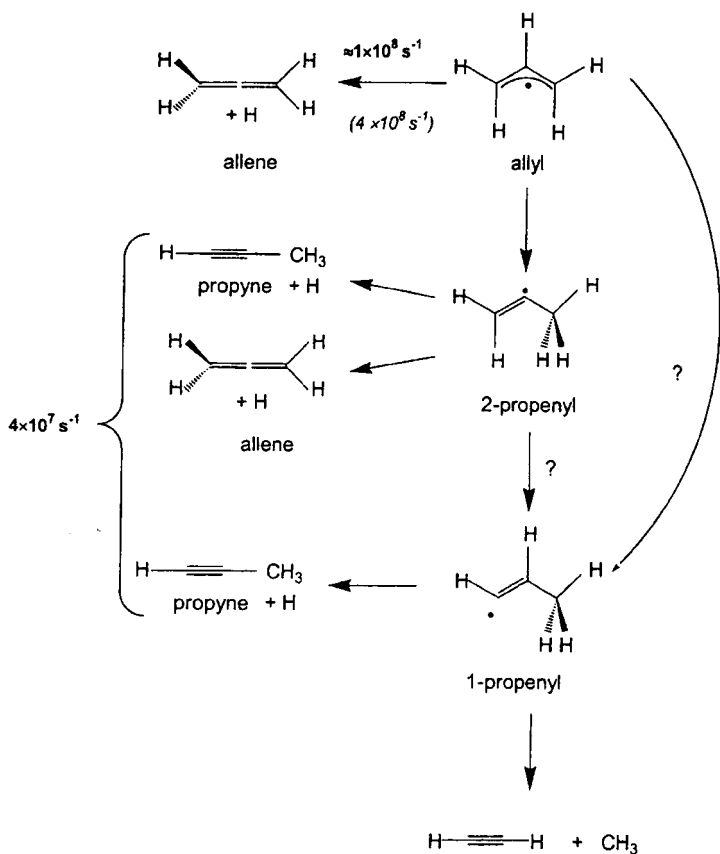


Fig. 22. Photofragment Doppler spectroscopy of C_3HD_4 revealing H-loss, and thus cleavage of the central C–H bond, to be the dominant reaction channel. The allene is the preferentially formed product. (From Deyerl *et al.*^{145,149})

REMPI TOFMS. A preference for the loss of the central hydrogen to form allene is demonstrated in the studies of partially deuterated allyl radicals (Fig. 22).^{145,148,149} The Doppler profile of the H-atom product indicates that $\sim 22\%$ of the excess energy is released into product translation, and when compared with a prior distribution, the product translational energy distribution peaks at higher value, suggesting a ~ 5 kcal/mol reverse barrier for the H-loss channel. A fast H-loss rate of $\sim 10^8$ s $^{-1}$ is observed experimentally, presumably due to the direct allene production channel.^{145,149} Simple RRKM calculations yield a rate of $\sim 4 \times 10^8$ s $^{-1}$, in reasonable agreement with the experimental values. A second H-loss channel is seen, which is believed to be the production of allene or propyne following isomerization to the 2-propenyl or 1-propenyl radical. This channel is associated with isotopic scrambling and thus is responsible for the small deuterium signal in the photofragment Doppler spectrum of D_2CCHCD_2 (Fig. 22).^{145,149} An experimentally measured slow H-loss rate of 4×10^7 s $^{-1}$ is possibly due to this second H-loss channel. RRKM calculations (using an *ab initio* value of 66 kcal/mol for the allyl to 2-propenyl radical isomerization barrier) have predicted that the direct formation of allene is favored by a factor of 2 to 3 over allene or propyne production via isomerization.^{145,149} This is in qualitative agreement with the experimental relative rates of the direct H + allene reaction channel and the product channels from isomerization to 2-propenyl. A summary of the unimolecular dissociation processes of the ground electronic state allyl radical is shown in Fig. 23.^{145,149}



Ref. 54: 16%

Fig. 23. Summary of the unimolecular dissociation processes of the ground electronic state allyl radical at 115 kcal/mol. Two competing pathways, formation of allene and isomerization to 2-propenyl (which subsequently dissociates into allene and propyne), are observed. The experimental (bold) and RRKM (italics) rates are given. The allene formation is the dominating channel. (From Fischer *et al.*¹⁴⁵)

Butler and co-workers have taken a unique approach to study the unimolecular dissociation of the vibrationally and rotationally hot allyl radical.^{150–152} They have examined the secondary C–H dissociation of the allyl radicals that are produced with high internal energies above the allyl dissociation thresholds in the primary photodissociation of allyl chloride and allyl iodide at 193 nm. The production of allene versus propyne (both at mass 40) from the secondary dissociation of the hot allyl radicals are

differentiated by their individual photoionization efficiency curves (with allene having a lower IP of 9.69 eV than 10.36 eV of propyne) by using a tunable VUV photoionization radiation from synchrotron radiation. The allene product is confirmed to be the main product of the allyl dissociation, and this result also indicates that the experimentally determined isomerization barrier of 48.6 kcal/mol from allyl to 2-propenyl is ~ 15 kcal/mol lower than the *ab initio* values. Some allyl radicals with internal energy as high as 15 kcal/mol above the 60 kcal/mol H + allene dissociation barrier are metastable, indicating significant centrifugal effects on the rotationally hot allyl radicals produced in the primary photodissociation of allyl iodide.^{151,152}

Using the same approach, Butler and co-workers have also investigated the allene/propyne product branching ratios in the unimolecular dissociation of the vibrationally and rotationally excited 2-propenyl ($\text{CH}_3\text{C}=\text{CH}_2$) radical (from 193 nm photolysis of 2-chloropropene)^{153,154} and 1-propenyl ($\text{CH}_3\text{CH}=\text{CH}$) radical (from 193 nm photolysis of 1-bromopropene).^{155,156} They have found that in the dissociation of the 2-propenyl radical with internal energies 0–18 kcal/mol above the H + propyne barrier, the H + propyne channel is dominant over the H + allene channel, and in 2-propenyl the barrier to the H + allene production is slightly higher than that to the H + propyne formation.^{153,154}

3.4. Alkoxy Radicals

3.4.1. Methoxy (CH_3O) and the Related Systems,

Thiomethoxy (CH_3S) and *Hydroxymethyl* (CH_2OH)

Methoxy (CH_3O): The spectroscopy and photochemistry of the methoxy ($\text{CH}_3\text{O}/\text{CD}_3\text{O}$) radical via the $\tilde{A}(^2\text{A}_1) \leftarrow \tilde{X}(^2\text{E})$ transition have been extensively studied.^{2,36,65,157,158} Unimolecular dissociation of the ground electronic $\tilde{X}(^2\text{E})$ state methoxy prepared in highly excited rotational and vibrational states via stimulated emission pumping has been studied by Temps and co-workers.^{35,159,160} As shown in Fig. 24,^{65,161} the $\text{CH}_3\text{O } \tilde{A}(^2\text{A}_1)$ excited state is bound and it undergoes predissociation via three repulsive states ($^4\text{A}_2$, $^2\text{A}_2$, and ^4E) to the CH_3 and $\text{O}(^3\text{P}_J)$ products. Fluorescence spectroscopy of the jet-cooled methoxy indicates that the predissociation process starts at an energy of 3793 cm^{-1} (relative to the vibrationless level of the $\tilde{A}(^2\text{A}_1)$ state) and corresponds to the energy of the 3_0^6 band of the $\tilde{A}(^2\text{A}_1)$ state.³⁶ Above the predissociation threshold, vibrational mode selectivity in the photofragmentation process is observed; understandably,

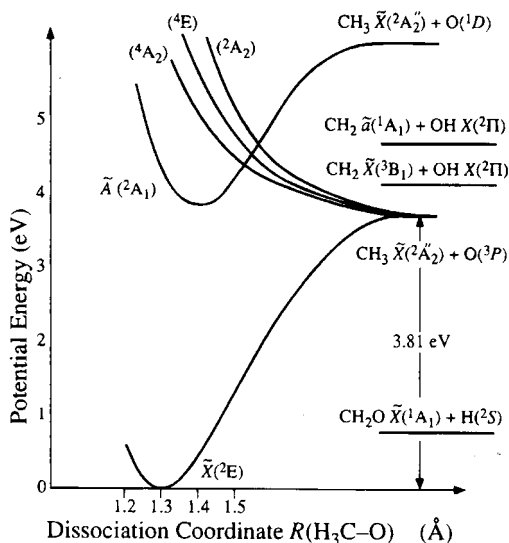


Fig. 24. Schematic C_{3v} potential energy surfaces for the methoxy radical as a function of C–O bond length. (From Osborn *et al.*⁶⁵)

the ν_3 (C–O stretch) mode tends to enhance the predissociation rates.³⁶ Similar study on CD_3O spectroscopy and photodissociation also reveals vibrational mode selectivity, with ν_3 being the major promoting mode for dissociation, and ν_2 , the umbrella mode, being not efficient.¹⁶²

Neumark and co-workers have studied the photodissociation dynamics of the $\text{CH}_3\text{O}/\text{CD}_3\text{O}$ radical using the fast radical beam photofragment translational energy spectroscopy.^{65,158} The photofragment yield spectra of CH_3O and CD_3O start at the 3_0^6 transition, indicating that the predissociation threshold is at 3775 cm^{-1} above $v = 0$ of the $\tilde{A}(^2A_1)$ state. The mode-specific effects are also observed in the photofragment yield spectrum: CH_3O has a main progression in the ν_3 C–O stretch and a combination band with one quantum of the e symmetry ν_6 methyl rock; CD_3O has the dominant ν_3 C–O stretch progression, along with the $3_0^2 2_0^1$ as the most prominent combination band involving the a_1 symmetry ν_2 umbrella motion. The main product channel observed is C–O bond fission. For both CH_3O and CD_3O , most of the available energy is partitioned into the $\text{CH}_3 + \text{O}$ product translation, and the translational energy distributions show that the ν_2 umbrella mode of the $\text{CH}_3(\text{CD}_3)$ fragment is excited. Photodissociation of CH_3O via the $3_0^6 6_0^1$ excitations results in more rotational excitation of

the products, consistent with sampling of non- C_{3v} geometries in the $\tilde{A}(^2A_1)$ state. Photodissociation of CD_3O via the $3^2_02^1_0$ excitations produces bimodal CD_3 product vibrational state distribution, with excitation of $\nu_2 = 0$ and $\nu_2 = 2$ always greater than that for $\nu_2 = 1$. This effect indicates that the energy distribution among parent vibrational modes strongly influences the vibrational distribution in the products.

Thiomethoxy (CH_3S): The potential energy surfaces of the thiomethoxy radical is shown in Fig. 25. Similar to methoxy, the bound $\tilde{A}(^2A_1)$ excited state predissociates via three repulsive states (4A_2 , 2A_2 , and 4E) to the CH_3 and $S(^3P_J)$ products.^{161,163,164} The spectroscopy of the $\tilde{A}(^2A_1)$ state of thiomethoxy and lifetimes of the vibrational levels of this state are examined by Pushkarsky and co-workers using various techniques of fluorescence spectroscopy.¹⁶⁵ Similar to methoxy, the predissociation of $CH_3S(\tilde{A}^2A_1)$ to the $CH_3 + S(^3P)$ products becomes predominant for the vibrational excitations involving $\nu_3 \geq 3$, and is mode selective with the ν_3 (C–S stretch) mode being the promoting vibration for predissociation.¹⁶⁵ A second nonradiative

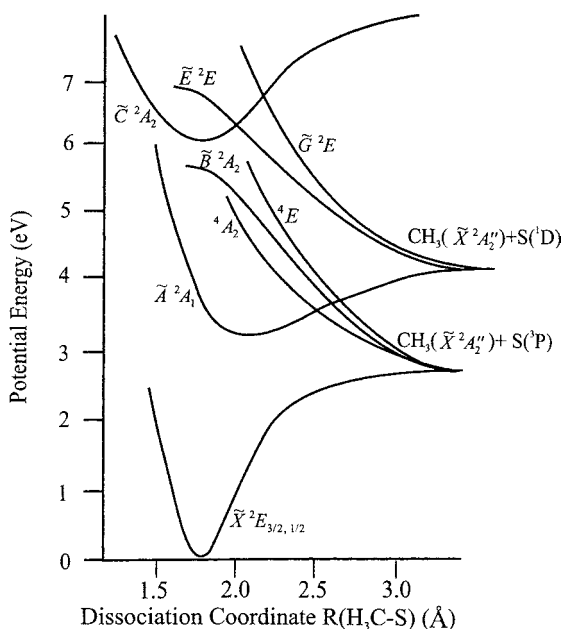


Fig. 25. Schematic C_{3v} potential energy surfaces for the CH_3S radical as a function of C–S bond length. (From Hsu *et al.*,¹⁶³ Cui *et al.*,¹⁶¹ and Bise *et al.*¹⁶⁴)

decay channel is suggested, possibly producing $\text{H} + \text{CH}_2\text{S}$ after internal conversion of $\tilde{A}^2\text{A}_1$ to $\tilde{X}(^2\text{E})$.¹⁶⁵

The photodissociation spectroscopy and dynamics of jet-cooled CH_3S and CD_3S radicals have also been studied by Neumark and co-workers using the fast radical beam photofragment translational spectroscopy.¹⁶⁴ The experiment is carried out via the predissociative $\tilde{A}(^2\text{A}_1) \leftarrow \tilde{X}(^2\text{E})$ band ($T_0 > 26400\text{ cm}^{-1}$) and the unstructured dissociative $\tilde{B}(^2\text{A}_1) \leftarrow \tilde{X}(^2\text{E})$ band near 45600 cm^{-1} . For the $\tilde{A}(^2\text{A}_1) \leftarrow \tilde{X}(^2\text{E})$ band, the $\text{CH}_3 + \text{S}$ product pathway is observed as the only one major channel. The photofragment yield spectra of CH_3S and CD_3S have extended 3_0^0 and $3_0^2 2_0^1$ progressions, with the 3_0^2 transition identified as the predissociation onset of the $\tilde{A}^2\text{A}_1$ state. The product translational energy $P(E_{\text{T}})$ distributions have resolved the CH_3 fragment vibrational and $\text{S}(^3\text{P}_J)$ fine-structure distributions. At photon energies $< 29000\text{ cm}^{-1}$, the vibrational and fine-structure distributions suggest that the predissociation is via the $^4\text{A}_2$ repulsive surface, while at higher energies, the ^4E state contribute more to the predissociation, increasing the vibrational excitation in the CH_3 fragment and changing the $\text{S}(^3\text{P}_J)$ fine-structure distributions. Similar to CH_3O , mode specificity in the photodissociation is observed: the $3_0^3 2_0^1$ and $3_0^4 2_0^1$ transitions lead to a larger excitation in the CH_3 fragment umbrella mode than the nearly isoenergetic 3_0^{n+3} transitions, suggesting that the umbrella mode couples to the dissociation coordinate less than the C–S stretch. The photofragment angular distributions are anisotropic: $\beta = -0.2$ to -1.0 , which is in agreement with perpendicular transition $\tilde{A}(^2\text{A}_1) \leftarrow \tilde{X}(^2\text{E})$. The photoproduct angular distributions become more anisotropic with the increased excitation in the ν_3 mode, corresponding to rapidly decreased excited state lifetime.

Photodissociation of CH_3S near 45600 cm^{-1} via the repulsive $\tilde{B}^2\text{A}_1$ state also predominantly produces $\text{CH}_3 + \text{S}(^3\text{P}_{2,1,0})$, with most of the available energy channelled into the product translation.¹⁶⁴ The anisotropy parameter $\beta = -0.98$ is consistent with the perpendicular electronic transition from the $\tilde{X}(^2\text{E})$ to the $\tilde{B}^2\text{A}_1$ state.¹⁶⁴ At higher energy of 193 nm (51800 cm^{-1}), photodissociation of CH_3S is shown to produce mainly $\text{CH}_3 + \text{S}(^1\text{D}_2)$, with $\text{S}(^1\text{D}_2) : \text{S}(^3\text{P}_J) = 85 : 15$.¹⁶³ At 193 nm , CH_3S is possibly excited to the bound $\tilde{C}^2\text{A}_2$ state, which then predissociates via a repulsive ^2E state to the $\text{CH}_3 + \text{S}(^1\text{D}_2)$ products (Fig. 25).¹⁶³

Hydroxymethyl (CH_2OH): The hydroxymethyl (CH_2OH) is a more reactive isomer of methoxy radical. The spectroscopy and photochemistry of jet-cooled CH_2OH via its $3s$, $3p_x$, and $3p_z$ Rydberg states (in

ascending order of energy) have been studied recently by Reisler and co-workers.^{166–169} The CH_2OH radicals are produced in a molecular beam via the photoinitiated reaction between Cl atoms with methanol. The highest-lying $3p_z$ Rydberg state has sharp absorption structured at 41000 cm^{-1} (shown in the REMPI spectrum) and a predissociation lifetime of $0.5 \pm 0.1\text{ ps}$.¹⁶⁶ The photo-predissociation of the jet-cooled CH_2OD and CD_2OH radical via the $3p_z$ Rydberg state produces formaldehyde and hydrogen atom: D atoms (detected by REMPI) appear as the major products from CH_2OD with no detectable amount of H photofragment, while only H atoms are produced in the dissociation of CD_2OH .¹⁶⁷ This also implies that the isomerization of hydroxymethyl to methoxy is unimportant. The product translational energy distribution is broad, indicating that the formaldehyde cofragment is produced in the ground electronic state but with a large internal energy excitation. The D-atom product from CH_2OD has an anisotropic angular distribution with an average $\beta = -0.6 \pm 0.3$, indicating that the dissociation is fast. Based on these results, Reisler and co-workers have suggested that the $3p_z$ Rydberg state predissociation involves nonadiabatic transitions from the initially excited Rydberg state to the ground state, with the final crossing occurring in a region of the potential energy surface that leads to direct O–D(H) fission without isomerization.¹⁶⁷

The spectroscopy and photodissociation of hydroxymethyl via the lower $3s$ and $3p_x$ Rydberg states are investigated by the depletion, REMPI, and photofragment yield spectroscopy methods.¹⁶⁸ The locations of the $3s$ and $3p_x$ Rydberg states identified in the experiments are in good agreement with the recent *ab initio* calculations.¹⁶⁸ The vibronic bands of the $2^2\text{A}'(3p_x) \leftarrow 1^2\text{A}''$ transition are much broader than those of $2^2\text{A}''(3p_z) \leftarrow 1^2\text{A}''$, and the $1^2\text{A}'(3s) \leftarrow 1^2\text{A}''$ transition is structureless. Photodissociation study of CH_2OD via the $3s$ state in the wavelength region $365\text{--}318\text{ nm}$ proceeds predominantly with the O–D bond fission pathway, while that via the $3p_x$ state produces both H and D products.^{168,169} In the photodissociation of CH_2OD via the $3s$ state, the translational energy distribution of the D-atom production channel is measured at 352.5 nm ; 69% of the available energy is partitioned into the product translation, implying that the ground state products $\text{CH}_2\text{O}(1^1\text{A}_1) + \text{D}$ are the main photodissociation channel.¹⁶⁹ The anisotropy parameter of the D channel is kinetic energy-dependent; the negative anisotropy parameter, $\beta = -0.7 \pm 0.1$, is consistent with the perpendicular $1^2\text{A}'(3s) \leftarrow 1^2\text{A}''$ transition. These experimental results, combined with the conical intersection calculations by Yarkony and co-worker,¹⁷⁰

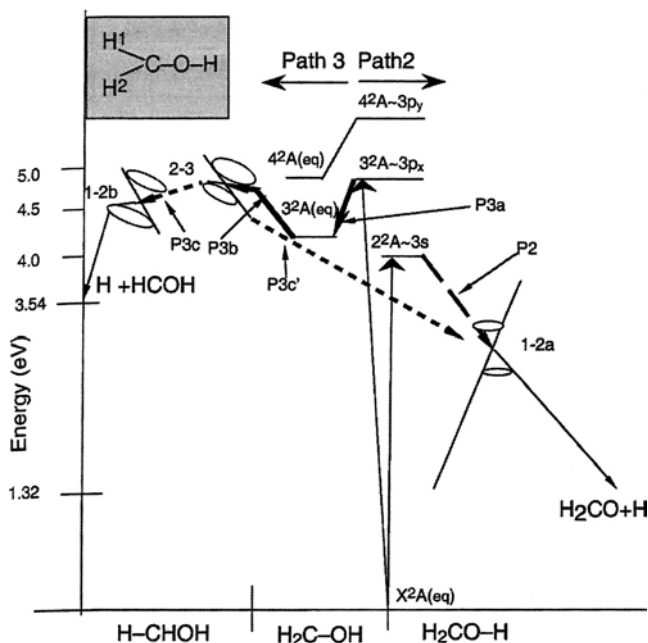


Fig. 26. Schematic representation of the decay mechanisms of the hydroxymethyl radical. The 3s Rydberg state and the ground state have a conical intersection leading to the ground state $\text{H}_2\text{CO} + \text{H}$ products. (From Hoffman *et al.*¹⁷⁰)

suggest that the O–D bond rupture involves crossing from the 3s potential energy surface to a repulsive region of the ground state surface at a large O–D bond distance (Fig. 26).¹⁶⁹ Note that this decay pathway of the CH_2OH 3s Rydberg state through a conical intersection is similar to that in its isoelectronic analog ethyl radical.³⁹ The progressive broadening of the absorption features from the uppermost $3p_z$ to the lowest 3s excited state is due to the increased surface couplings to lower electronic states, as shown in the recent calculations (Fig. 26)¹⁷⁰; and these couplings control the photodissociation dynamics and the reaction outcomes.^{168,169}

3.4.2. Ethoxy ($\text{CH}_3\text{CH}_2\text{O}$)

Photodissociation of ethoxy ($\text{C}_2\text{H}_5\text{O}$) radical in the photolysis wavelength of 270–220 nm has been investigated using fast radical beam photofragment translational spectroscopy by Neumark and co-workers.⁶⁶ The photofragment yield (PFY) spectrum in the range of 270–220 nm is structureless but exhibits abrupt increases in intensity at 260 and 225 nm, suggesting

possibly two different electronic transitions. No significant dissociation signal is observed in the region of 342–311 nm where the fluorescence from the $\tilde{B}^2A' \leftarrow \tilde{X}^2A''$ transition of C_2H_5O was observed, indicating that at least the lower vibrational levels of the \tilde{B}^2A' state of C_2H_5O is not dissociative.

The product mass distribution shows that throughout the entire absorption band, C_2H_5O dissociates primarily into the vinyl radical (C_2H_3) + H_2O , instead of $CH_2O + CH_3$, $C_2H_4 + OH$, or $C_2H_5 + O$. The technique is not sensitive to the $CH_3CHO + H$ and $CH_3CO + H_2$ channels. The translational energy distributions for the $C_2H_3 + H_2O$ channel are largely insensitive to the photon energy. In the region of $\lambda > 225$ nm, the $P(E_T)$ distributions for $C_2H_3 + H_2O$ from C_2H_5O dissociation have a single feature, peaking around 0.7 eV and extending up to 4 eV. At photon energies beyond the onset of the second electronic band (225 nm or 5.51 eV), a new feature appears at $E_T \leq 0.3$ eV that is attributed to the production of an excited state C_2H_3 .⁶⁶ Neumark and co-workers proposed a dissociation mechanism in which the excited ethoxy radicals isomerize through electronically-excited states of either the 1- or 2-hydroxyethyl radicals (rather than by internal conversion to the ground state) and then undergo dissociation to $C_2H_3 + H_2O$.

Photodissociation of ethoxy radical at 193 nm has been observed via the secondary photolysis of jet-cooled ethanol by Xu and co-workers.¹⁷¹ H-atom production channel from 193 nm photodissociation of ethoxy is shown to be a significant pathway, producing fast H atoms (with translational energy up to ~ 140 kcal/mol) and slow H atoms (peaking at ~ 8 kcal/mol) (Fig. 27). The major portion of the H atom from the secondary photodissociation of ethoxy is slow, corresponding to highly internally-excited CH_3CHO . The CH_3CHO can be in a highly vibrationally-excited ground state and/or electronically-excited state, and further decomposition of the highly-excited CH_3CHO is possible. The ethoxy radical can be excited to the \tilde{B}^2A' state or a higher electronic excited state by the 193.3-nm photon. The structureless and statistical-like translational energy distribution $P(E_T)$ is consistent with a unimolecular decomposition mechanism following radiationless processes from the higher excited state to the ground state or low-lying electronic states. The peak in the $P(E_T)$ of the secondary photodissociation would indicate an exit-channel dissociation barrier height of ~ 8 kcal/mol, close to the calculated value of 5.9 kcal/mol (the barrier height for the ground state $CH_3CHO + H$ recombination).¹⁷² Interestingly, the shape of the $P(E_T)$ of the H-production channel of ethoxy at 193 nm is similar to those of the $C_2H_3 + H_2O$ product channel of ethoxy in the region of 220–270 nm.⁶⁶

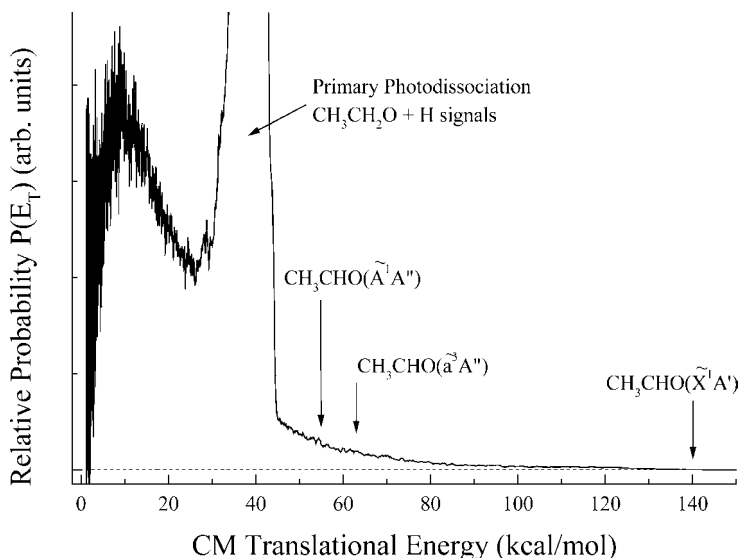


Fig. 27. Product translational energy distribution of the H-atom production channel in the secondary photodissociation of ethoxy radical at 193.3 nm. The onsets of the relevant electronic states of the possible CH_3CHO product are indicated in the figure. The signals from the primary photodissociation of ethanol are labelled. (From Xu *et al.*¹⁷¹)

3.4.3. Vinyoxy (CH_2CHO)

Vinyoxy (CH_2CHO) is important in both combustion and atmospheric chemistry, and it is also a prototypical unsaturated alkoxy radical. The spectroscopy and electronic structures of the \tilde{A}^2A' and \tilde{B}^2A'' states of CH_2CHO have been extensively studied.^{67,173–183} The \tilde{B}^2A'' LIF spectroscopy studies show that the \tilde{B} state fluorescence is abruptly quenched above 30200 cm^{-1} (only 1400 cm^{-1} above the \tilde{B}^2A'' state origin),^{174,175,177} as compared with the absorption spectrum that extends to higher energy 35700 cm^{-1} and peaks at $\sim 32500\text{ cm}^{-1}$.¹⁷³ The sharply depleted LIF spectrum implies that the \tilde{B}^2A'' state decays via fast nonradiative processes. This is confirmed by fluorescence depletion spectroscopy of jet-cooled vinyoxy from 30300 to 33900 cm^{-1} , which identifies sharp vibronic absorptions in this region where fluorescence is quenched.¹⁷⁶ The predissociation mechanism of the \tilde{B}^2A'' state vinyoxy radical was examined theoretically by Matsika and Yarkony.¹⁸⁴ It is shown that upon excitation the \tilde{B}^2A'' state decays via a sequence of internal conversions to the ground \tilde{X}^2A'' state. The $\tilde{B}^2A''\text{--}\tilde{A}^2A'$ radiationless transition is via an avoided crossing which is accessible after a barrier

of $\sim 2000\text{ cm}^{-1}$, while the $\tilde{B}^2A''-\tilde{A}^2A'$ conical intersections are too high in energy to participate in the predissociation of \tilde{B}^2A'' . The \tilde{A}^2A' then undergoes efficient radiationless transition to the \tilde{X}^2A'' ground state via easily accessible conical intersections.¹⁸⁴

The spectroscopy and photodissociation dynamics of the vinoxy radical $\tilde{B}^2A'' \leftarrow \tilde{X}^2A''$ transition have been investigated by Neumark and co-workers using fast radical beam photofragment translational spectroscopy.⁶⁷ The potential energy surfaces of the vinoxy radical and the dissociation channels and energetics are shown in Fig. 28. The \tilde{B}^2A'' state decays by predissociation starting from the origin transition of the $\tilde{B}^2A'' \leftarrow \tilde{X}^2A''$ band. The photofragment yield spectrum reveals several vibrational progressions of the \tilde{B}^2A'' state. The dissociation rate greatly increases above 1400 cm^{-1} , indicating the onset of fast predissociation processes and consistent with the results from spectroscopic and theoretical

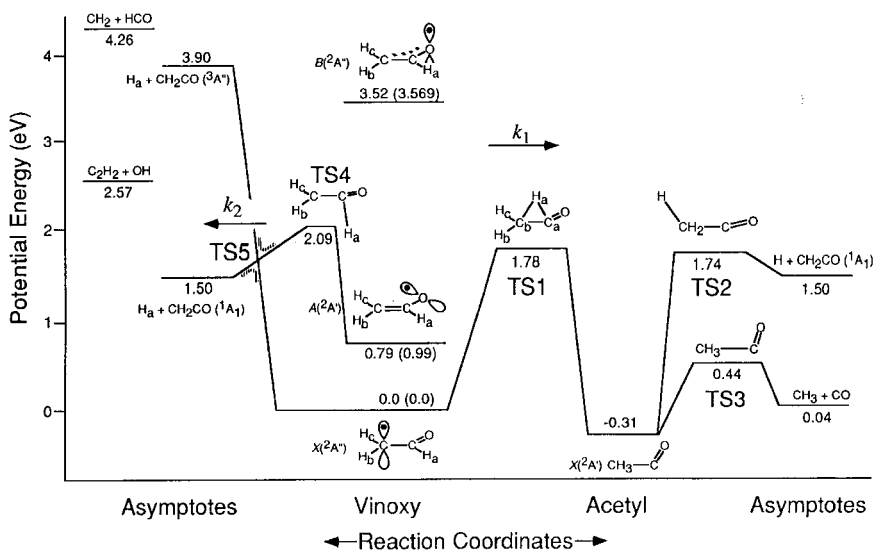


Fig. 28. Schematic of potential energy surfaces of the vinoxy radical system. All energies are in eV, include zero-point energy, and are relative to CH_2CHO (\tilde{X}^2A''). Calculated energies are compared with experimentally-determined values in parentheses. Transition states 1–5 are labelled, along with the rate constant definitions from RRKM calculations. The solid potential curves to the left of vinoxy retain C_s symmetry. The avoided crossing (dotted lines) which forms TS5 arises when C_s symmetry is broken by out-of-plane motion. (From Osborn *et al.*⁶⁷)

studies. The photofragment energy and angular distributions indicate that the dissociation occurs by internal conversions to the ground state potential energy surface, and the dissociation of the ground \tilde{X}^2A'' state leads to two product channels, $CH_3 + CO$ and $H + CH_2CO$, with a branching ratio of about 1:4.⁶⁷

The translational energy and angular distributions of the $CH_3 + CO$ channel are largely independent of the excited vibronic modes in the \tilde{B}^2A'' state (Fig. 29), which is consistent with a dissociation mechanism that ultimately involves the ground electronic state of vinoxy radical.⁶⁷ After the internal conversion to the ground state, the vinoxy radical could undergo 1, 2 H-shift isomerization to CH_3CO radical which subsequently dissociates into the $CH_3 + CO$ products. The shape of the translational energy distributions of the $CH_3 + CO$ channel indicate a significant exit channel barrier, and is shown to be determined by the CH_2CHO to CH_3CO isomerization barrier on the ground state potential energy surface (Fig. 28). Some limited information on the $H + CH_2CO$ product channel is obtained in the photodissociation of CD_2CDO . The product translational energy release indicates a small exit channel barrier. This barrier is thought to be formed by an avoided crossing between the $CH_2CHO(\tilde{X}^2A'')$ state (correlating in planar geometries with $H + CH_2CO(\tilde{a}^3A'')$) and the $CH_2CHO(\tilde{A}^2A')$ state (correlating with $H + CH_2CO(\tilde{X}^1A_1)$) (Fig. 28).⁶⁷

The H-atom production channel for the \tilde{B} -state photodissociation of jet-cooled vinoxy has also been examined in the photon energy region of 308–325 nm by Xu and co-workers using the Rydberg H-atom time-of-flight technique.¹⁸⁵ The vinoxy radical beam is produced by 193.3-nm photolysis of ethyl vinyl ether followed by supersonic expansion. The H-atom product signals observed in the experiment are from the vinoxy photodissociation, as confirmed by the H-atom product yield spectrum¹⁸⁵ that closely follows the absorption spectrum of vinoxy¹⁸⁵ and the product yield spectrum of the $CH_3 + CO$ product channel.⁶⁷ These three spectra are plotted in Fig. 30. The $H + CH_2CO$ product translational energy distributions for the \tilde{B}^2A'' state in the photon energy region of 308–325 nm are essentially the same; they are structureless, statistical-like distributions, peaking at $E_T \sim 10$ kcal/mol and with an average translational energy release $\langle E_T \rangle \sim 0.26E_{\text{avail}}$ (Fig. 31). Product angular distributions are isotropic at all the photolysis wavelengths. The observed dynamic information for the $H + CH_2CO$ channel is consistent with the unimolecular dissociation pathway of the $H + CH_2CO$ products, which likely occurs after internal conversion from the \tilde{B} state to the ground state of vinoxy.

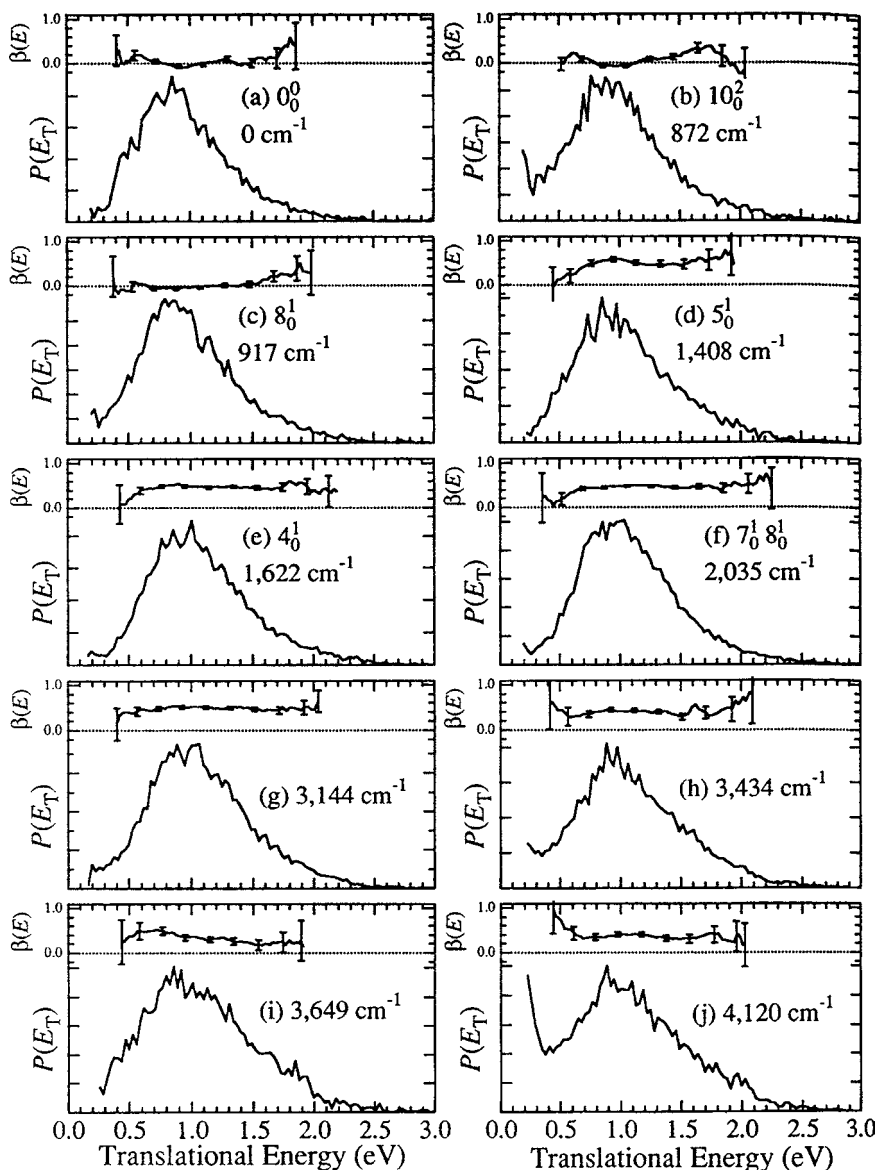


Fig. 29. Photofragment translational energy distributions $P(E_T)$ and angular distributions $\beta(E_T)$ for the $\text{CH}_3 + \text{CO}$ product channel of $\text{CH}_2\text{CHO}(\tilde{B}^2A'')$. Vibronic assignments are given in addition to the excess energy for each transition.

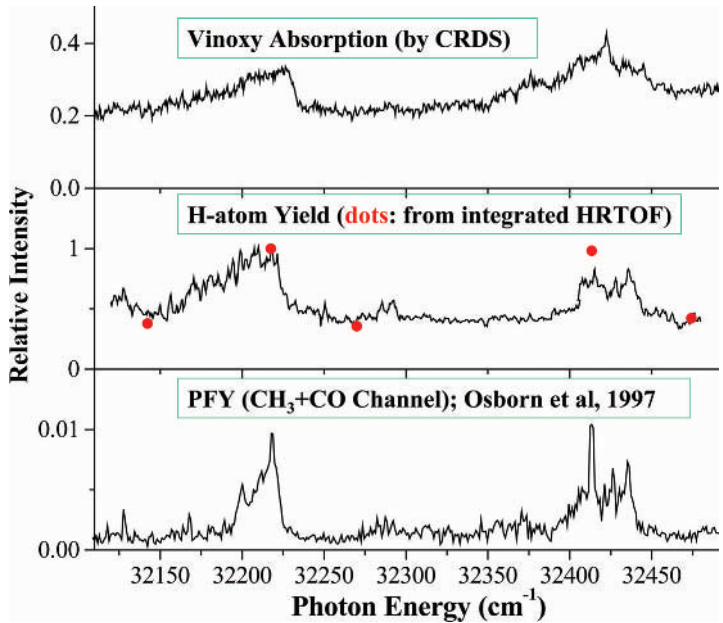


Fig. 30. Absorption spectrum of vinyoxy, H-atom product yield spectrum, and CH₃+CO product yield spectrum. (From Xu *et al.*¹⁸⁵ and Osborn *et al.*⁶⁷)

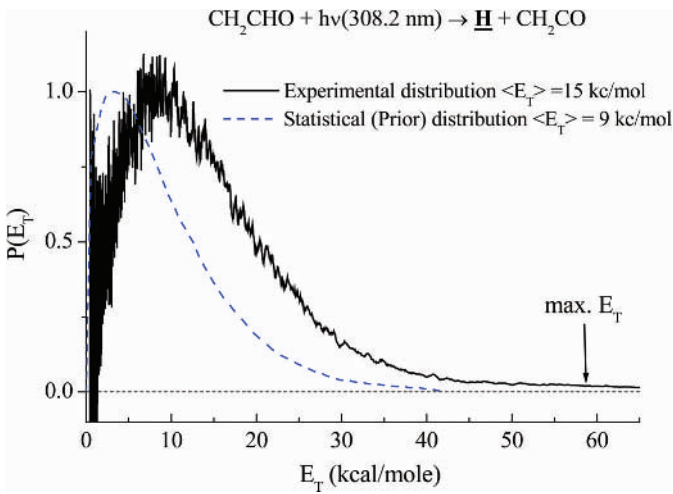


Fig. 31. Photofragment translational energy distribution $P(E_T)$ for the H + CH₂CO product channel of the CH₂CHO photodissociation at 308.2 nm. (From Xu *et al.*¹⁸⁵)

3.4.4. Cyclic Alkoxy

Continetti and co-workers have studied the photodissociation of cyclopropoxy ($c\text{-C}_3\text{H}_5\text{O}$) radical and cyclobutoxy ($c\text{-C}_4\text{H}_7\text{O}$) radical via photodetachment and dissociative photodetachment processes of cyclopropoxide ($c\text{-C}_3\text{H}_5\text{O}^-$) and cyclobutoxide ($c\text{-C}_4\text{H}_7\text{O}^-$), respectively, at 532 nm.¹⁸⁶ The $c\text{-C}_3\text{H}_5\text{O}$ radical is produced in both the ground $X(^2A'')$ state and the first excited $A(^2A')$ state in the photodetachment of $c\text{-C}_3\text{H}_5\text{O}^-$. The $X(^2A'')$ state is stable at lower levels of excitation, but with increasing internal energy, it dissociates into the $\text{HCO} + \text{C}_2\text{H}_4$ products. The $A(^2A')$ state completely dissociates into the $\text{HCO} + \text{C}_2\text{H}_4$. The correlated measurements of photoelectron and photofragment kinetic energies can provide dissociation energies: the $c\text{-C}_3\text{H}_5\text{O}$ radical is thermodynamically unstable with respect to $\text{HCO} + \text{C}_2\text{H}_4$ by -0.26 ± 0.07 eV. Cyclobutoxide undergoes only dissociative photodetachment to ground-state vinyloxy radical and ethylene. The $c\text{-C}_4\text{H}_7\text{O}$ radical is found to be thermodynamically unstable relative to dissociation into the $\text{C}_2\text{H}_3\text{O} + \text{C}_2\text{H}_4$ products by -0.45 ± 0.07 eV.

Continetti and co-workers have also investigated the photodetachment of cyclopentoxide ($c\text{-C}_5\text{H}_9\text{O}^-$). At both 532 and 355 nm, cyclopentoxide undergoes (1) photodetachment to stable cyclopentoxy or the ring-opened 5-oxo-pentan-1-yl radical and (2) dissociative photodetachment, producing the $\text{C}_3\text{H}_5\text{O} + \text{C}_2\text{H}_4$ photofragments.¹⁸⁷ The $c\text{-C}_5\text{H}_9\text{O}$ radical is unstable relative to $\text{C}_3\text{H}_5\text{O}$ and C_2H_4 by -0.12 ± 0.12 eV.

3.5. Others

Neumark and co-workers have utilized the fast radical beam photofragment translational spectroscopy to study the spectroscopy and photodissociation dynamics of a series of free radicals (in addition to those discussed above). These include CH_2NO ,¹⁸⁸ HCCO ,⁶² HNCN ,¹⁸⁹ N_3 ,⁶⁰ NCO ,^{59,190} CCO ,¹⁹¹ NCN ,¹⁹² CNN ,¹⁹³ and I_3 .¹⁹⁴ Houston and co-workers have examined photodissociation of the NCO radical at 193 nm.¹⁹⁵ Continetti and co-workers have investigated the dissociation of the formyloxyl (HCO_2 and DCO_2) radical via the dissociative photodetachment of HCO_2^- and DCO_2^- ,⁶⁴ and the dissociation of HOCO via the dissociative photodetachment of HOCO^- .⁶³ Davis and co-workers have studied the photodissociation of the H_2CN radical in the region of 274–288 nm using high- n Rydberg H-atom photofragment translational energy spectroscopy.¹⁹⁶

4. Conclusions

The studies of photodissociation dynamics of free radicals have provided a great amount of information about the photochemistry of free radicals. In these studies, the competing photoproduct branching pathways are characterized; the state and energy distributions of the photoproducts are measured, identifying the energy partitioning into various degrees-of-freedom (translational and internal (electronic, vibrational, and rotational)); and spatial distributions and vector properties of the products are monitored. The dynamic information of the free radical photodissociation thus obtained helps reveal the details of the dissociation mechanisms of the radicals energized by light, the natures of the electronic states and transitions states involved, the thermodynamics and reaction energetics of the radicals, and the complex nonadiabatic interactions of the multiple potential energy surfaces. As compared with the stable molecules, the low-lying electronic states of free radicals (e.g. the low-lying Rydberg states and the Rydberg/valence interactions in some radicals) complicate their photodissociation dynamics. Theoretical studies can be of great help in many cases.

It is clear that one of the major challenges in the experimental studies of free radicals is the preparation of radicals. The experimental designs (production of radicals and detection of radicals and photoproducts) are largely dependent on the particular radicals of interest. Nevertheless, many approaches have been taken, as seen in this review, to study the free radical photodissociation, and a great number of systems have been examined during the last couple of years. The sophistication in the experimental studies of free radical photochemistry has reached the level that has been available for the stable molecules. State-to-state photodissociation dynamics of free radicals have been demonstrated for a few small systems. Many more advances in the field of photodissociation dynamics of radicals are expected, and it is hoped that a more systematic and sophisticated understanding of free radical photochemistry can be developed.

Acknowledgments

The author's research work on photochemistry of free radicals has been supported by US National Science Foundation, ACS Petroleum Research Fund, Camille and Henry Dreyfus Foundation, A. P. Sloan Foundation, and UC Regents' Faculty Fellowships and Faculty Development Award.

References

1. J. C. Whitehead, *Rep. Prog. Phys.* **59**, 993 (1996).
2. S. C. Foster and T. A. Miller, *J. Phys. Chem.* **93**, 5986 (1989).
3. P. C. Engelking, *Chem. Rev.* **91**, 399 (1991).
4. X. Q. Tan, T. G. Wright and T. A. Miller, in *Jet Spectroscopy and Molecular Dynamics*, eds. J. M. Hollas and D. Phillips (Blackie Academic and Professional, London, 1995), p. 75.
5. P. Chen, in *Unimolecular and Bimolecular Reaction Dynamics*, eds. C. Y. Ng, T. Baer and I. Powis (Wiley & Sons, 1994), p. 371.
6. G. N. Robinson, G. M. Nathanson, R. E. Continetti and Y. T. Lee, *J. Chem. Phys.* **89**, 6744 (1988).
7. X. D. Peng, R. Viswanathan, G. H. Smudde and P. C. Stair, *Rev. Sci. Instrum.* **63**, 3930 (1992).
8. D. H. Fairbrother, K. A. Briggman, K. A. Dickens, P. C. Stair and E. Weitz, *Rev. Sci. Instrum.* **68**, 2031 (1997).
9. J. R. Dunlop, J. Karolczak and D. J. Clouthier, *Chem. Phys. Lett.* **151**, 362 (1988).
10. D. W. Kohn, H. Clauberg and P. Chen, *Rev. Sci. Instrum.* **63**, 4003 (1992).
11. H. W. Rohrs, C. T. Wickhamjones, G. B. Ellison, D. Berry and B. M. Argrow, *Rev. Sci. Instrum.* **66**, 2430 (1995).
12. J. L. Yao and E. R. Bernstein, *J. Chem. Phys.* **107**, 3352 (1997).
13. M. R. Cameron and S. H. Kable, *Rev. Sci. Instrum.* **67**, 283 (1996).
14. Z. A. Liu, R. J. Livingstone and P. B. Davies, *Chem. Phys. Lett.* **291**, 480 (1998).
15. P. Chen, S. D. Colson, W. A. Chupka and J. A. Berson, *J. Phys. Chem.* **90**, 2319 (1986).
16. J. A. Blush, J. Park and P. Chen, *J. Am. Chem. Soc.* **111**, 8951 (1989).
17. J. A. Blush and P. Chen, *J. Phys. Chem.* **96**, 4138 (1992).
18. H. Clauberg and P. Chen, *J. Am. Chem. Soc.* **113**, 1445 (1991).
19. H. Clauberg, D. W. Minsek and P. Chen, *J. Am. Chem. Soc.* **114**, 99 (1992).
20. D. W. Minsek and P. Chen, *J. Phys. Chem.* **94**, 8399 (1990).
21. X. Zhang, A. V. Friderichsen, S. Nandi, G. B. Ellison, D. E. David, J. T. McKinnon, T. G. Lindeman, D. C. Dayton and M. R. Nimlos, *Rev. Sci. Instrum.* **74**, 3077 (2003).
22. X. Zhang and P. Chen, *J. Am. Chem. Soc.* **114**, 3147 (1992).
23. H. S. Johnston, H. F. Davis and Y. T. Lee, *J. Phys. Chem.* **100**, 4713 (1996).
24. K. Mikhaylichenko, C. Riehn, L. Valachovic, A. Sanov and C. Wittig, *J. Chem. Phys.* **105**, 6807 (1996).
25. D. L. Monts, T. G. Dietz, M. A. Duncan and R. E. Smalley, *Chem. Phys.* **45**, 133 (1980).
26. M. Heaven, T. A. Miller and V. E. Bondybey, *Chem. Phys. Lett.* **84**, 1 (1981).
27. T. A. Miller, *Science* **223**, 4636 (1984).
28. D. E. Powers, J. B. Hopkins and R. E. Smalley, *J. Phys. Chem.* **85**, 2711 (1981).

29. P. Andresen, D. Häusler and H. W. Lülf, *J. Chem. Phys.* **81**, 571 (1984).
30. P. Andresen, N. Aristov, V. Beushausen, D. Häusler and H. W. Lülf, *J. Chem. Phys.* **95**, 5763 (1991).
31. A. D. Sappay and J. C. Weisshaar, *J. Phys. Chem.* **91**, 3731 (1987).
32. E. J. Hintsa, X. Zhao, W. M. Jackson, W. B. Miller, A. M. Wodtke and Y. T. Lee, *J. Phys. Chem.* **95**, 2799 (1991).
33. H. F. Davis and Y. T. Lee, *J. Phys. Chem.* **100**, 30 (1996).
34. D. W. Neyer, S. H. Kable, J. C. Loison, P. L. Houston, I. Burak and E. M. Goldfield, *J. Chem. Phys.* **97**, 9036 (1992).
35. A. Geers, J. Kappert, F. Temps and J. W. Wiebrecht, *J. Chem. Phys.* **99**, 2271 (1993).
36. D. E. Powers, M. B. Pushkarsky and T. A. Miller, *J. Chem. Phys.* **106**, 6878 (1997).
37. M. Ahmed, D. S. Peterka and A. G. Suits, *J. Chem. Phys.* **110**, 4248 (1999).
38. K. S. Xu and J. S. Zhang, *J. Chem. Phys.* **111**, 3783 (1999).
39. G. Amaral, K. S. Xu and J. S. Zhang, *J. Chem. Phys.* **114**, 5164 (2001).
40. M. Heaven, L. DiMauro and T. A. Miller, *Chem. Phys. Lett.* **95**, 347 (1983).
41. A. T. Droege and P. C. Engelking, *Chem. Phys. Lett.* **96**, 316 (1983).
42. P. C. Engelking, *Rev. Sci. Instrum.* **57**, 2274 (1983).
43. K. R. Comer and S. C. Foster, *Chem. Phys. Lett.* **202**, 216 (1993).
44. S. Sharpe and P. Johnson, *Chem. Phys. Lett.* **107**, 35 (1984).
45. K. N. Rosser, Q. Y. Wang and C. M. Western, *J. Chem. Soc., Faraday Trans.* **89**, 391 (1993).
46. K. Schreel, J. Schleipen, A. Eppink and J. J. ter Meulen, *J. Chem. Phys.* **99**, 8713 (1993).
47. R. Schlachta, G. M. Lask, S. H. Tsay and V. E. Bondybey, *Chem. Phys. Lett.* **155**, 267 (1991).
48. A. Thoma, B. E. Wurfel, R. Schlachta, G. M. Lask and V. E. Bondybey, *J. Phys. Chem.* **96**, 7231 (1992).
49. M. C. van Beek and J. J. ter Meulen, *Chem. Phys. Lett.* **337**, 237 (2001).
50. S. K. Bramble and P. A. Hamilton, *Meas. Sci. Technol.* **2**, 916 (1991).
51. D. T. Anderson, S. Davis, T. S. Zwier and D. J. Nesbitt, *Chem. Phys. Lett.* **258**, 207 (1996).
52. S. Davis, D. T. Anderson, G. Duxbury and D. J. Nesbitt, *J. Chem. Phys.* **107**, 5661 (1997).
53. W. W. Harper, S. A. Nizkorodov and D. J. Nesbitt, *J. Chem. Phys.* **116**, 5622 (2002).
54. W. W. Harper, D. A. Hostutler and D. J. Clouthier, *J. Chem. Phys.* **106**, 4367 (1997).
55. T. Motylewski and H. Linnartz, *Rev. Sci. Instrum.* **70**, 1305 (1999).
56. J. Xin, H. Y. Fan, I. Ionescu, C. Annesley and S. A. Reid, *J. Mol. Spectrosc.* **219**, 37 (2003).
57. K. Ikejiri, H. Ohoyama, Y. Nagamachi, T. Teramoto and T. Kasai, *Chem. Phys. Lett.* **379**, 255 (2003).
58. P. Zou, H. Kim and S. W. North, *J. Chem. Phys.* **116**, 4176 (2002).

59. D. R. Cyr, R. E. Continetti, R. B. Metz, D. L. Osborn and D. M. Neumark, *J. Chem. Phys.* **97**, 4937 (1992).
60. R. E. Continetti, D. R. Cyr, D. L. Osborn, D. J. Leahy and D. M. Neumark, *J. Chem. Phys.* **99**, 2616 (1993).
61. R. E. Continetti, in *Photoionization and Photodetachment*, Part 2, Advanced Series in Physical Chemistry, Vol. 10B, ed. C. Y. Ng (World Scientific Publishing, Singapore, 2000), p. 748.
62. D. L. Osborn, D. H. Mordaunt, H. Choi, R. T. Bise, D. M. Neumark and C. M. Rohlfing, *J. Chem. Phys.* **106**, 10087 (1997).
63. T. G. Clements, R. E. Continetti and J. S. Francisco, *J. Chem. Phys.* **117**, 6478 (2002).
64. T. G. Clements and R. E. Continetti, *J. Chem. Phys.* **115**, 5345 (2001).
65. D. L. Osborn, D. J. Leahy and D. M. Neumark, *J. Phys. Chem.* **A101**, 6583 (1997).
66. H. Choi, R. T. Bise and D. M. Neumark, *J. Phys. Chem.* **A104**, 10112 (2000).
67. D. L. Osborn, H. Choi, D. H. Mordaunt, R. T. Bise, D. M. Neumark and C. M. Rohlfing, *J. Chem. Phys.* **106**, 3049 (1997).
68. W. Hack, *Int. Rev. Phys. Chem.* **4**, 165 (1985).
69. M. N. R. Ashfold and J. D. Howe, *Annu. Rev. Phys. Chem.* **45**, 57 (1994).
70. J. J. Scherer, J. B. Paul, A. Okeefe and R. J. Saykally, *Chem. Rev.* **97**, 25 (1997).
71. M. D. Wheeler, S. M. Newman, A. J. Orrewing and M. N. R. Ashfold, *J. Chem. Soc., Faraday Trans.* **94**, 337 (1998).
72. M. Sablier and T. Fujii, *Chem. Rev.* **102**, 2855 (2002).
73. S. D. Chambreau, J. S. Zhang, J. C. Traeger and T. H. Morton, *Int. J. Mass Spectrom.* **199**, 17 (2000).
74. S. D. Chambreau and J. Zhang, *Chem. Phys. Lett.* **343**, 482 (2001).
75. M. N. R. Ashfold, I. R. Lambert, D. H. Mordaunt, G. P. Morley and C. M. Western, *J. Phys. Chem.* **96**, 2938 (1992).
76. H. Sato, *Chem. Rev.* **101**, 2687 (2001).
77. A. M. Wodtke and Y. T. Lee, *J. Phys. Chem.* **89**, 4744 (1985).
78. D. W. Chandler and P. L. Houston, *J. Chem. Phys.* **87**, 1445 (1987).
79. P. L. Houston, *J. Phys. Chem.* **100**, 12757 (1996).
80. *Imaging in Chemical Dynamics*, eds. A. G. Suits and R. E. Continetti (American Chemical Society, 2000).
81. *Imaging in Molecular Dynamics: Technology and Applications*, ed. B. Whitaker (Cambridge University Press, 2003).
82. L. Schnieder, W. Meier, K. H. Welge, M. N. R. Ashfold and C. M. Western, *J. Chem. Phys.* **92**, 7027 (1990).
83. W. D. Zhou, Y. Yuan and J. S. Zhang, *J. Chem. Phys.* **119**, 9989 (2003).
84. J. Brzozowski, P. Eрман and M. Lyyra, *Phys. Scr.* **17**, 507 (1978).
85. J. A. Gray and R. L. Farrow, *J. Chem. Phys.* **95**, 7054 (1991).
86. D. E. Heard, D. R. Crosley, J. B. Jeffries, G. P. Smith and A. Hirano, *J. Chem. Phys.* **96**, 4366 (1992).

87. J. J. L. Spaanjaars, J. J. Termeulen and G. Meijer, *J. Chem. Phys.* **107**, 2242 (1997).
88. R. A. Copeland, J. B. Jeffries and D. R. Crosley, *J. Mol. Spectrosc.* **143**, 183 (1990).
89. M. L. Sink, A. D. Banddrauk and R. Lefebvre, *J. Chem. Phys.* **73**, 4451 (1980).
90. S. Y. Lee and K. F. Freed, *J. Chem. Phys.* **87**, 5772 (1987).
91. S. Y. Lee, *J. Chem. Phys.* **103**, 3501 (1995).
92. D. R. Yarkony, *J. Chem. Phys.* **97**, 1838 (1992).
93. G. Parlant and D. R. Yarkony, *J. Chem. Phys.* **110**, 363 (1999).
94. S. J. Singer, K. F. Freed and Y. B. Band, *Adv. Chem. Phys.* **61**, 1 (1985).
95. C. Kalyanaraman and N. Sathyamurthy, *Chem. Phys.* **187**, 219 (1994).
96. B. Ruscic, A. F. Wagner, L. B. Harding, R. L. Asher, D. Feller, D. A. Dixon, K. A. Peterson, Y. Song, X. M. Qian, C. Y. Ng, J. B. Liu, W. W. Chen and D. W. Schwenke, *J. Phys. Chem.* **106**, 2727 (2002).
97. D. C. Radenovic, A. J. A. van Roij, D. A. Chestakov, A. Eppink, J. J. ter Meulen, D. H. Parker, M. P. J. van der Loo, G. C. Groenenboom, M. E. Greenslade and M. I. Lester, *J. Chem. Phys.* **119**, 9341 (2003).
98. R. A. Durie and D. A. Ramsay, *Can. J. Phys.* **36**, 35 (1958).
99. J. A. Coxon and D. A. Ramsay, *Can. J. Phys.* **54**, 1034 (1976).
100. M. Troler, R. L. Mauldin III and A. R. Ravishankara, *J. Phys. Chem.* **94**, 4896 (1990).
101. W. H. Howie, I. C. Lane, S. M. Newman, D. A. Johnson and A. J. Orr-Ewing, *Phys. Chem. Chem. Phys.* **1**, 3079 (1999).
102. I. C. Lane, W. H. Howie and A. J. Orr-Ewing, *Phys. Chem. Chem. Phys.* **1**, 3087 (1999).
103. A. Toniolo, M. Persico and D. Pitea, *J. Chem. Phys.* **112**, 2790 (2000).
104. S. Schmidt, T. Benter and R. N. Schindler, *Chem. Phys. Lett.* **282**, 292 (1998).
105. R. Flesch, J. Plenge, M. C. Schurmann, S. Kuhl, M. Klusmann and E. Ruhl, *Surf. Rev. Lett.* **9**, 105 (2002).
106. R. Flesch, J. Plenge, S. Kuhl, M. Klusmann and E. Ruhl, *J. Chem. Phys.* **117**, 9663 (2002).
107. P. W. McLoughlin, C. R. Park and J. R. Wiesenfeld, *J. Mol. Spectrosc.* **162**, 307 (1993).
108. G. Herzberg and J. Shoosmith, *Can. J. Phys.* **34**, 523 (1956).
109. G. Herzberg, *Proc. Roy. Soc.* **A262**, 291 (1961).
110. H. T. Yu, A. Sevin, E. Kassab and E. M. Evleth, *J. Chem. Phys.* **80**, 2049 (1984).
111. S. G. Westre, T. E. Gansberg, P. B. Kelly and L. D. Zeigler, *J. Phys. Chem.* **96**, 3610 (1993).
112. S. W. North, D. A. Blank, P. M. Chu and Y. T. Lee, *J. Chem. Phys.* **102**, 792 (1995).
113. S. H. S. Wilson, J. D. Howe, K. N. Rosser, M. N. R. Ashfold and R. N. Dixon, *Chem. Phys. Lett.* **227**, 456 (1994).

114. V. Dribinski, A. B. Potter, A. V. Demyanenko and H. Reisler, *J. Chem. Phys.* **115**, 7474 (2001).
115. S. V. Levchenko and A. I. Krylov, *J. Chem. Phys.* **115**, 7485 (2001).
116. A. B. Potter, V. Dribinski, A. Demyanenko and H. Reisler, *Chem. Phys. Lett.* **349**, 257 (2001).
117. S. V. Levchenko, A. V. Demyanenko, V. L. Dribinski, A. B. Potter, H. Reisler and A. I. Krylov, *J. Chem. Phys.* **118**, 9233 (2003).
118. H. R. Wendt and H. E. Hunziker, *J. Chem. Phys.* **81**, 717 (1984).
119. J. Munk, P. Pagsberg, E. Ratajczak and A. Sillesen, *J. Phys. Chem.* **90**, 2752 (1986).
120. B. H. Lendsfield III, P. E. M. Siegbahn and B. Liu, *J. Chem. Phys.* **81**, 710 (1986).
121. A. Sevin, H. T. Yu and E. M. Evleth, *J. Mol. Struct.: THEOCHEM* **104**, 163 (1983).
122. E. M. Evleth, H. Z. Cao, E. Kassab and A. Sevin, *Chem. Phys. Lett.* **109**, 45 (1984).
123. A. S. Zyubin, A. M. Mebel and S. H. Lin, *Chem. Phys. Lett.* **323**, 441 (2000).
124. M. R. A. Blomberg and B. Liu, *J. Chem. Phys.* **83**, 3995 (1985).
125. J. L. Brum, S. Deshmukh and B. Koplitz, *J. Chem. Phys.* **95**, 2200 (1991).
126. J. L. Brum, S. Deshmukh, Z. Wang and B. Koplitz, *J. Chem. Phys.* **98**, 1178 (1993).
127. T. Gilbert, T. L. Grebner, I. Fischer and P. Chen, *J. Chem. Phys.* **110**, 5485 (1999).
128. W. L. Hase, R. J. Wolf and C. S. Sloane, *J. Chem. Phys.* **71**, 2911 (1979).
129. Z. Y. Min, R. Quandt and R. Bersohn, *Chem. Phys. Lett.* **296**, 372 (1998).
130. H. E. Hunziker, H. Knepe, A. D. Mclean, P. Siegbahn and H. R. Wendt, *Can. J. Chem.* **61**, 993 (1983).
131. C. D. Pibel, A. McIlroy, C. A. Taatjes, S. Alfred, K. Patrick and J. B. Halpern, *J. Chem. Phys.* **110**, 1841 (1999).
132. M. Shahu, C. H. Yang, C. D. Pibel, A. McIlroy, C. A. Taatjes and J. B. Halpern, *J. Chem. Phys.* **116**, 8343 (2002).
133. M. B. Pushkarsky, A. M. Mann, J. S. Yeston and C. B. Moore, *J. Chem. Phys.* **115**, 10738 (2001).
134. A. Fahr, P. Hassanzadeh and D. B. Atkinson, *Chem. Phys.* **236**, 43 (1998).
135. A. M. Mebel, Y. T. Chen and S. H. Lin, *Chem. Phys. Lett.* **275**, 19 (1997).
136. J. H. Wang, H. C. Chang and Y. T. Chen, *Chem. Phys.* **206**, 43 (1996).
137. M. N. Paddon-Row and J. A. Pople, *J. Phys. Chem.* **89**, 2768 (1985).
138. P. Zhang, S. Irle, K. Morokuma and G. S. Tschumper, *J. Chem. Phys.* **119**, 6524 (2003).
139. A. M. Mann, X. Chen, V. A. Lozovsky and C. B. Moore, *J. Chem. Phys.* **118**, 4452 (2003).
140. D. A. Ramsay and P. Thistlethwaite, *Can. J. Phys.* **44**, 1381 (1966).
141. D. B. Atkinson and J. W. Hudgens, *J. Phys. Chem.* **103**, 4242 (1999).
142. A. Fahr, P. Hassanzadeh, B. Laszlo and R. E. Huie, *Chem. Phys.* **215**, 59 (1997).
143. H. J. Deyerl, I. Fischer and P. Chen, *J. Chem. Phys.* **111**, 3441 (1999).

- 144. T. L. Nguyen, A. M. Mebel, S. H. Lin and R. I. Kaiser, *J. Phys. Chem.* **105**, 11549 (2001).
- 145. I. Fischer and P. Chen, *J. Phys. Chem.* **106**, 4291 (2002).
- 146. S. G. Davis, C. K. Law and H. Wang, *J. Phys. Chem.* **103**, 5889 (1999).
- 147. D. Stranges, M. Stemmler, X. M. Yang, J. D. Chesko, A. G. Suits and Y. T. Lee, *J. Chem. Phys.* **109**, 5372 (1998).
- 148. H. J. Deyerl, T. Gilbert, I. Fischer and P. Chen, *J. Chem. Phys.* **107**, 3329 (1997).
- 149. H. J. Deyerl, I. Fischer and P. Chen, *J. Chem. Phys.* **110**, 1450 (1999).
- 150. M. L. Morton, L. J. Butler, T. A. Stephenson and F. Qi, *J. Chem. Phys.* **116**, 2763 (2002).
- 151. D. E. Szpunar, M. L. Morton, L. J. Butler and P. M. Regan, *J. Phys. Chem.* **B106**, 8086 (2002).
- 152. D. E. Szpunar, Y. Liu, M. J. McCullagh, L. J. Butler and J. Shu, *J. Chem. Phys.* **119**, 5078 (2003).
- 153. J. A. Mueller, J. L. Miller, L. J. Butler, F. Qi, O. Sorkhabi and A. G. Suits, *J. Phys. Chem.* **104**, 11261 (2000).
- 154. J. A. Mueller, B. F. Parsons, L. J. Butler, F. Qi, O. Sorkhabi and A. G. Suits, *J. Chem. Phys.* **114**, 4505 (2001).
- 155. M. L. Morton, J. L. Miller, L. J. Butler and F. Qi, *J. Phys. Chem.* **106**, 10831 (2002).
- 156. J. L. Miller, M. L. Morton, L. J. Butler, F. Qi, M. J. Krisch and J. N. Shu, *J. Phys. Chem.* **106**, 10965 (2002).
- 157. D. E. Powers, M. B. Pushkarsky and T. A. Miller, *J. Chem. Phys.* **106**, 6863 (1997).
- 158. D. L. Osborn, D. J. Leahy, E. M. Ross and D. M. Neumark, *Chem. Phys. Lett.* **235**, 484 (1995).
- 159. A. Geers, J. Kappert, F. Temps and J. W. Wiebrecht, *J. Chem. Phys.* **101**, 3618 (1994).
- 160. A. Geers, J. Kappert, F. Temps and J. W. Wiebrecht, *J. Chem. Phys.* **101**, 3634 (1994).
- 161. Q. Cui and K. Morokuma, *Chem. Phys. Lett.* **263**, 54 (1996).
- 162. B. E. Applegate, M. B. Pushkarsky and T. A. Miller, *J. Phys. Chem.* **103**, 1538 (1999).
- 163. C. W. Hsu, C. L. Liao, Z. X. Ma, P. J. H. Tjosses and C. Y. Ng, *J. Chem. Phys.* **97**, 6283 (1992).
- 164. R. T. Bise, H. Choi, H. B. Pedersen, D. H. Mordaunt and D. M. Neumark, *J. Chem. Phys.* **110**, 805 (1999).
- 165. M. B. Pushkarsky, B. E. Applegate and T. A. Miller, *J. Chem. Phys.* **113**, 9649 (2000).
- 166. V. Aristov, D. Conroy and H. Reisler, *Chem. Phys. Lett.* **318**, 393 (2000).
- 167. D. Conroy, V. Aristov, L. Feng and H. Reisler, *J. Phys. Chem.* **104**, 10288 (2000).
- 168. L. Feng, X. Huang and H. Reisler, *J. Chem. Phys.* **117**, 4820 (2002).
- 169. L. Feng, A. V. Demyanenko and H. Reisler, *J. Chem. Phys.* **118**, 9623 (2003).

170. B. C. Hoffman and D. R. Yarkony, *J. Chem. Phys.* **116**, 8300 (2002).
171. K. S. Xu, G. Amaral and J. S. Zhang, *J. Chem. Phys.* **111**, 6271 (1999).
172. C. Sosa and H. B. Schlegel, *J. Am. Chem. Soc.* **109**, 7007 (1987).
173. H. E. Hunziker, H. Knepe and H. R. Wendt, *J. Photochem.* **12**, 377 (1981).
174. G. Inoue and H. Akimoto, *J. Chem. Phys.* **74**, 425 (1981).
175. L. F. DiMauro, M. Heaven and T. A. Miller, *J. Chem. Phys.* **81**, 2339 (1984).
176. T. Gejo, M. Takayanagi, T. Kono and I. Hanazaki, *Chem. Lett.* **12**, 2065 (1993).
177. L. R. Brock and E. A. Rohlfing, *J. Chem. Phys.* **106**, 10048 (1997).
178. K. I. Barnhard, M. He and B. R. Weiner, *J. Phys. Chem.* **100**, 2784 (1996).
179. R. D. Mead, K. R. Lykke, W. C. Lineberger, J. Marks and J. I. Brauman, *J. Chem. Phys.* **81**, 4883 (1984).
180. L. S. Alconcel, H. J. Deyerl, V. Zengin and R. E. Continetti, *J. Phys. Chem.* **A103**, 9190 (1999).
181. M. Dupuis, J. J. Wendoloski and W. A. Lester, Jr., *J. Chem. Phys.* **76**, 488 (1982).
182. M. Yamaguchi, T. Momose and T. Shida, *J. Chem. Phys.* **93**, 4211 (1990).
183. M. Yamaguchi, *Chem. Phys. Lett.* **221**, 531 (1994).
184. S. Matsika and D. R. Yarkony, *J. Chem. Phys.* **117**, 7198 (2002).
185. K. Xu, G. Amaral, L. Wang and J. Zhang, in preparation.
186. L. S. Alconcel, H. J. Deyerl, M. DeClue and R. E. Continetti, *J. Am. Chem. Soc.* **123**, 3125 (2001).
187. L. S. Alconcel and R. E. Continetti, *Chem. Phys. Lett.* **366**, 642 (2002).
188. D. R. Cyr, D. J. Leahy, D. L. Osborn, R. E. Continetti and D. M. Neumark, *J. Chem. Phys.* **99**, 8751 (1993).
189. R. T. Bise, A. A. Hoops and D. M. Neumark, *J. Chem. Phys.* **114**, 9000 (2001).
190. A. A. Hoops, R. T. Bise, J. R. Gascooke and D. M. Neumark, *J. Chem. Phys.* **114**, 9020 (2001).
191. H. Choi, D. H. Mordaunt, R. T. Bise, T. R. Taylor and D. M. Neumark, *J. Chem. Phys.* **108**, 4070 (1998).
192. R. T. Bise, H. Choi and D. M. Neumark, *J. Chem. Phys.* **111**, 4923 (1999).
193. R. T. Bise, A. A. Hoops, H. Choi and D. M. Neumark, *J. Chem. Phys.* **113**, 4179 (2000).
194. H. Choi, T. R. Taylor, R. T. Bise, A. A. Hoops and D. M. Neumark, *J. Chem. Phys.* **113**, 8608 (2000).
195. S. Gomez, H. M. Lambert and P. L. Houston, *J. Phys. Chem.* **A105**, 6342 (2001).
196. E. J. Bernard, B. R. Strazisar and H. F. Davis, *Chem. Phys. Lett.* **313**, 461 (1999).

This page intentionally left blank

INDEX

- 1-propenyl, 501
- 2-propenyl, 501
- 2D ion imaging technique, 39
- 3D imaging technique, 39
- Abel transform, 287, 288
- abstraction reaction, 445
- adiabatic bend approximation, 412
- algebraic variational approach, 411
- alkoxy radicals, 501
- alkyl radicals, 484
- allyl, 497
- angle-specific kinetic energy
 - distribution, 28
- atom–diatom reactions, 410
- atom/radical reactions, 330
- B3LYP, 435
- barrier states, 48
- Bayesian analysis, 430
- benzene, 179
- Born–Oppenheimer approximation,
 - 383, 384, 386, 390, 391,
 - 393–396, 405
- Born–Oppenheimer breakdown, 386,
 - 390–392
- BrO, 484
- C–C insertion, 218
- C–H insertion, 218
- carbon atom C(³P), 329
- catalytic destruction of O₃, 283
- cavity ring-down spectroscopy, 473
- CCSD(T), 433, 435
- centrifugal sudden approximation,
 - 416, 450
- channel three, 179, 192
- Chapman, S., 282
- chloromethyl (CH₂Cl), 487
- Clebsch–Gordon coefficient, 419
- CIO, 481
- CMB experiments, 329
- complete nuclear permutation group,
 - 427
- confidence lengths, 430
- conical intersection, 25
- coupled-channel results, 450
- cross-section, 52, 420
- crossed molecular beam (CMB)
 - technique, 329
- cyclic alkoxy, 513
- cycloheptatriene, 196
- D₂ + OH, 437
- de-excitation, 390
- density functional theories, 433
- density-to-flux transformation, 13
- detection of free radicals, 472
- diatom–diatom reaction, 413
- diatomic radicals, 475
- differential cross-section, 33
 - state-resolved, 89
 - state-to-state, 3
- discrete variable representation, 417
- dissociation rate, 176
- dissociative ionization, 166
- Doppler effect, 2

- Doppler profile, 305
- Doppler-selected TOF technique, 3
- electric discharge, 470
- electron impact ionization, 228
- electron-hole pair, 383, 387–391
- electron-mediated vibrational energy transfer, 400
- electronic friction theory, 393
- electronically adiabatic approach, 394
- electronically nonadiabatic effects, 383, 393, 394, 401, 405
- electronically nonadiabatic influences, 393, 394
- electronically nonadiabatic interactions, 391, 404
- ethoxy ($\text{CH}_3\text{CH}_2\text{O}$), 506
- ethyl (C_2H_5), 489
- ethylbenzene, 201
- exchange reaction, 445
- exoelectron emission, 404
- experimental techniques of photodissociation dynamics, 474
- $\text{F} + \text{H}_2$, 67
- $\text{F} + \text{HD}$, 60
- first principles theory, 412
- four-wave mixing scheme, 91
- generation of free radical beams, 467
 - Grow*, 427, 434
- $\text{H} + \text{D}_2 \rightarrow \text{HD} + \text{H}$, 89
- $\text{H} + \text{D}_2$ reaction, 88
- $\text{H} + \text{D}_2\text{O}$, 445
- $\text{H} + \text{H}_2\text{O}$, 445
- $\text{H} + \text{HD}$, 72
- $\text{H}_2 + \text{OH}$, 437
- H_2O photochemistry, 89
- H_3O^+ , 455
- $\text{HD} + \text{OH}$, 437
- H-atom Rydberg “tagging”
 - time-of-flight (HRTOF) technique, 89, 90
- H-atom Rydberg tagging technique, 37
- Hartley band, 281, 283, 301
- high- n Rydberg atom time-of-flight (HRTOF) technique, 475
- hydroxyl radical (OH), 475
- hydroxymethyl (CH_2OH), 504
- hyperspherical coordinate approach, 411
- imaging technique, 285
- initial state-selected time-dependent wavepacket method, 412
- integral cross-section, 443
 - state-to-state, 453
- ion imaging, 163
- ion TOF, 37
- isotopic scrambling, 195, 197, 201
- Jacobi coordinates, 413, 417
- laser-induced fluorescence, 472
- mass spectrometer, 171
- methoxy (CH_3O), 501
- methyl (CH_3), 484
- minimum energy path, 425
- molecular symmetry group, 435
- Molina, M. J., 283
- Moller–Plesset perturbation theory, 433
- MP2, 433, 435
- multimass ion imaging, 163
- negative ion photodetachment, 471
- neighbor list, 436
- Newton diagram, 237
- Newton sphere, 9
- nonadiabatic reactions, 404
- nonadiabatic transition, 25, 320
- $\text{O}(^1\text{D}) + \text{H}_2$ reaction, 89
- $\text{O}(^1\text{D}_2)$ angular distributions, 290
- $\text{O}(^1\text{D}_2)$ speed distributions, 288
- $\text{O}(^3\text{P})$ angular distributions, 312
- $\text{O}(^3\text{P})$ speed distributions, 303
- $\text{O}_2(^1\Delta_g)$ angular distributions, 296
- OD, 479

- OH + D₂ reaction, 89
- odd oxygen, 283
- optical Doppler-shift, 37
- oxidative addition, 217
- ozone, 281

- perpendicular transition, 17
- PES construction method, 422
- photodetachment spectroscopy, 455
- photodissociation, 163
- photodissociation dynamics, 281
- photodissociation dynamics of free radicals, 466
- photodissociation of free radicals, 465
- photoelectron spectra, 457
- photoelectron spectroscopy, 455, 473
- photofragment translational spectroscopy, 164, 475
- photolysis, 469
- polyatomic multichannel reactions, 329
- potential energy surfaces, 421
- product distribution, 59
- propargyl (C₃H₃), 495
- propylbenzene, 201
- pyrolysis, 468

- QCISD, 433
- quantized transition states, 88
- quasi-classical trajectory results, 451

- radial cylindrical energy analyzer, 171
- rate constant, 420
- reaction cross-section, 421
- reaction dynamics, 329
- reaction path, 425
- reaction probability, 420
 - state-to-state, 453
- reaction rate constant, 421
- reactions of ground state oxygen
 - atom O(³P), 329
- reactive differential cross-sections, 329
- reactive flux, 421
- reactive resonance, 43, 60
- reactive scattering, 88, 329
- reduced dimensionality, 411

- resonance, 30
- resonance decay, 47, 58
- resonance pole, 51, 52
- resonance-enhanced multiphoton ionization, 2, 88, 472
- ring permutation, 192
- ring-opening dissociation, 180, 188, 189
- rotating bond approximation, 411
- rotational basis functions, 419
- Rowland, F. S., 283
- Rydberg-valence interactions, 15
- Rydbergization, 15

- scattering wavefunction, 420
- Schatz and Elgersma, 427
- seven-membered ring, 196, 197
- Shepard interpolation, 424
- singular value decomposition, 423
- soft electron-impact ionization, 329
- space-focusing condition, 8
- spectator bond, 445
- split operator method, 417
- stimulated emission pumping, 400
- stratosphere, 283

- thermal rate constant, 443
- thiomethoxy (CH₃S), 503
- third harmonic generation scheme, 14
- time delay, 53
- time-dependent quantum wavepacket approach, 412
- time-independent methods, 411
- time-of-flight, 2, 228
- toluene, 192
- total angular momentum basis functions, 415
- trajectory, 321
- transition metal catalysts, 216
- transition state, 455
 - early, 268
 - late, 269
 - multicentered, 220
- triatom-atom reaction, 417
- triplet state, 207

- unitary matrix, 423
- unsaturated aliphatic radicals, 493

- velocity mapping-ion counting
 - technique, 287
- velocity-flux contour maps, 26
- vibrational coupling to metal surface,
 - 387
- vibrational de-excitation, 389, 390
- vibrationally-inelastic processes, 400
- vinoxy (CH_2CHO), 508
- vinyl (C_2H_3), 493

- Walch–Dunning–Schatz–Elgersma PES, 437
- wavepacket propagation, 417
- Wigner rotation matrix, 419
- Wiley–McLaren, 307
- Wilson **B** matrix, 422

- Yang–Zhang–Collins–Lee global PES,
 - 437
- YZCL1 PES, 439
- YZCL2 PES, 439